

## *Optical Biopsy III*

**Robert R. Alfano**  
*Chair/Editor*

**23-24 January 2000**  
**San Jose, California**

*Sponsored by*  
SPIE—The International Society for Optical Engineering  
IBOS—International Biomedical Optics Society

20001020 010

Proceedings of SPIE  
Volume 3917

**REPORT DOCUMENTATION PAGE**Form Approved  
OMB No. 0704-0188

Public reporting burden for this collection of information is estimated to average 1 hour per response, including the time for reviewing instructions, searching data sources, gathering and maintaining the data needed, and completing and reviewing the collection of information. Send comments regarding this burden estimate or any other aspect of this collection of information, including suggestions for reducing this burden to Washington Headquarters Service, Directorate for Information Operations and Reports, 1215 Jefferson Davis Highway, Suite 1204, Arlington, VA 22202-4302, and to the Office of Management and Budget, Paperwork Reduction Project (0704-0188) Washington, DC 20503.

**PLEASE DO NOT RETURN YOUR FORM TO THE ABOVE ADDRESS.**

<b>1. REPORT DATE (DD-MM-YYYY)</b> 19-04-00		<b>2. REPORT DATE</b> Final Technical Report		<b>3. DATES COVERED (From - To)</b> 15-01-2000 to 14-07-2000	
<b>4. TITLE AND SUBTITLE</b>  Optical Biopsy III				<b>5a. CONTRACT NUMBER</b>	
				<b>5b. GRANT NUMBER</b> F49620-00-1-0135	
				<b>5c. PROGRAM ELEMENT NUMBER</b>	
<b>6. AUTHOR(S)</b>  Alfano, Robert R.				<b>5d. PROJECT NUMBER</b>	
				<b>5e. TASK NUMBER</b>	
				<b>5f. WORK UNIT NUMBER</b>	
<b>7. PERFORMING ORGANIZATION NAME(S) AND ADDRESS(ES)</b> Society of Photo-optical Instrumentation Engineers PO Box 10 Bellingham, WA 98227-0010 (SPIE)				<b>8. PERFORMING ORGANIZATION REPORT NUMBER</b>  Volume 3917	
<b>9. SPONSORING/MONITORING AGENCY NAME(S) AND ADDRESS(ES)</b> Air Force Office of Scientific Research 801 N. Randolph St. Room 732 Arlington, VA 22203-1977				<b>10. SPONSOR/MONITOR'S ACRONYM(S)</b> AFOSR/NE	
				<b>11. SPONSORING/MONITORING AGENCY REPORT NUMBER</b>	
<b>12. DISTRIBUTION AVAILABILITY STATEMENT</b>  Approved for Public Release					
<b>13. SUPPLEMENTARY NOTES</b>  ISBN 0-8194-3533-3					
<b>14. ABSTRACT</b>  This proceedings contains papers on the following topics: Fluorescence Biopsy, Light-Scattering Biopsy, Contrast Agents and Raman Biopsy, Women's Health and Light Scattering. Research results presented at the conference showed the advancement in the application of spectroscopy and optical techniques in the medical field. Mediphotonic technologies will provide the medical profession with a new set of light-based tools for future noninvasive diagnosis and treatment.					
<b>15. SUBJECT TERMS</b>  Light-scattering, Biopsy, Fluorescence					
<b>16. SECURITY CLASSIFICATION OF:</b>			<b>17. LIMITATION OF ABSTRACT</b>  SAR	<b>18. NUMBER OF PAGES</b>  268	<b>19a. NAME OF RESPONSIBLE PERSON</b> Marshall Weathersby
<b>a. REPORT</b> Non- Classified	<b>b. ABSTRACT</b>	<b>c. THIS PAGE</b>			<b>19b. TELEPHONE NUMBER (Include area code)</b> (360)676-3290

# PROGRESS IN BIOMEDICAL OPTICS AND IMAGING

Vol. 1, No. 11

## ***Optical Biopsy III***

**Robert R. Alfano**

*Chair/Editor*

**23-24 January 2000**

**San Jose, California**

*Sponsored by*

SPIE—The International Society for Optical Engineering

IBOS—International Biomedical Optics Society

*Published by*

SPIE—The International Society for Optical Engineering

**Proceedings of SPIE  
Volume 3917**

SPIE is an international technical society dedicated to advancing engineering and scientific applications of optical, photonic, imaging, electronic, and optoelectronic technologies.

AQM01-01-0003



The papers appearing in this book compose the proceedings of the technical conference cited on the cover and title page of this volume. They reflect the authors' opinions and are published as presented, in the interests of timely dissemination. Their inclusion in this publication does not necessarily constitute endorsement by the editors or by SPIE. Papers were selected by the conference program committee to be presented in oral or poster format, and were subject to review by volume editors or program committees.

Please use the following format to cite material from this book:

Author(s), "Title of paper," in *Optical Biopsy III*, Robert R. Alfano, Editor, Proceedings of SPIE Vol. 3917, page numbers (2000).

ISSN 1605-7422  
ISBN 0-8194-3533-3

Published by  
**SPIE—The International Society for Optical Engineering**  
P.O. Box 10, Bellingham, Washington 98227-0010 USA  
Telephone 360/676-3290 (Pacific Time) • Fax 360/647-1445

Copyright ©2000, The Society of Photo-Optical Instrumentation Engineers.

Copying of material in this book for internal or personal use, or for the internal or personal use of specific clients, beyond the fair use provisions granted by the U.S. Copyright Law is authorized by SPIE subject to payment of copying fees. The Transactional Reporting Service base fee for this volume is \$15.00 per article (or portion thereof), which should be paid directly to the Copyright Clearance Center (CCC), 222 Rosewood Drive, Danvers, MA 01923. Payment may also be made electronically through CCC Online at <http://www.directory.net/copyright/>. Other copying for republication, resale, advertising or promotion, or any form of systematic or multiple reproduction of any material in this book is prohibited except with permission in writing from the publisher. The CCC fee code is 1605-7422/00/\$15.00.

Printed in the United States of America.



# Contents

- vii *Conference Committee*
- ix *Introduction*

## SESSION 1 FLUORESCENCE BIOPSY I

---

- 2 **Design and performance of a real-time double-ratio fluorescence imaging system for the detection of early cancers [3917-02]**  
A. Bogaards, A. J. L. Jongen, E. Dekker, J. H. T. M. van den Akker, H. J. C. M. Sterenborg, Univ. Hospital Rotterdam (Netherlands)
- 9 **In-vivo autofluorescence of nasopharyngeal carcinoma and normal tissue [3917-03]**  
J. Y. Qu, Hong Kong Univ. of Science and Technology; P. W. Yuen, Queen Mary Hospital/Univ. of Hong Kong; Z. Huang, Hong Kong Univ. of Science and Technology; W. I. Wei, Queen Mary Hospital/Univ. of Hong Kong
- 16 **Characterization of human neoplastic and normal oral tissues by visible excitation and emission fluorescence spectroscopy [3917-05]**  
D. Koteeswaran, Government Aringnar Anna Memorial Cancer Hospital (India); N. Vengadesan, P. Aruna, Anna Univ. (India); K. Muthuvelu, Government Aringnar Anna Memorial Cancer Hospital (India); S. Bharghavi, Government General Hospital/Chennai Medical College (India); V. S. Gowri, S. Ganesan, Anna Univ. (India)

## SESSION 2 LIGHT-SCATTERING BIOPSY I

---

- 22 **Light-scattering microscope as a tool to investigate scattering heterogeneity in tissue [3917-06]**  
A. K. Popp, M. T. Valentine, Harvard Univ.; P. D. Kaplan, Unilever Research U.S.; D. A. Weitz, Harvard Univ.
- 33 **Light scattering from cells: the contribution of the nucleus and the effects of proliferative status (Invited Paper) [3917-07]**  
J. R. Mourant, M. Canpolat, C. Brocker, O. Espondo-Ramos, T. M. Johnson, A. Matanock, K. Stetter, J. P. Freyer, Los Alamos National Lab.
- 43 **Diffuse backscattering Mueller matrix analysis for tissue diagnostics with polarized light [3917-08]**  
A. H. Hielscher, S. Bartel, Downstate Medical Ctr./SUNY/Brooklyn

## SESSION 3 LIGHT-SCATTERING BIOPSY II

---

- 56 **Combination of diffuse reflectance and fluorescence imaging of turbid media [3917-09]**  
J. Y. Qu, J. Hua, Z. Huang, Hong Kong Univ. of Science and Technology
- 62 **Instrumentation for subsurface imaging in a clinical environment [3917-10]**  
S. G. Demos, M. C. Staggs, H. B. Radousky, Lawrence Livermore National Lab.; R. R. Alfano, CUNY/City College

- 67 **Elastic scattering spectroscopy in vivo: optical biopsies of cancers of the breast and GI tract** [3917-11]  
D. C. O. Pickard, G. M. Briggs, C. Saunders, S. Lakhani, National Medical Laser Ctr./Univ. College London (UK); P. M. Ripley, I. J. Bigio, Los Alamos National Lab.; S. G. Brown, National Medical Laser Ctr./Univ. College London (UK)
- 75 **Spectral polarization imaging of human prostate tissues** [3917-44]  
W. B. Wang, J. H. Ali, CUNY/City College; J. H. Vitenson, J. M. Lomberdo, Hackensack Univ. Medical Ctr.; R. R. Alfano, CUNY/City College

---

#### SESSION 4 CONTRAST AGENTS AND RAMAN BIOPSY

---

- 80 **Tumor-specific fluorescent contrast agents** [3917-12]  
S. I. Achilefu, R. B. Dorshow, J. E. Bugaj, R. Rajagopalan, Mallinckrodt Inc.
- 87 **Calcium detection of human hair and nail by the nanosecond time-gated spectroscopy of laser-ablation plume** [3917-14]  
M. Haruna, M. Ohmi, M. Nakamura, Osaka Univ. School of Allied Health Sciences (Japan); S. Morimoto, Osaka Univ. Graduate School of Medicine (Japan)
- 93 **Characterization of type I, II, III, IV, and V collagens by time-resolved laser-induced fluorescence spectroscopy** [3917-15]  
L. Marcu, D. Cohen, Cedars-Sinai Medical Ctr.; J.-M. I. Maarek, Univ. of Southern California; W. S. Grundfest, Cedars-Sinai Medical Ctr.
- 102 **Raman detection of carotenoid pigments in the human retina** [3917-16]  
W. Gellermann, I. V. Ermakov, R. W. McClane, Univ. of Utah; P. S. Bernstein, Univ. of Utah School of Medicine
- 109 **Global analysis of arterial fluorescence decay spectra** [3917-17]  
J.-M. I. Maarek, Univ. of Southern California; W. S. Grundfest, L. Marcu, Cedars-Sinai Medical Ctr.
- 119 **Optical biopsy with long-range nondiffracting beams** [3917-18]  
E. Goldfain, Welch Allyn, Inc.

---

#### SESSION 5 FLUORESCENCE BIOPSY II

---

- 130 **Blue LEDs feasibility for tissue fluorescence analysis** [3917-21]  
S. M. Dets, National Technical Univ. of Ukraine and Simon Fraser Univ. (Canada); N. A. Denisov, National Technical Univ. of Ukraine
- 139 **Laser-induced fluorescence spectrum of human colonic tissues by Monte Carlo modeling** [3917-22]  
Z. Huang, T.-C. Chia, S. Lee, W. Zheng, S. M. Krishnan, T.-K. Lim, H. M. Cheah, C. H. Diong, Nanyang Technological Univ. (Singapore); F. S. Choen, Singapore General Hospital
- 146 **Ultraviolet 2D fluorescence mapping system for the imaging of head and neck tumors** [3917-23]  
A. Katz, CUNY/City College; H. E. Savage, New York Eye and Ear Infirmary; F. Zeng, J. Rome, CUNY/City College; S. P. Schantz, S. A. McCormick, R. S. Cocker, New York Eye and Ear Infirmary; R. R. Alfano, CUNY/City College

- 150 **DNA and protein change in tissues probed by Kubelka-Munk spectral function [3917-47]**  
Y. Yang, CUNY/City College; E. J. Celmer, St. Vincent's Medical Ctr. of Richmond;  
J. A. Koutcher, Memorial Sloan-Kettering Cancer Ctr.; R. R. Alfano, CUNY/City College

---

**SESSION 6 OCT BIOPSY**

---

- 156 **Interferometric 2D and 3D tomography of photoelastic media [3917-25]**  
I. Patrickeyev, Institute of Continuous Media Mechanics (Russia); V. I. Shakhurdin, Perm State  
Technical Univ. (Russia)

---

**SESSION 7 OPTICAL PROPERTIES**

---

- 168 **Noninvasive determination of concentration of compounds in strongly absorbing biological tissue (Invited Paper) [3917-27]**  
R. A. Bolt, J. S. Kanger, F. F. M. de Mul, Univ. of Twente (Netherlands); X. Wu, S.-J. Yeh,  
O. S. Khalil, Abbott Labs.
- 176 **Effects of rough interfaces on a converging laser beam propagating in a skin tissue phantom [3917-28]**  
J. Q. Lu, K. Dong, X. H. Hu, East Carolina Univ.
- 184 **Experimental study of optical properties of porcine skin dermis from 900 to 1500 nm [3917-29]**  
Y. Du, M. J. Cariveau, G. W. Kalmus, J. Q. Lu, X. H. Hu, East Carolina Univ.

---

**SESSION 8 WOMEN'S HEALTH AND LIGHT SCATTERING**

---

- 194 **Spatial variation of fluorescence in human breast tissues [3917-30]**  
A. Pradhan, M. S. Nair, N. Ghosh, Indian Institute of Technology/Kanpur; A. Agarwal, G.S.V.M.  
Medical College (India)
- 200 **Ultraviolet and blue 2D fluorescence mapping of gynecological tissues [3917-31]**  
A. Katz, CUNY/City College; H. E. Savage, New York Eye and Ear Infirmary; Y. Yang, F. Zeng,  
J. Rome, CUNY/City College; S. A. McCormick, R. S. Cocker, New York Eye and Ear Infirmary;  
Y. Yu, Sarnoff Corp.; R. R. Alfano, CUNY/City College
- 204 **Visualization of photon propagation and abnormality detection [3917-33]**  
J. Ge, Z. Le, D. Y. Y. Yun, Univ. of Hawaii/Manoa
- 212 **Simulation comparisons on diffusion equation [3917-34]**  
J. Ge, S. Nie, V. Syrmos, D. Y. Y. Yun, Univ. of Hawaii/Manoa
- 219 **Distributed-source approach to image reconstruction in diffuse optical tomography [3917-35]**  
I. V. Yaroslavsky, A. N. Yaroslavsky, H. Battarbee, Louisiana State Univ./Shreveport Medical  
Ctr.; C. Sisson, Louisiana State Univ./Shreveport; J. Rodriguez, Louisiana State Univ./  
Shreveport Medical Ctr. and Centenary College of Louisiana
- 225 **In-vivo sized-fiber spectroscopy [3917-36]**  
T. P. Moffitt, S. A. Pahl, Oregon Medical Laser Ctr.

- 232    **Validation of self-reported skin color via analysis of diffuse reflectance spectra of skin**  
[3917-37]  
R. A. Weersink, Photonics Research Ontario (Canada); L. A. Marrett, Cancer Care Ontario  
(Canada); L. D. Lilge, Photonics Research Ontario (Canada); M. Purdue, Cancer Care Ontario  
(Canada); S. Walter, McMaster University (Canada)

---

**POSTER SESSION**

---

- 240    **Fluorescence study of normal, benign, and malignant human breast tissues** [3917-38]  
A. Pradhan, R. N. Panda, M. S. Nair, B. V. Laxmi, Indian Institute of Technology/Kanpur;  
A. Agarwal, A. Rastogi, G.S.V.M. Medical College (India)
- 244    **Stoke's and anti-Stoke's characteristics of anaerobic and aerobic bacterias at excitation  
of fluorecence by low-intensity red light: I. Research of anaerobic bacterias** [3917-40]  
V. I. Masychev, M. T. Alexandrov, Rosslyn Medical UK (Russia)
- 256    **Effects of scattering particle concentration on light propagation through turbid media**  
[3917-42]  
A. N. Bashkatov, E. A. Genina, V. I. Kochubey, V. V. Tuchin, Saratov State Univ. (Russia)
- 265    *Addendum*
- 267    *Author Index*

## Conference Committee

### *Conference Chair*

**Robert R. Alfano**, CUNY/City College

### *Program Committee*

**Irving J. Bigio**, Los Alamos National Laboratory  
**Stavros G. Demos**, Lawrence Livermore National Laboratory  
**Richard B. Dorshow**, Mallinckrodt Inc.  
**Israel Gannot**, Tel Aviv University (Israel)  
**Andreas H. Hielscher**, SUNY/Brooklyn  
**Feng Liu**, CUNY/City College  
**Barry R. Masters**, Uniformed Services University of the Health Sciences  
**Howard E. Savage**, Memorial Sloan-Kettering Cancer Center  
**Richard C. Straight**, University of Utah  
**Katarina Svanberg, M.D.**, Lund University Hospital (Sweden)  
**Sharon L. Thomsen, M.D.**, University of Texas at Austin  
**Wubao B. Wang**, CUNY/City College  
**Yizhong Yu**, Sarnoff Corporation

### *Session Chairs*

- 1 Fluorescence Biopsy I  
**Alvin Katz**, CUNY/City College
- 2 Light-Scattering Biopsy I  
**Irving J. Bigio**, Los Alamos National Laboratory  
**Stavros G. Demos**, Lawrence Livermore National Laboratory
- 3 Light-Scattering Biopsy II  
**Richard C. Straight**, University of Utah
- 4 Contrast Agents and Raman Biopsy  
**Wubao B. Wang**, CUNY/City College
- 5 Fluorescence Biopsy II  
**Asima Pradhan**, Indian Institute of Technology/Kanpur
- 6 OCT Biopsy  
**Richard B. Dorshow**, Mallinckrodt Inc.
- 7 Optical Properties  
**Singaravelu Ganesan**, Anna University (India)
- 8 Women's Health and Light Scattering  
**Alvin Katz**, CUNY/City College

## Introduction

The fifth conference on the advances in lasers and light spectroscopy to diagnose cancer and other diseases, now called Optical Biopsy, was held on January 23 and 24, 2000, in San Jose, California. Research results presented at the conference showed the advancement in the application of spectroscopy and optical techniques in the medical field. Mediphotonic technologies will provide the medical profession with a new set of light-based tools for future noninvasive diagnosis and treatment. Optical biopsy, one of the promising new noninvasive technologies, is poised to become an important new modality for the medical profession, as it does not require tissue removal or surgery.

Optical biopsy is the analysis of a biomedical sample using its characteristic optical properties. These characteristic properties will vary for different states of a tissue. Optical biopsy can be implemented in vivo without the removal of tissue. The methods and technologies presented at this conference provide new ways to characterize the physical and chemical changes occurring in tissues with and without contrast agents, thereby offering exciting possibilities for novel optical biopsy and optical imaging diagnostic and therapeutic approaches.

The conference was attended by researchers from many different countries around the world. Papers were presented on research using many different techniques to optically interrogate tissue, including fluorescence, fluorescence imaging, Raman scattering, elastic scattering, reflectance spectroscopy, absorption, polarization imaging, and optical coherence tomography.

The progress in the development of optical cancer detection methods toward clinical use was evidenced by the increased number of papers on in-vivo measurements. These papers focused on in-vivo native fluorescence from the oral cavity, upper aerodigestive tract, esophagus, and colon. Fluorescence 2D imaging in clinical applications is becoming the preferred diagnostic approach. In-vivo resonant Raman spectra was used to give information on the human retina. Results from the latest work on the use of optical methods for characterizing and diagnosing states of human tissues were exchanged.

I would like to thank Dr. Alvin Katz and Dr. Kestutis Sutkus of the City College of New York for their help with this conference.

**Robert R. Alfano**

## **SESSION 1**

### **Fluorescence Biopsy I**

# Design and performance of a real-time Double Ratio Fluorescence Imaging System for the detection of early cancers

A. Bogaards, A.J.L. Jongen, E. Dekker, J.H.T.M. van den Akker, H.J.C.M. Sterenberg  
Photodynamic Therapy and Optical Spectroscopy Programme,  
Daniel den Hoed Cancer Center, University Hospital, Rotterdam, the Netherlands

**Key words:** fluorescence imaging, double ratio, optical properties, cancer detection,  $\delta$ -aminolevulinic acid.

## Introduction

Fluorescence Imaging is an experimental clinical technique for tumor detection, which has been gaining interest over the last years. Existing fluorescence imaging devices commonly use imaging methods that are influenced by the absorption and scattering properties of the investigated tissue. This can lead to artifacts in tissue fluorescence (1,2,3) and may invalidate diagnoses. For several years we have been investigating a technique for measuring fluorescence signals independent on absorption and scattering properties, the Double Ratio measurement technique (2,4). The Double Ratio is the quotient of two Single Ratios excited at two different wavelengths. The present paper describes the design and performance of a novel real-time Fluorescence Imaging system based on the Double Ratio technique. Experiments were done on optical phantoms, animals (*in vivo*) and humans (*in vivo*) to prove the system's independence on optical properties. All experiments performed on animals and on human subjects were done according to protocols fulfilling all legal and ethical regulations.

Today, the gold standard for tumor detection of superficial tumors is visual inspection, followed by excision and histopathologic examination. Of course, it would be preferred to have a more accurate and possibly a less invasive tool. Over the last decade a number of non-invasive tumor detection techniques have been suggested (1,5). *In vivo* fluorescence imaging techniques can be divided into two different lines of approach: 1) Auto-fluorescence, and 2) Enhanced fluorescence. Auto-fluorescence is the native tissue fluorescence. Enhancing fluorescence is done with drugs acting as tumor markers. Both are excited with usually blue or UV light. The application of the drug can be topically, orally i.p. or i.v. Commonly used drugs are Hematoporphyrin (Hp) and  $\delta$ -aminolevulinic acid (5ALA) which induces PPIX as a fluorescent tumor marker. Other drugs are presently under clinical evaluation.

Fluorescent imaging devices used in the clinic today most often use one wavelength detection to obtain a fluorescent image. Other devices use two wavelengths for detection, for instance to obtain a red-green Ratio image. These so called Single Ratios (6) subtract autofluorescence and correct for variations in excitation fluence rate and geometrical factors. The latter two methods can be very useful for tissue with homogeneous optical properties, but the reliability of these methods is seriously compromised in those cases where the optical properties of the investigated tissue are not homogeneously distributed. Both methods have dependencies on variations in the optical properties of the investigated tissue, which are *not* related to malignancy. This may invalidate diagnostics. For instance single red-green ratios are seriously biased by the amount of blood and melanin within the tissue.

For several years we have been investigating a technique for measuring fluorescence signals which is intended to be *independent* on the optical properties, variations in excitation fluence and geometrical factors: The Double Ratio fluorescence measurement technique, where two wavelengths are used for excitation *and* two for detection. With this technique the resulting image is *only dependent* on the fluorophore concentration. Previous experiments over the last few years with the Double Ratio technique using point (fiber optic) measurements show good agreement with the theory (2,4). Now, one step further, we have developed a system able to produce Double Ratio images.

The present paper briefly describes the fundamentals on which the imaging technique is based, followed by a short description of the system design after which the performance of the novel system is discussed.



## Fundamentals

The Single and Double Ratios are defined as:

$$\text{Single Ratio}_i = \frac{F_{i,m}}{F_{i,n}} \quad \text{eq 1}$$

$$\text{Double Ratio} = \frac{\text{Single Ratio}_i}{\text{Single Ratio}_j} = \frac{F_{i,m} F_{j,n}}{F_{i,n} F_{j,m}} \quad \text{eq 2}$$

Where  $F$  is the fluorescence signal, the subscript  $i$  and  $j$  refer to the excitation wavelengths and the subscripts  $n$  and  $m$  refer to the detection wavelengths.

Sinaasappel et al. derived that the Double Ratio can be written as:

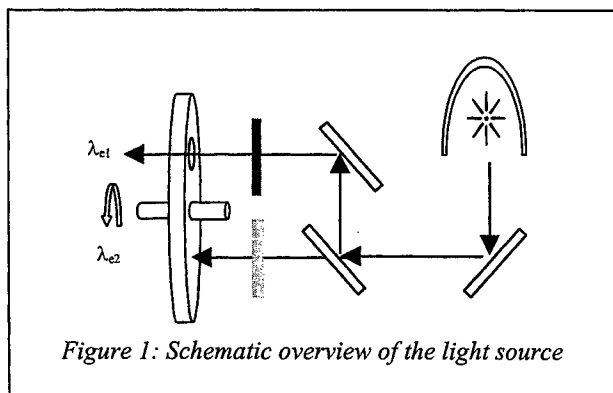
$$\text{Double Ratio} = \frac{1 + aC}{1 + bC} \quad \text{eq 3}$$

Where  $a$  and  $b$  are constants and  $C$  stands for the concentration of the fluorophore. As  $a$  and  $b$  can be derived from the fluorescence properties of the exogenous and endogenous (auto) fluorophores, the Double Ratio is dependent of the fluorophore concentration and artifacts caused by absorption, scattering and geometry are all cancelled out (4).

## System design

A novel system has been developed and build. This system can be used for: auto-fluorescence measurements, enhanced fluorescence measurements, processing into Single- and Double-Ratios. The fluorescence can be studied at a wide variety of wavelengths by exchanging detection and excitation filters.

The system consists of a light source for excitation, a CCD camera for detection and a PC for real time image processing. The used light source is an Oriel Photomax water-cooled lamp housing with a 200-Watt Xenon Mercury lamp. Through a beam splitter the output of the lamp is divided in two beams. With filters the desired wavelength (band) is chosen. A chopper is used to alternate between the two excitation wavelengths. The alternating lamp output is coupled into liquid light guides. Finally some optics illuminate the detection area. The camera is a Philips IP 800 with an intensified CCD operating at a normal video frequency of 50Hz. The camera has a sensitivity of 5 $\mu$ lux.



The optics used to focus the image on the camera are home made and consist of a first lens, a chopper wheel, a set of filters, a second lens unit and finally the camera. The second lens unit consists of four achromatic lenses designed to focus four equal images on the camera. The original, in the focal plane of the first lens, creates four similar images in the focal plane of the second lens where the CCD is positioned. By changing the first lens the magnification can be changed in such way that the detection area is either 1 or 3 square centimeters. The first hole in the chopper wheel illuminates the two images on the upper half of the CCD, whereas the second hole in the chopper wheel illuminates the two images on lower half of the CCD. The chopper in the camera is running synchronized with the chopper in the light housing, causing the following four equal images: 1.)  $F_{i,m}$ , 2.)  $F_{i,n}$ , 3.)

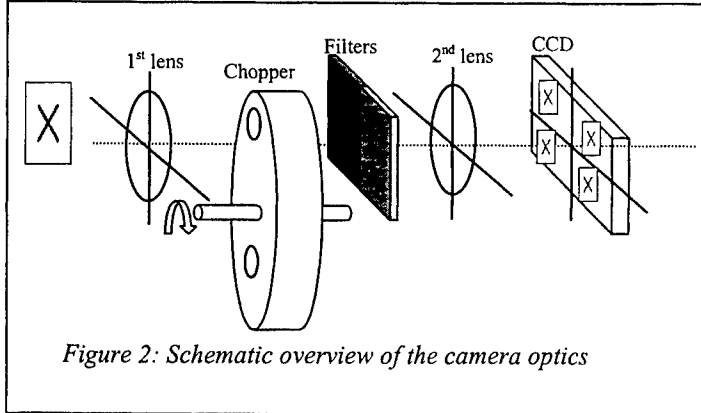


Figure 2: Schematic overview of the camera optics

$F_{j,m}$ , 4.)  $F_{j,n}$ . Software has been developed to operate the camera and process the images in real-time. The software has been written in IDL 5.2 running on a regular PC with a Windows NT4.0 platform.

The setup in the following experiments is configured to measure the PPIX fluorescence with the following excitation ( $\lambda_i$ ,  $\lambda_j$ ) and detection ( $\lambda_n$ ,  $\lambda_m$ ) wavelengths:

$\lambda_i$ : 405 nm, Oriel 56541

$\lambda_j$ : 435 nm, Oriel 56551

$\lambda_n$ : 550nm, Omega optical 550RDF42

$\lambda_m$ : 675nm, Omega optical 675DF110

To eliminate any excitation light to enter the camera a Schott KV500 filter is positioned in front of the first lens.

### Experiments

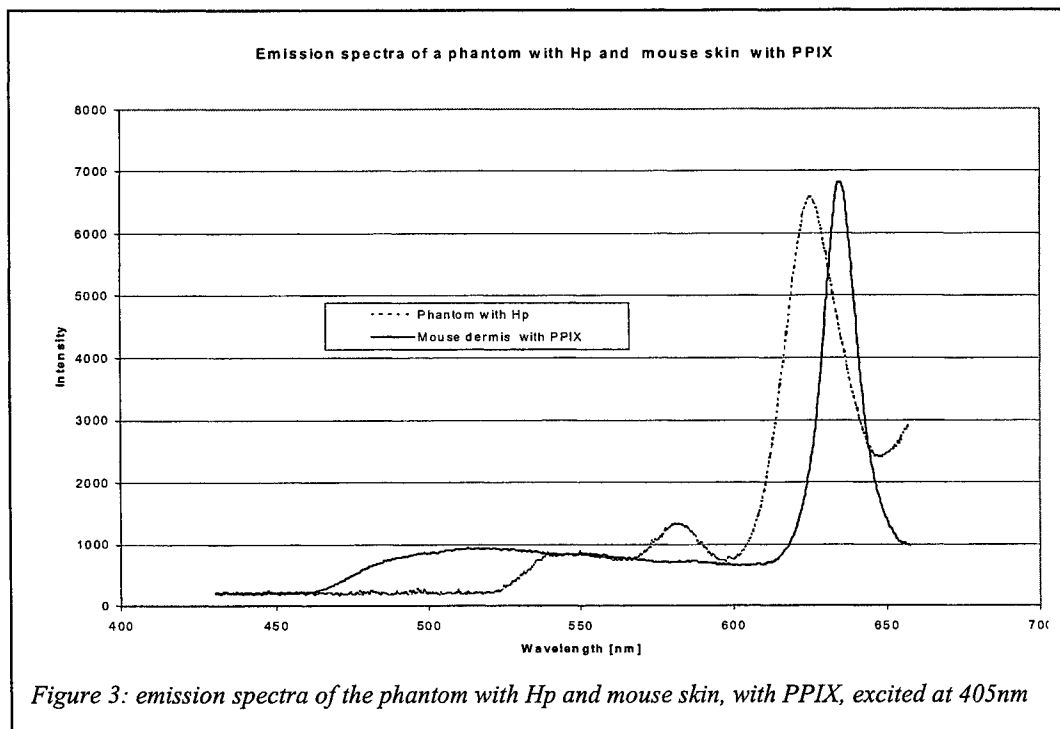
The following three 3 experiments have been performed:

1. Phantom Study: Ex vivo study of the dependence on optical properties,  $\mu_s$  and  $\mu_a$ .
2. Human Study: In vivo check of the independence of Double ratio on  $\mu_a$ .
3. Animal Study: In- and Ex Vivo feasibility study of localizing PPIX concentrations and tumors.

#### Phantom Study

Phantom studies have been performed to investigate the sensitivity of the Double Ratio to changes in the absorption coefficient  $\mu_a$  and scattering coefficient  $\mu_s$ . To create these properties aqueous solutions have been made with Intralipid10% as a scattering component and Evans blue as the absorbing component. To simulate the auto-fluorescence of the dermis and epidermis Fluoreceine was used. To simulate the PPIX fluorescence Hematoporphyrin (Hp) was used in a concentration sequence. Hp has, compared to PPIX, a similar absorption- and emission spectra and is more easily dissolved in aqueous solutions. Before adding HP to the phantom it was pre-diluted in a small amount acetone to enhance solubility in water.

To see how well the phantom represents reality, the emission spectrum of the phantom is compared with the emission spectrum of human tissue in the graph below.



Five different phantoms were made in total:

- Phantom 1:  $\mu_s = 80 \text{ cm}^{-1}$ ,  $\mu_a = 2.8 \text{ cm}^{-1}$
- Phantom 2:  $\mu_s = 120 \text{ cm}^{-1}$ ,  $\mu_a = 2.8 \text{ cm}^{-1}$
- Phantom 3:  $\mu_s = 80 \text{ cm}^{-1}$ ,  $\mu_a = 4.2 \text{ cm}^{-1}$
- Phantom 4:  $\mu_s = 244 \text{ cm}^{-1}$ ,  $\mu_a = 1.8 \text{ cm}^{-1}$ , corresponding to human dermis (3)
- Phantom 5:  $\mu_s = 313 \text{ cm}^{-1}$ ,  $\mu_a = 2.3 \text{ cm}^{-1}$ , corresponding to human liver (3)

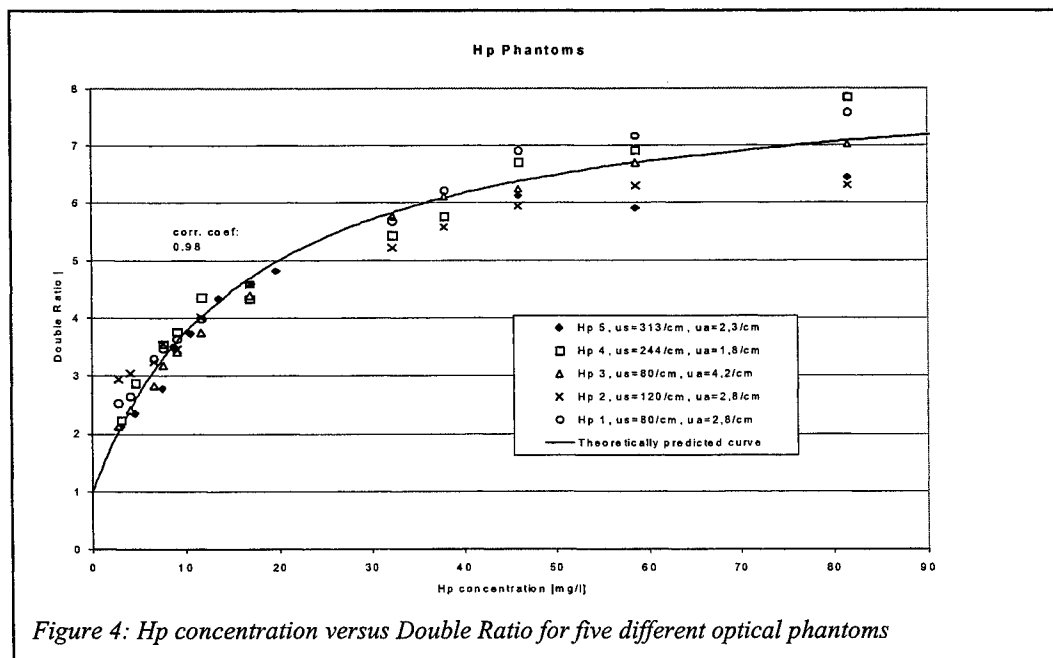


Figure 4 shows the DR versus Hp concentration for the five mentioned phantoms. Clearly visible is the independence of the Double Ratio of absorbing and scattering coefficient. The graph also shows a good correlation between the measured values and the theoretically predicted curve given by equation 3, which is plotted in the graph as well. We found a correlation coefficient of 0.98.

#### *Human experiments*

Previous studies show that absorption artifacts induced by melanin (2) can seriously compromise single red-green fluorescence ratios measured on the skin. To study these absorption artifacts in vivo we performed the following experiment. We studied pigmented moles on human Caucasian epidermis, comparing Single red-green Ratios with Double Ratios. We found two volunteers on which we selected two pigmented moles each. Topical administration with a solution of 20%  $\delta$ -ALA in 3% carboxymethylcellulose in water took place for half an hour. The gel was held into position with Tegaderm and was applied on the pigmented mole and surrounding unpigmented skin. After half an hour the Tegaderm was removed and the skin was cleaned with a gauze.

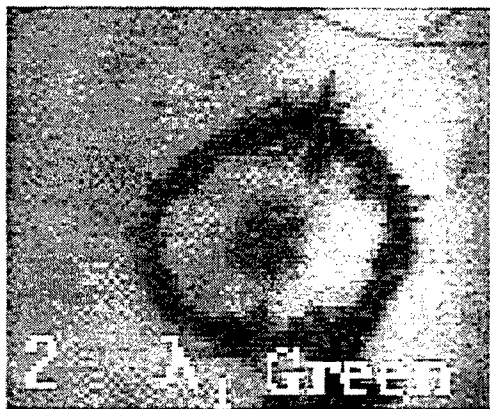


Figure 5: In vivo white light image a pigmented human mole. The position of the mole is indicated with a circle.

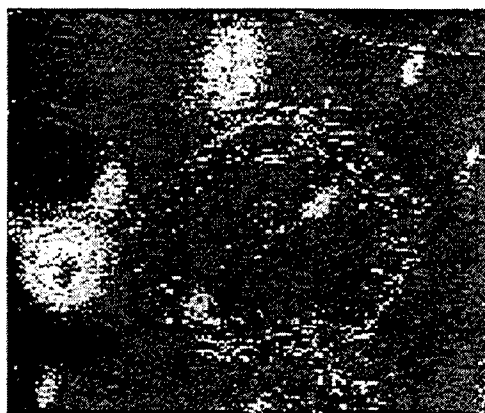


Figure 6: In vivo Double Ratio image of a pigmented human mole.

Figure 5 shows the white light image of a pigmented mole indicated with a pen circle around it. Figure 6 shows the Double Ratio image of this mole. The mole has disappeared in the Double Ratio image, which indicates that the Double ratio is independent on tissue color. The pen circle around the mole has not completely disappeared due to small artifacts in overlapping the four images. The whitish spots indicate an elevated PPIX concentration in the hair follicles.

#### *Animal Study*

An animal study has been performed to test whether the system is capable of localizing in vivo PPIX concentrations and tumors. For this study we used twenty hairless mice. Ten of these mice had visible skin tumors and chronically aged skin due to UVB irradiation. The other ten mice were used as control group. Topical administration with a solution of 20%  $\delta$ -ALA in 3% carboxymethylcellulose in water took place for half an hour. The gel was held into position with Tegaderm and was applied on control tissue and tumor tissue. After half an hour the Tegaderm was removed and the skin was cleaned with a gauze. Imaging took place six hours and twelve hours after ALA application.



*Figure 7: The rectangle in the mouse drawing shows the detection area.*

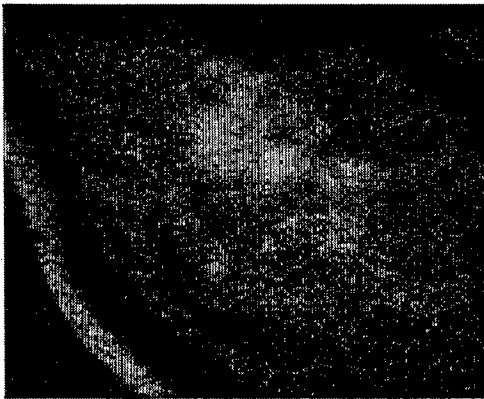


*Figure 8: Double Ratio image of visible tumors on 'normal' skin (in vivo)*

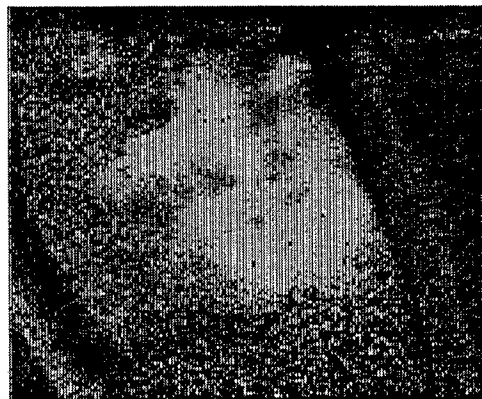


*Figure 9: Double Ratio image of visible tumors on chronically aged skin (in vivo)*

Figure 8 shows an in vivo Double Ratio image of a mouse with visible skin tumors. The image size is  $3\text{cm}^2$ . The white spots in the figure indicate the position of visible skin tumors with a size of approximately 2 to 3 mm with possibly some surrounding satellite tumors. This image shows distinctive tumors.

Figure 9 shows an in vivo Double Ratio image of a mouse with visible skin tumors and chronically aged skin. The image size is  $3\text{cm}^2$ . The white spots in the figure indicate the position of visible skin tumors with a size of approximately 2 to 3 mm. The tumors can hardly be discriminated due to the surrounding altered skin, which appears to accumulate as much PPIX as the tumor itself. White light examination with the naked eye showed altered skin with some tumors. Both images were taken at similar times after ALA application and have similar scales.

Six and twelve hours after ALA application ten mice were sacrificed, five mice with tumor and five mice with normal tissue. After that a region of the skin of approximately three square centimeters was cut out and imaged. The images of all twenty mice were then statistically analyzed comparing normal vs. tumor tissue. On average the difference between control and tumor tissue was found to be a factor 4. Twelve hours post ALA application and a factor 6 was found.

### **Conclusions**

The Double Ratio imaging device we developed performed excellently both on realistic optical phantoms, on skin tumors in mice and on a human mole. At present the device is being investigated in a series of clinical experiments.

## Acknowledgements

This work was supported by grants from the Dutch technology Foundation (AGN 443413) and the European community (BMH4 CT97-2260).

## References

1. G.A. Wagnieres, W.M. Star, B. C. Wilson, "In Vivo Fluorescence Spectroscopy and Imaging for Oncological Applications.", *J. Photochem. PhotoBiol.* **68**:603-632 (1998).
2. H.J.C.M. Sterenborg, A.E. Saarnak, R. Frank, M. Montamedi, "Evaluation of spectral correction techniques for fluorescence measurements on pigmented lesions", *J. Photochem. PhotoBiol.* **35**:159-165 (1996).
3. W.F. Cheong, S.A. Prahl, A.J. Welch, "A review of the optical properties of biological tissues", *IEEE J. Quant. Electron.* **26**: 2166-2185 (1990).
4. M. Sinaasappel and H.J.C.M. Sterenborg, "Quantification of the hematoporphyrin dervative by fluorescence measurement using dual-wavelength excitation and dual-wavelength detection", *Applied Optics* **32**:541-548 (1993).
5. S. Andersson-Engels, C.Klinenberg, K.Svanberg, S. Svanberg, "In vivo fluorescence imaging for tissue diagnostics, *Phys. Med. Biol.* **42**:815-824 (1997).
6. A.E. Profio, O.J. Balchum, F.Carstens, "Digital Background subtraction for fluorescence imaging", *Med. Phys.* **13**:717-721 (1986).

# In vivo autofluorescence of nasopharyngeal carcinoma and normal tissue

Jianan Y. Qu, PhD<sup>1</sup>, Po Wing YUEN, MD<sup>2</sup>, Zhijian Huang, PhD<sup>1</sup>  
and William I. WEI, MD<sup>2</sup>

<sup>1</sup>Department of Electrical and Electronic Engineering, Hong Kong University of Science and Technology, Clear Water Bay, Kowloon, Hong Kong, P.R. China

<sup>2</sup>Division of Otorhinolaryngology, The University of Hong Kong, Queen Mary Hospital, The University of Hong Kong, 102 Pokfulam Road, Hong Kong, P.R. China

## ABSTRACT

An optical imaging and spectroscopy system has been developed for the study of *in vivo* fluorescence of nasopharyngeal tissue through an endoscope. The system records the fluorescence signal in the imaging plane of the endoscopic system. This allows analyze the characteristics of the light induced fluorescence (LIF) spectra recorded by each pixel of the two dimensional detector which may be used for fluorescence endoscopic imaging. If the endoscope for fluorescence endoscopy is the same as one employed for the *in vivo* fluorescence study, the algorithms developed to distinguish the diseased tissue from normal tissue based on the *in vivo* fluorescence study should be highly reliable for fluorescence imaging of lesions. In this work, fluorescence spectra were collected from 27 full term patients. Different algorithms were tested for separation of cancerous lesions from normal tissue. High sensitivity and specificity were achieved.

**Keywords:** Fluorescence, spectroscopy, imaging, cancer

## 1. INTRODUCTION

Nasopharyngeal carcinoma (NPC) occurs with highest incidence and frequencies in Asian countries. Genetic factors, infection with the Epstein-Barr virus (EBV), and environmental factors are all implicated as being important for the development of NPC<sup>[1-4]</sup>. Screening of nasopharyngeal carcinoma is now carried out by checking individuals suspected of having NPC for elevated levels of serum IgA antibodies directed against EBV viral capsid antigen (VCA) and Early Antigen(EA) with subsequent nasoendoscopic biopsy of the nasopharynx. However, many malignant tumors and early lesions such as carcinoma *in situ* are small and have the flat surface. It is difficult to localize the small and flat lesions with an ordinary endoscopy. Random biopsies are usually conducted to screen for subclinical tumors. According to the statistic results, only 5.4% of patients with elevated serum EBV antibody titer had asymptomatic NPC in random biopsy of the nasopharynx<sup>[3]</sup>. The low incidence of pathological evidence of nasopharyngeal carcinoma suggests that majority of the screening program will suffer the unnecessary trauma caused by the random biopsy. Furthermore, patients with raised serum EBV antibody titer or with tumor removed need to have follow-up endoscopy and biopsy to rule out possible nasopharyngeal carcinoma, residual tumor or tumor recurrence. As a result, a remote imaging technique is desirable for early detecting malignant tumor and guiding the routine biopsy procedure.

Laser-induced fluorescence (LIF) of tissues depends on their biochemical and histomorphologic characteristics. LIF technology has already successfully demonstrated the capability to distinguish normal tissue from precancerous and early cancerous lesions at different human organs and body sites. Optical fiber probes were most commonly used for *in vivo* LIF spectroscopic study of tissue. However, the fluorescence imaging technique such as fluorescence endoscopy is more desirable and convenient for clinical diagnosis. The optics of endoscope is very different from fiber probe in terms of optical illumination and collection geometry. The endoscope collects information from much larger area than optical fiber probe used of point measurement. To separate the normal tissue from lesions, the algorithm for fluorescence image processing should be created based on the correlation between fluorescence spectra and pathologic results. The fluorescence spectra should be recorded from the location where the biopsy is taken for pathologic diagnosis. Also, the spectra must be collected by a system with the same geometry as endoscope employed. In this work, we built a multiple channel spectrometer for the study of characteristics of *in vivo* fluorescence signal recorded by an imaging system. Specifically, the spectrometry analyzed the LIF signal of tissue in the image plane of a conventional endoscopic system

during endoscopy. This allowed us to investigate the fluorescence signal received by each pixel of a two dimensional sensor proposed for recording the LIF image of the fluorescence endoscopy. First, we created a simple algorithm to detect nasopharyngeal carcinoma by using the ratio of fluorescence signals at two wavelength bands. Furthermore, we tested the algorithm involved with the fluorescence signals at three wavelength bands to compensate for the effect of blood absorption on the fluorescence signal. The performance of the algorithm should be more stable with reducing the distortion of tissue fluorescence signal by the variation of blood content. Finally, we discuss the possibility to further improve the sensitivity and specificity of the LIF imaging technique. Instead of using a general algorithm built on the spectral data collected from a group of subjects, we propose to make use of the difference of fluorescence signals between diseased and normal tissue within an individual to create a more robust algorithm for the detection of diseased tissue.

## 2. MATERIALS AND METHODS

The schematic diagram of the imaging and spectroscopy system for study of *in vivo* fluorescence signal is shown in Figure 1. The system was designed to be able to adapted to any endoscope. A 100 W mercury arc lamp filtered by a band pass filter in the wavelength range from 390 nm – 450 nm was used as excitation source. The excitation power at the endoscope tip is about 50 mW. The fluorescence and reflection of excitation from the tissue surface were imaged by a commercial endoscope. A dichroic mirror with cut-on wavelength at 470 nm divided the optical signal from the endoscope into the reflection and fluorescence channels. The image recorded by a CCD video camera in reflection channel was displayed on a monitor for the real time endoscopy. A long pass filter with cut-off wavelength at 470 nm was used to eliminate residual excitation light in the fluorescence channel. The fluorescence signal was collected by an optical fiber bundle with seven optical fibers of 200  $\mu\text{m}$  in diameter and NA 0.16. The fibers were evenly distributed in fluorescence image plane of the endoscope. When the separation of the endoscope distal tip and the imaged tissue surface was 15 mm, each single fiber sampled the signal from the area about 1mm in diameter on tissue surface. The sampling area is much smaller than the total illuminated area. The fluorescence signals received by the fibers were conducted to the entrance slit of an imaging spectrograph. The tips of optical fibers were placed in the entrance plane and lined up vertically. The fluorescence conducted by the fibers were then dispersed and imaged onto an intensified CCD (ICCD) camera. The images of CCD and ICCD were grabbed simultaneously by a frame grabber at rate of 25 frames per second. The spectra of a white light lamp shown in Figure 2a were formed by binning the seven spectral strips in the image vertically. The wavelength of the spectral measurement was calibrated by using a standard spectral lamp. The response of ICCD with fixed gain was in its linear region. A typical image grabbed from real time video with aiming marks is shown in Figure 2b.

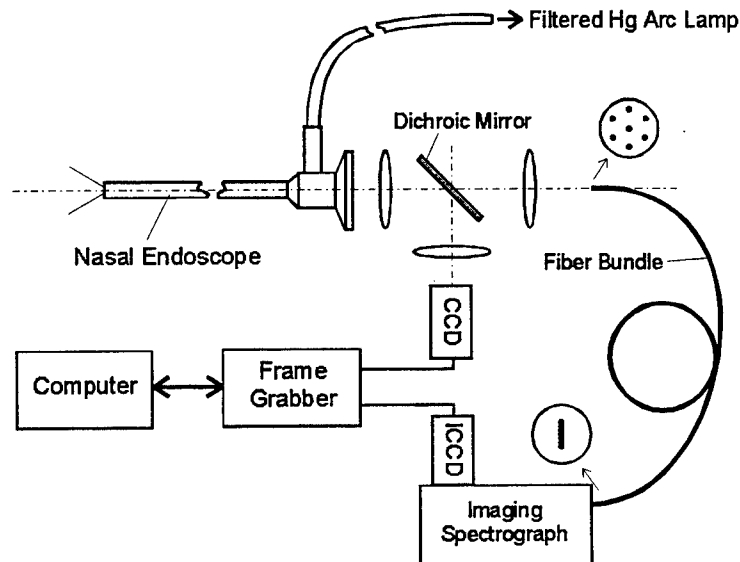


**Figure 1.** Arrangements for *in vivo* measuring tissue autofluorescence in the image plane of a nasal endoscopic imaging system.



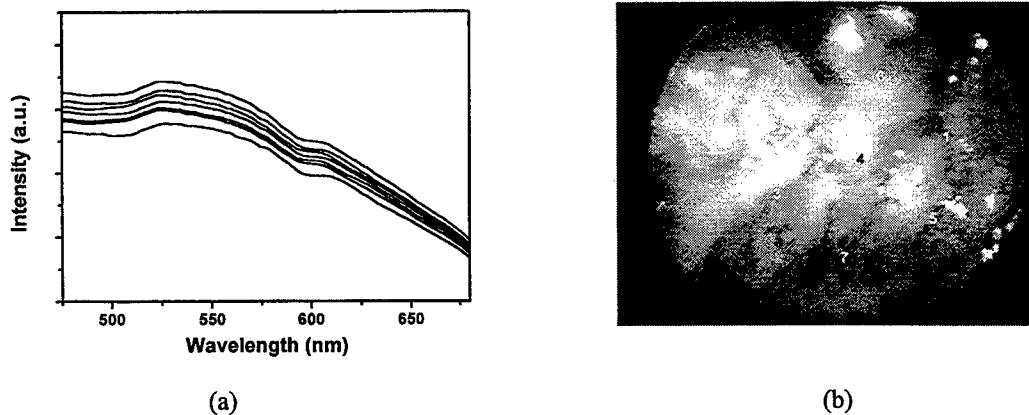


**Figure 2.** (a) Spectra formed by binning the spectral strips vertically. (b) Real time image recorded from the endoscope overlaid with aiming number marks of seven optical fibers. Each mark indicates the area aimed by a correspondent single fiber. Fluorescence signals are collected from seven sampling areas simultaneously. The highlighted number points the area of interest on the tissue surface where both fluorescence measurement and biopsy will be taken.

The *in vivo* fluorescence measurements have been conducted in the Department of Otorhinolaryngology and Department of Clinical Oncology at Queen Mary Hospital, The University of Hong Kong. A total of 27 subjects were enrolled in this study which lasted about six months. The fluorescence spectra were measured at the sites where biopsy specimens were taken. Histologic examinations on biopsies were then performed by the pathologists. This study was approved by the Ethical Committee of Queen Mary Hospital, the University of Hong Kong.

### 3. RESULTS AND CONCLUSIONS

We collected *in vivo* fluorescence on 110 biopsy sites from 27 subjects before the biopsy procedures were performed. In which, 58 were found to be normal, 52 exhibited carcinoma. Figure 3 illustrates typical fluorescence spectra acquired from nasopharyngeal sites. All fluorescence intensities are not calibrated due to variation of measurement geometry site by site. As can be seen, the spectral lineshapes vary not only individual by individual but within individual also. The peak emission wavelength of nasopharyngeal carcinoma and normal tissue occurs within  $\pm 10$  nm of 510 nm. The large variation of fluorescence intensity in the region of 530 – 590 nm and peak emission wavelength indicates that the blood content in tissue plays important role in the distortion of fluorescence signal recorded on the tissue surface<sup>[11,12,19,20]</sup>. During the fluorescence measurement procedure, the distance between the distal tip of endoscope and tissue surface was kept in the range from 10 to 15 mm. Although the distance was not calibrated, we observed that the fluorescence intensity from the nasopharyngeal carcinoma was generally lower than the normal tissue.

A simple algorithm based on the ratio of fluorescence signals at two wavelength bands was created to differentiate the nasopharyngeal carcinoma from the surrounding normal tissue. As discussed previously, the algorithm will be valid for the fluorescence endoscopic imaging system because the tissue fluorescence were analyzed in the image plane of the endoscope. A set of wavelength bands in the range from 470 – 700 that best separated the carcinoma and normal tissue was found by exhaustive search. The minimal bandwidth was set to 30 nm in the search. A very narrow bandwidth becomes not practical because the signal to noise ratio SNR is inversely proportional to the bandwidth and the performance of a fluorescence imaging system is strongly dependent on the SNR. The ratio of fluorescence signal in the short wavelength band vs. long wavelength band was calculated. An unpaired student's *t*-test was used to compare the ratio scores of the normal and carcinoma tissues. The separation of normal tissue from carcinoma was evaluated by the student's *t*-test result. The optimal wavelength bands for the ratio algorithm was found at  $500 \pm 25$  nm and  $640 \pm 40$  nm as shown in Figure 3. The ratio scores of the signals in the band of  $500 \pm 25$  nm vs.  $640 \pm 40$  nm from all measured fluorescence spectra are shown in Figure 4a. The distributions of the ratio scores for normal and carcinoma are displayed separately because of the slight

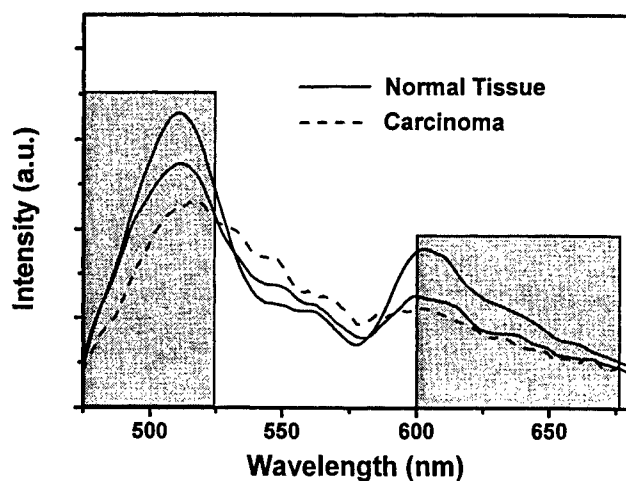


Figure 3. Typical *in vivo* autofluorescence emission spectra

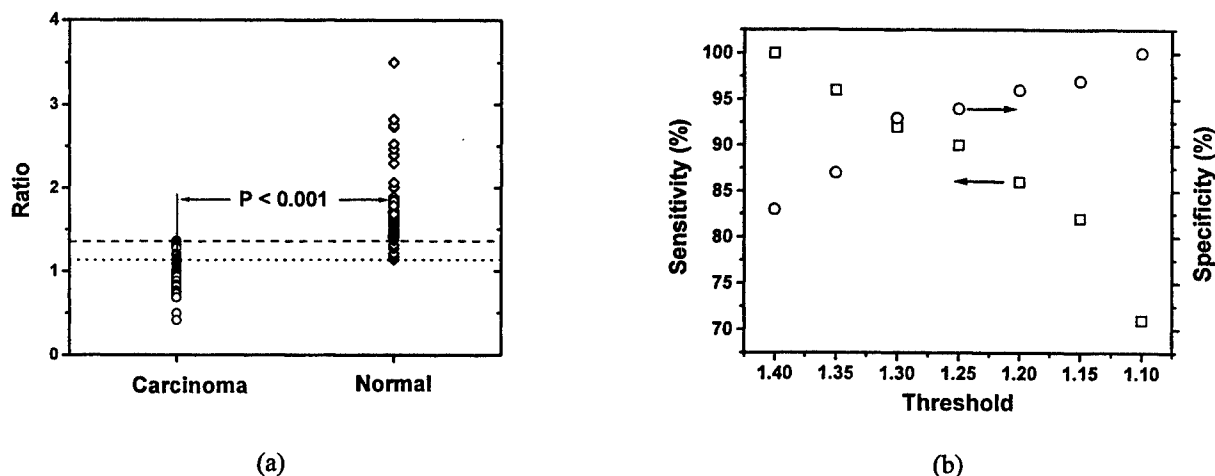


Figure 4. (a) Scatter plot for the scores of two wavelengths ratio algorithm. The circles and diamonds represent the scores of nasopharyngeal carcinoma and normal tissue, respectively. (b) Dependence of sensitivity and specificity of two wavelengths algorithm on the diagnostic threshold. The squares and circles represent the sensitivity and specificity, respectively.

overlapping between two groups. The mean ratio scores were  $1.78 \pm 0.48$  for normal nasopharyngeal tissue and  $0.99 \pm 0.20$  for the carcinoma. The *p*-value of student's *t*-test on the ratios for normal tissue and carcinoma was found to be smaller than 0.001. This indicates the significantly statistical difference ( $P < 0.001$ ) between two groups of scores. To further evaluate the performance of two wavelengths algorithm, we calculated the sensitivity and specificity of the algorithm as a function of decision thresholds. The sensitivity and specificity were defined as

$$\text{Sensitivity} = \frac{\text{True Positives}}{\text{True Positives} + \text{False Negatives}}$$

$$\text{Specificity} = \frac{\text{True Negatives}}{\text{True Negatives} + \text{False Positives}}$$

The dash and dot lines in Figure 4a represent the diagnostic thresholds for sensitivity of 100% and specificity of 100%, respectively. The dependence of sensitivity and specificity on diagnostic threshold are shown in Figure 4b. As can be seen, when the threshold is set to 1.30, the two wavelengths algorithm can achieve both sensitivity and specificity about 92%.

As discussed in the beginning of the section, the variation of blood content plays an important role in distortion of fluorescence spectra emitted from tissue surface. The result of an exhaustive search of the optimal set of wavelength bands for the ratio algorithm has reflected the effect of blood content on the fluorescence measurement. The optimal set of wavelength bands at  $500\pm 25$  nm and  $640\pm 40$  nm excludes the wavelength region of 530nm to 590 nm where the blood appears very strong absorption<sup>[19,20]</sup>. This indicates that the exhaustive search is a process to minimize the blood effect on the performance of the ratio algorithm. However, the absorption coefficient of blood in the wavelength band of  $500\pm 25$  nm is still much greater than  $640\pm 40$  nm<sup>[19,20]</sup>. To further reduce the effect of blood absorption and improve the accuracy of the diagnosis, we investigated an algorithm which compensated the variation of fluorescence signal in wavelength band of  $500\pm 25$  nm caused by blood absorption to some extent.

The algorithm was created by forming the dimensionless function

$$R = \frac{I(500 \pm 25)}{I(640 \pm 40)} \left( \frac{I(500 \pm 25)}{I(560 \pm 35)} \right)^k$$

in which fluorescence signals in three wavelength bands:  $500\pm 25$  nm,  $560\pm 35$  nm and  $640\pm 40$  nm were employed. The first term of  $R$ -function is the two wavelengths ratio. The second term includes the information of blood absorption and is used to compensate the effect of blood variation on the first term. A constant  $k$  was used to scale the blood effect on the score of the algorithm. It has been found in an exhaustive search that the best separation was achieved by setting the value of  $k$  about 0.51. Again, the result of an unpaired student's  $t$ -test was used as the criterion to determine the best separation and optimal value of constant  $k$ . The scores of  $R$ -function for normal and carcinoma tissues are shown in Figure 5a. The mean scores of  $R$ -function for normal and carcinoma tissues are  $1.95\pm 0.50$  and  $1.00\pm 0.21$ , respectively. The small  $p$ -value ( $<0.001$ ) demonstrates that the significantly statistical difference between two groups of scores. It has been noticed that the variances of  $R$ -function scores for normal and carcinoma tissues are at the same levels as the two wavelengths algorithm. However, the difference of mean score between the normal tissue and carcinoma is 0.95, compared to 0.79 of two wavelengths algorithm. This indicates that three wavelengths algorithm can separate the normal tissue and carcinoma better than two wavelengths algorithm. The dependence of sensitivity and specificity on the diagnostic threshold for three wavelengths algorithm is displayed in Figure 5b. The sensitivity of 98% and specificity of 95% can be achieved when the threshold is set to 1.35.

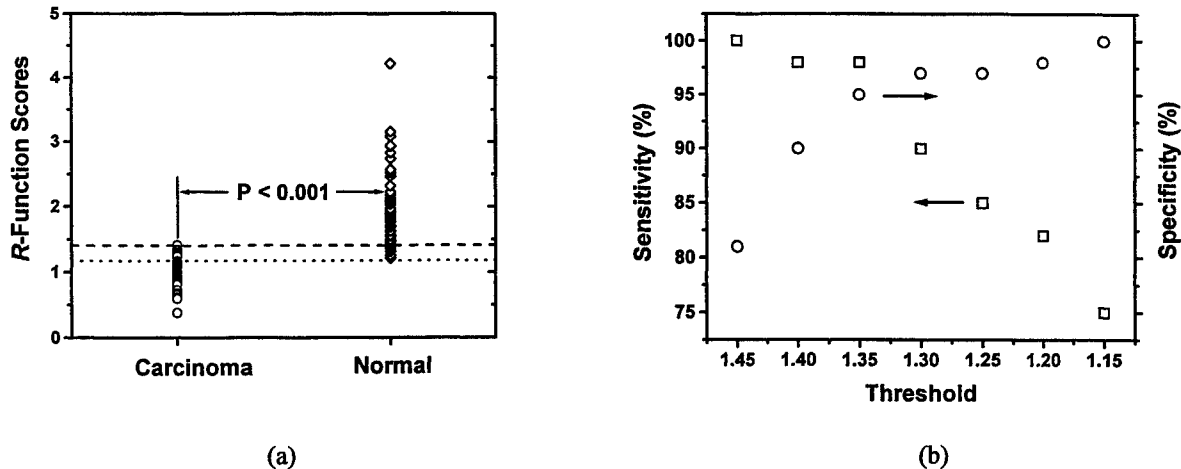


**Figure 5.** (a) Scatter plot for the scores of three wavelengths ratio algorithm. The circles and diamonds represent the scores of nasopharyngeal carcinoma and normal tissue, respectively. (b) Dependence of sensitivity and specificity of three wavelengths algorithm on the diagnostic threshold. The squares and circles represent the sensitivity and specificity, respectively.

In conclusion, we built a multiple channel spectrometer to analyze the light induced fluorescence spectra of nasopharyngeal carcinoma and normal tissue in the image plane of a standard nasal endoscope. The results of the study reported here demonstrate that a conventional endoscopic system with the feature of fluorescence spectral imaging can localize the nasopharyngeal carcinoma with high sensitivity and specificity. There is not a technical obstacle and cost problem to build a two wavelengths and three wavelengths imaging system for real time endoscopy<sup>[15-18]</sup>. The fluorescence endoscopy will offer unique information for the early detection of malignant nasopharyngeal tumors noninvasively. The method to investigate the tissue autofluorescence in our study can be generally used to create reliable algorithm for various fluorescence endoscopic imaging systems to detect diseased tissue on other organ sites. It should be pointed out that no subject with a subclinical cancerous lesion was found and examined in this six months pilot study. The pathological analysis showed that all biopsied sites, where the *in vivo* fluorescence spectra were measured, exhibited either normal or invasive carcinoma, although some carcinoma lesions are flat and unobservable. Furthermore, the exact biochemical and morphological basis for the difference in fluorescence spectral characteristics between normal and carcinoma tissue are currently unknown. In the future study, we will focus on investigating the autofluorescence of early lesion and develop the understanding of the basis of nasopharyngeal autofluorescence.

#### 4. REFERENCES:

1. Ho JHC. Genetic and environmental factors in nasopharyngeal carcinoma. In: W. Nakahara et al, eds. Recent Advances in Human Tumor Virology and immunology. Tokyo: University of Tokyo Press. 1971:275-95.
2. Ho JHC, Ng MH, Kwan HC, Chau JCW. Epstein-Barr virus-specific IgA and IgG serum antibodies in nasopharyngeal carcinoma. Br J Cancer 1976; 34: 655-9.
3. Wei WI, Sham JS, Zong YS, Choy D, Ng MH. The efficacy of fiberoptic examination and biopsy in the detection of early nasopharyngeal carcinoma. Cancer 1991; 67: 3127-3130.
4. Sham JS, Wei WI, Kwan WH, Chan CW, Kwong WK, Choy D. nasopharyngeal carcinoma - pattern of tumor regression after radiotherapy. Cancer 1990; 65:21.
5. Wagnieres GA, Star WM, Wilson BC. In vivo fluorescence spectroscopy and imaging for oncological applications. Photochemistry & Photobiology. 1998; 68:603-32.
6. Cothren RM, Richards-Kortum R, Sivak MV Jr., Fitzmaurice M, Rava RP, Boyce GA, Doxtader M, Blackman R, Ivanc TB, Hayes GB, Doxtader M, Blackman R, Ivanc T, Feld MS, Petras RE. Gastrointestinal tissue diagnosis by laser-induced fluorescence spectroscopy at endoscopy. Gastrointestinal Endoscopy. 1990; 36:105-11.
7. Hung J, Lam S, LeRiche JC, Palcic B. Autofluorescence of normal and malignant bronchial tissue. Lasers in Surgery & Medicine. 1991; 11: 99-105.
8. Ramanujam N, Mitchell MF, Mahadevan A, Thomsen S, Silva E, Richards-Kortum R. Fluorescence spectroscopy: a diagnostic tool for cervical intraepithelial neoplasia (CIN). Gynecologic Oncology. 1994; 52: 31-38
9. Qu J, MacAulay C, Lam S, Palcic B. Laser-induced fluorescence spectroscopy at endoscopy: tissue optics, Monte Carlo modeling, and in vivo measurements. Opt. Eng. 1995; 34: 3334-3343.
10. Zeng HS, Weiss A, Cline R, MacAulay CE. Real time endoscopic fluorescence imaging for early cancer detection in the gastrointestinal tract. Bioimaging. 1998; 6: 151-165.
11. Wu J, Feld MS, Rava RP. Analytical model for extracting intrinsic fluorescence in turbid media. Appl. Opt. 1993; 32:3585-3595
12. Gardner CM, Jacques SL, Welch AJ. Fluorescence spectroscopy of tissue: recovery of intrinsic fluorescence from measured fluorescence. Appl. Opt. 1996; 35: 1780-1792
13. Ramanujam N, Mitchell MF, Mahadevan A, Thomsen S, Malpica A, Wright T, Atkinson N, Richards-Kortum R. Development of a multivariate statistical algorithm to analyze human cervical tissue fluorescence spectra acquired in vivo. Lasers in Surgery & Medicine. 1996; 19:46-62
14. Tumer K, Ramanujam N, Ghosh J, Richards-Kortum R. Ensembles of radial basis function networks for spectroscopic detection of cervical precancer. IEEE Transactions on Biomedical Engineering. 1998; 45:953-61.
15. Andersson-Engels S, Johansson J, Svanberg K, Svanberg S. Fluorescence imaging and point measurements of tissue: applications to the demarcation of malignant tumors and atherosclerotic lesions from normal tissue. Photochemistry & Photobiology. 1991; 53:807-14.
16. Palcic B, Lam S, Hung J, MacAulay C. Detection and localization of early lung cancer by imaging techniques. Chest. 1991; 99:742-3.

17. Andersson-Engels S, Johansson J, Svanberg S. Medical diagnostic system based on simultaneous multispectral fluorescence imaging. *Applied Optics*, 1994; 33: 8022-8029.
18. Wagnieres GA, Studzinski AP, van den Bergh HE. An endoscopic fluorescence imaging system for simultaneous visual examination and photodetection of cancers. *Rev. Scient. Inst.* 1997; 68: 203-212.
19. van Kampen EJ, Zilstra WG. Determination of hemoglobin and its derivatives. In: H. Sobotka and C. P. Stewart, eds. *Advances in Clinical Chemistry*. New York: Academic. 1965: 8:158-187.
20. van Assendelft OW. Spectrophotometry of haemoglobin derivatives. Netherlands: Royal Vangorcum Ltd. 1970: 55-70.
21. Gonzalez RC, Woods RE. Digital imaging processing. New York: Addison-Wesley Pub. Co. Inc. 1993: 413-477.

# Characterization of Human Neoplastic and Normal Oral tissues by Visible Excitation and Emission Fluorescence Spectroscopy

D. Koteeswaran<sup>a</sup>, N. Vengadesan, P. Aruna, K. Muthuvelu<sup>a</sup>,  
S. Barghavi<sup>b</sup>, V.S. Gowri<sup>c</sup>, S. Ganesan\*

Division of Medical Physics and Laser Medicine, Department of Physics,  
Anna University, Chennai 600 025, INDIA.

<sup>a</sup>Govt. Arignar Anna Memorial Cancer Hospital, Kancheepuram 631 552, INDIA.

<sup>b</sup>Govt. General Hospital, Chennai Medical College, Chennai 600 001, INDIA.

<sup>c</sup>Department of Ocean Management, Anna University, Chennai 600 025, INDIA

## 1. ABSTRACT

The steady state native fluorescence emission and excitation spectra of human normal and cancerous oral tissues are studied in the visible region. The fluorescence excitation spectrum is recorded for 600 nm emission by scanning the excitation ( $\lambda_{ex}$ : 340 – 580 nm). The excitation spectrum of normal tissues has peaks at 406, 524 and 552 nm, whereas the cancerous tissues have peaks at 406, 513 and 552 nm respectively. The fluorescence emission spectra were also recorded at 405 and 560 nm excitations ( $\lambda_{em}$ : 430 – 700 nm;  $\lambda_{em}$ : 580 – 750 nm). The emission spectrum of cancerous tissues has two distinct peaks at 604 and 660 nm. It is also observed that there is a distinct difference between normal and cancerous tissues at 560 nm excitation. The ratio parameter  $R_1 = (I_{406} / I_{550})$  is introduced from the excitation spectrum for 600 nm emission and two ratio parameters  $R_2 = (I_{470} / I_{600})$  and  $R_3 = (I_{470} / I_{660})$  are introduced for the emission spectrum at 405 nm excitation. Among the three ratio parameters the  $R_1$  classifies the normal and cancerous tissues at a specificity and sensitivity of 83 % and 93 % respectively. A critical value of 1.8 is suggested for classifying the normal from cancerous tissues.

**Keywords:** Fluorescence, Excitation spectroscopy, oral cancer, optical diagnosis

## 2. INTRODUCTION

Oral cancer is predominantly related to the behavior of smoking, alcohol abuse, chewing of tobacco and betel nut. As tobacco chewing is habitual among rural community in India, oral cancer constitutes 30 % of the overall malignancy affecting the whole body. The carcinogenesis of oral cavity is a multi step process secondary to exposure to tobacco related carcinogens. The entire exposed mucosa is at risk for genetic damage, which will exist in varying stages of progression towards invasive disease. Discrimination of early stages of abnormal proliferation through some novel screening strategies may help to serve as an intermediate endpoint in chemo-preventive and behavior modification.

In this regard, native fluorescence spectroscopy (NFS) has been extended to the medical community to characterize various metabolic and pathological changes at cellular and tissue level. Porphyrin derivatives, which have preferential accumulation in tumor tissues, have been extensively used for diagnostic purpose in oncology.  $\delta$ -Aminolevulinic acid is frequently applied topically or systematically and used for diagnostic evaluations of tumors of skin<sup>1</sup>, bladder<sup>2</sup>, gastrointestinal tract and lung<sup>3</sup>. However, Protoporphyrin IX may accumulate in tumors with some degree of selectivity, because of the limited capacity of the enzyme, ferrochelatase<sup>4</sup>.

Currently, photophysical properties of intrinsic bio-molecules and their structure have also been considered as a useful tool to study various alterations in the functional, morphological and micro-environmental changes in cells and

---

\* Correspondence: E-mail : [sganesan@annauniv.edu](mailto:sganesan@annauniv.edu); Telephone: ++ 91-44- 2351723 Extn: 3154; Fax: ++91-44-4910740

tissues. Differences in the native fluorescence have been ascribed to various molecules such as tryptophan, tyrosine, phenylalanine, nicotinamide adenine dinucleotide – reduced form (NADH), flavin adenine dinucleotide (FAD), collagen, elastin and endogenous porphyrins in cells and tissues<sup>5</sup>. Studies in diagnostic oncology indicate that the native fluorescence spectroscopy of tissues can be exploited to distinguish normal from malignant conditions of breast<sup>6</sup>, cervix<sup>7</sup> and colon<sup>8</sup>. However, most of the reported data are based on the native fluorescence excitation and emission spectroscopy in the ultraviolet region. Only limited data are available on the applications of excitation and emission spectroscopy in the visible region. In this regard, we have already reported on the use of visible native fluorescence spectroscopy in discriminating different pathological conditions of oral cancerous tissues in 7,12 Dimethyl benz(a) anthracene induced hamster cheek pouch carcinogenesis<sup>9</sup>. In the present paper, we extended our study on human normal and cancerous oral tissues using both excitation and emission fluorescence spectroscopy in the visible region.

### 3. Materials and methods

#### 3.1. Tissue preparation

Tissue samples were collected from patients with oral malignancy (n = 14). Normal oral tissue samples (n = 6) at adjacent normal sites were also collected from selected patients. Each tissue sample was cut into two segments. One segment was sent to the pathologist for standard histopathological evaluation. The second segment was washed with 0.9% NaCl solution and stored at -4°C, until assay. Both normal and malignant tissues were homogenized and the homogenate was mixed with equal volume (1:1) of 1 N Perchloric acid and methanol. The mixture was vortexed using cyclomixer and centrifuged at 3000 rpm for 10 minutes. The clear supernatant thus separated was taken for spectral analysis.

#### 3.2. Steady state fluorescence measurement

The steady state fluorescence measurements in the visible region were performed using a Spectrofluorometer (Fluoromax – 2, SPEX, USA) at an excitation wavelength of 405 nm by scanning the emission monochromator ( $\lambda_{em} = 430 - 700$  nm). The excitation spectra were scanned between 340 – 580 nm, for 600 nm emission. Excitation and emission slit widths were set at 2 and 5 nm respectively for the measurement of fluorescence emission spectra and vice-versa for excitation spectra. The signals were detected using a red sensitive photomultiplier tube (R928 – Himatzu).

### 4. RESULTS

The excitation and emission fluorescence spectra were measured for both normal and tumor tissues extracted in perchloric acid – methanol mixture. The excitation scan was performed, by exciting the tissues in the wavelength region of

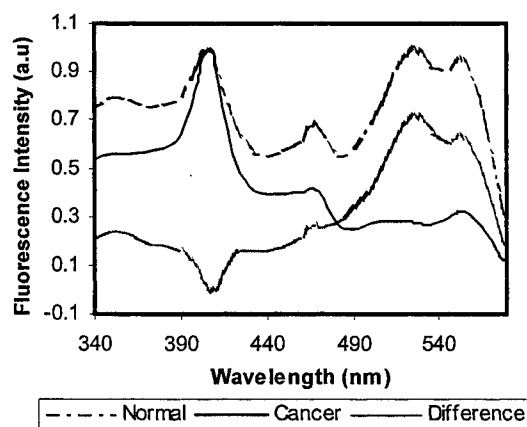


Fig. 1. Normalized Fluorescence excitation spectra for 600 nm emission

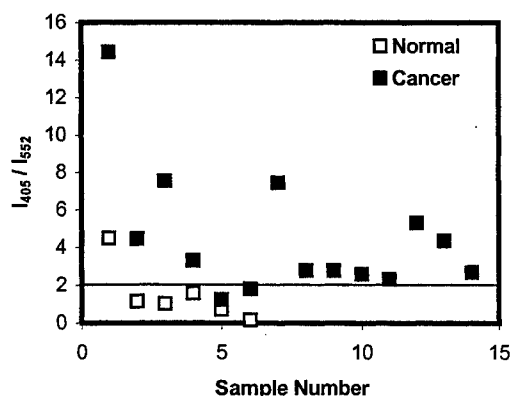


Fig. 2. Scatter plot of  $I_{405} / I_{552}$

340 – 580 nm and observing the emission at 600 nm. Fig.1 shows the normalized, average excitation spectra of both normal and cancerous tissue extracts along with their difference spectrum. Fig.1 shows the following salient features that discriminate normal tissues from cancerous tissues. The averaged excitation spectrum of normal samples shows three distinct peaks at 406, 524 and 552 nm, with almost same intensity. However, the averaged excitation spectrum of cancerous samples has a primary peak at 406 nm and two secondary peaks at 467 and 552 nm.

In order to quantify the results, we introduced the ratio parameter  $R_1 = I_{405} / I_{552}$  at 600 nm emission, where  $I_{405}$  and  $I_{552}$  are the relative excitation intensities at 405 and 552 nm respectively. Fig.2 shows the scatter plot of  $R_1$  for both normal and cancerous tissues.

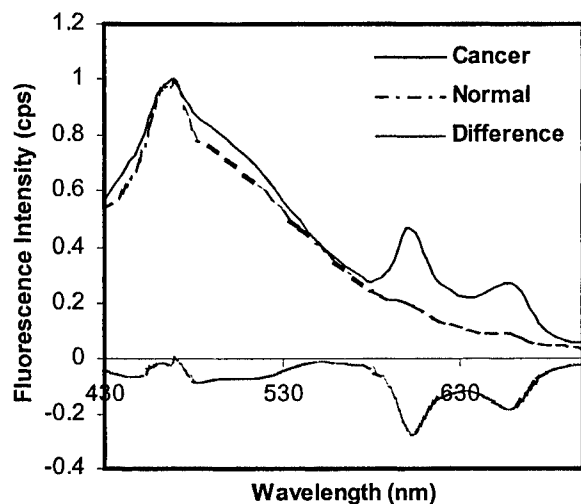


Fig.3. Normalized fluorescence emission spectra at 405 nm excitation

The emission scan of both normal and cancerous oral tissues were performed at 405 nm excitation ( $\lambda_{em} = 430 - 700$  nm). Fig.3 shows the normalized average fluorescence emission spectrum of tissue extracts of normal and cancerous subjects, along with their difference spectrum. It is observed that the average fluorescence spectrum of normal subjects shows a primary emission peak at 475 nm. However, the average spectrum of cancerous tissue extracts shows two additional emission peaks at 605 and 660 nm, which are absent in the case of normal. To evaluate the potentiality of native fluorescence emission spectroscopy in discriminating cancer tissues from normal, two ratio parameters,  $R_2 = I_{470} / I_{600}$  and  $R_3 = I_{470} / I_{660}$  were introduced. Here  $I_{470}$ ,  $I_{600}$  and  $I_{660}$  are the emission intensities in the native fluorescence emission spectra of normal and cancerous tissues, for 405 nm excitation. Figs.4 and 5 show the scatter plot of  $R_2$  and  $R_3$  for normal and cancerous subjects.

## 5. DISCUSSION

Although oral lesions are visible and easily detected compared with other organs, they continue to be an important health concern, the population at risk from this cancer is ranked second in Asian countries because of the exposure to tobacco products and alcohol.<sup>10</sup> Patients are often left with severe cosmetic and functional difficulties resulting from this disease and its treatment. This is partly as a result of the late stage at which these cancers present. The most common symptom of cancer of the oral cavity is a sore in mouth; however, diagnosis is often delayed because the pain associated with ulceration occurs quite late in this disease. Detection and treatment of precancerous and early cancerous lesions would decrease the mortality associated with this disease.<sup>11</sup>

Policard is considered to be the first to have recognized the presence of endogenous porphyrins in tumors.<sup>12</sup> Later, Ghadially examined the fluorescence of endogenous porphyrins and identified it as being a mixture consisting mainly of protoporphyrin with traces of coproporphyrin.<sup>13</sup> He also photographed the red fluorescence from animal and from human tumors, under Wood's lamp illumination. Ghadially et al demonstrated that a possible reason for the phenomenon of autofluorescence is that it is the result of microbial synthesis of porphyrins in necrotic areas of tumors.<sup>14</sup> But others have suggested that the native fluorescence may be due to certain porphyrin compounds in the body, formed by the degradation of hemoglobin, which is responsible for the characteristic autofluorescence at 630 and 690 nm. Although there is controversy concerning the origin of native fluorescence of endogenous porphyrins, it is still considered to be an important tumor marker in the characterization of tissues.

In this context, we have made an attempt to use native fluorescence excitation and emission spectroscopy of tissue extracts in Perchloric acid – methanol mixture, for discriminating cancerous tissues from normal. We have measured the fluorescence excitation spectra of normal and cancerous tissue extracts for 600 nm emission (Fig.1). The native fluorescence emission spectra of normal and cancerous tissues were measured at 405 nm excitation (Fig.3). The average excitation and emission spectra were generated for the two groups of normal and cancerous tissues.



The peak at 406 nm observed in the average excitation spectra of both normal and cancerous tissues may be due to the Soret absorption band of porphyrins. The excitation peak at 524 nm observed in the spectrum of normal tissues and the peak at 552 nm in the case of both normal and cancerous tissues may be due to the Q band of porphyrins, as the typical absorption spectrum of the porphyrins consists of two parts : the Soret band at 380 – 420 nm and the Q bands in the 480 – 650 nm region.<sup>15</sup> This observation is in agreement with the results of Yang et al., who observed excitation peaks around 400, 500, 525 and 570 nm in the acetone extracts of cancerous tissues.

In order to evaluate the potentiality of native fluorescence excitation spectroscopy in discriminating normal from cancer, a ratio parameter  $R_1$  was introduced. Fig.2 shows that a critical value of 1.8 for  $R_1$  misclassifies one normal sample as cancer, resulting in a specificity of 83 %. Also,  $R_1$  misclassifies 1 out of 14 cancer samples as normal, resulting in a sensitivity of 93 %.

In the case of fluorescence emission spectrum, the additional secondary emission peaks observed at 605 and 660 nm for 405 nm excitation, are characteristic of cancerous tissues and they may be attributed to the presence of endogenous porphyrins. Hua et al. have observed  $\delta$ -ALA induced endogenous porphyrin emission peaks at 605 and 660 nm in the case of animal tumor tissue extracts.<sup>16</sup> The emission peak at 475 nm observed in both normal and cancerous tissue extracts may be assigned to enzyme bound NADH. In order to compare the diagnostic potentiality of native fluorescence emission spectroscopy of tissues with that of excitation spectroscopy, the ratio parameters  $R_2$  and  $R_3$  were introduced. Figs.4 and 5 show that a critical value of 3.8 for  $R_2$  and 7.8 for  $R_3$  classify only 3 normal samples as normal resulting in a relatively low specificity of 50 %. However, out of 14 cancerous tissues, two were misclassified as normal resulting in a sensitivity of 86%.

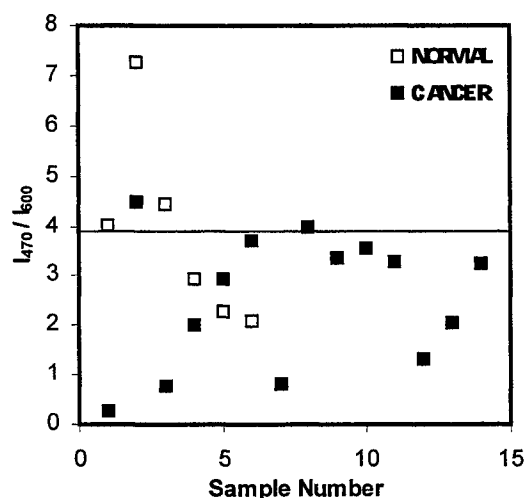


Fig. 4. Scatter plot for  $I_{470} / I_{600}$

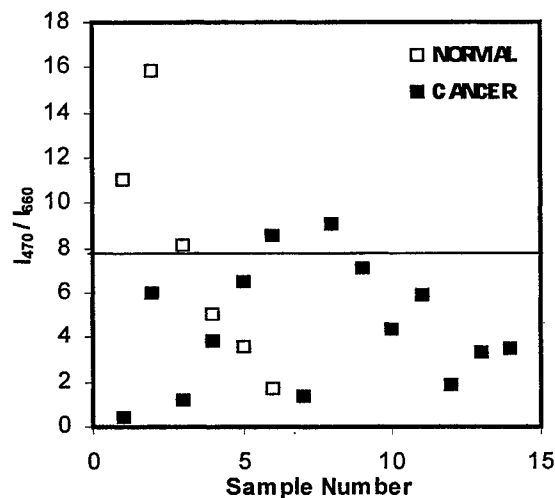


Fig. 5. Scatter plot for  $I_{470} / I_{660}$

It should be emphasized here that many of the reported works are based on the applications of ultraviolet excitation spectroscopy of tissues for the discrimination of cancer from normal. In this regard, we suggest that the present study using visible fluorescence excitation spectroscopy may eliminate the use of ultraviolet radiation in diagnostic oncology. Our results suggest that native fluorescence excitation spectroscopy of tissue extracts yields relatively higher sensitivity and specificity for discriminating cancerous tissues from normal, when compared to fluorescence emission spectroscopy. However, in order to increase the diagnostic potentiality of the present technique using excitation spectroscopy, further studies are to be carried out in detail with more sample population.

## 6. ACKNOWLEDGEMENT

We thank Department of Science and Technology, Govt. of India for the research grant. The author N.V thank Council for Scientific and Industrial Research (CSIR), Govt. of India for the research fellowship

## 7. REFERENCES

1. Kriegsmair, M., R. Baumgartner, R. Knuelchel, H. Stepp, F. Hofstadter and A. Hofstetter, "Detection of early bladder cancer by 5-aminolevulinic acid induced porphyrin fluorescence", *J. Urol.*, **155**, pp. 105 – 110, 1996.
2. Regula, J., A. J. MacRobert, A. Gorchein, G. A. Buonaccorsi, S. M. Thorpe, G. M. Spencer, A. R. W. Hatfield and S. G. Bown, "Photosensitization and photodynamic therapy of oesophageal, duodenal and colorectal tumors using 5 aminolevulinic acid induced protoporphyrin IX – a pilot study", *Gut*, **36**, pp. 67 – 75, 1995.
3. Huber, R. M., F. Gamarra, A. Leberig, H. Stepp, K. Rick and R. Baumgartner, "Inhaled 5-aminolevulinic acid (ALA) for photodynamic diagnosis and early detection of bronchial tumors : first experience in patients", Abstract book of 6<sup>th</sup> IPA meeting, Melbourne, Australia.
4. Q. Peng, K. Berg, J. Moan, M. kongshaug and J. M. Nesland, "5-Aminolevulinic acid – based Photodynamic therapy : Principles and Experimental Research", *Photochem. Photobiol.*, **65(2)**, pp. 235 – 251, 1997.
5. R. R. Alfano and S. S. Yao, "Human teeth with and without caries studied by visible luminescent spectroscopy", *J. Dent. Res.*, **60**, 120 – 122, 1981.
6. R. R. Alfano, B. B. Das, J. Cleary, R. Prudente and E. J. Celmer, "Light sheds light on cancer – distinguishing malignant tumors from benign tissues and tumors", *Bull. N. Y. Acad. Med.*, **67**, pp. 143 – 150, 1991.
7. W. S. Glassman, G. H. Liu, G. C. Tang, S. Lubicz and R. R. Alfano, "Ultraviolet excited fluorescence spectra from non-malignant and malignant tissues of the gynecological tract", *Lasers Life Sci.*, **5**, pp. 49 – 58, 1992.
8. C. R. Kapadia, F. W. Cutruzzola, K. M. O'Brien, M. L. Stetz, R. Enriquez and L. I. Decklebaum, "Laser induced fluorescence spectroscopy of human colonic mucosa", *Gastroenterology*, **99**, pp. 150 – 157, 1990.
9. N. Vengadesan, P. Aruna and S. Ganesan, "Characterization of native fluorescence from DMBA-treated hamster cheek pouch buccal mucosa for measuring tissue transformation", *Br. J. Can.*, **77(3)**, pp. 391 – 395, 1998.
10. C. C. Boring, T. C. Squires and T. Tony, Cancer statistics, *CA Cancer J. Clin.*, **41**, pp. 19 – 36, 1991.
11. S. R. Baker, Malignant neoplasms of the oral cavity, In *Otolaryngology – Head and Neck Surgery*, Cummings CW, J. M. Fredrickson, L. A. Harker, C. J. Krause and D. E. Schuller. (eds) pp. 1248 – 1305, Mosby Year Book : St. Louis.
12. A. Policard, "Etude sur les aspects offerts par des tumeurs experimentales examinees a la luminere de Wood", *Compte – rendus Soc. Biol.*, **91**, pp. 1423 – 1424, 1924.
13. F. N. Ghadially and W. J. P. Neish, "Porphyrin fluorescence of experimentally produced squamous cell carcinoma" *Nature*, **188**, pp. 1124, 1960.
14. F. N. Ghadially, W. J. P. Neish and H. C. Dawkins, "Mechanisms involved in the production of red fluorescence of human and experimental tumors", *J. Path. Bact.*, **85**, pp. 77 – 92, 1963.
15. Y. L. Yang, Ye YM, Li FM, Li YF and Ma PZ, "Characteristic autofluorescence for cancer diagnosis and its origin", *Lasers Surg. Med.*, **7**, pp. 528 – 532, 1987.
16. Z. Hua, S. L. Gibson, T. H. Foster and R. Hilf, "Effectiveness of  $\delta$ -Aminolevulinic acid –induced Protoporphyrin as a Photosensitizer for Photodynamic therapy *in vivo*", *Can. Res.*, **55**, pp. 1723 – 1731, 1995.

## **SESSION 2**

### **Light-Scattering Biopsy I**

# Light scattering microscope as a tool to investigate scattering heterogeneity in tissue

Alois K. Popp<sup>\*a</sup>, Megan T. Valentine<sup>a</sup>, Peter D. Kaplan<sup>b</sup>, David A. Weitz<sup>a</sup>

<sup>a</sup> DEAS and Physics Department, Harvard University, Cambridge, MA, 02138

<sup>b</sup> Unilever Research U.S., Edgewater, NJ, 07020

## ABSTRACT

Rayleigh light scattering has not yet been used for quantitative investigations of heterogeneous systems. Preconditions for such an experiment are a well defined scattering geometry and independent information about the local state of the sample. We have designed a new instrument that meets these criteria: a light- scattering microscope with simultaneous imaging. We demonstrate the ability to characterize local differences within one tissue type as well as global differences between tissue types. Real space images of the sample are taken by normal video microscopy techniques. The light scattering pattern is analyzed by the evaluation of wave- vector dependence (form factor) and scattering direction of the scattered intensity. Statistical analysis of scattering patterns show what is important for the characterization and classification of tissues and heterogeneous structures. Real space images provide context for scattering analysis. The light scattering microscope is a powerful tool for characterization of local structural order in inhomogeneous structures like tissues.

**Keywords:** Rayleigh light scattering, tissue optics, static light scattering, microscopy, heterogeneities

## 1. INTRODUCTION

In the pursuit of non-invasive measures of physiology and structure, the field of tissue optics has been growing rapidly in the 1990s. Many applications of tissue optics rely on differences in light scattering and absorption between different tissue types, such as tumor and non- tumor <sup>1, 2</sup>. Focussed on understanding these differences, a significant literature has appeared on the origin of light scattering in tissue <sup>3, 4</sup> (and references therein).

Researchers have primarily taken three different experimental approaches:

- (1) Photon transport measurements of tissue <sup>3, 5-11</sup> or tissue phantoms <sup>12-15</sup>, using various experimental geometries. Bulk tissue is best described as turbid media. Transport measurements focus on measuring bulk quantities like absorption, transmission or reflection coefficients. The values of these coefficients vary due to the physiological conditions of the sample as well as due to species- specific variability and differences in the techniques <sup>2, 16</sup>.
- (2) Averaged scattering experiments from dilute suspensions of cells and organelles to find the structures that are the main contributors to the light scattering from tissue <sup>17-20</sup>. It has been tried to relate the also measured optical properties of the tissues to the scattering from constituent organelles <sup>17</sup>.
- (3) Scattering measurement from excised tissue. Up to now, most of these investigations focussed on measuring average tissue scattering properties from mounted slices <sup>21, 22</sup>, using tissue slices of thicknesses between 100 and 1000  $\mu\text{m}$ .

Furthermore, various models have been developed for these approaches to describe the experimental results from transport measurements <sup>3, 23-25</sup> and light scattering from cells and cell suspensions theoretically <sup>26, 27</sup>.

This report is a novel example of the third approach. Working with thinner excised tissue slices (20  $\mu\text{m}$ ), we performed simultaneous microscopic imaging and scattering measurements of numerous small regions. The report discusses the technique, the differences between tissues and analyzes both the aggregate and individual statistical properties of scattering patterns with an eye towards describing the microscopic origins of light scattering in tissue. The principal result is that extra- and super-cellular tissue organization is responsible for a large fraction of the most distinctive qualitative features of scattering patterns.

We study the optical properties of thin unstained tissue slices with a newly designed light scattering microscope <sup>28</sup>.

\* Correspondence: Email: [alpopp@deas.harvard.edu](mailto:alpopp@deas.harvard.edu); Telephone: 617 496 8049; Fax: 617 496 3088

This microscope-based light-scattering apparatus allows us to both observe real space images and simultaneously perform static light scattering measurements. By using a collimated beam in the sample plane and imaging the sample simultaneously, we can select the scattering volume of interest and control the size and placement of the beam. The scattered light is imaged onto a CCD-detector. Previous attempts to use the microscope as a scattering platform either used a highly divergent beam in the sample plane which made interpreting static light scattering difficult<sup>29-31</sup>, or did not include imaging<sup>32</sup> which provides an intuitive if not always formal tool to help unravel scattering patterns.

The beam is not larger than 70  $\mu\text{m}$  in diameter. Therefore, we can directly relate scattering to the structures the light is scattered from by imaging on a lengthscale at which heterogeneities in the tissue can be resolved. Without a traditional, image based view of heterogeneities we see no way to understand the connection between scattering patterns and tissue structure. Little is known about how variations in tissue organization and structure contribute to light scattering in tissue. We do know that tissues show specific heterogeneities of sizes and organization. Hair, pores, sweat glands, epithelial layers, collagen fibers, lung alveoli, bile ducts and capillaries are only a few examples.

The data from light scattering experiment consists of the two-dimensional intensity distribution of the scattered light, which we can relate to the scattering angle by a simple calibration procedure and derive both the azimuthal averaged and fully anisotropic static form factor from the intensity distribution. These patterns are analyzed with statistical methods. But we can use the real space images to check on which structures the light is scattered from, a uniquely useful feature. We have successfully applied our technique to investigate heterogeneities inside different tissue types and are able to measure differences between tissue types due to the presence of specific heterogeneous structures. A tissue consisting of a well organized structure like striated muscle has a unique scattering pattern showing strong anisotropy in scattering.

## 2. EXPERIMENTAL METHODS

### 2.1. Design of the static scattering microscope

By using a commercially available inverted microscope (Leica DM-IRBE) with additional custom-made optical and mechanical components as shown in Figure 1, we perform simultaneous scattering measurements and imaging. A laser beam (Coherent Innova 304, 514.5 nm) is launched from a fiber optic coupler that is mechanically mounted to an extension of the microscope above the condenser. A series of neutral density filters and a linear polarizer attenuates the laser intensity to typically less than 50  $\mu\text{W}$ . A beamsplitting cube splits the laser intensity into two paths of equal intensity (accomplished by rotation of a linear polarizer). One path leads directly to a photodiode that monitors the input laser intensity, the other beam is coupled into the light path of the microscope by a dichroic mirror. It scatters from the sample and is collected at the detector. On the collection side of the sample, the objective lens of the microscope (plan-apochromatic, 100x magnification) with high numerical aperture (N.A.=1.4) collects both scattered light and unscattered transmitted beam. By using index-matching immersion oil to eliminate the air-glass interfaces at the condenser and objective, we can collect scattered photons up to an angle close to 90 degrees from aqueous samples. In the back focal plane of the objective (BFPO), all parallel rays are brought to a point. By collecting light in this plane, we collect photons through the same scattering angle,  $\theta$ . In the BFPO, the scattering angle depends only on the distance between the collection point and the center of the BFPO,  $\delta x \sim \sin \theta$ . In most objectives, the BFPO is inconveniently located just inside the objective's exit pupil. We built a projection system to re-image the BFPO in a more accessible plane above the internal housing of the microscope, through a phase telescope mounted on the camera port of the trinocular head. In the projected BFPO, we place a beamblock to remove the unscattered transmitted light. The beamblock consists of a 1mm diameter metal rod. The beamblock obscures light scattered at angles less than 3 degrees. One final relay lens re-images the scattering plane and beamblock, onto a 16 bit cooled CCD detector (Princeton Instruments, Model CCD-512SF) with a 512x512 array of 24  $\mu\text{m}$  square pixels. The intensity at each pixel can be measured using a variety of exposure times to increase dynamic range.

The incident laser beam is focussed to a point on the back focal plane (BFP) of the condenser, ensuring a collimated beam in the sample plane. With our design, a 1mm diameter laser beam forms a spot of 40 microns with a divergence angle of less than 10 mrad. We can increase or decrease the illuminated spot size with the addition of an enlarging or reducing telescope before the focussing lens at the field iris. Additionally, samples can be imaged via conventional bright-field microscopy by diverting a portion of the illuminating light to the side camera port, where a 8 bit CCD camera can record the real space images. We place a filter before the camera to block out the transmitted and scattered laser beam, and allow only the red portion of the illuminating halogen source to pass. This allows us to record both the real space image from the brightfield microscopy and the corresponding Fourier space image from the static light scattering. We perform several calibrations for the CCD detector, namely correcting for read-out noise, thermal noise, offset and pixel to pixel variations due to the quantum efficiency and area of each pixel by taking several pictures of a dark background and a uniformly illuminated ("flat") background. There is a final correction for flare at low angles. Flare is measured by scattering from an empty or solvent

filled sample chamber to find the amount of stray light. This flare intensity is then subtracted from the experimental data using an appropriate scaling factor to reflect the differences in input laser intensity between the two images. An attenuation factor is also used to compensate for the attenuation of the beam by the sample compared to the empty sample chamber. These corrections are typically small compared to the scattering intensity at even fairly large angles.

## 2.2. Raw data conversion and data analysis

On the CCD detector, we collect the intensity as a function of the radial distance of the scattered light towards the unscattered beam. To convert this distance- dependent function into a wave- vector dependence ('form factor'), we have to relate the radial distance to the wave vector of the beam and find the proportionality factor between them. We know that the radial distance of the scattered light on the BFPO (and therefore on the CCD detector) is proportional to the sine of the scattering angle:  $\delta x \sim \sin \theta$ . The (sample dependent) proportionality constant can be found by scattering from an object showing a calculable scattering pattern. We used a graticule for this calibration: Calculating the scattering angles of maxima and minima from the known distances of the gridlines ( $d$ ) using Bragg's law and measuring the appropriate positions of maxima and minima on the CCD detector ( $\delta x$ ), we can calculate the conversion factor  $C$ :

$$\sin \theta_G = \frac{m * \lambda}{d} = C * \delta x, \quad (1)$$

with  $\lambda$  being the wavelength of the laser beam and  $m$  the order of the maximum.

Using Snells law, we can apply this conversion to any sample  $S$  with known refractive index  $n_S$ :

$$\sin \theta_S = \frac{n_G}{n_S} * \sin \theta_G \quad (2)$$

Once the conversion from the distances into scattering angles is known, we can calculate the scattering wave vector  $q = 4\pi n \sin(\theta/2)/\lambda$ , where  $n$  is the index of refraction of the sample, and  $\lambda$  is the wavelength of the incident beam. In our data analysis, we have divided our scattering patterns into concentric rings of fixed wave- vector around the beam- center and have calculated the average intensity of each of all pixels inside the ring. Results are shown in section 3.

To present a picture of the measured sample which is as close to the average and to investigate the content, to which heterogeneities contribute to the average appearance of the sample, we have taken between 25 and 35 images and measurements of randomly selected spots on the sample. Furthermore, we have screened regions containing interesting heterogeneities to investigate the change in scattering from homogenous tissue to the heterogeneity. The measured and corrected scattering patterns have been converted into form factors. Additionally to that, anisotropy in the scattering patterns has been determined by calculating average intensities on a radial grid. The angular regions between  $0^\circ$  and  $10^\circ$  and between  $350^\circ$  and  $360^\circ$ , which were covered by the beam- block, have not been taken into account. In both cases the averaged intensities have been divided by the exposure time and the intensity of the incoming laser beam to allow comparison of measurements taken with different values of these parameters.

## 2.3. Sample processing

We have tried to keep the sample processing technique as simple as possible to prevent further artifacts due to sample processing<sup>3</sup>. Lung, skin and muscle have been directly frozen and stored in liquid nitrogen or a  $-70^\circ\text{C}$  freezer until the slicing procedure. The *Xenopus Sartorius* muscle and has been stored, sectioned and processed like the porcine samples. The frozen tissue samples were sectioned 20 microns thick, using a standard cryomicrotome. The slices were directly transferred from the knife to a small coverslip (18 mm x 18 mm), which was glued onto a microslide, using ultravacuum grease to seal the sample airtight. The samples were stored for 2 weeks at  $-20^\circ\text{C}$  or at  $4^\circ\text{C}$  overnight, if measured the next day.

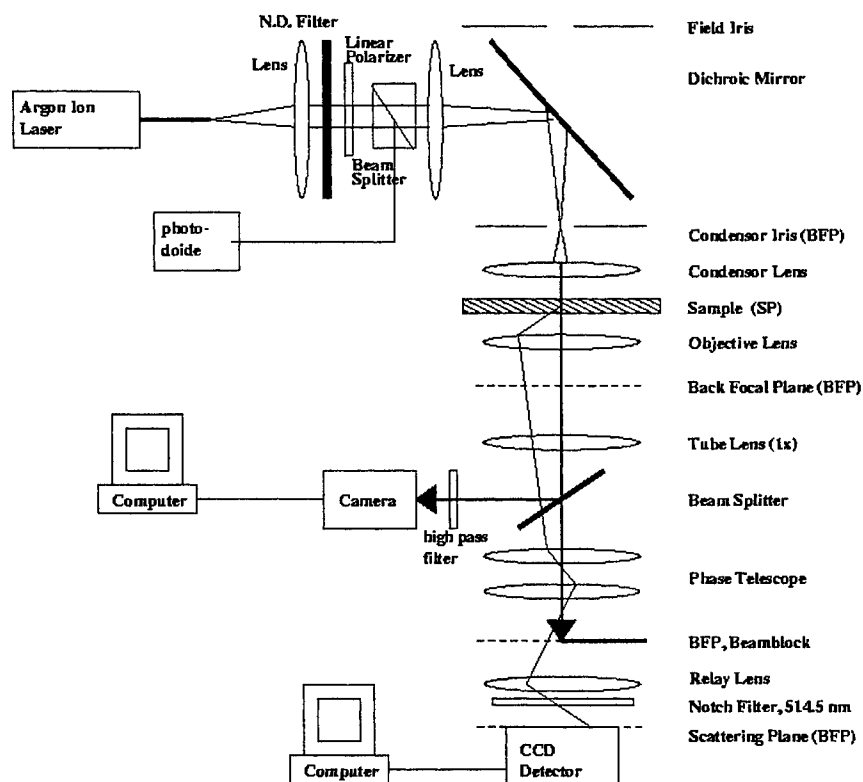


Fig. 1. Opto-mechanical design of the light scattering microscope.

### 3. RESULTS

#### 3.1. Scattering from muscle

The aim for this study was to use a well defined sample to compare visible and well understood structure, striated muscle, to scattered intensity patterns. In comparison to that, samples consisting of muscle fibers from more randomly, but predominantly crosssectionally oriented muscle have been measured. The obvious differences between orientations should be obvious in the scattering pattern. This represents a first step towards working on less obviously distinguishable tissues.

Striated muscles are a well described system<sup>33</sup>. The tissue is highly ordered, containing elongated cells enriched in actin- and myosin filaments giving the muscle its characteristic polar structure. We prepare longitudinal sections from precisely excised *Xenopus Sartorius* muscle and Porcine leg muscle. The randomly sectioned porcine muscle shows no directionality. The fiber bundles are randomly oriented, often perpendicular to the surface. In our approach to relate scattering from small, well defined spots of a size comparable to that of a muscle fiber bundle to the structure and morphology of the tissue, we took more than 30 single measurements of two slices of both tissues. Examples, real space images together with the scattering patterns, are shown in Fig.2. A comparison of the scattering images of Fig. 2 by eye shows the influence of orientation: The scattering pattern of the *Xenopus Sartorius* muscle has a preferred direction of scattering, whereas the porcine muscle tissue shows a relatively isotropic pattern. We calculated the form factor and directional analysis as described in the section 2.2., taking a value of 1.41 for the refractive index of muscle from the literature<sup>2</sup>. Not surprisingly, the pronounced difference in scattering patterns does not survive the process of azimuthal averaging - both tissue types obey the same power law, showing

no difference in decay between the highly ordered and the unordered muscle sample (Fig. 3, upper graph). This behavior has also been observed after averaging over all measurements (Fig 6). Differences in form factors have been found in terms of the total scattered intensity and the fine structure of the form factor of the Sartorius muscle. The observed differences in total scattered intensity can be due to a number of effects and need not be the result of differences in tissue organization, as discussed in <sup>2, 3</sup>. The differences in the anisotropy of the scattering pattern, however, are due to differences in tissue organization.

While, without azimuthal sensitivity, we find little to separate the two muscles, the directional analysis found striking differences between the well ordered Sartorius muscle and the porcine leg (Fig. 3, upper graph). Repeated rotation of the sample resulted in a change of the orientation of the fibers and therefore in the orientation of the streak-like feature seen in the scattering pattern, as shown in the directional analysis of three consecutive measurements after rotation of the sample (Fig.3, lower graph). With this experiment, we have shown that we can directly relate scattering pattern and microscopic image in the case of ordered tissue structures like muscle fibers oriented parallel to the surface of the coverslip. A detailed analysis of the preferred scattering direction showed maxima and minima in intensity along the streak-like features of the intensity distribution. They are also the reason for the fine-structure of the form factor of this sample. These need to be analyzed in detail, because they might be the contribution of cellular and sub-cellular components to the scattering, like previous experiments in backscattering geometry have shown <sup>34</sup>. Having understood the fine-structure, we might be able to relate our findings to tissue types that don't show a pronounced scattering in one direction. The ultimate aim is to use our knowledge about the origin of these features to explain the contribution from cellular components to scattering for other tissue types as well.

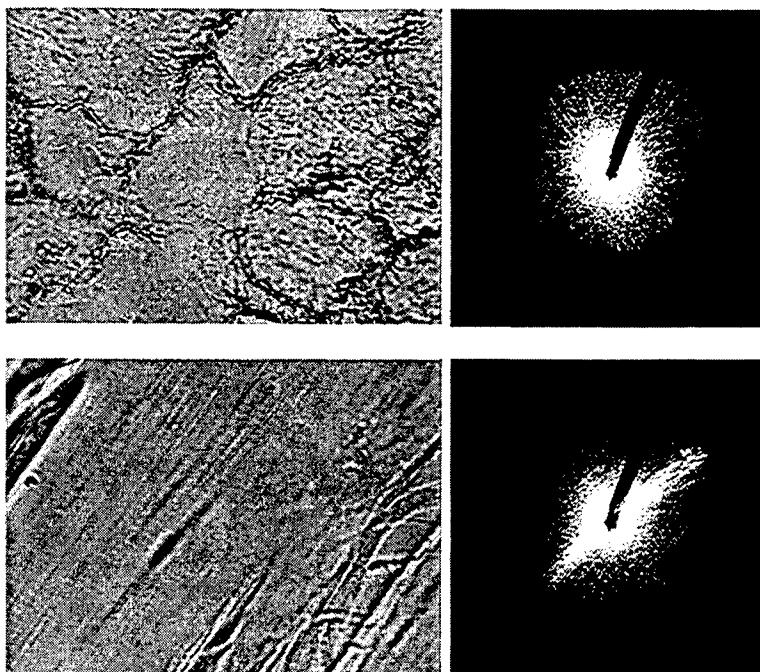


*Figure 2: Real space images (left) and scattering patterns (right) from different muscular tissues. On the upper half, predominantly crosssectional oriented fibers from a porcine leg muscle are shown. In the lower half, Xenopus Sartorius muscle with fibers oriented parallel to the surface of the coverslip can be seen. The real space images show a field of view of 60  $\mu\text{m}$  length. The scattering patterns are intensity distributions and show bright spots at high scattered intensity. Images show the surface the incident laser beam is directed to.*



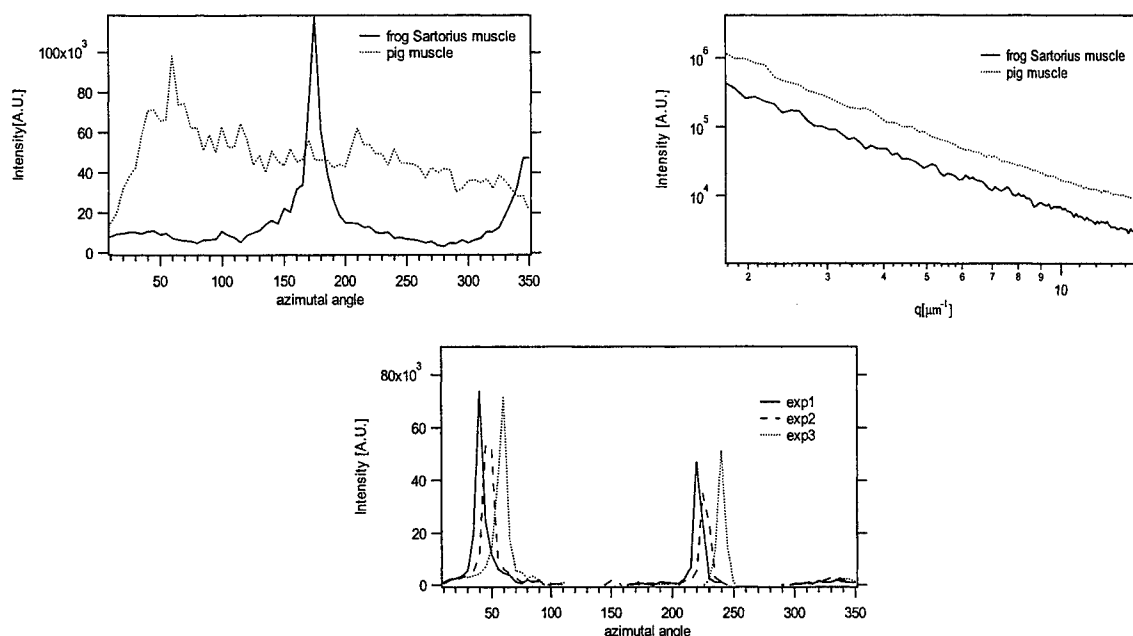


Figure 3: Directional analysis (upper right graph) and form factor analysis (upper left graph) of measurements from porcine muscle and *Xenopus Sartorius* muscle. Rotating the Sartorius muscle sample rotates the scattering pattern (lower graph).

### 3.2. Investigation of heterogeneities

Unlike muscle, many tissue types are inhomogeneous. Many organs consist of more than one tissue type, often showing super-cellular structures typical and functionally important for the organ. Some tissues like skin show structures consisting of a-cellular biological matter. Dermal tissue, for example, consists mainly of keratin fibers. Structures inside the skin like pores, sweat glands and hair lead to the idea that these heterogeneities contribute to measured average quantities in an important way. Furthermore, the stratum corneum shows a complex surface topology on a microscopic length scale, which contributes to the appearance of skin. As an example, we concentrate on the measurement of a small, well defined heterogeneity like a hair. Hairs in the tissue are surrounded by dense accumulations of fibrous connective tissue belonging to the dermis. A thickened basal lamina, the glassy membrane, separates the dermis from the epithelium of the hair follicle. The outer layers of follicular epithelium form at the external root sheath, followed by the internal root sheath and the cortex of the hair. As the material properties of tissue and hair (e.g. scatterer density, refractive index) that contribute to light scattering are different from one image to another, a prominent change in scattering patterns can be expected. We have performed our measurements in a scanning mode, probing the region containing a hair in a horizontally sectioned dermal slice of porcine skin. We took several measurements between regions of homogeneous tissue and the center of the hair. Here, the observed scattering patterns changes, when the hair is approximated, from an isotropic to a highly anisotropic scattering pattern. In the experiments with skin, the decay of the form factor does change with position in the tissue (Fig. 5). While approaching the root sheaths, the single form factors show a slower decay. It seems, however, that under certain conditions the form factor can be used to describe differences between tissues and heterogeneities present therein. A possible explanation for this effect is given in section 3.3., as this behavior of the form factor is also valid for averages of form factors.

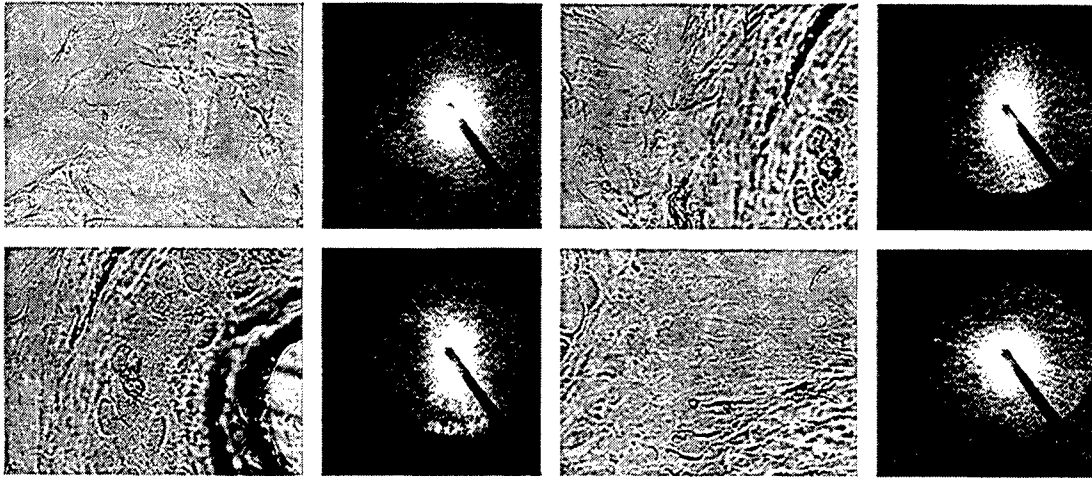


Fig 4: Scattering from skin in a scanning mode. Scattering images and real space images of a selection of experiments are shown. From upper left to lower right: Dermal tissue (experiment 25), approaching external root sheath (exp 33), approaching an internal root sheath (exp. 38), scattering from inhomogeneous tissue away from the hair. The form factors of each of these measurements are shown in Fig 5.

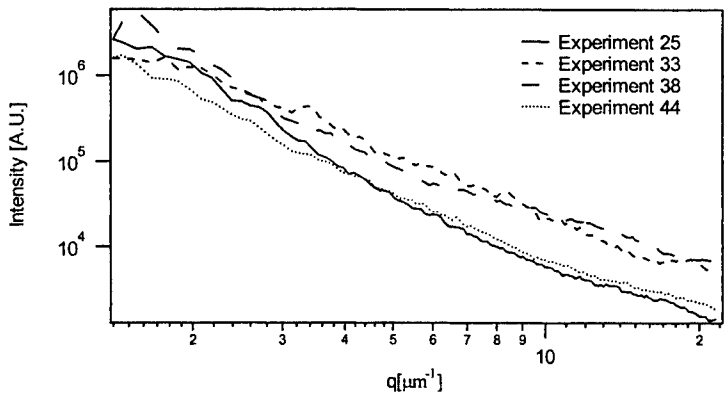


Figure 5: The decay of the form factors shows differences between tissue from the dermis (Experiments 25 and 44) and the heterogeneous region close to a hair (Experiments 33 and 38): The form factors of measurements approaching the external (Exp.33) or internal root sheath (Exp. 38) decay slower.

### 3.3 Averaging single measurements

To express the average optical properties of our samples, calculated as averaged form factor and anisotropy, we have simply added up the single form factors and anisotropies of every measurement and divided by the number of measurements. Averaging smoothes the fine structural features of single measurements and leads to a simpler description of the optical properties of a sample. Form factors calculated from raw data of single measurements often cannot be fitted to a power law. However, these averaged properties still contain the measured heterogeneities. Whenever heterogeneities are present, their optical properties contribute also to the average. Having measured several horizontally sectioned samples of porcine skin in various depths, we have calculated a simple average of the form factors for each slice. These average form factors have been fitted to the power law for the wave- vector dependence  $q^{-x}$  in a dynamic range between  $q = 2.7$  and  $11.9 \mu\text{m}^{-1}$ . For better comparison, the form factors have been normalized to the first point of the power law fit (Fig. 6). The value of the power

exponent  $x$  for all our skin samples ranged between  $-3.2$  and  $-3.7$ . Using an application of the theory of fractal dimensions to light scattering, the power law coefficient can be described in terms of fractal dimension:  $x = 6 - D_f$ . This law expresses our results in fractal dimensions. For all porcine skin samples,  $D_f$  reached values between  $2.3$  and  $2.8$ . A  $D_f$  between  $2$  and  $3$  is unique for randomly oriented surfaces<sup>35</sup>. Rayleigh scattering (Intensity  $\sim q^{-4}$ ) for example, can be explained to be scattering from perfectly smooth random surfaces.  $D_f$  increases towards  $3$  with increasing roughness of the surface. Microscopic imaging of our skin samples showed a relatively heterogeneous surface, especially in the epidermal layer. All other tissues showed a much slower decay coefficient  $x$  being about  $-2.5$  (Fig. 7). We assume that the decay of the form factor of skin tissue is mostly due to scattering from surfaces. With the approach of the fractal dimension, one could also explain the slower decay of the single form factors of the tissue measurements (Fig.5) by taking into account the complex surface topology around the hair. In other tissues, the substructure seems to be much more important. We are fully aware of the fact, that the fractal dimension approach includes the danger to oversimplify the complex material properties of tissue and heterogeneities which are probed by our scattering technique. For example, the nature of the material the light is scattered from, is not explained by this approach.

We have already shown that a form factor is not always the appropriate measure for the optical properties of tissue and that other forms of analysis like a calculation of the preferred scattering direction have to be used to investigate the optical properties of tissue precisely. Furthermore, more elaborate statistics tools have to be used in the future for our approach, as we are dealing with numerous measurements. Mean and standard deviation as well as the analysis with higher moments (data not shown) have already been shown to be useful to describe the differences in scattering directions. With the help of Fourier analysis, one might be able to compare the radial shape of single scattering patterns. Another approach to the analysis might include pattern recognition tools.

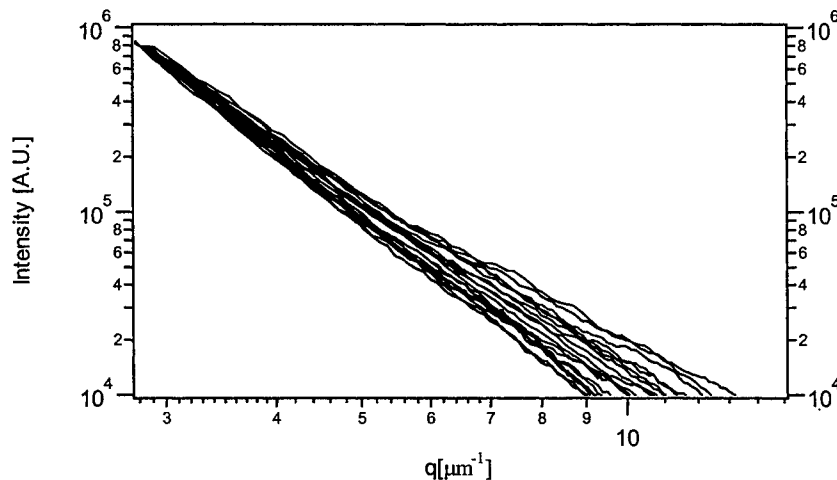


Figure 6: The azimuthally and spatially averaged form factors of 18 slices of porcine skin, normalized to the first point used for fitting. The decay can be fitted to a power law and has been found to result in a fractal dimension between  $2.3$  and  $2.7$ , which could be interpreted as scattering from randomly oriented surfaces of different roughness.

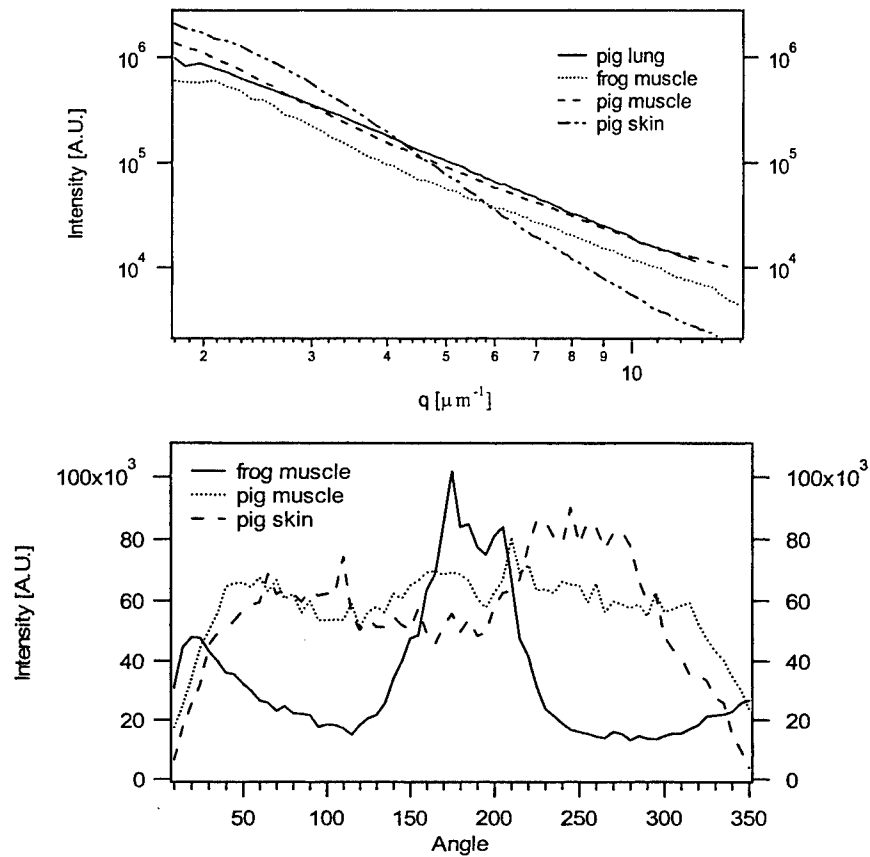


Figure 7: Averaged form factors and directional analysis for different tissues. The form factor decays with a power law coefficient of  $-3.7$  for skin, whereas all other tissue types show a decay with a coefficient close to  $-2.5$ . Averaging of all measurements of a *Xenopus* muscle sample under fixed orientation shows the almost constant direction of the muscle fibers throughout the sample. The porcine muscle average showed no preferred orientation of the fibers. The porcine skin sample showed a vague preferred direction, most probably due to the selection of spots.

#### 4.CONCLUSIONS

In this report, we have shown our initial observations gained by applying the light scattering microscope to tissue. We set out to see whether and how to distinguish tissues on the basis of their light scattering patterns. This effort is motivated by the observation that a significant fraction of pathologists observations of tissue involve recognizing the presence and absence of structural order in tissue slices. We performed light scattering and imaging of multiple tissues, always looking at small ( $70\text{ }\mu\text{m}$ ) spots from  $20\text{ }\mu\text{m}$  slices. We observe significant differences due to super- and extra-cellular structures and heterogeneities in  $20\text{ }\mu\text{m}$  thick tissue – these differences would not be systematically accessible without the scattering microscope.

Several strategies were employed to distinguish between scattering patterns. First, we analyze numerous measurements on randomly selected spots, to show how these single experiments contribute to average scattering. In this analysis, we look at the power law that describes the decay of the averaged form factors. We found, that skin is distinct from other tissues as its form factor decays with approximately  $q^{-3.2}$  to  $q^{-3.7}$  for wave vectors between  $q = 2.7\mu\text{m}^{-1}$  and  $q = 11.9\mu\text{m}^{-1}$ . A possible explanation in terms of scattering from randomly oriented surfaces has been given. The same analysis does not segregate different types of similar tissues, striated porcine muscle sample and striated *Xenopus Sartorius* muscle, despite quite different structures -- the *Xenopus* muscle has well aligned muscle fibers parallel to the surface of the coverslip, whereas the (randomly sectioned) porcine muscle showed fibers of all different orientations. These organizational differences appear when the azimuthal dependence is analyzed.

Our technique is very useful for the detection and measurement of heterogeneities in tissues, as we have simultaneous microscopic information about the region where we perform our light scattering experiment. Measurements from a common heterogeneity in skin like a hair have been shown as example how a heterogeneity and the region around it can be measured in a scanning fashion revealing local ordering and anisotropies not previously accessible by scattering. We see clearly that with microscopic spatial resolution, tissues can not be treated as homogenous media and that large structures, ordering and anisotropy over tens of microns is responsible for a significant fraction of the total scattered light.

Using thin tissue slices as samples, we keep our investigation close to patho- histological studies. It is apparent that the scattering pattern contains a signature of local structure and organization<sup>30, 36, 37</sup>. Further development of the analysis of these scattering patterns may be useful for automatically detecting certain types of order. It is unlikely that light scattering without microscopy would be a reliable tool for pathology as the real-space image is needed to provide context for scattering measurement. In particular, the mode of operation is likely to be one in which a pathologist focusses on a suspicious region and collects a scattering pattern which can be analyzed quantitatively for relevant order and organization. Further development towards pathology requires focussed work on a particular problem of interest.

### ACKNOWLEDGEMENTS

We are grateful to acknowledge the generous gift of excised frozen *Xenopus Sartorius* muscle from Pierre Tijssens (University of Pennsylvania). Furthermore, we'd like to thank David Boas (Massachusetts General Hospital) for the porcine tissue, Jia Quian Ren (Massachusetts General Hospital) for the possibility to use the cryomicrotome in his institute and Marge Lehman (Unilever Research) for preparing preliminary samples. This work was partially supported by a grant from Unilever Research.

### REFERENCES

1. J. R. Mourant, I. J. Bigio, J. Boyer, R. L. Conn, T. Johnson, and T. Shimada, "Spectroscopic Diagnosis of bladder cancer with elastic light scattering," *Lasers in Surg. Med.* **17**, pp. 350-357, 1995.
2. J. B. Fishkin, O. Coquoz, E. R. Anderson, M. Brenner, and B. J. Tromberg, "Frequency-domain photon migration measurements of normal and malignant tissue optical properties in a human subject," *Appl. Optics* **36**, pp. 10-20, 1997.
3. V. V. Tuchin, "Light scattering study of tissues," *Physics- Uspekhi* **40**, pp. 494-515, 1997.
4. V. V. Tuchin, S. R. Utz, and I. V. Yaroslavsky, "Tissue Optics, Light-Distribution, and Spectroscopy," *Optical Engineering* **33**, pp. 3178-3188, 1994.
5. D. A. Boas and A. G. Yodh, "Spatially varying dynamical properties of turbid media probed with diffusing temporal light correlations," *JOSA A*, **14**, pp. 192-213, 1997.
6. S. J. Matcher, M. Cope, and D. T. Delpy, "In vivo measurements of the wavelength dependence of tissue-scattering coefficients between 760 and 900 nm measured with time-resolved spectroscopy," *Appl. Optics* **36**, pp. 386-396, 1997.
7. H. Liu, D. A. Boas, Y. Zhang, A. G. Yodh, and B. Chance, "Determination of optical properties and blood oxygenation in tissue using continuous NIR light," *Physics in Medicine & Biology* **40**, pp. 1983-93, 1995.
8. J. Laufer, R. Simpson, M. Kohl, M. Essenpreis, and M. Cope, "Effect of temperature on the optical properties of ex vivo human dermis and subdermis," *Phys. Med. Biol.* **43**, pp. 2479-2489, 1998.
9. J. B. Dawson, D. J. Barker, D. J. Ellis, E. Grassam, J. A. Cotterill, G. W. Fisher, and J. W. Feather, "A theoretical and experimental study of light absorption and scattering by in vivo skin," *Phys. Med. Biol.* **25**, pp. 695-709, 1980.
10. A. Wiel, G. Bruls, and C. v. d. Leun, "Forward scattering properties of human epidermal layers," *Photochem. Photobiol.* **40**, pp. 231-242, 1984.
11. S. P. Treweek and J. C. Barbenel, "Direct measurement of the optical properties of human breast skin," *Med. Biol. Eng. & Comput.* **34**, pp. 285-289, 1996.
12. S. L. Jacques, C. A. Alter, and S. A. Prahl, "Angular dependence of HeNe laser light scattering by human dermis," *Lasers in Life Sc.* **1**, pp. 309-333, 1987.
13. D. A. Boas, M. A. O'Leary, B. Chance, and A. G. Yodh, "Scattering of diffuse photon density waves by spherical inhomogeneities within turbid media: analytic solution and applications," *Proceedings of the National Academy of Sciences of the United States of America* **91**, pp. 4887-91, 1994.
14. M. A. O'Leary, D. A. Boas, B. Chance, and A. G. Yodh, "Experimental Images of Heterogeneous Turbid Media By Frequency- Domain Diffusing-Photon Tomography," *Optics Letters* **20**, pp. 426-428, 1995.
15. E. M. Sevick, C. L. Burch, and B. Chance, "Near-infrared optical imaging of tissue phantoms with measurement in the change of optical path lengths," *Advances in Experimental Medicine & Biology* **345**, pp. 815-823, 1994.

16. W.-F. Cheung, S. A. Pahl, and A. J. Welch, "A review of the optical properties of biological tissues," *IEEE J. Quantum Electron.* **26**, pp. 2166-85, 1990.
17. J. R. Mourant, J. P. Freyer, A. H. Hielscher, A. A. Eick, D. Shen, and T. M. Johnson, "Mechanisms of light scattering from biological cells relevant to noninvasive optical- tissue diagnostics," *Appl. Optics* **37**, pp. 3586-3593, 1998.
18. R. Drezek, A. Dunn, and R. Richards-Kortum, "Light scattering from cells: finite difference time domain simulations and goniometric measurements," *Applied Optics* **38**, pp. 3651-3661, 1999.
19. B. Beauvoit, H. Liu, K. Kang, P. D. Kaplan, M. Miwa, and B. Chance, "Characterization of absorption and scattering properties for various yeast strains by time-resolved spectroscopy," *Cell Biophys.* **23**, pp. 91-109, 1993.
20. B. Beauvoit and B. Chance, "Time-resolved spectroscopy of mitochondria, cells, and tissues under normal and pathological conditions," *Mol. Cell. Biochem.* **184**, pp. 445-455, 1998.
21. M. J. C. Van Gemert, S. L. Jacques, H. J. C. M. Sterenborg, and W. M. Star, "Skin optics," *IEEE Transactions on Biomedical Engineering* **36**, pp. 1146-54, 1989.
22. J. F. Beek, P. Blokland, P. Posthumus, M. Aalders, J. W. Pickering, H. J. C. M. Sterenborg, and M. J. C. v. Gemert, "In vitro double-intergrating sphere optical properties of tissues between 630 and 1064 nm," *Phys. Med. Biol.* **42**, pp. 2255-2261, 1997.
23. A. H. Hielscher, R. E. Alcouffe, and R. L. Barbour, "Comparism of finite- difference transport and diffusion calculations for photon migration in homogenous and heterogenous tissues," *Phys.Med.Biol.* **43**, pp. 1285-1302, 1998.
24. S. R. Arridge, M. Cope, and D. T. Delpy, "The theoretical basis for the determination of optical pathlengths in tissue: temporal and frequency analysis," *Phys.Med.Biol.* **37**, pp. 1531-1560, 1992.
25. D. J. Smithies and P. H. Butler, "Modeling the distribution of laser light in port-wine stains with the Monte- Carlo method," *Phys.Med.Biol.* **40**, pp. 701-731, 1995.
26. G. Videen and D. Ngo, "Light scattering multipole solution for a cell," *J.Biomed.Opt.* **3**, pp. 212-220, 1998.
27. J. M. Schmitt and G. Kumar, "Optical Scattering properties of soft tissue: a discrete model," *Appl. Optics* **37**, pp. 2788-2797, 1998.
28. P. D. Kaplan, V. Trappe, and D. A. Weitz, "Light Scattering Microscope," *Appl. Optics* **38**, pp. 4151-4157, 1999.
29. T. Maeda and S. Fujime, "Quasielastic light scattering under optical microscope," *Rev. Sci. Instr.* **43**, pp. 566-567, 1972.
30. I. Nishio, T. Tanaka, S.-T. Sun, Y. Imanishi, and S. T. Ohnishi, "Hemoglobin aggregation in single red blood cells of sickle cell anemia," *Science* **220**, pp. 1173-1174, 1983.
31. I. Nishio, J. Peetermans, and T. Tanaka, "Microscope laser light scattering spectroscopy of single biological cells," *Cell Biophys.* **7**, pp. 91-105, 1985.
32. P. S. Blank, R. B. Tishler, and F. D. Carlson, "Quasielastic light scattering microscope spectrometer," *Appl. Optics.* **26**, pp. 351, 1987.
33. L. P. Gartner and J. L. Hiatt, *Color Textbook of Histology*. Philadelphia: W.B. Saunders Company, 1997.
34. L. T. Perelman, V. Backman, M. Wallace, G. Zonios, R. Manoharan, A. Nusrat, S. Shields, M. Seiler, C. Lima, T. Hamano, I. Itzkan, J. VanDam, J. M. Crawford, and M. S. Feld, "Observation of periodic fine structure in reflectance from biological tissue: A new technique for measuring nuclear size distribution," *Physical Review Letters* **80**, pp. 627-630, 1998.
35. B. A. Fedorov, B. B. Fedorovov, and P. W. Schmidt, "An analysis of the fractal properties of the surface of globular proteins," *J. Chem. Phys.* **99**, pp. 4076-4084, 1993.
36. J. A. Peetermans, B. D. Foy, and T. Tanaka, "Accumulation and diffusion of crystallin inside single fiber cells in intact chicken embryo lenses," *Proc. Natl. Acad. Sci.* **84**, pp. 1727-1730, 1987.
37. J. A. Peetermans, E. K. Matthews, I. Nishio, and T. Tanaka, "Particle motion in single acinar cells observed by microscope laser light scattering spectroscopy," *Eur. Biophys. J.* **15**, pp. 65-69, 1987.

## Light scattering from cells: the contribution of the nucleus and the effects of proliferative status

J. R. Maurant\*, M. Canpolat, C. Brocker, O. Esponda-Ramos, T. Johnson,  
A. Matanock, K. Stetter, and J.P. Freyer

MS E535, Bioscience Division, Los Alamos National Laboratory, Los Alamos, NM 87545

### ABSTRACT

As part of our ongoing efforts to understand the fundamental nature of light scattering from cells and tissues, we present data on elastic light scattering from isolated mammalian tumor cells and nuclei. The contribution of scattering from internal structures and in particular from the nuclei was compared to scattering from whole cells. Roughly 55% of the elastic light scattering at high-angles ( $>40^\circ$ ) comes from intracellular structures. An upper limit of 40% on the fractional contribution of nuclei to scattering from cells in tissue was determined. Using cell suspensions isolated from monolayer cultures at different stages of growth, we have also found that scattering at angles greater than about  $110^\circ$  was correlated with the DNA content of the cells. Based on model calculations and the relative size difference of nuclei from cells in different stages of growth, we argue that this difference in scattering results from changes in the internal structures of the nucleus. This interpretation is consistent with our estimate of  $0.2\ \mu\text{m}$  as the mean size of the scattering centers in cells. Additionally, we find that while scattering from the nucleus accounts for a majority of internal scattering, a significant portion must result from scattering off of cytoplasmic structures such as mitochondria.

### 1. INTRODUCTION

Elastic light scattering is a fundamental interaction of light with tissue. As light travels through tissue it is scattered in a manner dependent on the wavelength of light and on the structures within the tissue. Measurements of light transport through tissue are consequently sensitive to the structural features of tissue. Structural features are what pathologists often use for disease diagnoses. Therefore the measurement of light transport through tissue can potentially be a diagnostic tool. When a probe is placed on the surface of the tissue the measurement of light transport can be made noninvasively. A noninvasive technique for tissue biopsy and pathology could have several advantages over conventional pathology methods. For example, information could be obtained in real-time, making immediate treatment possible. Additionally, complications and sedatives associated with tissue removal can be eliminated.

There are several noninvasive optical techniques under development. Some methods primarily probe biochemical aspects of tissue<sup>1,2,3</sup>, while other techniques, such as elastic scattering spectroscopy and optical coherence tomography (OCT) measure quantities directly related to light scattering<sup>4,5</sup>. In elastic-scattering spectroscopy broad band light is typically incident on the tissue through an optical fiber. Light that has passed through the tissue is then collected by an adjacent optical fiber and the spectral intensities are measured. The wavelength dependent spectrum of the tissue contains information about both the biochemical and morphological features of the tissue. Optical coherence tomography is an imaging technique in which the intensity of backscattered light from different locations within the tissue is measured at a resolution of  $\sim 10\ \mu\text{m}$ . The results described in this paper are most relevant to elastic-scattering spectroscopy and OCT, but also have relevance to the other optical techniques because all measurements of light transport in tissue are affected by light scattering.

The development of noninvasive optical methods requires a fundamental understanding of how light scatters from structures within tissue. From what structures does light scatter? How sensitive is light scattering to changes in structural features? Can the changes in specific structural features be quantitated from measurements of light scattering? Several research groups have begun addressing these questions. In earlier work, we demonstrated that the average effective radius of the scattering centers in a suspension of fibroblast cells is roughly  $0.2\ \mu\text{m}$ , and that there is a wide distribution of sizes with some scatterers being at least  $1\ \mu\text{m}$  in radius<sup>6</sup>. Therefore, much of the scattering must be from small structures within the nuclei and cytoplasmic organelles. Mitochondria have been suggested as a major source of scattering, particularly in cells containing a large fraction of mitochondria<sup>7</sup>, and chemically induced megamitochondria have been shown to alter the light scattering properties of cells<sup>8</sup>. Phase contrast microscopy reveals that cell membranes and nuclei cause significant phase shifts compared to other cell components and they therefore are expected to be a major source of light scattering<sup>9</sup>. Theoretical computations of light scattering from cells have elucidated some interesting facts regarding the contribution of nuclei. When

\* Correspondance: email: [jmourant@lanl.gov](mailto:jmourant@lanl.gov); Tel: (505) 665-1190

nuclei are modeled as a homogeneous structure, high angle scattering is not significantly altered as nuclear size is increased. However, when the nucleus is assumed to be heterogeneous, high-angle scattering increases with nuclear size<sup>10</sup>.

The general goal of this work is to examine light scattering from mammalian cells and nuclei using experimental methods. Light scattering processes related to the interface of the cell membrane with the surrounding media are investigated. The contribution of the nuclei to scattering from whole cells is also determined. Finally, evidence is presented that light scattering from both isolated nuclei and cells is correlated with DNA content, and the possibility that these changes in light scattering are due to changes in nuclear morphology is discussed.

## 2. METHODS

### 2.1 Angular dependent light scattering measurements

Measurements of angular dependent scattering were made as described earlier<sup>6</sup>. Briefly, a HeNe laser was incident on the solution of cells or nuclei. The angular dependent light scattering intensity was measured from 6° to 173° using a photomultiplier tube that was rotated around the sample. When a concentration of cells between  $1 \times 10^5$  and  $2 \times 10^5$  cells/mL was used, there was at most one scattering event over the pathlength of the sample cell. For a few of the measurements, a higher concentration of cells was used in order to overcome the background scattering from the media. By measuring different dilutions, it was determined that the effect of multiple scattering was negligible between about 30° and 150°. Nuclei were found to have a lower cross-section for scattering than cells and were measured at a concentration of  $5 \times 10^5$  nuclei/mL.

### 2.2 Elastic-scatter spectra of cell suspensions

Cells were suspended at a concentration of  $1 \times 10^8$  cells/mL in an open 15 mL volume (depth = 3 cm, length = 3 cm, width = 1.9 cm) sample cell. The container was black on the inside in order to minimize edge effects. Measurements were made with a fiber optic probe placed on the surface of the cell suspension. The optical fibers were 200  $\mu$ m in diameter, the center-to-center separation was 550  $\mu$ m and all fibers had a numerical aperture of 0.22. The optical illumination and detection instrumentation was described in an earlier publication<sup>11</sup>.

### 2.3 Calculation of scattering from spheres

Mie theory was used to calculate scattering coefficients, and the angular dependence of scattering from spheres. The code of Bohren and Huffman<sup>12</sup> was modified in order to calculate scattering from a distribution of sphere sizes. When modeling nuclei, they were assumed to be spherical in shape. The radius was taken to be  $\sim 4.5 \mu$ m as determined by image analysis. A standard deviation in radius of 2.2  $\mu$ m was used based on Coulter counter analysis of the nuclear volume distribution. A value of 1.39 was used for the index of the nuclei<sup>13</sup> and a measured value of 1.332 for phosphate buffered saline (PBS) was used for the medium index.

### 2.4 Cell growth

The highly tumorigenic rat fibroblast cell clone, MR1, used in this study was derived from myc-transfected Fisher 344 rat embryo fibroblasts by transfection with the point-mutated T24Ha-ras-oncogene<sup>14</sup>. Cell suspensions were obtained from monolayer cultures by treatment for 10 minutes with 0.25% trypsin in a phosphate-buffer (pH 7.4) containing 1 mM EDTA and 25 mM HEPES, followed by the addition of complete DMEM. Growth curve experiments showed that monolayers of MR1 cells reached a plateau in growth at  $\sim 6 \times 10^5$  cells/cm<sup>2</sup>. Based on these data, exponentially-growing cell suspensions were obtained from monolayer cultures harvested at a cell density of less than  $2 \times 10^5$  cells/cm<sup>2</sup>, while plateau-phase suspensions were obtained from monolayer cultures harvested at greater than  $6 \times 10^5$  cells/cm<sup>2</sup>. The proliferative status of each of these suspensions was confirmed by flow cytometric DNA content analysis as described below. Exponentially-growing cells were composed of 45% G<sub>1</sub>-phase cells, 40% S-phase cells and 15% G<sub>2</sub>-phase cells, while plateau-phase cells were 85% G<sub>1</sub>-phase, 5% S-phase and 10% G<sub>2</sub>-phase.

### 2.5 Counting of cells and nuclei and volume analysis of cells

Suspensions of cells and nuclei were counted and the distribution of cell volumes determined using an electronic particle counter (Coulter Electronics) essentially as described previously<sup>15</sup>. Cell volume distributions were processed to calculate a mean cell volume from the region not containing acellular debris. Mean volumes were also calculated from the nuclei distributions, but these underestimated the true volume of the nuclei as measured by image analysis (see below) by  $\sim 50\%$ , probably due to the presence of electrically-conductive pores in the nuclear membrane. However, nuclei volume distributions were used to both separate nuclei from smaller debris for accurate counting, and to estimate the degree of nuclei clumping.

### 2.6 Nuclei isolation

Two methods of nuclei isolation were used. One method used a sucrose gradient to separate the nuclei from other cell structures obtained upon lysing of the cell membrane. One set of experiments was performed with nuclei isolated by the this



method. We switched to a method adapted from a technique originally developed for flow cytometry of isolated nuclei<sup>16</sup> because it is much faster and resulted in fewer problems with nuclei clumping. Electronic volume distributions and image analysis (see below) documented that these procedures produced a suspension of isolated nuclei with little residual cytoplasm and less than 15% of the nuclei in clumps, primarily doublets. Nuclei recovery was 80-100% of the starting cell population. The final nuclei suspension were kept in ice-cold PBS until light scatter analysis.

## 2.7 Image analysis

Unfixed cells and nuclei were stained with Hoechst 33342, a DNA specific fluorophore and fluorescein isothiocyanate (FITC), a protein specific chromophore. Images were obtained using a fluorescent microscope interfaced to a computer workstation using commercial image analysis software. Filters were set first to image the Hoechst fluorescence, thereby obtaining an image of the nuclei, then changed to image the FITC fluorescence, thereby obtaining an image of the whole cell for the same microscopic field. The images were processed using standard software (NIH Image) to obtain geometric mean diameters from measurements of the major and minor axes of each nucleus/cell. A total of 200-300 measurements were averaged to obtain an estimate of the cell and nuclear size. Size measurements were essentially identical for the nuclei using the two different filter sets, demonstrating that the nuclei isolation procedure produced nuclei with little residual cytoplasm. Images of 10  $\mu\text{m}$  diameter fluorescent polystyrene spheres were collected for each filter set at the same microscopic magnification and processed using the same settings as for the cells and nuclei. All diameter values have been corrected using the diameter calibration obtained from the microsphere measurements.

## 2.8 Cell cycle analysis

DNA content flow cytometry was used to characterize the proliferative status of the cells as described in detail elsewhere<sup>16</sup>. Briefly, a suspension of  $1 \times 10^6$  cells in 1 mL of PBS was fixed in 70% ethanol, then washed with phosphate-buffered saline (PBS) and stained with the nucleic acid stain propidium iodide (50  $\mu\text{g/mL}$ ) in combination with RNase (100  $\mu\text{g/mL}$ ) to remove cellular RNA and ensure a fluorescence signal proportional to DNA content. DNA content histograms containing 10,000 cells were then collected using a commercial flow cytometer (FACSCalibur<sup>TM</sup>). DNA content histograms were deconvoluted using a commercial software package (Multicycle<sup>TM</sup>) to estimate fractions of cells in the G<sub>1</sub>-, S- and G<sub>2</sub>-phases of the cell cycle. These histograms had a G<sub>1</sub>-phase peak with a coefficient of variation less than 4%, allowing routine cell cycle analysis which can resolve the different phases with a 2-3% error.

## 2.9 Manipulation of the media's refractive index

The addition of protein to PBS increases its refractive index. Ovalbumin or BSA (3 gm/ml) were added to PBS, mixed and then filtered through 0.4 and 0.2  $\mu\text{m}$  filters to remove undissolved protein. The exact refractive index of the protein solutions was measured based on the principal of minimum deviation<sup>17</sup>.

# 3. RESULTS

## 3.1 Scattering from internal cellular structures

In order to determine how much of the elastic light scattering was from the cell nucleus or other intracellular structures and how much was related to the cell membrane interface with PBS, we made measurements of cells in media with different indices of refraction. The underlying principle of these experiments is that when the index of refraction difference between the scatterer and the surrounding media is reduced, the intensity of scattering will be reduced<sup>12</sup>. Therefore, when the index of refraction of the medium outside a cell is increased so that it is closer to that of the cell, scattering from the interface between the cell membrane and the external medium will be reduced. Scattering from internal cellular structures, however, will not be affected. For the experiments, equal numbers of cells were suspended in either PBS, with a measured refractive index ( $n$ ) of 1.332, or in a PBS based protein solution. Two sets of measurements were performed. In one set scattering from cells suspended in BSA with  $n = 1.345$  were compared to scattering from cells suspended in PBS. In the other set of measurements, scattering from cells in ovalbumin solution with  $n = 1.343$  were compared to scattering from cells suspended in PBS. Analysis of the size distributions of cells in the different media before and after light scatter assay demonstrated that there were no measurable changes in cell size induced by incubation in these protein solutions. Cell counts before and after light scatter measurement showed a decrease in cell number of <5% during the measurement, probably due to cell adherence to the measuring chamber. Results calculated from our angular dependent scattering measurements are shown in Figure 1. The scattered light intensity at small angles ( $< 20^\circ$ ) was significantly greater when the cells are immersed in PBS with a low refractive index than when they are immersed in a protein solution with a higher refractive index. At larger angles the scattering was not strongly affected by changing to a medium of different index.

In order to learn as much as possible from our experimental results, we performed model calculations to understand the effects of changing the refractive index of the medium. The scattering coefficients of spheres in media of different indices were computed as described in the Methods section. The ratio of scattering coefficients for spheres immersed in media with indices of 1.330 and 1.345 is plotted as a function of scatterer size in Figure 2. The ratio was only weakly dependent on scatterer

size, but it was strongly dependent on the refractive index of the spheres. The closer the refractive index of the spheres was to that of the media, the greater the effect of changing the medium index. The effect of changing the medium refractive index on scattering as a function of angle was also investigated. For scatterers ( $n = 1.4$ )  $1\text{ }\mu\text{m}$  and smaller in radius, the ratio of light scattering intensity in the medium of lower index (1.332) to light scattering intensity in the medium of higher index (1.345) did not depend strongly on angle. For larger spheres, the ratio decreased for angles less than about  $15^\circ$ . There were also oscillations as a function of angle for narrow distributions of sphere sizes, but these averaged out when a broader distribution was used. In conclusion, for a distribution of scatterer sizes, scattering at all angles was affected similarly by changing the medium refractive index, with the exception of angles less than about  $15^\circ$ .

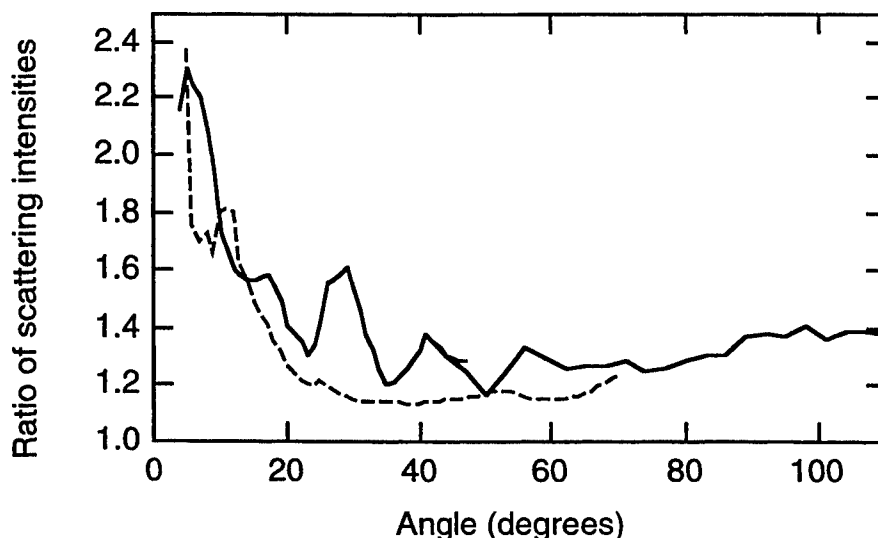


Figure 1. Experimentally determined ratio of scattering from cells immersed in media of low and high indices of refraction. The media of low index had a refractive index of 1.332 in both cases. The media of higher index had  $n = 1.345$  for the solid curve and  $n = 1.343$  for the dashed curve. Data at higher angles are not shown because of interference from scattering off of protein molecules dissolved in the media.

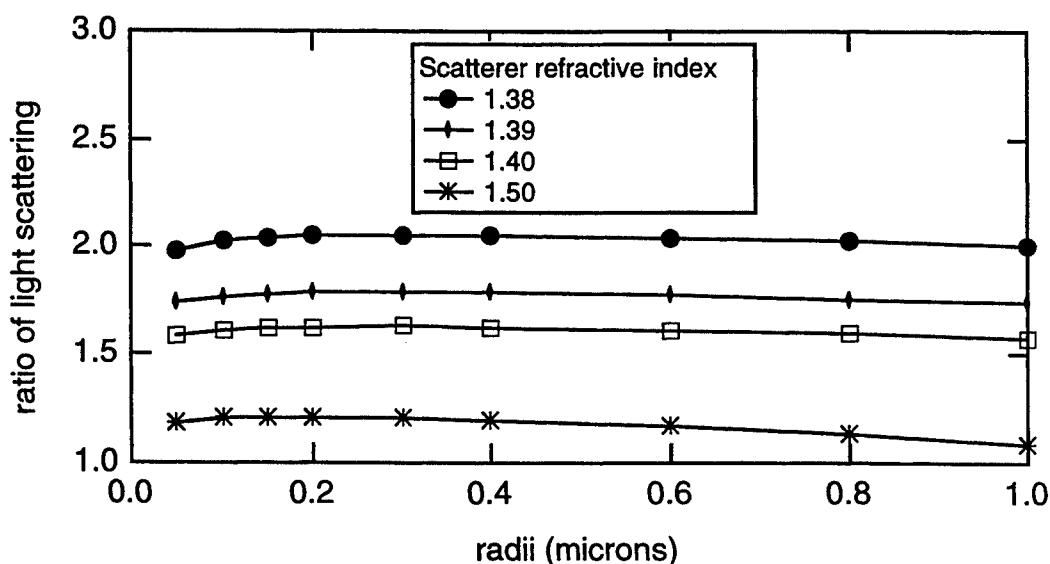


Figure 2. Theoretical calculations of the ratio of the scattering coefficients for spheres immersed in media of different refractive indices. The abscissa is sphere size.

We can conclude from the modeling results and Figure 1 that there was significant scattering at small angles from cell structures that are in contact with the medium. However, at larger angles ( $>40^\circ$ ) the effect on elastic scattering of increasing the external index of refraction was much smaller. Assuming a value for the index of refraction of the cell structures in contact with the medium of 1.38 and 1.3 as the ratio of scattering from cells suspended in media with low and high indices of refraction (Figure 1), the fraction of scattering from particles internal to the cell can be estimated from the data at angles above  $40^\circ$ . The scattering in the low refractive index medium is given by  $I_{nc} + I_c$ , where  $I_{nc}$  is the intensity of scattering from structures not in contact with the medium and  $I_c$  is the intensity of scattering from structures in contact with the medium. In the medium of high refractive index, the scattering from the particles in contact with the medium is reduced by about a factor of 2.1 and the scattering is given by  $I_{nc} + 0.48 \cdot I_c$ . Using the fact that the ratio of scattering in the low and high refractive index media is 1.3, we calculate that ~55% of the elastic light scattering at angles greater than  $40^\circ$  was from internal cellular structures when the cells are immersed in PBS.

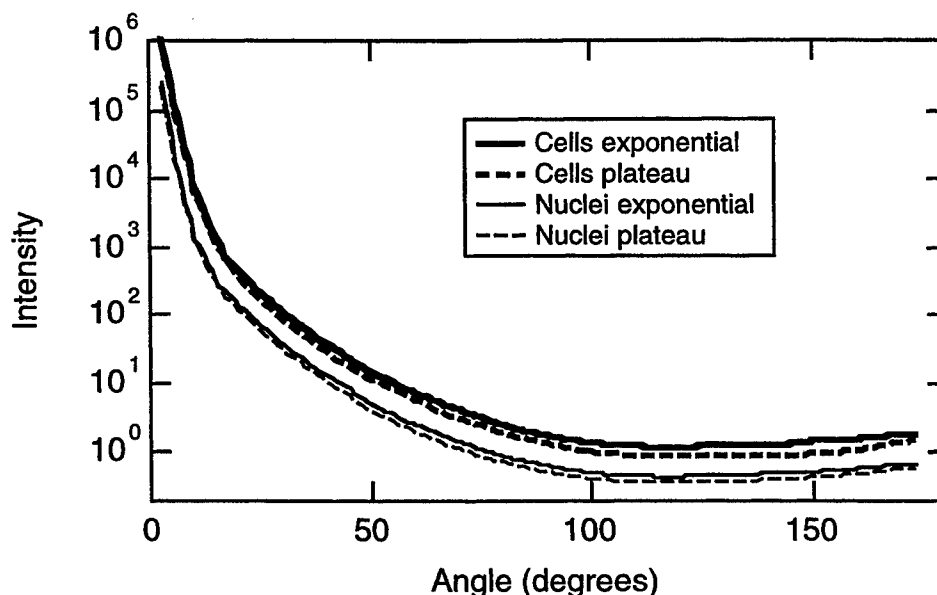


Figure 3. Scattered light intensity from cells and nuclei as a function of angle. The curves have been corrected to represent scattering equal number densities of cells and nuclei.

### 3.2 Scattering from cells in the exponential and plateau phases of growth

The average DNA content of cells harvested in the exponential phase of growth will be different from the average DNA content of cells harvested in the plateau phase of growth, since MR1 cells are known to arrest in the  $G_1$ -phase of the cell cycle at growth plateau<sup>15</sup>. Therefore, harvesting cells in different growth stages provides a means of determining whether light scattering is correlated with DNA content. For each experiment, two sets of cells were harvested. In some cases the cells were at similar points on the growth curve, in other cases they were different. Measurements were made of angular dependent light scattering, and the DNA content of the cells was determined by flow cytometric DNA content analysis as described in the Methods section. DNA content was quantitated with a single parameter with Equation 1, where  $\%G_2$ ,  $\%S$ , and  $\%G_1$  refer to the percent of cells in the  $G_2$ ,  $S$ , and  $G_1$  phases of the cell cycle, respectively. The basis of Eq. 1 is that cells in the  $G_2$  phase in the cell cycle have two copies of their DNA and therefore have twice as much DNA; cells in the  $S$  phase are in the process of duplicating their DNA and therefore have on average about 1.5 times as much DNA as cells in the  $G_1$  phase of the cell cycle. The fraction of cells in the different stages of the cell cycle were determined.

$$\text{DNA index} = 2 \cdot (\%G_2) + 1.5 \cdot (\%S) + (\%G_1) \quad (1)$$

Figure 3 shows representative data from one experiment where the cells were harvested in the exponential and plateau phases of growth. At large angles, the cells harvested in the exponential phase of growth scatter more than those harvested in the plateau phase of growth. To quantify changes in high angle scattering, the integral of the scattering intensity between  $110^\circ$  and  $140^\circ$  was calculated. A ratio of the DNA indices and a ratio of the high angle scattering intensities were computed for each individual experiment. As shown in Figure 4, cell suspensions with larger DNA contents scatter more light than cell suspensions with smaller DNA contents. For example, when one of the suspensions measured contains more DNA than the

other, it also has significantly more scattering between  $110^\circ$  and  $140^\circ$ . Clearly, there is a correlation between light scattering at large angles and cellular DNA content.

Elastic scatter spectra of cells in the exponential and plateau phases of growth were also measured. The results for three separate experiments are quite similar, as shown in Figure 5. The slope of the elastic-scatter spectra was steeper for the cells harvested in the exponential phase of growth than for the cells harvested in the plateau phase of growth. Since the wavelength dependence of scattering is generally steeper for smaller particles<sup>6</sup>, this result indicates that the average size of the scatterers is probably smaller for the exponential phase cells.

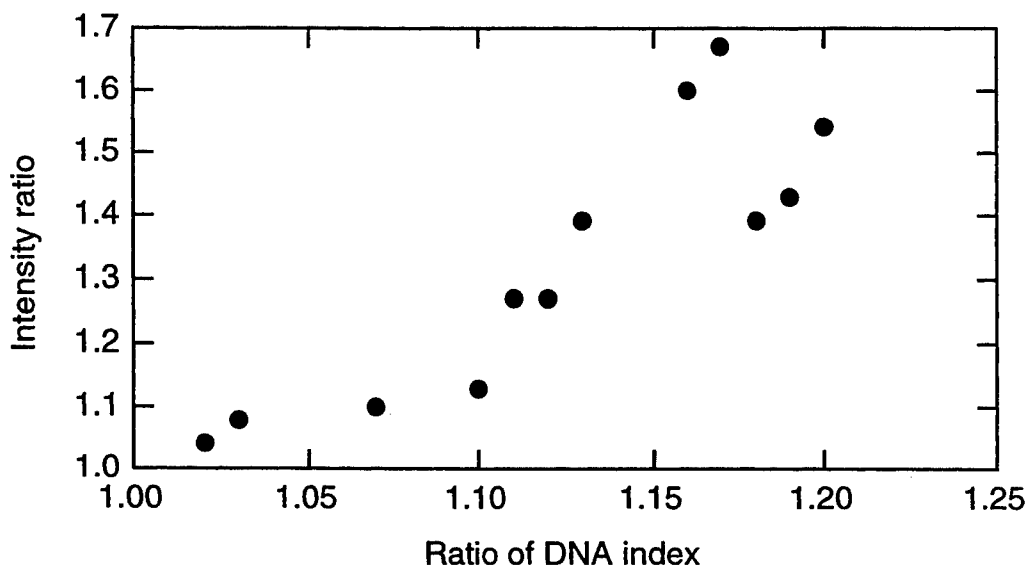


Figure 4. Each data point is the result of measurements of two suspensions of cells. In some cases the cells suspensions contained similar amounts of DNA in other cases one suspension contained significantly more DNA than the other. The ratio of the DNA content of the two suspensions is plotted on the abscissa. The ratio of the scattering intensities from  $110^\circ$  to  $140^\circ$  is plotted on the ordinate.

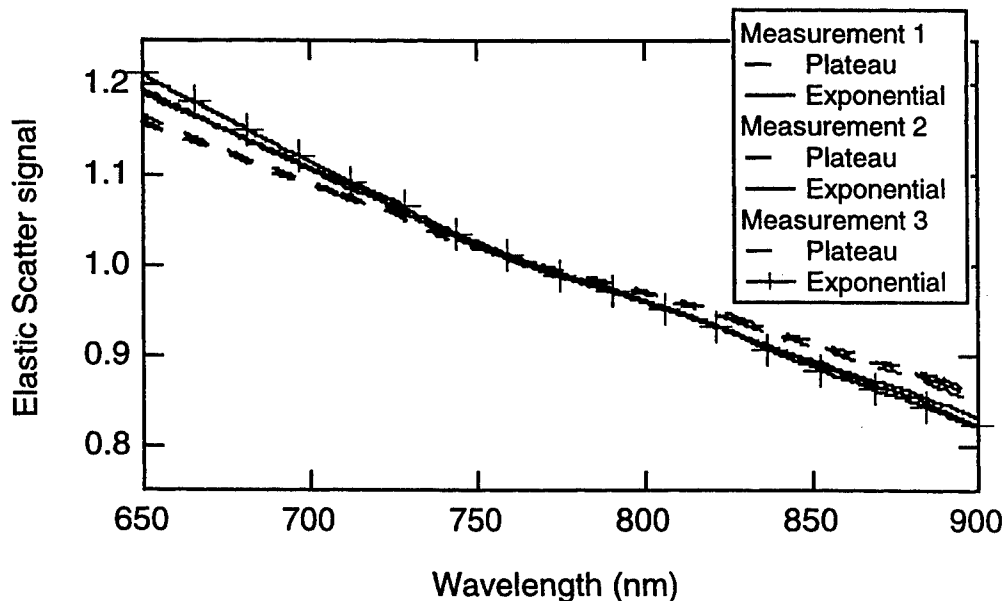


Figure 5. Diffuse reflectance of cell suspensions as a function of wavelength. Results from three separate experiments are shown. The data were normalized such that the area under all of the curves is the same from 650 to 900 nm.

### 3.3 Scattering from isolated nuclei

The primary issue we wish to address by examination of isolated nuclei is how much of the scattering from mammalian cells is due to scattering from the nuclei. Nuclei were isolated from cells harvested in the exponential and plateau phases of growth as described in the Methods section. Angular dependent scattering measurements were made of cells and the corresponding isolated nuclei. By dividing the results for isolated nuclei by the results for whole cells, we obtained an estimate of the contribution of nuclei to scattering from whole cells.

Figure 3 shows the results of angular dependent scattering measurements from one experiment. As discussed in the Section 2, cells harvested in the exponential phase of growth scatter more at large angles than cells harvested in the plateau phase of growth. Figure 3 also demonstrates that the nuclei isolated from cells in the exponential phase of growth scatter more at large angles than nuclei isolated in the plateau phase of growth. In Figure 6 we show the ratio of light scattering intensity from nuclei to that from intact cells. For both the exponential and the plateau phase cells, the contribution of the nuclei to the overall scattering from the cells appears to increase with angle. This result held for each of the four individual experiments.

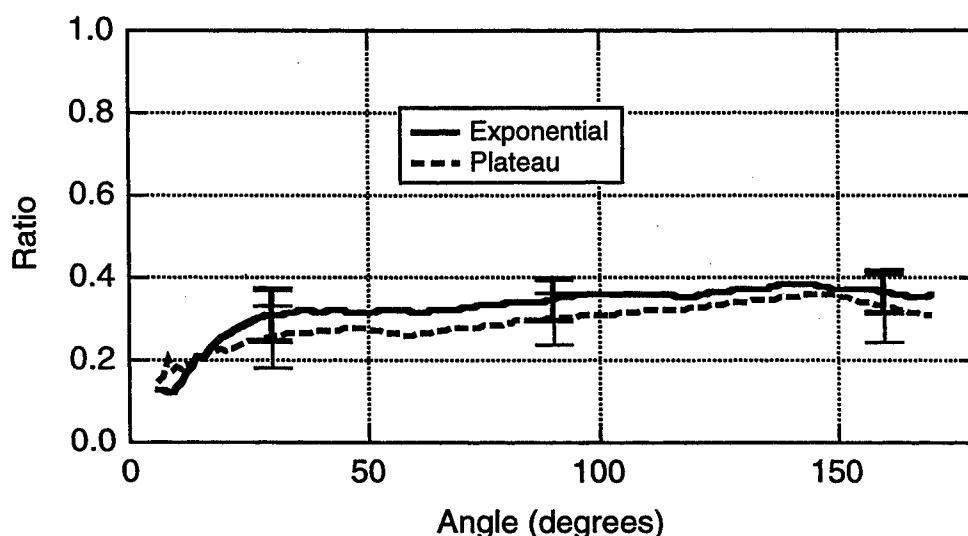


Figure 6. Ratio of light scattering from nuclei and cells as a function of angle. The two curves are each the average of four different experiments. Error bars, calculated as the standard deviation of the four measurements, are given for a few points.

For one of the four experiments (the one in which the nuclei were isolated via the sucrose gradient method), image analysis of the cells and nuclei was performed. The average size of the cells obtained by image analysis was compared to the size obtained by electronic volume analysis. The average diameters of the exponential and plateau phase cells from image analysis were  $14.5\text{ }\mu\text{m}$  and  $12.4\text{ }\mu\text{m}$ , respectively. The electronic volume results for the two cell suspensions were  $14.6$  and  $12.7\text{ }\mu\text{m}$ , respectively, demonstrating that the image analysis technique was accurate. As explained in the Methods section, electronic volume measurements of isolated nuclei were not possible due to the structure of the nuclear membrane. Nuclei isolated from cells harvested in exponential and plateau phases were measured by image analysis and found to have average diameters of  $9.0 \pm 0.18$  and  $9.1 \pm 0.18\text{ }\mu\text{m}$ , respectively. The diameter of the nuclei in intact exponential phase cells was also measured by image analysis and found to be  $8.9 \pm 0.18\text{ }\mu\text{m}$ . These results indicate that there is at most a  $0.4\text{ }\mu\text{m}$  difference in the average diameter of nuclei harvested in the exponential and plateau phases of growth. To test whether this difference could be responsible for the difference in high angle scattering, model calculations were performed assuming homogeneous nuclei. Nuclei with a diameter of  $9.4\text{ }\mu\text{m}$  were found to scatter slightly less at large angles ( $110^\circ$  to  $140^\circ$ ) than nuclei with a diameter of  $9.0\text{ }\mu\text{m}$ . This difference in scattering, however, is too small to explain the experimental results. The ratio of large angle scattering for the model calculations was only 1.08 compared to the experimentally observed ratio of 1.4 comparing nuclei from exponential- and plateau-phase cells.

## 4.0 DISCUSSION

Morphological features have traditionally been used by pathologists to diagnose disease. Recently, it has been proposed that light scattering could provide a noninvasive method of obtaining information about morphological features. The exact nature of the sensitivity and specificity of light scattering to morphological changes, however, has not yet been elucidated. The aim of this paper is to contribute to our knowledge of how changes in specific cellular features affect light scattering. In particular we are interested in cellular features that are known to have significance for pathology.

Morphological features of the nucleus such as size have traditionally been used by pathologists to diagnose malignancy. The relationship of these parameters to optical measurements are being investigated. Perelman et al have published the results of an analysis of diffuse reflectance measurements for determination of nuclear size assuming homogeneous nuclei<sup>18</sup>. Internal nuclear structures can also be important markers for pathological diagnosis. For example, large nucleoli and clumped chromatin are characteristic of anaplasia<sup>19</sup>. We aimed to directly investigate whether light scattering is sensitive to changes of the internal structure of the nucleus. The same experiment performed with the cells of comparing scattering when the scatterers were immersed in media of two different indices was attempted. Unfortunately, we found that scattering from the nuclei increased in the ovalbumin solution. Electronic volume measurements indicated that there was no change in nuclear size upon immersion in an ovalbumin solution. Therefore, we attribute this effect to ovalbumin leaking into the nucleus. Nuclear membranes are known to pass proteins of less than 60 kD in molecular weight<sup>20</sup>.

It is possible to obtain insight into light scattering from internal structures of nuclei by combining model calculations and experimental results. Model calculations presented in the Results section as well as those by Drezek et al.<sup>10</sup> demonstrate that a change in size of a homogeneous nuclei can not be responsible for the increased high angle scattering observed for cells and nuclei harvested in the exponential phase of growth. Additionally, our image analysis results did not show any change in the size of the nuclei. Therefore, we contend that the greater high angle light scattering from nuclei populations with greater DNA content is due to scattering off of internal structures. The elastic-scattering spectra indicate that the average size of the scatterers is smaller in the exponential phase cells. This result is consistent with increased scattering from small structures within the nuclei, although we can not rule out that this is an effect of structures in the cytoplasm, since cells harvested in the exponential phase of growth are bigger than cells harvested in the plateau phase of growth. We know that exponential-phase MR1 cells contain more mitochondria than cells from plateau-phase cultures<sup>21</sup>.

Figure 4 demonstrated that high angle light scattering is sensitive to DNA content. Recently there has been interest in using DNA ploidy and S-phase fraction for assessing disease status and predicting treatment outcomes<sup>22, 23, 24, 25</sup>. For example, DNA ploidy has been shown to be associated with poor outcome for gastric cancer<sup>26</sup>. This raises the issue of whether the elastic-scattering/diffuse-reflectance measurements that are possible in a clinical setting are also sensitive to DNA content. In recent work, we have demonstrated that when elastic-scattering is performed with the source and detector in close proximity, the collected light intensity depends on the probability of high angle scattering events<sup>26</sup>. Therefore, we expect that elastic-scattering spectroscopy is sensitive to DNA content. In support of this idea, we have shown in Figure 5 that elastic-scatter measurements of suspensions of cells harvested in different growth phases are reproducibly different.

Our results with cells harvested in different growth phases indicate that scattering from intact cells is probably sensitive to changes in the nuclei. However, the entire difference in scattering of the cells can not be attributed to only changes in the nuclei. Figure 6 indicates that the nuclei are responsible for less than 40% of the scattering from cells in suspension at any given angle, while Fig. 3 and the other angular dependent measurements of scattering from nuclei demonstrate that the ratio of scattering from exponential and plateau phase nuclei is less than 1.5. These numbers predict that the ratio of scattering in exponential and plateau phase cells should be less than 1.2. Figure 4 demonstrates that much larger values are obtained. Therefore, there must be differences in the cell cytoplasm. In fact, we have found that cells harvested in the exponential phase of growth are 1-2  $\mu\text{m}$  larger in diameter than those harvested in the plateau phase of growth, and contain more mitochondria<sup>22</sup>. Further studies are required to elucidate which other intracellular structures contribute to high-angle elastic light scattering.

## 5.0 CONCLUSIONS

High angle light scattering from both cells and isolated nuclei can be correlated with DNA content. The increased scattering of replicating versus nonreplicating cell populations is partly attributed to increased scattering from the nuclei and partly attributed to increased scattering from the cytoplasm. This is consistent with the fact that nuclei were shown to be the source of only about 40% of the scattering from whole cells in suspension.

For this work to be applied clinically, it will be necessary to show that noninvasive optical measurements of epithelial tissue are sensitive to replication rate and/or DNA content. As a first step elastic-scatter measurements of suspensions of replicating and non-replicating cells were made and wavelength-dependent differences were found. We expect our results on cell

suspensions to extrapolate to epithelial tissue because it primarily consists of cells. Nonetheless, in epithelial tissue the cells are in direct contact with each and therefore, the exact nature of the sensitivity of light scattering to DNA content and/or replication rate needs to be elucidated in this situation. In addition, measurement methods that can sensitively and specifically measure scattering properties without interference from absorption need to be developed.

### ACKNOWLEDGEMENTS

We appreciate the work of Mr. David Quintana and Ms. Adrienne Stephenson in preparing cells for measurement and for isolation of nuclei. We also acknowledge the assistance of Drs. Stephan Burde and Babetta Marrone with obtaining and processing images of cells and nuclei. Finally, we acknowledge the assistance of Ms. Mona Khalil in collecting and analyzing the flow cytometric DNA content distributions. This work was supported by grant CA-71898 from the National Cancer Institute, grant ES-07845 from the National Institute of Environmental Health Sciences, and grant RR-01315 from the Division of Research Resources, National Institutes of Health. Finally, we note that a version of this paper has been submitted to the Journal of Biomedical Optics.

### REFERENCES

1. Richards-Kortum R, Sevick-Muraca E, "Quantitative optical spectroscopy for tissue diagnosis," *Ann. Rev. Phys. Chem.* **47**, 555-606 (1996).
2. R. Manoharan, Y. Wang Y, and M. S. Feld, "Histochemical analysis of biological tissues using Raman-spectroscopy," *Spectrochimica Acta Part A-Molecular and Biomolecular Spectroscopy*, **52**, 215-249 (1996).
3. M. Diem, S. Boydston-White, and L. Chiroboga, "Infrared spectroscopy of cells and tissues: Shining light onto a novel subject," *Appl. Spec.* **53**, 148A - 161A (1999).
4. I. J. Bigio, J. R. Mourant, "Ultraviolet and visible spectroscopies for tissue diagnostics: fluorescence spectroscopy and elastic-scattering spectroscopy," *Phys Med. Biol.* **42**, 803-814 (1997).
5. J. G. Fujimoto, B. Bouma, G. J. Tearney, S. A. Boppart, C. Pitris, J. F. Southern, and M. E. Brezinski, "New Technology for high-speed and high-resolution optical coherence tomography," *Annals of the New York Academy of Sciences*, **838**, 95-107 (1998).
6. J. R. Mourant, J. P. Freyer, A. H. Hielscher, A. A. Eick, D. Shen, T. M. Johnson, "Mechanisms of light scattering from biological cells relevant to noninvasive optical tissue diagnostics," *Applied Optics* **37**, 3586-3593 (1998).
7. B. Beauvoit, T. Kitai, and B. Chance, "Contribution of the mitochondrial compartment to the optical properties of the rat liver: A theoretical and practical approach" *Biophys. J.* **67**, 2501-2510 (1994).
8. B. Beauvoit and B. Chance, "Time-resolved spectroscopy of mitochondria, cells and tissues under normal and pathological conditions," *Molecular and Cellular Biochemistry* **184**, 445-455 (1998).
9. J. Beuthan, O. Minet, J. Helfmann, M. Herrig, and G. Muller, "The spatial variation of the refractive index in biological cells," *Phys. Med. Biol.* **96**, 369-382 (1996).
10. R. Dreze, A. Dunn, and R. Richards-Kortum, "Light scattering from cells: finite-difference time-domain simulations and goniometric measurements," *Appl. Opt.* **38**, 3651-3663 (1999).
11. T. M. Johnson, and J. R. Mourant, "Polarized wavelength-dependent measurements of turbid media," *Optics Express* **4**, 200-216 (1999).
12. C. F. Bohren, and D. R. Huffman, *Absorption and scattering of light by small particles*. Wiley-Interscience, New York (1983).
13. A. Brunsting, and P. F. Mullaney, "Differential light scattering from spherical mammalian cells," *Biophys. J.* **14**:493-453 (1974).
14. L.A. Kunz-Schughart, A. Simm and W. Mueller-Klieser, "Oncogene-associated transformation of early passage rodent fibroblasts is accompanied by large morphologic and metabolic alterations," *Oncol. Reports* **2**:651-661 (1995).
15. J.P. Freyer, "Rates of oxygen consumption for proliferating and quiescent cells isolated from multicellular tumor spheroids," *Adv. Exp. Med. Biol.* **345**: 355-342 (1994).
16. A. Krishan, "Rapid flow cytofluorometric analysis of mammalian cell cycle by propidium iodide staining," *J. Cell Biol.* **66**: 188-193 (1975).
17. F. A. Jenkins, and H. E. White, *Fundamentals of Optics*, McGraw-Hill (1976), pp 30-32.
18. L. T. Perelman, V. Backman, M. Wallace, G. Zonios, R. Manohoran, A. Nurst, S. Shields, M. Seiler, C. Lima, T. Hamano, I. Itzkan, J. van Dam, J. M. Crawford, "Observation of periodic fine structure in reflectance from biological tissue: A new technique for measuring nuclear-size distribution," *Phys. Rev. Lett.* **80**, 627-630.
19. R. S. Cotran, V. Kumar, S. L. Robbins, "Pathologic Basis of Disease," W. B. Saunders, Philadelphia (1994).

20. H. Lodish, D. Baltimore, A. Berk, S. L. Zipursky, P. Matsudaira, J. Darnell, *Molecular Cell Biology* Scientific American Books New York (1995) pg. 840.
21. L.A. Kunz-Schughart, R.A. Habbersett and J.P. Freyer, "Mitochondrial-Function In Oncogene-Transfected Rat Fibroblasts Isolated From Multicellular Spheroids," *Am. J. of Physiology - Cell Physiology*, 42:C1487-C1495 NOV 1997
22. F. Collin, A. Chassevent, F. bonichon, G. Bertrand, P. Terrier, and J.-M. Coindre, "Flow cytometric DNA content analysis of 185 soft tissue neoplasms indicates that s-phase fraction is a prognostic factor for sarcomas," *Cancer* 79, 2371-2373 (1997).
23. F. Esteban, D. S. deVega, R. Garcia, R. Rodriguez, J. Manzanares, A. Almeida, S. Tamames, "DNA content by flow cytometry in gastric carcinoma: Pathology, ploidy and prognosis," *Hepato-gastroenterology* 46, 2039-2043 (1999).
24. J. S. Ross, C. E. Sheehan, R. A. Ambros, T Nazeer, T. A. Jennings, R. P. Kaufman, H. A. G. Rifkin, and B. V. S. Kallakury, "Needle biopsy DNA ploidy status predicts grade shifting in prostate cancer," *Am. J. Surg. Path.* 23, 296-301 (1999).
25. M. Abad, J. Ciudad, M. R. Rincon, I. Silva, J. I. Pazbouza, A. Lopez, A. G. Alonso, A. Bullon, and A. Orfao, "DNA aneuploidy by flow-cytometry is an independent prognostic factor in gastric-cancer," *Analytical Cellular Pathology* 16, 223-231 (1998).
26. M. Canpolat, J. R. Maurant, "Quantifying the importance of high angle scattering events to light-transport through turbid media measured in a backscattering geometry," submitted to *Physics in Medicine and Biology*.



# Diffuse backscattering Mueller matrix analysis for tissue diagnostics with polarized light

Andreas H. Hielscher\* and Sebastian Bartel  
State University of New York - Downstate Medical Center  
Dept. of Pathology, 450 Clarkson Ave., Brooklyn, New York 11203

## ABSTRACT

We have developed a Monte Carlo algorithm that calculates all sixteen, two-dimensional elements of the diffusing backscattering Mueller Matrix for highly scattering media. Using the Stokes-Mueller formalism and scattering amplitudes calculated with Mie theory, we are able to consider polarization dependent photon propagation in highly scattering media. The numerically computed matrix elements are compared to experimental data obtained from particle suspensions with different particle sizes and fibroblast cell suspensions. The numerical results show good agreement in both azimuthal and radial direction with the experimental data, and suggest that in the fibroblast suspensions subcellular structures with a typical size of 200 to 300 nm dominate the backscattering behavior.

**Keywords:** Polarization, photon migration, Monte Carlo, scattering, turbid media, infrared imaging.

## 1. INTRODUCTION

In recent years there has been an increasing interest in the propagation of polarized light in randomly scattering media, especially for medical applications. For example, Emile *et al.*<sup>1</sup> and Demos *et al.*<sup>2</sup> proposed the use of polarized light to isolate ballistic photons from the diffuse background and enhance the spatial resolution in optical tomographic methods. In other applications that are aimed at the in-vivo characterization of biological tissue the investigation of backscattered light is of particular interest. Jacques *et al.*,<sup>3</sup> and Demos *et al.*<sup>4</sup> investigated the utilization of backscattered polarized light to beneath-the-surface imaging. Other studies suggest that relevant information may be obtained by measuring the spatially dependent response of a medium to a polarized point source.<sup>5,6,7</sup> In this case a linearly polarized, collimated laser beam is focussed onto the medium and the multiple-scattered, diffusely backreflected light is recorded with a CCD camera. Using collinear or crossed analyzer in front of the camera, one obtains two-dimensional, polarization-dependent, surface-intensity maps, which show characteristic two- or fourfold symmetries. It has been demonstrated that these patterns can be used to determine the scattering coefficient  $\mu_s$ , anisotropy factor  $g$ , and the average particle size of polystyrene-sphere and biological-cell suspensions.<sup>6</sup>

Beyond obtaining surface intensity maps of linearly polarized light with crossed or collinear source-detector arrangements, many other configurations are possible. For example, one may vary the degree between the optical axes of the linear polarizers and analyzer, or include circularly or elliptically polarized light into the measurements. It can be shown that a total of 16 intensity measurements suffice to obtain the so-called Mueller matrix, which may be used to describes any optical system.<sup>8,9,10</sup> This 4x4-matrix operator completely determines the transformation of an arbitrary incident polarization state. In the case of diffusely backscattered light from a point source each matrix element is represented by a two-dimensional surface map.<sup>11</sup> Hielscher *et al* showed that suspensions that differ in the size of their scatter centers (e.g. polystyrene spheres) show distinctively different backscattering Mueller matrices.<sup>6</sup> Difference can also be found between the Mueller matrices of cells suspensions containing tumorigenic and non-tumorigenic fibroblast cells.<sup>11</sup>

In addition to experimental studies several groups have developed numerical Monte Carlo models that describe polarized light propagation in scattering media.<sup>7,12,13,14</sup> Only Kattawar *et al.*<sup>7</sup> and Rakovic *et al.*<sup>14</sup> used these simulations to compute the effective backscattering Mueller matrix and compared it to experimental results obtained from suspension of spheres with a diameter of 2020 nm. They were able to reproduce the azimuthal symmetry in all 16 matrix, but obtained only poor agreement in the radial dependence.

In this work we extend the existing approaches and simulate polarization dependent photon propagation through multiply scattering media. In our simulation we fully considers both polar-angle  $\phi$  and azimuthal-angle  $\theta$  dependent

\* Correspondence: Email: ahielscher@netmail.hscbklyn.edu; WWW: <http://recon2.hscbklyn.edu>; Telephone: 718 270 4562; Fax: 718 270 3313

scattering as proposed by Mie theory and we follow each photon until it is either absorbed or leaves the medium. By propagating the Stokes vector along with each photon, we can trace the polarization-state of individual photons and determine the effective backscattering Mueller matrix. Our approach differs from the algorithm developed by Kattawar and Rakovic in that they only consider the polar-angle dependent scattering and estimate the contribution of each scattered photon by an escape function from a particular scattering location.<sup>7,14</sup>

In the following section we will first briefly review the basic concept of Monte Carlo techniques and the Stokes-Mueller formalism. Subsequently we will give a detailed description of how the Stokes-Mueller formalism is combined with the Monte Carlo technique to properly consider polarisation dependent light scattering and propagation. Simulation results for 204-nm-diameter and 2040-nm-diameter sphere suspensions are compared to experimental results. The results are used to interpret backscattering experiments on suspensions that contain rat fibroblast cells.

## 2. NUMERICAL MODEL

### 2.1. Stokes-Mueller Formalism

The basis of our Monte Carlo code for polarized light scattering is an algorithm previously developed by Wang and Jacques.<sup>15,16</sup> The individual photon paths are traces from a pencil-beam, normally incident on a slab geometry. The transport pathlength  $s$  between scattering events is sampled randomly from the normalized distribution  $\rho(s) = \mu_t \exp(-\mu_t s)$ , where  $\mu_t = \mu_a + \mu_s$  is the interaction coefficient. A detailed description of Wang et al's algorithm as well as experimental validation can be found elsewhere.<sup>15,16,17,18</sup> Here we concentrate on the adaptation of this code to consider polarized light.

To include polarization effect into the standard Wang-Jacques code we employ the Stokes-Mueller formalism of polarized light. The Stokes notation is to be favored over the also widely used Jones formalism, since the latter does not allow for the treatment of depolarizing effects.<sup>8,19,20</sup> Neglecting the absolute phase, a given state of polarization can be completely described in terms of its intensities by a Stokes vector:<sup>8,9,10,21</sup>

$$\mathbf{S} = \begin{pmatrix} S_0 \\ S_1 \\ S_2 \\ S_3 \end{pmatrix} = \begin{pmatrix} \langle |E_l|^2 + |E_r|^2 \rangle \\ \langle |E_l|^2 - |E_r|^2 \rangle \\ \langle E_l^* E_r + E_l E_r^* \rangle \\ i \langle (E_l^* E_r - E_l E_r^*) \rangle \end{pmatrix}, \quad (1)$$

where  $E_r, E_l$  are two orthogonal electrical field components in a plane perpendicular to the propagation direction. The Stokes parameter  $S_i$  are ensemble averages (or time averages in case of ergodic, stationary processes) as indicated by the  $\langle \rangle$ . Therefore, no coherence effects are considered. The parameters are real and obey the inequality

$$S_0^2 \geq S_1^2 + S_2^2 + S_3^2. \quad (2)$$

In this equation the equality holds for 100 percent polarized light. The degree of polarization  $\Phi$  is defined by

$$\Phi = \sqrt{S_1^2 + S_2^2 + S_3^2} / S_0. \quad (3)$$

When the Stokes vectors are used to describe the propagation of light through optical components such as lenses, polarizers, retarders, etc. each of these optical elements can be uniquely represented by a 4x4 Mueller matrix,  $M$ . By multiplying the Stokes vector of the incident light with the appropriate Mueller matrix, one obtains a new Stokes vector for the transmitted or scattered beam. An arrangement of several optical components is described mathematically by successive multiplication of the corresponding matrix operator,

$$\mathbf{S}' = \mathbf{M}_n \cdot \dots \cdot \mathbf{M}_2 \cdot \mathbf{M}_1 \cdot \mathbf{S} \quad (4)$$

## 2.2. Polarized Light Propagation in Multiple Scattering Media

When the Stokes-Mueller formalism is employed to describe scattering events, the Stokes vector  $\mathbf{S}$  is defined with respect to the scattering plane,  $\Sigma$ , which contains the direction-vectors of the in- and outgoing beam.  $E_l$  is chosen to be in the scattering plane and  $E_r$  is orthogonal to the scattering plane (Fig.1). In multiple scattering media, this plane of reference changes with each scattering event, so that the Stokes vector  $\mathbf{S}_{r,l}$  of a scattered state is, in general, different from  $\mathbf{S}_{r,l'}$ , the one that is subjected to the next scattering event. In order to keep track of a photon's polarization state as it undergoes multiple scattering events, it is assigned the four component Stokes vector  $\mathbf{S}$  and a local co-ordinate system ( $e_r, e_l, e_3$ ) in which  $\mathbf{S}$  is defined. The local tripod is chosen so that  $e_3$  points in the direction of propagation, while  $e_l$  and  $e_r$  are oriented parallel and perpendicular to the plane of reference respectively (Fig. 2). Both  $\mathbf{S}$  and ( $e_r, e_l, e_3$ ) have to be modified upon each scattering event. Knowledge of the reference system is crucial to a correct interpretation of the current Stokes vector.

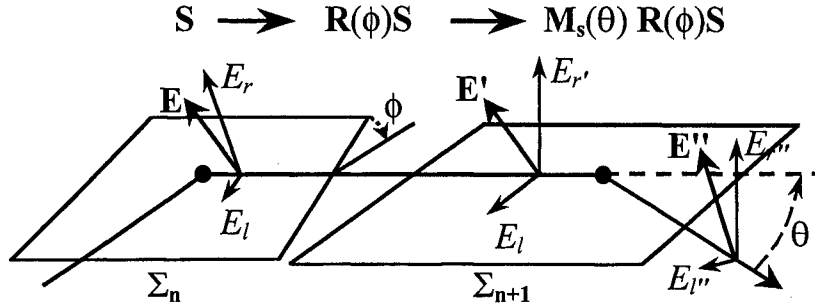


Fig. 1: Transformation of incident Stokes vector  $\mathbf{S}$  into scattering plane by rotation  $\mathbf{R}(\phi)$  and subsequent scattering by single-scattering Mueller matrix  $\mathbf{M}_s(\theta)$ .

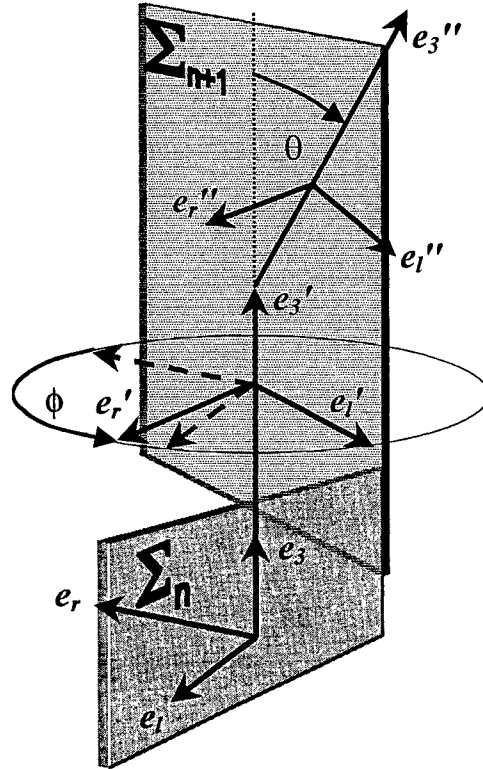


Fig.2: Local coordinate systems of photon prior to and after scattering. The photon is incident from below. First local coordinate system ( $e_r, e_l, e_3$ ) is rotated about  $e_3$  to obtain ( $e'_r, e'_l, e'_3$ ). This is followed by a rotation about  $e'_r$ , which results in the local coordinate system ( $e''_r, e''_l, e''_3$ ). The scattering plane is denoted by  $\Sigma_{n+1}$ .

Assume the deflection angles  $\theta$ ,  $\phi$  have already been fixed properly, then the Stokes vector and the local tripod are updated as follows (Fig.2):

- i) We project the incident Stokes vector (Eq.1) given in the coordinate system  $(e_r, e_b, e_3)$  into the scattering plane. The corresponding coordinate systems are connected by a rotation  $\mathbf{R}(\phi)$

$$\mathbf{S}_{r'l'} = \mathbf{R}(\phi) \cdot \mathbf{S}_{r1} \quad (6)$$

where  $\phi$  is the tilting angle between successive scattering planes and  $\mathbf{R}(\phi)$  is given by

$$\mathbf{R}(\phi) = \begin{pmatrix} 1 & 0 & 0 & 0 \\ 0 & \cos(2\phi) & \sin(2\phi) & 0 \\ 0 & -\sin(2\phi) & \cos(2\phi) & 0 \\ 0 & 0 & 0 & 1 \end{pmatrix} \quad (7)$$

The Stokes vector  $\mathbf{S}_{r'l'}$  is now given with respect to the new coordinate system  $(e'_r, e'_l, e'_3)$ . Next, we apply the single scattering Mueller matrix  $\mathbf{M}_s(\theta)$  to obtain the Stokes vector  $\mathbf{S}'_{r''l''}$  of the scattered photon, hence

$$\mathbf{S}'_{r''l''} = \mathbf{M}_s(\theta) \cdot \mathbf{S}_{r'l'} = \mathbf{M}_s(\theta) \cdot \mathbf{R}(\phi) \cdot \mathbf{S}_{r1} \quad (8)$$

The elements of the Mueller matrix  $M_s$  are calculated by Mie-theory with a code given by Bohren and Huffman.<sup>25</sup> The Stokes vector  $\mathbf{S}'_{r''l''}$  is now given with respect to the new coordinate system  $(e''_r, e''_l, e''_3)$ .

- ii) We rotate the local coordinate system  $(e_r, e_b, e_3)$  prior to scattering about  $e_3$  and  $e'_r$  to obtain the system  $(e''_r, e''_l, e''_3)$  of the outgoing photon (Fig. 2). This step involves standard rotational matrices and is easily performed, since we are dealing with the basis vectors in their eigensystem, e.g.

$$e'_r = e_r = \mathbf{D}_3(\phi) \cdot e_r \quad (9)$$

$$e'_r = \begin{pmatrix} \cos(\phi) & -\sin(\phi) & 0 \\ \sin(\phi) & \cos(\phi) & 0 \\ 0 & 0 & 1 \end{pmatrix} \begin{pmatrix} 1 \\ 0 \\ 0 \end{pmatrix} = \begin{pmatrix} \cos(\phi) \\ \sin(\phi) \\ 0 \end{pmatrix} \quad (10)$$

and similarly

$$e'_l = \begin{pmatrix} -\cos(\theta)\sin(\phi) \\ \cos(\theta)\cos(\phi) \\ \sin(\theta) \end{pmatrix} \quad (11)$$

$$e'_3 = \begin{pmatrix} \sin(\theta)\sin(\phi) \\ -\sin(\theta)\cos(\phi) \\ \cos(\theta) \end{pmatrix} \quad (12)$$

The sense of direction of the above rotations has to be carefully considered: While the Stokes vector is being expressed in a rotated system, the three basis vectors are actively being rotated, demanding for the transpose matrix, or a negative angle  $\phi$ .

- iii) As it stands the system  $(e''_r, e''_l, e''_3)$  is given with respect to  $(e_r, e_b, e_3)$ . To be able to determine the Stokes vector in terms of a fixed system and eventually apply a 'detector' to exiting photons,  $(e''_r, e''_l, e''_3)$  has to be expressed in terms of the global system  $(x,y,z)$ . For any vector  $\mathbf{a}$ , given locally we obtain the xyz-representation according to

$$\mathbf{a}_{x,y,z} = e_r a_r + e_l a_l + e_3 a_3 \quad (13)$$

So far we have not explicitly specified any single scattering matrix  $\mathbf{M}_s$ . Mueller matrices for single scattering particles of arbitrary shape and composition can be derived from Mie theory.<sup>22</sup> In this work we only considered isotropically distributed, spherical particles, which reduces the Mueller matrix to 4 independent elements:

$$M_s(\theta) = \begin{pmatrix} m_{11} & m_{12} & 0 & 0 \\ m_{12} & m_{11} & 0 & 0 \\ 0 & 0 & m_{33} & m_{34} \\ 0 & 0 & -m_{34} & m_{33} \end{pmatrix} \quad (14)$$

However, our approach is easily extended to the general case by substituting the appropriate single scattering matrix. We used a source code by Bohren and Huffman<sup>22</sup> to determine the scattering amplitudes from which the  $m_{ij}$  are derived.

### 2.3. Sampling of $\theta$ and $\phi$

Let us now consider the actual sampling of  $\theta$  and  $\phi$ . Generally, an incident plane wave is scattered over the whole solid angle resulting in an intensity distribution  $I(\theta, \phi)$ . Since we are dealing with discrete photon packets and, consequently, discrete deflection angles, it is necessary to either properly sample  $(\theta, \phi)$  or to punish certain packets, depending on their new direction. The preferred approach is to directly sample  $(\theta, \phi)$  so that the probability density  $\rho$  of a packet being scattered under these angles is proportional to the expected intensity  $I(\theta, \phi) = S'_o(\theta, \phi)$ . We obtain  $\rho$  in terms of the Stokes components of an incident state by applying Eq. (7) and Eq. (8)

$$\begin{aligned} \rho(\theta, \phi) \propto I(\theta, \phi) = S'_o(\theta, \phi) = & m_{11}(\theta) S_0 \\ & + m_{12}(\theta) (S_1 \cos(2\phi) + S_2 \sin(2\phi)) \\ & + m_{13}(\theta) (S_2 \cos(2\phi) - S_1 \sin(2\phi)) \\ & + m_{14}(\theta) S_3 \end{aligned} \quad (15)$$

where  $m_{ij}$  are the elements of the single scattering Mueller matrix  $M_s$ . Note that equation 15 introduces an explicit dependence on the incident polarization state as well as on the azimuth angle  $\phi$ , as demanded by Mie theory. This differs from the approach by Kattawar, which assumes the scattered intensity  $I(\theta, \phi)$  to be proportional to the  $m_{11}$  element of the single scattering matrix.

The sampling of  $I(\theta, \phi)$  according to equation 15 from uniformly generated random numbers is performed using the rejection method.<sup>23</sup> First two angles  $(\theta, \phi)$  are randomly chosen and Eq. 15 is evaluate to yield a number  $S'_o(\theta, \phi)$  between 0 and 1. Than a third number  $S_{\text{rand}}$  between 0 and 1 is randomly generated. If  $S_{\text{rand}} \leq S'_o(\theta, \phi)$  the scattering angles for the next scattering event are fixed to  $(\theta, \phi)$ . If  $S_{\text{rand}} > S'_o(\theta, \phi)$  a new pair of angles and a new value  $S_{\text{rand}}$  are randomly chosen until  $S_{\text{rand}} \leq S'_o(\theta, \phi)$ .

### 2.4. Photon Detection

The goal of this work is to determine the backscattering Mueller matrix  $M = \{m_{ij}\}$  defined by

$$\mathbf{S}' = \mathbf{M} \cdot \mathbf{S} \quad (16),$$

which connects any incident Stokes vector  $\mathbf{S}$  with the outgoing vector  $\mathbf{S}'$  of backscattered light. Although, the Mueller matrix for a random distribution of homogeneous spheres is known to have only 7 independent elements,<sup>14</sup> we explicitly recorded all 16 elements. This allowed us to perform consistency checks and verify the validity of our approach.

A total of 16 linear independent measurements with linear and circular polarizers and analyzers in different azimuthal arrangements are required to determine  $\mathbf{M}$ . Note that except for  $m_{11}$  none of the matrix elements is directly accessible by a single direct measurement. Instead, one has to solve the set of linear equations generated by Eq. (16).<sup>8,9,19</sup> A detailed description of how to derive the actual matrix elements from linear combinations of intensity measurements has been given by Bickel<sup>10</sup> and Hielscher.<sup>11</sup>

Since in our simulation we are able to access the Stokes components directly rather than only intensities, a total of 4 runs with the orthogonal basis vectors

$$\mathbf{S}^1 \equiv (1, 0, 0, 0)^T, \quad \mathbf{S}^2 \equiv (1, 1, 0, 0)^T, \quad (17a,b)$$

$$\mathbf{S}^3 \equiv (1, 0, 1, 0)^T, \quad \mathbf{S}^4 \equiv (1, 0, 0, 1)^T, \quad (17c,d)$$

is sufficient to determine all elements of the backscattering Mueller matrix. Consider an incident unpolarized photon in state  $\mathbf{S}^j$ . Upon it exiting from the medium, we record its Stokes components in the auxiliary matrix  $\hat{m}_i^j$ :

$$\hat{m}_1^j = S_1^j, \quad \hat{m}_2^j = S_2^j, \quad \hat{m}_3^j = S_3^j, \quad \hat{m}_4^j = S_4^j, \quad (18)$$

where the superscript  $j = 1..4$  indicates one of the incident vectors in Eq. (17) and the subscript refers to the component of the detected vector  $\mathbf{S}$ . In general, if the incident polarization state is  $\mathbf{S}^j$ , the resulting Stokes vector is added to the  $j^{\text{th}}$  column of  $\hat{m}_i^j$ . Since Stokes vectors are additive, they may simply be summed up to yield the average 'answer' of the medium. Finally, the average contribution of an incident state  $\mathbf{S}^j$  to the  $i^{\text{th}}$  component of a recorded Stokes vector  $\mathbf{S}$  is contained in  $\hat{m}_i^j$ .

It is now straightforward to determine the actual backscattering Mueller matrix  $\mathbf{M} = \{m_{ij}\}$ , from the following set of equations:

$$(\hat{m}_1^1, \hat{m}_2^1, \hat{m}_3^1, \hat{m}_4^1)^T = \mathbf{S}'^1 = \mathbf{M} \cdot \mathbf{S}^1 \equiv (m_{11}, m_{21}, m_{31}, m_{41})^T \quad (19a)$$

$$(\hat{m}_1^2, \hat{m}_2^2, \hat{m}_3^2, \hat{m}_4^2)^T = \mathbf{S}'^2 = \mathbf{M} \cdot \mathbf{S}^2 \equiv (m_{11} + m_{12}, m_{21} + m_{22}, m_{31} + m_{32}, m_{41} + m_{42})^T \quad (19b)$$

$$(\hat{m}_1^3, \hat{m}_2^3, \hat{m}_3^3, \hat{m}_4^3)^T = \mathbf{S}'^3 = \mathbf{M} \cdot \mathbf{S}^3 \equiv (m_{11} + m_{13}, m_{21} + m_{23}, m_{31} + m_{33}, m_{41} + m_{43})^T \quad (19c)$$

$$(\hat{m}_1^4, \hat{m}_2^4, \hat{m}_3^4, \hat{m}_4^4)^T = \mathbf{S}'^4 = \mathbf{M} \cdot \mathbf{S}^4 \equiv (m_{11} + m_{14}, m_{21} + m_{24}, m_{31} + m_{34}, m_{41} + m_{44})^T. \quad (19d)$$

Equations (19a) -(19d) provide 16 equations, one for each vector component of the 4 vectors, for a total of 16 unknowns  $m_{ij}$ .

## 2.5. Depolarization

Some remarks shall be made concerning the depolarization of light in the photon picture: After a large number,  $n$ , of scattering all four components of the Stokes vector are effectively mixed and the resultant vector  $\mathbf{S}^{(n)}$  is given in a randomly oriented coordinate system. Extending Eq. (8) to successive scattering of an incident Stokes vector  $\mathbf{S}$  we can write

$$\mathbf{S}^{(n)} = \mathbf{M}(\theta_n)\mathbf{R}(\phi_n)\dots\mathbf{M}(\theta_2)\mathbf{R}(\phi_2)\cdot\mathbf{M}(\theta_1)\mathbf{R}(\phi_1)\cdot\mathbf{S} \quad (20)$$

where  $\theta_n$  is the  $n^{\text{th}}$  scattering angle and  $\phi_n$  is the azimuthal angle between scattering planes  $(n-1)$  and  $n$ .

It is interesting to note that the matrix product (Eq. 20) is actually not changing the degree of polarization  $\Phi$  of individual photons. Any incident state with  $\Phi = 1$  will remain 100 percent polarized as it undergoes multiple scattering events. Only the nature of polarization will change, which means that the components  $S_1$ ,  $S_2$ , and  $S_3$  change while  $\Phi$  in Eq. (3) stays constant. However, in Monte Carlo simulations where a large number of independent photons are launched, the observed polarization state is an incoherent superposition of all possible contributions from Eq. 20, which yields

$$\mathbf{S}_{\text{eff}}^{(n)} = \sum_i \mathbf{S}_i^{(n)} = \sum_i \mathbf{M}(\theta_{n,i})\mathbf{R}(\theta_{n,i})\dots\mathbf{M}(\theta_{2,i})\mathbf{R}(\theta_{2,i})\cdot\mathbf{M}(\theta_{1,i})\mathbf{R}(\theta_{1,i})\cdot\mathbf{S}, \quad (21)$$

where  $i$  indicates the sum over all detected photons. Therefore, the effective Stokes vector will generally yield  $\Phi < 1$  and we find the medium to be depolarizing.

### 3. RESULTS

#### 3.1. Problem Setup

For the Monte Carlo simulations we have to choose the wavelength  $\lambda$  of the incident light, particle size and concentration, the wavelength-dependent refractive indices of polystyrene ( $n_p = 1.58$  @  $\lambda = 543$  nm) and water ( $n_w = 1.33$  @  $\lambda = 543$  nm), and the absorption coefficient  $\mu_a$ . These parameters fix the single scattering matrix  $\mathbf{M}_s$ . The simulated phantom is a semi-infinite, randomly distributed ensemble of scatterers. To match experimental geometries, the absorption can be set to 100 percent outside a region of interest, e.g. the physical boundaries of a beaker that contains a particle suspension. We implemented the Monte Carlo code on a cluster of 5 LINUX workstation each of them with two 450MHz Pentium processors. On this cluster simulations with  $10^8$  photons were completed in less than 16 hours. In general we found that the larger the particle size the more photons need to be launch to get a good signal to noise ratio in the Mueller matrix images. With increasing particle size the scattering phase-function becomes more and more forward peaked. Therefore, it takes more and more scattering events for a photon to get turned around and being able to escape the medium in the backward direction.

To validate the polarization-dependent Monte-Carlo algorithms, we compare computed results with experimental data. The experimental setup for studying the polarization state of diffusely backscattered light is described in detail elsewhere.<sup>11</sup> Here we restrict the description to the major components. We use a focussed He-Ne laser ( $\lambda = 543$ nm), whose beam is normally incident onto the medium. The emerging light is projected through an intermediate image plane onto a 14-bit CCD camera. To avoid the strong specular reflection from the surface of the medium and only record multiply scattered light an optical mask (2-mm diameter) is placed in the intermediate image plane. The tissue phantom consists of aqueous mono disperse polystyrene-sphere-suspensions with particles of 204 nm and 2040 nm in diameter. The respective concentrations are chosen so that the resulting reduced scattering coefficient  $\mu_s'$  equals  $1.9\text{cm}^{-1}$ . For the recording of the backscattering intensity measurements approximately 30 ml of each suspension are placed in a beaker with an opening of 4 cm in diameter.

#### 3.2. Comparison of Numerical and Experimental Results

Figures 3a,b displays the numerically and experimentally obtained Mueller matrix for 204-nm-particle suspensions, respectively. Each matrix element is given as a two-dimensional image of the surface, 40x40 mm in size. The laser beam (diameter  $d < 500$   $\mu\text{m}$ ) is orthogonally incident in the center of each element. In the Monte Carlo simulation (Fig. 3a) a photon collection grid of 60x60 pixels is used that limits the spatial resolution to  $\approx 0.67$  mm. This grid size was necessary to improve the signal to noise ratio in each pixel. The experimental data (Figs. 3b) was obtained with a 300x300 grid resulting in a resolution of  $\approx 0.13$  mm. However, to better compare simulations and experiments the experimental data was also projected onto a 60x60 grid. All 16 matrix elements are normalized to the maximum intensity of the respective  $m_{11}$  element, so that the amplitudes range from -1 to +1. Also note that in the experiment an optical mask was used to reduce the specularly backreflected light at the laser incident point. This mask is visible in Fig. 3b as a gray spot in the center of all matrix elements.

First of all, we note the excellent overall agreement between simulation and experiment. The basic symmetries and structures are recovered for each matrix element as well as the backscattering Mueller matrix as a whole. This is true for the azimuthal and radial dependencies. As expected, the diffuse reflectance given by element  $m_{11}$  is independent of the azimuth. It has similar radial extent in all figures, owing to the identical  $\mu_s'$  in all experimental and simulated phantoms. For the 204-nm-spheres suspension the last row and column are close to zero, while pronounced patterns are observed in columns and rows 1 through 3. The strong lobes in  $m_{12}$ ,  $m_{13}$ ,  $m_{21}$ , and  $m_{31}$ , that are characteristic for suspensions of the small polystyrene particles, are accurately reproduced in the simulation. In the case of the 2040-m-spheres suspensions (not shown) the first row and column are almost zero, except for the  $m_{11}$ -element. The 4 central elements have a similar symmetry compared to the smaller sphere suspensions but show a significantly larger radial extent and higher amplitude.

#### 3.3. Influence of Particle Size

To study in more detail the effects of particle size on the diffuse backscattering Mueller matrix, we performed Monte Carlo simulation for particle suspensions containing spheres with diameters from 200 to 600 nm. The reduced scattering coefficient  $\mu_s' = (1-g) \mu_s = 1.9\text{ cm}^{-1}$  was chosen the same for all simulation. The results are shown in Figs. 3a, c, d, e, and f. First we notice that in all cases the elements  $m_{14}$  and  $m_{41}$  are basically zero over the entire surface. Furthermore, the elements  $m_{24}$ ,  $m_{34}$ ,  $m_{42}$ , and  $m_{43}$  are almost zero with only weak azimuthal variations very close to the light incident point in

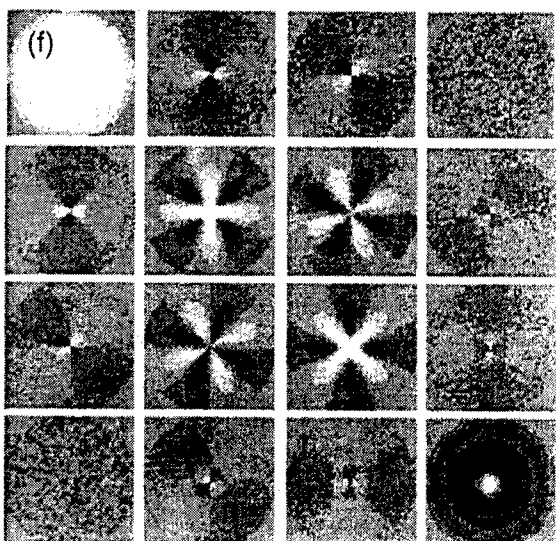
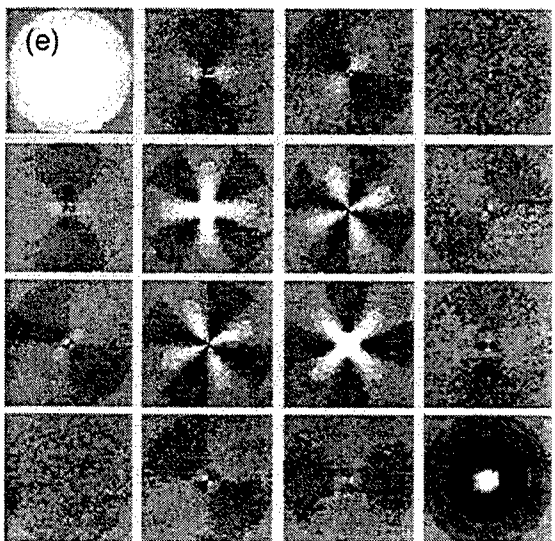
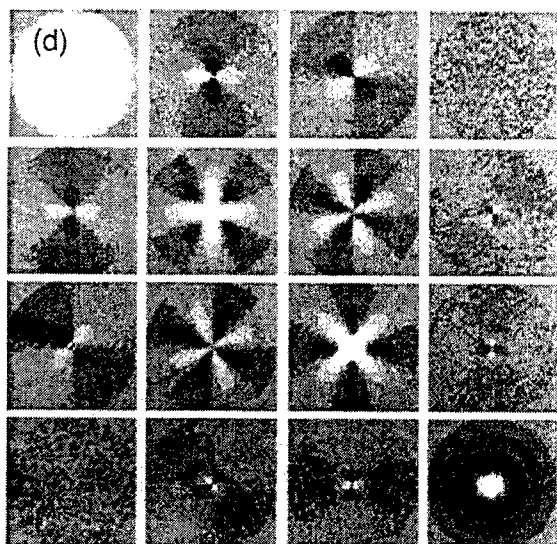
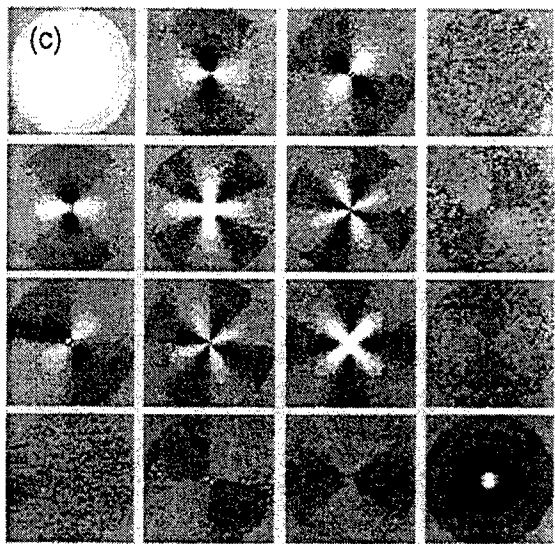
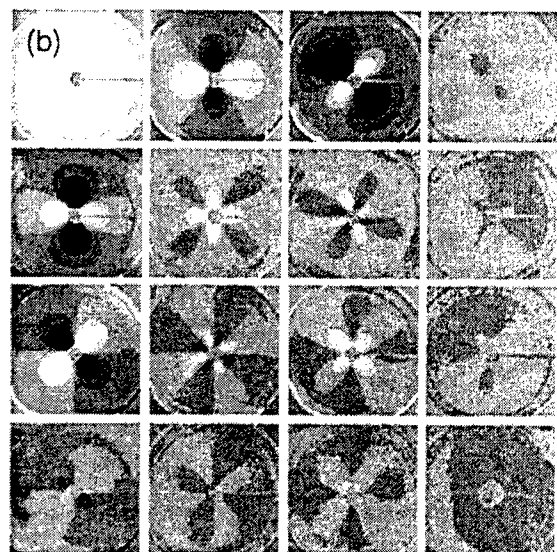
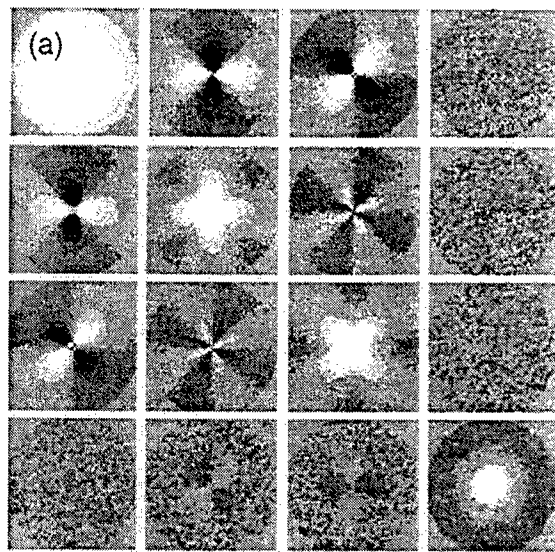




**Fig. 3** (previous page): Mueller matrices for diffusely backscattered light. Each of the six matrices has 16 two-dimensional elements that are 4 cm x 4 cm in size. Shown are results of Monte Carlo simulations for suspensions containing particles with different diameters [(a) 204 nm, (c) 300 nm, (d) 400 nm, (e) 500 nm, and (f) 600 nm]. Figure (b) displays results from an experiment on a polystyrene-spheres suspension containing particles with a diameter of 204 nm. In all case we set  $\mu_s' = 1.9 \text{ cm}^{-1}$  and  $\mu_a = 0.05 \text{ cm}^{-1}$ .

the center. The strongest changes with particle size are observed in the elements  $m_{12}$ ,  $m_{13}$ ,  $m_{21}$ , and  $m_{31}$ . For 200-nm-diameter and 300-nm-diameter spheres suspensions these elements show a strong 4-fold symmetry with some areas having values larger than zero and other areas having values smaller than zero. For the 500-nm-diameter and 600-nm-diameter spheres suspensions  $m_{12}$ ,  $m_{13}$ ,  $m_{21}$ , and  $m_{31}$  are almost zero. The four elements in the center of the Mueller matrix,  $m_{22}$ ,  $m_{23}$ ,  $m_{32}$ , and  $m_{33}$  also change with particle size, however, the effects are less pronounced as compared to changes in the  $m_{12}$ ,  $m_{13}$ ,  $m_{21}$ , and  $m_{31}$  elements. Finally, one can observe a drastic change in the  $m_{44}$  element going from the suspension containing 200-nm-diameter spheres (Fig. 3a) to the suspension containing 300-nm-diameter sphere. For the 200-nm case this element is almost zero except close to the center, where the values are larger than zero. In the 300-nm case, as well as for larger particles, the  $m_{44}$  element is notably smaller than zero.

### 3.4. Comparison of Simulations with Experiments on Fibroblast Cell Suspensions

We also compared the simulations to experimental data obtained from fibroblast cell suspensions. How these suspension were prepared is described in detail elsewhere.<sup>6</sup> An example is shown in Fig. 4a. Displayed in that figure is the diffuse backscattering Mueller matrix for a fibroblast cell suspension that contains approximately  $10^8$  tumorigenic MR1e cells/cm<sup>3</sup>. We found that this Mueller matrix resembles monodisperse suspensions containing polystyrene spheres with a diameter of 200 to 300 nm (Fig. 4b - same as Fig. 3c). The  $m_{21}$ ,  $m_{31}$ ,  $m_{21}$ ,  $m_{31}$ ,  $m_{22}$ ,  $m_{33}$ ,  $m_{23}$ , and  $m_{32}$  elements of the cell-suspension are similar to the same elements of the 300-nm spheres suspension, while the  $m_{44}$  element is comparable to the  $m_{44}$  element of the 204-nm spheres suspension (Fig. 3a). This suggests that the backscattering from the cell suspension is dominated by structures or particles within that have a typical size of approximately 200-300nm. The average diameter of the MR1e cells is approximately 10  $\mu\text{m}$ . Therefore the major scatterers in the suspensions have to be subcellular structures or particles. A possible candidate are mitochondria, which range in size from 200 to 1000  $\mu\text{m}$ . However, further studies are necessary to confirm this hypothesis. For example, the current Monte Carlo code only simulates media with one type of spherical particles, while the cell suspensions consists of a variety of differently sized and shaped particles.

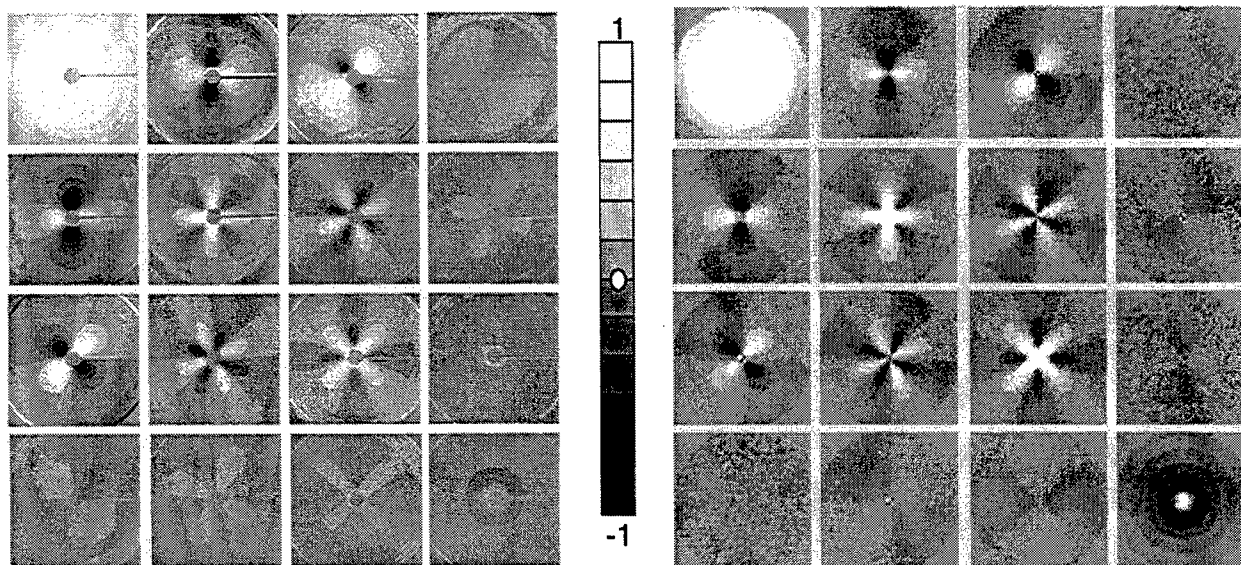


**Fig. 4:** Comparison of the experimentally determined diffuse backscattered Mueller matrix for tumorigenic MR1e fibroblast cell suspension (a-left) and the simulated Mueller matrix for a suspension with 300-nm diameter polystyrene spheres (b-right, same as Fig. 3c).

## 4. SUMMARY

We have developed a Monte-Carlo-based algorithm that accurately calculates all 16, two-dimensional diffuse backscattering Mueller matrix elements of strongly scattering media. The code keeps track of the polarization state, given by the Stokes vector, of individual photons propagating through the medium. Each single-scattering event is treated

according to Mie-theory. We compared simulations of multiple-scattered light to experiments on 204-nm-diameter spheres suspensions. The simulations well reproduces the 2-dimensional backscattering intensity patterns of all 16 elements of the diffuse backscattering Mueller matrices. Furthermore, we used the Monte Carlo code to study the influence of the size of the scatteres in a particle suspension on the diffuse Mueller matrix. We found that the of all matrix components the  $m_{12}$ ,  $m_{13}$ ,  $m_{21}$ , and  $m_{31}$  elements appear most sensitive to change in particle size. In addition, we showed that experimental data obtained from a suspension that contained tumorigenic MR1e fibroblast cells resembled the simulated results for 200 to 300-nm-diameter polystyrene-spheres suspensions. Because the fibroblast cells have an average diameter of approximately 10  $\mu\text{m}$ , our findings suggests that sub-cellular components or structures are responsible for the backscattering characteristic. The developed algorithm provides a tool to examine the effects of different particle sizes and optical properties on observable backscattering polarization patterns from highly scattering. This allows for future systematic studies regarding the characterization of biological tissue by its diffuse backscattering Mueller matrix.

## ACKNOWLEDGEMENTS

We would like to thank Mr. Ketelsen, system administrator at the at the Konrad Zuse Institute, Berlin ZIB, for his valuable advice in the process of implementing the parallel C-code. This work was supported in part by the Dean's Office of the College of Medicine at the State University of New York (SUNY) Downstate Medical Center in Brooklyn, NY.

## REFERENCES

1. O.Emile, F..Bretenaker, A.Le Floch, "Rotating polarization imaging in turbid media," *Opt. Lett.* **21**, No. 20, 1706-1708 (1996)
2. S.G. Demos and R.R. Alfano, "Tempral gating in highly scattering media by the degree of optical polarization," *Opt. Lett.* **21**, No.2, 161-163 (1996)
3. S.L. Jacques, A. Gutsche, J. Schwartz, L. Wang, and F.K. Tittel, "Video reflectometry to extract optical properties of tissue in-vivo," in *Medical optical Tomography : Functional Imaging and Monitoring*, G. Mueller, B. Chance, R.R. Alfano, S.R. Arridge, J. Beuthan, E. Gratton, M. Kaschke, B.R. Masters, S. Svanberg, and P. van der Zee, eds. Vol. ISII of SPIE Institute Series 211-226 (1992)
4. S.G. Demos, and R.R. Alfano, "Optical polarization imaging," *Appl. Opt.* **36**, 150-155 (1997).
5. S.L. Jacques, L.H. Wang, D.V. Stephens, and M. Ostermeyer, "Polarized light transmission through skin using video reflectometry: toward optical tomography of superficial tissue layers," in *Lasers in Surgery: Advanced Characterization, Therapeutics, and Systems VI*, R. R. Anderson, ed., Proc. SPIE **2671**, pp. 199-220 (1996).
6. A.H. Hielscher, J.R. Mourant, I.J. Bigio, "Influence of particle size and concentration on the diffuse backscattering of polarized light from tissue phantoms and biological cell suspensions," *Appl. Opt.* **36**, 125-135 (1997).
7. G.M. Kattawar, M.J. Rakovic, and B.D. Cameron, "Laser backscattering polarization patterns from turbid media: Theory and experiment," in *Advances in Optical Imaging and Photon Migration* J.G. Fujimoto and M.S. Patterson (eds.), OSA TOPS **21**, 105-110 (1998)
8. C. Brosseau, *Fundamentals of Polarized Light*, (John Wiley & Sons, New York, NY, 1998)
9. E. Collett, *Polarized Light: Fundamentals and Applications*, (Marcel Dekker, New York, NY, 1993)
10. W.S. Bickel and W.M. Bailey, "Stokes vectors, Mueller matrices, and polarized light scattering," *Am. J. Phys.* **53**, 468-478 (1985).
11. A.H. Hielscher, A.A. Eick, J.R. Mourant, D. Shen, J.P. Freyer, and I.J. Bigio, "Diffuse backscattering Mueller matrices for highly scattering media," *Optics Express* **1**, 441-454, (1997). (<http://epubs.osa.org/oearchive/pdf/2826.pdf>)
12. N.V. Voshchinnikov and V.V. Karjukin, "Multiple scattering of polarized radiation in circumstellar dust shells," *Astron. Astrophys.* No.288, 883-896 (1994)
13. H.T. Chuah and H.S. Tan, "A monte Carlo backscatter model for radar backscatter from a half-space random medium," *IEEE Transactions on geoscience and remote sensing*, **27**, No.1, 86-93 (1998)
14. M.J. Rakovic, G.W. Kattawar, M. Mehrübeoglu, B.D. Cameron, L.V. Wang, S. Rastegar, G.L. Cote, "Light backscattering polarization patterns from turbid media: theory and experiments," *Applied Optics* **38**, No. 15, 3399-3408 (1999).
15. L.H. Wang, Jacques S.L., "Optimized radial and angular positions in Monte Carlo modeling," *Medical Physics*, **21**, 1081-1083 (1994).
16. L.H. Wang, S.L. Jacques, and L. Zheng, "MCML-Monte Carlo modeling of light transport in multilayered tissues," *Comput. Methods Programs Biomed.* **47**, 131-146 (1995)

- 
17. L.H. Wang and S.L. Jacques, "Monte Carlo modeling of light transport," in *Optical-Thermal Responses of Laser Irradiated Tissue*, A.J. Welch and M. van Gemert (New York: Plenum), pp. 73-100 (1995) (source code available at <http://omlc.ogi.edu/software/mc/index.html>)
  18. A.H. Hielscher, L. Wang, F.K. Tittel, S.L. Jacques, "Influence of boundary conditions on the accuracy of diffusion theory in time-resolved reflectance spectroscopy of biological tissues," *Physics in Medicine and Biology* No.40, 1957-1975, 1995
  19. R.M.A. Azzam, N. M. Bashara, *Ellipsometry and Polarized Light*, (Elsevier North-Holland, New York, NY, 1977)
  20. D.G.M. Anderson, R. Barakat, "Necessary and sufficient conditions for a Mueller matrix to be derivable from a Jones matrix," *J. Opt. Soc. Am.* **11**, No. 8, 2305-2319 (1994)
  21. C.F. Bohren, D. Huffman, *Absorption and Scattering of Light by Small Particles*, (John Wiley & Sons, New York, NY, 1998)
  22. H.C. Van de Hulst, *Light Scattering by Small Particles* (Dover Publications Inc., New York, NY, 1981)
  23. I. Lux and L. Koblinger, *Monte Carlo Particle Transport Methods: Neutron and Photon Calculations*, (CRC Press, Boca Raton, FL, 1991)



## **SESSION 3**

### **Light-Scattering Biopsy II**

# Combination of Diffuse-reflectance and Fluorescence Imaging of Turbid Media

Jianan Y. Qu, Jianwen Hua and Zhijian Huang

Department of Electrical and Electronic Engineering, Hong Kong University of Science and Technology, Clear Water Bay, Kowloon, Hong Kong, P. R. China

## ABSTRACT

We have used the cross-polarization method to eliminate the specular reflection and enhance the diffusive back-scattering of polarized fluorescence excitation light from the turbid media. The image of the ratio between fluorescence and cross-polarized reflection provides a map of the fluorescence yield, defined as the ratio of the autofluorescence emission to the illumination incidence, over the surface of the turbid media when excitation and collection of fluorescence are highly inhomogeneous. The simple ratio imaging technique shows the feasibility to detect early cancer, which usually starts from the superficial layer of tissue, based on the contrast in the fluorescence yield between lesion and normal tissue.

**Keywords:** Fluorescence, diffuse reflection, tissue, imaging

## 1. INTRODUCTION

Optical spectroscopy has been widely used in chemical analysis of biological samples. Since the mid-80s, the use of this technology for tissue classification has become a new approach in non-invasive medical diagnostics. In particular, the methods involved with laser-induced fluorescence (LIF) to characterize pathological states in human tissue have been extensively investigated<sup>[1-7]</sup>. The tissues are usually classified based on the spectral characteristics of endogenous tissue fluorescence (autofluorescence). Careful *in vivo* studies on several organ sites with an optical fiber catheter revealed that the fluorescence yield of early lesions were almost always lower than that of the surrounding normal tissues, although the spectral lineshapes of early lesions and normal tissues vary both from individual by individual and within an individual<sup>[4-7]</sup>. The algorithms based on the contrast in fluorescence yield between lesion and normal tissue can be used to discriminate early lesions. However, the point by point diagnosis by the use of an optical fiber catheter of fixed fluorescence excitation and collection geometry is not practical in clinical application. An imaging technique is desirable.

For examination of large area by an imaging device, recorded fluorescence power are strongly affected by the geometrical effects such as separation of the source-sample-detector, incident/emission angles and irregularity of sample surface. Without a mechanism to calibrate or compensate the geometrical effects, it is extremely difficult to compare the fluorescence yield at different sites in the imaged area, especially for *in vivo* measurements. Several groups have pursued different ways for mapping of fluorescence yield over the surface of turbid media. A non-imaging approach based on ratio of fluorescence intensity to reflection showed that the geometrical effects could be compensated, but the artifacts caused by the specular reflection of the tissue surface created much false positive<sup>[2,3]</sup>. In ref. [6], an effort combining ultrasound and fluorescence spectroscopy showed that the accuracy of tissue characterization was improved by compensating the detector-sample separation, though the dependence of fluorescence intensity on the incident/emission angle was uncertain. A digital image processing method was reported to eliminate the geometrical effects in fluorescence imaging by taking the ratio of the fluorescence image to itself processed by the "moving average algorithm", a type of low pass filter<sup>[7]</sup>. However, to ensure smoothing out the lesions and keeping the excitation and collection nonuniformities in the reference image, the algorithm requires that the lesion width is much smaller than the imaged area. Furthermore, if the spatial frequency of the low fluorescence areas caused by geometrical effects is overlapping with that of lesion, this low pass filter based image processing method will be unable to distinguish the lesion from the geometrical artifacts. In this study we introduce an imaging technique that allows for mapping of the fluorescence yield over the surface of a turbid medium by correcting the excitation and collection nonuniformities.

## 2. MATERIALS AND METHODS

The technique is based on a simple hypothesis. The reflection of the excitation light from the turbid media consists of three components: specular reflection, non-diffusive backscattering (such as single scattering) and diffusive backscattering. The diffusive components carry the information of excitation and collection geometry. Therefore, the geometrical effects of fluorescence imaging may be corrected by normalizing the fluorescence signal to the diffusive reflection recorded from the same site. Experimentally, a cross-polarization method can be used to reject the specular reflection and extract the diffusive components from the total reflection of excitation light. The tissue like sample (turbid medium) is illuminated with linearly polarized fluorescence excitation light and, by the use of a polarization analyzer, the cross-polarized image is recorded. Since forward scattering dominates the light propagation in the human tissue, the cross-polarized components in the reflection are mainly due to the multiple scattering and highly diffusive. The information carried in the cross polarization image are predominantly from beneath the superficial layer<sup>[8,9]</sup>. The specular reflection and superficial information (mainly due to the single back-scattering), which cause the artifacts in correction of geometrical effects, are almost completely removed in the cross-polarized image. Taking the ratio of the fluorescence signal against the cross-polarized reflection recorded from the same position, a normalized fluorescence image is formed.

The experimental arrangement is shown in Figure 1. A laser with 200 mW output at wavelength of 457 nm delivered the excitation onto the tissue phantom through a linear polarizer and microlenses. The fluorescence and reflection signals from the sample were collected by a commercial endoscope and imaged to an 8-bit CCD camera. The angle between the optical axes of the endoscope and illumination optics was about 15°. Both the divergent angles of the illumination optics and collection angle of the endoscope were about 38°. The imaged area on the sample surface was about 12×12 mm at  $\theta = 0^\circ$ . The holder of a long-pass filter with cut-off wavelength at 470 nm and a polarizer with the polarization axis perpendicular to that of excitation light allowed for easily recording the fluorescence or cross-polarized images. The fluorescence and cross-polarized images were grabbed by a frame-grabber. To improve the signal to noise ratio, the fluorescence image was formed by taking average of 16 image frames.

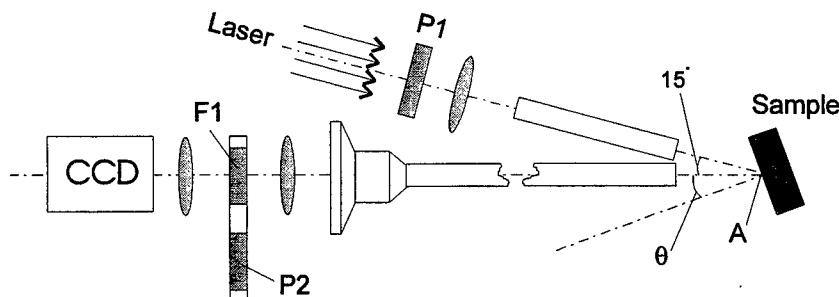


**Figure 1.** Schematic diagram of the experimental setup used to collect the fluorescence and cross-polarized reflection images. F1: long pass filter; P1, P2: polarizers with polarization axis perpendicular to each other;  $\theta$ : angle between the optical axis of endoscope and the normal of sample surface.

Tissue-simulating phantoms were made of gelatin with 20% solids dissolved in boiling deionized water, polystyrene spheres (0.55  $\mu\text{m}$  in diameter), fluorescent dye mixture and dominantly absorbing blood with red cells hemolyzed. The contents of blood, which determined the absorption coefficients ( $\mu_a$ ) of tissue phantoms used in this study, were 2.5%, 5%, 7.5% and 10% by-volume, respectively. The concentrations of polystyrene spheres, the dominant scatterers in the phantoms, were set to 0.25%, 0.35% and 0.5% by-weight, respectively. The scattering coefficients ( $\mu_s$ ) and anisotropy factor ( $g$ ) of tissue phantoms were calculated by Mie theory<sup>[10,11]</sup>. In the wavelength region of 450 - 700 nm,  $\mu_s$  for the concentrations of polystyrene microsphere at 0.25%, 0.35% and 5% were ranged from 95-39  $\text{cm}^{-1}$ , 133-55 and 189-78  $\text{cm}^{-1}$ , respectively. The  $g$  factor were ranged from 0.9-0.82. The composition of fluorescent dye mixture was carefully controlled to ensure its spectral lineshape similar to that of the autofluorescence of human tissue in the range of 450-700nm<sup>[14,5]</sup>. The absorption coefficients of dye mixture in all tissue phantoms were kept at least a factor of 10 smaller than that of 2.5% blood, the lowest level of blood content in all phantoms. The absorption of dye mixture was negligible. This ensured the linearity between the fluorescence yield and the dye content in a phantom. The optical properties ( $\mu_a$ ,  $\mu_s$  and  $g$ ) of all phantoms were in the range of human tissue<sup>[12]</sup>.

### 3. RESULTS AND CONCLUSIONS

In the first experiment, we demonstrate that the excitation and collection nonuniformities of fluorescence imaging of the homogeneous tissue phantom with flat surface can be corrected by the ratio imaging method. The optical properties of six phantoms were set by the combination of three blood contents (2.5%, 5%, and 7.5%) and two microsphere concentrations (0.25% and 0.5%). In practice, the geometry of imaging was changed by rotating the sample along the axis across the point-A and perpendicular to the plane of the page in Figure 1. The fluorescence and cross-polarized images were collected from all tissue phantoms at  $\theta = 0^\circ$ – $60^\circ$  with increment of  $15^\circ$ . For a fair comparison, the mean gray levels of all the fluorescence images and ratio images of fluorescence against cross-polarized reflection have been adjusted to 128, half of the full gray levels of an 8-bit image. The typical fluorescence and the ratio image are shown in Figure 2. The histograms of the gray level in the figure indicate the homogeneity of image. As can be seen in Figure 2, the gray level of fluorescence image varies in wide range, while the gray level of ratio image has a very narrow distribution around 128, the mean gray level. It was found that standard deviation (S.D.) of gray level for the fluorescence images recorded from all six tissue phantoms varied from 24 to 39 at  $\theta = 0^\circ$ – $60^\circ$ . In contrast, S.D. of all ratio images was below 3 and not sensitive to  $\theta$  and optical properties of samples. This indicates that the geometrical effects have been corrected to a great extent.

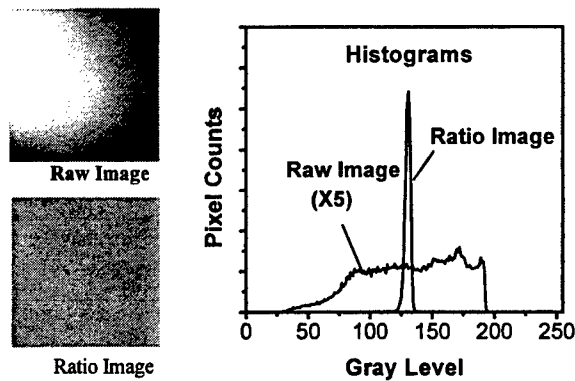


**Figure 2.** Images collected from a sample with blood content of 2.5% and 0.5% microsphere at  $\theta = 30^\circ$ .

The second experiment was designed to evaluate the performance of the ratio imaging technique on inhomogeneous tissue-like turbid media. To build an inhomogeneous tissue phantom, parts of homogeneous sample were replaced with the sample of different optical properties or fluorescence yield. The structures of three representative inhomogeneous samples are shown in Figure 3. The simulating lesions of fluorescence contrast phantom were made with the sample of the same optical properties and fluorescence yield about 82% of surrounding sample. Two holes of depth  $\sim 2.5$  mm were made to represent the irregularity of the sample surface and create interference for identification of simulating lesions. The absorption contrast phantom was made with samples of different  $\mu_a$  and the same  $\mu_s$ . The scattering contrast phantom was made with samples of different  $\mu_s$  and same  $\mu_a$ . The fluorescence dye content was uniform in both phantoms. The raw fluorescence and ratio images of fluorescence contrast tissue phantoms are displayed in Figure 4. Apparently, one can not distinguish the simulating lesions from the holes in the raw fluorescence image of fluorescence contrast phantom. In contrast, only the simulating lesions appear clearly, and the difference in fluorescence yield between simulation lesion and normal tissues were recovered. To explore the possibility to simplify the technology by using the similar approaches reported in ref. [2,3], we took the ratio of fluorescence to direct reflection. The direct reflection and ratio images shown in Figure 4 demonstrate that the false signals caused by the specular reflection create severe interference to identify the signal of simulating lesions. Comparing the raw and ratio images of absorption contrast phantom in Figure 5, it was found that the change of fluorescence signal caused by difference of blood content was corrected. This indicates that the effect of absorption variation on diffusive reflection and fluorescence may cancel each other. We observed that the variation of scattering property in scattering contrast phantom has not been corrected in the ratio image. This is because the cross-polarized reflection is much more sensitive to the scattering properties than fluorescence as shown in Figure 5. The variation of tissue scattering property may introduce artifacts to the ratio imaging technique. However, the scattering coefficient is mainly



determined by the tissue structure. The scattering difference between the premalignant early lesion and normal tissue may not be significant due to their histological similarity.

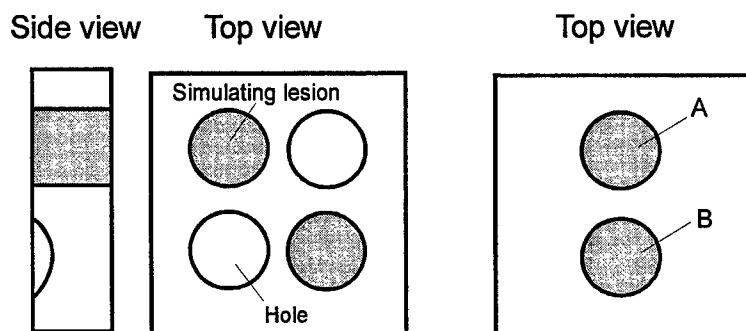
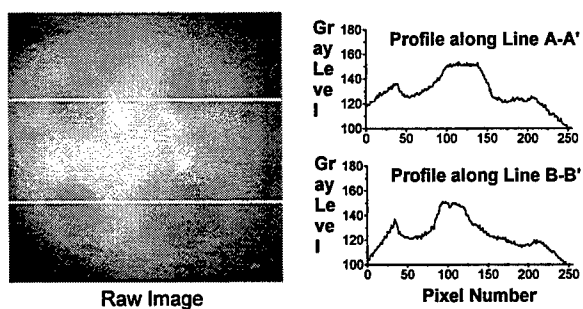
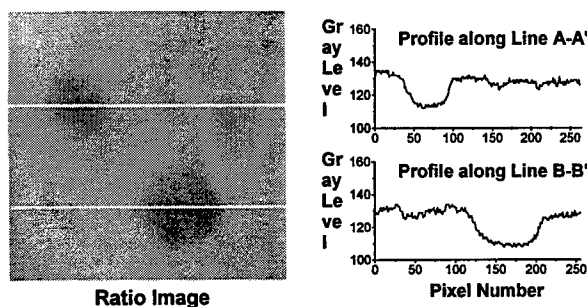


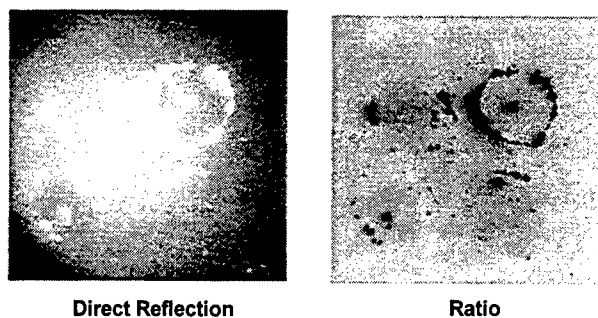
**Figure 3.** Structures and compositions of inhomogeneous phantoms. Left: Fluorescence contrast, Blood content: 5%, Concentration of microsphere: 0.35%; Right: For absorption contrast, Microsphere: 5%; Blood: 10% in area A, 2.5% in area B and 5% in surroundings. For scattering contrast, Blood: 5%; Microsphere: 0.5% in area A, 0.35% in area B and 0.25% in the surroundings.



(a)



(b)



(c)

**Figure 4.** Experimental results for fluorescence contrast phantom: (a) Raw fluorescence image and line profile analysis, (b) Ratio image and line profile analysis, (c) Direct reflection and ratio images.

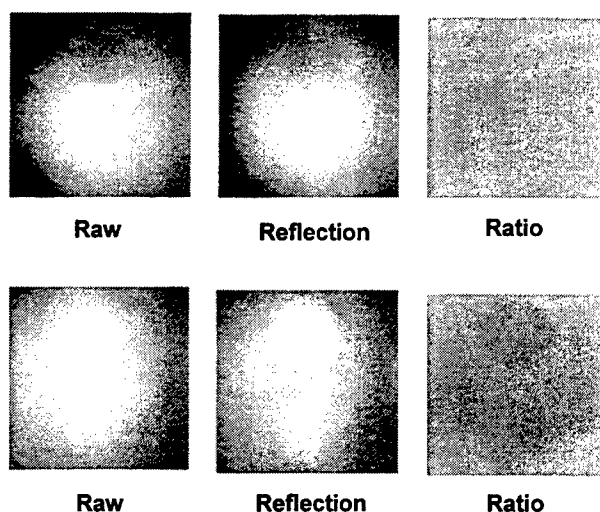


**Figure 5.** Raw fluorescence, cross-polarized reflection and ratio images recorded from absorption contrast phantom (above) and scattering contrast phantom (below).

It should be pointed out that most of human tissues have multiply layered structure and the distribution of endogenous fluorophores as the function of depth. The evaluation of the ratio imaging method on the real tissue may be more complicated. Our future work will be focused to study the *in vivo* examination on various tissues by using a specially designed endoscopic system based on the concepts reported in this paper. The effect of possible variation in tissue structure/scattering on the mapping of fluorescence yield will also be investigated.

This research is supported by Hong Kong Research Grants Council grant CA97/98.EG01 and Hong Kong University of Science and Technology.

#### 4. REFERENCES

1. G.A. Wagnieres, W.M. Star and B.C. Wilson, Photochem. & Photobiol., **68**, 603 (1998)
2. A.E. Profio, D.R. Doiron and J. Sarnaik, Med. Phys., **11**, 516 (1984)
3. P. Lenz, Rev. Sci. Instrum., **59**, 930 (1988)

4. N. Ramanujam, M.F. Mitchell, A. Mahadevan, S. Thomsen, E. Silva and R. Richards-Kortum, *Gynecologic Oncology*, **52**, 31 (1994)
5. J. Qu, C. MacAulay, S. Lam and B. Palcic, *Opt. Eng.*, **34**, 3334 (1995)
6. S. Warren, K. Pope, Y. Yazdi, A.J. Welch, S. Thomsen, A.L. Johnston, M.J. Davis and R. Richards-Kortum, *IEEE Trans. Biomed. Eng.*, **42**, 121 (1995)
7. T.D. Wang, J. van Dam, J.M. Crawford, E.A. Preisinger, Y. Wang and M.S. Feld, *Gastro.*, **111**, 1182 (1996)
8. S.G. Demos and R.R. Alfano, *Appl. Opt.* **36**, 150, (1997)
9. G.D. Lewis, D.L. Jordan and P.J. Roberts, *Appl. Opt.* **38**, 3937 (1999)
10. A.J. Durkin, S. Jaikumar and R. Richards-Kortum, *Appl. Spectro.*, **47**, 2114 (1993)
11. M. Kohl, M. Essenpreis and M. Cope, *Phys. Med. Biol.*, **40**, 1267 (1995)
12. W.F. Cheong, S.A. Prahl and A.J. Welch, *IEEE JQE*, **QE-26**, 2166 (1990)

# Instrumentation for subsurface imaging in a clinical environment

S. G. Demos, M. Staggs, H. B. Radousky

Lawrence Livermore National Laboratory, PO Box 808, L-411, Livermore, CA 94551.

Tel.: (925) 423 3388, Fax: (925) 423 2463

and

R. R. Alfano

Institute for Ultrafast Spectroscopy and Laser, CCNY, J-419, 138 Str. & Convent Ave., New York, NY. 10031

## ABSTRACT

The aim of this effort is to test the feasibility to develop endoscopic optical imaging technology for cancer screening inside the human body. The degree of success of such optical imaging instrumentation depends on the presence of optical differences among the various tissue components of interest of a body part or organ. Our research approach involves the utilization of the spectral polarization difference imaging technique incorporated into endoscopic imaging modalities. To establish methodology for optimum operation, we have build a compact imaging system for *in-vitro* studies of human tissue samples of interest in a clinical environment.

**Key words:** Polarization, Tissues, Backscattering, Imaging, Fluorescence

## 1. INTRODUCTION

The presence of characteristic optical "signatures" of various tissue components is key to the success of any photonic imaging modality for biomedical applications. These optical "signatures" may arise from differences in the biochemical and/or structural characteristics of the tissues. The differences in the cellular level (size of the cells, density and cell makeup) between cancer tissue when compared to normal tissue offers the promise for the development of optical imaging technology particularly suitable for cancer detection.

Optical endoscopes and other similar modalities are currently widely used to observe the interior of the human body. Endoscopes operate under white light illumination to provide color images of the human part under examination using a video system or other equivalent apparatus. Figure 1 shows conventional images (converted in gray-scale) of human bladder from two patients using an endoscope (cystoscope) frequently used by urologists. Brighter features in these images arise from cancer lesions located on the surface of the bladder tissue. Images are approximately 2-cm in diameter. Eighty percent of bladder cancer cases are superficial, that is they are above the muscle. These after resection recur about 50% of the times. When the tumors become muscle invasive overall, the 21/2 year survival is about 50%. Thus, there is a real need to be able

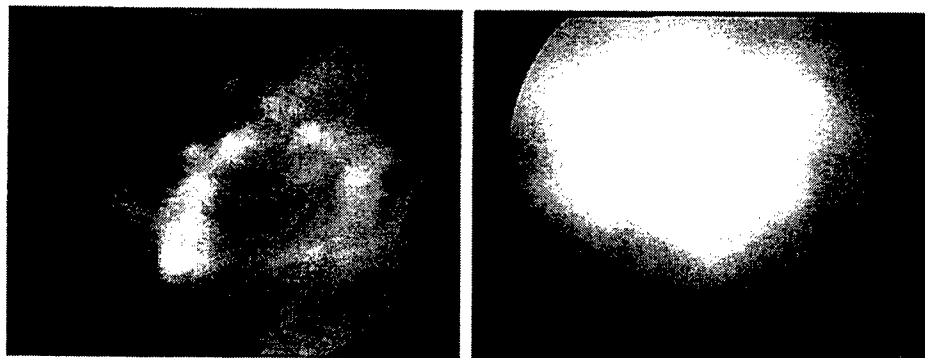


**Figure 1:** Images of human bladder from two patients obtained using a cystoscope. Brighter features arise from cancer lesions located on the surface of the tissue.

to identify which of the tumors will progress, and there is a need to be certain that a tumor truly is not muscle invasive. Bladder cancer is a clinical example that clearly demonstrates the need for a deep-subsurface imaging modality.

This work represents an effort to develop an imaging technology for non-invasive analysis and imaging of tissues and chemical distributions in the body with imaging depth of up to 1 centimeter. The approaches examined are adaptable to existing endoscopic imaging modalities to allow for employment inside the human body. One of the approaches we are examining embodies the spectral polarization difference imaging (SPDI) technique [1,2] which can offer deep subsurface imaging (up to 1-cm) based on changes in scattering and absorption at particular wavelengths [2]. In addition, far-red and near infrared emission imaging under red photoexcitation is examined as a complementary method to SPDI for differentiating various tissue components [3]. This method is suitable for surface and 1-millimeter depth subsurface imaging. For certain applications such as for cancer detection, the above techniques may provide an adequate tool for noninvasive disease detection and characterization inside the human body.

## 2. EXPERIMENTAL APPROACH

The SPDI technique utilizes spectral and polarization filtering of the backscattered light under polarized illumination to detect and enhance the visibility of an "object" located on the surface or below the surface. The sample is illuminated with linearly polarized light and using an analyzer, the perpendicular polarization image components are recorded for different illuminating wavelengths. It has been shown that the surface image information is almost completely carried by the parallel image while the perpendicular image contains predominantly information from beneath the surface [1]. The images obtained at different illuminating wavelengths are formed by photons that have reached a different penetration depth inside the tissue due to differences in scattering and/or absorption. In general, longer in wavelengths photons can reach a larger penetration depth. Utilization of different illuminating wavelengths in combination with polarization techniques and subsequent inter-image operations lead to the removal of the image component of the outer tissue layers and enhancement of the image information from the inner layers of the tissue. Choosing the appropriate illumination wavelength, images at different depth zones are effectively captured.

Images shown in figure 1 indicate that there are optical differences between normal and cancer bladder tissues that can be exploited by an optical imaging and/or diagnostic tool. The construction of such an imaging modality that is based on the SPDI technique is possible using existing technology and components developed for medical endoscopes with the incorporation of the appropriate modifications. Such modifications should include polarized multi-wavelength illumination of the sample and selection of the cross-polarized image components. The arrangement of the optical components of an endoscopic imaging system based on the SPDI technique is shown in figure 2. The illumination is obtained from a white

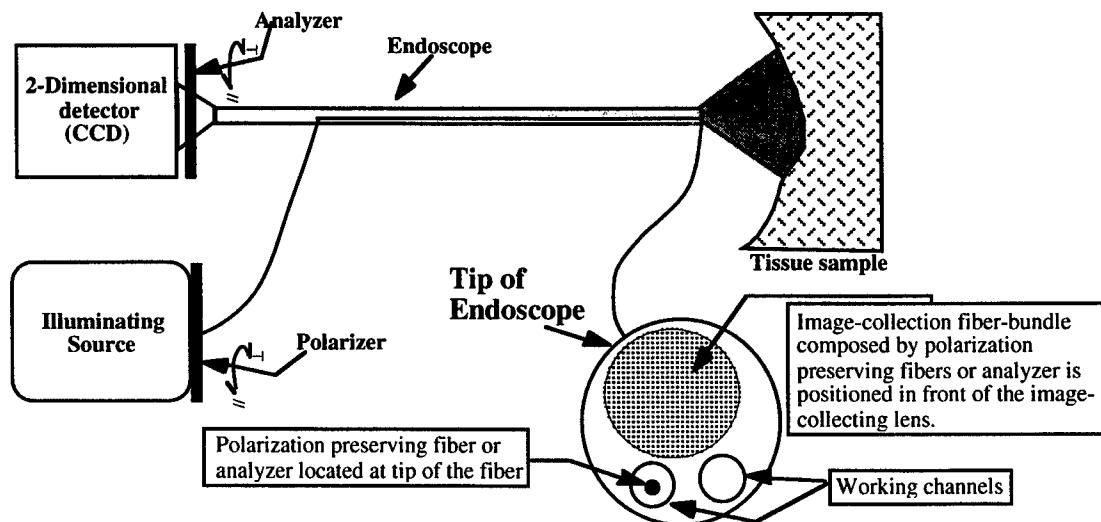


**Figure 2:** The arrangement of the optical components of an endoscopic imaging system that incorporates the SPDI subsurface imaging technique

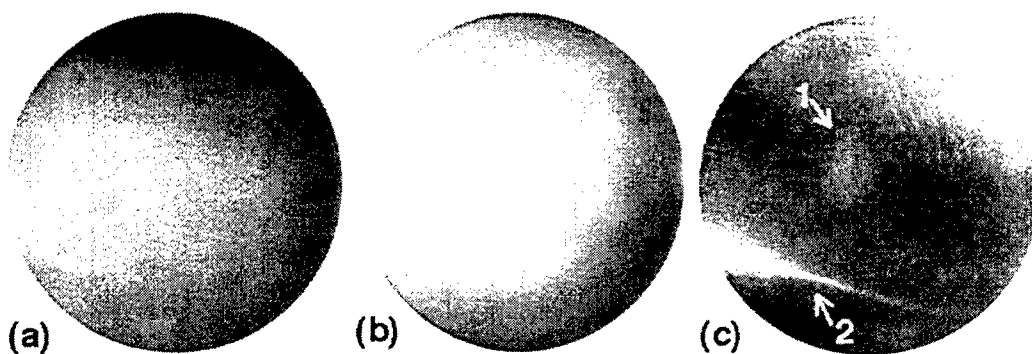


**Figure 3:** Images of a breast chicken tissue sample that contains fat (“1”) and tendon (“2”) tissue lesions located 1-cm and 0.5-cm, respectively, below the surface of the sample. The perpendicular polarization image components under 690-nm (a) and 820-nm (b) illumination. The SPDI image obtained using 970-nm and 820-nm illumination (c).

light source or from diode lasers. This light is coupled into a fiber that reaches near the sample through the endoscope’s working channel. A polarizer and optical filters are positioned between the illumination source and the fiber to ensure polarized illumination of the sample at different wavelengths. In this configuration, a polarization preserving illumination fiber is required for proper operation. Alternatively, a polarizer may be placed at the tip of the illumination fiber in order to guarantee polarized illumination of the sample without the need of a polarization preserving fiber. The scattered light is collected by the endoscope’s lens and an appropriate analyzer is used to select the perpendicular polarization image component. The imaging lens of the endoscope may be composed by an image-collection fiber-bundle made by polarization preserving fibers. In this case, the analyzer can be located at the end of the endoscope (in front of the CCD). Alternatively, the analyzer may be positioned in front of a standard image-collecting fiber-bundle or other type of specialized endoscope lens designs. The polarizer and analyzer are always cross-polarized. A CCD camera or other equivalent modality is used to record the digitized images from the sample. Depth profiling of the tissue structures observed using the SPDI technique is achieved using different illumination wavelengths.

The digitized images obtained using this technique will show intensity variations that will be subject to interpretation. This is demonstrated in preliminary experiments using animal tissues and an image collection lens that is similar to those used in cystoscopes for imaging of the bladder. The illumination was obtained from a white light source that is coupled into a fiber and delivered into the sample. Using appropriate optical filters (F) at the input of the fiber, illumination of the sample with light at different wavelength was achieved. A polarizer was positioned at the output of the illumination fiber. A second polarizer with its polarization axis oriented perpendicular to the first polarizer was positioned in front of the imaging lens. Figures 3a and 3b show images of a 2-cm thick breast chicken tissue sample under 690-nm and 820-nm illumination. The sample was prepared using three breast chicken tissue layers. The top layer was 0.5-cm thick and consisted of homogenous breast tissue. The second layer was also 0.5-cm thick but it contained a tendon lesion on its surface. In the middle of the surface of the third, 1-cm thick, breast tissue layer, a  $\approx 4$ -mm in diameter, 2-mm thick fat lesion was positioned and sandwiched between the second and third breast tissue layers. The three layer, 2-cm thick, sample was placed between two glass slides and slightly compressed to a uniform thickness. The SPDI image obtained using 970-nm and 820-nm illumination is shown in figure 3c. Two features observed in this image denoted as “1” and “2” show the fat tissue (“1”) and tendon tissue (“2”) lesions located 1-cm and 0.5-cm, respectively, below the surface of the sample. Figures 2a and 2b demonstrate that these features are not visible or difficult to be identified when direct images are recorded even when polarization filtering (to reject the less scattered photon on the outer tissue layers) or NIR illumination wavelengths (to reach larger photon propagation depths) are used. Using white light illumination and color video imaging (typical operation of endoscopes), these two tissue lesions located below the surface are not visible and it would be impossible for the operator to detect. These results demonstrate that the application of the SPDI technique for endoscopic imaging is possible.

To test the operational concepts for endoscopic imaging and cancer detection in a clinical environment, we have built a prototype instrumentation to perform *in-vitro* measurements of human tissue samples as they become available immediately after surgery. Figure 4a shows a photograph of this prototype instrument. This instrumentation will allow to utilize various illumination wavelengths and sources to test the ability to distinguish between normal tissue and malignant or benign tumors in various body parts as well as identify the best possible approaches for endoscopic imaging and cancer detection.. The primary focus of this investigation will be the application of this technology for the detection of cancer in bladder, colon, prostate and kidney. Figure 4b shows the schematic layout of the key optical components of this first version of the system. The experimental setup involves polarizers (P) and appropriate optical filters (F) while diode lasers and a white light source are used as the illumination sources. There are three different concepts that will be examined.

To test the first concept (light scattering approach for implementation of the SPDI technique), a white light source is used to illuminate the sample at different wavelengths selected by optical filters located on a filter wheel and the two polarization image components in the backscattering geometry will be recorded. The experimental results obtained using human tissue samples will reveal differences between normal and cancerous tissue components and provide information on the applicability of the SPDI subsurface imaging technique to address the problem of cancer detection.

The second concept to be tested involves imaging of various tissue types using the near infrared emitted light under 633-nm excitation. The experiments will be performed by incorporating polarization selection to enhance the volume of information. These measurements will reveal differences between normal and cancerous tissue components by comparing the intensity of the NIR emission images, the totally polarized NIR emission images and the degree of polarization of the emission images.

The third concept to be tested utilizes the degree that light depolarizes as it propagates through tissue to probe the structural characteristics of tissue components of interest [4,5]. For this purpose, polarized laser light at 820-nm will be used to illuminate the sample and the degree of polarization of the transmitted light through the tissue will be used for imaging. Different tissue structures (such as a suspicious tissue lesions in a field of normal tissues) will be imaged by comparing the intensity of the image formed by a) the overall transmitted light  $[(I(//)+I(\perp))/I_0]$ , b) the polarized transmitted light  $[(I(//)-I(\perp))/I_0]$  and c) the degree of polarization of the transmitted light  $[(I(//)-I(\perp))/(I(//)+I(\perp))]$ . This method may be particularly suitable for *in-vitro* prostate imaging and cancer detection to assist the pathologist intensify suspicious lesion for quick pathology assessment.

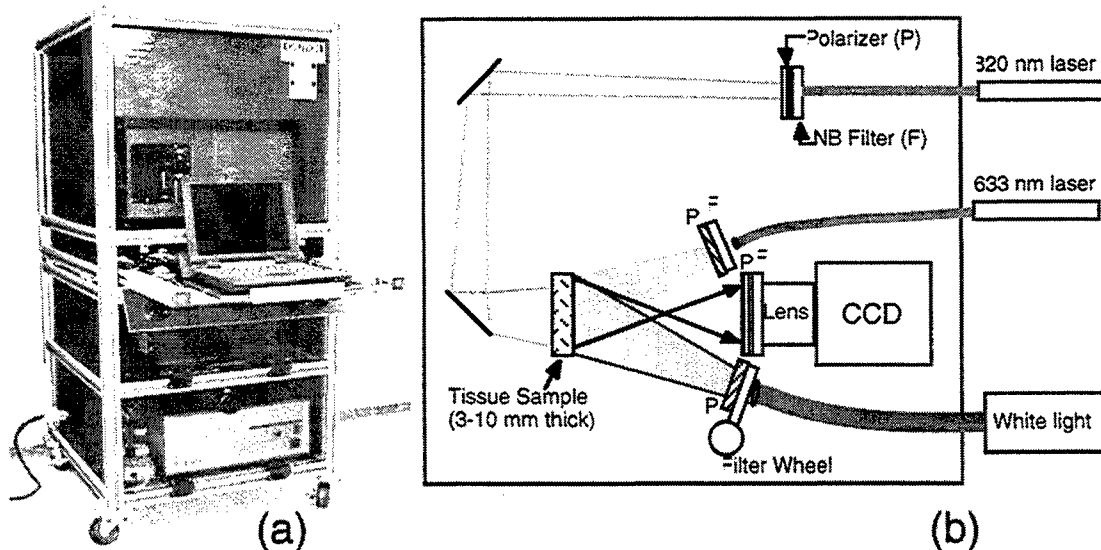


**Figure 4:** a) Photograph of the prototype instrumentation to perform *in-vitro* measurements of human tissue samples immediately after surgery. Its compact size and computer controlled operation enables its implementation in a clinical environment. b) Schematic layout of the key optical components of this system. The experimental setup involves polarizers (P) and appropriate optical filters (F) while diode lasers and a white light source coupled with optical fibers are used to illuminate the sample.

### 3. DISCUSSION

To successfully treat and cure a cancer patient, early detection and appropriate selection of existing anti-cancer treatments for each patient are of great importance. Except for skin cancer, all the other types of cancer occur inside the body and are very difficult to be detected at early stages. A large percentage of these cancers occur inside the body that can be reached and viewed using various types of endoscopes. Stomach, cervix, uterus, colon, rectum, bronchus and bladder cancers could be detected at early stages when they are best treated if a suitable minimally invasive endoscopic screening system existed. In addition, such an endoscopic screening system could assist in monitoring the development on a cancer tumor(s) for an assessment of the success of the treatment of the patient with chemotherapy or other method.

The images obtained using the approaches discussed in this work will be able to provide information of different tissue structures on the surface and below the surface. The utilization of this technology incorporated into different types of existing endoscopes with the appropriate modifications can be realized using low cost off-the-shelf components, will be user friendly requiring no particular specialization nor exposure of the operator to any harmful radiation and will be minimally invasive for the patient. This technology may also find applications in other areas of basic and clinical research as well as in clinical diagnostics. If appropriate optical "signature(s)" exists, this method could be useful for the diagnosis of clinical disease, early detection/screening, for identifying the presence of toxicant or drugs at specific target sites in the body, for determining the concentrations of these agents on the target sites of interest for monitoring individual therapies, for assessing pharmacokinetic and pharmacodynamics in basic and clinical research and in forensic analysis.

### 4. CONCLUSION

An endoscopic imaging system for surface and subsurface imaging for clinical applications may only require small modifications of existing endoscopes to provide inexpensive technology which the medical personnel is already familiar with. As a result, this technology can become an easily accessible screening and diagnostic tool to the medical community due to the anticipated low cost of acquisition and operation and the limited expertise and training required. This imaging technology may find application in the early detection/screening of cancer, in providing minimally invasive monitoring of the tumor's response to various stages of treatments and in assisting during surgery by providing information on the depth of penetration of the tumor. Studies and testing in a clinical environment are in progress.

### ACKNOWLEDGMENTS

This work was performed at Lawrence Livermore National Laboratory under the auspices of the U.S. Department of Energy under Contract W-7405-Eng-48 through the Institute for Laser Science and Applications, Materials Research Institute, the U.S. Department of Energy Center of Excellence at City College of New York and the California Cancer Research Program.

### REFERENCES

1. S. G. Demos and R.R. Alfano, "Optical Polarization Imaging" *Applied Optics*, **36**, 150-155, (1997).
2. S. G. Demos, H. B. Radousky and R.R. Alfano "Subsurface imaging using the Spectral Polarization Difference technique and NIR illumination", *Optical Tomography and Spectroscopy of Tissue III*, B. Chance and R. R. Alfano, Eds., SPIE **3597**, 406-410, 1999.
3. Gang Zhang, S. G. Demos, and R.R. Alfano, "Far-red and NIR spectral wing emission from tissues under 532 nm and 632 nm photo-excitation", *Lasers in the Life Sciences*, **9**, 1-16 (1999).
4. S. G. Demos, H. Savage, Alexandra S. Heerdt, S. Schantz and R. R. Alfano, "Time-resolved degree of polarization for human breast tissue", *Opt. Comm.*, **124**, 439-442, (1996).
5. S. G. Demos, H. Savage, Alexandra S. Heerdt, S. Schantz and R.R. Alfano, "Polarization Filter for Biological Optical Imaging", *Photochemistry and Photobiology*, **66**, 821-825 (1997).



# Elastic Scattering Spectroscopy In-Vivo: Optical Biopsies of Cancers of the Breast and GI Tract

David C. O. Pickard<sup>1a</sup>, Gavin M. Briggs<sup>a</sup>, Christobel Saunders<sup>a</sup>, Sunil Lakhani<sup>a</sup>, Paul M. Ripley<sup>b</sup>, Irving J. Bigio<sup>b</sup>, Stephen G. Bown<sup>a</sup>

<sup>a</sup>National Medical Laser Centre, Division of Surgical Specialities, Royal Free and University College Medical School, University College London, First Floor, Charles Bell House, 67-73 Riding House Street, London, W1P 7PN, UK

<sup>b</sup>Bioscience Division, Los Alamos National Laboratory, Los Alamos, NM 87545

## ABSTRACT

Elastic scattering or diffuse reflectance spectroscopy offers the possibility of distinguishing between normal and neoplastic tissue with a relatively simple optical measurement. The measurement of the relative reflection of light has previously been shown to be sensitive to the size and distribution of both intra and inter-cellular structures as well as absorption from chromatophores which are present in the tissue. By coupling a white light source and spectrometer to optic fibres it is possible to construct probes which can be inserted percutaneously or intra-operatively into breast tissue or which can pass down the channel of an endoscope and take in-vivo spectra of diseased and normal tissue in the Gastro-Intestinal tract. Spectra are reported from a large number of patients with a variety of benign, metaplastic, dysplastic and cancerous conditions. Some differences that have been observed in these spectra are discussed and the merits and disadvantages of "optical biopsy" as an in-vivo diagnostic tool are examined. It is shown that to a relatively high degree of sensitivity and specificity it is possible to distinguish cancerous from normal tissue in a number of cases. The methods of distinguishing spectra and some possible modalities for their improvement are discussed.

**Keywords:** Optical Biopsy, Elastic Scattering, Breast Cancer, Diagnosis, Barrett's Oesophagus

## 1. INTRODUCTION

Breast cancer is one of the largest killers of women in the developed world. Breast cancer represents 30% of all new cancers in American women and between 1 in 8 American and 1 in 12 European women will develop breast cancer at some point. However 5-year survival rates are standing at 62-76% in Western Europe and improving. Prompt and efficient detection and diagnosis of breast cancer is important to the effectiveness of the treatments and the long-term prognosis of the patients. Detection can be undertaken in a number of ways. Breast self examination is promoted in many countries and a program of referral from local general practitioners to breast clinics at specialist centers detects most palpable lumps, i.e. those that can be felt externally. Several countries also run screening programs which offer women mammograms at regular intervals. In the United Kingdom women between the ages of 50 and 64 are offered 3 screening every 3 years. These can be very useful in detecting micro-calcification, which may be associated with cancers. Screening can often identify tumours long before the associated lumps would have become palpable. Women with a family history of disease or other high risk factors are often monitored more closely.

A number of different optical techniques are being investigated for the detection and diagnosis of cancerous lesions in the breast. These include, at the far end of the electromagnetic spectrum, the x-ray scanning or mammographic techniques, far infra-red techniques to discover increases of blood flow associated with tumours either by the additional heat given off from neo-vascularization or by direct observation of the vessels in transmission. In other areas of cancer detection and diagnosis fluorescence and Raman spectroscopy have also been used to identify tumours.

Approximately 1 in 10 members of the population of developed nations will suffer from acid reflux, from the stomach into the lower oesophagus, at some point in their lives. In a mild form this is a temporary discomfort commonly known as

<sup>1</sup> Correspondence: D. Pickard; Email: D.Pickard@ucl.ac.uk; Tel: +44 (0)20 7679 9084; Fax: +44 (0)20 7813 2828; Supported by US Army Materiel Command.

heartburn. In cases of chronic reflux between 1 in 5 and 1 in 10 patients will go on to develop a condition known as Barrett's oesophagus. In Barrett's oesophagus the squamous epithelium of the oesophageal tube undergoes changes, in a process known as metaplasia, to resemble the columnar epithelium of the upper intestine. Barrett's oesophagus is reasonably straightforward to recognise during white light endoscopy, where the metaplastic epithelium takes on a red velvety appearance. In approximately 10% of those patients that develop long-segment Barrett's oesophagus the epithelium may become dysplastic. This dysplasia does not appear significantly different from normal Barrett's under white light endoscopy, but its severe form is known to be a pre-malignant condition and carries a very significant risk of adenocarcinomas of the lower oesophagus and gastro-oesophageal junction. Currently the only method of screening patients for dysplasia in Barrett's is regular random quadrant biopsies at 2-cm intervals throughout the Barrett's segment. The challenge is to recognise the pre-malignant dysplasia as early as possible so that it can be treated before it has a chance to progress further.

## 2. ELASTIC SCATTERING SPECTROSCOPY

Elastic-scattering spectroscopy (ESS), sometimes called "diffuse reflectance spectroscopy", has been studied as a technique that can be used for minimally invasive optical diagnosis or "optical biopsy". This has been shown to have the potential to distinguish dysplasia and cancer from normal and benign conditions [1-3], as well as being able to differentiate different types of normal tissues. The main advantages of using an optically based system such as ESS for diagnosis are directly related to the technologies these systems employ. The use of fine gauge optical fibers for the delivery and collection of diagnostic light, results in the construction of "optical probes" that are compatible with current clinical instrumentation used for minimally invasive procedures, such as core-biopsy needles, endoscopes, laparoscopes, colposcopes and cystoscopes. The other major benefits of optical biopsy are related to the computerized-automation of the system, which facilitates the rapid (<1s) acquisition of spectroscopic data. This system has the potential of reducing costs and risk by preventing the unnecessary surgical excision of suspicious lesions that may be non-malignant or eliminating further surgical procedures due to incomplete removal of malignant tissue. As a diagnostic aid it may also offer the advantage of a reduced waiting-time for the result, which could therefore minimize the related patient anxiety. The clinical instrumentation based upon ESS has been described in previous publications that reported earlier clinical studies [1-2]. Elastic-scattering spectroscopy (ESS), when performed using an optical fiber based probe with an appropriate optical-geometry [4], is sensitive to the size and structure of the sub-cellular components that change upon transformation to pre-malignant or malignant conditions (e.g., the nucleus, mitochondria, etc.).

## 3. OPTICAL BIOPSIES WITH THE ESS SYSTEM

The optical biopsy system consists of a flashlamp, an optical probe, a spectrometer and a computer to control these components and record the elastic scattered spectrum. A diagrammatic representation of the components of the system is given in figure one. The spectrometer, flashlamp and power supply are contained in a briefcase sized unit to which the computer and optical probe are attached. The flashlamp is a pulsed xenon arc lamp that emits light between approximately 300 and 900 nanometres. This light is coupled into an optic fibre that carries the light to the tissue. A second fibre collects the light from the tissue and transfers it back to the spectrometer. The spectrometer analyses the light between approximately 350-900 nm using a diffraction grating and CCD array. The computer controlling the unit is in general a lap-top for portability with a 486 or better chip and running some form of the windows operating system.

A number of different designs of optical probe exist for obtaining spectra from a variety of different types of tissue and using different methods. All of the optical probes have two SMA connectors to couple the send and receive fibres to the flash lamp and spectrometer respectively. The probes are generally 2 to 3 metres in length to allow them to be used by surgeons while maintaining sterility or to be passed through the channel of an endoscope. The tip of the probe presents the fibre tips to the tissue at a fixed separation. This tip may be made of large gauge stainless steel for hand held uses, thinner rigid designs for use through core cut needles and flexible tips for use through endoscopes.

To obtain a spectrum the probe is placed in contact with the tissue under investigation. With the current design of probes the probe must be held as close to perpendicular to the tissue so that both fibres are in complete contact. In order for the light to be collected by the receive fibre it must be reflected through one hundred and eighty degrees. This takes place through a series of elastic scattering events that are represented in figure two. The scattering coefficients will vary with wavelength and the size of the particles in the scattering medium and can be predicted, to first order, by Mie theory. The spectrum will not only be a product of the scattering events but also of absorption by chromophores in the tissues, such as

haemoglobin from blood and beta-carotene in adipose tissue. This absorption can give indications of the state of vascularization and indeed oxygenation in the tissue but can also overwhelm the spectrum. It may sometimes be necessary to wipe or wash the tissue to prevent this absorption washing out the spectrum.

#### **4. USES OF ESS IN BREAST CANCER DIAGNOSIS**

In the present study the optical biopsy system is being used in a number of different ways to investigate ways it might be used in the diagnosis and treatment of breast cancer. The first study investigates how the system might be used in a clinical environment along with core cut biopsies, to provide an in-situ diagnosis that could then be confirmed by conventional histology. The second investigation looks at how the system may be used as a surgical aid to identify cancerous tissue during excision, and prevent any tumour being left in the patient. Lastly the study looks at whether elastic scattering spectroscopy may give any information on the status of sentinel nodes, which are important to the staging of the disease and the prognosis of patients.

##### **1. Percutaneous (Clinical) Biopsy**

Percutaneous biopsies are routinely performed to obtain histological diagnosis when suspicious lumps have been found on clinical examination or when opacities have been observed during routine mammogram screening. Previously these biopsies have been obtained from a minor surgical procedure or via fine needle aspiration (FNA). Aside from the accuracy of histological information obtained during a minor lumpectomy the disadvantages of a surgical procedure are clear (especially if surgery may need to be repeated to complete the excision). Fine needle aspiration although very inexpensive is becoming less and less used especially within the United States due to doubts over the accuracy of the cytology results and worries of the chances of false negative diagnoses as only a few cells are sampled.

The alternative is to take biopsies in which a macroscopic core of tissue is removed from the lump percutaneously but using a large gauge needle. Two methods and systems are widely used for obtaining these 'core' biopsies. In the first, referred to as core-cut, the 14-gauge biopsy needle consists of a hollow sleeve, with an internal rod that has an 3/4 inch long recessed section near its tip. The needle is positioned within the suspicious lump either manually or using some variety of image guidance (digital mammography or Ultrasound - US). The 'gun' attached to the needle is primed and then when it is 'fired' two things happen in very quick succession. Firstly the inner part of the needle is shot forward an inch or so into the tissue to expose the recessed section into which tissue that has just been pushed aside by the needle can relax. The outer section of the needle is next pushed over the inner and this cuts out the 'core' of tissue within the recessed section. The needle is then removed and the core is sent for standard histopathological analysis.

The second device known as a mammotome also uses a two part needle, but within this device the recessed space contains a series of holes, which when a vacuum is applied will 'suck' tissue into the recess before the cutting sheath is drawn over. This results in larger biopsy specimens, which can be important in cancerous tissue which being much stiffer than normal tissue does not relax as quickly and may result in inadequate specimens. This system may also be used in conjunction with image guidance. In either of the systems, to increase the chances of an adequate biopsy and decrease those of false negative diagnoses, several core cuts may be taken, sometimes as many as a dozen, traversing the lump at different angles and in different planes.

The optical biopsy system can be used in conjunction with either of these core biopsy devices. In both cases the internal apparatus is removed and the probe is inserted down the inner sheath. When a spectrum has been acquired the probe is removed, the inner part of the biopsy kit replaced and a standard biopsy obtained. In order to match the spectra to the histological diagnosis at as near as possible the same site the far end of the biopsy core is marked with black ink before it is sent to the pathology labs. Currently the majority of our core-cut biopsies are obtained in theatre from the unconscious patient but prior to them being prepped for the operation. In future we intend to take more spectra from patient in clinics under local anaesthetic, more accurately reflecting the one of the roles we see the probe being put to eventually. Unfortunately the diameters of probe are incompatible with the needles used in FNA, however it would also be hard to compare with the cytology results which are obtained along quite a long track.

##### **2. Tumour Bed Measurements**

Mastectomy (total breast amputation) has been the treatment of choice for breast cancer since the late 19<sup>th</sup> century. Recently however, modern breast surgery has seen a trend towards more conservative procedures where most of the breast tissue is retained. Such procedures are referred to as wide local excisions or lumpectomies. Although recurrence rates following these procedures are slightly higher than for mastectomy patients, long term survival rates are unaffected and obviously by conserving the breast, the cosmetic and psychological effects are much reduced.

When a tumour or suspicious lump is removed in a surgical procedure it is important that the margins, or edges of the excision are clear from malignant tissue which might otherwise continue to proliferate. To ensure this, the specimen from a wide local excision may be sent for frozen section (where the lump is snap frozen and sliced) to ensure that the tumour does not extend too close to any of the margins. This is a time consuming, and due to the risks of extended or repeated anaesthesia, possibly dangerous procedure. If the tumour bed, or the margins of the excised sample, could be tested for residual cancer during or immediately after the operation and an instant diagnosis could be gained this would obviously be preferable.

For the purposes of this study spectra were acquired from patients after the tumour had been excised. First the area was examined manually by the surgeon, feeling for any small lumps or other odd features in the remaining tissue. Prospective sights were marked with ink (not actually on the site but in a triangle of points around it), spectra were acquired, and then small tissue biopsies were obtained using forceps. Obviously the proportion of positive margins will hopefully be very low but using this technique it is possible to obtain very accurate correlation between the tissue examined, its histology, and the elastic scattering spectra. Some work is also in progress on measuring the degradation in spectra from those taken *in-situ* and those taken from tissue that has been excised. This is done using time series of experiments to understand how the spectrum changes with tissue de-oxygenation and cooling and to examine whether *ex-vivo* spectra provide similar diagnostic information as those taken *in-situ*.

### 3. Sentinel Node Measurement

The lymphatic system consists of a network of small vessels (rather like tiny veins) connecting a series of lymph nodes (glands). Its main functions are to drain extra-cellular fluid back into the circulation and also trap infectious agents such as bacteria and viruses in the lymph nodes where the 'infection fighting' white cells are congregated. The drainage from the breast tissue is to a network of nodes which are mostly situated in the axilla (underarm), although there are also some in the sub-clavicular regions and behind the sternum. When tumours spread to other areas of the body the most common route for this metastasis to take place is through the lymphatic system. To assess the staging of the cancer it is therefore important to know if the tumour has metastasised to the lymphatic system. The sentinel node is the first node (usually in the axilla) to which the tissue surrounding the breast tumour drains. The phrase 'sentinel node' is somewhat misleading because the structure of the lymphatic system may lead to several nodes being primary drainage points, and in this case all nodes must be investigated. Various methods can be used to find this primary node. Two of the most common are the use of a dye or radioactive isotope tracer.

A dye, frequently blue, is injected into the breast and given time to diffuse through the tissue and begin to drain into the lymphatic system. Different techniques suggest injecting the dye around the tumour itself, in the skin above the tumour or simply below the aureola. If injected subcutaneously the blue dye can lead to permanent marking of the skin in a manner analogous to tattooing although it generally disappears by one year. In most cases the sentinel node biopsy is part of a procedure involving some breast tissue excision, and in this case the discoloured skin will also be removed. With the radioactive marker techniques a solution, usually containing technetium, is injected in advance of the operation. Radio-imaging can then be used to find the approximate position of the sentinel node, whether there are multiple nodes to find, and sometimes also if there is a secondary focus of tumour. During the operation the nodes are located using a Geiger counter with appropriate shielding.

Once the sentinel node (nodes) has been located, it is removed and sent for histopathology. Often this is done as a frozen section, analogous to the procedure defined above. The analysis of the node has significant repercussions for the prognosis of the patient and the further treatment of the disease. If the node shows no evidence of metastasized cancer then it is termed negative and barring recurrence the disease can be assumed completely removed. If the node proves to be positive, the patient will require the rest of the axillary nodes to be removed and assessed (axillary clearance). The overall number of positive nodes has implications for further treatment, namely chemotherapy, and also is one of the most important indicators of prognosis.

In this study lymph nodes were examined after dissection to establish whether elastic scattering spectroscopy could distinguish positive from negative nodes. Because the nodes were examined ex-vivo the restrictions on sterility of the system were less severe. The lymph nodes dissected can range in size from a few millimeters to several centimeters in diameter. Although it may be possible for the surgeon to approximately determine the status of the nodes by hand, because nodes containing tumour will tend to be firmer to the touch, decisions on axillary clearance will always await the pathology result. The nodes to be examined were bivalved, which means they were cut almost in two along their major axes and spread open for examination. Cytology imprints were obtained from the nodes as an alternative method of diagnosis, by pressing the bivalved surface onto the surface of a slide. Spectra were obtained from a point judged to be at the centre of the node and from a couple of points at the periphery, or cortex, where it is known that partial replacement will be first observed. The node was then sent for standard pathological examination and the results compared to the spectra. The axilla contains between 10 and 30 identifiable nodes and after axillary clearance it was possible to perform biopsies on several nodes, some of which would be positive and some negative.

The use of blue dye to identify the sentinel nodes could possibly prove problematic when obtaining elastic scattering spectra for diagnostic purposes. The dye used at the Middlesex hospital was Patente Bleu V, a dye of the triphenylmethane class which is also used in food colouring under the European classification number E131. This dye has a well known spectrum and although its partial or complete removal from the spectrum may be possible its maximum absorption at approximately 630nm did not appear to interfere with the results to a great extent.

## 5. RESULTS

A number of patients previously diagnosed with Barrett's oesophagus were recruited at the Middlesex Hospital in central London. The patients had been referred for upper gastrointestinal (UGI) endoscopy examinations to monitor the progress of their conditions. During the UGI procedures a set of normal biopsies were to be obtained to test for dysplasia within the segments of Barrett's mucosa. The so-called random quadrant biopsies involved taking four pieces of tissue at a particular level of the oesophagus and repeating this process at 2cm intervals throughout the Barrett's segment. Informed consent, as regulated by the local ethics committee, for the optical biopsy procedure and any additional biopsies was obtained. Prior to each of the quadrant biopsies being obtained the optical probe was inserted through the biopsy channel of the endoscope and held against the wall of the oesophagus while a spectrum was obtained. Immediately afterward a standard biopsy was obtained from the same spot, as judged by the endoscopist. The biopsy samples were submitted separately for conventional histopathological diagnosis, and when the results returned they were matched up with the appropriate spectral traces.

Two different automated methods of spectral classification were employed to assess the degree of correlation between pathology and spectral pattern differences: artificial neural networks and hierarchical cluster analysis. Artificial neural networks (ANNs) were selected for study because of the expectation that they would prove to be a generally useful method of tissue spectral classification. ANNs are well suited for classification in systems where model-based classification is difficult. Such is the case with ESS spectra of GI tissue because of the remarkable heterogeneity of tissue types with consequent broad variability in optical scattering and absorption properties. Hierarchical cluster analysis (HCA) was employed to examine the variability within the spectra from the view of different measures of spectral properties.

Figures three and four show examples of elastic scattering spectra obtained from benign and malignant breast tissue and positive and negative sentinel nodes. The figures are reproduced from Bigio et al. (2000) [3]. The spectra are displayed in a ratioed form in which the ratio of the observed elastically scattered spectrum has been ratioed [too many ratio's] to a reference spectrum taken from a sample of Spectralon™. Spectralon is a material with a very flat diffuse spectral response in the interval of interest. The spectra have also had any residual light from background illumination removed and have been smoothed and scaled appropriately. Lastly the spectra have been normalised to the area beneath the curves to allow better comparison.

Figure three shows spectra from 'normal', fibro-fatty and malignant breast tissue. In addition to the presence of Haemoglobin absorption bands at approximately 410, 550 and 575 nm it is also possible to see differences in the slopes and particularly in the absorption characteristics between 450 and 500 nm. Such differences may be explained by the absorption of beta-carotene in adipose tissue but have not as yet been fully accounted for. The figure also shows some evidence of differences in the optical properties of different tissues in the ultra-violet end of the spectrum. Figure four shows examples

of spectra from normal and metastatic (positive) sentinel nodes, again differences in the UV and blue-green regions of the spectrum are apparent.

## 6. REFERENCES

- 1) J.R. Maurant, I.J. Bigio, J. Boyer, T. Johnson, J. Lacey, A.G. Bohorfoush & M. Mellow, "Elastic scattering spectroscopy as a diagnostic tool for differentiating pathologies in the GI tract..." J. Biomed. Opt. 1, 192-199 (1996).
- 2) J.R. Maurant, I.J. Bigio, J. Boyer, R.L. Conn, T. Johnson & T. Shimada, "Spectroscopic diagnosis of bladder cancer with elastic light scattering," Lasers in Surgery and Medicine 17, 350-357 (1995).
- 3) I.J. Bigio, S.G. Bown, G. Briggs, C. Kelley, S. Lakhani, D. Pickard, P.M. Ripley, I.G. Rose & C. Saunders, "Diagnosis of breast cancer using elastic-scattering spectroscopy: preliminary clinical results" Accepted for publication in J. Biomed. Opt. (2000)
- 4) J.R. Maurant, J. Boyer, A. Hielscher and I.J. Bigio, "Influence of the scattering phase function on light transport measurements in turbid media performed with small source-detector separations", Optics Letters 21, pp.546-548 (1996).

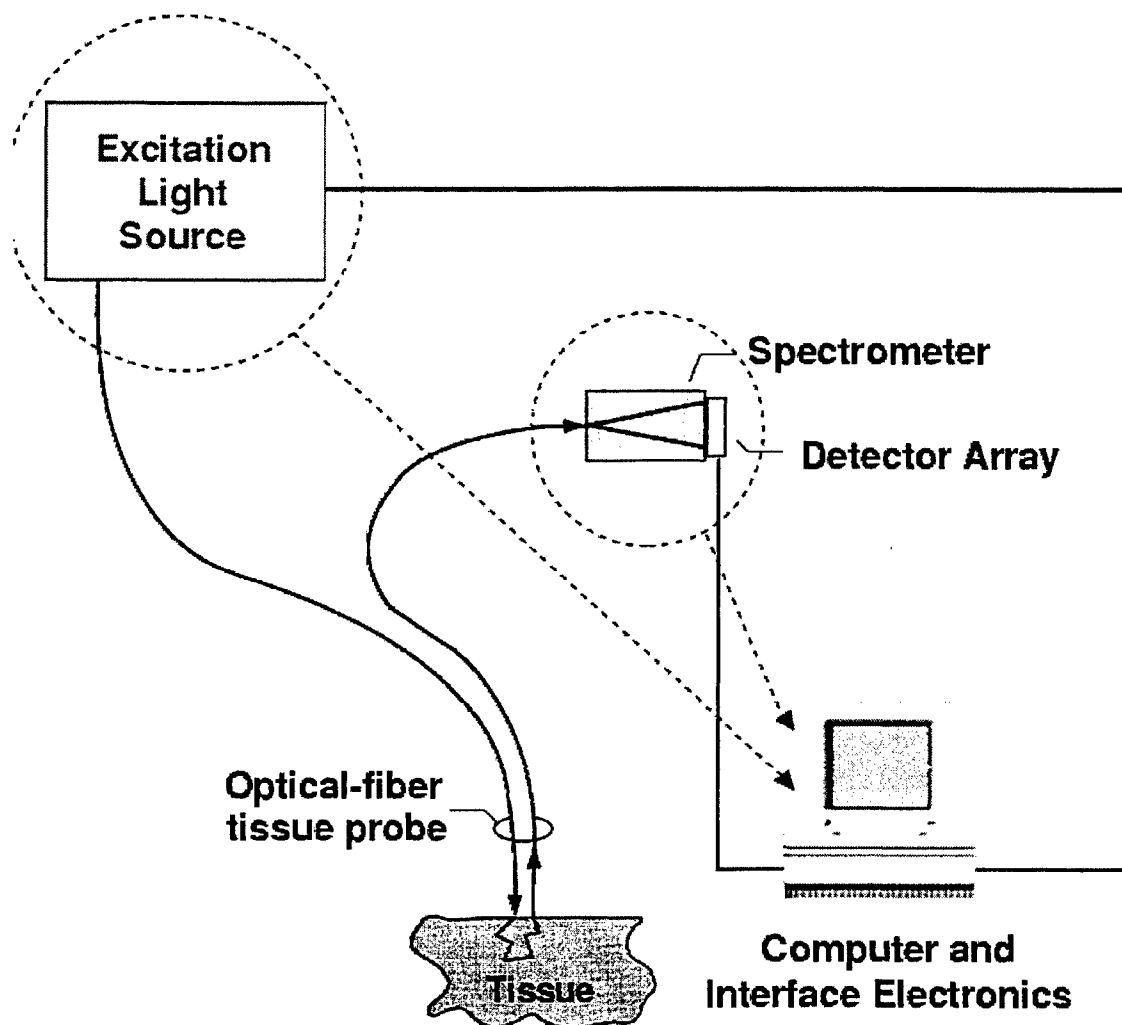


Figure 1  
Schematic diagram of the principal components of the ESS diagnostic system. All components (except for the fiber probe) are located inside a small, portable chassis.

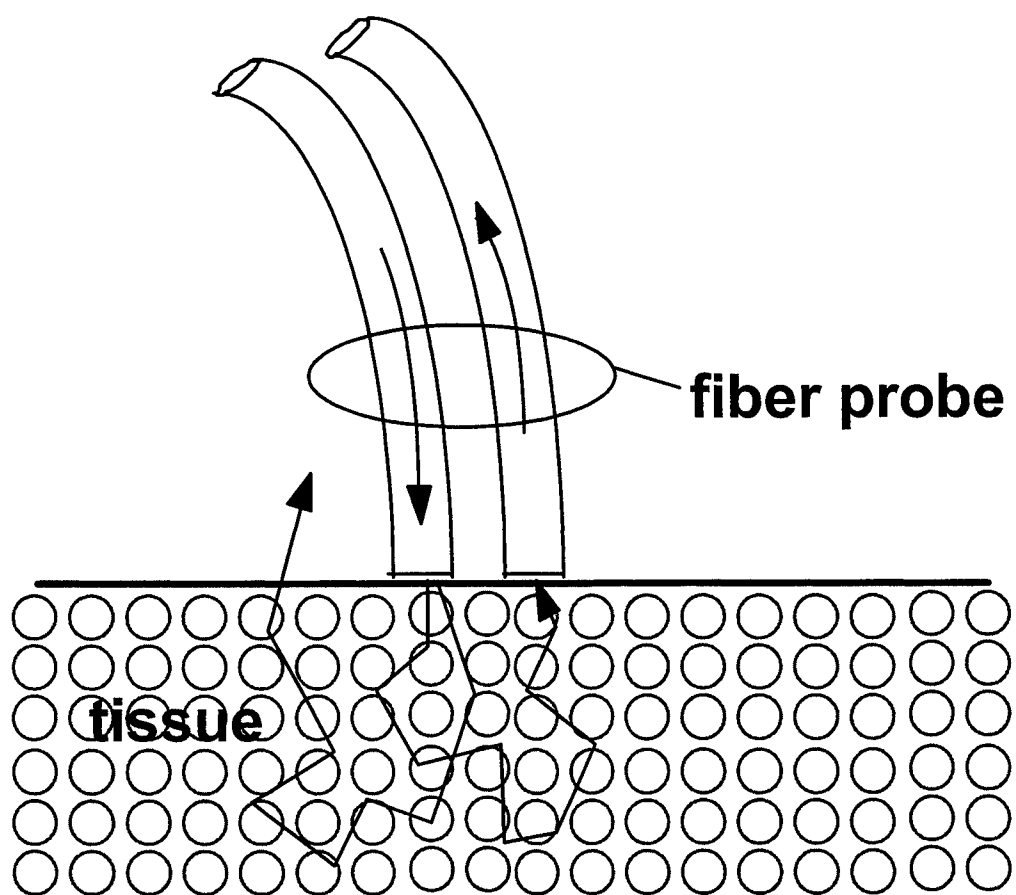


Figure 2  
Depiction of the optical geometry for the fiber-optic probe.

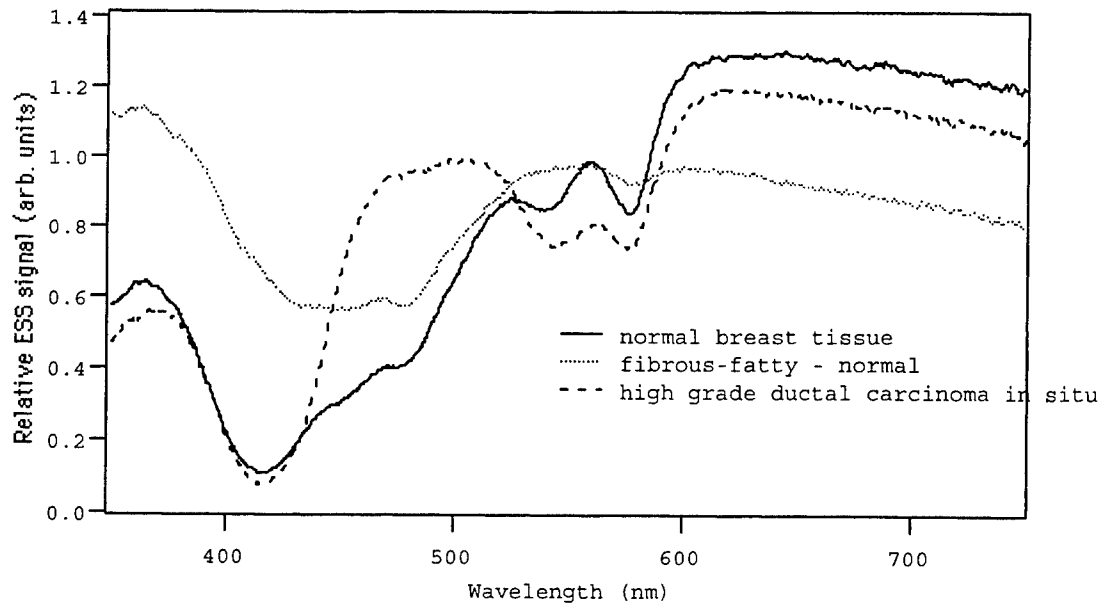


Figure 3  
Examples of ESS spectra for normal and malignant breast tissue conditions.

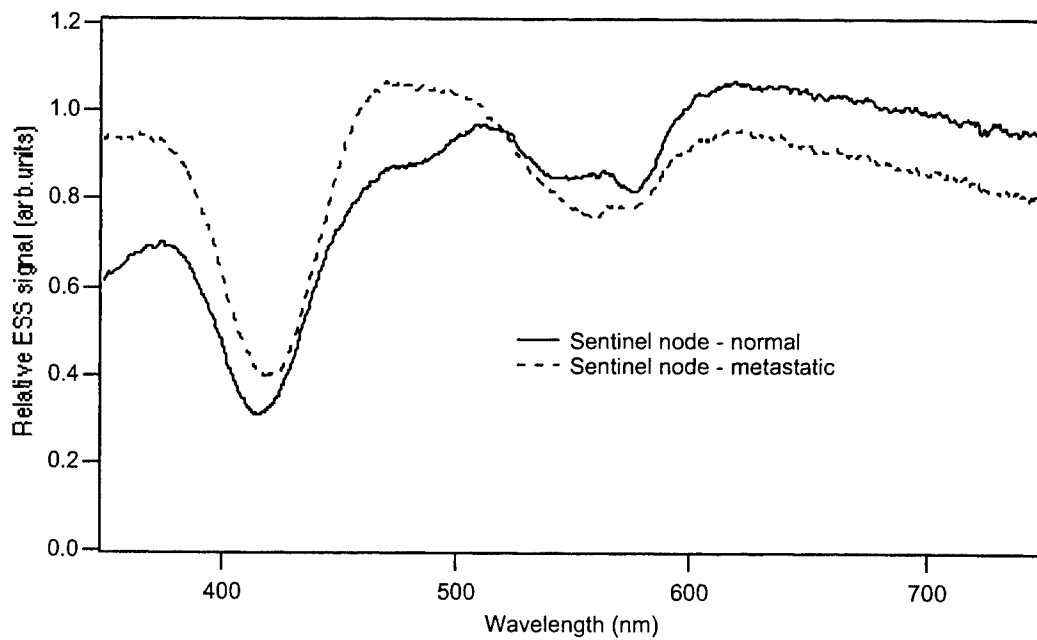


Figure 4  
Examples of ESS spectra for a reactive node, without tumor and for node containing metastatic tumor.



# Spectral polarization imaging of human prostate tissues

W. B. Wang<sup>a</sup>, J. H. Ali<sup>a</sup>, J. H. Vitenson<sup>b</sup>, J. M. Lombardo<sup>c</sup>, and R. R. Alfano<sup>a</sup>

<sup>a</sup>Institute for Ultrafast Spectroscopy and Lasers, and New York State Center for Advanced Technology for Ultrafast Photonic Materials and Applications, Department of Physics, The City College of the City University of New York, New York, NY 10031,

<sup>b</sup>Urology and <sup>c</sup>Pathology Departments at Hackensack University Medical Center, 30 Prospect Avenue, Hackensack, NJ 07601.

## ABSTRACT

Human prostate in-vitro tissues were studied using near infrared spectral polarization imaging. Different imaging methods using the light scattered or emitted from prostates tissues and contrast agents were performed on various model samples, which consisted of a small piece of absorber or prostate tissue dyed with indocyanine green embedded inside a large piece of prostate tissue at different depths. Small foreign objects with a diameter of ~1 mm hidden inside the host prostate tissues at depths of 3.0 mm, 4.5 mm and 8.5 mm were imaged and identified using the scattering light, tissue emission wing and contrast agent emission light imaging methods, respectively.

**Keywords:** Human prostate, light scattering, absorption, emission, contrast agent, spectral and polarization imaging.

## 1. INTRODUCTION

Prostate cancer has a high incidence and mortality rate for men. Every year, nearly 180,000 new prostate cancer cases are diagnosed, and about 37,000 deaths annually are caused by prostate cancers in U.S.<sup>1</sup> The early stage prostate cancers, designed T1-2 ("T" for "tumor"), are confined to the prostate gland or surrounding area, and are easy to be neglected because they are not likely to threaten life at this stage. The more developed cancers may spread to the lymph nodes (N+) or bones (M1), causing persistent and increasing pain, abnormal function, and death. The detection and treatment of early small prostate cancers are most important to prevent death attributable to prostate cancers.

Current techniques for detection of prostate cancers have limited accuracy. The regular methods for monitoring prostate cancers are the prostate specific antigen (PSA) blood test and a digital rectal examination (DRE). When the PSA level is elevated or the DRE abnormal, there is a one-in-three chance that cancer is present. This can only be confirmed by a needle biopsy of the prostate. In the biopsy, a number of cores of prostate tissue are taken with a thin needle guided into selected regions of the prostate with an ultrasound probe.<sup>1</sup> Since the ultrasound imaging has poor spatial resolution and contrast, and needle biopsy is invasive, better methods are needed to develop high resolution and noninvasive techniques to detect early small prostate cancers.

Based on spectral and polarization properties of the light propagated, scattered, absorbed and emitted from turbid media and contrast agents,<sup>2-6</sup> we have developed spectral polarization imaging methods to enhance the ability to image objects hidden inside turbid media and tissues.<sup>4-6</sup> A prototype wide-band near infrared (NIR) spectral polarization imaging instrument was built, and has been used for imaging measurements on human prostate tissues at Hackensack University Medical Center (HUMC) under the IRB approval.

In this paper, we present our NIR spectral polarization imaging studies on human prostate tissues. The NIR region considered by our measurements consists of wavelengths ranging from 650 nm to 900 nm. The model prostate samples were made with a small piece of absorber or prostate tissue stained with indocyanine green dye sandwiched by large pieces of prostate tissues. The depth of the foreign objects underneath the surface of the host prostate tissues was varied from a millimeter to a centimeter to obtain the critical imaging depths. The measured results show that the longer wavelength NIR light and emission imaging methods are preferred for detecting deeply hidden objects.

## 2. EXPERIMENTAL METHODS

Fig.1 shows a photograph of our prototype wide-band NIR spectral polarization imaging instrument. Light from a white light source is used to illuminate a sample with an average power of  $\sim 50 \mu\text{W}/\text{cm}^2$ , which is much lower than the critical illumination level given by FDA. The illumination wavelength is selected by wide-band pass filters (550-900 nm, FWHM=40 nm) placed on a multiple filter wheel, which can be rotated to the desired filter position by computer control to select the appropriate wavelength. The images formed by light scattered or emitted from the sample are recorded by a CCD camera. The detection wavelength is selected by rotating a similar set of band pass filters placed on the second multiple filter wheel located in front of the detector. Polarizer  $P_1$  is used to choose the linear polarization of the illumination, and polarizer  $P_2$  is placed in front of the CCD for selecting the detection polarization. The images can be recorded when the detection polarization is parallel or perpendicular to that of illumination.<sup>4</sup>

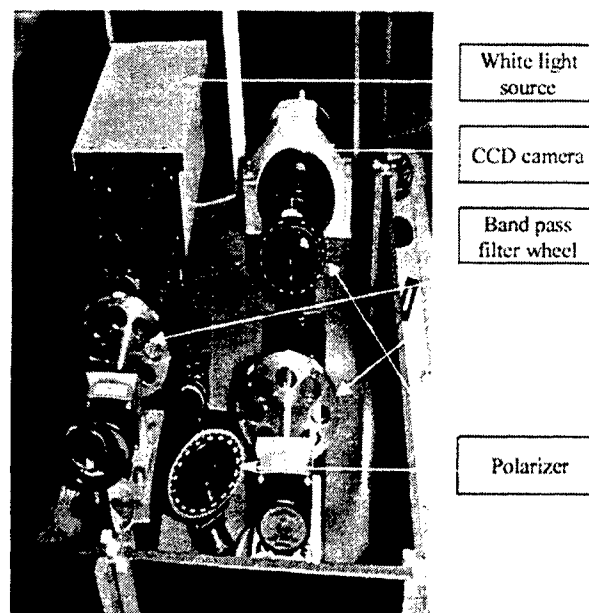


Fig.1 The photograph of the wide-band NIR spectral polarization imaging unit.

For scattered light imaging, the same illumination and detection band pass filters are used. For emission light imaging, the band pass range of the detection (imaging) filter is longer than that of illumination so that the pump light is blocked, and only the light emitted from the sample is collected by the CCD camera.

Since the scattering and emission properties of the hidden foreign objects and prostate tissues are different, both scattered and emitted NIR light images can be used to identify the objects hidden inside prostate tissues.

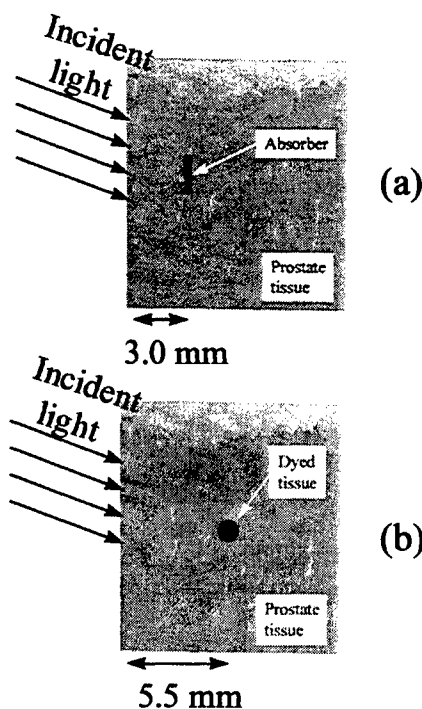


Fig. 2 The diagram of model prostate samples made of (a) a small wire piece of absorber, and (b) a tiny dot piece of prostate tissue dyed with indocyanine green embedded inside large pieces of prostate tissue layers.

The prostate tissues were obtained from four autopsy cases at HUMC, ranging in age from 57 to 70 years, who died of conditions unrelated to the prostate. The prostate tissues were cut into a number of large slices with thickness varied from 1.0 mm to 4.5 mm. Several model samples were made for the imaging measurements with a small piece of foreign object (absorber or dyed prostate tissue) sandwiched by a number of large pieces of prostate tissue layers. The depths of the foreign objects underneath the surface of the host prostate tissues were varied from millimeter to centimeter to obtain the critical depths of different imaging methods.

## 3. EXPERIMENTAL RESULTS

### 3.1. Scattering Light Imaging

The sample used for the scattering light imaging measurements consisted of a small wire piece of absorber ( $\Phi 1 \text{ mm} \times 6 \text{ mm}$ ) embedded inside large slices of prostate tissue ( $\sim 30 \times 20 \text{ mm}$ ) with a depth of  $\sim 3 \text{ mm}$  from the surface of the host tissue as shown in Fig.2(a). During the measurements, the illumination and detection wavelengths were kept same when they were changed by rotating the two filter wheels. In this way, the emission light is blocked, and the CCD camera only collects the light scattered from the sample.

The scattered light images for the sample described in Fig.2(a) were recorded at the wavelengths of 550 nm, 600 nm, 750 nm and 800 nm with  $P_1 \perp P_2$ , and are shown in Figs.3(a) - 3(d). It can be seen that the object (absorber) can not be distinguished by the 550 nm image, but it can be clearly identified as a

thin dark line by the 800 nm image. As the wavelength increases from 550 nm to 800 nm, the visibility of the object improves. The wavelength dependence of the image quality of the scattered light images can be explained by the relative absorption spectrum of the prostate tissue shown in Fig.4(a). The relative absorption of the prostate tissue decreases when the wavelength increases from 400 nm to NIR. The short wavelength (such as 550 nm and 600 nm) light was absorbed strongly by the surface and near surface layers of the prostate tissue, and could not reach the object deeply embedded in the host tissue. In this case, the scattered light images is formed by the light scattered only from the surface and near surface tissue layers with almost no contribution from the object, and, therefore, the object can not be identified. In contrast, the larger penetration of the longer wavelength NIR light in prostate tissues enables them to reach the deeper object. Once the NIR light reaches the object, the difference of scattering and absorption properties between the foreign object and the surrounding tissues is reflected in the image, and therefore, the foreign object can be identified by the NIR scattering images.

The scattering light imaging measurements were extended to other prostate tissue samples with objects embedded at depth of 3.5 mm and deeper. The results show that at the same low illumination intensity of  $\sim 50 \mu\text{W}/\text{cm}^2$ , objects could not be observed with depth more than 3.0 mm even from the images obtained at longer wavelengths of 750 - 850 nm.

### 3.2. Tissue Emission Wing Imaging

The tissue emission wing images are formed by the light emitted from prostate tissues at the NIR wing range. The tissue emission wing images

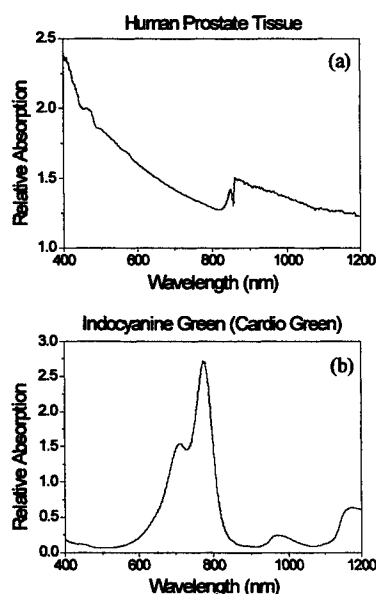


Fig.4 The relative absorption spectrum for human prostate tissue (a), and indocyanine green dye (b).

to 750 nm are shown in Fig.5. The salient feature of the images is that the dyed object can not be distinguished by images

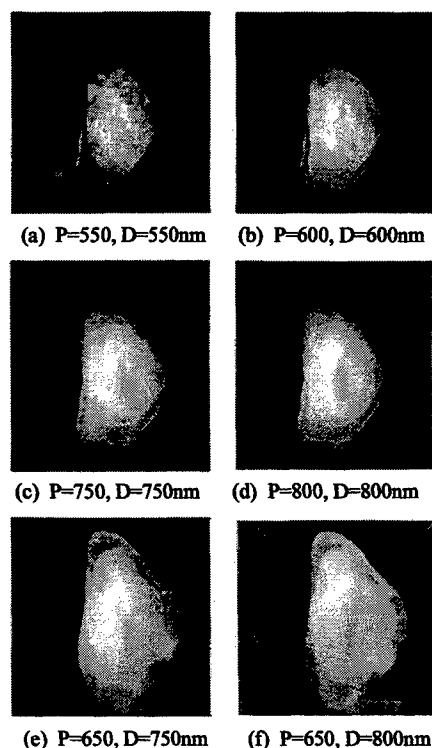


Fig.3 (a)-(d) The scattering light images recorded at wavelengths from 550 nm to 800 nm; and (e)-(f) the tissue emission wing images recorded at 750 nm and 800 nm with 650 nm pump. The sample consists of a small piece of absorber hidden in the host prostate tissue at depth of 3.0 mm. P: pump, D: detection wavelengths.

for the sample indicated by Fig.2(a) recorded at 750 nm and 800 nm with 650 nm pump are shown in Figs. 3(e) and 3(f). In tissue emission wing imaging measurements, the images recorded by CCD camera were formed by light emitted, not scattered, from the sample. The critical depth for which the object can be identified from the tissue emission wing image was found 4.5 mm. This improvement of detection depth compared with the scattering light imaging can be understood because the signal light in the tissue emission wing imaging travels much shorter distance than that in the scattering light imaging.

### 3.3. Contrast Agent Emission Light Imaging

The sample used for the contrast agent emission light imaging measurements consisted of a tiny dot piece ( $\Phi \sim 1.0 \text{ mm}$ ) of prostate tissue dyed with indocyanine green (cardio green) embedded inside a large piece of prostate tissue ( $\sim 20 \times 16 \text{ mm}$ ) about 5.5 mm from the surface of the host tissue as shown in Fig.2(b). Since the emission from the contrast agents is much stronger and more polarized than tissue emission, introducing contrast agents to the NIR spectral polarization imaging technique is expected to further improve the imaging depth and resolution.<sup>4-6</sup>

The contrast agent emission light images for the sample described in Fig.2(b) recorded at 800 nm (or 850 nm) with different pump wavelengths from 550 nm to 750 nm are shown in Fig.5. The salient feature of the images is that the dyed object can not be distinguished by images

obtained with short wavelength (550 nm and 600 nm) pump, while the object can be identified by the images obtained with longer wavelengths (700 nm and 750 nm) pump. When the pump wavelength increases, the visibility of the dyed object increases dramatically. This improvement can be seen more clearly by their image intensity distribution of a cross section taken from a same number row of the different images as shown on the right side of Fig.5. This pump wavelength dependence can be explained from the measured relative absorption spectra of prostate tissue and indocyanine green shown in Fig.4. With NIR wavelengths (700 nm and 750 nm) pump, the light can penetrate the prostate tissue and reach the dyed object. In addition, the absorption of indocyanine green at 700 nm and 750 nm is strong, and the emission from the dye is much stronger than that of native emission from prostate tissues.<sup>6</sup> As a result, the dyed object can be clearly distinguished by those contrast agent emission light images.

The contrast agent emission light imaging measurements were extended to the samples with the dyed tissue embedded at depths of more than 5.5 mm. The results show that the dyed dot tissue with a diameter of ~1 mm embedded at 8.5 mm can still be distinguished, which indicates that the contrast agent emission imaging has higher sensitivity and resolution than that of scattering light and tissue emission wing imaging without contrast agents.

#### 4. CONCLUSION

We have performed and compared different spectral polarization imaging methods on human prostate samples using light scattered or emitted from prostate tissues and foreign objects to obtain the experimental criteria necessary for imaging objects within prostate tissues. The measured results show that small foreign objects with a diameter of ~1 mm hidden inside the host prostate tissues at depths of 3.0 mm, 4.5 mm and 8.5 mm can be identified using the scattering light, tissue emission wing and contrast agent emission light imaging methods, respectively.

#### 5. ACKNOWLEDGEMENTS

This research was supported in part by DOE Center for Optical Imaging and Cancer Diagnosis, and New York State Technology Foundation. We would like to thank Mr. A. Jackson at HUMC for his help on preparation of prostate model samples.

#### 6. REFERENCES

1. D. J. Tindall and P. T. Scardino, "Defeating prostate cancer: Crucial directions for research — except from the report of the Prostate Cancer Progress Review Group (Review)", *Prostate*, **38**(2), 166-171 (1999); and P. T. Scardino, "Prostate cancer: detection, treatment, and prevention", *Newsweek*, Nov.1, 1999, PP 11-12.
2. J. M. Schmitt, A. H. Gandjbakhele, and R. F. Bonner, "Use of polarization light to discriminate short-path photons in a multiply scattering medium", *Appl. Opt.* **31**, 6535 (1992).
3. G. Porter, P. J. Sadkowski and C. J. Tredwell, "Picosecond rotational diffusion in kinetic and steady state fluorescence spectroscopy", *Chem. Phys.* **49**, 416 (1977).
4. W. B. Wang, S. G. Demos, J. Ali, R. R. Alfano, "Imaging fluorescent objects embedded inside animal tissues using polarization difference technique", *Optics Communications*, **142**, 161 (1997).
5. S. G. Demos, W. B. Wang, and R. R. Alfano, "Imaging objects hidden in scattering media with fluorescence polarization preservation of contrast agents", *Appl. Optics*, **37**, 792 (1998).
6. W. B. Wang, S. G. Demos, J. Ali, Gang Zhang, and R. R. Alfano, "Visibility enhancement of fluorescent objects hidden in animal tissues using spectral fluorescence difference method", *Optics Communications*, **147**, 11 (1998).

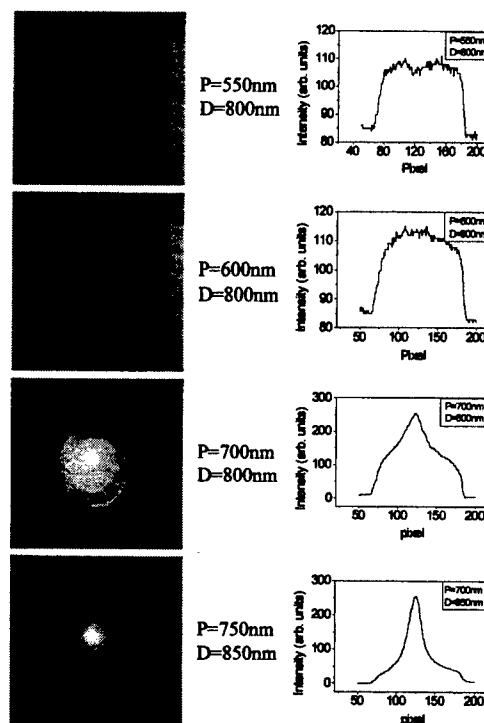


Fig.5 The contrast agent images recorded at 800 nm (or 850 nm) with different pump wavelength varied from 550 nm to 750 nm. The sample consists of a tiny dot piece of prostate tissue dyed with indocyanine green embedded inside a large piece of prostate tissue at depth of 5.5mm. P: pump, D: detect wavelengths.

## **SESSION 4**

### **Contrast Agents and Raman Biopsy**

# Tumor Specific Fluorescent Contrast Agents

Samuel Achilefu\*, Richard B. Dorshow, Joseph E. Bugaj, and Raghavan Rajagopalan

Mallinckrodt Inc., PO Box 5840, St. Louis, MO 63134-0840

## ABSTRACT

Several dyes are currently used for various biomedical applications due to their biocompatibility and high molar absorptivity. Localization of dyes in tumors may be mediated by several factors such as leaky vasculature and high metabolic activity in proliferating cells. However, these mechanisms of action make it difficult to differentiate inflammation from benign or malignant tumors. In order to enhance their tumor specificity, dyes have been conjugated to biomolecules that target unique factors in various diseased states. However, such large biomolecules can elicit adverse immunogenic reactions in humans, and are often preferentially taken up by the liver. Furthermore, for solid tumors which may rely on diffusion of the biomarkers from the vasculature, penetration of large dye conjugates is not favorable. To overcome these problems, we designed and synthesized novel dye-peptide conjugates that are receptor specific. The efficacy of these new fluorescent contrast agents was tested *in vivo* in well-characterized rat tumor lines. The resulting optical images demonstrate that successful specific tumor targeting was achieved.

**Keywords:** peptide-dye conjugates, targeting agents, contrast agents, tumors detection, dyes, fluorescence, indocyanine green, contrast agents

## 1. INTRODUCTION

Interest in the early detection of tumors has increased recently as a result of the increasing number of deaths caused by this disease. Currently, different forms of roentgenography, scintigraphy, ultrasound and magnetic resonance imaging techniques have been approved for use in humans.<sup>1</sup> In general, contrast agents are used to enhance the differentiation of normal from abnormal tissues by non-specific entrapment or exclusion of the agents from the cancer cells. Recently, optical imaging has been proposed as an alternative tumor detection method with great potential in clinical diagnosis.<sup>2</sup> Among other advantages over conventional modalities, the optical approach neither uses ionizing radiation nor radioactive materials, and a wealth of information can be extracted from tissue interaction with light in the electromagnetic region of interest.

While detection of tumors are possible without a contrast agent, biocompatible dyes with high molar absorptivity and fluorescent quantum yield enhance detection sensitivity. Localization of these dyes in tumors can be mediated by several factors, including leaky vasculature and high metabolic activity in proliferating cells. However, these mechanisms of action make it difficult to differentiate inflammation from benign or malignant tumors, hence, diagnoses rely largely on the expertise of the radiologist, which is prone to human error. Further, non-specific contrast agents accumulate in many tissues, thus, requires prolonged waiting period for them to clear from normal tissues. However, several tumors are known to overexpress specific receptors which could be used to different them from normal cells. Thus, to enhance tumor specificity, ligands for the receptors can be used as delivery vehicles for contrast agents. Several studies by scintigraphic imaging have demonstrated the feasibility of tumor detection with antibodies and other large biomolecules. Adaptation of this approach to optical imaging has been published.<sup>3,4</sup> However, such large molecules are rapidly and preferentially taken up by the liver and can elicit adverse immunogenic reactions in humans. For solid tumors which rely on the diffusion of biomarkers from the vasculature, the penetration of large dye conjugates is not favorable due to net positive pressure within the tumor.<sup>5</sup> Hence, a better method to specifically deliver dye conjugates to tumors is highly desirable.

Recent studies in nuclear medicine have demonstrated that attachment of chelating agents to small molecular peptides can be used to target tumors without loss of receptor affinity of the peptides.<sup>6</sup> This approach has several advantages over the use of non-specific agents or conjugation of the agents to large biomolecules, including rapid localization on tumors, rapid clearance from blood and the possibility to synthesize several peptide derivatives without resorting to expensive natural products. Our goal in this study is to evaluate the use of small peptide-dye conjugates in tumor detection. To this end, we designed and synthesized novel dye-peptide conjugates that are receptor specific. The efficacy of the new fluorescent

contrast agents was evaluated *in vivo* in a well-characterized rat tumor lines using a simple continuous wave fluorescence imaging apparatus.

## 2. MATERIALS AND METHODS

### 2.1 Synthesis

#### 2.1.2 Synthesis of bispropylcarboxymethylindocyanine dye (Cypate)

Cypate was prepared by the reaction of a mixture of 1,1,2-trimethyl-[1H]-benz[e]indole and 3-bromopropanoic acid in 1,2-dichlorobenzene. Reaction of the brown solid precipitate obtained with glutacanaldehyde dianil monohydrochloride in ethanol gave a green solution. Evaporation of the solvent and lyophilization of the residue gave cypate as dark green flakes (Figure 1B).

#### 2.2.2 Synthesis of Cytate-1

Octreotate, a somatostatin receptor ligand, was prepared by standard Fmoc solid phase synthesis<sup>7</sup> and the two cystein residues per molecule were cyclized into a disulfide bond on solid support with thallium trifluoroacetate to give the cyclic peptide. Reaction of cypate with the peptide on solid support and subsequent peptide cleavage from the resin with trifluoroacetic acid gave the crude product which was purified by HPLC to give the desired compound in 99.5% HPLC purity (Figure 1C).

#### 2.2.3 Synthesis of bombesinate

Similar procedure described above was used to prepare bombesinate which has affinity for bombesin receptors. This peptide is linear, hence, does not require the cyclization step described above. HPLC purity was >99.5% (Figure 1D).

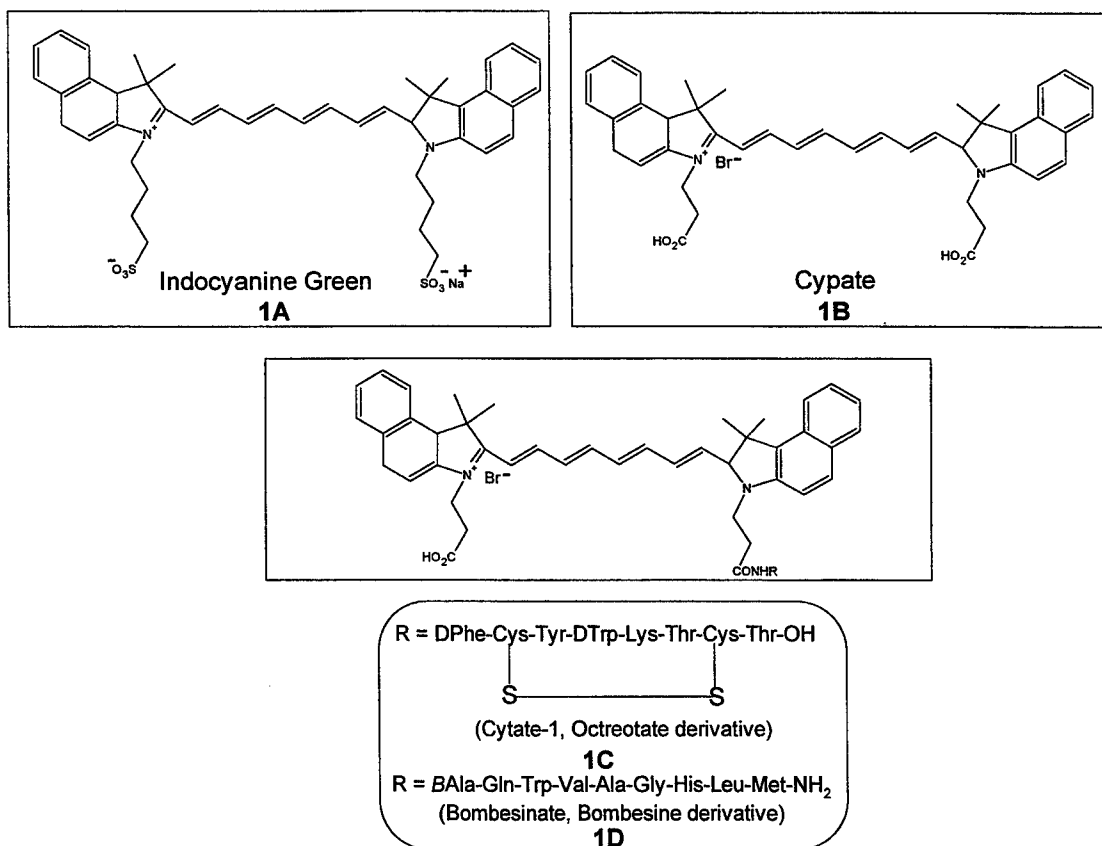


Figure 1: Structures of ICG, cypate and peptide-dye conjugates

## 2.2 Animal protocols

### 2.2.1 Pancreatic ductal adenocarcinoma (DSL 6A) tumor

DSL 6A tumors were induced in male Lewis rats in the left flank area by the introduction of material from a solid (donor) implant and the tumors were palpable in approximately 14 days. The animals were anesthetized with rat cocktail (xylazine; ketamine; acepromazine 1.5: 1.5: 0.5) at 0.8ml/kg via intramuscular injection. The area of the tumor (left flank) was shaved to expose tumor and surrounding surface area. A 21 gauge butterfly equipped with a stopcock and two syringes containing heparinized saline was placed into the later tail vein of the rat. Patency of the vein was checked prior to administration of the indocyanine Green (ICG) dye via the butterfly apparatus. Each animal received 500  $\mu$ L of a 0.42 mg/mL solution of ICG in water. The images obtained at 2 and 30 minutes post injection are shown in Figure 2A.

### 2.2.2 Prostatic carcinoma (R3327-H) tumor

R3327-H tumors were induced in young male Copenhagen rats in the left flank area from a solid implant. These tumors grow very slowly and palpable masses were present 4-5 months post implant. The images obtained at 2 and 30 minutes post injection are shown in Figure 2B.

### 2.2.3 Pancreatic acinar carcinoma (CA20948) tumor

Rat pancreatic acinar carcinoma expressing the SST-2 receptor (CA20948) were induced by solid implant technique in the left flank area and palpable masses were detected 9 days post implant. The images obtained at 2 and 30 minutes post injection are shown in Figure 2C.

## 2.3 Imaging apparatus and procedure

A non-invasive *in vivo* fluorescence imaging apparatus was employed to assess the efficacy of contrast agents developed for tumor detection in animal models. A LaserMax Inc. laser diode of nominal wavelength 780 nm and nominal power of 40 mW was used. The detector was a Princeton Instruments model RTE/CCD-1317-K/2 CCD camera with a Rodenstock 10 mm F2 lens (stock #542.032.002.20) attached. A 830 nm interference lens (CVI Laser Corp. part # F10-830-4-2)) was mounted in front of the CCD input lens such that only emitted fluorescent light from the contrast agent was imaged. Typically, an image of the animal was taken pre-injection of contrast agent. This image was subsequently subtracted (pixel by pixel) from the post injection images. However, the background subtraction was never done once the animal had been removed from the sample area and returned at a later time for images taken several hours post injection.

## 3. RESULTS & DISCUSSION

Prior to evaluating our novel tumor receptor-targeted conjugates, we examined the clearance profile of the non tumor specific dye ICG (Figure 1A). Tumor retention of ICG in different tumor lines is shown in Figure 2. As shown in Figure 2, ICG can localize in certain tumors (DSL6/A and Dunning R3327H) by a non-specific mechanism of action, induced primarily as a result of the presence of leaky vasculatures around the tumor. However, this dye was unable to localize in a rat pancreatic acinar carcinoma over-expressing the SST-2 receptor (CA20948) for a prolonged period of time. Biodistribution studies showed that the ICG preferentially accumulated in the liver, as expected, and subsequently excreted through the intestine. A combination of these observations clearly indicates that non-tumor specific dyes such as ICG cannot differentiate inflammation from tumors. Hence, this approach may result in several false positives or negatives and cannot be relied upon for clinical prognosis.



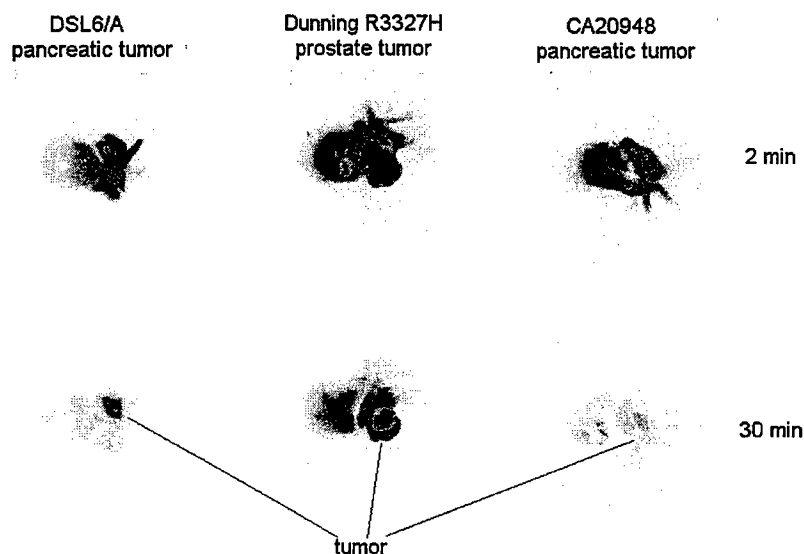


Figure 2. *In vivo* ICG uptake in rats with different tumor lines at 2 and 30 minutes post-administration.

As a control experiment, 500  $\mu$ L of 0.42 mg/mL aqueous ICG solution was administered to a rat with a CA20948 tumor on its flank. Time sequence images are shown in Figure 2. At one minute post-injection, a high level of fluorescence (black on this gray scale image) is noted at the liver and at the tumor locations. By 10 minutes post-injection, localization in the liver was evident with concomitant clearance for the remainder of the animal including the tumor mass. At sixty minutes post-injection, the rat had moved slightly such that the fluorescence from the liver is masked, but the flank with the tumor is still directed at the camera and has essentially only the residual fluorescence of the rest of the body. Thus ICG is not retained in this tumor.

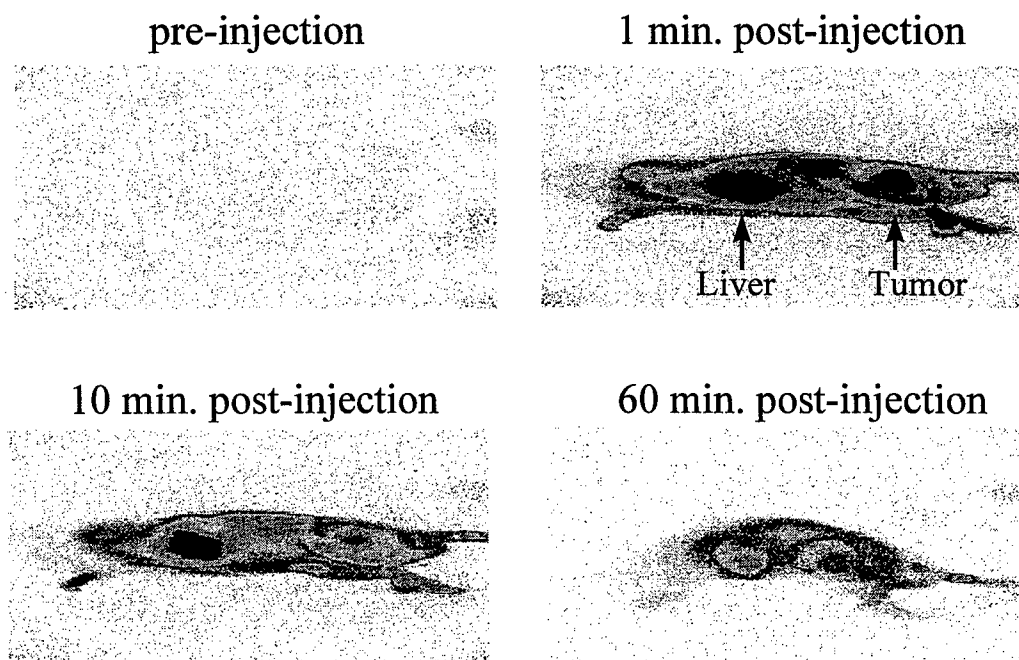


Figure 3: Time dependent ICG uptake and washout in rat with a CA20948 tumor on flank.

Figures 4 and 5 show the clearance profile of the cyanine dye, cypate, in two tumor lines (CA20948 and AR 42J) before its conjugation with receptor-avid peptides. Cypate, like ICG, is not retained in either *in vivo* tumors.

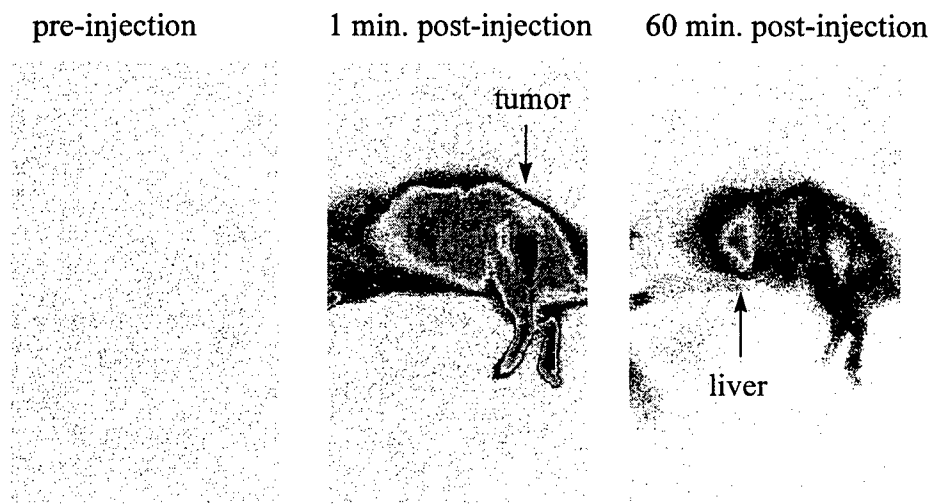


Figure 4: Uptake of cypate in rat with a CA20948 tumor on flank.

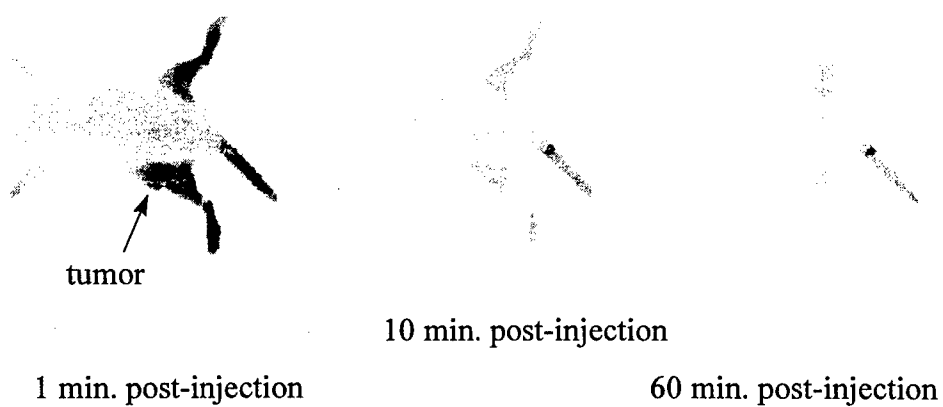


Figure 5: Uptake of cypate in rat with an AR 42-J tumor on flank.

The feasibility of using tumor specific peptide-dye conjugates to detect tumors is illustrated in Figures 6 and 7. A 500  $\mu$ L of a 0.5 mg/mL aqueous Cytate 1 solution was administered to a rat with a CA20948 tumor on its flank. Time sequence images are shown in Figure 6. Localization of the tumor was evident as early as ten minutes post-injection. By ninety minutes, the tumor is well-delineated, with the remaining non-tumor tissues indicating clearance of the agent. Retention of the dye-peptide is still observed in the tumor at 24 hours post-injection (not shown), further verifying receptor specificity of this dye-peptide conjugate.

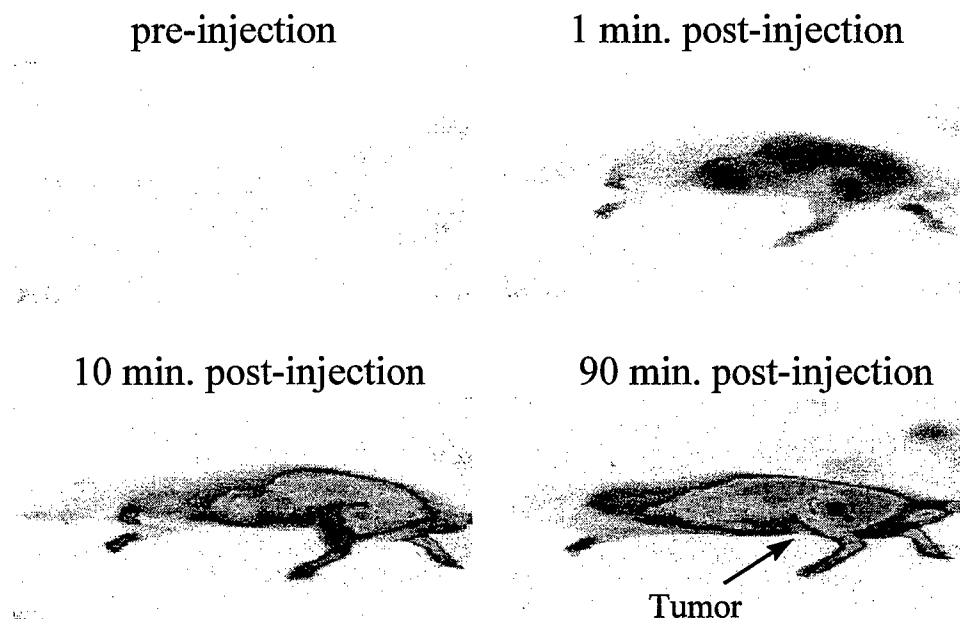


Figure 6: Uptake of cytate-1 in rat with a CA20948 tumor on flank.

In Figure 7, bombesinate is shown to localize in a CA20948 rat tumor *in vivo*. Thus, two dye-peptide conjugates have demonstrable targeting capability.

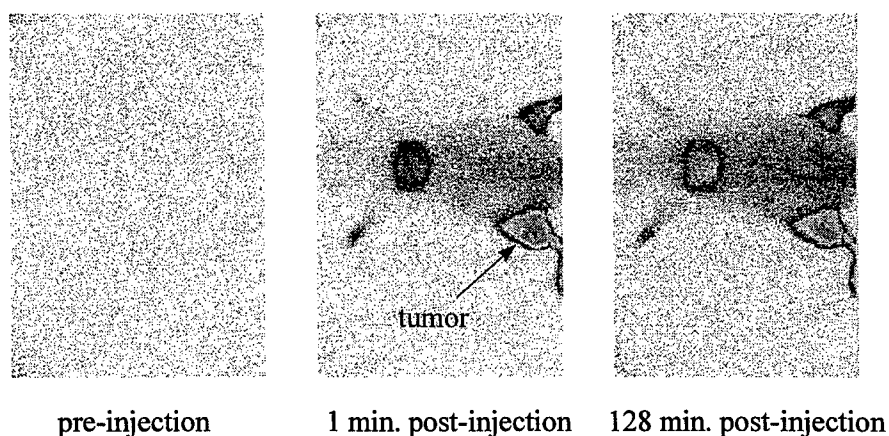


Figure 7: Uptake of bombesinate in rat with a CA20948 on flank.

#### 4. SUMMARY

The rat pancreatic acinar carcinoma over-expressing the SST-2 receptor became an interesting tumor line for evaluation of receptor-specific dye-peptide conjugates for several reasons. As discussed above, we have demonstrated that ICG has only a transient retention this tumor line. Further, CA20948 is known to over-express SST-2 receptor. A logical approach would, therefore, involve the conjugation of dyes to biomarkers that have high affinity for this receptor. Fortunately, several somatostatin analogues have been demonstrated by scintigraphy to target SST-receptor.<sup>8</sup> A commercial product based on targeting somatostatin tumor receptor, OctreoScan, is currently used for the detection of neuroendocrine tumors.<sup>9</sup> However, the active targeting component of this imaging agent is a small 8-amino acid peptide and it was not evident that attachment of large dye molecules to an analogue of this peptide, octreotate, will not conceal the peptide's ability to localize in tumors. The use of small peptides has several advantages over large biomolecules, including ease of synthesis of a variety of compounds for potential combinatorial screening of new targets, reproducibility of high purity compounds, diffusiveness to solid tumors, and the ability to incorporate a variety of functional groups to modify the pharmacokinetics of the peptide-dye conjugates. Consequently, we evaluated the feasibility of using small peptide-dye conjugates in tumor imaging by the optical modality.

This approach required the synthesis of functionalizable dyes for the attachment of the peptides. We developed a method to conjugate the dyes on peptides by solid phase synthesis, a process which is amenable to automated synthesis. In formulating the conjugates for *in vivo* use, we discovered that addition of some biocompatible organic solvents such as dimethyl sulfoxide (DMSO) preserved the dye fluorescence.

#### 5. CONCLUSION

Our results indicate that small peptide-dye conjugates can be effective in tumor imaging by the optical modality as has been demonstrated in nuclear medicine. Both cytat-1 and bombesinate localized for over 24 hours in tumors known to over-express somatostatin and bombesin receptors whereas dyes devoid of the receptor targeting component were not retained in these tumors.

#### 6. ACKNOWLEDGMENTS

The authors wish to thank R. Randy Wilhelm (mass spectrometry), Michelle A. Schmidt (peptide chemistry), and Hermo Jimenez (dye chemistry) for their various contributions.

#### REFERENCES

1. D.D. Shaw, "Contrast media: Directions for the 1990s," *Investigative Radiology* **28**, pp. S138-139, 1993.
2. A. Yodh and B. Chance, "Spectroscopy and imaging with diffusing light," *Physics Today* **48**, pp. 34-40, 1995.
3. B. Ballou, G.W. Fisher, A. S. Waggoner, D. L. Farkas, J.M. Reiland, R. Jaffe, R.B. Mujumdar, and T.R. Hakala, "Tumor labeling in vivo using cyanine-conjugated monoclonal antibodies," *Cancer Immunol. Immunother.* **41**, pp. 257-263, 1995.
4. K. Licha, A. Becker, F. Kratz, and W. Semmler, "New contrast agents for optical imaging: Acid-cleavable conjugates of cyanine dyes with biomolecules," in *Biomedical Imaging: Reporters, Dyes, and Instrumentation*, Darryl J. Bornhop, Christopher Contag, Eva M. Sevcik-Muraca, Editors, Proceedings of SPIE Vol. **3600**, pp. 29-35 (1999).
5. R.K. Jain, "Barriers to drug delivery in solid tumors," *Scientific American* **271**, pp. 58-65, 1994.
6. M. de Jong, W.A.P. Breeman, W.H. Bakker, P.P.M. Kooij, B.F. Bernard, L.J. Hofland, T.J. Visser, A. Srinivasan, M.A. Schmidt, J.L. Erion, J.E. Bugaj, H.R. Macke, and E.P. Krenning, "Comparison of <sup>111</sup>In-labeled somatostatin analogues for tumor scintigraphy and radionuclide therapy," *Cancer Research* **58**, pp. 437-441, 1998.
7. E. Atherton, *Fluorenylmethoxycarbonyl-polyamide solid phase peptide synthesis: General principles and development*. Information Press, Oxford, 1989.
8. W.H. Bakker, E.P. Krenning, W.A.P. Breeman, J.W. Koper, P.P. Kooij, J.-C. Reubi, J.G. Klijn, T.J. Visser, R. Docter, and S.W. Lamberts, "Receptor scintigraphy with a radioiodinated somatostatin analogue: radiolabeling, purification, biological activity, and in vivo application in animals," *J. Nucl. Med.* **31**, pp. 1501-1509, 1990.
9. D.J. Kwekkeboom, E.P. Krenning, G.S. Kho, W.A.P. Breeman, and P.M. Van Hagen, "Somatostatin receptor imaging in patients with sarcoidosis," *Eur. J. Nucl. Med.* **25**, pp. 1284-1292, 1998.

---

\*Correspondence: Email: Samuel.Achilefu@mkg.com; Phone: (314) 654-3485; Fax: (314) 654-5337

# Calcium detection of human hair and nail by the nanosecond time-gated spectroscopy of laser-ablation plume

Masamitsu Haruna<sup>\*a</sup>, Masato Ohmi<sup>a</sup>, Mitsuo Nakamura<sup>\*\*a</sup> and Shigeto Morimoto<sup>b</sup>

<sup>a</sup>School of Allied Health Sciences, Faculty of Medicine, Osaka University

1-7 Yamada-Oka, Suita, Osaka 565-0871, Japan

<sup>b</sup>Department of Geriatric Medicine, Graduate School of Medicine, Osaka University

2-2 Yamada-Oka, Suita, Osaka 565-0871, Japan

## ABSTRACT

We demonstrate the nanosecond time-gated spectroscopy of plume in laser ablation of biological tissue, which allows us to detect calcium (Ca) with high sensitivity by the use of either an ultraviolet (UV) or a near-infrared (near IR) laser pulse. Clear and sharp peaks of  $\text{Ca}^+$  appear in the luminescence spectrum of laser-ablation plume although the Ca content is only 0.1% in human hair and nail. Luminescence peaks of sodium atom (Na) and ionized carbon ( $\text{C}^+$ ) are also detectable. This specific spectroscopy is low invasive because a single low-energy laser pulse illuminates the tissue sample, and it does not require any poisonous sensitizers like fluorescence dye. This method, therefore, is a promising candidate for optical biopsy in the near future. In particular, Ca detection of human hair may lead to new diagnoses, including monitor of daily intake of Ca and a screening diagnosis of osteoporosis.

**Keywords:** Tissue laser ablation, Plume luminescence, Time-gated spectroscopy, Calcium detection

## 1. INTRODUCTION

Laser ablation has the advantage that biological tissue can be removed layer by layer, leading to smooth cutting surface of the tissue with less affection of the surrounding tissue. Besides the use for such a surgical knife, the tissue ablation has been used for the refractive surgery of cornea<sup>1</sup> and the surgery of vascular.<sup>2</sup> For improvement of these surgeries, the dynamic analyses of the tissue ablation were made by observation of time-transitional images of laser-ablation plume with the high-speed framing camera and the stroboscopic photography and microscopy.<sup>3-5</sup> Thus, the tissue ablation has traditionally been used as the therapeutic techniques. On the other hand, recently, there has been considerable interest in the use of tissue laser ablation as a diagnostic tool. In this case, the diagnosis was performed by the time-gated spectroscopy of the emission light of laser-ablation plume, as reported by several research groups.<sup>6-9</sup> S. Andersson-Engels et al. reported the plume spectra of a calcified plaque in an aortic wall and urinary stone, where the 308-nm XeCl excimer laser pulse of 20ns was used as the light source and the spectra were obtained 500ns after illumination of the laser pulse.<sup>6</sup> Many peaks of Ca and  $\text{Ca}^+$  were observed over the wavelength range of 350nm to 650nm. The time-gated spectroscopy of the plume was also used to study pulsed-laser fragmentation of biliary calculi.<sup>7</sup> Luminescence spectra of ablation products of atherosclerotic aorta were investigated using the 2.5- $\mu\text{m}$  Holmium YAG laser pulse of 250 $\mu\text{s}$  and the XeCl laser pulse of nearly 60ns.<sup>8,9</sup> All these reports indicated that the time-resolved spectroscopy of laser-ablation plume is potential for a destructive characterization of biological tissue, but there has been no proposal for the actual diagnostic application.

In this paper, we demonstrate detection of trace elements of human hair and nail by the nanosecond time-gated spectroscopy of the plume luminescence in the UV and near IR laser ablation. In particular, this specific spectroscopy can provide highly sensitive detection of  $\text{Ca}^+$  which may lead to a novel diagnosis, including monitor of daily intake of Ca and a screening diagnosis of osteoporosis.

## 2. EXPERIMENTAL SETUP

The experimental setup for study of the plume luminescence is shown in Fig. 1. The Q-switched Nd:YAG laser is used as the light source which supplies laser pulses of five to several tens nanoseconds at 1064, 532 and 266nm with the repetition rate of 10Hz. Among a time series of laser pulses, a single pulse is picked up by the electronic shutter, and is

---

\*Correspondence: Email: haruna@sahs.med.osaka-u.ac.jp; TEL: +81-6-6879-2572; FAX: +81-6-6879-2469

\*\*M. Nakamura is now with NEC Co., 1753, Shimonumabe, Nakahara-ku, Kawasaki, Kanagawa 211-8666, Japan

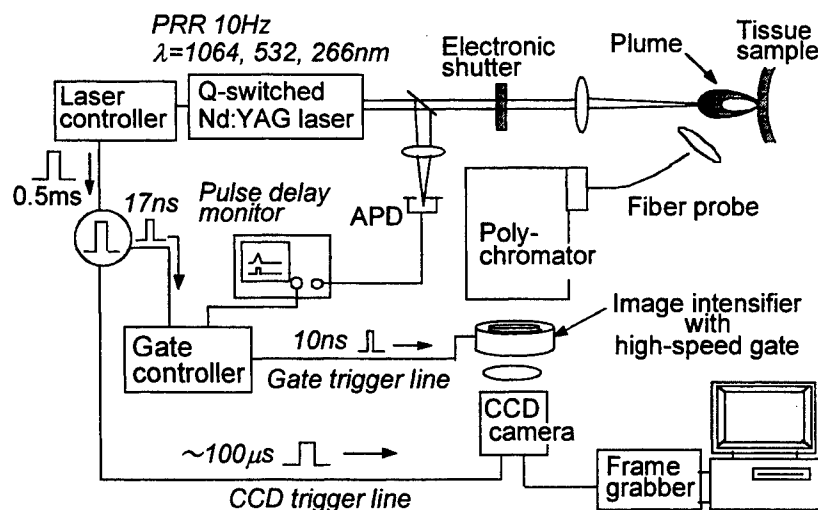


Fig. 1 Experimental setup for the nanosecond time-gated spectroscopy of tissue-ablation plume.

loosely focused on a tissue sample where a focused spot size is around  $150\mu\text{m}$  in diameter. The laser-ablation plume is then ejected from the tissue surface, and develops normal to the surface. Emitting light from the plume is captured by a fiber probe with  $960\text{-}\mu\text{m}$  core diameter, followed by being diffracted with the polychromator. The spectroscopic image is gated with a time slot as short as  $10\text{ns}$  in synchronization with the illuminating laser pulse, as shown in Fig. 1. The time slot is adjustable at the desirable delay time  $t_d$  after the laser pulse illuminates the tissue sample. The adjustment accuracy of  $t_d$  is here less than  $1\text{ns}$  because jitter of a trigger pulse is below  $0.5\text{ns}$  in the laser controller. The time-gated spectroscopic image is intensified, and the time-serial image data are then fed into a frame grabber via a CCD camera. In the spectroscopic image, the image intensities are integrated along an array of pixels corresponding to a certain wavelength, resulting in the plume-luminescence spectrum in the wavelength range of  $350$  to  $700\text{nm}$  with a resolution of  $1\text{nm}$ .

### 3. TIME-GATED SPECTROSCOPY OF PLUME LUMINESCENCE

#### 3. 1 Near IR laser ablation

In the experiment, human nail, hair and tooth were used as the tissue sample. The  $1064\text{-nm}$  laser pulse illuminated a piece of human nail where the laser pulse energy was  $17\text{ mJ}$ . Time-gated luminescence spectra of laser-ablation plume were measured for different values of the delay time  $t_d$ , as shown in Fig. 2. In the ablation, the laser pulse is focused on the tissue surface. The leading edge of the laser pulse is absorbed instantaneously on the surface, where air and water are then decomposed to form plasma.<sup>10,11</sup> According to our dynamic analysis of tissue ablation, the plasma absorbs a considerable part of the pulsed laser energy, and grows rapidly in the reverse direction of the incident laser pulse.<sup>5</sup> It looks like a spindle-shaped brilliant plume, along the focusing beam, whose spectrum includes several peaks of nitride ion ( $\text{N}^+$ ) over the wavelength range of interest, as shown in Fig. 2. This plume-like plasma is partial shielding of the tissue sample against the laser pulse. On the other hand, the remaining energy of the laser pulse is absorbed via the plasma by the tissue itself, as a result, the tissue ablation is made with generation of a real plume which grows normal to the tissue surface as if it chases the plume-like plasma. This plume consists of ionized and non-ionized elements, molecules and clusters of the tissue sample itself.

Our experimental result of Fig. 2 reflects clearly the tissue ablation dynamics, as described above. At the early stage of the ablation (when the delay time  $t_d$  is less than  $300\text{ns}$ ), the plume-like plasma consists of a largely structureless continuum corresponding to high electron temperature. The luminescence peaks of  $\text{N}^+$  ion are sufficiently strong to shadow luminescence peaks of ionized trace elements of the real plume. As the plasma cools down, it is then possible to obtain sharp luminescence peaks of  $\text{Ca}^+$  at  $394$  and  $397\text{nm}$ , as shown in Fig. 2. These luminescence peaks decrease gradually with time. In our result, luminescence peaks of  $\text{Ca}$  and other trace elements are suppressed because of relatively low laser fluence.

### 3.2 UV laser ablation

The 266-nm laser pulse was used for ablation of human hair to minimize difference of laser absorption due to hair colors, where the pulse energy was 17mJ with the pulse width of 5.5ns. In the case of the UV laser ablation, air break occurs near the focal plane of the lens, resulting in dissociation of nitrogen. To avoid air break, the hair sample was set nearly 1mm short of the focal plane. The light spot size on the hair sample was adjusted to be 200 $\mu$ m which was almost twice as thick as human hair so that optical alignment was made easily with respect to the hair sample. The time-transient spectra of the plume luminescence is shown in Fig. 3. Generally, the UV laser ablation is characterized by earlier excitation of trace elements, because both thermal and photochemical effects contribute to the tissue ablation. Accordingly, sharp emission peaks of  $\text{Ca}^+$  appear at  $t_d=300$ ns, as shown in Fig. 3, which is nearly 100ns earlier compared to the case of the near IR laser ablation.

Besides the  $\text{Ca}^+$  peaks, one can find clearly luminescence peaks of sodium atom (Na) at 589nm and ionized carbon ( $\text{C}^+$ ), as shown in Fig. 4.  $\text{C}^+$  originates from keratin which is a main component of hair.

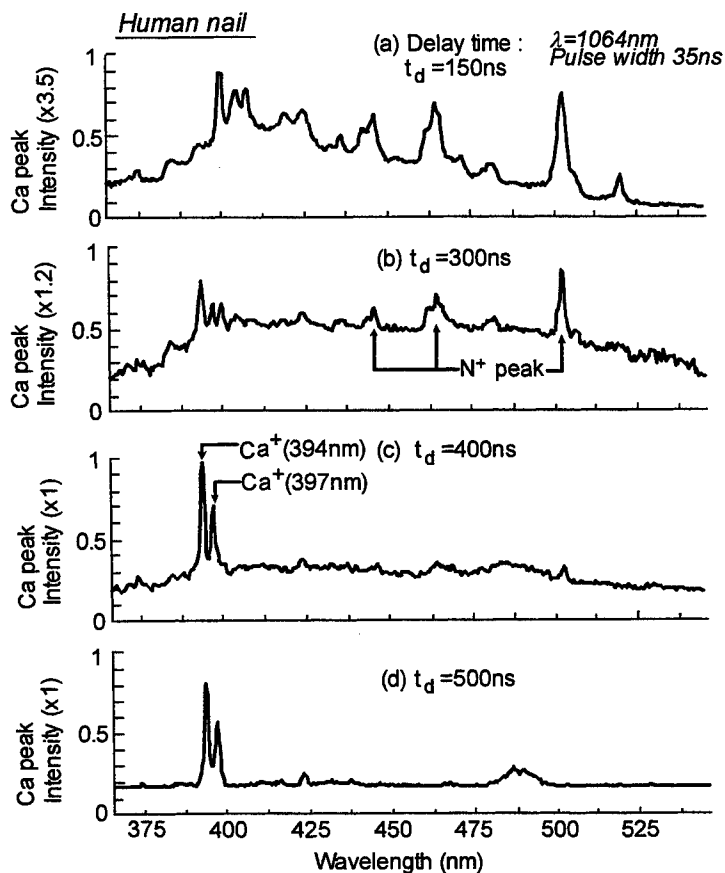


Fig. 2 Time-gated luminescence spectra of the plume in ablation of human nail by the 1064-nm near IR laser pulse, where the time gate width is 10ns.  $t_d$  is the delay time after illumination of the laser pulse.

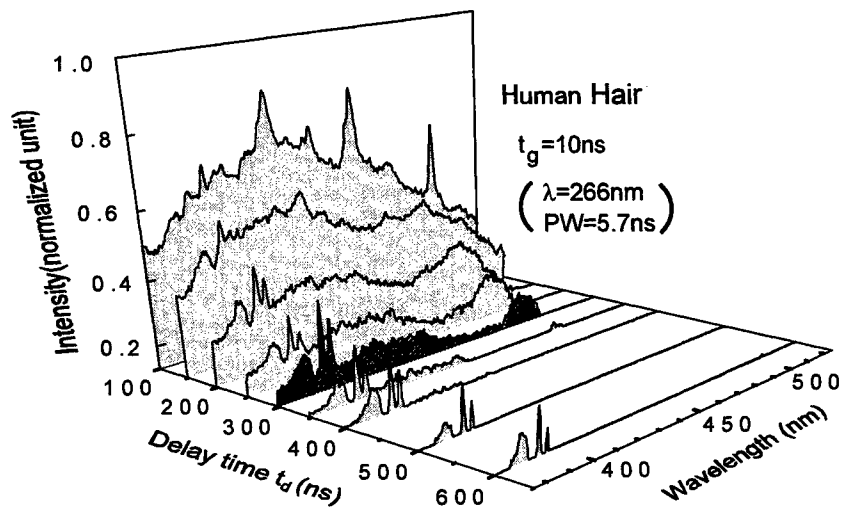


Fig. 3 Time-transient spectra of the plume luminescence of human hair in ablation by the 266-nm UV laser pulse.

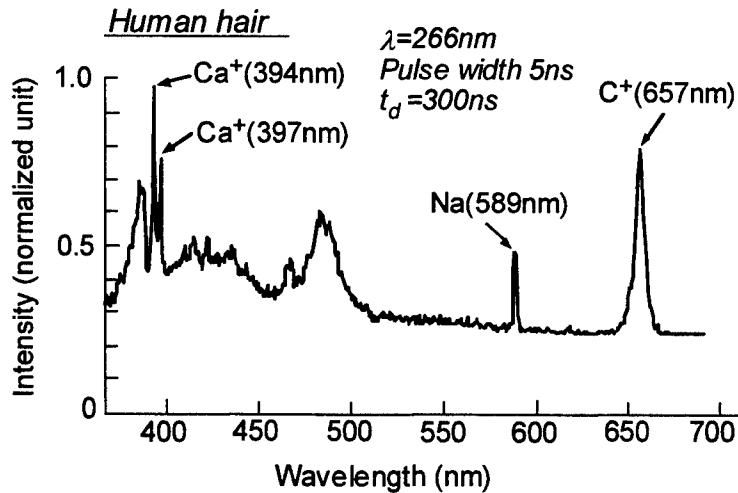


Fig. 4 Ca detection of human hair by the UV laser ablation.  
Na and C<sup>+</sup> are detected as well.

#### 4. CALCIUM DETECTION OF HUMAN HAIR TOWARD A NEW DIAGNOSIS

10 to 15-mm long hairs having roots were used as the sample. Calcium detection of the hair sample was made by measurement of the peak intensity of Ca<sup>+</sup> at 394nm in the plume luminescence spectra. It is here noted that the hair surface is usually contaminated by some chemicals and dust particles. In the experiment, the Ca<sup>+</sup> peak intensity was measured with respect to the shot number of the illuminating laser pulse, as shown in Fig. 5, where the ablation was made for five different points of the hair sample. For all the ablation points, the first shot gives us abnormally high peak intensity of Ca<sup>+</sup>, while the peak value of Ca<sup>+</sup> reduces suddenly to a half or less in the second shot and it is almost the same in the successive laser shots. This fact indicates that the surface contamination includes a considerable amount of additional calcium. Fortunately, the laser ablation has the advantage of easy removal of the surface contamination by the first laser pulse, and therefore, the second laser pulse is used for detection of Ca contained in hair. Fig 6 is the microscope photograph of the hair sample after ablation of the second laser pulse. In addition, the Ca<sup>+</sup> peak intensity of a black hair is apparently higher by 20% or more than that of a white hair when both are taken in the same person. In contrast, dependence of the Ca<sup>+</sup> peak intensity upon the hair diameter is not clear in our experiment because of individual difference.

Successively, more than 30 female hair samples were collected to measure the Ca<sup>+</sup> peak intensity over a wide range of age. The measurement result is shown in Fig. 7. Although the data were scattered remarkably due to individual

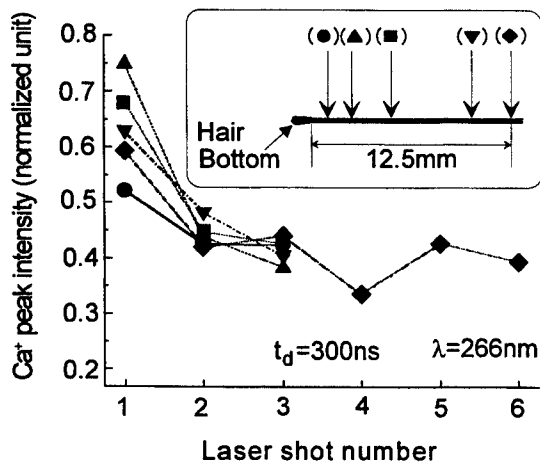


Fig. 5 Variation of Ca<sup>+</sup> peak intensity with the shot number of UV laser pulses.

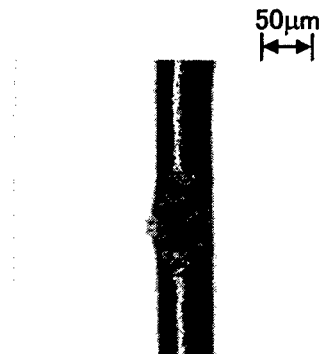


Fig. 6 Microscope photograph showing the hair surface after UV laser ablation of two laser pulses.



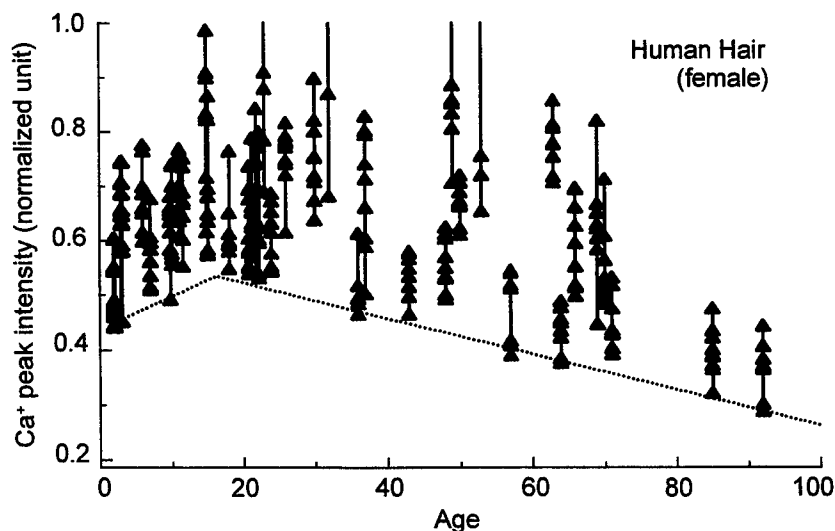


Fig. 7  $\text{Ca}^+$  peak intensity vs age for female hair samples.

difference, the minimum values seem to align with some regularity. The  $\text{Ca}^+$  peak intensity becomes maximum around 20 years old, and decreases gradually with age. Scattering of the data due to individual difference is more remarkable in the mature and old ages. These features are almost consistent with the age dependence of bone mineral density (BMD) measured by the dual-energy X-ray absorptiometry (DEXA).<sup>12</sup> On the other hand, for male hairs, there is no remarkable reduction of the  $\text{Ca}^+$  peak intensity over 60 years old. The male hairs of young age exhibit a lower  $\text{Ca}^+$  peak intensity compared to that of the female hair.

The qualitative examination has been presented, as described above, on the basis of our experimental results. However, we have a problem to be solved in order for quantitative analysis of the Ca content of hair. This problem is due to the fact that the hair diameter ranges from 60 to 120  $\mu\text{m}$ . In fact, the peak value of  $\text{Ca}^+$  is not only determined by the Ca contents of the hair itself, but also influenced by the hair diameter. This means it is difficult to compare quantitatively the Ca content for different hair samples. A possible solution is to measure the ratio of two peak values of  $\text{Ca}^+$  and  $\text{C}^+$  in the luminescence spectrum of plume, as shown in Fig. 4. This way may lead to a novel biomedical-optics measurement and diagnosis, including monitor of daily intake of Ca and a screening diagnosis of osteoporosis before the existing DEXA.

## 5. CONCLUSION

We have demonstrated the nanosecond time-gated spectroscopy of laser ablation plume of biological tissue. In particular, this specific spectroscopy is very sensitive to calcium in human hair and nail. Clear and sharp peaks of  $\text{Ca}^+$  appear in the luminescence spectra of laser-ablation plume although the Ca content is only 0.1% in human hair and nail. In comparison with the existing fluorescence diagnoses, this method has the advantages that trace elements such as Ca, Na, K, etc can be detected with much higher sensitivity, UV, visible and near IR laser pulses are available if the pulse width is around 10ns with the low repetition rate, and any poisonous sensitizers like fluorescence dyes are not needed. Our method is also low invasive because a single nanosecond laser pulse with relatively low energy illuminates the tissue sample for diagnosis. Accordingly, the time-gated spectroscopy of laser-ablation plume presented here is a promising candidate for optical biopsy in the near future.

## ACKNOWLEDGMENTS

The authors are grateful to N. Ohtuka, H. Ueki and F. Namba for their helpful assistance when they were at Osaka University, and R. Konoshita, Osaka University, for his intensive work in improvement of the spectroscopic system. This research is supported by Grant-in-Aid for Scientific Research (B) (2) (Subject #11480256) and Grant-in-Aid for Exploratory Research (Subject #11875015) from Japan Society for the Promotion of Science, for which we express our gratitude.

## REFERENCES

1. for example, C. A. Puliafito, R. F. Steinert, T. F. Deutsch, F. Hillenkamp, E. J. Dehm, and C. M. Adler, "Excimer laser ablation of the cornea and lens," *Ophthalmol.* **92**, No. 6, pp. 741-748, 1985.
2. for example, J. M. Isner., P. G. Steg, and R. H. Clarke, "Current status of cardiovascular laser therapy, 1987," *IEEE J. Quantum Electron.* **23**, No. 10, pp. 1756-1771, 1987.
3. K. T. Schomacker, Y. Domankevitz, T. J. Flotte, and T. F. Deutsch, "Co:MgF<sub>2</sub> laser ablation of tissue: effect of wavelength on ablation threshold and thermal damage," *Lasrs Surg. Med.* **11**, pp141-151, 1991.
4. S. Fujisaka, T. Ito, and K. Sato, "High-speed imaging study of excimer laser ablation of bone," *Review Laser Eng.* **22**, No. 7, pp. 552-558, 1994 (*in Japanese*).
5. Y. Shimaoka, M. Nakamura, M. Ohmi, and M. Haruna, "Nanosecond stroboscopic microscope for laser ablation of biological tissue," Tech. Dig. Pacific Rim Conf. Lases & Electro-Optics (CLEO/PR), FF3, pp. 261-262, Makuhari, Chiba, Japan July 1997.
6. S. Andersson-Engels, J. Johansson, and S. Svanberg, "Fluorescence diagnosis and photochemical treatment of diseased tissue using lasers: Part I," *Analyt. Chemist.* **61**, No. 24, pp. 1367A-1373A, 1989.
7. P. Teng, N. S. Nishioka, R. R. Anderson, and T. F. Deutsch, "Optical studies of pulsed-laser fragmentation of biliary calculi," *Appl. Phys. B* **42**, pp. 73-78, 1987.
8. L. I. Deckelbaum, J. J. Scott, M. L. Stetz, K. M. O'Brien, and G. Baker, "Detection of calcified atherosclerotic plaque by laser-induced plasma emission," *Lasers Surg. Med.* **12**, pp. 18-24, 1992.
9. A. A. Oraevsky, S. L. Jacques, G. H. Pettit, F. K. Tittel, and P. D. Henry, "XeCl laser ablation of atherosclerotic aorta: luminescence spectroscopy of ablation products," *Lasers Surg. Med.* **13**, pp. 168-178, 1993.
10. B. Zysset, J. G. Fujimoto, C. A. Puliafito, R. Birngruber, and T. F. Deutsch, "Picosecond optical breakdown: tissue effects and reduction of collateral damage," *Lasers Surg. Med.* **9**, pp. 193-204, 1989.
11. R. O. Esenaliev, A. A. Oraevsky, and V. S. Letokhov, "Laser ablation of atherosclerotic blood vessel tissue under various irradiation conditions," *IEEE Trans. Biomed. Eng.* **36**, No. 12, pp. 1188-1194, 1989.
12. H. Orimo et al., "Diagnostic standard of primary osteoporosis," *Osteoporosis Japan* **3**, pp. 111-116, 1995 (*in Japanese*).

# Characterization of Type I, II, III, IV, and V collagens by time-resolved laser-induced fluorescence spectroscopy

Laura Marcu<sup>\*a</sup>, David Cohen<sup>a</sup>, Jean-Michel I. Maarek<sup>b</sup>, Warren S. Grundfest<sup>a</sup>

<sup>a</sup> Laser-Research & Technology Development, Cedars-Sinai Med.Ctr. Los Angeles, CA 90048

<sup>b</sup> Biomedical Engineering, University of Southern California, Los Angeles, CA 90089

## ABSTRACT

The relative proportions of genetically distinct collagen types in connective tissues vary with tissue type and change during disease progression (atherosclerosis, tumor), development, wound healing, aging. This study aims to 1) characterize the spectro-temporal fluorescence emission of five different types of collagen (Type I to V) and 2) assess the ability of time-resolved laser-induced fluorescence spectroscopy to distinguish between collagen types. Fluorescence emission of commercially available purified samples was induced with nitrogen laser excitation pulses and detected with a MCP-PMT connected to a digital storage oscilloscope. The recorded time-resolved emission spectra displayed distinct fluorescence emission characteristics for each collagen type. The time domain information complemented the spectral domain intensity data for improved discrimination between different collagen types. Our results reveal that analysis of the fluorescence emission can be used to characterize different species of collagen. Also, the results suggest that time-resolved spectroscopy can be used for monitoring of connective tissue matrix composition changes due to various pathological and non-pathological conditions.

**Keywords:** Time-Resolved Laser Induced Fluorescence, collagen types, fluorescence impulse response function, noninvasive tissue characterization.

## 1. INTRODUCTION

Fluorescence emission information could provide a possible method to separate the fluorescence contributions of component molecules in the tissue based on their different spectrum and lifetime. Consequently, numerous studies<sup>1-5</sup> have suggested that laser-induced fluorescence spectroscopy (LIFS) represents a potential tool for non-intrusive characterization of biological tissue. Since time-resolved information improves the specificity of fluorescence measurements, a time-resolved LIFS technique is desirable for tissue characterization.

Collagen, the major component of the connective tissue, is now recognized as one of the most important natural fluorescent tissue component. Within the large collagen family of proteins, at least 13 genetically distinct types<sup>6</sup> have been identified. Each collagen type has a unique tissue specificity. Generally, Types I, II, III, IV, and V are the major collagen types.<sup>7,8</sup> Type I collagen, the prevalent collagen in vertebrate organisms, is the common collagen of tendon, skin, bone, blood vessels wall. Type II collagen is largely found in cartilages. Type III collagen is usually found in association with Type I collagen in a variety of muscular and elastic tissue, such as artery, uterine leiomyoma, skin. Type IV and V collagens has been identified as the collagens of basement membrane and detected in aortic tissue, placental membranes, bone, dermis, corneal stroma. The relative proportions of the distinct collagen types in a given tissue vary in certain pathological conditions (tumor type or tumor progression, atherosclerosis progression), throughout development, and during wound healing.<sup>6-8</sup> Also, the collagen structure is altered with increasing age and by UV-light exposure (photoaging).<sup>9,10</sup>

Collagen molecules are composed of three polypeptide chains ( $\alpha$ -chains). At least 20 polypeptide chains are involved in forming the molecular conformation of the various collagen types.<sup>8</sup> The amino-acids composition and cross-links of each  $\alpha$ -chain may vary with species and tissue type or be altered during disease progression, healing process, development, aging and photoaging.<sup>10-12</sup> Based upon chromatographic techniques, the fluorescence of collagen family of molecules has been attributed to

\* Correspondence: E-mail: lmarcu@bmsrs.usc.edu

various amino-acids and amino-acid crosslinks.<sup>8,13</sup> For instance, various components of collagen were found to absorb in far-UV (aromatic amino acids: phenylalanine, tyrosine), mid-UV (carbonyl components, aldol condensation cross-links, keto-amine cross-links) and near-UV (pyridinoline).<sup>8,13</sup> Also, differences in fluorophores composition were identified between i) bovine Achilles tendon, cartilage, bone, dentine, vitreous humor and ii) rat tail tendon, skin, cornea.<sup>8</sup>

Attempts to use time-resolved LIFS for characterization of tissue collagen composition have been scarce.<sup>4,5,15</sup> The goals of this study are: 1) to characterize the fluorescence emission of the main genetically distinct types of collagen molecules, Types I, II, III, IV, and V and 2) to assess the ability of time-resolved laser-induced fluorescence spectroscopy to distinguish between collagen types. The results of this work could be useful for monitoring connective tissue changes as a result of a various pathological (cancer, atherosclerosis) and non-pathological (development, healing, aging) conditions.

## 2. MATERIALS AND METHODS

**Instrumentation.** The experimental setup used for this study was similar to that used in our previous studies.<sup>5,14,15</sup> Briefly, the pulses of a nitrogen laser (337 nm emission, 3 ns duration), were focused into a fluorescence probe and directed to the sample. The fluorescence emission was collected by the fluorescence probe, directed into a scanning monochromator (bandpass 5 nm), and detected by a gated multi-channel plate photomultiplier tube placed at the monochromator exit slit. The photomultiplier output was amplified and recorded with a digital oscilloscope (0.5 ns sampling rate, 500 MHz bandwidth). A fraction of the excitation source output beam was directed toward two fast silicon detectors. One detector was used to trigger the gate and delay generator, which in turn gated the photomultiplier. The second detector was used to trigger the oscilloscope to begin sweeping the photomultiplier output and to monitor laser pulse-to-pulse shape and energy variation. A personal computer interfaced (GPIB) with the digital oscilloscope and with the monochromator stepper motor driver was used to control data acquisition, data transfer from the oscilloscope, and monochromator wavelength scanning.

**Samples.** Fluorescence measurements were recorded from commercially available samples of five genetically distinct types of collagen: Type I insoluble from bovine Achilles tendon, Type I acid soluble from calf skin, Type I acid soluble from rat tail, Type II acid soluble from bovine tracheal cartilage, Type II acid soluble from bovine nasal septum, Type III acid soluble from human placenta, Type IV acid soluble from human placenta, Type V acid soluble from human placenta (Sigma Chemical, St. Louis, Missouri). The samples (powder form) were studied at room temperature.

**Experimental procedures.** The fluorescence response pulses were measured for 360-510 nm spectral range (5 nm increment). To improve the signal-to-noise ratio, each recorded fluorescence pulse represented the average of 16 consecutive fluorescence pulses. To determine the reproducibility of fluorescence response across the emission spectrum, ten successive fluorescence transients were recorded at three wavelengths 390, 430, and 470 nm. Three fluorescence measurement sequences were recorded for each collagen compound. Each measurement sequence was obtained from three different areas of the samples that had never been exposed to laser irradiation. The energy output of the laser at the tip of the excitation fiber was adjusted to 0.6 mJ/pulse. During a single measurement sequence (370 seconds), the energy total fluence delivered to the sample was <1.2 mJ/mm<sup>2</sup>. In a previous study<sup>5</sup> we reported that this fluence minimizes the photobleaching of collagen emission. After each measurement sequence, the monochromator was tuned to a wavelength slightly below the laser line. The average of sixteen laser pulses reflected by the sample was used to represent the temporal profile of the laser pulse. The background noise was measured with the monochromator tuned to 400 nm.

### *Data analysis.*

1) The time-integrated spectra (conventional spectral fluorescence emission) was constructed from the measured fluorescence response pulses by integrating each pulse as a function of time for each investigated wavelength. The constructed fluorescence spectra was corrected for background noise, corrected for nonuniform instrumental system response measured with a calibrated irradiance light source (Oriel, 63358) and normalized by dividing the fluorescence intensity at each emission wavelength by the peak fluorescence intensity. The reconstructed spectrum was characterized by discrete fluorescence intensities ( $I_w$ ) that showed the variation of fluorescence intensity as a function of wavelength. To describe the fluorescence emission band shape, two parameters were used a) the position of the peak fluorescence maximum and b) the fluorescence bandwidth at half-maximal amplitude (FWHM) measured on the long wavelength range of the peak emission.

2) The time-resolved spectra (fluorescence impulse response function  $I_f(\tau)$  (FIRF)) was determined by deconvolving the measured laser pulse from the measured fluorescence pulses at each wavelength across the spectrum. The deconvolution

method adopted was based upon Least-Square iterative reconvolution technique combined with Laguerre expansion of kernels technique. Five Laguerre function were used for expansion. The method was previously<sup>15,16</sup> fully described. To characterize the dynamics of fluorescence decay, two sets of parameters were used a) the average lifetime estimated as the time at which the FIRF crossed the 1/e mark, b) the decay constants obtained by approximating the FIRF with a biexponential function.

$$I_f(t) = a_1 e^{-t/\tau_1} + a_2 e^{-t/\tau_2}$$

In the biexponential model, parameters  $\tau_1$  and  $\tau_2$  represented the fast-term and the slow-term decay constants. Ratio  $A_1 = a_1/(a_1+a_2)$  represent the fractional contribution of the fast-decay component to the fluorescence impulse response function.

3) Data are reported as mean  $\pm$  SE. The level of significance used was  $p < 0.05$ . Variance analysis (one-way ANOVA), applied to the time-dependent parameters ( $\tau$ ,  $\tau_1$ ,  $\tau_2$ ,  $A_1$ ), was employed to evaluate the effect of emission wavelength on the dynamics of fluorescence decay. The differences among individual means were assessed with a post-hoc comparison test (Student-Newman-Keuls).

### 3. RESULTS AND DISCUSSION

*Type I collagen.* The time-resolved fluorescence spectra of collagen from bovine Achilles tendon (BAT) differs from those measured on collagen from calf skin (CS) and rat tail (RT). Whereas the emission of CS and RT collagen were nearly similar (Figure 1).

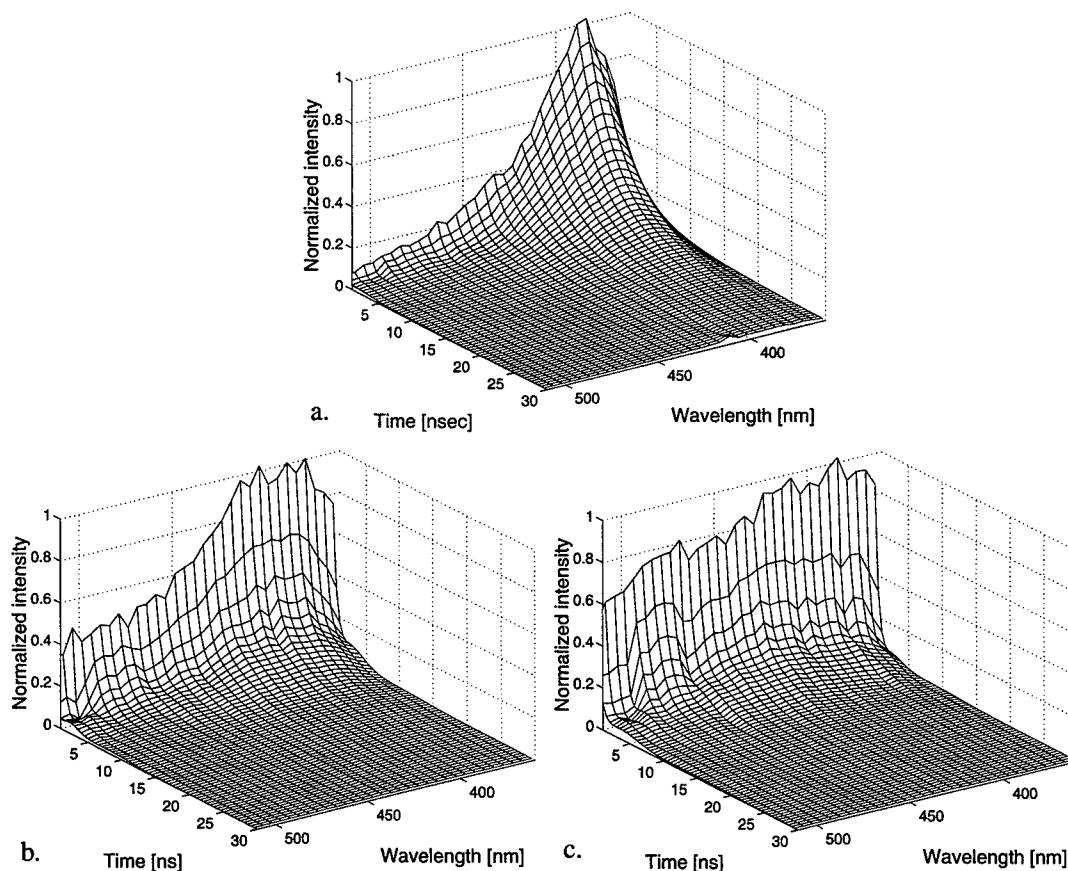


**Figure 1.** Collagen Type I spectro-temporal fluorescence impulse function. a) from bovine Achilles Tendon; b) from calf skin; c) from rat tail.

The emission spectra of CS and RT collagen was broader and presented a red shifted peak compared to that of BAT collagen (Table 1). The time-resolved emission (at peak region) of CS and RT collagen decayed faster and exhibited shorter lifetimes compared to that of BAT collagen (Table 1). The decay characteristics,  $\tau_1$ ,  $\tau_2$  and  $A_1$  are represented in Fig. 2.

**Table 1:**

Collagen Type	Source	Peak max. (nm)	FWHM <sup>a</sup> (nm)	5% I <sup>b</sup> <sub>max</sub> (390 nm) (ns)	$\tau_f$ (390 nm) (ns)
Type I	BAT	380	35 ± 2	19.0	5.2±0.2
	CS	420	73 ± 3	8.0	1.05±0.1
	RT	400	55±2	10.0	1.45 ± 0.1
Type II	NS	380	30 ± 2	22.0	6.1 ± 0.2
	TC	380	30 ± 2	23.0	6.2 ± 0.2
Type III	HP	385	60 ± 2	15.0	2.95±0.1
Type IV	HP	410	80 ± 4	7.5	1.25 ± 0.1
Type V	HP	405	80 ± 3	7.0	1.05±0.1

- a. Full-width at half maximum measured on the long wavelength site of the peak emission.  
b. Decay time of emission intensity to 5% of its value at time 0.

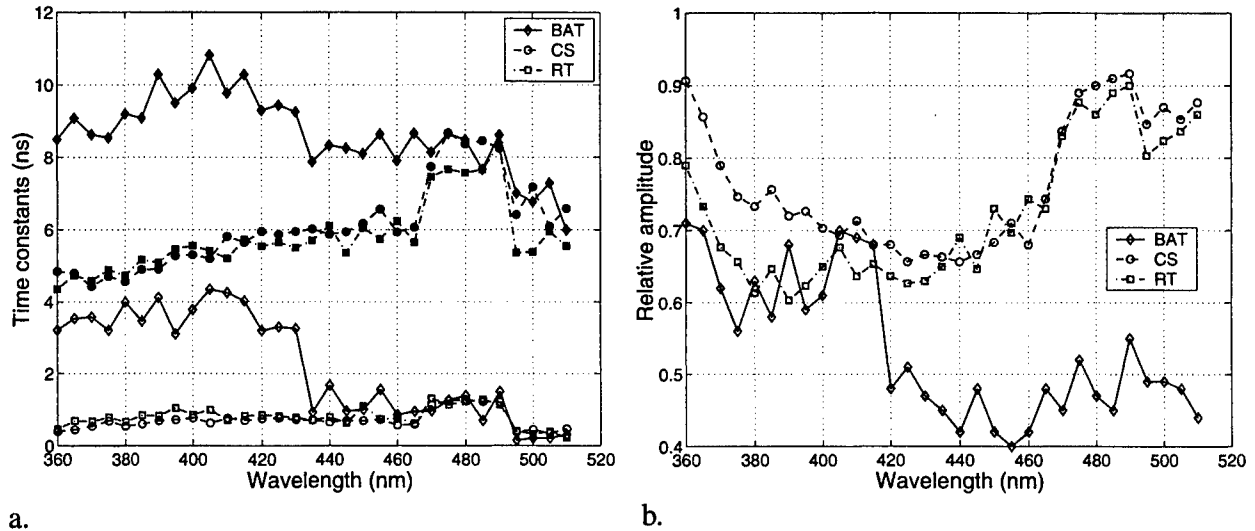


**Figure 2.** Collagen Type I fluorescence decay characteristics. a) time decay constants:  $\tau_1$  (open symbols),  $\tau_2$  (close symbols); b) fractional contribution of the fast-decay component to FIRF:  $A_1$ . Each value represents the average over three measurement sets.

Significant shorter time decay constant (at 390 nm:  $\tau_1 = 0.9$  ns;  $\tau_2 = 5$  ns) were retrieved for CS and RT collagen in contrast to those for BAT collagen ( $\tau_1 = 4.0$  ns;  $\tau_2 = 10$  ns). Also, for CS and RT collagen the decay constants values increased as a function of wavelength (470 nm:  $\tau_1 = 1.3$  ns;  $\tau_2 = 7.5$  ns). Whereas for BAT collagen, the decay constants significantly decreased at wavelengths  $>430$  nm ( $\tau_1 = 1.3$  ns;  $\tau_2 = 8.0$  ns). Still, ratio  $A_1$  showed opposite trends: a gradual increase from values around 0.65 (region of main peak emission) to  $\sim 0.85$  (470 - 490 nm range) for CS and RT collagen and a step decrease from 0.6 (region of main peak emission) to  $\sim 0.45$  (wavelengths  $>430$  nm) for BAT collagen.

Previous studies<sup>1-5</sup> have described the spectral emission characteristics of insoluble BAT collagen and acid-soluble CS and RT collagens for a broad range of excitation wavelengths. Changes of emission band shapes as function of excitation wavelength it has been noted.<sup>1,2</sup> Also, early reports<sup>9,13</sup> have identified differences between spectral emission of insoluble BAT collagen and that of acid-soluble RT and CS collagens. These differences were attributed to the distinct sets of fluorophores that characterizes Type I collagen originating from different tissues. The 3-hydroxy-pyridinium crosslink, pyridinoline (peak absorption at 325 nm), has been identified as responsible for BAT collagen peak fluorescence emission around 390 nm. The presence of different fluorophores was suggested to generate the peak emission at 420-440 nm (excitation 350-370 nm) for RT collagen and 430-435 nm (excitation 350) for CS collagen. Pyridinoline content of rat tail tendon and skin was found<sup>17</sup> negligible ( $<0.002$  residue/1000 residues) compared to Achilles tendon (rat: 0.017; bovine: 0.16). The time-resolved emission spectra of collagen family of molecules has been investigated to a much less extend. Only a few reports<sup>4,15</sup> have described the time-resolved characteristics of BAT collagen. However, to our knowledge, the time-resolved spectra of other collagen types has not been reported:

The spectral emission characteristics of Type I collagens investigated in present study are in agreement with those described in early studies<sup>2,4,15</sup> that used for excitation wavelengths in near-UV range. Also, the time-resolved spectra characteristics of BAT collagen concord with those early reported.<sup>4,15</sup> Additionally, we characterized the time-resolved emission of acid-soluble CS and RT collagens. The significant faster dynamics of fluorescence decay identified for CS and RT collagens relative to BAT collagen 1) confirms the early chromatographic studies that suggested the presence of different fluorophores in skin and tail collagens compared to Achilles tendon collagen; 2) indicates that pyridinoline is a long lived fluorescent component (lifetime  $> 5$  ns) which can be easily distinguished from the other fluorescent constituents of skin and tail collagens.

*Type II collagen.* The fluorescence emission of collagen from nasal septum (NS) was similar to that of collagen from tracheal cartilage (TC). Their emission characteristics are depicted in Figs. 3-4 and Table 1. The overall characteristics of Type II collagen fluorescence emission were similar to those of BAT Type I collagen, except for, a slightly narrow emission band, a longer emission time and an increased contribution of  $A_1$  at wavelengths  $>430$  nm.

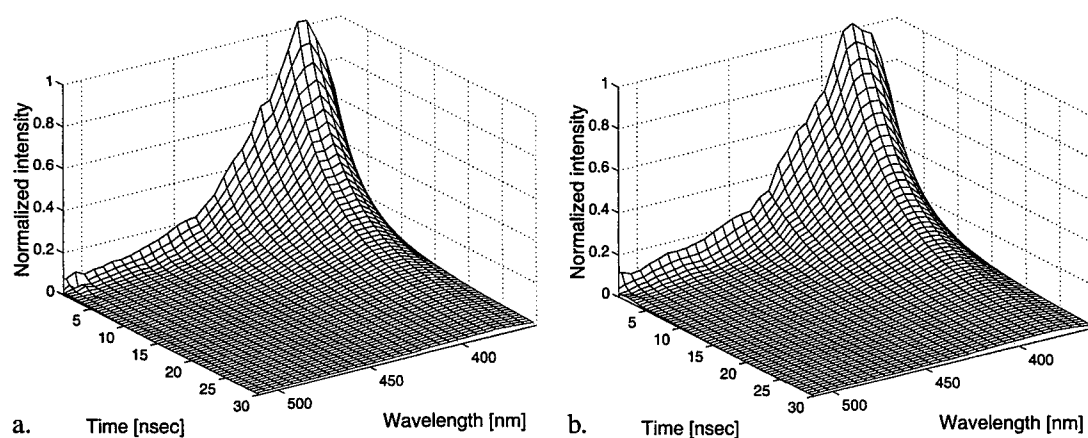


**Figure 3.** Collagen Type II spectro-temporal fluorescence impulse function. a) from bovine nasal septum; b) from bovine tracheal cartilage.

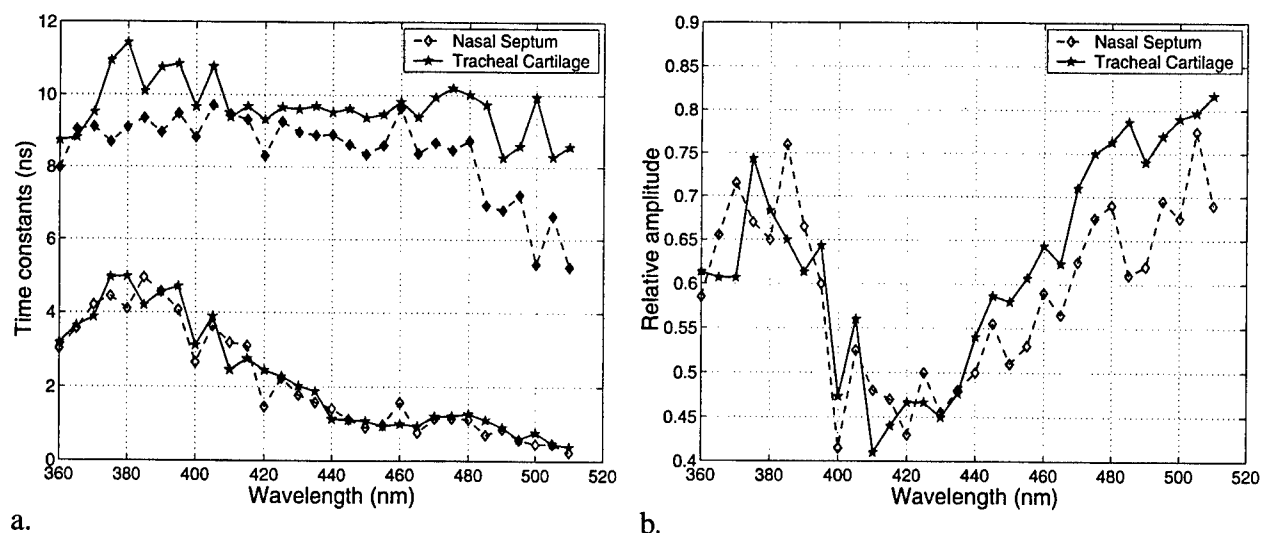


**Figure 4.** Collagen Type II fluorescence decay characteristics. a) time decay constants:  $\tau_1$  (open symbols),  $\tau_2$  (close symbols); b) fractional contribution of the fast-decay component to FIRF:  $A_1$ . Each value represents the average over three measurement sets.

Chromatographic analysis<sup>18</sup> have identified pyridinoline as an abundant component of cartilage collagen. The time-resolved spectra determined in this study for both NS and TC collagen present similarities with BAT collagen emission but not with RT and CS collagen, thus suggesting that upon 337 nm excitation pyridinoline dominates the fluorescence emission of Type II collagen. The long time decay determined for both collagen cartilage samples correlates with the results for BAT collagen that indicate pyridinoline as a long lived fluorescent component.

**Type III collagen.** The fluorescence emission characteristics are shown in Table 1 and Fig. 5-6. The emission spectra was significant (~2 times) broader and slightly (5 nm) red shifted compared to that of BAT Type I and Type II collagens. Also, the dynamics of the fluorescence decay was faster. These trends were reflected by all time-dependent parameters, lifetime and decay constants (Fig. 6 and Table 1). The time of emission decreased along the spectrum, mainly due to increased contribution of  $A_1$  parameter.

The spectral emission of Type III collagen has been previously reported for 308 nm (380 nm peak emission; 70 nm FWHM)<sup>3</sup>, and 325 nm (390 nm, 30 nm)<sup>2</sup> excitation, but to our knowledge, no information is available regarding its time-resolved emission. The chromatographic separation of Type III a-chains from Type I a-chain revealed differences in their cyanogen bromide peptides, cross-linked by disulfide bonds, different hydroxyproline crosslink (4-hydroxy-pyridinium).<sup>19</sup> These compositional differences, probably, originate the distinct fluorescence emission characteristics of Type III collagen when compared to Type I collagens.

**Type IV collagen.** The time-resolved emission spectra of Type IV collagen (Fig. 5-6) resembled closely the emission of CS and RT Type I collagens. However, a few differences were observed compared to CS and RT Type I collagen. For instance, we determined a 10 nm shift (blue compared to CS, red compared to RT) of peak emission, a broader emission, and slight faster decay (Table 1).

**Type V collagen.** The fluorescence emission characteristics are shown in Table 1 and Fig. 5-6. The fluorescence emission characteristics were similar those of Type IV collagens and, consequently, to those of CS and RT Type I collagen.



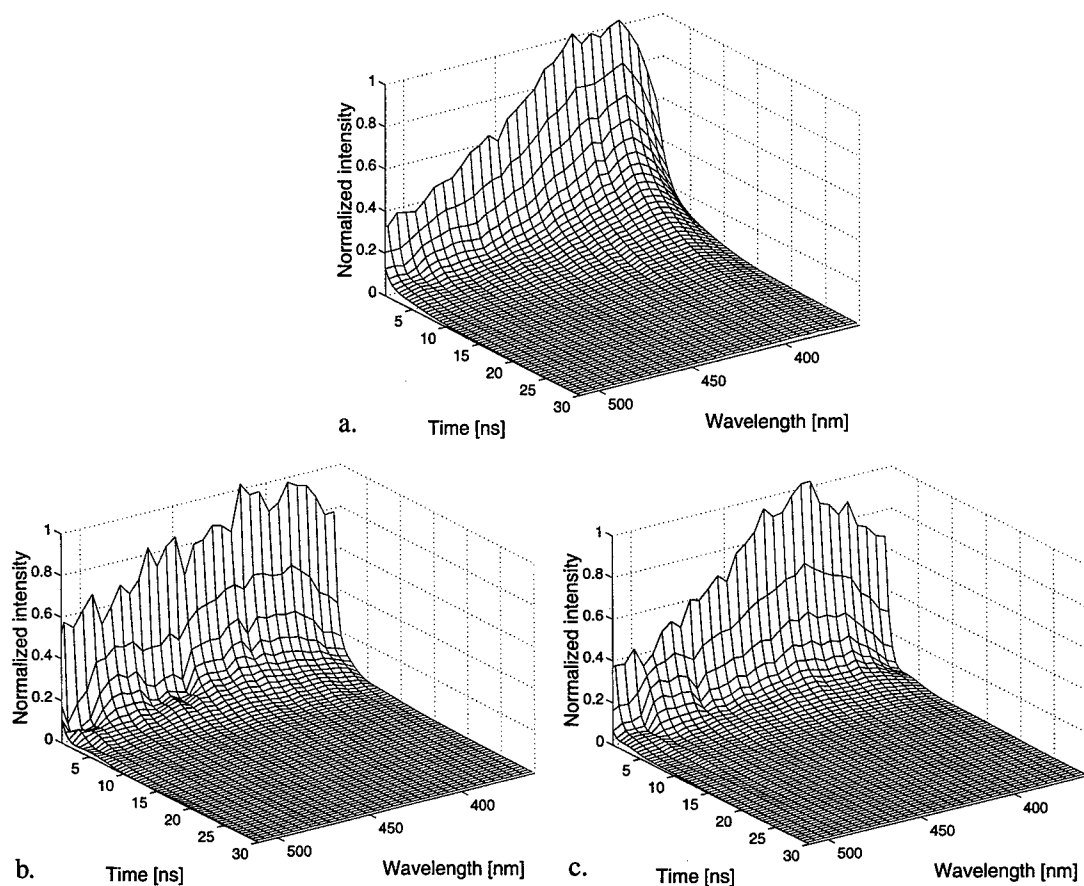


**Figure 5.** Spectro-temporal fluorescence impulse function of collagen: a) Type III; b) Type IV; c) Type V. All three collagen types are from human placenta.

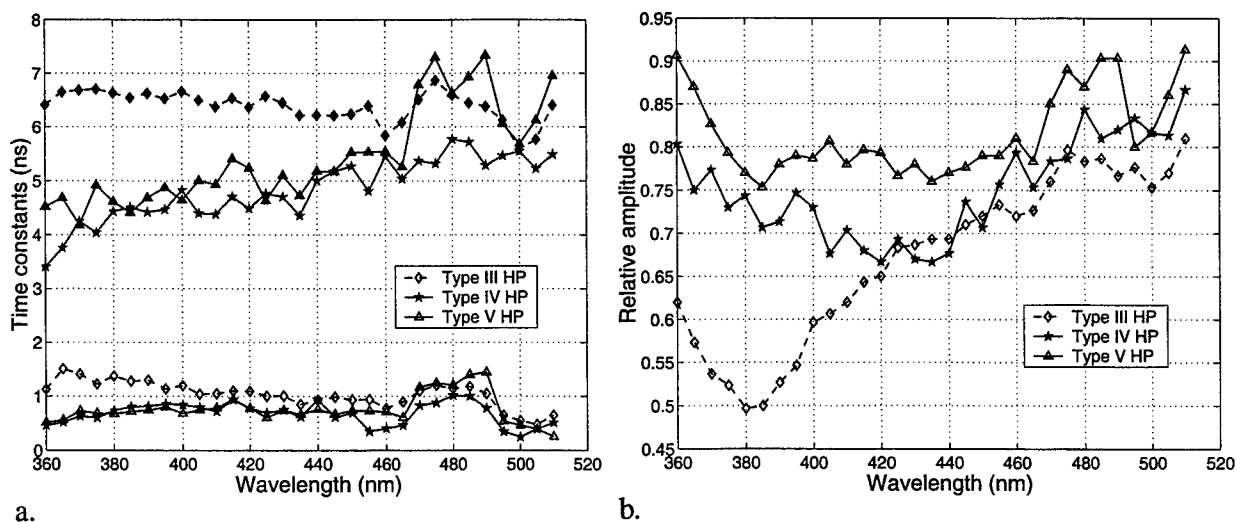


**Figure 6.** Collagen Types III, IV, V fluorescence decay characteristics. a) time decay constants:  $\tau_1$  (open symbols),  $\tau_2$  (close symbols); b) fractional contribution of the fast-decay component to FIRF:  $A_1$ . Each value represents the average over three measurement sets.

Both Type IV and V collagens are primarily found in basement membrane structure and contain more than one unique polypeptide chain. Although we were not able to infer from literature the origin of their emission upon near-UV excitation, the fast emission decay retrieved for these collagens suggest that pyridinoline, the main fluorescent component of Type I BAT collagen and Type II collagen, is less likely to contribute to Type IV and V fluorescence.

#### 4. CONCLUSION

This study demonstrated that time-resolved fluorescence information can discriminate: 1) Type I collagen in skin and tail tendon from Type I collagen in Achilles tendon; 2) all Type I collagen from Type III collagen; 3) Type II collagen from all other types except Type I Achilles tendon; 4) Type III collagen from Types IV and V collagens. Our results are in agreement with the chromatographic analysis of collagen types composition. Collagen is a constant component of solid tumors matrix, normal and atherosclerotic arterial walls, and skin but varies in quantity and type. Defining the amount and kinds of collagen of various tissues at particular stages (disease, age, healing, etc) can be useful in a) defining the extent of tissue transformation and 2) tissue diagnose. Consequently, our results suggest time-resolved laser-induced fluorescence technique as a potential tool for quantification of collagen matrix transformations in various tissues and non-invasive diagnostic.

#### ACKNOWLEDGEMENTS

This work was supported in part by the Biomedical Simulations Resource at University of Southern California, Los Angeles.

#### REFERENCES

1. J. J. Baraga, R. P. Rava, P. Taromi, C. Kittrell, M. Fitzmaurice, and M. S. Feld, "Laser Induced Fluorescence Spectroscopy of Normal and Atherosclerotic Human Aorta Using 306–310 nm Excitation". *Laser Surg. Med.*, **10**:245–261, 1990.
2. L. I. Laifer, K. M. O'Brien, M. L. Stetz, G. R. Gindi, T. J. Garrand, L. I. Deckelbaum, "Biochemical basis for the difference between normal and atherosclerotic arterial fluorescence", *Circulation*, **80**:1893–1901, 1989.
3. W. Yan, M. Perk, A. Chagpar, Y. Wen, S. Stratoff, W. Schneider, B. Jugdutt, J. Tulip, A. Lucas, "Laser-Induced Fluorescence: III. Quantitative Analysis of Atherosclerotic Plaque Content", *Lasers Surg. Med.*, **16**:164–178, 1995.
4. S. Andersson-Engels, L. Laert, R. Berg, M. A. D'Hallewin, J. Johansson, U. Stenram, K. Svanberg, and S. Svanberg, "Fluorescence characteristics of atherosclerotic plaque and malignant tumors. In *SPIE* **1426**: 31–43, 1991.
5. Marcu L, Grundfest W.S., Maarek J.M., "Photobleaching of arterial fluorescent compounds: characterization of elastin, collagen, and cholesterol time-resolved spectra during prolonged ultraviolet irradiation", *Photochem. Photobiol.* **69**:713–721, 1999.
6. S. Katsuda, Y. Okada, T. Minamoto, Y. Oda, Y. Matsui, and I. Nakanishi, "Collagens in Human Atherosclerosis. Immunohistochemistry analysis using collagen type-specific antibodies", *Arterioscler Thromb.* **12**:494–502, 1992.
7. K.G. McCullagh, V. C. Duance, and K. A. Bishop, "The distribution of collagen types I, III and V (AB) in normal and atherosclerotic human aorta", *J. Path.* **130**:45–55, 1980. laser-induced fluorescence spectroscopy
8. E. J. Miller and S. Gay, "The collagens: An overview and update", *Methods in Enzymology* **144**:3–41, 1987.
9. E. Fujimori, Changes induced by ozone and ultraviolet light in type I collagen. Bovine Achilles tendon collagen versus rat tail tendon collagen, *Eur. J. Biochem.* **152**:299–306, 1985.
10. E. Schwartz, F. A. Cruickshank, C. C. Christensen, J. S. Perlish, and M. Lebwohl. Collagen alterations in chronically sun-damaged human skin., *Photochem. Photobiol.* **58**:841–844, 1993.
11. R. W. Glanville, D. Breitkreutz, M. Meitinger, and P.P. Fietzek, "Completion of the amino-acid sequence of the  $\alpha 1$  chain from type I calf skin collagen", *Biochem J.* **215**:183–189, 1983.
12. M. J. Barnes, and L. F. Morton, "Presence of Type III collagen in guinea-pig dermal scar", *Biochem J.* **157**:263–266, 1976.
13. J. M. Menter, G. D. Williamson, K. Carlyle, C. L. Moore, and I. Willis, "photochemistry of type I acid-soluble calf skin collagen: dependence on excitation wavelength", *Photochem. Photobiol.* **62**:402–408, 1995.
14. Marcu L., Maarek J.M., Grundfest W.S. "Time-resolved laser-induced fluorescence of lipids involved in development of atherosclerotic lesion lipid-rich core". In *Optical Biopsy II*, SPIE **3250**:158–167, 1998.

15. J-M. I. Maarek, L. Marcu, W. J. Snyder, W. S. Grundfest, Time-resolved fluorescence spectra of arterial fluorescent compounds: reconstruction with Laguerre expansion technique. *Photochem. Photobiol.* In press, 2000
16. V. Z. Marmarelis, "Identification of Nonlinear Biological Systems Using Laguerre Expansions of Kernel". *Ann. Biomed. Eng.*, **21**:573-589, 1993.
17. D. Fujimoto and T. Moriguchi, "Pyridinoline, a non-reducible crosslink of collagen", *J. Biochem.* **83**: 863-867, 1978
18. J-J Wu and D. R. Eyre," Identification of hydroxypyridinium cross-linking sites in Type II collagen of bovine articular cartilage", *Biochemistry* **23**:1850-1857, 1994.
19. E. H. Epstein, "[ $\alpha 1(\text{III})$ ]<sub>3</sub> Human skin collagen. Release by digestion and preponderance in fetal life", *J. Biol. Chem.* **249**:3225-3231, 1974.

# Raman Detection of Carotenoid Pigments in the Human Retina

Werner Gellermann<sup>a</sup>, Igor V. Ermakov<sup>a</sup>, Robert W. McClane<sup>a</sup>,  
and Paul S. Bernstein<sup>b</sup>

<sup>a</sup>Department of Physics and Dixon Laser Institute  
University of Utah, Salt Lake City, UT 84112

<sup>b</sup>Department of Ophthalmology, Moran Eye Center,  
University of Utah School of Medicine, Salt Lake City, UT 84132

## ABSTRACT

We have used resonance Raman scattering as a novel, non-invasive, *in-vivo* optical technique to measure the concentration of carotenoid pigments in the human retina. Using argon laser excitation we are able to measure two strong carotenoid resonance Raman signals at 1159 and 1525 wave numbers, respectively. The required laser power levels are within the limits given by safety standards for ocular exposure. Of the approximately ten carotenoid pigments found in normal human serum, the species lutein and zeaxanthin are concentrated in high amounts in the cells of the human macula, which is a ~ 5 mm diameter area of the retina in which the visual acuity is highest. These carotenoids give the macula a characteristic yellow coloration, and it is speculated that these molecules function as filter to attenuate photochemical damage and/or image degradation under bright UV/blue light exposures. In addition, they are thought to act as free-radical scavenging antioxidants. Studies have shown that there may be a link between macular degenerative diseases, the leading cause of blindness in the elderly in the United States, and the presence or absence of the carotenoids. We describe an instrument capable of measuring the macular carotenoids in human subjects in a non-invasive, rapid and quantitative way.

**Keywords:** Raman Scattering, Resonance Raman Spectroscopy, retina, macula, carotenoids, age-related macular degeneration

## 1. INTRODUCTION

Human serum normally contains about ten species of carotenoid pigments. Two of these pigments, the xanthophyll carotenoids lutein and zeaxanthin, are also found in the retina, more specifically, in the cells of the macula lutea, the five to six millimeter diameter central area of the retina in which the visual acuity is highest [1-5]. While zeaxanthin is concentrated centrally, lutein dominates in more peripheral regions. As a consequence of their strong optical absorption in the blue/green spectral range, that occurs as broad absorption band near 450 nm, these carotenoids give a characteristic yellow coloration to the macula.

The macular carotenoids lutein and zeaxanthin are known to act as a filter to attenuate photochemical damage and/or image degradation from short wavelength visible light [6,7]. In addition, they are thought to act as free-radical scavenging antioxidants [6,7]. Studies have shown that there is an inverse correlation between high dietary intakes and blood levels of lutein and zeaxanthin and risk of age-related macular degeneration (AMD), the leading cause of blindness in the elderly in the United States [8,9].

We have investigated resonance Raman scattering as a new approach for non-invasive optical measurement of the retinal carotenoid pigments. Potentially this laser spectroscopy technique could be an objective and specific technique to non-invasively quantify macular pigment levels in human subjects and thus be a major advance in the study and possible prevention of macular degeneration diseases.

## 2. STRUCTURE AND OPTICAL PROPERTIES OF CAROTENOIDS

Carotenoids are chain-like molecules similar to polyenes regarding their structure and optical properties. Fig. 1 shows the molecular structures for the three carotenoid species  $\beta$ -carotene, zeaxanthin, and lutein. All three species contain 9 alternating conjugated carbon double and single bonds, respectively. Both ends of the conjugated chain have an attached ionone ring, and four methyl groups are attached along the polyene backbone. Compared to  $\beta$ -carotene, lutein and zeaxanthin have an additional OH radical attached to the ionone rings. Zeaxanthin differs from lutein in the location the additional carbon double bond in the ionone rings.

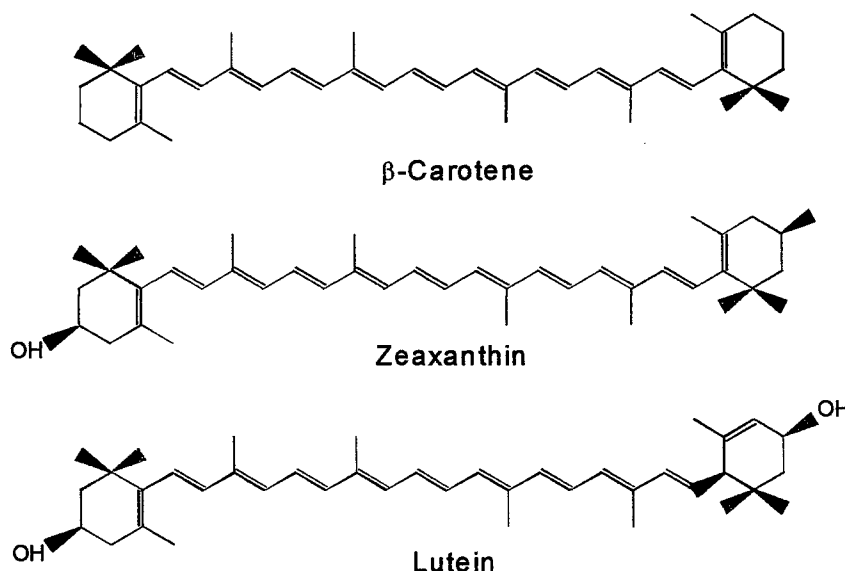


Fig. 1 Molecular structures of the three carotenoid species  $\beta$ -carotene, zeaxanthin, and lutein.

The electronic absorptions of carotenoid solutions (tetrahydrofuran) are strong in all cases and occur in broad bands ( $\sim 100$  nm width) in the  $\sim 450 - 460$  nm region. They show clearly resolved vibronic substructure with a spacing of  $\sim 1400$   $\text{cm}^{-1}$  in the cases of lutein,  $\beta$ -carotene and zeaxanthin. Laser excitation of the carotenoids in the long-wavelength shoulder of their absorption bands results in weak luminescence. For all three carotenoids this luminescence is characterized by a very small Stokes shift ( $\sim 70$  nm) and in the case of lutein and  $\beta$ -carotene a vibronic substructure appears in their band shapes. Most striking, however, is the fact that the luminescence signals are extremely weak, requiring a sensitive photomultiplier in combination with a photon counter for their detection. Comparing the signal strengths of the luminescence to organic dyes in the same experimental setup we estimate the quantum efficiencies  $\eta$  of the carotenoids to be of the order of  $10^{-5}$ .

The observed optical properties can be understood within the concept of the configuration coordinate diagram for the carotenoid molecules, which is illustrated in Fig.2. Shown here are the energies of the carotenoid molecule's three lowest states as a function of a configuration coordinate. The configuration coordinate represents the displacement of a normal coordinate of the molecule's constituent atoms from equilibrium position. In this picture, optical excitation of the molecule's conjugated  $\pi$ -electron leads in a fully electric-dipole allowed vibronic transition from the  $1^1A_g$  singlet ground state to the  $1^1B_u$  singlet excited state. Following excitation of the  $1^1B_u$  state, the molecule then relaxes very rapidly (within  $\sim 200$ - $250$  fs in  $\beta$ -carotene [10]) via nonradiative transitions to the bottom of the  $1^1B_u$  state. From here, two competing deactivation channels exist for the excited molecule: a) radiative transition back to the  $1^1A_g$  ground state, and b) nonradiative relaxation to another excited singlet state,  $2^1A_g$ , which is known to lie *below* the  $1^1B_u$  state in polyenes. Obviously, the nonradiative deactivation channel b) is very effective in the optical pumping cycle of the carotenoids, thus yielding only a very low luminescence quantum efficiency for channel a). Furthermore, once in level  $2^1A_g$ , the electronic emission to the ground state is symmetry- forbidden. The combination of a low  $1^1B_u \rightarrow 1^1A_g$  luminescence efficiency

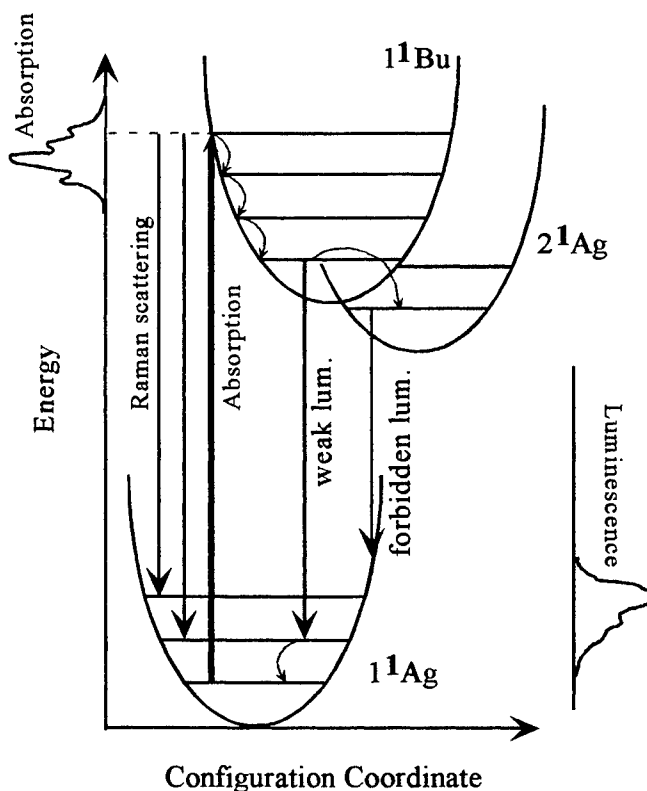


Fig. 2 Configuration coordinate diagram for lowest energy levels of carotenoid molecules, with indicated optical excitation, non-radiative relaxation, luminescence, and Raman transition channels.

( $10^{-5}$ - $10^{-4}$  in  $\beta$ -carotene [10]), and the absence of  $2^1A_g \rightarrow 1^1A_g$  fluorescence, results in extremely low luminescence signals for carotenoid molecules. This fact allows us to explore the resonant Raman scattering response of the molecular vibrations which is usually orders of magnitude weaker than a fully electric dipole allowed and therefore potentially masking luminescence transition (see Fig.2).

### 3. RESONANCE RAMAN SPECTROSCOPY OF CAROTENOIDS

In our initial experiments we used a conventional research-grade Raman setup to measure carotenoids in solutions and human flat-mounted retinas. As excitation sources, the vertically polarized 4880 or 5145 Å lines of an argon laser were used. The laser power was reduced to several mW with a neutral density filter and the laser plasma lines were eliminated with a combination of a 600 lines/mm grating and a slit. The laser was directed through a beam splitter and weakly focused onto the sample with a 10 cm focal length lens. The backscattered light was imaged onto the entrance slit of a Raman spectrometer with the beam splitter and an additional lens. The Raman spectrometer (Spex Triplemate) employed two stray light rejection gratings with 300 lines/mm, a dispersion grating with 1200 lines/mm, and a liquid-nitrogen cooled silicon CCD detector array with 25  $\mu$ m pixel width.

In Fig. 3 we show Raman spectra obtained for a solution of lutein spotted on filter paper. We observe strong and clearly resolved Raman signals superimposed on a weak fluorescence background under resonant laser excitation. The Raman response is characterized by two prominent Stokes lines at 1158 and 1525  $\text{cm}^{-1}$  (corresponding to wavelength shifts of 292 and 393 Å, respectively, for 4880 Å excitation), with the 1255  $\text{cm}^{-1}$  line being the stronger one. These lines originate [11], respectively, from carbon-carbon single-bond and double-bond stretch vibrations of the conjugated backbone. In addition, a weaker but clearly distinguishable Stokes signal appears at 1008  $\text{cm}^{-1}$ , which is attributed to rocking motions of the

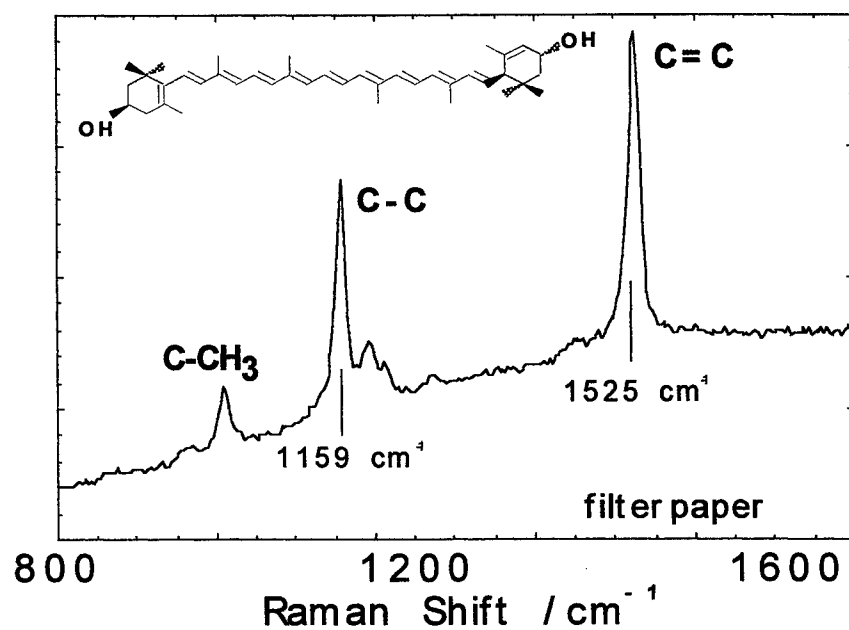


Fig.3. Resonance Raman spectrum of lutein spotted on filter paper.

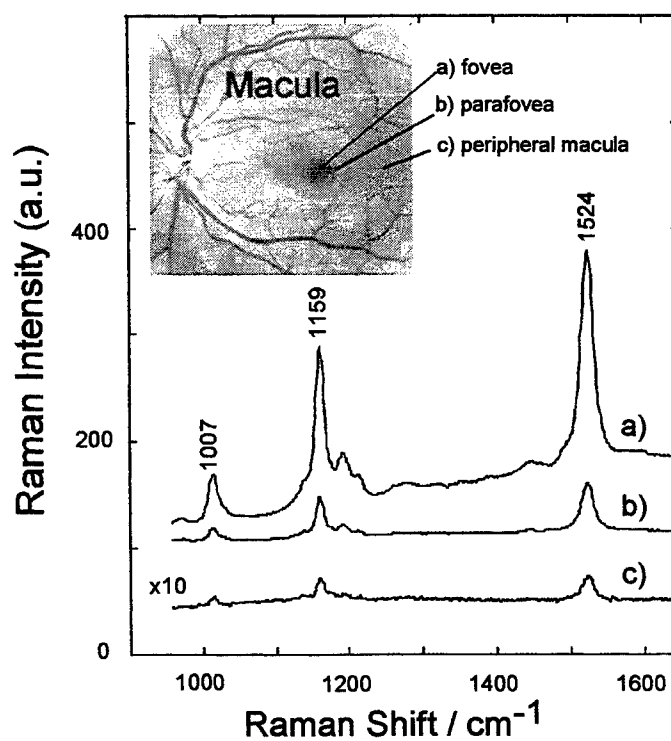


Fig.4 Resonance Raman spectrum of flat-mounted human retina.

molecule's methyl components [11]. This result demonstrates that strong Raman signals with excellent signal-to-noise ratio can even be readily obtained even for extremely thin, film-like samples.

Proceeding to ocular tissues we measured next the resonant Raman response of flat-mounted human retinas. Usable signals can be obtained with either the 4880 or 5145 Å argon laser lines. Ordinarily, the 4880 Å line is preferred over the 5145 Å line since carotenoid Raman signal strength is three times higher at 4880 Å, and background luminescence is lower. A typical result is shown in Figure 4.

The Raman spectra obtained for the macula are remarkably similar to the spectra of the lutein solution shown in Fig. 4. The peaks at  $\sim 1159$  and  $\sim 1524$   $\text{cm}^{-1}$  are obtained with good signal-to-noise ratio when the beam is aimed at the foveal and parafoveal areas (traces a and b), and they decrease by at least a factor of 30 as the beam is moved toward the peripheral retina (trace c). This behavior correlates well with the known distribution of carotenoids in the human retina as determined by high-performance liquid chromatography (HPLC) or psychophysically [1,12,13].

We find that other human ocular structures such as the cornea, lens, vitreous, retinal pigment epithelium, choroid, and sclera do not generate any detectable or interfering Raman signals under comparable conditions. We were also able to demonstrate a linear correlation between Raman signal strength and actual macular carotenoid levels as determined by HPLC.

For the development of a Raman detection system useful for living humans, the light exposure of the retina has to be limited to a maximum permissible dose, which according to ANSI Z136.1 standards is  $2.7 \text{ J/cm}^2$  (equivalent to a laser power density at the retina of  $2.7 \text{ mW/mm}^2$  for 10 seconds) [14]. For this purpose we constructed a compact, fiber-based Raman system with high light throughput and interfaced it to a fundus camera to facilitate locating the macula in the retina. The experimental layout is shown in Figure 5. The excitation laser beam is routed via fiber, holographic rejection filter,

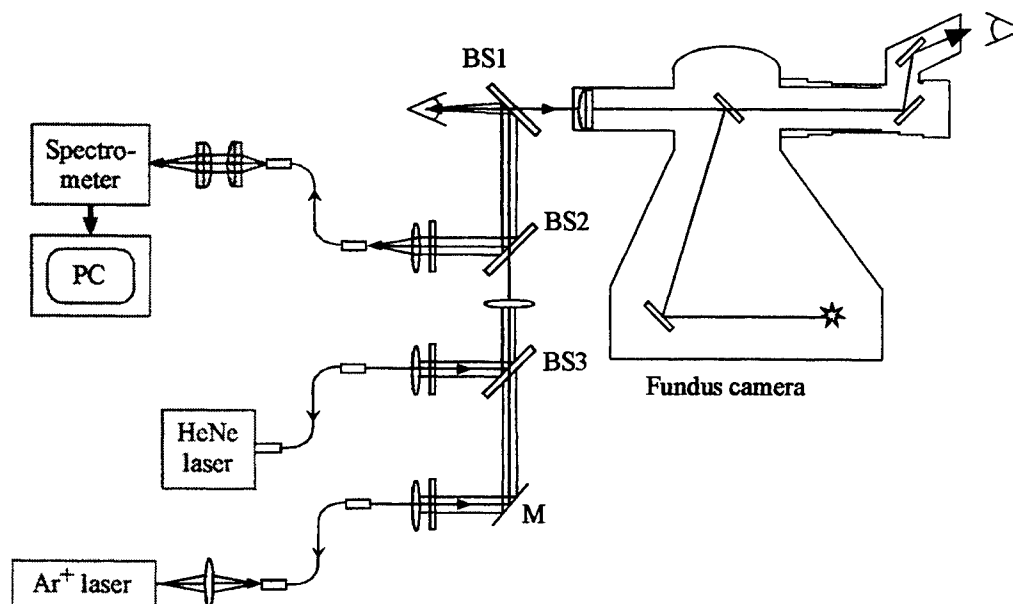


Fig. 5 Experimental setup showing light delivery and collection optics of fiber-based Raman spectrometer interfaced with fundus camera.



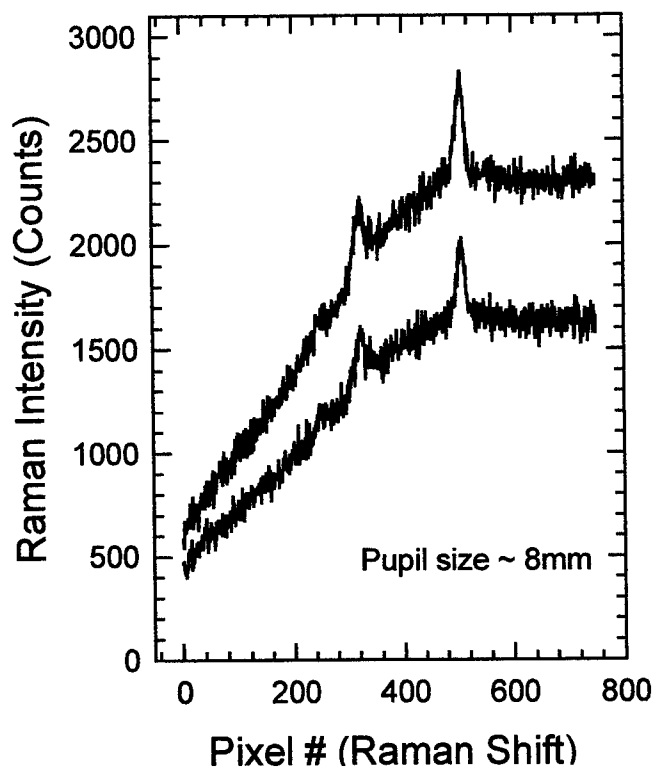


Fig. 6 Raman spectra from retina of healthy volunteer, measured with dilated pupil. The two traces correspond to two separate measurements, and clearly show the carotenoid Raman signals superimposed on a fluorescence background.

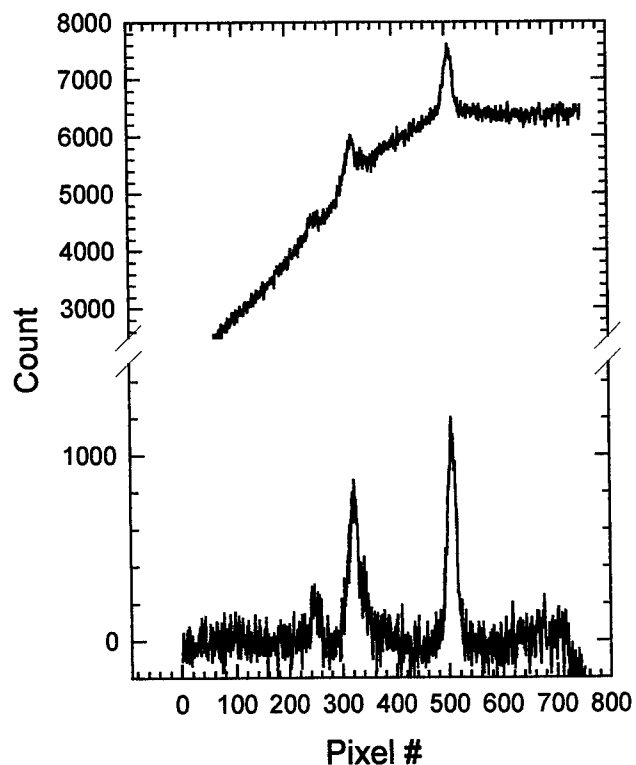


Fig. 7 Raman spectra of healthy human volunteer, measured with dilated pupil, and averaged over three individual measurements. Top trace: before background subtraction; bottom trace: after subtraction of fluorescence background.

dichroic beamsplitter and focusing lens to the human eye. The Raman-scattered light is collected in 180 degree backscattering geometry with the same lens and routed through beam splitter, laser band pass filter and fiber bundle to a spectrograph. He-Ne laser aids as a pilot beam and can be detected on a macula with a fundus camera. The Raman spectra are recorded with a cooled CCD camera and displayed on a computer screen.

In Fig. 6 we show Raman spectra from the macula of a healthy volunteer, measured with a dilated pupil (diameter about 8 mm). The figure shows two traces corresponding to two separate measurements and clearly shows the appearance of the carotenoid Raman signals superimposed on a broad fluorescence background. In these measurements the laser power was 300  $\mu$ W, the exposure time 1 sec., and the spot diameter on the macula was 1 mm. This corresponds to a real dose of 38 mJ/cm<sup>2</sup>, a value which is about 70 times lower than the maximum permissible safe dose of 2.7 J/cm<sup>2</sup>.

Spectra with further increased signal-to-noise ratio could be obtained by measuring several individual Raman spectra, followed by simple averaging of the spectra. This can be seen from Fig. 7 where we show Raman spectra of the macula of the same volunteer averaged over three consecutive measurements. The upper trace corresponds to the three averaged spectra and the bottom trace to the same spectra after subtraction of the fluorescence background.

#### 4. CONCLUSION

In conclusion, we showed that Raman scattering has the potential to be an outstanding new tool for the noninvasive measurement of macular carotenoids in the human retina. It is remarkable that strong Raman signals with good signal-to-noise ratio can be obtained from the most light sensitive area of the human retina at surprisingly low laser intensities that fall within safety standards. Because there is accumulating evidence that increased macular carotenoid levels may be protective against visual loss from AMD, this technique may prove to be important in assessing risk of visual loss in patients prone to develop AMD. Those patients found at risk could attempt to raise their macular carotenoid levels through dietary modification or nutritional supplements, and their response to intervention could be monitored using the same device. A prototype Raman instrument for use on humans in a clinical setting is currently under development.

#### 5. REFERENCES

1. D. M. Snodderly, P. K. Brown, F. C. Delori, & J. D. Auran, *Invest. Ophthalmol. Vis. Sci.* **25**, 660 (1984).
2. D. M. Snodderly, J. D. Auran, & F. C. Delori, *Invest. Ophthalmol. Vis. Sci.* **25**, 674 (1984).
3. R. A. Bone, J. T. Landrum, & S. L. Tarsis *Vision Res.* **25**, 1531 (1985).
4. G. J. Handelman, D. M. Snodderly, A. J. Adler, M. D. Russett, & E. A. Dratz, *Methods in Enzymology* **213**, 220 (1992).
5. J. D. M. Gass, *Stereoscopic Atlas of Macular Disease* (fourth edition), Mosby, St. Louis (1997).
6. W. Schalch, in *Free Radicals and Aging*, eds. Emerit, I. & Chance, B. (Birkhauser Verlag, Basel Switzerland), 280 (1992).
7. D. M. Snodderly, *Am. J. Clin. Nutr.* **62S**, 1448S (1995).
8. Eye Disease Case Control Study Group *Arch. Ophthalmol.* **111**, 104 (1993).
9. J. M. Seddon, U. A. Ajani, R. D. Sperduto, R. Hiller, N. Blair, T. C. Burton, M. D. Farber, E. S. Gragoudas, J. Haller, D. T. Miller, L. A. Yannuzzi, & W. Willett, *J. Am. Med. Assoc.* **272**, 1413 (1994).
10. A. P. Shreve, J. K. Trautman, T. G. Owens, and A. C. Albrecht, *Chem. Phys. Letters* **178**, 89 (1991).
11. Y. Koyama, I. Takatsuka, M. Nakata, and M. Tasumi, *J. Raman Spectroscopy* **19**, 37 (1988).
12. D. M. Snodderly, J. D. Auran, F. C. Delori, *Invest. Ophthalmol. Vis. Sci.* **25**, 647 (1984); R. A. Bone, J. T. Landrum, S. L. Tarsis, *Vision Res.* **25**, 1531 (1985); G. J. Handelman, D.M. Snodderly, A. J. Adler, M. D. Russet, E. A. Dratz, *Methods in Enzymology* **213**, 220 (1992).
13. J. T. Landrum, R. A. Bone, M. D. Kilburn, *Advances in Pharmacology*, (H. Seis, Ed.), Academic Press, New York, 1996, ps. 537-556; B. R. Hammond, E. J. Johnson, R. M. Russell, N. I. Krinsky, K.-J. Yeum, R. B. Edwards, D. M. Snodderly, *Inv. Ophthalmol. Vis. Sci.* **38**, 1795 (1997); B. R. Hammond, B. R. Wooten, D. M. Snodderly, *J. Opt. Soc. Am. A* **14**, 1187 (1997).
14. F. C. Delori, J. S. Parker, M. A. Mainster, *Vision Res.* **20**, 1099 (1980); ANSI Z136.1-1993, *American National Standards for Safe Use of Lasers* (American National Standards Institute, New York, 1993).

# Global analysis of arterial fluorescence decay spectra

Jean-Michel I. Maarek<sup>a</sup>, Warren S. Grundfest<sup>b</sup>, Laura Marcu<sup>b</sup>

<sup>a</sup>Department of Biomedical Engineering, University of Southern California  
Los Angeles, CA 90089-1451

<sup>b</sup>Laser Research and Technology Development, Cedars Sinai Medical Center  
Los Angeles, CA 90048

## ABSTRACT

Global analysis of time-resolved fluorescence measured at multiple emission wavelengths was applied to simulated fluorescence spectra and arterial fluorescence spectra. Fluorescence of human aortic samples was produced with nitrogen laser excitation. Simulated spectra had decay characteristics in the range expected from previous studies of artery tissue. For both types of spectra, the emission decay was analyzed with global analysis to model the decay with a sum of exponentials. Decay constants were held fixed across wavelengths while pre-exponential coefficients were wavelength-dependent. For the simulated spectra, global analysis was compared to the traditional method in which decay constants and pre-exponential coefficients are assumed wavelength-dependent. On the simulated data, three decays could be reliably estimated by global analysis even when only two exponential decays were identified with the traditional method. On the arterial data, the intermediate decay and the long decay significantly increased between normal samples and fibrous plaque (1.7 to 2.5 ns; 7.0 to 8.4 ns). The pre-exponential coefficient of the long decay was larger in the blue range of the spectrum for the samples with advanced atherosclerosis. We conclude that global analysis markedly improves the recovery of exponential decay trends in time-resolved fluorescence spectra. Application to artery tissue fluorescence reveals characteristic spectral changes associated with atherosclerosis.

**Keywords:** time-resolved fluorescence, global analysis, simulation, atherosclerosis, nitrogen laser, aorta.

## 1. INTRODUCTION

A large body of research has reported on the diagnostic potential of fluorescence spectroscopy for detection and classification of atherosclerotic lesions. Most studies focused on the analysis of continuous wave fluorescence spectra of artery tissue to describe spectral changes associated with atherosclerosis<sup>1,2,3,4</sup>. A few studies also reported differences in the time-dependent decay of the fluorescence between healthy arterial wall and atherosclerotic lesions<sup>5,6,7,8,9,10</sup>. In these studies, the finite duration of the laser excitation pulse required that the intrinsic fluorescence decay be extracted from the experimental data by deconvolution of the experimental fluorescence transient from the laser pulse transient. Characteristics of the fluorescence decay were usually summarized by fitting the intrinsic decay with a weighted sum of exponentials. When the transient fluorescence emission was measured at more than one wavelength, the multi-exponential approximation was traditionally performed independently for each wavelength, either as part of the deconvolution<sup>5,6,7</sup> or after the deconvolution was carried out through other means<sup>8,9,10</sup>. Knutson and colleagues<sup>11</sup> reported on a class of approximation methods dubbed "global analysis" that can be applied when relations exist between the individual decay curves. A typical situation in which global analysis has been tested is one in which the decay constants (lifetimes) were assumed to be invariant across wavelengths. This situation would correspond to attributing the composite fluorescence emission of a sample to several monoexponential fluorophores with differing emission spectra. Knutson and colleagues<sup>11</sup> showed that global analysis resulted in increased model testing sensitivity leading to a more accurate estimation of the order of the exponential approximation. In addition, the exponential parameters were more accurately estimated with global analysis when compared to the traditional method.

To our knowledge, global analysis has never been applied to the analysis of time-resolved fluorescence spectra of artery tissue. Therefore, the present study had two goals. First, we investigated the applicability of global

analysis to simulated tissue spectra that had similar characteristics to actual tissue spectra measured with our experimental setup. Second, we used global analysis to describe the decay characteristics of artery tissue fluorescence for tissue samples with different degrees of atherosclerosis.

## 2. MATERIALS AND METHODS

### 2.1 Time-resolved fluorescence spectra of aortic tissue

The experimental setup, experimental procedures, and characteristics of the artery samples were described previously<sup>8,9,10</sup>. Briefly, the samples were illuminated with laser pulses from a nitrogen laser ( $\lambda$ : 337 nm; pulse width: 3 ns FWHM) that were directed to the sample by the illumination channel of an Oriel fluorescence probe (Oriel, model 77558). The sample fluorescence was spectrally separated with a monochromator and measured one wavelength at a time with multi-channel plate photomultiplier tube (Hamamatsu, model R2024U) connected to a digital storage oscilloscope (Tektronix, model TDS 620A; sampling period: 0.5 ns). The fluorescence response was measured for 29 wavelengths from 370 to 510 nm (5-nm increment). For three wavelengths (390, 430, 470 nm), the measurements were repeated 10 times thus yielding a total of 56 fluorescence measurements for each sample. The laser input waveform was measured after the sample fluorescence as the reflected intensity on the tissue surface.

Fluorescence measurements were carried out on human aortic specimens obtained from 13 cadavers (11 – 85 years old; median age: 49 years). After the fluorescence measurements, the samples were fixed in formalin and processed for histologic observation and classification. The samples were classified using the Stary classification of atherosclerotic lesions<sup>12,13</sup>. Eighty samples could be unequivocally assigned to one of six classes in the Stary classification (normal to type V lesion). The retained lesion types spanned the range from healthy arterial tissue to fatty streaks (type II lesion), to atheroma (type IV lesion), and fibrous lesion (type V lesion).

For each wavelength of emission, the fluorescence impulse response function was retrieved by numeric deconvolution using the laser pulse waveform as input and the fluorescence transient as output. The deconvolution method used a basis of discrete time Laguerre functions to expand the impulse response function<sup>8,14</sup>. The parameters of the expansion were iteratively adjusted to minimize the quadratic distance between the experimentally measured fluorescence transient and its computed counterpart (the convolution of the impulse response function with the experimental laser input pulse). The impulse response functions were assembled in a two-dimensional (time, wavelength) array, the time-resolved fluorescence spectrum. The time-resolved spectrum represented the intrinsic fluorescence decay as a function of time for the different wavelengths of emission.

### 2.2. Simulated time-resolved fluorescence spectra

Impulse response functions for the simulated time-resolved fluorescence spectra were constructed as arrays of exponential decay terms. Each array column represented the fluorescence impulse response function at one wavelength of emission:

$$I_{\lambda}(m) = a_{S,\lambda} e^{-mT/\tau_S} + a_{I,\lambda} e^{-mT/\tau_I} + a_{L,\lambda} e^{-mT/\tau_L}$$

where  $T$  is the sampling period (0.5 ns). The short, intermediate, and long decay constants ( $\tau_S$ ,  $\tau_I$ , and  $\tau_L$ ) were wavelength-independent. The corresponding pre-exponential terms ( $a_{S,\lambda}$ ,  $a_{I,\lambda}$ ,  $a_{L,\lambda}$ ) varied with wavelength in a linear fashion. The simulated time-resolved fluorescence spectra were composed of 58 columns that corresponded to the tissue fluorescence responses measured at wavelengths 360 – 510 nm in the experimental measurements (5 nm increment). The fluorescence impulse response functions were repeated 10 times for three wavelengths in the simulated spectra (390, 430, and 470 nm).

Three situations were considered that are summarized in the table below. Model 1 had decay constants that were relatively far apart (14 to 1 ratio between longest and shortest decay constant). This model was studied

with two levels of Gaussian white noise superimposed on the impulse response function. The signal-to-noise ratio (SNR) was estimated as the ratio of the signal variance over the noise variance. Model 2 had two closely spaced decay constants. It was used to simulate fluorescing samples containing two fluorophores with similar decay constants. This model was studied without noise. Model 3 had three decay constants that were closer to each other than the decay constants of model 1 (4.5 to 1 ratio between longest and shortest decay constant). This model was studied with the lower noise level only (SNR = 60 dB). Note that all three models had decay constants that were in the expected range for decay constants measured on arterial fluorescent compounds and artery tissue<sup>7,8,10,14</sup>. The decay constants ranged from 1 to 14 times the value of the sampling period used in the experimental study.

	Decay constants (ns)	Pre-exponential terms	Noise
Model 1	$\tau_S = 0.5, \tau_I = 2.0, \tau_L = 7.0$	Linear variation [0 – 1]	SNR=60 dB, SNR=40 dB
Model 2	$\tau_S = 0.5, \tau_I = 7.0, \tau_L = 7.5$	Linear variation [0 – 1]	0
Model 3	$\tau_S = 1.0, \tau_I = 3.0, \tau_L = 4.5$	Linear variation [1 – 0.5]	SNR=60 dB

### 2.3. Estimation of exponential decay trends in time-resolved spectra

The decay characteristics of the time-resolved fluorescence spectra were first estimated with a two exponential approximation of the decay, which was then compared to a three exponential approximation of the decay. Two methods were used to compute the parameters of the multi-exponential approximations: global analysis and the “traditional” method. In the global analysis method, the decay constants were held fixed for all wavelengths<sup>11</sup>. The pre-exponential coefficients were allowed to vary with wavelength. In the traditional method, decay constants and pre-exponential coefficients were allowed to vary with wavelength. For the three exponential approximation, analysis of a time-resolved spectrum required the estimation of three pre-exponential terms per wavelength + three decay constants (177 parameters for the simulated spectra). With the traditional method, analysis of a time-resolved spectrum required the estimation of three pre-exponential terms per wavelength + three decay constants per wavelength (348 parameters for the simulated spectra).

Estimation of the parameters of the multi-exponential approximation was performed using a simplex search method. The F test was applied to the residual sum of squares to determine if the improvement in the fit from a two exponential model to a three exponential model was statistically significant<sup>15</sup>. All computations were performed with the software MATLAB (The Mathworks).

## 3. RESULTS

### 3.1. Simulations – model 1

Figure 1 presents an example of fluorescence impulse response for model 1 ( $a_S = 0.5, a_I = 0.75, a_L = 1.0$ ) superimposed with Gaussian white noise such that the SNR = 60 dB (Fig. 1a) or 40 dB (Fig. 1b).

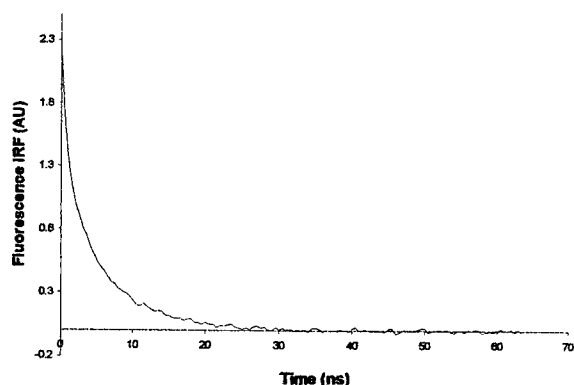


Fig 1a: noisy input with SNR = 60 dB

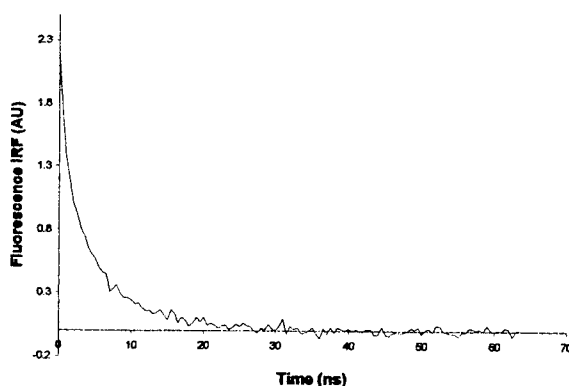


Fig 1b: noisy input with SNR = 40 dB

For the noisy model 1 response with a SNR = 60 dB, both the global analysis method and the traditional method yielded a significant improvement in the fit when a three exponential approximation was used as opposed to a two exponential model. Approximation of the simulated spectrum with the global analysis algorithm yielded values of the decay constants  $\tau_s = 0.5$  ns,  $\tau_i = 2.0$  ns,  $\tau_L = 7.0$  ns. When the traditional analysis method was used and the decay curves were approximated one at a time, the decay constants varied around the noise-free values of model 1 (Fig 2a). The variations of the pre-exponential coefficients around the noise-free values (dashed lines) are shown in Fig. 2b when the global analysis method was used and in Fig. 2c when the traditional method was used. The illustrations clearly show that the global

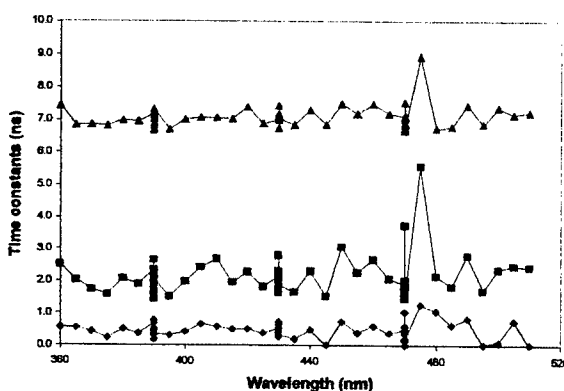


Fig 2a: decay constants – without global fit

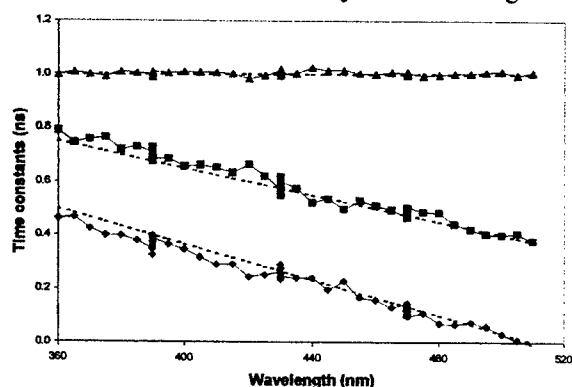


Fig 2b: pre-exponential coefficients – global fit

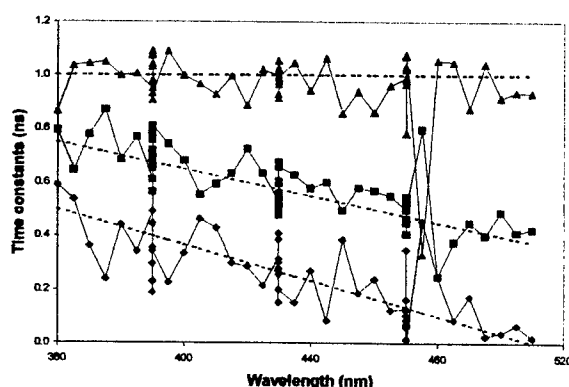


Fig 2c: pre-exponential coefficients – without global fit

analysis algorithm produced a much tighter fit for the pre-exponential coefficients when compared to the traditional method.

When the level of noise was higher (SNR = 40 dB), the global analysis method continued to show a statistically significant improvement in the fit when a three exponential model were used as opposed to a two exponential model. The estimated decay constants had values equal to  $\tau_s = 0.6$  ns,  $\tau_i = 2.3$  ns,  $\tau_L = 7.0$  ns. The pre-

exponential coefficients followed the pattern of variations of the noise-free values of model 1 (Fig. 3a) albeit with more variability around the trends of the latter when compared to the results obtained with the lower noise level.

With the traditional method, the improvement in the fit produced by a three exponential model was not statistically significant over the two exponential model. This would lead one to reject the three exponential model in favor of the simpler (but erroneous) two exponential model. The decay constants of the best two exponential fit (Fig 3.b) were such that one decay constant with value around 6 ns accounted for the 7 ns decay term in model 1. A second decay constant with value around 1 ns accounted for the 0.5 ns and 2 ns terms in the fluorescence IRF of model 1. The variations of the decay constants around their mean values were similar to the variations observed for a successful approximation (compare Fig 3.b with Fig. 2.a). These trends would support the two exponential model and lead one to miss the third decay term altogether. Results for the model 1 simulations illustrate one situation for which the global analysis method is superior to the traditional method: that of experimental noise in the estimated fluorescence impulse response function.

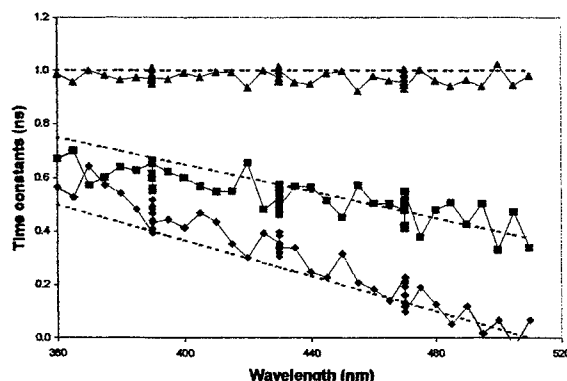


Fig 3a: pre-exponential coefficients – global fit

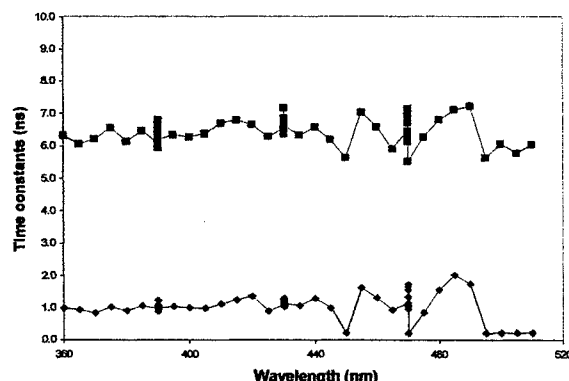


Fig 3b: decay constants – without global fit

### 3.2. Simulations – model 2

Approximation of the model 2 decay with a three exponential model yielded a statistically significant improvement of the fit for both the global analysis method and the traditional method. With the global analysis method, the decay constants of model 2 were correctly retrieved ( $\tau_S = 0.5$  ns,  $\tau_I = 7.0$  ns,  $\tau_L = 7.5$  ns). With the traditional method, only the short decay constant was correctly retrieved (Fig 4a). The long decay constant had a value around 7.35 ns in between the 7.0 and the 7.5 ns decay terms. An artifactual intermediate decay ranged between 2.0 and 7.5 ns. The pre-exponential coefficients were correctly estimated with the global analysis method (Fig. 4b) whereas only the pre-exponential coefficient of the short decay term was correctly retrieved with the traditional

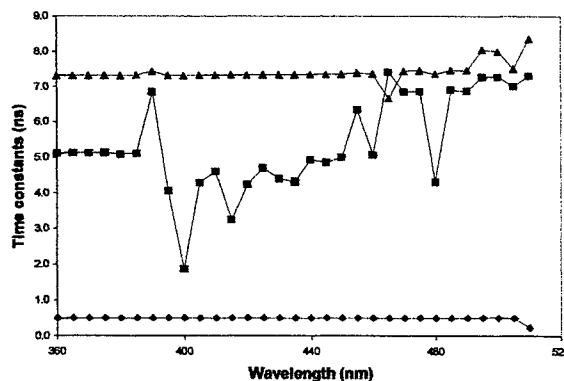


Fig 4a: decay constants – without global fit

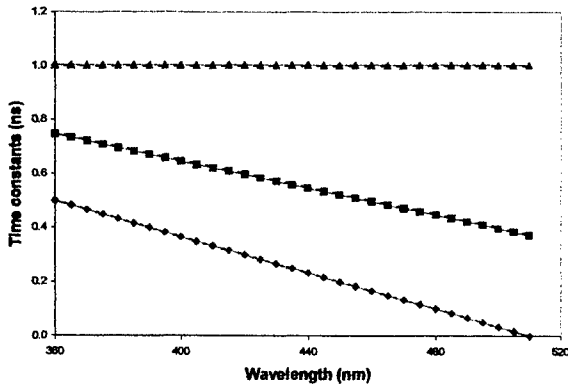


Fig 4b: pre-exponential coefficients – global fit

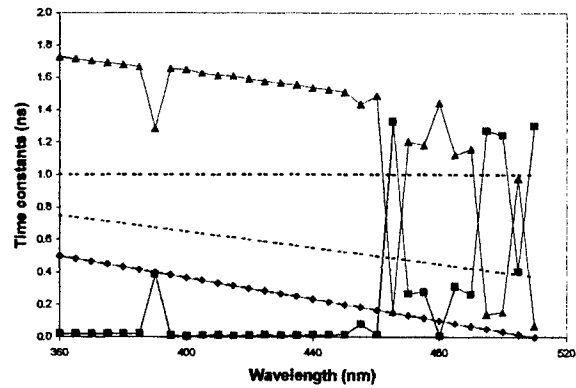


Fig 4c: pre-exponential coefficients – without global fit

method (Fig. 4c). The pre-exponential coefficient of the long decay term was overestimated, accounting for both the intermediate decay and the long decay terms. The coefficient associated with the artifactual intermediate decay was close to 0 in the blue range of the spectrum and presented strong variations at higher wavelengths. The model 2 simulations illustrate a second situation in which the global analysis method yields better results than the traditional method: that of two decay constants of similar magnitude in the fluorescence impulse response function.

### 3.3. Simulations – model 3

For the model 3 decay with a low level of noise (SNR = 60 dB), only the global analysis method registered a significant improvement in the fit when a three exponential model was used as opposed to a two exponential model. The decay constants ( $\tau_s = 1.0$  ns,  $\tau_i = 3.0$  ns,  $\tau_L = 4.5$  ns) correctly reproduced the decay constants of the model. The pre-exponential coefficients followed the trends of the noise-free values (Fig. 5a). The decay constants retrieved with the traditional method and a two exponential model are shown in Fig. 5b. The short decay and long decay terms are slightly overestimated when compared to the noise-free values of model 3. Yet, the decay constants show moderate variations across the spectrum which hide the fact that a third decay term is not accounted for by the fit. For these simulations, the traditional method fails because the decay constants have similar magnitude (although further apart than those of model 2) and because of noise superimposed to the fluorescence impulse response function. In contrast, the global analysis method successfully yields the correct parameters of the model.

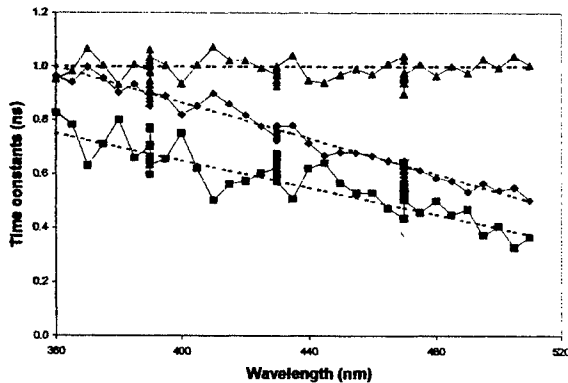


Fig 5a: pre-exponential coefficients – global fit

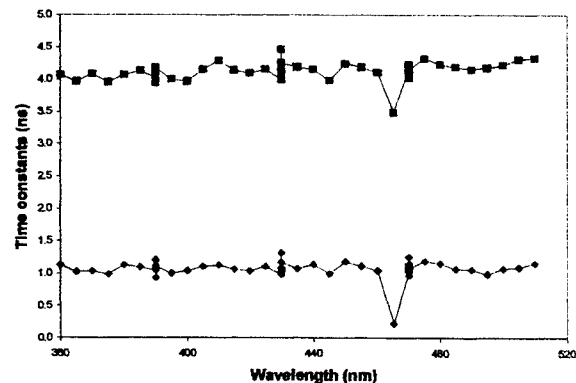


Fig 5b: decay constants – without global fit

Based on results of the simulation study, the global analysis method is better at estimating the model order, decay constants, and pre-exponential coefficients of fluorescence impulse functions with dynamics in the range of the expected decay trends for arterial fluorescence decay. The global analysis method was applied to the fluorescence decay spectra of arterial tissue to identify trends in the decay that change with the progression of atherosclerosis.



### 3.4. Fluorescence decay characteristics of aortic specimens

The short decay constant  $\tau_s$  ( $0.4 \pm 0.1$  ns) was not different for the different types of lesion identified in the samples of artery considered in this study. In contrast, the intermediate decay constant and the long decay constants significantly increased as the severity of the lesions increased from normal to type V lesions (Fig. 6). The intermediate decay constant  $\tau_i$  increased by approximately 0.6 ns for lesion types IV and V when compared to the other lesion types. The largest increase of the long decay constant  $\tau_L$  (0.9 ns) was observed between type I and type II lesions. Note that the values of the decay constants measured on artery tissue were similar to the values used for model 1 in the simulation study.

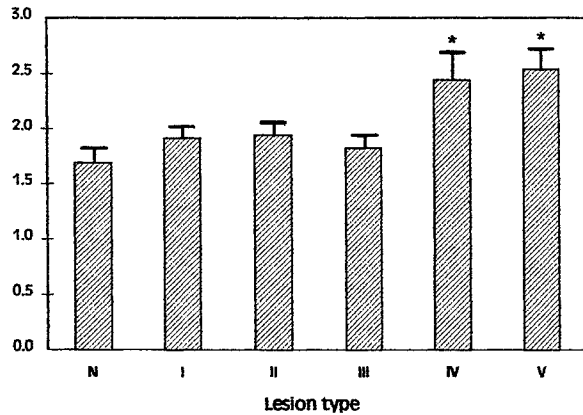


Fig 6a: intermediate decay constant – artery samples

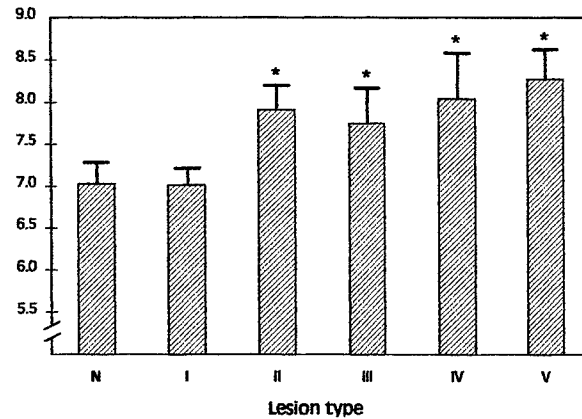


Fig 6b: long decay constant – artery samples

For all lesion types, fractional amplitude  $A_I$  ( $A_I = a_I / (a_S + a_I + a_L)$ ) decreased as the emission wavelength increased to 420 nm (Fig. 7a). Parameter  $A_I$  reached a plateau between 420 and 465 nm. For all tissue types, fractional amplitude  $A_I$  increased in the 470 – 490 nm range when compared to the values of  $A_I$  in midrange of the spectrum (420–465 nm). The increase was substantially larger for atherosclerotic lesions when compared to normal arterial wall. For wavelengths above 490 nm, amplitude  $A_I$  was slightly below the value observed in the midrange of the spectrum.

Fractional amplitude  $A_L$  was approximately independent of wavelength for normal arterial wall and type I lesions (Fig. 7b), except for a small dip at 470 – 490 nm in type I lesions. Type II lesions was associated with a reduced value of  $A_L$  over the whole wavelength range when compared to type I lesions. For type III – type V lesions, amplitude  $A_L$  at 390 nm was substantially larger than the value of  $A_L$  observed for the other tissue types at that same wavelength,  $A_L$  being largest for type V lesions. For these lesions, fractional amplitude  $A_L$  returned to the level observed in normal tissue for wavelengths between 420 and 465 nm. Parameter  $A_L$  decreased in the 470 – 490 nm range in comparison to its midrange values.

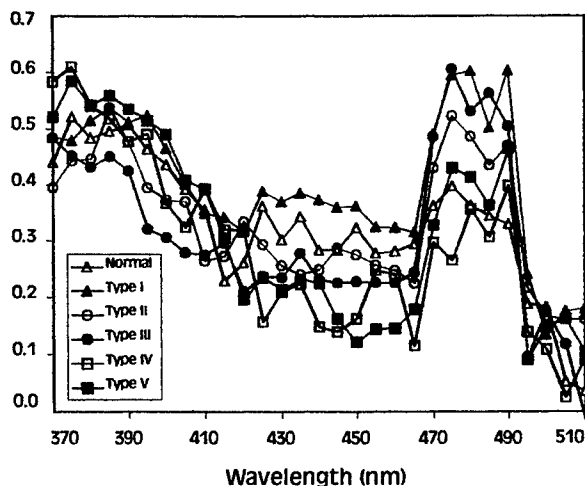


Fig 7a: fractional amplitude – intermediate decay term

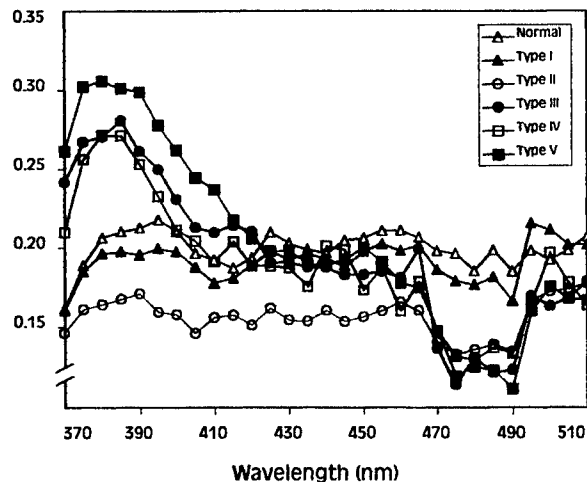


Fig 7b: fractional amplitude - long decay term

#### 4. DISCUSSION

This study shows that global analysis markedly improves the estimation of multiexponential decay characteristics of time-resolved fluorescence emission spectra. We found using simulated data that estimation of the model order was more robust and the parameter values were more accurately retrieved when global analysis was used as opposed to the traditional approximation procedure (one wavelength at a time). Application of global analysis to estimate decay parameters of artery fluorescence spectra allowed us to recover three individual decay terms in the fluorescence impulse response function. The decay constants and the pre-exponential terms varied characteristically with the progression of atherosclerosis.

Multiexponential approximations have been used by ourselves<sup>8,9,10,14</sup> and several other groups<sup>5,6,7</sup> to approximate the time-dependent decay of fluorescence of arterial fluorophores and tissue samples. To the best of our knowledge, the present study is the first in which a global analysis approach was used to estimate the parameters of the exponential approximation. Global analysis methods take advantage of the relationships that exist between fluorescence decay curves measured for different values of a parameter (in our case, the emission wavelength). These methods have been shown to greatly increase the accuracy of the recovered decay constants and pre-exponential amplitudes<sup>11</sup>. In the present study, the simulated data were sampled at the same rate as the time-resolved fluorescence spectra of artery tissue measured with our experimental setup. The decay constants of the simulated data were in the range expected from previous studies of arterial fluorophores and tissue samples. The simulations showed that global analysis was superior to the traditional fitting methods in terms of correctly estimating the approximation order and in terms of assigning values to the parameters of the exponential fit.

For complex systems like the arterial wall, the decay constants of the exponential approximation are usually not interpretable in terms of individual fluorophores but mainly serve to represent different trends in the decay<sup>16</sup>. In that sense, traditional fitting methods may suffice to characterize changes in the fluorescence decay trend that accompany a disease process like atherosclerosis. However, when one attempts to identify the fluorescence signatures of potential fluorescing species in a sample, the simulations show that there is advantage in using the information contained in the whole two-dimensional time-resolved spectrum all at once. Thus, global analysis should allow for a more precise detection of the response of fluorescing species like elastin, lipids, and collagen in the time-resolved emission spectra of artery tissue.

Andersson-Engels and colleagues<sup>5</sup> used a picosecond excitation system at 337 nm to evaluate the fluorescence decay characteristics of aortic and coronary samples at 380, 437, and 480 nm. Normal arterial wall and samples with thin or thick fibrotic plaque (type IV and type V lesions) were examined. These authors found as we did three exponential components in the fluorescence decays of normal arterial tissue and atherosclerotic

lesions. The decay constants they found at 380 nm for normal samples ( $\tau_s = 0.2$  ns,  $\tau_1 = 1.7$  ns,  $\tau_L = 6.0$  ns) and for thick fibrous lesions ( $\tau_s = 0.4$  ns,  $\tau_1 = 2.5$  ns,  $\tau_L = 7.5$  ns) were comparable to the decay constants found in our data. In their study however, the decay constants varied with wavelength such that the values at 480 nm for normal samples ( $\tau_s = 0.4$  ns,  $\tau_1 = 2.4$  ns,  $\tau_L = 8.5$  ns) and fibrous lesions ( $\tau_s = 0.4$  ns,  $\tau_1 = 2.4$  ns,  $\tau_L = 8.7$  ns) were not different. The fractional amplitudes were also not different in the red range of the spectrum between normal arterial wall and fibrous lesions. In our study, the largest difference for the fractional amplitudes was found to exist in the blue range of the spectrum with only small differences in the red range of the spectrum. The higher variability of the estimated parameters that is intrinsic to traditional fitting methods could be a disadvantage for detecting small fluorescence decay differences between different tissue types.

In conclusion, we showed that global analysis was superior to traditional fitting methods for the recovery of exponential decay trends in simulated time-resolved fluorescence spectra of artery tissue. Characteristic changes in exponential decay parameters derived from the time-resolved spectra were related to the type of atherosclerotic lesion assigned to aortic samples by histology.

## 5. ACKNOWLEDGEMENTS

This work was supported in part by the American Heart Association, Greater Los Angeles Affiliate (#1082-GI), the Powell Foundation, and the Medallions Group, Cedars Sinai Medical Center.

## 6. REFERENCES

1. Laifer LI, O'Brien KM, Stetz ML, Gindi GR, Garrand TJ, Deckelbaum LI. "Biochemical basis for the difference between normal and atherosclerotic arterial fluorescence". *Circulation* **80**:1893-1901, 1989.
2. Yan WD, Perk M, Chapgar A, Wen Y, Stratoff S, Schneider WJ, Jugdutt BI, Tulip J, Lucas A. "Laser-induced fluorescence: III. quantitative analysis of atherosclerotic plaque content". *Lasers Surg. Med.* **16**:164-178, 1995.
3. Morguet AJ, Gabriel RE, Buchwald AB, Werner GS, Nyga R, Kreuzer H. "Single-laser approach for fluorescence guidance of excimer laser angioplasty at 308 nm: evaluation in vitro and during coronary angioplasty". *Lasers Surg. Med.* **20**:382-393, 1997.
4. Baraga JJ, Taroni P, Park YD, An K, Maestri A, Tong LL, Rava RP, Kittrell C, Dasari RR, Feld MS. "Ultraviolet laser induced fluorescence of human aorta". *Spectrochim. Acta A* **45**:95-99, 1989.
5. Andersson-Engels S, Johansson J, Svanberg S. "The use of time-resolved fluorescence for diagnosis of atherosclerotic plaque and malignant tumours". *Spectrochim. Acta A* **46**:1203-1210, 1990.
6. Andersson-Engels S, Johansson J, Svanberg K, and S. Svanberg S. "Fluorescence imaging and point measurements of tissue: applications to the demarcation of malignant tumors and atherosclerotic lesions from normal tissue". *Photochem. Photobiol.* **53**:807-814, 1991.
7. Andersson-Engels S, Baert L, Berg R, D'Hallewin MA, Johansson J, Stenram U, Svanberg K and Svanberg S. "Fluorescence characteristics of atherosclerotic plaque and malignant tumors". *SPIE* **1426**:31-43, 1991.
8. Maarek JM, Marcu L, Grundfest WS. "Characterization of atherosclerotic lesions with laser-induced time resolved fluorescence spectroscopy". *SPIE* **3250**:181-189, 1998.
9. Maarek JM, Marcu L, Grundfest WS, Fishbein M. "Classification of aortic atherosclerotic lesions with time-resolved fluorescence spectroscopy". *SPIE* **3600**, 192-200, 1999.
10. Marcu L, Maarek JM, Fishbein M, Grundfest WS. "Atherosclerotic lesions classification by time-resolved laser induced fluorescence spectroscopy: clinical identification of lipid-rich lesions". *J. Am. Coll. Cardiol.* **33**:66A, 1999.
11. Knutson JR, Beechem JM, Brand L. "Simultaneous analysis of multiple fluorescence decay curves: a global approach". *Chem. Phys. Lett.* **102**:501-507, 1983.
12. Stary HC, Chandler AB, Glagov S, Guyton JR, Insull W Jr, Rosenfeld ME, Schaffer SA, Schwartz CJ, Wagner WD, Wissler RW. "A definition of initial, fatty streak, and intermediate lesions of atherosclerosis". *Arterioscler. Thromb.* **14**:840-856, 1994.
13. Stary HC, Chandler AB, Dinsmore RE, Fuster V, Glagov S, Insull W Jr, Rosenfeld ME, Schwartz CJ, Wagner WD, Wissler RW. "A definition of advanced types of atherosclerotic lesions and a histological classification of atherosclerosis". *Arterioscler. Thromb. Vasc. Biol.* **15**:1512-1531, 1995.

14. Maarek JM, Snyder WJ, Grundfest WS. "Time-resolved laser-induced fluorescence of arterial wall constituents: deconvolution algorithm and spectro-temporal characteristics". SPIE **2980**:278-285, 1997.
15. Landaw EM, DiStefano III JJ. "Multiexponential, multicompartamental, and noncompartmental modeling. II. Data analysis and statistical consideration". Am. J. Physiol. **246**, R665-R677, 1984.
16. Lakowicz JR. *Principles of Fluorescence Spectroscopy*, 51-91, Plenum Press, New York, 1983.

# Optical biopsy with long-range nondiffracting beams

Ervin Goldfain

Welch Allyn Inc, Skaneateles Falls, NY 13153

## ABSTRACT

Most current configurations for optical biopsy contain fiber optic bundles at both the delivery and receiving ends of the optical system. Some layouts include distal lenses to either collimate or focus the incident light at various depth locations across the tissue. The inherent beam divergence, along with the highly scattering nature of the living tissue, are known to limit the penetration depth of the probe and the spatial or temporal resolution of the detected signal.

In this work we study a novel modality for tissue illumination based on the use of long-range nondiffracting beams (LRNB). LRNB represent narrow-width light pencils with a constant or linearly varying axial intensity that propagate over large distances without diffractive spreading. Recent tests have demonstrated that LRNB exhibit insignificant intensity distortions when operated as beacon beams through atmospheric turbulence. Our numerical and software simulations show that LRNB may offer the potential for larger penetration depth and enhanced contrast over setups using conventional laser beams. Clinical applications include diagnosis, laser surgery and photodynamic therapy.

**Keywords:** optical biopsy, tissue imaging, biomedical spectroscopy, nondiffracting beams, Bessel beams, axicon.

## 1. INTRODUCTION

Standard beam delivery systems for optical biopsy are based upon fiber optic bundles or optical components such as conventional lenses or light concentrators. The probing beam is either collimated or focused on various depth locations inside the tissue volume. It is well known that the inherent beam divergence, along with the occurrence of multiple photon scattering and absorption events inside the tissue, degrade the spatial and temporal resolution of the detected signal.

A number of approaches have been introduced to offset this challenge, including confocal imaging and spectroscopy,<sup>1,2</sup> phase-shift detection,<sup>3,4</sup> and time-gated techniques using low-coherence interferometry<sup>5-9</sup>.

The main drawback of these approaches is that, for thick tissue, a vast majority of transmitted photons is discarded and the scarcity of detected light with the shortest propagation length limits the achievable gain in resolution<sup>10,11</sup>. For instance, time-gated mammography generally fails to distinguish an inhomogeneity smaller than approx. 10 mm., which falls short of the resolution required for a routine screening of breast disease<sup>10</sup>. In thick tissue, an ultrashort pulse will typically broaden by many orders of magnitude during a detection time window comparable to the duration of the probing pulse<sup>11</sup>.

We report in this work a novel strategy for tissue illumination based on the use of long-range nondiffracting beams (LRNB). LRNB are produced by using several techniques<sup>12,13</sup> such as placing an annular ring in the focal plane of a well corrected lens, via phase filters, refractive or holographic axicons, or spherically aberrated optical systems. Recent experiments have demonstrated that LRNB exhibit minor intensity distortions when used as beacon beams through atmospheric turbulence<sup>14</sup>. It is worth mentioning here that acoustic nondiffracting beams have been studied in conjunction with 2D and 3D ultrasound imaging<sup>15</sup>.

The paper is organized as follows: the first section briefly describes the theory underlying LRNB, the second section deals with a numerical comparison between conventional and LRNB excitation modes as applied to the steady-state fluorescence spectroscopy of thick tissue. The third section reports results of a Monte Carlo simulation comparing time-gated imaging under conventional and LRNB illumination. Conclusions and future challenges are outlined in the last section.

## 2. OPTICAL DESCRIPTION OF THE NONDIFFRACTING BEAM

The nondiffracting beam belongs to a class of solutions of the wave equation which are invariant with respect to diffraction from one plane of propagation to the next. The simplest nontrivial example of a nondiffracting beam is the zero-order Bessel wave<sup>16</sup>:

$$E(x, y, z, t) = E_0 \cdot J_0(\alpha \cdot \rho) \cdot \exp[-i \cdot (\omega \cdot t - \beta \cdot z)] \quad (1)$$

in which :

$$0 \leq \alpha \leq \left( \frac{2 \cdot \pi}{\lambda} \right) \quad (2)$$

$$\rho^2 = x^2 + y^2$$

with "x,y" denoting beam coordinates in a plane normal to the propagation direction "z", "λ" being the wavelength, "t" the time, "ω" the angular frequency, "E<sub>0</sub>" the electric field amplitude and J<sub>0</sub> the zero-order Bessel function. The beam parameter "β" satisfies the relationship:

$$\beta^2 = \left( \frac{2 \cdot \pi}{\lambda} \right)^2 - \alpha^2 \quad (3)$$

Fig.1 shows the plot of the Bessel beam in the (x,y) plane. The central peak has a width proportional to "α" and is generally surrounded by several concentric rings that may be suppressed by truncating the beam with annular stops<sup>17</sup>.

It can be shown that, if the beam is generated through apertures with custom transmission functions<sup>18,19,20</sup>, the axial beam intensity becomes linearly dependent on the propagation distance according to:

$$I(x, y, z) = I_0 \cdot (a + b \cdot z) \cdot [J_0(\alpha \cdot \rho)]^2 \quad (4)$$

in which:

$$I(x, y, z) = (|E(x, y, z, t)|)^2 \quad (5)$$

$$I_0 = (E_0)^2$$

and where the real coefficients "a" and "b" satisfy the condition:

$$a + b \cdot z > 0 \quad (6)$$

The range over which the axial beam intensity yields a uniform or a linearly varying profile follows the construction of the beam forming optics. Controlling the amount of spherical aberration introduced by the lens system or the cone angle of the linear axicon are typical examples of how a desired distance range may be achieved in practice<sup>20,21</sup>.

### 3. SIMULATION RESULTS

#### 3.1 Steady-state fluorescence spectroscopy in thick tissue

In this section we perform numerical evaluations of the fluorescent signal emitted by a generic fluorophore source under steady-state conventional (Gaussian beam) and LRNB excitation. It is assumed that the fluorophore is deeply buried in an isotropic semi-infinite slab of homogeneous tissue which can be modeled as a highly scattering medium. To make the comparison relevant, it is assumed that both conventional and LRNB ballistic components of the excitation light are focused on the fluorophore at depth ( $-z_f$ ) and that both focal spots are subjected to the same average intensity (measured in flux per unit area).

Referring to fig. 2 and taking into account (4), the intensity distribution for the ballistic component of the excitation light attenuated by scattering and absorption losses is described by<sup>22</sup>:

$$I(\rho, z)_G = I_{0,G} \cdot \left[ \frac{w_0(z_0)}{w(z)} \right]^2 \cdot \exp \left[ -2 \cdot \left( \frac{\rho}{w(z)} \right)^2 \right] \cdot \exp[-\mu_t \cdot (z + z_f)] \quad (\text{Gaussian beam}) \quad (7)$$

$$I(\rho, z)_{\text{LRNB}} = I_{0,\text{LRNB}} \cdot [a + b \cdot (z + z_f)] \cdot [J_0(\alpha \cdot \rho)]^2 \cdot \exp[-\mu_t \cdot (z + z_f)] \quad (\text{LRNB})$$

In the above  $w_0(z_0)$  stands for the Gaussian beam waist at the depth of focus " $z_0$ ":

$$w_0(z_0) = \sqrt{\frac{\lambda \cdot z_0}{\pi}} \quad (8)$$

$w(z)$  is the waist at any arbitrary depth " $z$ ":

$$w(z) = w_0(z_0) \cdot \sqrt{1 + \left( \frac{z}{z_0} \right)^2} \quad (9)$$

and " $\mu_t$ " is the total transport coefficient. Setting equal average intensity of the focal spot for both ballistic modes amounts to integrating (7) over the radial coordinate  $\rho$  and dividing by the linear extent of the focal spot, that is:

$$\frac{\int_0^{\rho_0} I(\rho, 0)_{\text{LRNB}} d\rho}{\rho_0} = \frac{\int_0^{w_0(z_0)} I(\rho, 0)_G d\rho}{w_0(z_0)} \quad (10)$$

in which the integrated intensity is carried out at  $z = 0$  and  $\rho_0$  represents the effective radius of the LRNB focal spot. In the framework of diffusion theory it can be shown that the beam intensity at depth  $(-z_f)$  may be expressed as<sup>23</sup>:

$$I(-z_f) = I_s \cdot K(-z_f) \quad (11)$$

where  $I_s$  is the beam intensity on the tissue surface and  $K(-z_f)$  is a depth-dependent function. For a given excitation beam intensity, the local fluorescence emission rate is represented by the product:

$$f(-z_f) = \gamma \cdot I(-z_f) \cdot \mu_{a,f,\lambda}(-z_f) \quad (12)$$

with  $\gamma$  denoting the quantum fluorescence yield and  $\mu_{a,f,\lambda}(-z_f)$  the fluorophore absorption coefficient for the excitation wavelength  $\lambda$ . Combining the above, the fluorescent signal reaching the tissue surface takes the form<sup>23</sup>:

$$F(0) = \int_0^\infty E(0, -z_f) \cdot f(-z_f) dz_f = \gamma \cdot I_s \cdot \int_0^\infty E(0, -z_f) \cdot K(-z_f) \cdot \mu_{a,f,\lambda}(-z_f) dz_f \quad (13)$$

where  $E(0, -z_f)$  is the total intensity that reaches a single point on the tissue surface. This quantity depends on fluorophore location and on the optical properties of the tissue. Let "g" denote the ratio of the fluorescent signal produced under LRNB excitation to the one produced by Gaussian excitation. From (7) and (13) it follows that:

$$g = \frac{F_{LRNB}(0)}{F_G(0)} = \frac{I_{s, LRNB}}{I_{s, G}} = \frac{I_{0, LRNB} \cdot a \cdot [J_0(\alpha \cdot \rho)]^2}{I_{0, G} \cdot \left[ \frac{w_0(z_0)}{w(z_f)} \right]^2 \cdot \exp \left[ -2 \cdot \left( \frac{\rho}{w(z_f)} \right)^2 \right]} \quad (14)$$

Fig. 3 represents plots of the gain "g" versus fluorophore depth "zf" ( in absolute value ) corresponding to the following choice of constructive parameters ( $\lambda = 920$  nm,  $I_{0, LRNB} = I_{0, G} = a = 1$ ) :

$\alpha_1 = 18.781 \text{ mm}^{-1}$	$w_{0,1} = .125 \text{ mm}$	$\rho_{0,1} = .100 \text{ mm}$
$\alpha_2 = 15.026 \text{ mm}^{-1}$	$w_{0,2} = .150 \text{ mm}$	$\rho_{0,2} = .125 \text{ mm}$
$\alpha_3 = 12.526 \text{ mm}^{-1}$	$w_{0,3} = .180 \text{ mm}$	$\rho_{0,3} = .150 \text{ mm}$



The graph indicates that , for a given fluorophore depth, the gain "g" scales up with the reduction in the focal spot size " $\rho_0$ ". This may be an attractive alternative for the spectroscopy of deeply buried small-size fluorophores, which may otherwise be inaccessible with conventional pencil-like beams.

### 3.2 Time-gated imaging through thick tissue

#### 3.2.1 Comparison of the depth-dependent intensity distributions

In this section we use (7) to study an example of time-gated imaging through thick tissue. Assuming that both the diffusive and the snake components of the illumination beam are rejected via time-gating, we again set the focal spot intensity to be equal on average for the ballistic component, according to (10). In addition, we assume that both beams are being focused halfway through tissue thickness and have a comparable spot diameter. This additional assumption puts the Gaussian and the LRNB modes on equal footing insofar as the ability to generate a resolvable transmitted signal or an acceptable imaging contrast.

Figs. 4 and 5 show the 3D intensity plots corresponding to the ballistic components of the LRNB and Gaussian modes at the focal spot ( $z = 0$ ) and deeper depth locations ( $z > 0$ ). The vertical axis indicates intensity, the horizontal axis contained in the intensity cross section denotes the radial coordinate ( $\rho$ ) and the third axis corresponds to the depth coordinate ( $z$ ). The inhomogeneity is buried at  $z_i = 50$  mm below the tissue surface. Note that all units have been normalized to a set of arbitrary values. The parameters of this numerical simulation are chosen as follows:

$$\begin{array}{ll} \lambda = 920 \text{ nm} & w_0 = .125 \text{ mm} \\ I_{0,\text{LRNB}} = I_{0,\text{G}} = 1 & \rho_0 = .100 \text{ mm} \\ a = 0, b = .02 \text{ mm}^{-1} & \mu_t = 1.04 \text{ mm}^{-1} \\ \alpha = 18.781 \text{ mm}^{-1} & z_i = 50 \text{ mm} \end{array}$$

#### 3.2.2 Monte Carlo raytracing

In this section we show comparative results of a statistical raytracing simulation of time-gated imaging through thick tissue (fig. 6). Using a commercially available software package, a large number of raypaths ( $2 \cdot 10^6$ ) is randomly traced through a stack of two diffusing layers with a fully absorbing inhomogeneity embedded at half of the overall thickness. The Gaussian beam is delivered through a planoconvex lens and the nondiffracting beam is generated using a refractive axicon . The comparison between the two illumination modes is based upon the contrast function, which is defined as:

$$C(\%) = \frac{I_{\max} - I_{\min}}{I_{\max}} \cdot 100 \quad (15)$$

in which  $I_{\max}$  and  $I_{\min}$  stand for the maximum and minimum peaks of the detected intensity distribution. As before, we rely on the assumption that time-gating is fully efficient in the sense that only the ballistic component survives detection. The focal spot intensity and size are set equal for both illumination modes. The inhomogeneity diameter is denoted by "d" and the thickness of each layer by "t". The axicon profile is described by the linear function:

$$z = (-.003) \cdot r \quad (16)$$

where "z" and "r" are the axial and radial coordinates of the axicon surface. The rest of simulation parameters are as follows:

<u>input source</u> : step-index fiber optic, core diameter .500 mm	<u>operating wavelength</u> : $\lambda = 700$ nm
<u>illumination numerical aperture</u> : .25	<u>emitted flux</u> : 100 mW
<u>overall tissue thickness</u> : 100 mm (2.t)	<u>focal spot size</u> : 3 mm
<u>focal spot intensity</u> : .025 lumen/mm <sup>2</sup>	<u>total transport coefficient</u> ( $\mu_t$ ): 1.04 mm <sup>-1</sup>

#### 4. CONCLUSIONS

A side by side analysis of the Gaussian beam and LRNB illumination modes has been developed. Simulation results point out that LRNB may be superior in terms of penetration depth and signal contrast for the characterization and diagnosis of thick tissue. Additional modeling and experimental work are required to validate these preliminary findings. One is specifically interested in further exploration of clinical benefits, dynamic range, as well as potential limitations associated with the LRNB modality.

#### 5. REFERENCES

1. D. S. Dilworth, E. N. Leith and J. L. Lopez, "Imaging absorbing structures within thick diffusing media", *Appl. Opt.* **29**, 691-698 (1990).
2. D. S. Dilworth, E. N. Leith and J. L. Lopez, "Three-dimensional confocal imaging of objects embedded within thick diffusing media", *Appl. Opt.* **30**, 1796-1803 (1991).
3. M. S. Patterson, J. D. Moulton, B. C. Wilson, K. W. Berndt and J. R. Lakowicz, "Frequency-domain reflectance determination of the scattering and absorption properties of tissue", *Appl. Opt.* **30**, 4474-4476 (1991).
4. J. B. Fiskin and E. Gratton, "Propagation of photon-density waves in strongly scattering media containing an absorbing semi-infinite plane bounded by a straight line", *JOSA A* **10**, 127-140 (1993).
5. H. P. Chiang, W. S. Chang and J. Wang, "Imaging through random scattering media by using cw broadband interferometry", *Opt. Lett.* **18**, 546-548 (1993).
6. M. R. Hee, J. A. Izatt, J. M. Jacobson and J. G. Fujimoto, "Femtosecond transillumination optical coherence tomography", *Opt. Lett.* **18**, 950-952 (1993).
7. M. E. Brezinski *et al.*, "Optical Biopsy with Optical Coherence Tomography", *Advances in Optical Biopsy and Optical Mammography*, Annals of the New York Academy of Sciences, New York, vol. 838, 68-74 (1998).
8. J. G. Fujimoto *et al.*, "New Technology for High-Speed and High-Resolution Optical Coherence Tomography", *Advances in Optical Biopsy and Optical Mammography*, Annals of the New York Academy of Sciences, New York, vol. 838, 95-107 (1998).
9. B. E. Bouma *et al.*, "High-resolution optical coherence tomographic imaging using a mode-locked Ti:Al<sub>2</sub>O<sub>3</sub> laser source", *Opt. Lett.* **20**, 1486-1488 (1995).
10. J. C. Hebden and Simon R. Arridge, "Imaging through scattering media by the use of an analytical model of perturbation amplitudes in the time domain", *Appl. Opt.* **35**, 6788-6796 (1996).
11. J. C. Hebden, D. J. Hall, M. Firbank and D. T. Delpy, "Time-resolved optical imaging of a solid tissue-equivalent phantom" *Appl. Opt.* **34**, 8038-8047 (1995).
12. R. M. Herman and T. A. Wiggins, "Production and uses of diffractionless beams", *JOSA A* **8**, 932-942 (1991).
13. R. M. Herman and T. A. Wiggins, "High-efficiency diffractionless beams of constant size and intensity", *Appl. Opt.* **33**, 7297-7306 (1994).
14. T. Aruga *et al.*, "Nondiffracting narrow light beam with small atmospheric turbulence-influenced propagation", *Appl. Opt.* **38**, 3152-3156 (1999).
15. This reference is located at <www.ifi.uio.no/~fox/abstract.htm>.
16. W. Lauterborn, T. Kurz and M. Wiesenfeldt, "Coherent Optics", Springer-Verlag, Berlin Heidelberg, 24, (1995).
17. Z. Jaroszewicz, J. Sochacki, A. Kolodziejczyk and L. R. Staronski, "Apodized annular-aperture logarithmic axicon: smoothness and uniformity of intensity distributions", *Opt. Lett.* **18**, 1893-1895, (1993).

18. Z. Jiang, Q. Lu and Z. Liu, "Propagation of apertured Bessel beams", Appl. Opt. **34**, 7183-7185, (1995).
19. S. Y. Popov, A. T. Friberg, "Linear axicons in partially coherent light", Opt. Eng. **34**, 2567-2573, (1995).
20. R. M. Herman and T. A. Wiggins, "Apodization of diffractionless beams", Appl. Opt. **31**, 5913-5915, (1992).
21. T. Aruga and S. W. Li, "Super high resolution for long-range imaging", Appl. Opt. 2795-2799, (1999).
22. J. Ying, F. Liu and R. R. Alfano, "Spatial distribution of two-photon-excited fluorescence in scattering media", Appl. Opt. **38**, 224-229, (1999).
23. T. J. Farrel *et al.*, "Modeling of photosensitizer fluorescence emission and photobleaching for photodynamic therapy dosimetry", Appl. Opt. **37**, 7168-7183, (1998).

## 6. PLOTS

**FIG. 1**

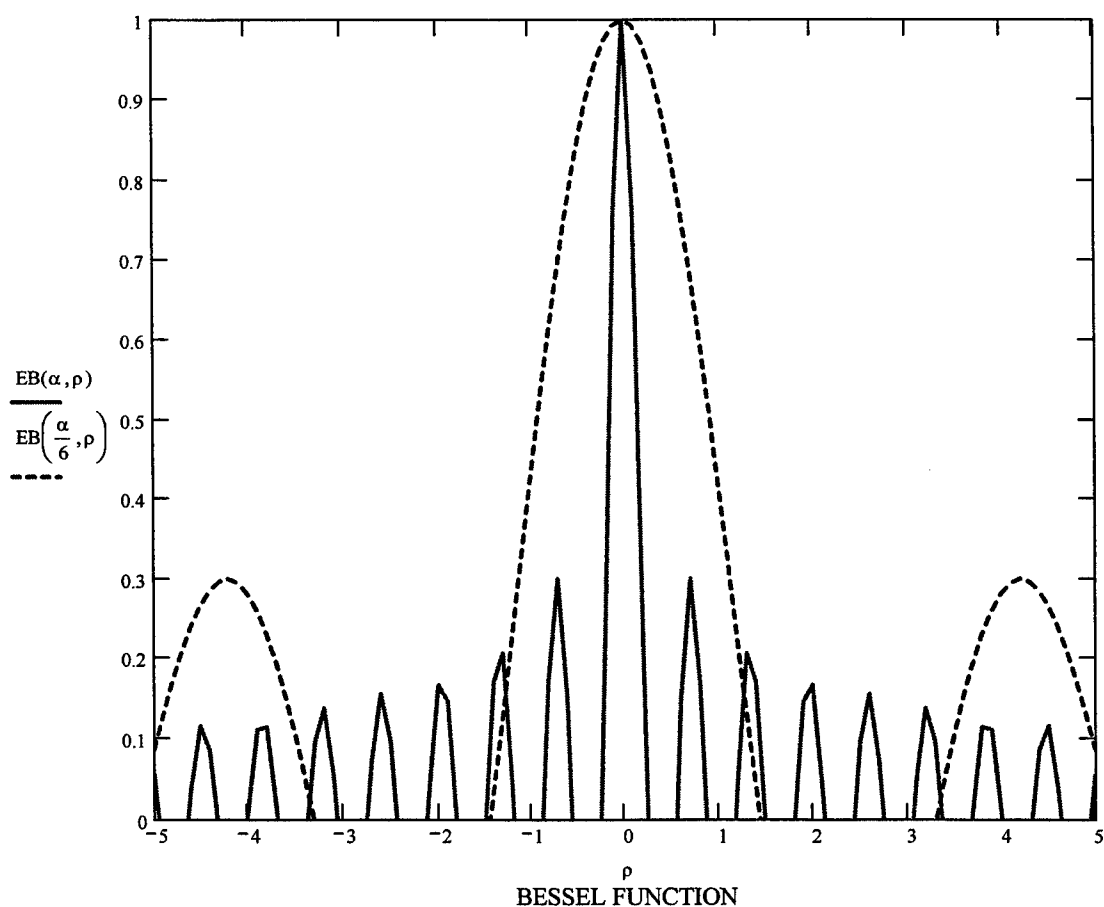


FIG. 2

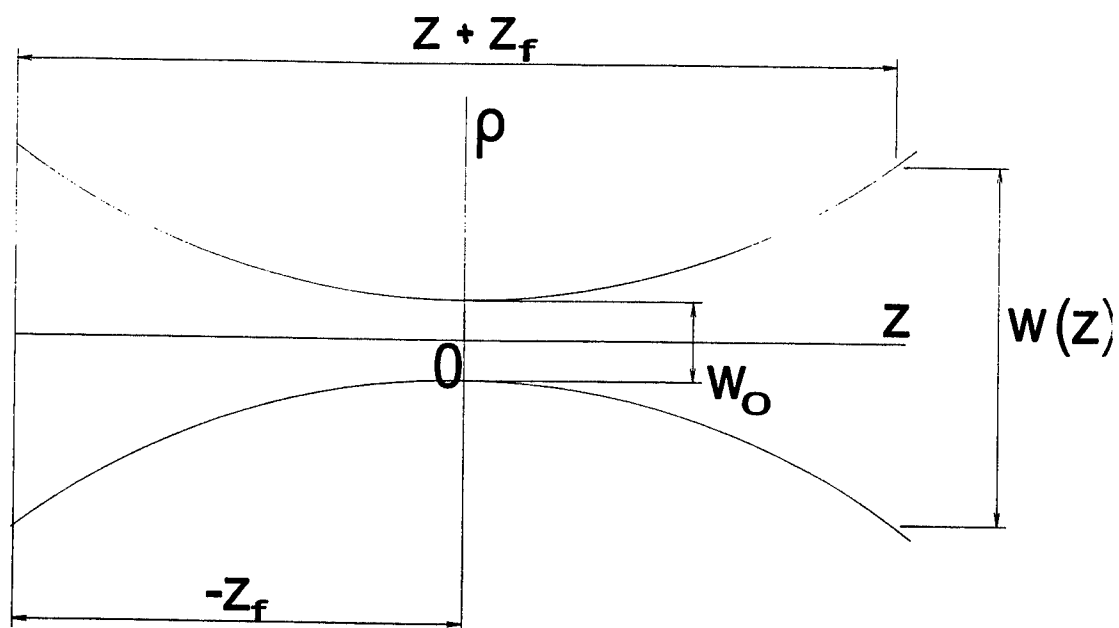


FIG. 3

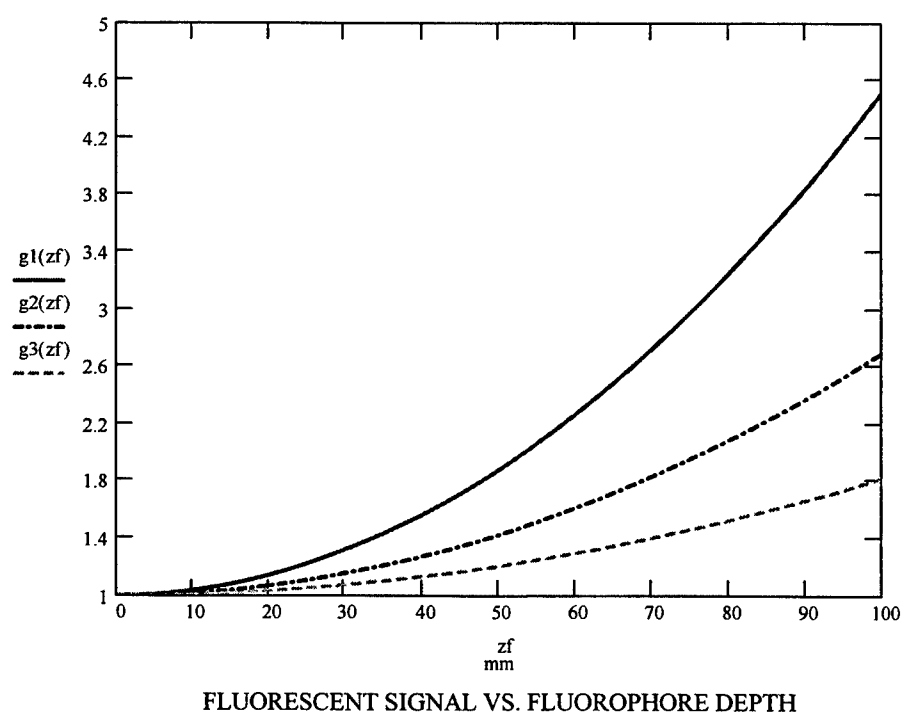


FIG. 4

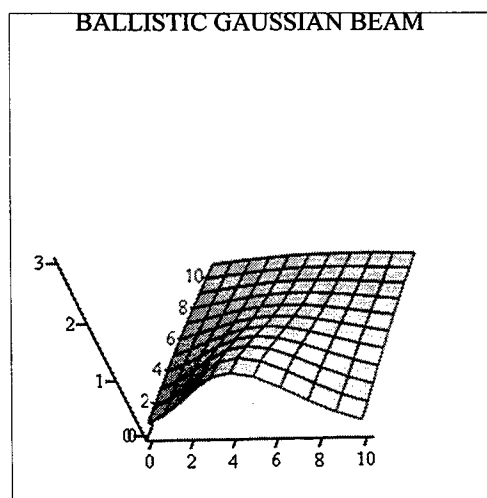


FIG. 5

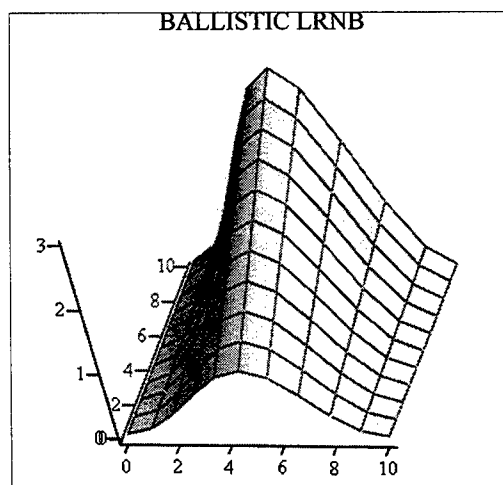
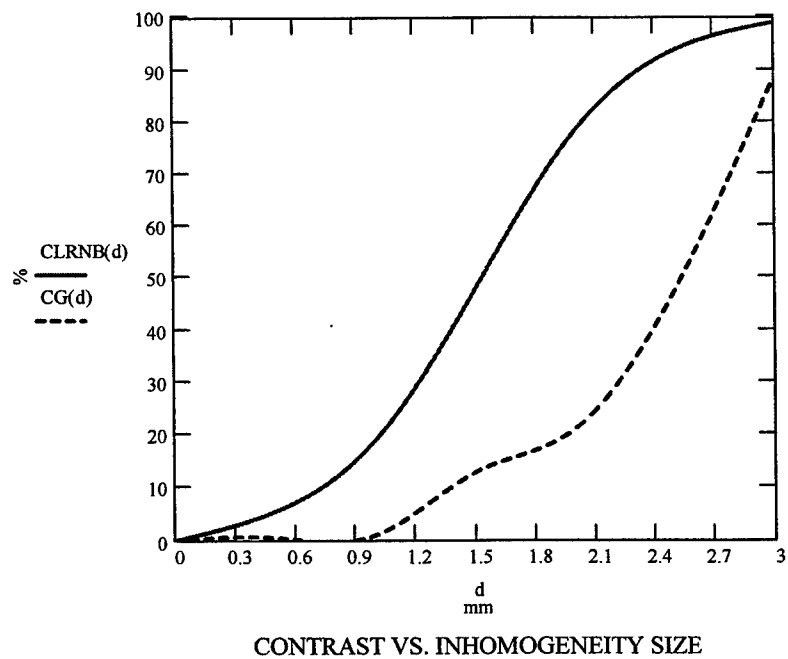


FIG. 6





## **SESSION 5**

### **Fluorescence Biopsy II**

# Blue LED's Feasibility for Tissue Fluorescence Analysis

Sergiy Dets<sup>a,b</sup>, Nikolay Denisov<sup>a</sup>

<sup>a</sup> Optical Engineering Department, National Technical University of Ukraine "KPI", Kyiv, Ukraine

<sup>b</sup> School of Engineering Science, Simon Fraser University, Burnaby, BC, Canada V5A 1S6

## ABSTRACT

We considered the limited number of light-induced fluorescence applications for marketed ultra-bright blue LED's where they can compete with versatile laser sources. Satisfactory optical output and miniature size as well as low power consumption of blue LED's emitting at 470 nm allow to consider them as a promising alternatives to metal vapor or gas lasers used in many express LIF applications. Available to authors LED's from Hewlett Packard, Micro Electronics Corp., Nichia Chemical Industries Ltd. and Toyoda Gosei Co. were tested to comply with demands to a tissue excitation source for portable spectrometers. The optical performance of LED's has shown that selected group of InGaN LED's could be successfully used for that. The miniature illuminator that includes LED, focusing condenser, filter set and distal fiberoptic light concentrator was designed and tested in conjunction with portable CCD-equipped spectrometer. Operating in dark condition the proposed LED illuminator provides the level of fluorescence signal sufficient to detect spectral abnormalities in human Caucasian skin and excised gastrointestinal samples. All tissue autofluorescence data taken under LED illumination were compared with readings under He-Cd laser excitation and showed a good match. A new diagnostic designs based on LED's were considered for clinical use.

**Keywords:** blue LED, light-induced fluorescence, light concentrator, tissue spectroscopy.

## 1. INTRODUCTION

The light-induced fluorescence spectroscopy (LIFS) for diagnostics of biological tissues has been well set up for several decades. In clinics the fluorescence microscopy and cytometry become routine procedures to characterize quantitatively the vast majority of human pathologies. Both non- and imaging fluorescence *in-vivo* oncological applications of LIFS have been proved to be helpful for detection of early-stage lesions when conventional diagnostic tools do not provide needed urgency and accuracy. Technique of *in vivo* fluorescence measurements usually operates by the optical contrast between normal and abnormal tissue areas, which is characterized by the shape of emission spectra, and often is expressed simply by an intensity ratio in red and green spectral regions (R/G ratio)<sup>1</sup>. And for some fluorescence diagnostic applications, where the detection procedure together with its quantitative expressions are quite developed (cutaneous malignancies, oral and lung cancers etc.), the pragmatic way to introduce the LIFS seems to ease the accessibility of LIF systems to practitioners. Technically, most non-imaging LIF measuring systems operating in cw or pulsed mode consist of a bright excitation light source, focusing system, optical filters, fiberoptic delivery/collecting system, and focusing lens coupled optically with detector of spectroanalyzer. Such opto-electronic systems, especially those aimed for *in vivo* express-analysis and using simple algorithm, frequently have inadequate "price/efficiency" proportion which do not allow them out of research laboratories. The significant progress was made here by the introduction of miniature PC plug-in CCD-spectrometers, which clinically are easy to operate in combination with various fiberoptic probes. Meantime, the dimensions of traditional fluorescence excitation light sources such as filtered Hg arc lamps, different types of lasers: Ar<sup>+</sup>-, He-Cd-, Kr<sup>+</sup>-, N<sub>2</sub>-, excimer- or dye lasers etc. basically do confine the creation of miniature handheld LIF system for *in-vivo* express operation.

Recent achievements in photonics technology *viz.* development of InGaN violet laser diode (NLHV500A from Nichia Chemical Industries<sup>2</sup>) and InGaN light-emitted diodes (LED's) irradiating in blue region of optical spectrum has enabled to introduce them in designing of small-size LIF systems. The advantage given by laser diode module to LIF system is smaller dimensions ( $\varnothing 44.5\text{mm} \times 222\text{mm}^3$ ,  $\varnothing 38\text{mm} \times 144\text{mm}^4$ ) and output power of 4-5 mW at blue wavelength region about 405 nm. While the available on market blue LED's are characterized by lower output in broader spectral range compare to lasers, which happens to be a crucial drawback for fluorescence applications involving strong absorbing tissues, besides they still possess miniature size, reliability and very competitive price. There is a successful introduction of blue LED light source engineered by Ocean Optics Inc., USA for fluorescence measurements of liquids *via* optical fibers<sup>5</sup>.

In this study we analyze optical characteristics of currently available powerful blue LED sources, consider the design of output optics to develop small and compact LED illumination module enable to perform basic point LIF measurements on



tissue in conjunction with portable fiberoptic spectrometer. The results of LED-induced fluorescence of different human tissues were compared with data collected during laser-induced fluorescence measurements.

## 2. ASPECTS OF OPTICAL DESIGN

### 1. Blue LED's

Most blue LED's are available in clear lamp type packages with diameter of 3mm or 5mm incorporating aspherical focusing optics to form sharp spatial radiation pattern. The basic properties of blue LED, that make it applicable to compact LIF system are high output power, both narrow radiation directivity and bandwidth at half peak emission. As high optical output and directivity are important for efficient fluorescence excitation through fiberoptic probes, the narrow bandwidth at short wavelength spectral region defines the region of tissue fluorescence observation and subsequent diagnostic algorithm. Thus, spectrally, a "good" blue LED's one would expect among GaN/SiC emitters that provide spectral maximum at 430 nm. However, these widely available LED's (*e.g.* CB290 Super Blue LED from Cree Research, Bright Blue LED #276-311 from Radioshack™, LB 5416 from Siemens Microelectronics etc.) look obsolete in contest of LIF tissue measurements as their radiant flux are far less the necessary power output. The second generation of LED based on InGaN chips emitting about 470 nm with much higher intensities was selected for further optical testing. We measured spatial directivity and optical power of several samples of the most powerful 5mm- LED's available from four suppliers: MBB51TAH-T of Micro Electronics Corp., HLMP-CB15 of Hewlett Packard (both USA), E1L51-3B and NSPB500XS of Toyoda Gosey Co. and Nichia Chemical Industries (both Japan), respectively. All LED's were connected through ballast resistor of 200 Ohm and DC powered as recommended by supplier (3.5-4.0V, 20-30 mA, NB: Surprisingly, pulse operation of blue LED's did not lead to important output gain). Goniometrically measured angular distribution of blue light from above blue LED's have given  $2\theta = 30 \pm 5^\circ$  in accordance with manufacturer data. Measurements of LED's optical power performed by calibrated power meter (Newport, USA) both have indicated some discrepancy of measured characteristics vs. ones specified by manufacturer (Cf. second column in Table 1). From above experiment NSPB500XS and E1L51-3B LED's showed the most powerful optical output of 1.57 and 1.35 mW, respectively. Besides, these two LED's proved much better flux stability compare to MBB51TAH-T and HLMP-CB15 group, which is expressed by standard deviation in Table 2:

Table 2.

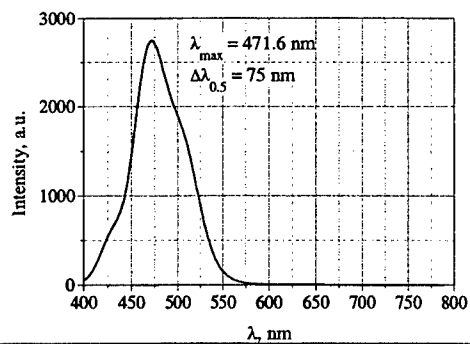
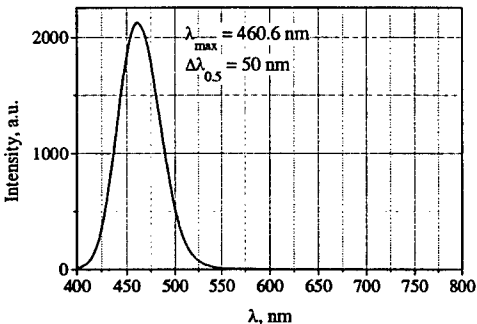
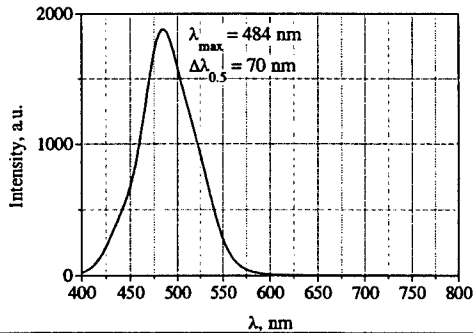
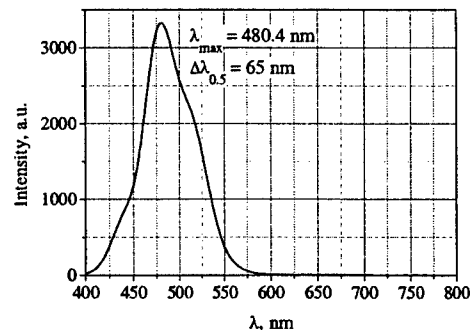
LED, number of samples n	Standard deviation of optical power, mW
MBB51TAH-T, n=3 pcs.	0.234
E1L51-3B, n=3 pcs.	0.007
HLMP-CB15, n=5 pcs.	0.041
NSPB500XS, n=3 pcs.	0.007

Measurements of spectral characteristics performed by fiberoptic spectrometer S2000 (Ocean Optics, USA) showed substantial emission maximum variance among all LED samples, which is illustrated by typical spectral graphs in Table 1 (Note: graphs are not reciprocally scaled along their intensity axis). As one can see, in disagreement with expected emission peak at  $\lambda_{\max} = 470$  nm all available LED's of type E1L51-3B gave peaks around  $\lambda_{\max} = 460$  nm with halfwidth  $\Delta\lambda_{0.5}$  of 50 nm, which made this powerful LED a reasonable choice to be a tissue excitation source.

### 2. Optical filtration of LED emitting light

Transmission characteristics of cut-off optical filters in excitation and collecting channels of LIF system, respectively, where defined by the limitation of spectral region of tissue registration of fluorescence to 530-700 nm. Therefore, in collecting channel we used orange cut-off glass filter OG530 (Schott, USA) as it has  $\tau_\lambda = 80\%$  transmission in fluorescence zone and sharp front at 530 nm blocking blue spectral component. The corresponding shortwave pass filter was located in front of the LED and provided the high transmission ( $\tau_\lambda > 80\%$ ) of blue component as can be seen on spectrum graphs in Fig. 1.

Table 1.

LED, number of samples $n$	Mean measured optical power $P$ at the distance $L$	Spectral graph
MBB51TAH-T from Micro Electronics Corp. ( $n=3$ )	$L = 2 \text{ cm}: P = 1.122 \text{ mW}$ $L = 0 \text{ cm}: P = 1.850 \text{ mW}$	
E1L51-3B from Toyoda Gosey ( $n=3$ )	$L = 2 \text{ cm}: P = 1.340 \text{ mW}$ $L = 0 \text{ cm}: P = 1.870 \text{ mW}$	
HLMP-CB15 from Hewlett Packard ( $n=5$ )	$L = 2 \text{ cm}: P = 0.632 \text{ mW}$ $L = 0 \text{ cm}: P = 0.800 \text{ mW}$	
NSPB500XS from Nichia Chemical Industries ( $n=3$ )	$L = 2 \text{ cm}: P = 1.574 \text{ mW}$ $L = 0 \text{ cm}: P = 2.0 \text{ mW}$	

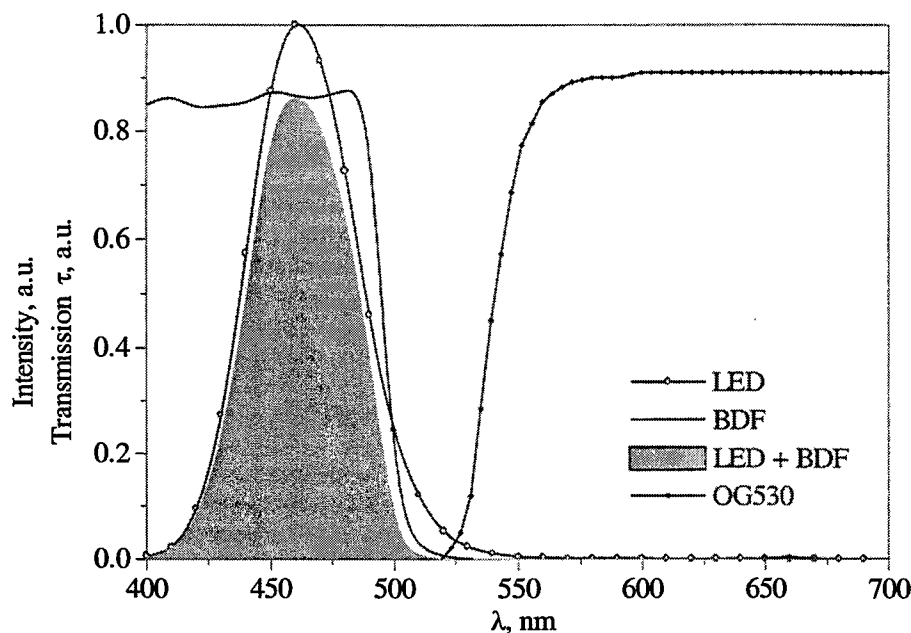


Fig.1. Spectral design of LIF system. Transformation of emission light of LED by blue dichroic filter (BDF) provides effective light use  $\eta_{\text{eff}}$  and blocks unnecessary green light component, whereas filter OG530 installed in receiving channel enables high transmission of fluorescence signal from tissue to spectrometer. Emission graphs are shown for E1L51-3B diode.

As good LIF system with LED source has to provide the optimal balance between energy delivered to tissue for excitation and possibly wider spectral region to enable R/G ratio algorithm, we estimated the effective light use  $\eta_{\text{eff}}$  for each LED type:

$$\eta_{\text{eff}} = \frac{\int I_{\lambda}^{\text{LED}} \cdot \tau_{\lambda} \cdot d\lambda}{\int I_{\lambda}^{\text{LED}} \cdot d\lambda} \cdot 100\%,$$

where  $\int I_{\lambda}^{\text{LED}} \cdot d\lambda$  and  $\int I_{\lambda}^{\text{LED}} \cdot \tau_{\lambda} \cdot d\lambda$  are integral values of LED intensity, respectively, before and after BDF was inserted.

Resulting data for LED's and BDF with transmission curve  $\tau_{\lambda}$  from Fig. 1 are collected in Table 3.

Table 3.

LED	$\eta_{\text{eff}}, \%$
E1L51-3B	83
MBB51TAH-T	61
NSPB500XS	53
HLMP-CB15	42

Generalizing data in Tab.1 & 3 we chose E1L51-3B from Toyoda Gosey as a light source for further design of LIF system, for the reason that this LED combined with the BDF provides the best intensity output  $[P \times \eta_{\text{eff}}]/100\%$  e.g. providing more than 1 mW output at the distance of  $L = 2\text{cm}$ .

### 3. Opto-mechanical composition of LED illuminating module.

The technical realization of LED illuminator for compact LIF system has based on standard 5mm- or 3-mm (with LED holder) LED's incorporating aspherical lenses. For practical reasons the common way to include the excitation source in LIF system is optical coupling with bifurcated multifiber probe separating excitation and collecting channels of LIF system. The probe was built according to coaxial "1+7 fibers" scheme with one 400 $\mu$ m- illumination fiber (NA=0.22) surrounded by seven 300 $\mu$ m- silica fibers (NA=0.22). Having length of 1.5 m and outer diameter of 2.8 mm, the probe design makes it applicable for both external as well as internal tissue measurements performed through biopsy channels of standard endoscope. LED illuminator and entrance hole of portable spectrometer S2000 (Ocean Optics, USA) were coupled directly to correspondent fiber end equipped with SMA-905 connector. To couple LED and probe the condenser able to form a spot of 300  $\mu$ m in diameter at the proximal end of illumination fiber was developed. In effect, LED condenser consisted of three stock lenses (#32010, #31854 and #45082, Edmund Scientific<sup>6</sup>) arranged according to the scheme ()(|() (See Fig.2). Optical filtration of LED light is done by placing the miniature BDF at the entrance of the SMA-905 connector of the probe. Cut-off filter OG530 is positioned at another SMA-905 connector before entrance hole of spectroscope S2000. Complete design of LED illumination module provides the incorporation of battery power supply lasting for 6 h of continuous autonomous operation (See Fig. 3).

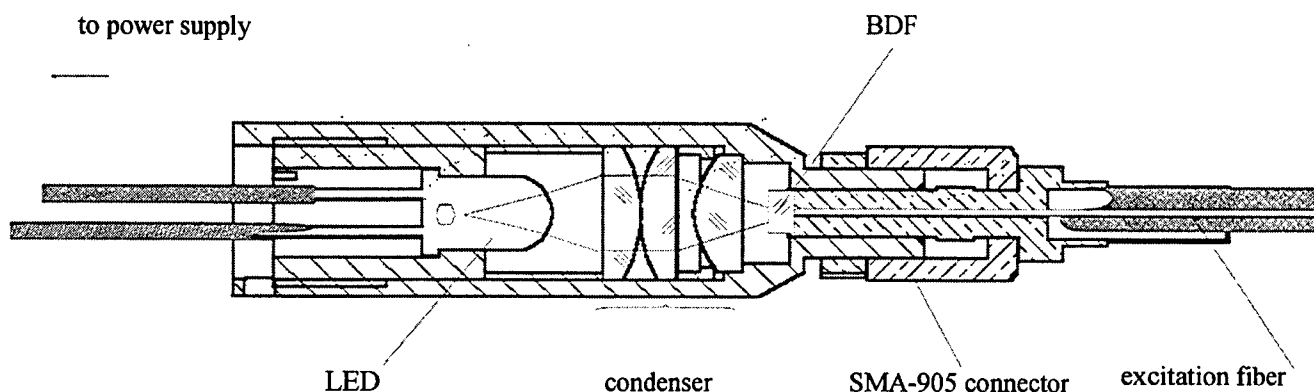


Fig. 2. Cross-section of LED illuminating module design.

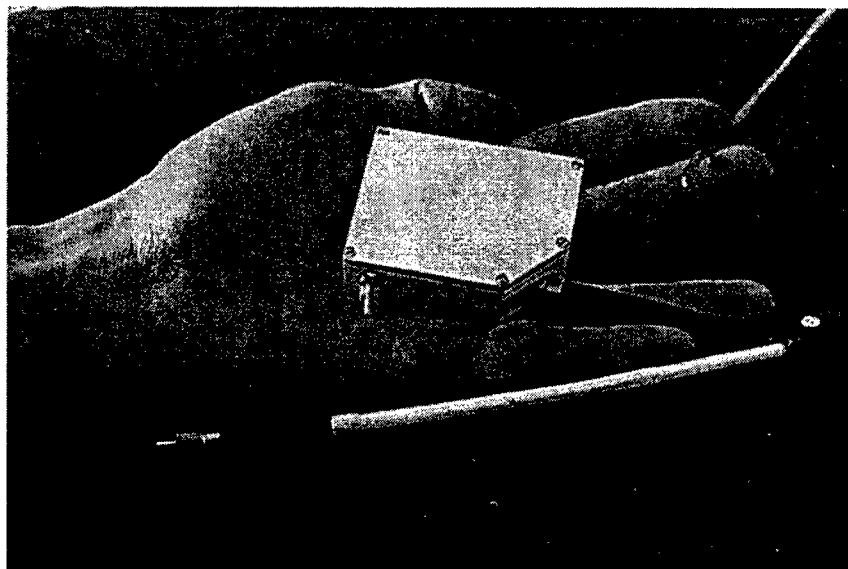


Fig. 3. Autonomous LED illuminating module for cutaneous fluorescence applications.

#### 4. Concentrating optics

To compensate Fresnel and transmission losses along the optical path from LED to tissue, which can exceed 35% of initial LED intensity and, simultaneously, to be able to provide the necessary power density at the tissue surface, the distal end of coaxial fiberoptic probe was equipped with a solid glass conical light concentrator. As shown in Fig. 4, the fiberoptic concentrator is operating in the direct contact with tissue to provide light collection from central excitation fiber of 400  $\mu\text{m}$  and illuminate tissue surface with higher power density, simultaneously gathering the fluorescence signal and coupling it to peripheral collecting zone of seven 300 $\mu\text{m}$ -fibers of the probe. Concentrator entrance spherical surface has the diameter of 2 mm and contact tip is 240  $\mu\text{m}$ . The efficiency of optical system of concentrator that consists of a monolithic glass cone having the excitation fiber at its focal plane, is estimated by two coefficients viz. sensor optical efficiency (SOE) and tip coupling efficiency (TCE) introduced elsewhere<sup>7</sup> as:

$$\begin{cases} \text{SOE} = \tau_T \cdot \tau_{fr} \cdot (k_\Sigma)^{FT} \cdot (k_\Sigma)^{TF} \\ \text{TCE} = \tau_{fr} \cdot (k_P)^{TF} / \tau_T \cdot (k_P)^{FT} \end{cases},$$

where  $\tau_T$  and  $\tau_{fr}$  are transmittance coefficients inside the probe into the direction of excitation and collecting, respectively;  $k_\Sigma$  – fiber-tissue (FT superscript) matching coefficient and  $k_P$  – packing coefficient in tissue-fiberoptic probe direction (TF). And for the conical light concentrator the power density gain on the tissue surface  $K_D$  can be expressed as:

$$K_D = \tau_T \cdot \left( \frac{R_{fe}}{R_t} \right)^2, \text{ see description to Fig. 4.}$$

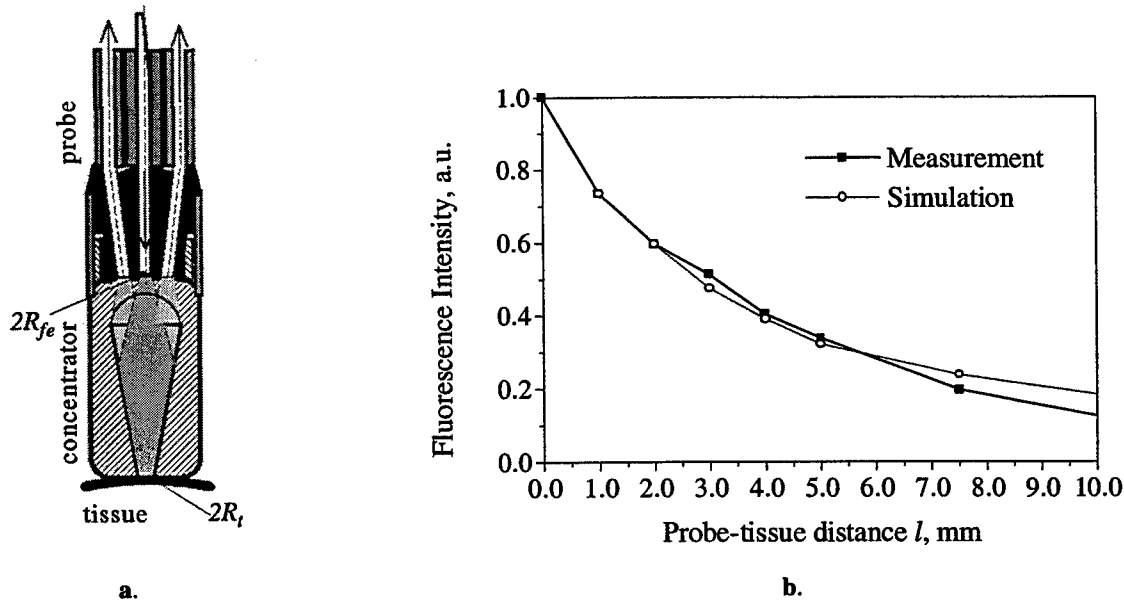


Fig. 4. Conical light concentrator is characterized by the diameter of contact tip  $2R_t$  and central fiber of excitation area  $2R_{fe}$  (a). Concentrator is optimized for the probe scheme of "1 exciting +7 collecting" fibers, and  $2R_t$  is equal to 240  $\mu\text{m}$ . The withdrawal of the concentrator tip from the tissue surface results in exponential ( $\sim e^{-l/4}$ ) decay of the fluorescence signal next to spectroscopy detector (b). Fluorescence measurements are conducted with above probe/concentrator configuration for normal stomach polyp (3x3x5mm) using He-Cd laser ( $\lambda = 442 \text{ nm}$ ,  $P = 15 \text{ mW}$ ) for excitation, whereas the simulated curve is the result of ray-tracing modeling of blue light and 560 nm-fluorescence under condition the latter has uniform angular distribution.

If supposed the fluorescence intensity is linearly proportional to power density on the tissue surface, the attachment of concentrator to probe gives the effect of power density rise presented in Table 4.

Table 4.

Coefficient	"1+7" probe	"1+7"probe with attached concentrator
$\tau_T$ , FT path	1.0*	0.6816
$\tau_{fr}$ , TF path	0.0840	0.2755
SOE	0.0403	0.0901
TCE	0.0630	0.3032
$K_D$	1.0*	1.8932

\*) arbitrary units

The lower transmittance  $\tau_T$  is resulting from Fresnel reflection losses at first optical surface of the concentrator, however, gathering properties of concentrator optics provides almost 2 times increase of power density from blue LED illuminating module up to 1.6 W/cm<sup>2</sup> at tissue surface. The attractive practicability of concentrator is that having the length of 5.5 mm it can be polished at its tip surface without significant undermining the light collecting abilities.

## 5. Tissue fluorescence measurements

To demonstrate the capabilities of the LIF system of measuring fluorescence we check its operation *in vitro* as well as *in vivo* using, respectively, excised biopsy samples from gastrointestinal tract with suspected dysplasia and normal skin of two Caucasian volunteers. All measurements were conducted in dark room conditions with no administration of any photosensitizing agent *e.g.* they were autofluorescence measurements.

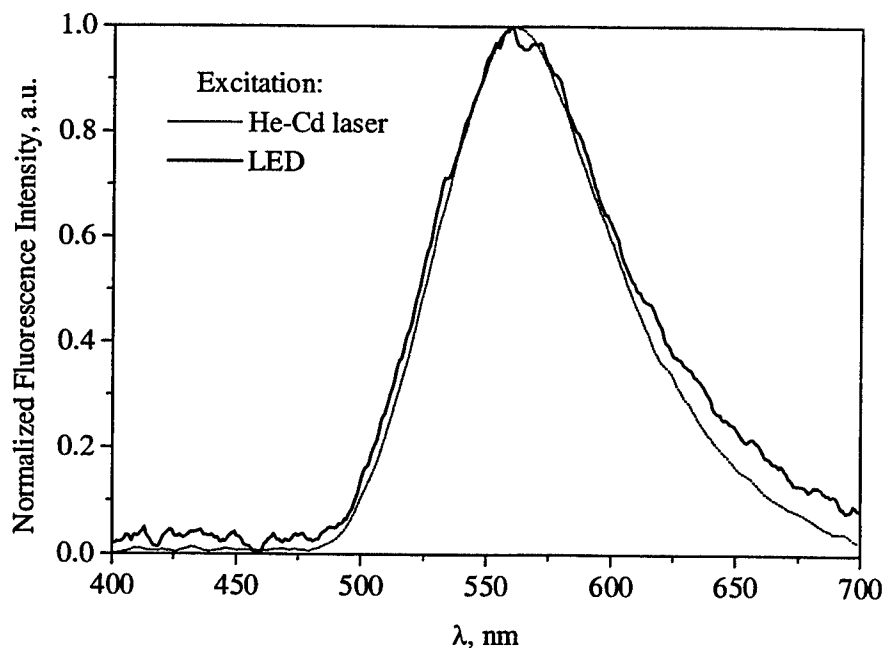


Fig. 5. Normalized fluorescence spectra of benign stomach polyp measured via LIF system using He-Cd laser ( $\lambda = 442$  nm,  $P = 15$  mW) and LED illuminating module. Measurements were conducted the same way for both sources in direct contact to tissue with attached probe concentrator.

Two sample sets from gall bladder walls and stomach polyp having minor dysplastic changes were examined using technique of autofluorescence diagnostics. Examined LIF system included LED module, fiberoptic probe with attached concentrator and portable spectrometer S2000 connected to PC. Each individual spectral measurement with LED illumination module was repeated after excitation source substitution by He-Cd laser ( $\lambda = 442 \text{ nm}$ ) to check the spectral differences. In Fig. 5 the normalized fluorescence spectra of benign stomach polyp is shown. As we see, the noise in autofluorescence spectrum using LED excitation is higher compare to 442 nm light excitation from 15mW-laser, nevertheless both curves a rather identical. Furthermore, two gall bladder samples histologically diagnosed with dysplasia were examined fiberoptically with LED equipped LIF system using R/G ratio algorithm. As a result, respectively, normal area of gall bladder and dysplasia were characterized by ratio of 0.94 and 1.48, and that was confirmed with He-Cd laser. The *in vivo* autofluorescence measurements of healthy skin from the arm area were performed with LED excitation and gave higher R/G ratio values of 0.47-0.5 seemingly as a result of lesser hemoglobin presence compare to gastrointestinal tissue.

### 3. DISCUSSION

Miniature fluorescence point measurement system utilizing LED as an excitation source has been shown to have a potential in tissue fluorescence analysis. We considered the introduction of presently available InGaN LED's emitting at blue spectrum as a part of compact LIF system, exploiting basic point measurement strategy. Based upon spectral and photometric data of LED's we arrange them in descending order of their practicability for fluorescence diagnostics of tissue:

- i. E1L51-3B from Toyoda Gosey,
- ii. MBB51TAH-T from Micro Electronics Corp.,
- iii. NSPB500XS from Nichia Chemical Industries,
- iv. HLMP-CB15 from Hewlett Packard

The 5mm-LED of E1L51-3B is our choice for application in miniature LED illuminating module as it combines high output power (1.34 mW at 2 cm distance), narrow radiation directivity ( $2\theta < 30^\circ$ ) and has emission peak at 460 nm. Its comparatively narrow emission halfwidth makes E1L51-3B convenient to keep R/G ratio algorithm after filtration in excitation and collecting channels of LIF system. The opto-mechanical implementation of 5 mm- and 3 mm LED's was found based on miniature design of simple three component condenser system consisting of widely available lenses and standard fiber optic connectors. Developed design of contact light concentrator attached to multifiber probe resulted in about two-fold increase of power density at the tissue surface  $K_D$ , compensating optical losses along the LED-Tissue path. The miniature LIF system included autonomous LED illuminating module, bifurcated multifiber probe with concentrator and fiberoptic spectrometer S2000 (Ocean Optics, USA) was tested clinically. We compared the autofluorescence readings form living and excised human tissues of different morphological structure and state *e.g.* polyp, gall-bladder, skin, using He-Cd laser and LED illumination module and the result proved the applicability of the latter for tasks of autofluorescence diagnosis.

Authors are seeking further improvement and miniaturization of proposed LIF system in using coatings for condenser optics, replacement of CCD-spectrometer with simpler photodiode comparative circuit providing the R/G ratio readings only, as well as rapidly changing situation on the optoelectronic market would result in bringing new LED products with preferred optical characteristics (*e.g.* see information about deep blue LED Chips<sup>8</sup>).

### 4. ACKNOWLEDGEMENT

Authors thank Dr. I.Melnik and P. Kowalski for helpful advises and Dr. A. Buryi for his excellent guidance during clinical experiments. S.D. acknowledges the financial support of A.E.Inc. and personally its President Prof. A. Rawicz (School of Eng. Sci., SFU) who has contributed heavily at each stage of the study.

### 5. REFERENCES

1. A.E. Profio, D.R. Doiron and J. Sarnaik, "Fluorometer for endoscopic diagnosis of tumors", *Med. Phys.* Vol. 11. pp.512-520, 1984.

- 
2. Specifications of NLHV500 Laser Diode from Nichia Corp., Japan; at <http://www.la.mesh.ne.jp/nichia/vlaser-e.htm> ; Version: September 1, 1999.
  3. "Blue-Violet Diode Laser System", Coherent Inc. – Preliminary product information, November 1999.
  4. "Blue Laser Module", Preliminary product information of Power Technology Inc., "Photonics Spectra", October 1999.
  5. Specifications of LS-450 Blue LED Pulsed Light Source from Ocean Optics, USA; [http://www.oceanoptics.com/ProductSheets/LS\\_450.asp](http://www.oceanoptics.com/ProductSheets/LS_450.asp) ; Version: December 1999
  6. "1999. Optics and Optical Instruments Catalog", Edmund Scientific Co., Barrington, NJ, 1998.
  7. N.A. Denisov, S.E. Griffin, "Contact fiber probes for in-vivo optical spectroscopy: comparative analysis", Optical Biopsy II, *Proc. SPIE*, Robert R. Alfano; Ed., Vol. 3250, pp. 44-55, 1998.
  8. Specifications of Super Bright LED Chips CXXX-CB290-E1000 from Cree Research Inc., USA; [http://www.cree.com/products/led/gsic\\_led.htm](http://www.cree.com/products/led/gsic_led.htm) ; Version: December 1999.



# Laser-induced Fluorescence Spectrum of Human Colonic Tissues by Monte Carlo Modeling

Zhiwei Huang<sup>1,\*</sup>, Teck-Chee Chia<sup>1</sup>, Sing Lee<sup>1</sup>, Wei Zheng<sup>2</sup>, SM Krishnan<sup>2</sup>, Tuan-Kay Lim<sup>2</sup>  
Horn Mun Cheah<sup>1</sup>, Cheong Hoong Diong<sup>1</sup>, Francis Seow Choen<sup>3</sup>

<sup>1</sup>School of Science, Nanyang Technological University, Singapore 259756

<sup>2</sup>School of EEE, Nanyang Technological University, Singapore 639798

<sup>3</sup>Department of Colorectal Surgery, Singapore General Hospital, Singapore 169608

## ABSTRACT

Based on the microscopic properties of colonic tissues, a five-layer colon optical model was developed to calculate the excitation light distribution in the tissue and the fluorescence escape function from the tissue by Monte Carlo simulations. The theoretically modeled fluorescence spectrum fits well to the experimental results, demonstrating that the microscopic properties of tissue applied in the colon optical model can be quantitatively correlated with the macroscopic autofluorescence measurements.

**Keywords:** fluorescence microscopy and imaging, laser-induced intrinsic fluorescence, fluorescence escape function, tissue optics, Monte Carlo modeling.

## 1. INTRODUCTION

In recently years, there have been many reports on the laser-induced autofluorescence (LIAF) macroscopic spectroscopies of human colonic tissues in the literature [1-3]. However, only a few groups investigated the LIAF microscopic spectroscopy and imaging of human colonic tissues using visible laser light. The microfluorophore distributions in tissues have not been studied in detail by separating the different tissue layers in the colon, and the spectral differences of different colon layers have not been reported either. A lack of knowledge on the exact fluorophore molecules and their spatial distribution inside the colon tissue make it difficult to explain some of the macroscopic measurements. We find that the macroscopic autofluorescence observed at the tissue surface is different from the intrinsic fluorescence of different tissue layers in colon tissue [4]. In fact, the re-emitted fluorescence spectrum is affected by tissue optical properties. Tissue re-absorption and scattering can distort the shape of the detected autofluorescence spectrum. Other factors such as the fluorophore distribution in tissue, the quantum yield of tissue fluorophores, the geometry of tissue sample, the boundary conditions and the light excitation/detection arrangement [5-6] may also affect the measured autofluorescence spectra. To improve the understanding of tissue autofluorescence process emitted from the colonic tissue, a five-layer colon optical model was developed in this study to simulate the excitation laser light distribution in the tissue as well as the autofluorescence escape process from the tissue. The contributions of each tissue layer in the colon to the total autofluorescence signal at the tissue surface are estimated based on this theoretical modeling. The tissue autofluorescence spectrum ranging from 470 to 750 nm was also modeled in terms of tissue microscopic optical properties. Note that this theoretical model is based on (1) the histological organization of colonic tissues; (2) fluorophore micro-distributions in the colon; (3) the intrinsic fluorescence spectra inside the colon, and (4) the available optical properties of colonic tissues.

\*Correspondence to the author, at the Division of Physics, School of Science, Nanyang Technological University, 469 Bukit Timah Road, Singapore 259756. Email: zwhuang@nie.edu.sg; Tel:+65-4605670; Fax:+65-4698952

## 2. METHODOLOGY

### 2.1 The Optical Model of Colon Tissue

The microscopic properties and images of autofluorescence emissions in human colonic tissues were studied under a microspectrophotometric (MSP) system [7]. Fig. 1 shows the typical microscopic autofluorescence image of the colon tissue section. It is found that the normal colon tissue consists of a well-defined layer structure, mainly consisting of the mucosa, the submucosa, and the muscularis propria. The mean thickness of each tissue layer measured from the 86 colon sections was estimated as: (i) epithelium,  $60 \pm 20 \mu\text{m}$ ; (ii) lamina propria,  $440 \pm 130 \mu\text{m}$ ; (iii) muscularis mucosa,  $60 \pm 20 \mu\text{m}$ ; (iv) submucosa,  $540 \pm 160 \mu\text{m}$ ; and (v) muscularis propria,  $800 \pm 210 \mu\text{m}$ .

Therefore, human colonic tissue can be simplified as a five-layer colon optical model that related to the microscopic fluorescence properties of tissues and to the published optical parameters of colonic tissues [8-14]. Table 1 outlines this model by providing data for the optical parameters ( $\mu_a$ ,  $\mu_s$ ,  $g$ ) and tissue thickness,  $d$ , refractive index,  $n$ , at 442 nm for each colon layer. To model the fluorescence escape process, optical parameters for the colon model at other wavelengths are also required. We compiled the data of each colon layer at 29 different wavelengths from 470 to 750 nm in 10-nm intervals using the data from the literature [8-13]. For example, Table 1 also lists the optical parameters for fluorescence wavelength at 510 nm.

Table 1 Tissue optical parameters ( $\mu_a$ ,  $\mu_s$ ,  $g$ ,  $n$ ,  $d$ ) of the five-layer colon optical model for Monte Carlo simulations at 442 and 510 nm, respectively.

Tissue Optical Parameters	Epithelium	Lamina Propria	Muscularis Mucosa	Submucosa	Muscularis Propria
$\mu_a$ ( $\text{cm}^{-1}$ )	2.1	2.9	4.5	7.5	6.0
	2.0	1.0	3.2	2.6	3.0
$\mu_s$ ( $\text{cm}^{-1}$ )	200	130	112	116	12
	180	90	70	81	70
$g$	0.94	0.92	0.94	0.94	0.94
	0.94	0.92	0.94	0.94	0.94
$n$	1.38	1.38	1.39	1.38	1.39
	1.38	1.38	1.39	1.38	1.38
$d$ ( $\mu\text{m}$ )	60	440	60	540	800

<sup>(a)</sup>Note that in each row, the first and the second sets of data correspond to the optical parameters at 442 and 510 nm, respectively.  $\mu_a$  is the absorption coefficient ( $\text{cm}^{-1}$ );  $\mu_s$  is the scattering coefficient ( $\text{cm}^{-1}$ );  $g$  is the scattering anisotropy;  $n$  is the tissue refractive index; and  $d$  is tissue thickness.

### 2.2 The Intrinsic Fluorescence Spectra

Fig. 2 shows a typical intrinsic fluorescence spectra of different colon layers measured from a 10- $\mu\text{m}$  normal tissue section under excitation laser light at 442 nm [4]. The intrinsic fluorescence of various tissue layers in colon differs in both the spectral shape and intensity of the fluorescence emission, suggesting that fundamentally different fluorophores may be present in the respective colon layers. The superficial layers (epithelium and lamina propria) are characterised by a fluorescence intensity significantly lower than that of the connective inner layers (muscularis mucosa and submucosa tissues). Thus fluorescence from the submucosa dominates over the fluorescence from the mucosal layer, and fluorescence from the muscularis propria of normal colon is extremely weak. From Fig. 2, it is also found that the spectral shape of colon autofluorescence observed from bulk tissues is quite different from the intrinsic spectra of different layer colon tissues. This is actually caused by the effects of tissue optics. Therefore, the studies on colon autofluorescence microscopy and imaging confirm that the major fluorescing fluorophores are located in the muscularis mucosae and submucosal layers, and thus provide the fundamental knowledge for Monte Carlo modeling of laser-tissue interactions.

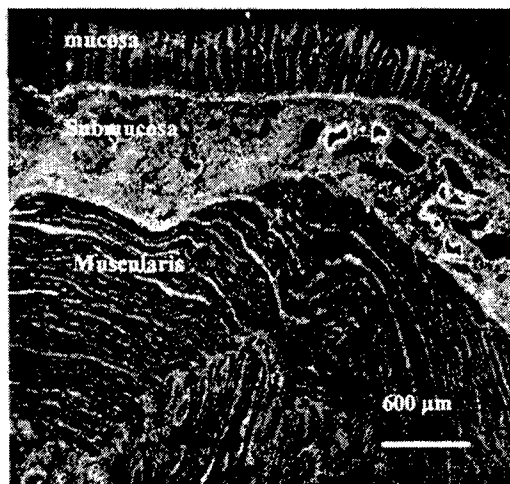


Fig. 1 Typical autofluorescence image of a 10-μm colon section obtained by the MSP system using laser excitation light at 442 nm. Magnification 40×.

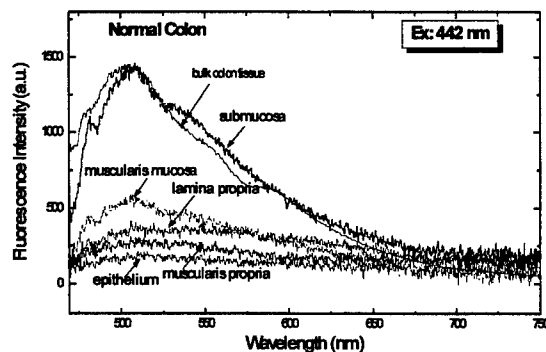


Fig. 2 The intrinsic autofluorescence spectra of normal colon fluorophores at different tissue layers of a 10-μm normal colon tissue section obtained by the MSP system under 442 nm laser light excitation. The macroscopic autofluorescence spectrum of the bulk colon tissue is also shown for comparison.

### 2.3 The Intrinsic Fluorescence Coefficient $\beta(\lambda_{ex}, \lambda_{em}, z)$

The intrinsic fluorescence coefficient,  $\beta(\lambda_{ex}, \lambda_{em}, z)$ , is denoted as the product of the absorption coefficient of the fluorophore,  $\mu_{a, fluor}$  ( $\text{cm}^{-1}$ ), and the quantum yield  $Y$  for fluorescence emissions. Within a tissue layer,  $\beta$  can be considered as a constant and therefore can be denoted as a function of  $z$ . Using the MSP system, one can measure the relative  $\beta$  distributions inside the tissue. The fluorophore density  $\rho(z)$  can be calculated from the digital autofluorescence image. The intrinsic spectra of different tissue layers measured with the MSP (Fig. 2) were normalised to equivalent overall integral intensity (the areas from 470 to 750 nm under each normalised intrinsic spectral curve are the same), and is denoted as  $I_{intrinsic}(\lambda_{ex}, \lambda_{em}, z)$ , which is dimensionless. Then the  $\beta$  can be obtained using [15]:

$$\beta(\lambda_{ex}, \lambda_{em}, z) = \rho(z) \times I_{intrinsic}(\lambda_{ex}, \lambda_{em}, z)$$

Fig.3 shows an example of the intrinsic fluorescence coefficient  $\beta(\lambda_{ex}=442\text{nm}, \lambda_{em}=510\text{nm}, z)$  distribution (relative values) inside the model colon tissue obtained from the MSP measurements of colon tissue sections.

### 2.4 Escape Function $E(\lambda_{em}, r, z)$ of Fluorescence

Once a fluorophore emits a fluorescence photon, that photon must reach the surface and escape to be observed. The escape function  $E(\lambda_{em}, r, z)$  is the surface distribution as a function of radial position ( $r$ ) of escaping photons from a point source of fluorescence at depth  $z$  and radial position  $r=0$  within a tissue of thickness  $D$ . It can be calculated by Monte Carlo simulation. The unit of  $E$  is in  $\text{cm}^{-1}$ . Simulations were conducted for a series of depths ( $z$ ) inside the tissue, using the optical parameters for the fluorescence wavelengths of interest.

### 2.5 Total Observed Fluorescence $F(\lambda_{ex}, \lambda_{em}, z)$

The escape functions for the point fluorescence sources  $E(\lambda_{em}, r, z)$  were convolved with the distribution of the fluorescence sources  $[\beta(\lambda_{ex}, \lambda_{em}, z) \cdot \Phi(\lambda_{ex}, r, z, \theta)]$ , yielding the total observed fluorescence,  $F(\lambda_{ex}, \lambda_{em}, z)$ , in units of  $W/\text{cm}^2$ , escaping at the tissue surface [16]

$$F(\lambda_{ex}, \lambda_{em}, r) = \int_0^D \int_0^{2\pi} \int_0^\infty \Phi(\lambda_{ex}, r', z', \theta') \beta(\lambda_{ex}, \lambda_{em}, z') E(\lambda_{em}, \sqrt{r^2 + r'^2 - 2rr' \cos \theta'}) r' dr' d\theta' dz'$$

The convolution in the above equation can be implemented numerically using discrete values for  $\Phi$  and  $E$  that were generated by the Monte Carlo simulation, and the experimentally determined  $\beta$ . The Monte Carlo simulation program (MCML simulation code) [17] was used to calculate the excitation light distribution inside the colon tissue which was modeled as a five-layer structure. To calculate the fluorescence escape function, the source code was modified to simulate the light propagation process for an isotropic fluorescence point source buried at depth  $z$  inside the tissue. One million photons were launched in each simulation.

### 3. MONTE CARLO MODELING RESULTS AND DISCUSSION

#### 3.1 The Excitation Laser Light (442 nm) Distribution inside Colon Tissue

Fig. 4 shows the Monte Carlo simulation results of the 442 nm excitation light distribution,  $\Phi$ , as a function of tissue depth,  $z$ . It is found that the mucosa is the tissue layer mainly involved in the irradiation procedure and that, on considering an average mucosa thickness of 560  $\mu\text{m}$ , only 15-30 % of the incident light fluence can reach the underlying structure, i.e., the submucosal layer. Very little 442 nm light further penetrates into the muscularis propria layer (tissue depth  $>1$  mm), thus the muscularis propria tissue has a negligible contribution to total measured autofluorescence signal under the 442 nm light excitation.

#### 3.2 Fluorescence Point Sources and Total Fluorescence

By the Monte Carlo method, we simulated one hundred fluorescence point sources at different depths inside the colon tissue ( $z$  ranged from 0 to 1000  $\mu\text{m}$ ), each emitting 1,000,000 photons isotropically. A series of the point fluorescence sources were distributed along the  $z$ -axis.

Fig. 5 shows an example of the fluorescence escape function  $E(\lambda=510 \text{ nm}, r, z)$  of fluorescence point sources located at depths 9.85, 132.17, 510.64, and 804.54  $\mu\text{m}$  inside the colon. It is found the peak value of the escape function is strongly dependent on the depth of point source. Less fluorescence can reach the top surface from deeper point sources, and the distributions are less peaked. The maximum value of the epithelium escape function is approximately 50, 200, and 610 times larger than that of the fluorescence sources arising from the lamina propria, the muscularis mucosa, and the submucosa, respectively.

Fig. 6 shows the total fluorescence  $F(\lambda=510 \text{ nm}, r)$  at the surface of colon tissue from tissue layers of a 10- $\mu\text{m}$  thickness at depths of 9.85, 132.17, 510.64, and 804.54  $\mu\text{m}$ , respectively. It is found that when  $z$  increases, the maximum height of fluorescence decreases, while its width increases. Thus, the light from a point fluorescence source inside the tissue will be attenuated and spread into a circular spot at the tissue surface when it escapes from the tissue. It is also found that even for the point source located at a depth of 800  $\mu\text{m}$ , the FWHM of  $F(\lambda, r)$  is only 1.2 mm, which is still much smaller than the fluorescence collection size (4 mm) of our detection system [18]. This indicates that the spectral distortion caused by the excitation/collection geometry in this study can be ignored, and the one-dimensional approximation for calculating the observed fluorescence is also valid.

Fig. 7 shows the fluorescence escape function  $E(\lambda=510\text{nm}, z)$  versus the depth of the fluorescence source inside the colon tissue.

#### 3.3 Estimation of Fractional Contributions of Different Tissue Layers to the Total Observed Autofluorescence

The product of the  $\Phi(z)$ ,  $E(z)$ , and  $\beta(z)$  versus tissue depth  $z$  is shown in Fig. 8. Integration of the curve in Fig. 8 yields fractional contributions of different tissue layers in colon to the total observed fluorescence signal. It is found that in normal colonic tissue, about 70% of the 510-nm fluorescence at the colonic tissue surface originates from the mucosal tissue, 30% comes from the underlying submucosal tissue. The muscularis-fat tissue contributes nearly nothing to the observed fluorescence signal. This is the results caused by the low rate of both the excitation light distribution inside the tissue and the fluorescence escape efficiency (Figs. 4 and 7). The above theoretical predictions indicate that tissue autofluorescence measurement is a surface enhanced technique. The reliability of the above predictions has been proven in the tissue photobleaching experiment [18].

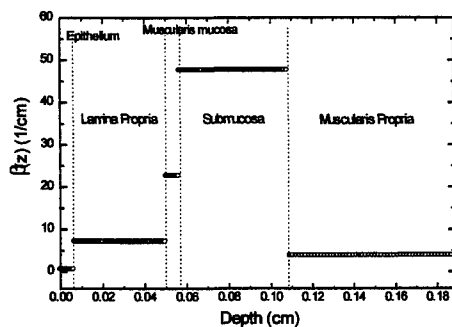


Fig. 3 The intrinsic fluorescence coefficient,  $\beta$ , as a function of tissue depth,  $z$ , inside the model colon tissue for 510 nm fluorescence under laser light excitation at 442 nm.

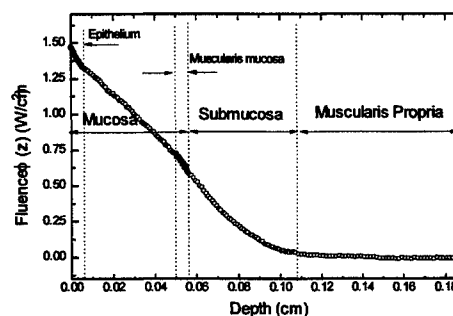


Fig. 4 The 442-nm laser light distribution,  $\Phi$ , as a function of tissue depth in colon by Monte Carlo simulations. The normal incident beam is assumed as an infinite wide in diameter with power density of  $1 \text{ W/cm}^2$ .

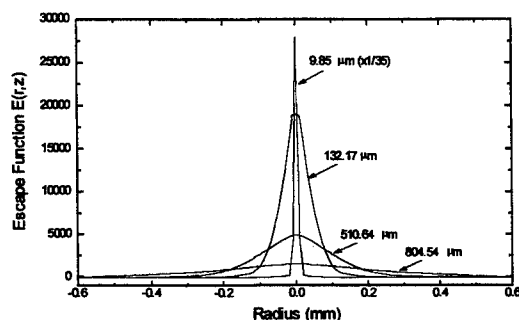


Fig. 5 Escape function  $E(\lambda_{em}=510 \text{ nm}, r, z)$  of fluorescence point source at tissue depths of 9.85, 132.17, 510.64, and 804.54  $\mu\text{m}$ , respectively.

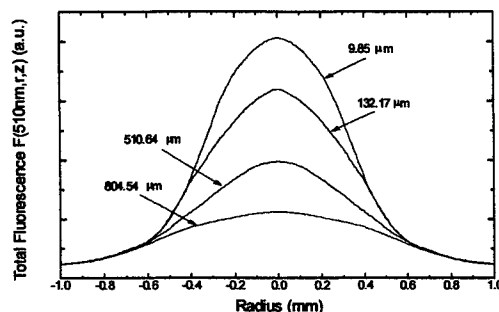


Fig. 6 The total fluorescence  $F(\lambda_{em}=510 \text{ nm}, r)$  at the surface of colon tissue from tissue layers of  $10\text{-}\mu\text{m}$  thickness at depths of 9.85, 132.17, 510.64, and 804.54  $\mu\text{m}$ , respectively.

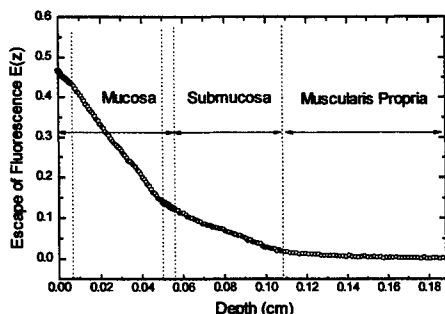


Fig. 7 Fluorescence escape function  $E(z)$  versus the depth of the point source inside the normal colon tissue (Fluorescence wavelength: 510 nm).

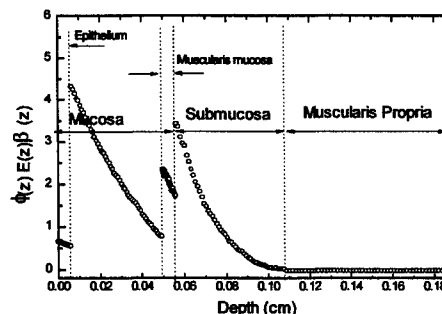


Fig. 8 The  $\Phi(z) \cdot E(z) \cdot \beta(z)$  function versus tissue depth,  $z$ .

### 3.4 Comparison of the Modeled Autofluorescence Spectrum with the Experimental Results

With a specific excitation/collection geometry (a large illumination area and a small detection area), we find that although the intensity of *in vitro* macroscopic autofluorescence varies from different tissue specimens, the spectral line-shape of autofluorescence does not vary significantly, and the spectral maximum position of autofluorescence nearly remains constant at  $506 \pm 2$  nm. It should be noted that the details of the spectral line-shape in 530-590 nm do change from case to case due to the tissue re-absorption of the fluorescence light and the variation in the amount of the various absorption chromophores in the blood [19]. The oxyhaemoglobin found *in vitro* in the specimens is an artefact caused by diffusion of hemolysed blood into the vascular wall after surgical resections.

Fig. 9 shows the modeled colon autofluorescence spectrum and the experimental autofluorescence spectra. For comparison purpose, each curve is normalized to a maximum intensity of 100. It is found that the modeled spectrum shows a prominent green fluorescence peak at 510 nm, which is close to the experimental peak position of 506 nm. The 4-nm wavelength shift between the experimental and the modeled peak positions could have arisen from our simulation errors using 10-nm interval. The effects of the absorption at 540 and 580 nm on autofluorescence light by blood [16] are also found in both the experimental spectra and the Monte Carlo simulation curve. From Fig. 9, it is found that the theoretical curve lying in the regions of 470-520 nm and 600-750 nm fits well to the experimental data since light absorption by blood in this two regions is relatively small [20]. However, the big difference between the experimental and the calculated autofluorescence spectra appears over the strong haemoglobin absorption band of 530-590 nm [19, 20]. This difference is due to the increased haemoglobin absorption in colon tissues, indicating that the data on microscopic properties of tissue for the 530-590 nm fluorescence used in the theoretical modeling may not truly reflect the actual situation in the bulk colon tissue. Thus, variation in the blood amount would play a major role at wavelengths of 530-590 nm, suggesting that the optical parameters evaluated from *in vitro* situations for Monte Carlo simulation should be handled cautiously for an *in vivo* evaluation.

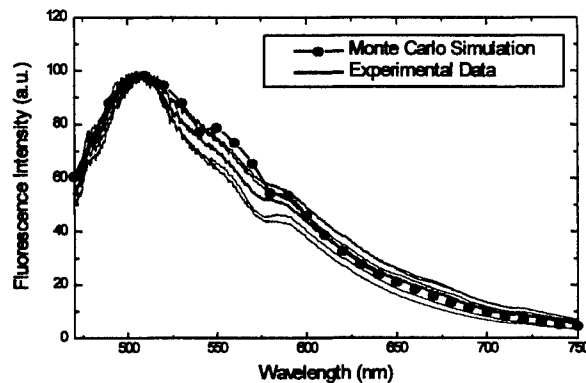


Fig. 9 Comparison of the modeled fluorescence spectrum by Monte Carlo simulations with the experimental autofluorescence spectra

## 4. CONCLUSIONS

Based on the five-layer colon optical model, we have calculated the excitation light distribution inside the tissue, the fluorescence escape function and the tissue autofluorescence spectrum by Monte Carlo simulations using the measured intrinsic fluorescence properties of colon tissues, such as fluorophore micro-distributions, the intrinsic fluorescence spectra, and optical parameters. The Monte Carlo simulation results of total observed fluorescence at the tissue surface show that with the arrangement of a large illumination area and a small detection area, a less distorted fluorescence spectra can be obtained. The theoretically modeled spectrum agrees well with the experimental fluorescence spectrum in the non-absorption wavelength band of blood, indicating that the microscopic properties of tissue applied in the colon optical model can be well correlated with the macroscopic autofluorescence measurements. Therefore, the use of the theoretical optical colon model by Monte Carlo simulations, considering the microscopic properties of colon and the intrinsic fluorescence distribution in colon, will allow us to optimise the experimental conditions that improve the modification of autofluorescence characteristics, thus approaching an *in vivo* autofluorescence measurements at endoscopy.

## 5. ACKNOWLEDGEMENTS

This work was supported by the Research Grant NIE RP 26/98 CTC.

## REFERENCES

1. S.von.Holstein, C.Nilsson, S.Andersson-Engels, R.Willen, B.Walther, K.Svanberg, Detection of adenomacarcinoma in Barretts's oesophagus by means of laser induced fluorescence, *Gut*, 39, 711-716 (1996).
2. K.T.Schomacker, J.K.Frisoli, C.C.Compton, T.J.Flotte, J.M.Richter, N.S.Nishioka, et al., Ultraviolet laser-induced fluorescence of colonic tissue: Basic biology and diagnostic potential, *Lasers Surg. Med.*, 12, 63-78 (1992).
3. T.J.Romer, M.Fitzmaurice, R.M.Cothren, et al., Laser-induced fluorescence microscopy of normal colon and dysplasia in colonic adenomas: Implications for spectroscopic diagnosis. *Am. J. Gastroentero.* 90, 81-87 (1995).
4. ZW Huang, TC Chia, S Lee, W Zheng, S M Krishnan, Laser-induced autofluorescence microscopy of colonic tissues. Presented on the LASERS' 99, Dec 1999, Quebec, Canada.
5. A.J.Welch, C.Gardner, R.Richards-Kortum, E.Chan, G.Criswell, J.Pfefer, S.Warren, Propagation of fluorescence light. *Lasers Surg. Med.*, 21, 166-178 (1997).
6. J.Wu, M.S.Feld, R.P.Rava, Analytical model for extracting intrinsic fluorescence in turbid media. *Appl. Opt.*, 32, 3585-3595 (1993).
7. ZW Huang, TC Chia, CH Diong, S Lee, W Zheng, SM Krishnan, T.K.Lim, Laser-induced microscopic autofluorescence imaging of human colonic tissues. *SPIE*, Vol. 3863, 316-321 (1999).
8. R.Marchesini, E.Pignoli, S.Tomatis et al., Ex Vivo Optical properties of human colon tissue, *Lasers Surg.Med.*, 15, 351-357 (1994).
9. R.S.DaCosta, L.Lilge, J.Kost et al., Confocal fluorescence microscopy, microspectrofluorimetry and modeling studies of laser induced fluorescence endoscopy (LIFE) of human colon tissue *SPIE* Vol. 2975, 98-107 (1997).
10. G.I.Zonios, R.M.Cothren, J.T.Arendt, et al., Morphological Model of Human Colon Tissue Fluorescence *IEEE Trans Bio Eng.*, 43, 113-122 (1996).
11. G.Bottiroli, R.Marchesini, A.C.Croce, M.Dal Fante, et al., Autofluorescence of normal and tumor mucosa of human colon. A comprehensive analysis, *SPIE*, Vol. 1887, 205-212 (1994).
12. J.Qu, C.MacAulay, S.Lam, B.Palcic, Laser-induced fluorescence spectroscopy at endoscopy: tissue optics, Monte Carlo modeling, and *in vivo* measurements, *Opt. Eng.*, 34, 3334-3343 (1995).
13. J.Qu, C.MacAulay, S.Lam, B.Palcic, Optical properties of normal and carcinomatous bronchial tissue, *Appl. Opt.*, 33, 7397-7405 (1994).
14. R.Marchesini, S.Fumagalli, E.Pignoli, A.E.Sichirillo, S.Tomatis et al., Light-induced fluorescence of human colon tissue: dependence on histological and histochemical properties studied by means of a simplified model for simulation. *SPIE*, Vol. 2324, 76-83 (1995).
15. H.Zeng, C.MacAulay, D.I.McLean, B.Palcic, Reconstruction of *in vivo* colon autofluorescence spectrum from microscopic properties by Monte Carlo simulation. *J.Photochem. Photobiol. B:Biol.*, 38, 234-240 (1997).
16. M.Keijer, R.Richards-Kortum, S.L.Jacques, M.S.Feld, Fluorescence spectroscopy of turbid media: autofluorescence of the human aorta. *Appl. Opt.*, 28, 4286-4292 (1989).
17. L.H.Wang, S.L.Jacques, Monte Carlo Modeling of Light Transport in Multi-layered Tissues in Standard C, University of Texas, M.D.Anderson Cancer Center, 1992.
18. TC Chia, ZW Huang, CH Diong, C Seow Changes in autofluorescence emission intensities of human colon tissues due to photobleaching processes *SPIE*, Vol.3568, 11-18 (1999).
19. L.S.L.Arakaki, M.J.Kushmerick, D.H.Burns, Myoglobin oxygen saturation measured independently of hemoglobin in scattering media by optical reflectance spectroscopy. *Appl. Spectrosc.*, 50, 697-707 (1996).
20. I.J.Bigio, J Boyer, T.M.Johnson, J.L.R.Mourant, R.Conn, A.Bohorfoush, Optical diagnostics based on elastic scattering: an update of clinical demonstrations with the optical biopsy system, *SPIE*, Vol.2324, 46-54 (1994).

# Ultraviolet 2-D fluorescence mapping system for the imaging of head and neck tumors

A. Katz<sup>a</sup>, Howard E. Savage<sup>b</sup>, Fanon Zeng<sup>a</sup>, Jayson Rome<sup>a</sup>, Stimson P. Schantz<sup>c</sup>,  
Steven A. McCormick<sup>b</sup>, Rubina S. Cocker<sup>b</sup>, and R. R. Alfano<sup>a\*</sup>

<sup>a</sup>Institute for Ultrafast Spectroscopy and Lasers,  
The City College of New York, New York, NY 10031

<sup>b</sup>Dept. of Pathology, New York Eye and Ear Infirmary, New York, NY 10003

<sup>c</sup>Dept. Of Otolaryngology, New York Eye and Ear Infirmary, New York, NY 10003

## ABSTRACT

Fluorescence images of *ex vivo* head and neck tissues were acquired at multiple combinations of emission and excitation wavelengths. The wavelength combinations were selected to map different tissue molecules and structures whose fluorescence signatures have been used to detect cancer. Fluorescence maps were generated by ratioing fluorescence image intensities. These ratio maps enhanced the ability to recognize regions of tumor and other features in tissues. Histopathological analysis was performed on the tissue samples. Location and shape of features observed in the fluorescence images were correlated with structures observed in histopathology.

**Keywords:** Optical Biopsy, Native fluorescence, Oral cavity cancer detection, Thyroid cancer

## 1. INTRODUCTION

Fluorescence spectroscopy is a real-time, non-invasive method which can detect, *in vivo*, molecular, chemical and structural changes in tissues caused by malignancy, before there is visual indication. In this work, 2-D fluorescence images of *ex vivo* head and neck tissues were acquired at multiple combinations of emission and excitation wavelengths. The wavelength combinations were selected to identify and map different tissue molecules (collagen, tryptophan, elastin, NADH) whose fluorescence signatures have been used to detect changes due to the onset of cancer. This work is part of an effort to develop a real time imaging system which will use fluorescence to identify and map cancerous and precancerous regions of tissues.

Fluorescence was first applied to the detection of cancer in tissue by Alfano *et al*<sup>1</sup> and has since been extended to tissues of many different origins. The use of excitation and emission spectroscopy in the UV has produced diagnostic accuracies greater than 90% using algorithms based on ratios of emission intensities at key wavelengths.<sup>2-3</sup> *In vivo* fluorescence measurements of the oral cavity for cancer detection were first performed by a group at Memorial Sloan Kettering Cancer Center.<sup>4-9</sup> Multiple emission and excitation scans were employed in this study. Significant spectral differences were observed between the control and cancer patients, as well as differences, within patients, between normal and precancerous tissue.<sup>10-13</sup> High diagnostic accuracy was achieved using algorithms based on intensity ratios at different combinations of emission and excitation wavelengths corresponding to the absorption and/or emission bands of collagen, tryptophan, elastin and NADH. Algorithms based on intensity ratios have the advantage of being independent of fluctuations in excitation power and collection geometry.

The goal of this project is to develop and test a fluorescence imaging system which, in addition to detecting cancer or precancer, can identify and image different structures found in head and neck tissues which may provide useful information to the physician. In this work, fluorescence images were acquired from various head and neck tissues including tongue, parotid gland, thyroid and floor of mouth. Features observed in the images were compared to structures identified by histopathological analysis.

## 2. MATERIALS AND METHODS

The salient features of the imaging system used to acquire the fluorescence images is as follows: The excitation source

---

\*Correspondence: Email: [alfano@scisun.sci.cuny.cuny.edu](mailto:alfano@scisun.sci.cuny.cuny.edu), Telephone: 212-650-5531; Fax: 212-650-5530.



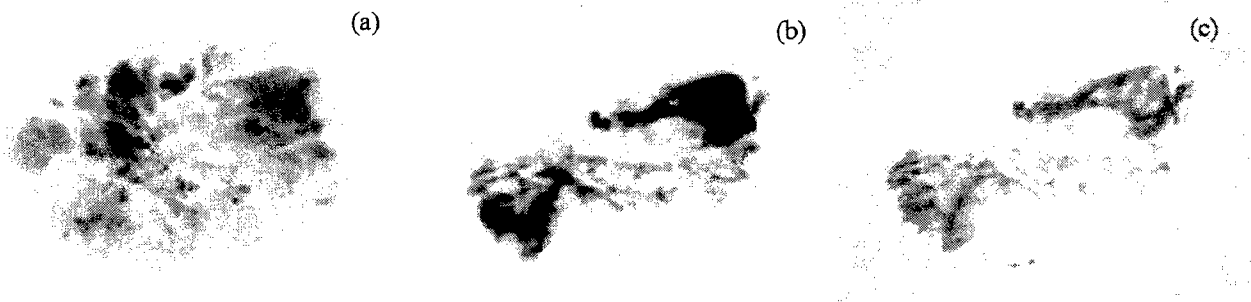


**Figure 1(a-c).** Base of tongue squamous cell carcinoma fluorescence images at  $\lambda_{em} = 380$  nm. (a) 300 nm excitation. (b) 340 nm excitation. (c)  $I_{340}/I_{300}$  ratio. Images have been inverted.

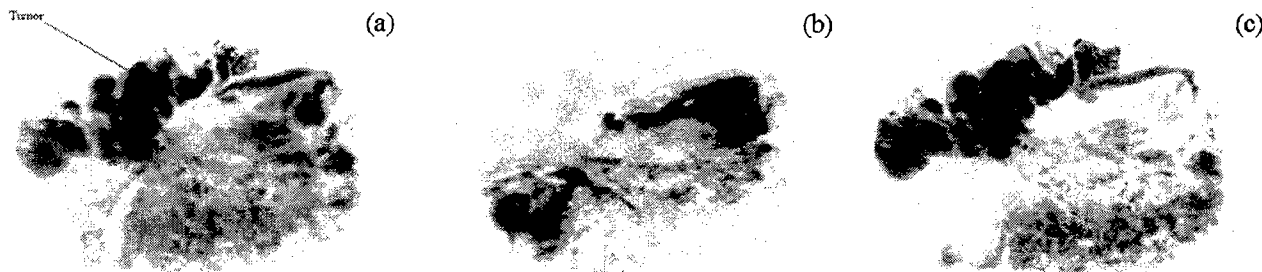


**Figure 2(a-c).** Base of tongue squamous cell carcinoma fluorescence images with  $\lambda_{ex} = 300$  nm. (a) 340 nm emission. (b) 440 nm emission. (c)  $I_{340}/I_{440}$  ratio. Images have been inverted, i.e. darker areas are higher intensity or ratio.

is a high power xenon lamp providing broad band excitation in the UV and blue spectral regions. The excitation light was delivered to the sample by a UV transmitting liquid light pipe. Excitation intensity at the sample site was approximately  $0.5 \text{ mW/cm}^2$ . The light pipe was positioned to excite the sample at close to normal incidence in order to optimize uniformity of illumination. Excitation wavelength selection was controlled by narrow band interference filters. The fluorescence was collected by a multi element UV lens and imaged onto the photo cathode of a UV sensitive image intensifier. The image magnification was varied among the samples to allow the entire sample to fit into the camera frame. Selection of emission wavelength was also controlled by narrow band interference filters. The fluorescence signal was amplified by the image intensifier and relayed to a monochrome CCD video camera. The output of the CCD was transferred to a frame grabber mounted in a Personal Computer. Images were captured at  $640 \times 480$  pixels at a rate of 30 frames per second.

Fresh tissues were acquired from the Department of Otolaryngology at New York Eye and Ear Infirmary (NYEEI). Samples were stored at  $4^\circ\text{C}$ , but otherwise untreated prior to acquisition of the fluorescence images. Images were acquired at five different excitation/emission wavelength combinations: The first filter combination primarily measures tryptophan emission. The second filter combination measures emission from collagen, elastin and NADH. The third combination measures emission from NADH and elastin. The fourth combination primarily measures collagen emission; 340 nm is the absorption peak, and 380 nm is the emission peak of collagen. The fifth filter combination also measures emission from NADH and elastin. For each wavelength combination, 25 frames were acquired and stored for averaging and further processing. The spatial resolution of this system is approximately  $100 \mu\text{m}$ , and is limited by the image intensifier resolution.

After completion of the fluorescence measurements, the samples were placed in formalin and returned to the NYEEI Department of Pathology for histopathological analysis.

### 3. ANALYSIS OF FLUORESCENCE IMAGES

All the samples exhibited some similar spectral characteristics in their respective fluorescence images. The tumor regions of the samples consistently demonstrated weaker emission at  $\lambda_{em} = 440$  nm than the non-tumor regions. The regions of normal tissue exhibited higher emission than the cancer samples at  $\lambda_{em} = 380$  nm for  $\lambda_{ex} = 340$  nm excitation, while for 300 nm excitation no clear differences were observed in the 380 nm emission intensity.

These spectral difference between normal and cancer tissue regions can be observed in the base of tongue sample whose fluorescence images are shown in Figs. 1(a) and (b). The region in the upper part of the sample was diagnosed by pathology as a squamous cell carcinoma while the rest of the sample consisted of normal tissue. Fig. 1(a) shows the  $I_{340}$  emission with  $\lambda_{ex} = 300$  nm. Fig. 1(b) shows the  $I_{440}$  emission with  $\lambda_{ex} = 300$  nm. The images have been inverted such that darker areas represent higher emission intensity. The cancer region demonstrated higher tryptophan emission ( $\lambda_{em} = 340$  nm) as compared to the normal region. However, the NADH emission ( $\lambda_{em} = 440$  nm), from the cancer region was significantly weaker than from the normal region. These differences can be further highlighted by generating ratio maps of the  $I_{340}$  and  $I_{440}$  images. The  $I_{340}/I_{440}$  ratio map is shown in Fig. 1(c), in which the cancer region exhibited a significantly higher  $I_{340}/I_{440}$  ratio than the normal region. In Fig. 1(c) areas of higher ratio are shown as darker regions.

Examination of the 380 nm emission images from the same sample also show large differences between the cancer and normal regions. The 380 nm emission images with  $\lambda_{ex} = 300$  nm and  $\lambda_{ex} = 340$  nm are shown in Figs. 2(a) and 2(b), respectively. At  $\lambda_{ex} = 300$  nm, the  $I_{380}$  image does not show large differences in emission intensity between the normal and tumor regions. However, for  $\lambda_{ex} = 340$  nm, the normal tissue region exhibits much stronger emission than the cancer region. This is a result of the exciting light not being able to penetrate the thicker basal cell layer of the tumor and exciting the collagen located underneath. The  $I_{340}/I_{300}$  ratio map, shown in Fig. 2(c), clearly delineates the cancer region, marked by a low  $I_{340}/I_{300}$  ratio, from the normal region with a high  $I_{340}/I_{300}$  ratio.

The ability of fluorescence imaging to locate and identify tumor regions as well as other structures in tissues is evidenced in the image shown in Fig. 3. This figure shows the 380 nm emission image ( $\lambda_{ex} = 340$  nm) from a papillary carcinoma of the thyroid surrounded by a collagen capsule. Pathological analysis identified the center of the capsule as a papillary carcinoma. The carcinoma has broken out of the capsule and spread to other areas of the thyroid as identified in Fig. 3. Pathology also identified regions of normal thyroid, connective tissue, and fibrous tissue in the sample. These regions are indicated in the Figure. It is observed that the collagen capsule, as expected, has very strong emission at 380 nm. The fibrous and connective tissue with high collagen content also exhibit strong 380 nm emission, while the cancer regions exhibit weak collagen emission. The location of the break in the capsule where the tumor has broken out can be identified by the low intensity area towards the bottom of the collagen ring. Below, and on either side of the capsule are regions of weak collagen signal surrounded by stronger signal areas. The weak signal areas have been identified by pathology as pockets of tumor surrounded by higher collagen content fibrous tissue. The normal tissue region towards the top of the sample has also has higher 380 nm emission than the tumor areas. The normal connective tissue on the upper right, with its higher collagen content is seen to have higher emission intensity than the other regions, with the exception of the capsule.

The  $I_{340}/I_{440}$  fluorescence ratio image from this same sample is shown in Fig. 4. As seen in the figure, the ratio from the cancerous regions are greater than from the normal regions. The pockets of tumor towards the bottom of the

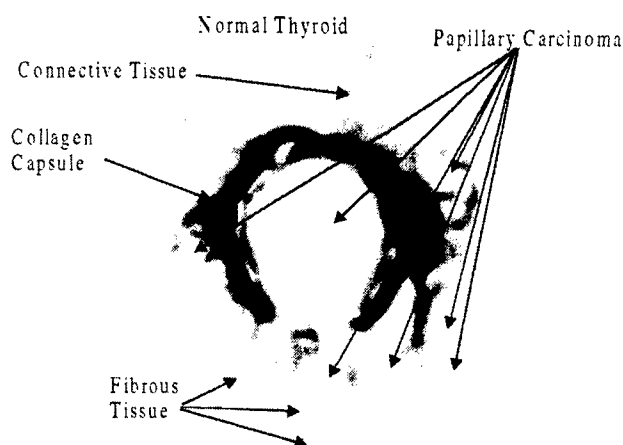


**Figure 3.** Fluorescence image from papillary carcinoma of the thyroid surrounded by a collagen capsule. The tumor has broken out of the bottom of the capsule,  $\lambda_{ex} = 340$  nm,  $\lambda_{em} = 380$  nm. Darker regions represent higher intensity.

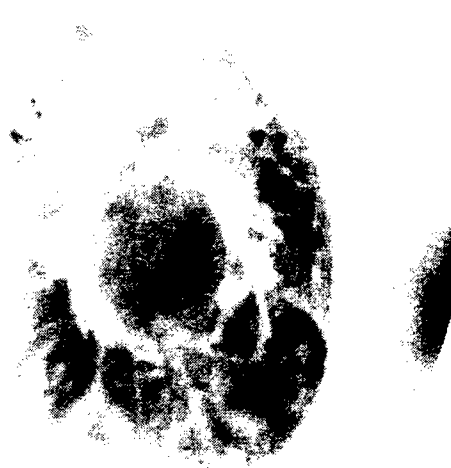


**Figure 4.** Fluorescence Ratio,  $I_{340}/I_{440}$ , image from a thyroid papillary carcinoma.  $\lambda_{ex} = 300$  nm.

sample are identified by the high ratio areas surrounded by low ratio areas of fibrous tissue. The collagen capsule has an exceptionally low ratio. This is the result of collagen re-absorption of the 340 nm emission signal.

#### 4. CONCLUSIONS

This work demonstrates that fluorescence imaging at multiple wavelengths in the ultraviolet coupled with intensity ratio maps generated from these images, can be used to identify regions of tumor and other structures in tissues. Ratio maps generated by dividing the  $I_{340}$  emission image by the  $I_{440}$  emission image, and dividing the  $I_{380}$  emission image with 340 nm excitation by the image with  $I_{300}$  excitation show clear differences between regions of tumor and normal tissue regions. The extension of this work to *in vivo* measurements may provide physicians with a valuable clinical tool to aide in the identification of tumor.

#### ACKNOWLEDGMENTS

This work has been supported by grants from NASA and the Department of Energy.

#### REFERENCES

1. R. R. Alfano, D. Tata, J. Cordero, P. Tomashefsky, F. W. Longo, and M. A. Alfano, "Laser induced fluorescence spectroscopy from native cancerous and normal tissues," *IEEE J Quantum Electron*, 20, 1507-1511 (1984).
2. R. R. Alfano, B. B. Das, J. Cleary, R. Prudente, and E. J. Celmer, "Light sheds light on cancer - distinguishing malignant tumors from benign tissues and tumors," *Bull. N. Y. Acad. Med.*, 67, 143-150 (1991).
3. B. B. Das, W. L. Glassman, R. R. Alfano, J. Cleary, R. Prudente, E. Celmer, and S. Lubicz, "UV-fluorescence spectroscopic technique in the diagnosis of breast, ovarian, uterus, and cervix cancer," *Laser-Tissue Interaction II*, 1427, S. L. Jacques, Ed., 368-373, SPIE Proceedings, Los Angeles, CA, 1991.
4. H. E. Savage, V. Kolli, J. Zhang, R. R. Alfano, P. G. Sacks, and S. P. Schantz, "Tissue autofluorescence spectroscopy: *in vivo* alterations may reflect cellular proliferation," *Advances in laser and light spectroscopy to diagnose cancer and other diseases*, 2135, R. R. Alfano, Ed., 16-25, SPIE, Los Angeles, CA, 1994.
5. H. E. Savage, P. G. Sacks, V. Kolli, D. Harris, and S. P. Schantz, "Intrinsic tissue fluorescence can identify retinoic acid induced changes in a multicellular tumor spheroid (MTS) model," *Head and Neck*, 16, 495 (1994).
6. H. E. Savage, V. Kolli, J. Ansley, R. Y. Chandawarkar, R. R. Alfano, and S. P. Schantz, "Innate tissue fluorescence of the oral mucosa of controls and head and neck cancer patients," *Advances in laser and light spectroscopy to diagnose cancer and other diseases II*, 2387, R. R. Alfano, Ed., 2-14, SPIE Proceedings, San Jose, CA, 1995.
7. H. E. Savage, V. Kolli, S. Saha, J.-C. Zhang, M. Glasgold, P. G. Sacks, R. R. Alfano, and S. P. Schantz, "Development of *in vitro* models to elucidate mechanisms of intrinsic cellular and tissue fluorescence," *Advances in laser and light spectroscopy to diagnose cancer and other diseases II*, 2387, R. R. Alfano, Ed., 44-56, SPIE Proceedings, San Jose, CA, 1995.
8. S. P. Schantz, H. E. Savage, P. Sacks, and R. R. Alfano, "Native cellular fluorescence and its application to cancer prevention," *Environ Health Perspect*, 105 Suppl 4, 941-4 (1997).
9. S. P. Schantz, V. Kolli, H. E. Savage, G. Yu, J. P. Shah, D. Harris, A. Katz, R. R. Alfano, and H. A. G., "In Vivo Native Cellular Fluorescence and Histological Characteristics of Head and Neck Cancer," *Clinical Cancer Research*, 4, 1177-1182 (1998).
10. V. K. Kolli, H. E. Savage, and S. P. Schantz, "In vivo tissue autofluorescence of neoplastic aerodigestive tract mucosa," *Head and Neck*, 16, 488 (1994).
11. V. R. Kolli, A. R. Shaha, H. E. Savage, P. G. Sacks, M. A. Casale, and S. P. Schantz, "Native cellular fluorescence can identify changes in epithelial thickness *in vivo* in the upper aerodigestive tract," *Amer. J. Surg.*, 170, 495-498 (1995).
12. V. R. Kolli, H. E. Savage, and S. P. Schantz, "In vivo native cellular fluorescence can identify changes in the oral mucosal thickness," *Proceedings of the American Association of Cancer Research* (1995).
13. V. R. Kolli, H. E. Savage, T. J. Yao, and S. P. Schantz, "Native cellular fluorescence of neoplastic upper aerodigestive mucosa," *Arch. Otolaryngol. Head Neck Surg.* (1996).

# DNA and protein changes in tissues Probed by Kubelka Munk Spectral Function

Yuanlong Yang\*, Edward J. Celmer (MD)\*\*, Jason A Koutcher (MD)\*\*\* and R. R. Alfano\*

\* Institute for Ultrafast Spectroscopy and Lasers. New York State Center for Advanced Technology for Ultrafast Photonic Materials and Applications. The City College, and Graduate School of the City University of New York. NY 10031.

\*\*St. Vincent's Medical Center of Richmond, Department of Pathology, Staten Island, NY 10310-1699

\*\*\*Memorial Sloan-Kettering Cancer Center, New York, NY.10021

## ABSTRACT

Normal, fibroadenoma, malignant, and adipose breast tissues were investigated using Kubelka-Munk Spectral Function (KMSF). The spectral features in KMSF were identified and compared with absorption spectra determined by transmission measurements. A specified spectral feature measured in adipose tissue was assigned to  $\beta$ -carotene, which can be used to separate fat from other molecular components in breast tissues. The peaks of (KMF) at 260nm and 280nm were attributed to DNA and proteins. The signal amplitude over 255nm to 265nm and 275nm to 285nm were found to be different for malignant fibroadenoma, and normal tissues.

Keywords: *Diffuse reflectance spectroscopy, Breast Cancer Diagnose, Optical biopsy DNA, proteins,*

## 1. INTRODUCTION

In our previous results, the fluorescence (1), excitation (2), and diffuse reflectance spectra (3) from different types human breast tissues have been studied as a potential clinical tool for cancer screening purposes. These characteristics may be reflected in the absorption spectra of these tissues. Due to multiple photon scattering, direct measurement of absorption spectra of tissues by conventional transmission means is not easily done. Bigio and co-workers investigated elastic scattering spectroscopy in the visible region for diagnosis of tissue pathologies (4). They claimed the spectrum of scattering light is different for different tissues.

In this paper, the diffuse reflectance spectrum and Kubelka-Munk function from breast tissues was obtained to give information about the changes in tissues. The spectral features of the Kubelka-Munk function were attributed to hemoglobin (oxygenated and deoxygenated hemoglobin), collagen, and  $\beta$ -carotene (in adipose tissue), proteins and nucleic acid components. The averaged amplitude of K-M function at 275nm to 285nm and 255nm to 265nm can be used to produce a criterion to distinguish malignant from fibroadenoma and benign breast tissue

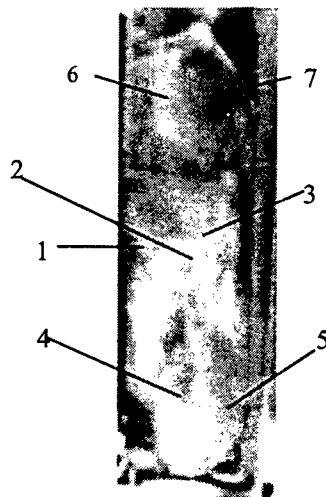


**Figure 1.** Photograph of typical specimen in cuvette. The specimen was diagnosed as poorly differentiated carcinoma. Diffuse reflectance method gave results on location as follow:

	1	2	3	4	5	6	7
$f_{275285}$	10.9	13.0	2.0	14.2	15.3	3.5	12.3
$f_{255265}$	14.1	30.5	1.64	31.4	38.1	3.6	13.6
$f_{480}$	0.03	0.04	0.12	0.06	0.41	0.10	0.06

## 2. MATERIALS

Excised benign, adipose, fibroadenoma and malignant breast tissue samples were obtained from St. Vincent Hospital, Memorial Sloan Kettering Cancer Center, and National Disease Research Interchange (NDRI). Specimens were neither chemically treated nor frozen prior to spectroscopic measurements. Samples of random shapes were mounted in a 1cm×1cm×5cm commercial quartz cuvette and closely attached to its inner surface for measurement of spectra. Usually, the spectra were measured at up to 3 different location of the sample. The photograph of typical specimen in the cuvette was displayed in Fig. 1. The malignant breast tissue specimens were classified into carcinoma *in situ*, infiltrating or invasive carcinoma, and mixed *in situ* and invasive (part *in situ* and part invasive) according to the pathology report. 25 invasive carcinoma, 22 mixed *in situ* and invasive, 14 fibroadenoma, 44 benign, and 31 adipose specimens have been studied. The pathological classifications of these specimens were displayed in Table 1.

The diffuse reflectance, fluorescence, and excitation spectra were performed from same spot of the sample, using an automated dual lamp-based spectrophotometer (Mediscience Technology Corp. CD scanner.). The measurements of diffuse reflectance spectra were selected using synchronized scan mode, in which the emission and excitation monochromators were scanning on the same wavelengths synchronously. The diffuse reflectance spectrum was scanned from 250nm to 650nm.

Table 1. Pathological classification of specimens.

No.	Description	Total
Malignant		
1	Ductal carcinoma	41
2	Lobular carcinoma	2
3	Mixed ductal and lobular carcinoma	3
4	Mucinous carcinoma	1
Benign		
1	Fibrocystic change	13
2	Benign and native tissue	31
Fibroadenoma		14
Adipose		31

As a reference standard,  $\beta$ -carotene crystal was obtained commercially from Sigma Co. And was dissolved in alcohol. The concentration of the carotene solution was 0.8 mg/ml. The small particles of  $Ti_2O_3$  (0.2 $\mu$ ) were added into carotene solution to enhance the scattering signal during diffuse reflectance measurements.

## 3. MODEL

Kubelka and Munk function obtained from diffuse reflectance is (5,6)

$$f \equiv (1 - R_\infty)^2 / 2R_\infty = k/s, \quad (1)$$

The function  $f$  is the ratio of absorption to scattering coefficients

In our experiment, the standard scatter is certified Spectralon<sup>TM</sup> 99% Reflection Standard (Labsphere, North Sutton, NH). Where

$$R_{\infty \text{ sample}} / R_{\infty \text{ STD}} = r_\infty. \text{ And}$$

$$f(r_\infty) = (1 - r_\infty)^2 / 2r_\infty = k/s. \quad (2)$$

Taking the logarithm of K-M function gives:

$$\text{Log } f(r_\infty) = \text{log } k - \text{log } s \quad (3)$$

Plotting  $\text{log } f(r_\infty)$  against the wavelength for a particular sample, the curve obtained corresponds to the absorption spectrum of the compound with intercept displacement given by  $-\text{log } s$  in the ordinate axis.

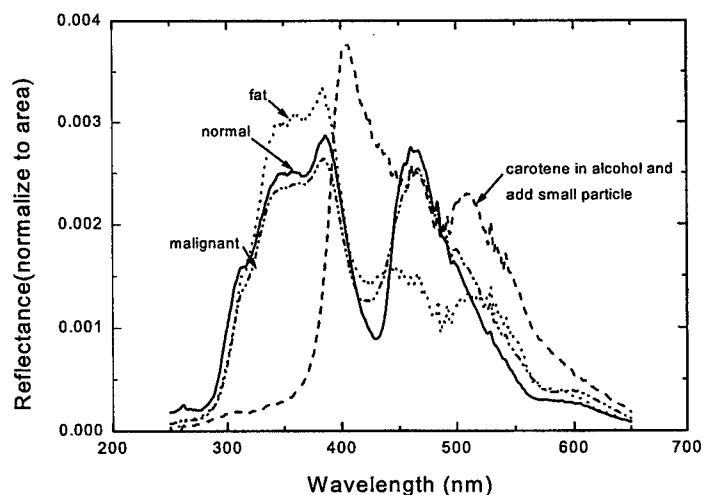


**Figure 2** Diffuse reflectance spectra of benign, malignant, adipose tissue and  $\beta$ -carotene solution. The  $\beta$ -carotene is dissolved in alcohol. The concentration is 0.8 mg/ml. The small particle  $Ti_2O_3$  (0.2 $\mu$ ) was added into carotene solution during diffuse reflectance measurement. All of the spectra have been normalized to area.

#### 4. RESULTS

The diffuse reflectance was measured from several types of tissues and chemicals from 250nm to 650nm. These reflectance spectra were displayed in Fig. 2. The K-M function from  $\beta$ -carotene solution, adipose, benign and malignant tissues were generated from the diffuse reflectance spectrum. The corresponding K-M functions were displayed in Fig. 3.

From Fig. 3, one noticed several peaks near 550nm, 480nm, 420nm, 280nm and 265nm. The absorption spectrum of  $\beta$ -carotene solution was also plotted in Fig. 3 for comparison. There was no carotene peak at 480nm in K-M function of benign or malignant breast tissues. The feature of  $\beta$ -carotene peak definitely appeared in adipose tissue. The averaged amplitude of K-M function at 480nm for different tissue was shown in Table 2. From Table 2 one can noticed that only adipose tissue gave higher amplitude ( $0.87\pm0.39$ ) at 480nm than other tissues.

Table 2. The amplitude of K-M function at 480nm for different kind of breast tissue.

	Invasive	Mixed	Benign	Fibroadenoma	Adipose
$f(r_{\infty})_{480nm}$	$0.22\pm0.27$	$0.14\pm0.10$	$0.12\pm0.11$	$0.12\pm0.09$	$0.87\pm0.39$

Some features can be found in the K-M curves of malignant, fibroadenoma and benign breast tissue. The peak near 280nm was appeared for all kind of tissue, but the amplitude was different. The amplitude of malignant was higher than fibroadenoma and benign tissue. This peak is corresponding to the absorption of proteins. The another peak near 265nm only appeared for malignant tissue. This peak is corresponding to the absorption of DNA. For fibroadenoma, the peak of K-M curve near 280nm is uncertain. Some specimen was higher some was lower but no 265nm peak was observed as compared to malignant tissue.

The averaged value of amplitude of K-M function from 275nm to 285nm and 255nm to 265nm were selected as the parameter to characterize the benign, fibroadenoma and malignant (invasive carcinoma and carcinoma *in situ*) breast tissues. The data of K-M function,  $f(r_{\infty})$ , and logarithm K-M function,  $\log f(r_{\infty})$ , averaged at 275nm to 285nm and 255nm to 265nm for various tissues were shown in Table 3. The values of

$f(r_{\infty})_{275nm-285nm}$  and  $f(r_{\infty})_{255nm-265nm}$  had higher value for malignant and lower value for benign tissue, such as  $f(r_{\infty})_{275nm-285nm}$ , the averaged value was  $13.11\pm10.39$  for invasive carcinoma,  $5.23\pm4.16$  for mixed carcinoma, and  $0.88\pm0.69$  for benign tissue. The values of  $f(r_{\infty})_{275nm-285nm}$  for these different tissues was different. This parameter could be used as criteria to separate benign from malignant tissue but failed to separate fibroadenoma from malignant tissue. The averaged value of  $f(r_{\infty})_{275nm-285nm}$  and  $f(r_{\infty})_{255nm-265nm}$  for fibroadenoma was  $5.23\pm5.69$  and  $3.62\pm4.41$  separately. It had higher value than benign tissue.

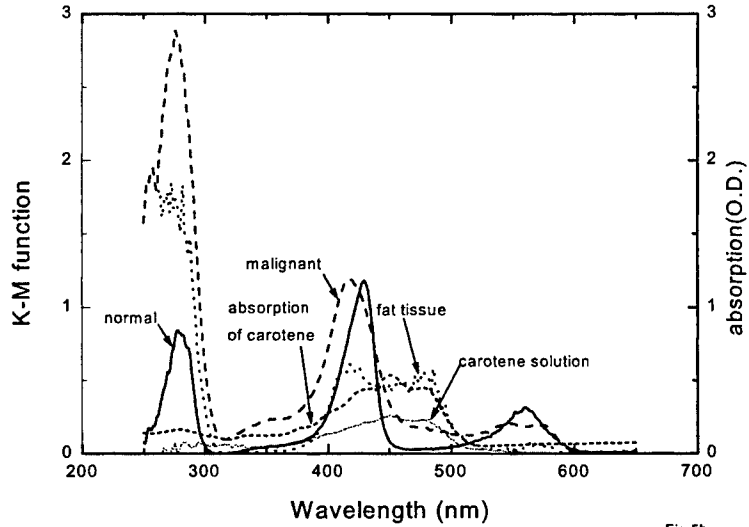


Fig.5b

Figure 3. The corresponding Kubelka-Munk functions of  $\beta$ -carotene solution, adipose, benign and malignant tissues transformed from diffuse reflectance spectrum. The absorption spectrum of  $\beta$ -carotene solution determined by transmission measurement was also presented for comparison.

Table 3: The averaged value of K-M function  $f(r_{\infty})$  and logarithm K-M function ( $\log f(r_{\infty})$ ) at 275nm–285nm and 255nm–265nm for different kind of breast tissues.

Type of specimen	Averaged at 275nm to 285nm		Averaged at 255nm to 265nm	
	$f(r_{\infty})$	$\log f(r_{\infty})$	$f(r_{\infty})$	$\log f(r_{\infty})$
Invasive carcinoma	13.11±10.39	0.98±0.39	19.05±18.70	1.06±0.52
Mixed invasive and <i>in situ</i>	5.23±4.16	0.58±0.36	8.78±13.30	0.65±0.50
Benign	0.88±0.69	-0.15±0.29	0.66±0.70	-0.36±0.39
Fibroadenoma	5.23±5.69	0.48±0.46	3.62±4.41	0.24±0.56
Adipose	4.92±0.69	0.50±0.44	8.32±10.31	0.55±0.68

Fibroadenomas are usually found in young women. It, the most common neoplasm of the breast, is a tumor composed of epithelial and stromal elements that originates from the terminal duct lobular unit. It is important to distinguish fibroadenoma from malignancy. From Table 3, it was found the averaged amplitude of  $f(r_{\infty})_{255\text{nm}-265\text{nm}}$  was higher than  $f(r_{\infty})_{275\text{nm}-285\text{nm}}$  for malignant tissue and lower for benign and fibroadenoma tissue. The another ratio parameter  $A=[f(r_{\infty})_{275\text{nm}-285\text{nm}}]/[f(r_{\infty})_{255\text{nm}-265\text{nm}}]$  was selected. The statistical averaged values, standard deviations and peak position of Gaussian fit curve of parameter A were given in Table 4. To explore the difference of parameter A for different kind of tissues had significant or not? The 't test' was calculated. The P value was equal to zero for either group the invasive carcinoma and fibroadenoma or group the mixed and fibroadenoma. The difference of A parameter between these two groups was significantly.

Table 4. The averaged value of parameter  $A=[f(r_{\infty})_{275\text{nm}-285\text{nm}}]/[f(r_{\infty})_{255\text{nm}-265\text{nm}}]$  for different kind breast tissues.

Type of specimen	$A=[f(r_{\infty})_{275\text{nm}-285\text{nm}}]/[f(r_{\infty})_{255\text{nm}-265\text{nm}}]$	
	Statistical mean value and standard deviation	Gauss fit center and width
invasive	0.93±0.52	0.85±0.35
Mixed invasive and <i>in situ</i>	0.89±0.36	0.85±0.31
Benign	1.97±1.42	1.49±0.84
Fibroadenoma	1.82±0.56	1.64±0.48

In conclusion, for malignant tissues, the proteins absorption was higher and the DNA absorption was found. For benign tissues, the absorption of proteins was lower and less DNA absorption was found. For fibroadenoma tissue, sometimes even the proteins absorption was as higher as malignant tissue, but less DNA absorption was found. Connected the change of absorption of DNA and proteins, malignant can be separated not only from benign tissue and also from fibroadenoma.

This research was supported by Organized Research of CUNY and DOE (Department of Energy).

## 5. REFERENCES

1. R. R. Alfano, Das Bidyut B., Joseph Cleary, Romulo Prudente, Edward J. Celmer. "Light sheds light on cancer-distinguishing malignant tumor from benign tissue and tumors The Bulletin of the New York Academy of Medicine (1991). 67 143-150,
2. Yuanlong Yang, A. Katz, Edward J. Celmer, Magaret Zarawska-Szczepaniak, and R. R. Alfano. "Fundamental Differences of Excitation Spectrum between Malignant and Benign Breast Tissues" Photochemistry and Photobiology (1997) 66(4): 518-522
3. N. Zhadin, Y. Yang, S. Ganesan, N. Ockman, R. R. Alfano. "Enhancement of the Fluorescence Cancer Diagnostic Method of Tissues Using Diffuse Reflectance and the Analysis of Oxygenation State." SPIE Proceeding (1996) 2697: 142-148
4. Irving J. Bigio, Judith R. Mourant, James Boyer and Tamara M. Johnson. "Invited: Elastic scattering spectroscopy for diagnosis of tissue pathologies" OSA TOPS on Biomedical Optical Spectroscopy and Diagnostics 1996, Vol. 3, p14-19, Eva Seveck-Muraca and David Benaron (eds.)
5. P. Kubelka and F. Munk. "Ein beitrag zur optik der farbanstriche" Z. Tech. Phys.(1931) 12, p.593
6. Wesley, WM. Wendlandt and Harry G. Hecht, "Reflectance Spectroscopy" p. 55-65, Interscience Publishers (1966)





## **SESSION 6**

### **OCT Biopsy**

# Interferometric 2D and 3D tomography of photoelastic media

Igor Patrickeyev\*, Valentin Shakhuridin\*\*

\* Institute of Continuous Media Mechanics, Perm, Russia

\*\* Perm State Technical University, Perm, Russia

## ABSTRACT

The experimental study of mechanical stress distribution in biological tissues in-vivo is of interest for some biomedical applications. This work considers the problem of light and stressed tissue interaction and the inverse problem of stress field reconstruction in 2D and 3D cases. Optical tomography is one of the most promising methods of solving these problems. This technique involves the reconstruction of the refractive index field using the measurements of waveform distortion. The reconstruction of stress field requires establishing the relation of the stress tensor to the variation of refraction index. A simple photoelastic model is a reasonable first approximation due to normal functioning of biological tissue. The propagation equation that describes the light propagation through the optically active elastic media obtained in the solving of the forward problem in terms of geometric optics approach. Interferometric, shlieren and depolarization methods of experimental data acquisition are considered. In general, 3D state of a stressed tissue should be described by six components of the stress tensor, but only three propagation equations appear to be independent. To close the system of equations, we have used three partial differential equilibrium equations with appropriate boundary conditions. The system of equations of interferometric tomography is studied in detail. In this case, the separation of stress tensor components results from analytical solving in the Radon domain. For special case of 2D deformation we need only one propagation equation and two equilibrium equations. It is shown that 3D problem can not be reduced to 2D problem in the general case of tensor field tomography. This sends us in search of special 3D algorithms. The use of wavelets is one of perspective ways of tomographic reconstruction under strong noise. 2D and 3D algorithms of the inverse Radon transform through inverse wavelet transform in noisy conditions have been developed.

**Keywords:** photoelasticity; interferometric method; tomography

## 1. INTRODUCTION

This work presents a new method of reconstruction of a stress field in the framework of a simple elastic model. This work has its origin in continuum mechanics where elastic media are currently of no concern because they are thought to be well - investigated. However, from a biomedical standpoint the elastic model is still interesting in the light of the normal tissue functioning. Possible applications of the method proposed are in-vivo diagnostics and monitoring.

## 2. PHOTOELASTIC RELATION AND LIGHT TRANSPORT EQUATION

The electromagnetic wave propagating through the anisotropic medium in the direction  $s$  splits into two waves, which have mutually perpendicular planes of polarization, as shown in Fig 1. These waves have different phase velocities or, in other words, the anisotropic medium can be characterized by two refractive indices dependent on the direction  $s$ .

The light transport equation obtained in terms of the geometric optics approach is derived as the solution of the wave equation

$$\frac{1}{c^2} \frac{\partial^2}{\partial t^2} D_i + \frac{\partial^2}{\partial x_i \partial x_j} E_j - \frac{\partial^2}{\partial x_j^2} E_i = 0, \quad (1).$$

where  $E$  is the electric intensity,  $D$  is the electric induction, and  $\epsilon$  is permittivity.

-----

Further information: contact Igor Patrickeyev, e-mail: [pat@icmm.ru](mailto:pat@icmm.ru), <http://www.icmm.ru/~pat>

In contrast to the anisotropic medium in which  $\epsilon$  is a tensor, the isotropic medium is characterized by a scalar permittivity.

Let us suppose that the tissue behaves in the same manner as the elastic medium. This model is a reasonable first approximation for the normal tissue functioning. In this case the Maxwell equation for piezoelectric effects defines the relationship between the permittivity and stress tensors

(2)

$$\epsilon_{ij} = [\epsilon_0 + (c_1 + 2c_2)\sigma_0]\delta_{ij} + (c_1 - c_2)\sigma'_{ij},$$

Here  $\epsilon_0$  is the permittivity of the initial (stress-free) medium,  $\sigma$  is the stress tensor, and  $c_1$  and  $c_2$  are the piezo-optic coefficients.

The permittivity tensor can be represented as an ellipsoid whose orientation and dimensions depend on the permittivity tensor components. Each central cross-section of the ellipsoid is an ellipse corresponding to the birefringence in the normal direction  $s$ . The ellipse axes are equal to refractive indices  $n$  defined as the square root of  $\epsilon$ .

In the special case of axial loading, each cross-section has two axes, one dependent on  $s$  and the other independent of  $s$ . These axes are the refractive indices of extraordinary ray  $n_e$  and ordinary ray  $n_0$ . The case when loads are directed along  $x_3$  is shown in Fig. 2. Here the ellipsoid is the ellipsoid of rotation. It has one optical axis coincident with the direction of loading. The birefringence effect caused by external loads is described for index  $n_e$  by equation

$$n_e = n_0 \sqrt{\frac{\epsilon_0 + c_1 \sigma_3}{\epsilon_0 + s_3^2 c_1 \sigma_3}}, \quad (3)$$

Here  $n_0$  is the refractive index in the stress-free medium. The maximal value of  $n_e$  corresponds to  $s$  perpendicular to loads (or the  $x_3$  axis in example) is

$$\left(\frac{n_e}{n_0}\right)_{\max} = \sqrt{1 + \frac{c_1 \sigma_3}{n_0^2}}.$$

If the loads have similar direction at each point, then the stress state will be described by the stress tensor component  $\sigma$  only. This value can be obtained from a scalar tomographic experiment in which the ray goes through 3D medium at different angles. The integral optical effects - rotation of the polarization plane or deviation of the ray from the rectilinear path - caused by the difference in refractive indices can be measured when the ray leaves the medium.

In 3D case the ellipse can have different orientations. Hence, unlike the scalar tomography where each medium point gives the same value independent of the direction of the light ray  $s$ , in 3D case the ellipsoid cross-sections depend on  $s$ . The integral optical effects depend on  $s$  as well. The principal values of the permittivity tensor  $\epsilon_1$  and  $\epsilon_2$  can be expressed in terms of the tensor component of the cross-section perpendicular to  $s$  as

$$\epsilon_{1,2} = \frac{1}{2}[(\epsilon_{11} + \epsilon_{22}) \pm \sqrt{(\epsilon_{11} - \epsilon_{22})^2 + 4(\epsilon_{12})^2}].$$

We have derived the same expression for the refractive index by expanding the square root into series and have retained the first terms for the case of weak birefringence. The substitution of this expression into equation (2) gives the final result

$$n_{1,2} = n_0 + \frac{c_1 + 2c_2}{2n_0} \sigma_0 + \frac{c_1 - c_2}{4n_0} [(\sigma_{11} + \sigma_{22}) \pm \sqrt{(\sigma_{11} - \sigma_{22})^2 + 4(\sigma_{12})^2}].$$

All above expressions are written in local coordinates. Equations of the absolute coordinate system are more complicated. The tomographic experiment is not reduced to translucence of a medium on independent parallel planes as in scalar tomography.

The tomographic experiment planning is required to answer the following questions. Which optical parameter should be measured in the experiment and how to reconstruct the stress field via experimental results? There are many methods of data acquisition different in their requirements to equipment and capability to reconstruct stresses. One of the well-defined methods is integrated photoelasticity. With this method, the difference in optical paths  $\Delta\zeta$  is measured

$$\Delta\zeta = \frac{c_1 - c_2}{4n_0} \int \sqrt{(\sigma_{ij} b_i b_j - \sigma_{ij} q_i q_j)^2 + 4(\sigma_{ij} b_i q_j)^2} ds. \quad (5)$$

The obtained data depend non-linearly on the stress tensor components. Hence we can reconstruct the stress by solving the system of non-linear equations. However this solution is effective in some special cases only. The other method suggests the measurement of the sum of optical paths by an interferometer. In contrast to the above method, we have the linear dependence of the measured parameter on stress tensor components. This linearity allows us to solve analytically the equation system. The value obtained by this method is expressed by equation

$$l(r, \vec{e}) = \int [f(\vec{x}) + s_i s_j g_{ij}(\vec{x})] \delta(\langle \vec{x} | \vec{e} \rangle - r) d\vec{x}, \quad (6)$$

which involves the following functions:  $f$  being proportional to  $\sigma$  and  $g$  describing the medium anisotropy.

Normally the tomographic problems are formulated in terms of the Radon transform. In other words, the acquired value can be redefined by the Radon transform operator

$$l(r, \vec{e}) = \mathcal{R}_2 f(r, \vec{e}) + s_i s_j \mathcal{R}_2 g_{ij}(r, \vec{e}). \quad (7)$$

The shadow method can be represented as the variation of the interferometric method. With this method we can measure the angular deviation of the ray path from rectilinearity. The value acquired by this method can be written in the Radon form

$$\theta(r, \vec{e}) = \mathcal{R}'_2 f(r, \vec{e}) + s_i s_j \mathcal{R}'_2 g_{ij}(r, \vec{e}), \quad (8)$$

In this equation the radial derivative of Radon image is given in a concise form

$$\mathcal{R}'_n f(r, \vec{e}) = \frac{\partial \mathcal{R}_n f(r, \vec{e})}{\partial r}. \quad (9)$$

From equations (7) and (8) it follows that all stress components contribute to a measured value. The stress field reconstruction based on the measured data belongs to the class of ill-posed problems. With Tikhonov's classification in mind, we can note that this problem is not completely defined for most stress states. In other words, the number of independent light transport equations is less than the number of unknown variables. In the event of scalar tomography we have one light transport equation, and, therefore, only the mean value of stress can be reconstructed. In 3D case we have extended the scope of plane tomography and suggest a new experimental scheme. It must be emphasized that in the general case we have only three independent light transport equations, whereas the complete description of the stress state requires six stress tensor components. Because of this, the obtained experimental information is sufficient only for some special cases of the stress state. Thus, for 3D case we need additional equations.

### 3. EQUILIBRIUM EQUATIONS

To close the system of light transport equations, the equilibrium equations with corresponding boundary conditions have been used

$$\begin{aligned}\frac{\partial \sigma_{11}}{\partial x_1} + \frac{\partial \sigma_{12}}{\partial x_2} + \frac{\partial \sigma_{13}}{\partial x_3} + v_1^* &= 0, \\ \frac{\partial \sigma_{12}}{\partial x_1} + \frac{\partial \sigma_{22}}{\partial x_2} + \frac{\partial \sigma_{23}}{\partial x_3} + v_2^* &= 0, \\ \frac{\partial \sigma_{13}}{\partial x_1} + \frac{\partial \sigma_{23}}{\partial x_2} + \frac{\partial \sigma_{33}}{\partial x_3} + v_3^* &= 0.\end{aligned}\tag{10}$$

In this expression  $v^*$  denotes volume loads. It is interesting to note that in the proposed method the surface loads are assumed to be concentrated in the near-surface volume. This statement was numerically illustrated in [1]. The equilibrium equations can be written in the Radon form taking into account the relation between the Radon transform of the function derivative and the radial derivative of the Radon image of this function

$$\Re_n \left[ \frac{\partial \xi(x_1 \dots x_n)}{\partial x_j} \right] = e_j \Re'_n \xi(r, \bar{e}),\tag{11}$$

The final expression for 3D case is as follows

$$\begin{aligned}\cos \psi \cos \phi \Re' \sigma_{11} + \cos \psi \sin \phi \Re' \sigma_{12} + \sin \psi \Re' \sigma_{13} + \Re v_1^* &= 0, \\ \cos \psi \cos \phi \Re' \sigma_{12} + \cos \psi \sin \phi \Re' \sigma_{22} + \sin \psi \Re' \sigma_{23} + \Re v_2^* &= 0, \\ \cos \psi \cos \phi \Re' \sigma_{13} + \cos \psi \sin \phi \Re' \sigma_{23} + \sin \psi \Re' \sigma_{33} + \Re v_3^* &= 0.\end{aligned}$$

In this expression,  $\phi$  and  $\psi$  denote the angular coordinates of vector  $\bar{e}$  in spherical coordinates.

### 4. ANALYTICAL SOLUTIONS FOR RADON IMAGES IN 2D AND 3D CASES

Now we can separate the stress components. The proposed method is based on the analytical solution in Radon space.

The special case of the plane stress state in 3D medium is described by three stress tensor components. A priori known that the remaining components are equal to zero. The complete system consists of one light transport equation and two equilibrium equations

$$\theta = \mathfrak{R}'_2 f + s_1^2 \mathfrak{R}'_2 g_{11} + s_2^2 \mathfrak{R}'_2 g_{22} + 2s_1 s_2 \mathfrak{R}'_2 g_{12},$$

$$\cos \varphi \mathfrak{R}'_2 \sigma_{11} + \sin \varphi \mathfrak{R}'_2 \sigma_{12} + \mathfrak{R}_2 v_1^* = 0,$$

$$\cos \varphi \mathfrak{R}'_2 \sigma_{12} + \sin \varphi \mathfrak{R}'_2 \sigma_{22} + \mathfrak{R}_2 v_2^* = 0.$$

(12)

Finally, the solution of this system yields equation

$$\mathfrak{R}'_2 \sigma_{11} = \sin^2 \varphi k_2 M - \cos \varphi \mathfrak{R}_2 v_1^* + \sin \varphi \mathfrak{R}_2 v_2^*,$$

$$\mathfrak{R}'_2 \sigma_{22} = \cos^2 \varphi k_2 M + \cos \varphi \mathfrak{R}_2 v_1^* - \sin \varphi \mathfrak{R}_2 v_2^*,$$

$$\mathfrak{R}'_2 \sigma_{12} = -\cos \varphi \sin \varphi k_2 M - \sin \varphi \mathfrak{R}_2 v_1^* - \cos \varphi \mathfrak{R}_2 v_2^*,$$

(13)

where the Radon images of components are expressed via experimentally measured values and boundary conditions and  $M$  denotes

$$M = \theta - \cos \varphi \mathfrak{R}_2 v_1^* - \sin \varphi \mathfrak{R}_2 v_2^*.$$

A general solution for 3D case can be derived in the same way. First, we should close the system by combining three equilibrium equations with corresponding boundary conditions and three light transport equations. This system in a concise form is

$$\begin{cases} \theta_k = \mathfrak{R}'_3 f + s_{i < k} s_{j < k} \mathfrak{R}'_3 g_{ij}, & k = 1, 2, 3 \\ e_j \mathfrak{R}'_3 \sigma_{ij} + \mathfrak{R}_3 v_i^* = 0, & i = 1, 2, 3. \end{cases}$$

(14)

Then we obtain the solution for functions  $f$  and  $g$

$$\mathfrak{R}'_3 f = \frac{I + V}{2 - c},$$

$$\mathfrak{R}'_3 g_{11} = (I - I_1 + 2V_1) - [1 + (1 - 2c)e_1^2] \mathfrak{R}'_3 f,$$

$$\mathfrak{R}'_3 g_{22} = (I - I_2 + 2V_2) - [1 + (1 - 2c)e_2^2] \mathfrak{R}'_3 f,$$

$$\mathfrak{R}'_3 g_{33} = (I - I_3 + 2V_3) - [1 + (1 - 2c)e_3^2] \mathfrak{R}'_3 f,$$

$$\mathfrak{R}'_3 g_{12} = \frac{I(1-e_1^2-e_2^2)-I_1(1-e_2^2)-I_2(1-e_1^2)-2e_2V_1-2e_1V_2+2e_1^2e_2^2(1-2c)\mathfrak{R}'_3f}{-2e_1e_2},$$

$$\mathfrak{R}'_3 g_{23} = \frac{I(1-e_2^2-e_3^2)-I_2(1-e_3^2)-I_3(1-e_2^2)-2e_3V_2-2e_2V_3+2e_2^2e_3^2(1-2c)\mathfrak{R}'_3f}{-2e_2e_3},$$

$$\mathfrak{R}'_3 g_{13} = \frac{I(1-e_1^2-e_3^2)-I_1(1-e_3^2)-I_3(1-e_1^2)-2e_3V_1-2e_1V_3+2e_1^2e_3^2(1-2c)\mathfrak{R}'_3f}{-2e_1e_3},$$

where

$$I = I_1 + I_2 + I_3, \quad V = V_1 + V_2 + V_3$$

$$I_i = (1-e_i)\theta_i, \quad V_i = e_i\mathfrak{R}_3 v_i^*.$$

And finally, we can write the Radon images of all components

$$\mathfrak{R}'_3 \sigma_{22} = \frac{2n_0}{c_1+2c_2} \mathfrak{R}'_3 f + \frac{4n_0}{c_2-c_1} \mathfrak{R}'_3 g_{22},$$

$$\mathfrak{R}'_3 \sigma_{11} = \frac{2n_0}{c_1+2c_2} \mathfrak{R}'_3 f + \frac{4n_0}{c_2-c_1} \mathfrak{R}'_3 g_{11},$$

$$\mathfrak{R}'_3 \sigma_{33} = \frac{2n_0}{c_1+2c_2} \mathfrak{R}'_3 f + \frac{4n_0}{c_2-c_1} \mathfrak{R}'_3 g_{33},$$

$$\mathfrak{R}'_3 \sigma_{12} = \frac{4n_0}{c_2-c_1} \mathfrak{R}'_3 g_{12},$$

$$\mathfrak{R}'_3 \sigma_{13} = \frac{4n_0}{c_2-c_1} \mathfrak{R}'_3 g_{13},$$

$$\mathfrak{R}'_3 \sigma_{23} = \frac{4n_0}{c_2-c_1} \mathfrak{R}'_3 g_{23}.$$

(15).

## 5. RECONSTRUCTION ALGORITHMS

We have solved the problem for Radon images analytically and now it is necessary to calculate the inverse Radon transform numerically. There are many tomographic algorithms and most of them are used for 2D reconstruction from projections. We have developed a new algorithm, which belongs to the class of so-called «p - filtering» and can be adapted for 2D and 3D cases. The algorithm involves filtering and back projecting. In practice, for stable reconstruction, it is necessary to provide the data denoising at high frequencies. Usually, this operation is introduced into the filtering technique.

Figures 3 and 4 shows the filter gain - frequency curves, which are linear and parabolic in 2D and 3D cases, respectively. These curves are plotted for the noiseless data. To obey the regularization requirement, we should suppress the signal at high frequencies. As a result, the gain curve tends to zero in this domain. This decreases the accuracy of reconstruction but ensures its stability. Thus, we can obtain the stress components from their Radon images or radial derivatives of Radon images.

The new algorithm is based on the wavelet transform and allows us to perform the data denoising simultaneously with reconstructing. Let us recall the definition of the Radon transform

$$\mathcal{R}_n f(r, \vartheta) = \int_{R^n} f(\bar{x}) \delta(\langle \bar{x} | \vartheta \rangle - r) d\bar{x} \quad (16)$$

This equation describes the projection on a secant hyperplane. For 2D case the hyperplane is a straight line, and for 3D a plane. By means of the wavelet analysis, we can redefine the Radon transform as a singular wavelet transform, where T is the translation,  $\Omega$  is the rotation and D is the dilation operators as

$$\mathcal{R}_n f(r, \vartheta) = \int_{R^n} f(\bar{x}) (T' \Omega^\vartheta D^a \delta)(\bar{x}) d\bar{x} \quad (17)$$

The  $\delta$ -function is not a wavelet in a strict sense, because its mean value is not equal to zero and it is an invariant to dilation. However, all main principles of the wavelet analysis are applicable to this function. For example, each projection line can be obtained by means of rotations and translation of a fixed straight line. The wavelet image of the function is related to its Radon-image

$$\tilde{f}(\bar{b}, a, \varphi) = \frac{1}{a} \mathcal{R} f(\langle \bar{b} | \vartheta \rangle, \varphi) \quad (18)$$

This result was obtained by Mattias Holschneider in 1990 [2].

Hence we can reconstruct the function from its wavelet image at noiseless scales. For this, we should take the synthesizing wavelet h that will compensate the singularity of  $\delta$ -function.

$$f(\bar{x}) = \lim_{\varepsilon \rightarrow 0, \rho \rightarrow \infty} \int_{\varepsilon}^{\rho} \frac{da}{a} \int_0^{2\pi} d\varphi \int_{-\infty}^{\infty} \tilde{f}(\bar{b}, a, \varphi) (T^{\bar{b}} \Omega^\vartheta D^a h)(\bar{x}) d\bar{b}$$



## **6. CONCLUSION**

Finally, the proposed method can be outlined as follows:

- 1) The acquired data and a priori information are processed on computer to tabulate the separated Radon images and to numerically reconstruct the stress tensor components according to the scheme shown in Figure 5.
- 2) The proposed approach is intended to reconstruct the stress state of a medium in 3D case. It can be simplified by applying the additional information in the event of special stress states.

## **ACKNOWLEDGEMENT**

Presentation of this work at conference is supported by RFBR travel grant 00-01-10504.

## **REFERENCES**

1. I.Patrickeyev, V.Shakhuridin, "Boundary conditions in the research of stress/strain state by Radon transform method", Proceeding of OE/LASE #2146-50, Los Angeles, January, 1994.
2. M.Holschneider, "Inverse Radon Transform through inverse wavelet transform", Prep.No P2364 CPT90, C.N.R.S. (Feb.1990).

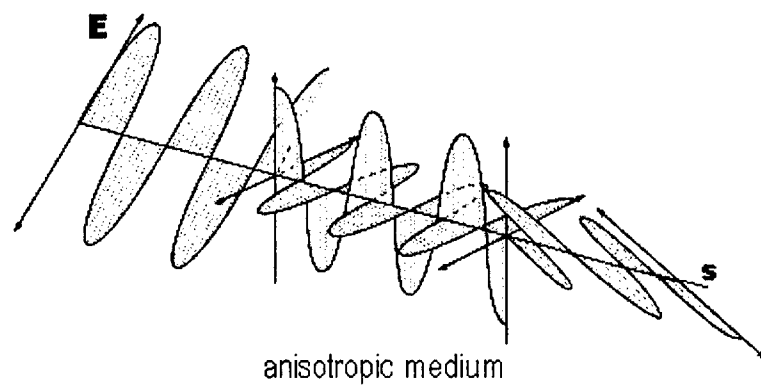


**Fig. 1.**

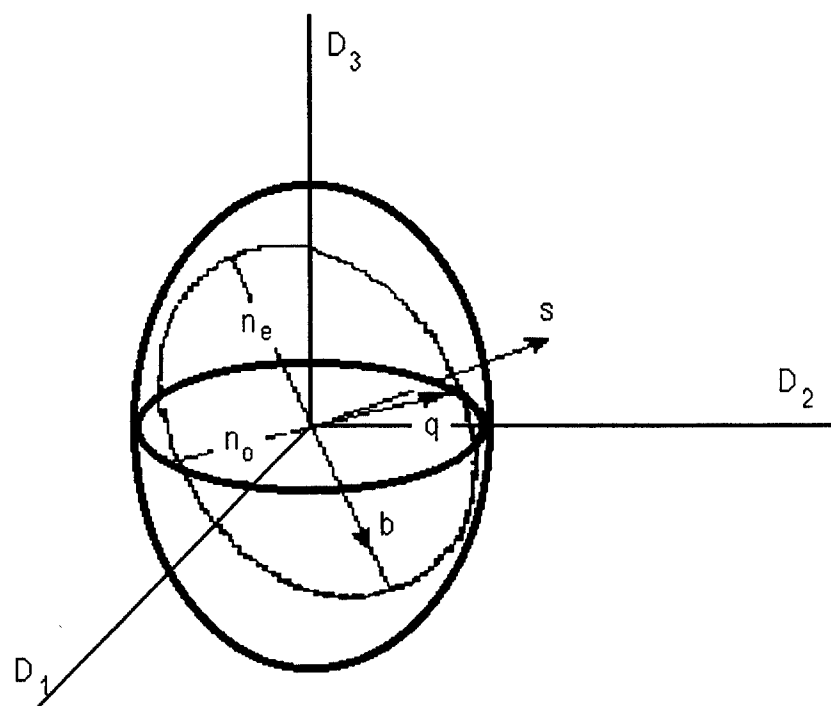


**Fig. 2**

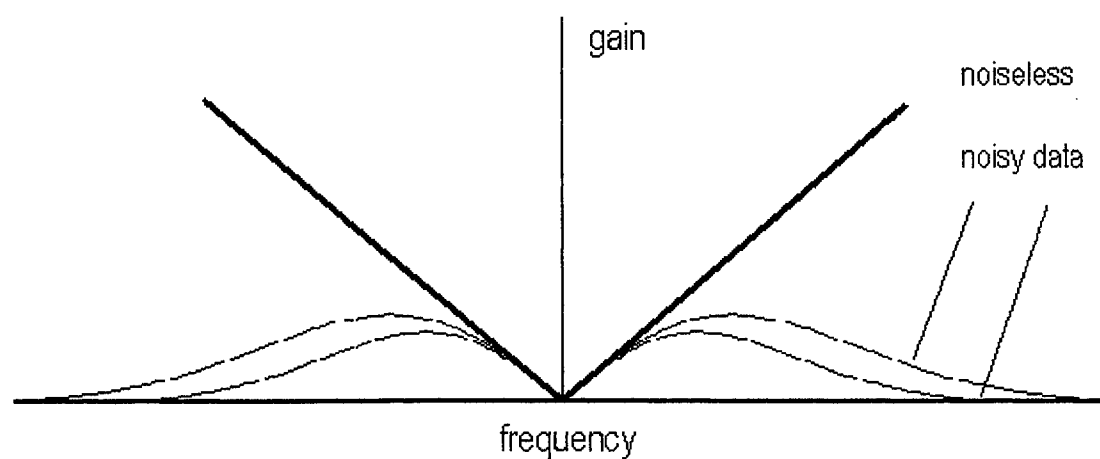


Fig. 3

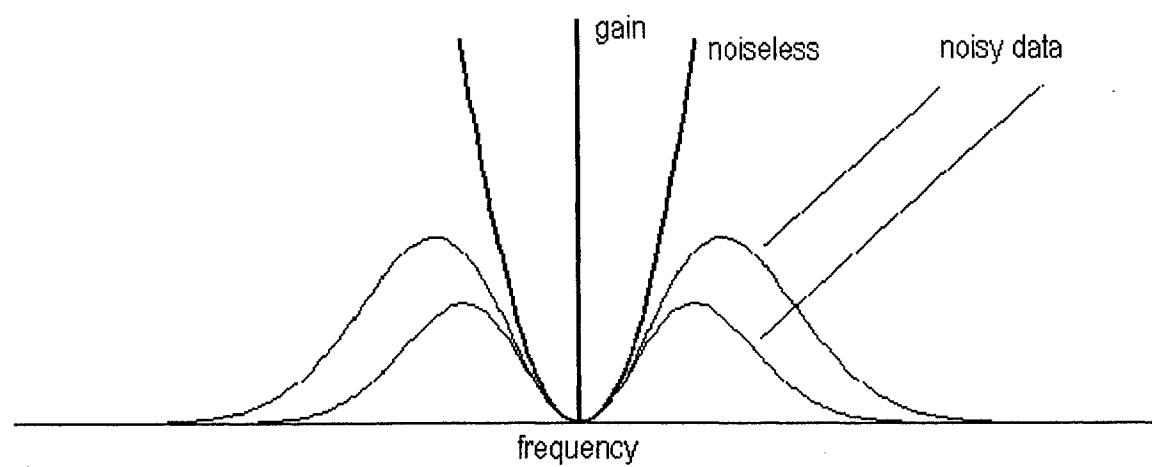


Fig. 4



## **SESSION 7**

### **Optical Properties**

# Non-invasive determination of concentration of compounds in strongly absorbing biological tissue

René A. Bolt<sup>1¶a</sup>, Johannes S. Kanger<sup>a</sup>, Frits F. M. de Mul<sup>a</sup>,  
Xiaomao Wu<sup>b</sup>, Shu-Jen Yeh<sup>b</sup>, and Omar S. Khalil<sup>b</sup>

<sup>a</sup>University of Twente, Enschede, the Netherlands

<sup>b</sup>Abbott Laboratories, Abbott Park, IL 60064, The United States of America

## ABSTRACT

We describe a non-invasive method for the determination of optical parameters of highly scattering media, such as biological tissue. An advantage of this method is that it does not rely on diffusion theory, thus it is applicable to strongly absorbing media and at small source-detector separations. Monte Carlo simulations and phantom measurements are used to illustrate the achievable accuracy of the system. The method was applied to non-invasive in-vivo tracking of haemoglobin concentration in biological tissue. The results correlated well to clinically (invasively) determined Hb concentrations.

**Keywords:** Tissue Optics, Light Scattering, In Vivo measurement, Haemoglobin, Analytes, Non-Invasive, Optical Parameters.

## 1. INTRODUCTION:

The use of optical methods for non-invasive determination of tissue and blood components has advanced in the last few years. Pulse oximetry<sup>1</sup>, laser Doppler flowmetry<sup>2</sup>, bilirubin determination in neonates and oxygen saturation in tissue are just a few examples<sup>3</sup>. The common phenomena that are detected are changes in the absorption and scattering properties of tissue as a result of the variation in concentration of a compound or a structural change in tissue. The experimental procedure usually involves measurement of reflectance, transmittance of a tissue at a specific body site and correlating the optical parameters with clinical data. Most algorithms rely on the hypothesis that the tissue is highly scattering and can be modelled as a semi-infinite homogeneous slab. This simplifying assumption is based upon the observations in some occasions that photons undergo many scattering events before being detected, the scattering coefficient of tissue at the wavelength of observation is much larger than the absorption coefficient, and the medium is homogeneous. Some of these requirements are difficult to fulfil in human tissue, skin tissues in particular, partly because of the high absorption of haemoglobin and other pigments at near-infrared wavelengths. We describe a method that does not depend on the diffusion theory approximation, thus it can be used at wavelengths where absorption by the tissue is high and can be applied for the in-vivo determination of haemoglobin in tissue.

---

<sup>¶</sup> e-mail r.a.bolt@tn.utwente.nl, Bio Physical Techniques Group, Department of Applied Physics, University of Twente, P/O Box 217, NL-7500 AE Enschede, the Netherlands. Phone (+31) 53 489 3157, Fax (+31) 53 489 1105

## 2. BACKGROUND:

Although invasive methods for the determination of body components are established for the diagnosis of a variety of diseases, non-invasive measurements offer several advantages. Alleviating pain and biohazard contamination are two major advantages. Secondly, difficulty of obtaining sufficient samples from paediatric and geriatric patients is also reduced. The potential for developing rugged non-invasive devices for testing for hematoma, internal body injuries, port-wine stains, bilirubinemia in neonates, anaemia, and other metabolic disorders and tissue structural defects enhances patient care and ease of early detecting and treating various diseases. Non-invasive determination of these components is predicated upon the ability to determine tissue optical parameters in a simplified way, such as presented in this paper.

## 3. THEORY:

Several theoretical approaches can be followed to deduce the optical parameters of tissue and hence the concentration of analytes or structural features. Analytical approaches, such as the diffusion theory approximation, require the validity of a number of assumptions. Among others, the medium must be predominantly scattering ( $\mu_s' \gg \mu_a$ ), and the detected light must have been multiply scattered in the medium (long diffusion path)<sup>4,5,6</sup>. Numerical methods, such as the Monte Carlo simulations, do not have these requirements but are computation-intensive and time consuming. It is not always possible to fulfil the requirements of the analytical approach in measurements on human body parts. For instance, the absorption of haemoglobin in the relevant region of its spectrum is of the same magnitude as the scattering of tissue. In a medium with significant absorption, the diffusion theory approximation can not be used. The Monte Carlo approach, on the other hand, is universally applicable but it is very laborious to do an inversion, *i.e.*, to extract the optical parameters from the experimental data. To overcome this problem, we developed a 2-dimensional diagram, which relates the measured data directly to the scattering and absorption coefficients, as suggested by Groenhuis et al<sup>7,8</sup>. In our system, the tissue is illuminated with a

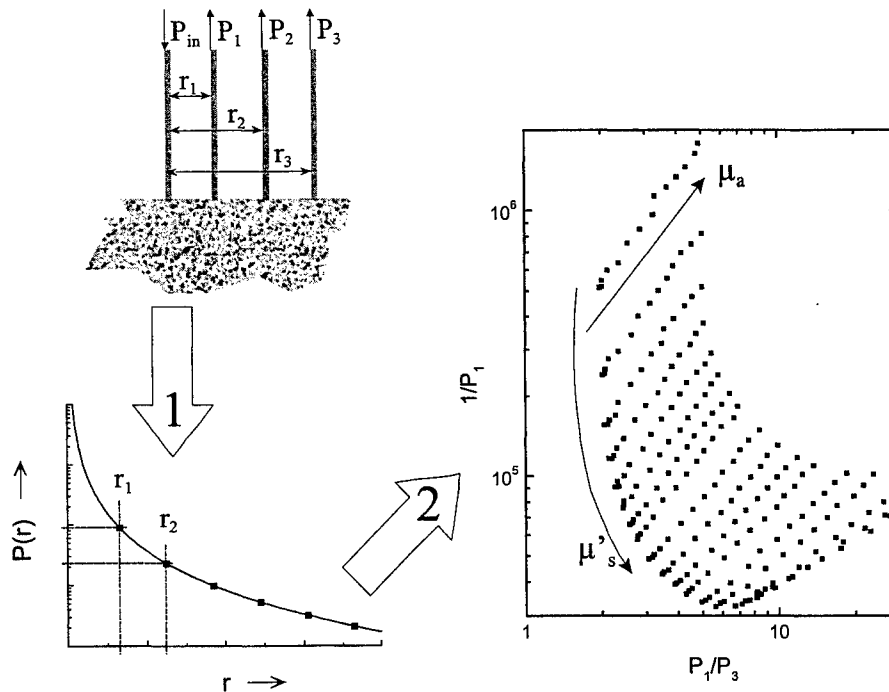


**Figure 1.** The principle of our method: we use a fibre probe to measure the reflected intensities  $P_1, P_2, P_3$  at radial distance  $r_1, r_2$  and  $r_3$  (Spatially Resolved Diffuse Reflectance measurement, SRDR). Then we insert a pair of these reflectance data in a 2-dimensional reference diagram. The figure shows such a diagram relating  $P_1$  and  $P_3$  on one hand to the absorption  $\mu_a$  and reduced scattering  $\mu'_s$  on the other hand. The reference diagram can be calculated using Monte Carlo simulations, or be determined from phantom measurements. To derive the optical parameters from the diagram, we use a Matlab interpolation program.

fibre, and reflected light is detected at two or more radial distances  $r_1$  and  $r_2$ , as indicated in figure 1. Thus the level of the reflectance curve is measured at two source-detector distances, namely at a small and a larger source-detector separations. In this aspect it differs from the method suggested by Bevilacqua et al, where the level and the slope are determined at a single distance by adapting a fit-function to measured reflectances at multiple radial distances<sup>9,10</sup>. We then use a reference grid to relate the two reflectance measurements  $P_1$  and  $P_2$  to the absorption and reduced scattering coefficient  $\mu_a$  and  $\mu'_s$  of the tissue. The grid is created from Monte Carlo simulations<sup>11</sup> on light propagation in a tissue model and calibrated with experimental data on phantoms with known optical properties. To find the optical parameters of an unknown sample, the reflectance data is processed using an interpolation program written in Matlab to get the absorption and scattering coefficients from the grid. As an example, the absorption coefficients of the tissue were obtained in such way and were correlated with the haemoglobin values determined from venous blood using clinical reference methods.

#### 4. EXPERIMENTS:

**4.1 Experimental set-up for the spatially resolved diffuse reflectance measurement (SRDR):** We constructed two different experimental set-ups, both using optical fibres for light delivery, multiple wavelength selection in the visible and near infrared and light detection at several radial distances from the source. The light-source is a 100-Watt QTH lamp (Oriel 66181) powered by a radiometric power supply (Oriel 68735). In one set-up, we use interference filters (Corion, 10 nm bandwidth) for the wavelength selection. A chopper (SR541, Stanford Research) is used to modulate the light source, and detection takes place by a silicon photodiode (Hamamatsu S-2386) and a lock-in amplifier (SR830, Stanford Research). Using a Labview program, the data are read into a personal computer via the IE<sup>3</sup> interface. This system is depicted in figure 2.

A second system uses four individual fibre spectrometers (Carl Zeiss MMS Vis-Enh modules, 14 bit dynamic range) for light detection, and does not use the chopper and filter wheel. Readout of these modules is by a dedicated interface (TEC-5, FEE-003-Vx Front-end electronics, MUX-4 Multiplexer, and PD-ISA 16V3 interface card) using a Labview program. Although these modules do not allow the use of phase sensitive detection (making the set up more sensitive to disturbances by, e.g., ambient light), they have an advantage over the filter-wheel system. We can simultaneously measure four fibres (and therefore four radial distances) over the wavelength range of 400 to 1100 nm (3 nm per pixel resolution). This enables us to measure reflection spectra, instead of reflection values at a number of discrete wavelengths. This is clearly a big advantage for spectroscopy applications, such as the detection of compounds in human tissue.

For both systems, an identical probe was used. This consists of 7 fibres (Custom built, Fiberguide Industries, using Fiberguide AFS400/440N fibre, core diameter 400  $\mu\text{m}$ , numerical aperture 0.22). One fibre is used for light delivery to the sample, the others for detection, for normalisation purposes we included a reference fibre. The probe geometry is depicted in Figure 2b.

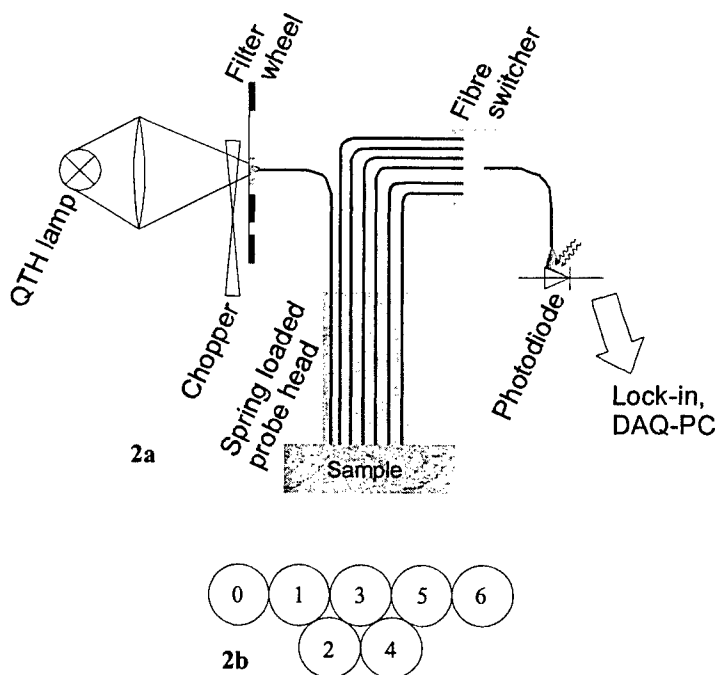


**Figure 2a/b.** Sketch of the experimental set up. In 2a, the set up is shown with a filter wheel, lock-in system, and a silicon photodiode for detection. In another arrangement, we leave out the chopper and lock-in system, and replace the filter wheel by a four-channel fibre spectrometer system (see text).

Fig. 2b shows the arrangement of the fibres in the probe head. Fibre 0 is used for light delivery, fibres 1 through 6 for detection. Fibre size is 400/440  $\mu\text{m}$ . The reference fibre is not shown.



**4.2 Reference grid generation: Monte Carlo simulations.** Monte Carlo simulations<sup>11</sup> were performed in parallel with the experimental determination to generate a reference grid. A series of simulations based on Intralipid phantoms (with a wide range of absorption and scattering coefficients) were run to create the reference grid. The scattering phase function was calculated from Mie theory, in such a way that the anisotropy factor  $g$  matches the values known from literature<sup>12</sup>. A number of experimental data points were run for samples with optical properties within the range used for calculating the reference grid. Using the scheme discussed above, the optical properties of “unknown” samples could be determined by interpolation. The accuracy of the absorption and scattering coefficients is believed to be better than  $\pm 10\%$ .

The experimental set-up and the method of determination of the absorption and scattering coefficients were applied to dye solutions in Intralipid suspensions. As a reference sample, we used diluted Intralipid samples without added dye.

We prepared a mixture of Intralipid and dye (Evans blue), and determined the absorption and scattering spectra of both components individually using a Shimadzu spectrophotometer (solid lines in Figure 3). Then we measured the reflectances at 2 distances using our fibre probe depicted in Figure 2. Using the separation technique described above, we calculated back from the reflectance values to the absorption and scattering spectrum of the mixture. The results are shown in Figure 3 (dotted lines). In the region of maximum absorption (around 625 nm), however, there is some cross-talk between absorption and scattering. This results in an underestimation of the scattering coefficient. We expect that we can minimise this effect by optimising the probe geometry and the analysis algorithm.

The absorption and scattering spectra determined with our method for the mixture of Intralipid and dye are in good agreement with the known spectra of the components, corrected for the concentrations used for preparing the mixture.

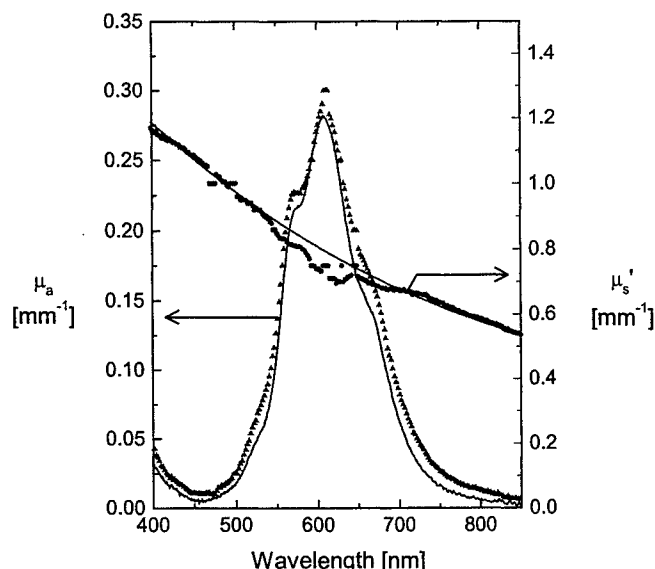


**Figure 3** Absorption and scattering spectra for Intralipid and dye measured separately using the spectrophotometer (solid line), and the absorption and scattering spectrum for an according mixture of Intralipid and dye, as determined using our method as outlined in section 3, theory.

**4.3 Phantom measurements and accuracy of the method:** In order to determine the achievable accuracy, we ran a number of test measurements. First of all, we used solid phantoms (white translucent nylon, white Delrin, and Spectralon) to determine the intrinsic stability of the measurements. In this situation, all variations in the measurement are caused by the set-up, and not by the phantom. In our measurements, we determine the ratio between the various fibres (e.g.,  $P_1/P_2$  and  $P_{ref}/P_1$ ). Therefore we focussed on these ratios. We found that these values are stable to typically 0.05% for the solid phantom measurements. Thus, the smallest measurable change in ratio is about 0.05%.

We used the set-up to determine the actual accuracy based on liquid phantom measurements. We prepared a series of Intralipid plus dye samples, the optical parameters of which are shown in table 1.

**Table 1.** Optical parameters of the samples used for simulation and test measurements. In essence, the samples are centred on sample E, with variations of plus and minus 20% in the scattering and absorption coefficient. Samples consist of Intralipid and dye (Ecoline Dark Green)

Sample	400 nm		500 nm	
	$\mu_a$ [mm <sup>-1</sup> ]	$\mu'_s$ [mm <sup>-1</sup> ]	$\mu_a$ [mm <sup>-1</sup> ]	$\mu'_s$ [mm <sup>-1</sup> ]
A	0.0721	2.11	0.0030	1.73
B	0.0721	2.53	0.0030	2.07
C	0.0721	3.03	0.0030	2.48
D	0.0901	2.11	0.0037	1.73
E	0.0901	2.53	0.0037	2.07
F	0.0901	3.03	0.0037	2.48
G	0.1081	2.11	0.0045	1.73
H	0.1081	2.53	0.0045	2.07
I	0.1081	3.03	0.0045	2.48
Water absorption	$1.7 \times 10^{-5}$		$2.6 \times 10^{-5}$	
Anisotropy factor (g)	0.868		0.810	

**Figure 4.** Scattering of Intralipid and absorption of Ecoline 602 as a function of wavelength, determined from collimated transmission measurements.

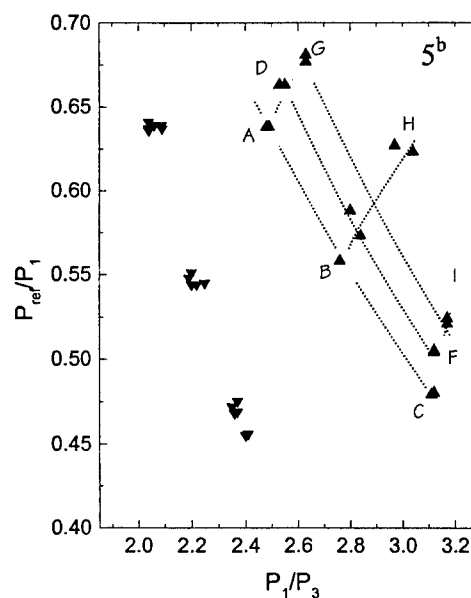
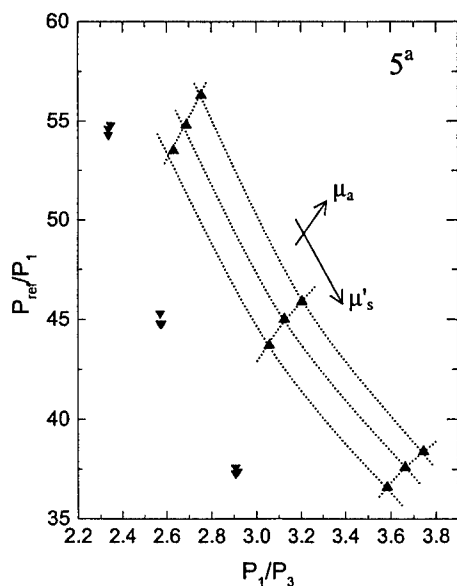
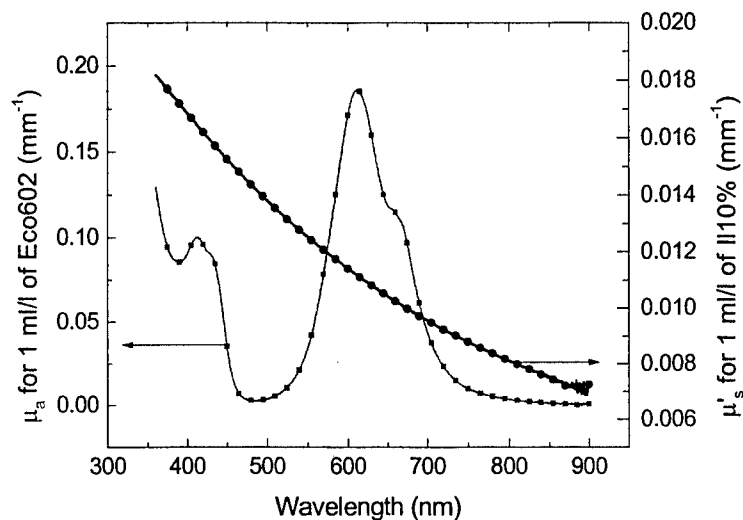


**Figure 5.** Simulations (5a) and measurements (5b) of the diagram for the sample optical parameters shown in Table 1. ▲ indicates data for 400 nm, ▼ indicates data obtained for 500 nm. Each experimental data point is an average over 20 measurements, the standard deviation is typically 0.1% or better. The digits correspond to those in table 1.

We used diluted Ecoline 602 (dark green) as a dye. This is a purely absorbing, non-scattering ink. The scattering part of the solution was diluted Intralipid 10%, which is mainly scattering (absorption is assumed to be mainly water absorption, this is consistent with the findings by van Staveren<sup>12</sup>). The samples were prepared by volumetric dilution of stock suspensions; the absorption and scattering coefficients of which were determined from collimated transmission measurements. Of each sample, we prepared 2 identical items. The optical parameters of Ecoline 602 and Intralipid are shown in figure 4.

In order to compare the data to theoretical predictions, we ran a series of Monte Carlo simulations for a semi-infinite medium with a transparent probe surface. These simulations give us similar data as the measurements (reflectance versus source-detector separation). From these data, we calculated a theoretical grid, following the procedure outlined in figure 1. The results for wavelengths of 400 and 500 nm are shown in figure 5a.

We then ran the 9 samples through the experimental procedure, and again the grid was calculated. The experimental results at 400 and 500 nm are shown in figure 5b. Each data point in this grid represents an average over 20 measurements. The smallest detectable change in optical parameters (at 400 nm) is approximately  $3 \times 10^{-4} \text{ mm}^{-1}$  in absorption coefficient, and  $1.5 \times 10^{-3} \text{ mm}^{-1}$  in reduced scattering coefficient, assuming averaging of 20 measurements and a signal to noise ratio of 1. Between 500 nm and 800 nm, the accuracy is improved by a factor of 3 or more due to higher sensitivity of the system.

In the experiments, we see that sample H is not on its expected position; this is caused by an error in preparing the sample. About 25% too much dye was added, resulting in a change in absorption relative to the 'central sample' (sample E) of +50%, instead of the expected 20%. This is consistent with its position in figure 4b.

The shape of the diagrams calculated from Monte Carlo simulations and from experimental data is not completely identical. This is explained by the fact that the simulations do not exactly match the measurement geometry. For the measurements, we use a probe with a reflecting (metal) area around the 7 fibres. The Monte Carlo simulations are done with a completely transparent, non-scattering layer on top, in a geometry where all of the probe-surface acts as a detector. Thus, in the simulation all photons that are emitted from the surface are detected in the probe. Effectively, this corresponds to a black probe surface, as can be seen from Monte Carlo simulations<sup>13</sup>. In the experiments, photons that emerge from the sample can be reflected back from the probe surface into the sample, thus altering the reflectance values, angular distribution, path length distribution, and other characteristics of the reflected photons (see for example US patent 5,825,488<sup>14</sup>). These effects can change measured reflectance by 10% or more. The impact of this effect on the diagram depends on the distances between the fibres, and also on the optical parameters of the material. Consequently the diagram is deformed relative to the diagram predicted from Monte Carlo calculations, and also the  $P_1/P_3$ -axis values are altered. The y-axis ( $P_{\text{ref}}/P_1$ ) is also shifted, but this is caused by a normalisation effect (the Monte Carlo simulations are normalised differently than the measurements). The difference between simulations and experiments would vanish by performing simulations based on the exact probe geometry. This, however, introduces a tremendous increase in calculation time. Only recently, we acquired a suitable computer system (Sun HPC450, 4x400MHz UltraSparcII processor and 4 GB of internal memory) to handle this task. In the near future, we will use this system for elaborate simulations.

In both the simulations and the experiments, the diagram at 400 nm is much broader in the absorption-direction than at 500 nm. This is caused by the fact that the absolute values of absorption, as well as absolute changes in absorption, are much larger at 400 nm.

Data for duplicate samples measurements are shown in Figure 5b. Two supposedly identical samples were prepared for each combination of optical parameters shown in Table 1. This was done by preparing 100 ml of sample volume, then equally dividing it over two identical sample containers. Data points for duplicate samples did not coincide. This effect is most clearly seen for the 'central' sample (E in table 1) and for sample H. It is not caused by differences in optical coupling between probe and sample; lifting the sample from the probe, then re-seating it exactly reproduces the data points. Therefore, we conclude that it is caused by small differences in sample optical parameters. This also indicates the difficulty of producing well-defined reference samples. We are working on a high-frequency modulated system to determine the exact optical parameters of the samples in an independent way<sup>15</sup> to solve this problem.

**4.4. In-vivo measurements: haemoglobin detection.** The experimental set-up was used to obtain the spatially resolved diffused reflectance of the forearms of 10 human subjects in a similar way as in the test measurements. We also did a series of calibration measurements on known samples, as well as extended Monte Carlo simulations. Then the absorption coefficients of the tissue at several wavelengths were determined through the 2-dimensional diagram method described above. Typical absorption and scattering spectra of human blood are shown in figure 6.

We found that a linear relationship exists between a linear combination of these absorption coefficients and the concentration of haemoglobin determined by a clinical reference method on venous puncture samples obtained from the same subjects (see figure 7).

Most of these 10 subjects were tested three times over a period of three weeks according to an approved protocol. The total number of data points was 26. Linear least squares fitting of the venous blood haemoglobin concentration and the tissue absorption coefficients at different wavelengths yielded the expression

$$[\text{Hb}], \text{ g/dL} = 12.65 + 1.474 \mu_a(590) - 25.97 \mu_a(750) + 18.93 \mu_a(800) + 2.54 \mu_a(950),$$

where  $[\text{Hb}]$  is the concentration of haemoglobin in grams per 100  $\text{cm}^3$  (dL) of venous blood,  $\mu_a(\lambda)$  is the absorption coefficient of the tissue (in  $\text{cm}^{-1}$ ) at wavelength  $\lambda$  (nm). The correlation coefficient  $r = 0.83$  and the standard error of calibration = 0.73 g/dL (5.5%).

Tissue absorption at wavelengths in the haemoglobin absorption region shows reasonably good correlation with the venous blood haemoglobin concentration. This correlation includes person to person variations, errors in repositioning the optical probe with respect to the body site, blood perfusion effects, change in skin properties, and change in subject's physiological conditions over a three-week period.

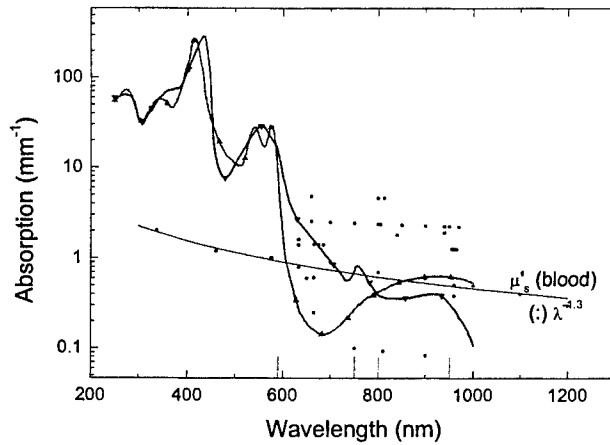


**Figure 6.** Typical absorption spectra of oxygenated (▲) and de-oxygenated (▼) haemoglobin, and scattering spectrum of human blood (compiled from literature).

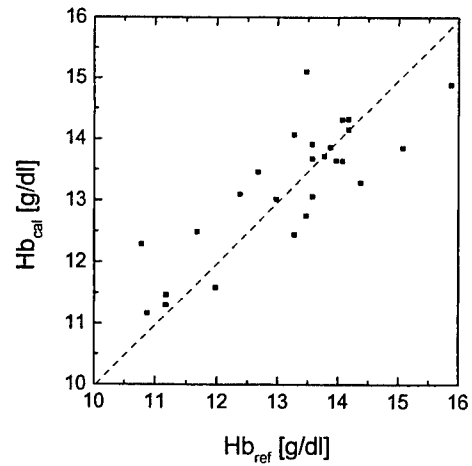


**Figure 7.** Haemoglobin content calculated from the absorption coefficients at 590, 750, 800, and 950 nm compared to the values determined from venous blood haemoglobin concentration. Correlation-coefficient  $r$  is 0.83

## 5. SUMMARY:

We constructed a non-invasive optical probe and accompanying algorithm to determine the optical properties of human body parts. The probe and calculation method is applicable to materials with high absorption, such as blood, and has been used to deduce the concentration of haemoglobin in tissue of human subjects.

Small changes in optical parameters can be detected with our approach ( $10^{-4} \text{ mm}^{-1}$  and  $5 \times 10^{-4} \text{ mm}^{-1}$  in absorption and reduced scattering coefficient, typical tissue parameters are  $0.2\text{--}0.5 \text{ mm}^{-1}$  for the absorption coefficient, and  $1\text{--}5 \text{ mm}^{-1}$  for the reduced scattering coefficient of dermis).

The method is suitable for in-vivo accurate determination of tissue optical parameters, but the achievable accuracy largely depends on the availability of well-defined reference samples and accurate simulations.

-----//-----

## 6. REFERENCES:

1. Y. Mendelson, "Pulse oximetry: theory and applications for noninvasive monitoring" *Clin Chem*; 38:1602-1607(1992)
2. A. P. Shepard and P. A. Oberg, eds, *Laser-Doppler blood flowmetry*, Kluwer Academic Publishers, Boston, 1990
3. S. L. Jacques, I. Saidi, A. Ladner, and D. Oelberg, "Developing an optical fiber reflectance spectrometer to monitor bilirubinemia in neonates" *SPIE Proceedings* 2975:115-124(1997)
4. W. M. Star, "Diffusion theory of light transport", in *Optical Thermal Response of Laser-Irradiated Tissue*, A. J. Welch and M. J. van Gemert, Eds, Plenum Press, NY, 1995, p 131-206
5. S. A. Prahl "The diffusion approximation in 3 dimensions", in *Optical Thermal Response of Laser-Irradiated Tissue*. A. J. Welch and M. J. van Gemert, Eds, Plenum Press, NY, 1995, p 207-231
6. R.A. Bolt and J.J. ten Bosch, "On the determination of optical parameters for turbid material" *Waves in Random Media*, 4:233-242(1994)
7. R.A.J. Groenhuis, J.J. ten Bosch and H.A. Ferwerda, "Scattering and absorption of turbid materials determined from reflection measurements. 1: Theory" *Applied Optics* 16:2456-2462 (1983)
8. R.A.J. Groenhuis, H.A. Ferwerda, and J.J. ten Bosch, "Scattering and absorption of turbid materials determined from reflection measurements. 2: Measuring method and calibration" *Applied Optics* 16:2463-2467 (1983)
9. F. Bevilacqua, D. Piguet, P. Marquet, J. D. Gross, B. J. Tromberg, and C. Depeursinge, "In vivo local determination of tissue optical properties", *SPIE Proceedings*; 3194:262-268(1998)
10. F. Bevilacqua, D. Piguet, P. Marquet, J. D. Gross, B. J. Tromberg, and C. Depeursinge, "In vivo local determination of tissue optical properties: applications to human brain", *Applied Optics* 38: 4939-4950 (1999)
11. F.F.M. de Mul, M.H. Koelink, M.L. Kok, P.J. Harmsma, J. Greve, R. Graaff, J.G. Aarnoudse, "Laser Doppler Velocimetry and Monte Carlo Simulations on Models for Blood Perfusion in Tissue", *Applied Optics*, 34: 6595-6611 (1995).
12. H.J. van Staveren, C.J.M. Moes, J. Van Marle, S.A. Prahl, and M.J.C. van Gemert, "Light scattering in Intralipid-10% in the wavelength range of 400-1100 nm", *Applied Optics*, 30: 4507-4541 (1991).
13. I.M. Kempson, "Preparation of correlated LDF and spectral measurements", internal report (honours project), May 1999.
14. M. Kohl, M. Cope, M. Essenpreis, D. Boesker, "Method and apparatus for determining analytical data concerning the inside of a scattering matrix", United States Patent 5,825,488 (1998).
15. A. Dergatchev, R.A. Bolt, and F.F.M. de Mul, "Determination of concentration of compounds in inhomogeneous turbid media by high-frequency modulated light", *Advances in Optical Imaging, Photon Migration, and Tissue Optics*, OSA technical digest (Optical Society of America, 1999), pp. 267-269

# Effects of Rough Interfaces on a Converging Laser Beam Propagating in a Skin Tissue Phantom

J. Q. Lu\*, K. Dong, X. H. Hu

Department of Physics, East Carolina University, Greenville, NC 27858

## ABSTRACT

Light propagation in a turbid medium such as the skin tissue depends on both the bulk optical properties and the profiles of the interfaces where mismatch in the refractive index occurs. In this paper we present recent results of investigations on the light distribution inside a human skin tissue phantom for an incident converging laser beam and its dependence on the roughness of the interfaces. The human skin tissue is modeled by a two-layer structure with a thin layer of epidermis on top of the dermal layer. Within each layer, the tissue is considered macroscopically homogeneous and the two interfaces, between ambient medium, epidermis and dermis, are treated as random rough surfaces. The distribution of laser light with wavelength near  $1\mu\text{m}$  in the tissue phantom is considered using a recently developed method of Monte Carlo simulation. The dependence of the light distribution on the surface roughness and index mismatch are presented, and their relevance to the possible laser surgery under skin surface and the measurements of optical properties of the skin tissues is discussed.

## 1. INTRODUCTION

Understanding the optical properties of human skin has presented a challenging problem to biomedical physics<sup>1</sup> and theoretical modeling of light propagation in the skin tissues has attracted active attention in the past few years.<sup>2</sup> The radiative transfer theory<sup>3</sup> has served as the framework for the modeling within which various numerical approaches have been pursued. In spite of the intense computing requirement, the Monte Carlo simulation, using a random walk model of photons, has acquired considerable preference over others for its simple algorithm and ability to provide nearly exact solutions for three-dimensional problems of light propagation and distribution under practical boundary conditions for collimated beam.<sup>4-7</sup> The effect of skin tissue structure on light propagation has been previously investigated through layer models with optically smooth interfaces between the layers, their results offered some guidelines in the studies of skin tissue optics.<sup>8-10</sup> In reality, however, the skin layer interfaces are randomly rough in nature, and it is desired that the effect of these rough interfaces be quantitatively understood. Accurate modeling of light distribution in these cases can help to understand the interplay between tissue morphology and light distribution and to provide insight on developing new methods to treat various lesions in skin dermal layer with focused laser beams.<sup>11</sup> In pursuing in this direction, we have recently developed a method of Monte Carlo simulation that is capable of directly calculating the light distribution inside a turbid medium for laser beams of any configuration and tissue interfaces of arbitrary profiles.<sup>12,13</sup> In this method, each photon in the input beam is individually tracked in the time domain according to the boundary condition and phantom geometry within the framework of radiative transfer theory. The computation efficiency of this method is achieved through a "time-slicing" procedure by exploiting the linear relation between the photon pathlength and its travel time for the spatial distribution of photon density.<sup>12</sup> In this report, we present a two-layer model of human skin tissue with rough interfaces and numerical simulations on the light distribution of a converging laser beam propagating in the tissue phantom using the Monte Carlo method.

## 2. SKIN MODELING

Skin is considered the largest and heaviest organ of the human body and its superficial structure is composed of two primary layers: epidermis and the underlying dermis.<sup>14</sup> The epidermis consists of keratinising sub-layers supported by the dermal layer of the dense fibro-elastic connective tissue containing glands and hairs. In average, the dermis is about 3 mm thick, while the thickness of epidermis varies between 50 and  $150\mu\text{m}$ . The epidermis is the most superficial layer of the skin and forms the interface between skin tissue and ambient environment. The epidermis can be divided further into five sub-layers and the structure of the outermost sub-layer determines the roughness of the skin surface. The principal cells of the epidermis are keratinocytes which gradually migrate from the deepest stratum to the surface and is sloughed off in a process called desquamation. The cornified and outermost sub-layer of the epidermis is the stratum corneum which has a thickness of approximately  $10\mu\text{m}$ .<sup>15</sup> The stratum corneum contains 15 to 20 layers of flattened, non-nucleated, keratinized cells called corneocytes which are filled with filaments of keratin. The corneocyte cells are dead, dehydrated and flat with an average size

approximately  $1\mu\text{m}$  or less in the direction perpendicular to the skin surface. Since the corneocytes are arranged in vertical columns that resemble stacks of flat plates, the fluctuation of skin surface height is expected to be about a fraction of the cell size in the perpendicular direction. The lateral diameters of the corneocytes lie in the neighborhood of a few tens micrometers. Therefore, we expect that the average peak-valley distance in the surface plane of the skin tissue to be a fraction of the lateral sizes of the corneocytes.

Since only the light distribution in the upper dermis within 2mm from the skin surface is concerned, we adopt a two-layer model of the human skin to reduce the computation time and memory requirements for generating and storage of the rough interface profiles used in our Monte Carlo simulations. In this two-layer model, the epidermis layers is treated as an infinite slab in the transverse x-y plane with an average thickness  $d$  along the z-axis while the dermis as a semi-infinitely large medium below the dermoepidermal junction, as shown in Fig. 1. Each layer is assumed macroscopically homogeneous and has its own set of optical parameter: refractive index  $n_i$ , absorption coefficient  $\mu_{ai}$ , scattering coefficient  $\mu_{si}$  and mean cosine of the scattering angle or the anisotropy factor  $g_i$  with  $i=1$  for epidermis and 2 for dermis. The dominant absorber to the near-infrared laser radiation at wavelengths near  $1\mu\text{m}$  in the epidermis is melanin and we choose  $\mu_{a1} = 5.0\text{mm}^{-1}$ ,  $\mu_{s1} = 10.0\text{mm}^{-1}$  and  $g_1 = 0.9$ .<sup>7</sup> In the dermal layer the principal absorber is hemoglobin which absorbs the near-infrared light near  $1\mu\text{m}$  weakly. Therefore, the bulk absorption coefficient of the dermis is chosen to be smaller than that of the epidermis:  $\mu_{a2} = 0.5\text{mm}^{-1}$ , with  $\mu_{s2} = 5.0\text{mm}^{-1}$  and  $g_2 = 0.9$ .<sup>7</sup> The skin surface, or the interface with the ambient medium of refractive index  $n_0$ , and the dermoepidermal junction are modeled in the same fashion as rough interfaces, to be discussed in more details next.

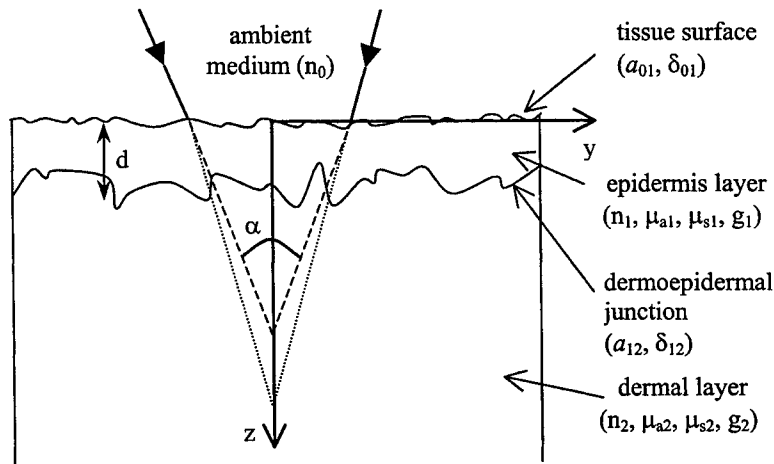


Fig. 1  
A schematic drawing of the two-layer model for human skin tissue with a converging laser beam of cone angle  $\alpha$  incident on the surface. The average thickness of the epidermis is assumed to be  $d=60\mu\text{m}$ .

### 3. ALGORITHMS

Considering a beam of light incident on a tissue phantom with rough interfaces, the photons will be refracted locally and randomly from its incident direction when passing through a rough interface. After entering the phantom, the photons will experience random scattering and absorption. As a result of these events, the light distribution in the tissue will vary as the beam propagates, and that is the interest of this report. The principles of tracking photons inside a skin tissue phantom used in this report have been described in Refs. 12 and 13. Here we concentrate only on the part of the algorithms that are related to the photon tracking near the rough interfaces. In order to study the effect of the surface roughness on light propagation in human skin, we employ a statistical technique to model the two interfaces of the epidermis layer by generating random surfaces from stochastic processes. In a stochastic process a sequence of values is drawn from a corresponding sequence of jointly distributed random variables. The method of generating a rough surface from stochastic processes has been used widely to study the multiple scattering of electromagnetic waves from random rough surfaces.<sup>16-18</sup>

The stochastic modeling of the rough interfaces in human skin utilizes an ensemble of randomly rough surfaces for each interface schematically shown in Fig. 1. The first surface, i.e., the interface between an ambient medium and epidermis, is described by a surface profile  $z = \zeta_1(\vec{R})$  while the second surface, i.e., the interface between the epidermis and dermis, is described by a surface profile  $z = d + \zeta_2(\vec{R})$ . Where  $\vec{R} = (x, y)$  is the position in the xy-plane. The surface profile functions, namely  $\zeta_1(\vec{R})$  and  $\zeta_2(\vec{R})$ , are statistically independent and each of them is assumed to be a stationary Gaussian

stochastic process characterized by a zero-mean and Gaussian surface height correlation function as expressed in the following equation:

$$\langle \zeta_i(\bar{R}) \rangle = 0, \quad (1)$$

$$\langle \zeta_i(\bar{R}) \zeta_i(\bar{R}') \rangle = \delta_i^2 \exp[-(\bar{R} - \bar{R}')^2 / a_i^2]. \quad (2)$$

where  $i=1, 2$  for the first (at  $z = 0$ ) and second (at  $z = d$ ) interface, respectively. The parameter  $\delta$  is the rms height of the surface departure from flatness that indicates the vertical fluctuation, and the parameter  $a$  is the transverse correlation length of the surface roughness describing the average lateral distance between the peak and valley in the surface profile. The angle brackets denote an average over the ensemble of realized surface profile. Numerically, each surface profile function in the ensemble, say  $\zeta(\bar{R}) = \zeta_i(\bar{R})$ , is generated from an uncorrelated Gaussian distribution of random numbers  $X(\bar{R})$  through a convolution integration

$$\zeta(\bar{R}) = X(\bar{R}) * G(\bar{R}) = \frac{2\delta}{a\sqrt{\pi}} \int X(\bar{R}') \exp\left[-\frac{2(\bar{R} - \bar{R}')^2}{a^2}\right] d\bar{R}', \quad (3)$$

where  $X(\bar{R})$  is the random height at position  $\bar{R}$  on the surface. To achieve high computing efficiency, the profile function is obtained through fast Fourier transformations as

$$\zeta(\bar{R}) = \frac{1}{2\pi} \int x(\bar{Q}) g(\bar{Q}) \exp[i\bar{Q}\bar{R}] d\bar{Q}, \quad (4)$$

where  $x(\bar{Q})$  and  $g(\bar{Q})$  are the Fourier transformations of  $X(\bar{R})$  and  $G(\bar{R})$ , respectively. In Monte Carlo simulations, results from individual samples of a rough surface ensemble are averaged to obtain the statistical distribution of light in the skin phantom. An example of  $\zeta(\bar{R})$  generated with the above procedures is shown in Fig.2 in which the scale of the z-axis is decreased so that the details of the surface fluctuation can be seen.

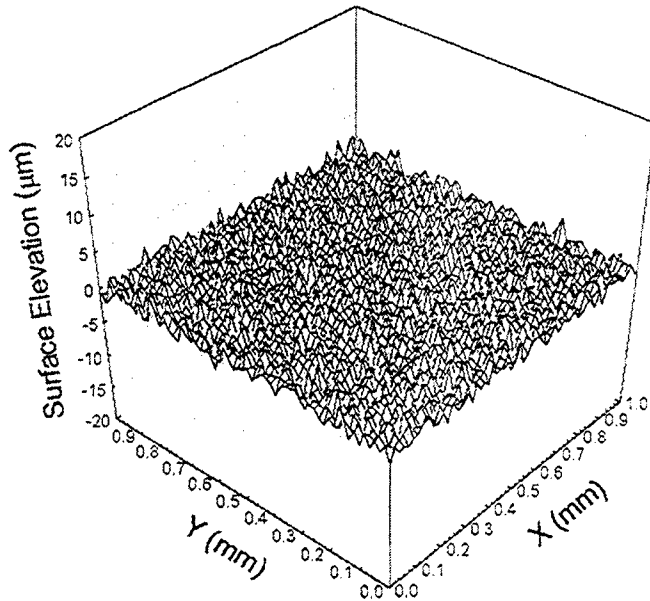


Fig. 2  
A rough surface profile generated in the x-y plane at  $z = 0$  with the rms height  $\delta = 1\mu\text{m}$  and the lateral correlation length  $a = 10\mu\text{m}$ .

An important part of photon tracking in the neighborhood of the interface is to decide if the photon reflects from or transmits through the interface when it is incident on the interface. For this purpose, the incident angle  $\phi_i$  of the tracked photon with respect to the surface normal of the interface needs to be calculated to determine the fate of the photon. For a given interface with profile function  $\zeta(\bar{R})$ , the surface normal has to be calculated locally by obtaining the partial derivatives of the surface



profile function,  $\zeta'_x$  and  $\zeta'_y$ , at the point of the incidence. The unit vector of the surface normal, pointing downward with the direction of z-axis, is given by

$$\hat{n} = \frac{(-\zeta'_x \hat{x} - \zeta'_y \hat{y} + \hat{z})}{\sqrt{\zeta'^2_x + \zeta'^2_y + 1}} \quad (5)$$

where  $\hat{x}$ ,  $\hat{y}$  and  $\hat{z}$  are the unit vectors along respective axes.

Light reflection and transmission occur at an interface between two media with mismatched refractive indices. In the statistical model of Monte Carlo simulation, the fate of photon is determined locally in the following procedures. A uniformly distributed random number RND ( $0 \leq \text{RND} \leq 1$ ) is generated once the tracked photon enters into the grid cell at the interface separating the incident medium with  $n_i$  from the other with  $n_r$ . If RND is smaller than the reflectance  $R$ , the photon will be reflected in a direction pointed by a unit vector  $\hat{r}$ . Otherwise, it will refract into the other medium along a direction  $\hat{t}$ . The reflectance  $R$  is calculated from the incident angle  $\phi_i$ ,  $n_i$  and  $n_r$  based on the Fresnel's formulation, averaged in both s- and p-polarization since the light within the radiative transfer theory is treated as photons without polarization

$$R = \frac{1}{2} \left[ \left\{ \frac{\tan(\phi_i - \phi_r)}{\tan(\phi_i + \phi_r)} \right\}^2 + \left\{ \frac{\sin(\phi_i - \phi_r)}{\sin(\phi_i + \phi_r)} \right\}^2 \right] \quad \text{for } \phi_i > 0, \quad (6)$$

$$R = \left( \frac{n_r - n_i}{n_r + n_i} \right)^2 \quad \text{for } \phi_i = 0.$$

In the above formula, the refraction angle  $\phi_r$  is related to the incident angle  $\phi_i$  by the Snell's law:  $n_i \sin \phi_i = n_r \sin \phi_r$ .

Furthermore, if we define a unit vector  $\hat{i}$  pointing in the direction of the incident photon, the following relations can be derived to find the directions of reflected and refracted photons

$$\hat{r} = 2 \cos \phi_i \hat{n} + \hat{i}, \quad (7)$$

$$\hat{t} = \frac{\sin(\phi_r - \phi_i)}{\sin \phi_i} \hat{n} + \frac{n_i}{n_r} \hat{i}. \quad (8)$$

#### 4. RESULTS

To study the effect of rough interfaces in skin tissue on the light distribution, we simulated the propagation of a converging laser beam in our two-layer skin model with the time-slicing Monte Carlo model.<sup>12, 13</sup> The converging laser beam is of Gaussian profile and incident on a tissue phantom as shown in Fig. 1 with the beam axis centered on the z-axis. The beam has a cone angle  $\alpha=30^\circ$  in the ambient medium and its radius at  $z=0$ , or the interface between the ambient medium and the tissue phantom, is adjusted to make the geometrical focal point at  $z=1\text{mm}$  in the skin phantom below the surface. Once the beam enters the tissue phantom, the unattenuated portion of the beam is assumed to proceed as a spherical wave toward a geometric focal point on the z-axis without considering diffraction. This treatment is consistent with the radiative transfer theory. An ensemble of 60 randomly generated rough surfaces are used for each of the two interfaces and a total of  $2.1 \times 10^8$  photons are tracked in each case to obtain light distributions for all cases of simulation.

The light reflection and refraction at an interface are results of the mismatch in the refractive index. Because of the extremely complicated nature of skin tissue optics, no accurate database is available for the wavelength and tissue type dependence of the index in human skin. To ensure the clinical relevance of our simulation results, we choose tissue refractive index from a range based on existing literature to study the effect of index mismatch at rough interfaces. The refractive index  $n_2$  of the skin dermis has been often cited between 1.37 and 1.5<sup>2</sup>, and we choose it to be 1.41 for our simulation in the near-infrared region near  $1\mu\text{m}$ . The refractive index of the stratum corneum, consisting of dehydrated cells, has been considered as 1.55.<sup>15, 19</sup> Since we consider most the cases of water as the ambient medium in contact with the stratum corneum, we assume the refractive index  $n_1$  of the epidermis to be of three values between that of water near 1.33 and 1.55:  $n_1 = 1.43, 1.45$ , and  $1.50$ . Throughout the calculations, the optical parameters for the first tissue layer are fixed at  $\mu_{a1} = 5.0\text{mm}^{-1}$ ,  $\mu_{s1} = 10.0\text{mm}^{-1}$ , and  $g_1 = 0.9$ ; and the second tissue layer  $\mu_{a2} = 0.5\text{mm}^{-1}$ ,  $\mu_{s2} = 5.0\text{mm}^{-1}$ , and  $g_2 = 0.9$ , these values are based on earlier discussions. Also fixed in the calculations are the transverse correlation lengths of both rough surfaces which are kept at  $a_{01}=20\mu\text{m}$  and

$a_{12}=80\mu\text{m}$ , and the mean thickness of the epidermis layer to be about  $60\mu\text{m}$ , according to previous discussions. The rms height of the first surface  $\delta_{01}$  will be varied from  $0.1$  to  $0.4\mu\text{m}$  and that of the second surface  $\delta_{12}$  from  $10$  to  $30\mu\text{m}$  based on low power micrograph of the vertical section of the human skin.<sup>14</sup>

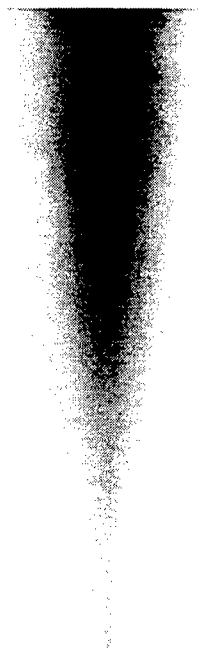


Fig. 3 A 2D image of light distribution in the y-z plane with the gray-scale proportional to the photon density and  $-0.5\text{mm} \leq y \leq 0.5\text{mm}$  and  $0 \leq z \leq 1.5\text{mm}$ . The parameters of the two-layer skin tissue model are given by  $n_0=1.0$ ,  $n_1=n_2=1.41$ ,  $\delta_{01}=0.2\mu\text{m}$ ,  $\delta_{12}=20\mu\text{m}$ .

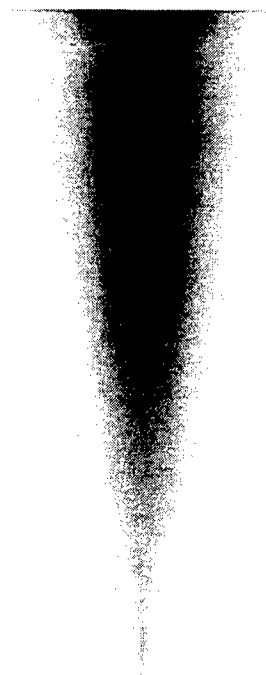


Fig. 4 Similar gray-scale image of light distribution as that in Fig 3 with following parameters changed:  $n_0=1.33$ ,  $n_1=1.45$  and  $\delta_{12}=10\mu\text{m}$ .

We first investigate the effects of surface roughness at the skin surface (i.e. the first interface) on the light distribution inside tissue by setting the index of epidermis the same as that of the dermis, and here the ambient medium is assumed to be air ( $n_0 = 1.0$ ). Shown in Fig. 3 is an example of the two-dimensional image of simulated light distributions inside the two-layer phantom of human skin tissue in gray-scale graphs under such conditions with other parameters given by  $n_1=n_2=1.41$ ,  $\delta_{01}=0.2\mu\text{m}$ ,  $\delta_{12}=20\mu\text{m}$ . The dermoepidermal junction can not be clearly seen because of the index matching at the junction even though the two layers have different scattering characterizations. Due to the cylindrical symmetry of the problem, the light distribution in the two-layer model can be quantitatively analyzed from the z-dependence of the photon density on the z-axis with simple 2D plots. The case shown in Fig. 3 is displayed in Fig. 5 (the curve with the lowest peak at  $z=1.0\text{mm}$ ). The 2D plot gives us a better view of the photon density variation as the light penetrates into the tissue phantom and the dermoepidermal junction now can be clearly identified. On the other hand, photons inside the tissue may be divided into one part associated with the photons suffered deflection at the two interfaces and/or scattering in bulk and another part associated with the undisturbed photons suffered neither deflection nor scattering. For a focused beam the latter part will be brought

together at the focal point, thus form a peak in photon density at the focal spot,  $z = 1.00\text{mm}$ , observed in both Figs. 3 and 5. When the roughness of the skin surface is decreased to  $\delta_{01}=0.1\mu\text{m}$ , the peak at  $z=1.0\text{mm}$  is significantly increased, as also shown in Fig. 5. This means that smoother surface deflects less photons.

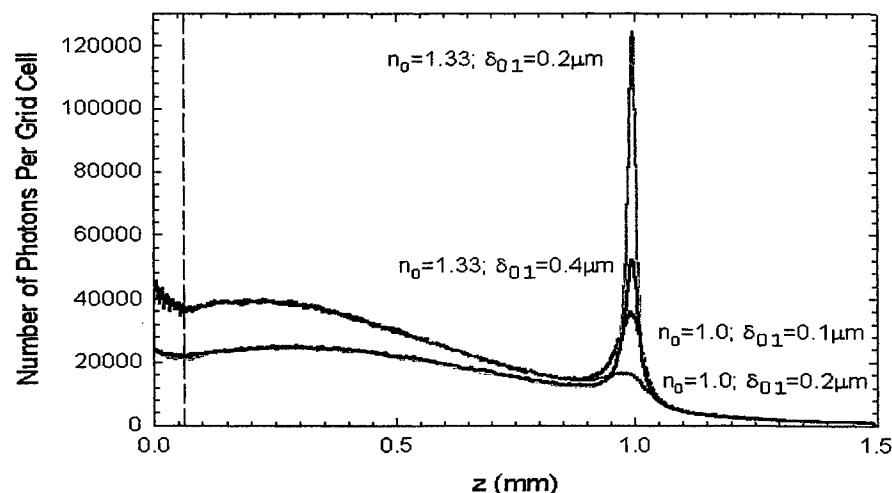


Fig. 5

The  $z$ -dependence of the photon density along the  $z$ -axis. Results from 4 simulations are displayed with different index of the ambient medium  $n_0$  and surface roughness at the skin surface  $\delta_{10}$ . All other parameters remain the same:  $n_1=n_2=1.41$ ,  $a_{01}=20\mu\text{m}$ ,  $\mu_{a1}=5.0\text{mm}^{-1}$ ,  $\mu_{s1}=10.0\text{mm}^{-1}$ ,  $g_1=g_2=0.9$ ,  $a_{12}=80\mu\text{m}$ ,  $\delta_{12}=20\mu\text{m}$ ,  $\mu_{a2}=0.5\text{mm}^{-1}$ ,  $\mu_{s2}=5.0\text{mm}^{-1}$ . The dashed line indicates the position of the dermoepidermal junction.

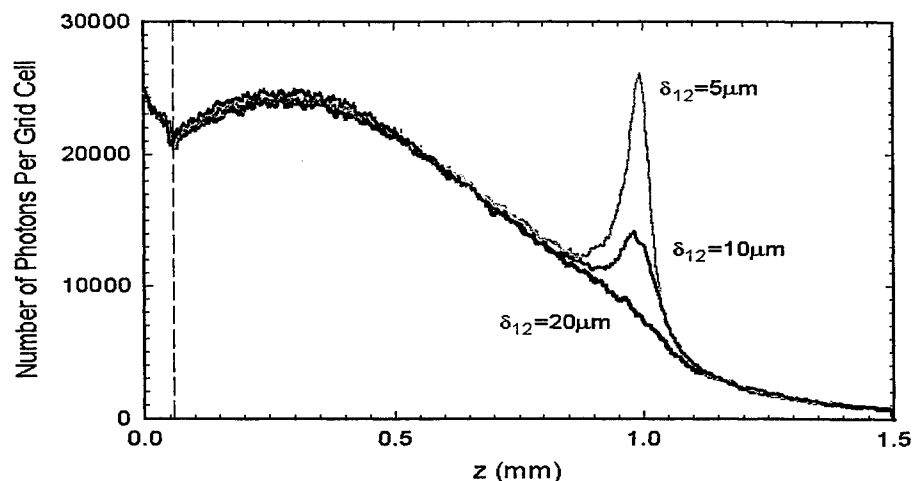


Fig. 6

The  $z$ -dependence of the photon density along the  $z$ -axis. Results from 3 simulations are displayed with different surface roughness at the dermoepidermal junction, i.e.  $\delta_{12}$ . All other parameters remain the same:  $n_0=1.33$ ,  $n_1=1.45$ ,  $a_{01}=20\mu\text{m}$ ,  $\delta_{01}=0.2\mu\text{m}$ ,  $\mu_{a1}=5.0\text{mm}^{-1}$ ,  $\mu_{s1}=10.0\text{mm}^{-1}$ ,  $g_1=g_2=0.9$ ,  $a_{12}=80\mu\text{m}$ ,  $n_2=1.41$ ,  $\mu_{a2}=0.5\text{mm}^{-1}$ ,  $\mu_{s2}=5.0\text{mm}^{-1}$ . The dashed line indicates the position of the dermoepidermal junction.

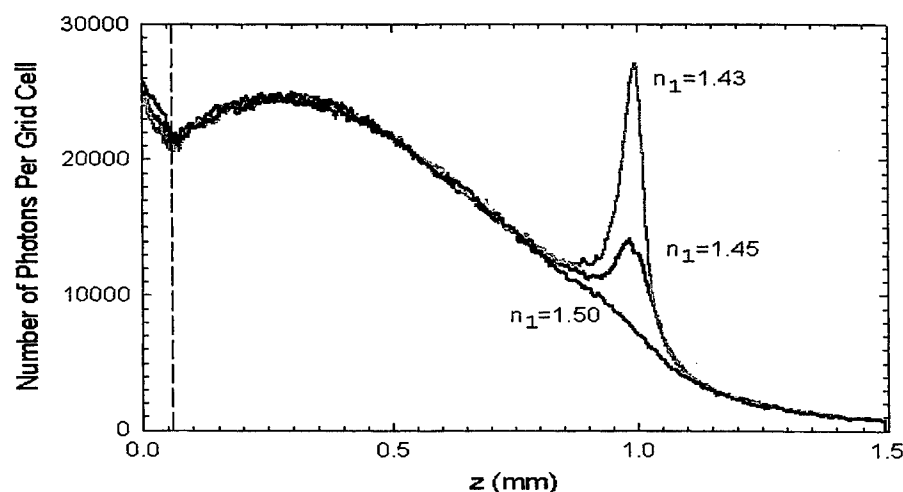


Fig. 7

The  $z$ -dependence of the photon density along the  $z$ -axis. Results from 3 simulations are displayed with different index of epidermis  $n_1$ . All other parameters remain the same:  $n_0=1.33$ ,  $a_{01}=20\mu\text{m}$ ,  $\delta_{01}=0.2\mu\text{m}$ ,  $\mu_{a1}=5.0\text{mm}^{-1}$ ,  $\mu_{s1}=10.0\text{mm}^{-1}$ ,  $g_1=g_2=0.9$ ,  $a_{12}=80\mu\text{m}$ ,  $\delta_{12}=10\mu\text{m}$ ,  $n_2=1.41$ ,  $\mu_{a2}=0.5\text{mm}^{-1}$ ,  $\mu_{s2}=5.0\text{mm}^{-1}$ . The dashed line indicates the position of the dermoepidermal junction.

We then study the effects of index mismatch at the skin surface on the light distribution by using water as the ambient medium ( $n_0 = 1.33$ ), again we have set the index of epidermis the same as that of the dermis. The result for the same surface parameters as that of Fig. 3 (i.e. are  $n_1 = n_2 = 1.41$ ,  $\delta_{01} = 0.2\mu\text{m}$ ,  $\delta_{12} = 20\mu\text{m}$ ) show a much higher peak at the focal point  $z = 1.00\text{mm}$ , for comparison purpose the  $z$ -dependent curve is also plotted in Fig.5. Comparing with the former two cases where air was the ambient medium, the beam radius at the skin surface reduces from 0.188 to 0.252mm for present case to keep the focal point at the same  $z$ -position  $z=1\text{mm}$  because of stronger refraction at the skin surface now. Consequently, for the same total number of incident photons, the photon density near the skin surface is lower than that of the two cases with air as the ambient medium. As the photons travel deeper into the tissue phantom, however, the difference starts to disappear since the bulk scattering begin to dominate the light distribution. When the surface roughness of the skin surface is doubled to  $\delta_{01} = 0.4\mu\text{m}$  with other parameters kept unchanged, the peak at the focal point is decreased as expected, but it is still much higher than that of the cases when air is the ambient medium. This set of results shows that while we can not reduce the roughness at the skin surface very much, but reducing the mismatch of the index at the skin surface can effectively reduce the light deflection.

When the index of epidermis is set to be different from that of dermis, dermoepidermal junction becomes more visible, as demonstrated by a two-dimensional image of simulated light distributions inside the two-layer phantom of human skin tissue in the gray-scale graph in Fig. 4. Here the index mismatch is 0.04 with  $n_1 = 1.45$  and  $n_2 = 1.41$ , and the other parameters are  $n_0 = 1.33$ ,  $\delta_{01} = 0.2\mu\text{m}$ , and  $\delta_{12} = 10\mu\text{m}$ . The effects of the index mismatch and surface roughness at the dermoepidermal junction are studied separately with different values of surface roughness  $\delta_{12}$  in Fig. 6 and different epidermis refractive index  $n_1$  in Fig. 7. It is clear from these results that the index mismatch at the two rough interfaces cause a portion of the incident photons to deviate from their trajectories which is significant in comparison with bulk scattering even at an optical depth of, neglecting the absorption,  $\mu_s z = 10 \times 0.06 + 5 \times 0.94 = 5.3$ .

## 5. DISCUSSION

The results presented in this report provide a quantitative analysis of the effect of surface roughness on the light distribution of a converging laser beam propagating in a two-layer skin tissue model. Two important conclusions can be drawn from these results.

Firstly, the effect of the index mismatch at the inherently rough tissue surface has to be carefully considered in determining the optical parameters of soft biological tissues. Conventional procedures of determining the absorption coefficient  $\mu_a$ , scattering coefficient  $\mu_s$  and the anisotropy factor  $g$  are to experimentally measure the collimated transmittance  $T_c$ , diffuse transmittance  $T_d$  and diffuse reflectance  $R_d$  with tissue samples from which the optical parameters  $\mu_a$ ,  $\mu_s$  and  $g$  are inversely calculated via certain theoretical model within the framework of the radiative transfer theory.<sup>20, 21</sup> The roughness of the interfaces at the tissue surface and inside tissue samples has not been considered and the deflection of photons at these interfaces in real tissue samples has been implicitly included as part of bulk scattering in theoretical modeling. This certainly leads to the overestimation of the scattering coefficient  $\mu_s$ . Depending on the particular structure of the tissue and sample configuration, the overestimation can be significant based on our simulation results. For example, the undeflected and unscattered photons in our simulations arrive at the focal spot and constitute the part of the photon density above the background. As shown in Fig. 5 for the same surface profile, the density of these photons is dramatically reduce from a factor of 10 larger than the background when water is assumed as the ambient medium to less than the background when water is replaced by air.

Secondly, our results indicate that the refractive index plays an important role in the tissue optics involving rough interfaces and illustrate the importance to accurately determine the refractive index of biological tissues in the spectral region of interest. The measurement of refractive index, however, has remained as a challenge for turbid media such as biological tissues. One possible method is to combine spatial filtering technique with immersion of the sample in the liquid of known index. The index of the tissue sample can be determined when the undisturbed portion of the transmitted light is increased to a maximum when a clear liquid of known index is used to match that of the tissue sample.

## ACKNOWLEDGEMENT

This work was partly supported by National Science Foundation under grant #PHY-9973787, National Institute of Health under grant #R15GM/OD55940-01, and North Carolina Super Computer Center through time allocation on SGI Origin 2000.

## REFERENCES

1. I.A. Magnus, *Dermatological Photobiology* (Oxford, 1976)
2. M.J.C. van Gemert, S.L. Jacques, H.J.C.M. Sterenborg, W.M. Star, "Skin optics", *IEEE Trans. Biomed. Eng.*, **36**, 1146 (1989)
3. S. Chandrasekhar, *Radiative Transfer*, Oxford University Press, London, 1950
4. B. C. Wilson, G. Adams, "A Monte Carlo model for the absorption and flux distributions of light in tissue," *Med. Phys.*, **10**, 824-830 (1983).
5. M. Keijzer, S. T. Jacques, S. A. Prahl, A. J. Welch, "Light distributions in artery tissue: Monte Carlo simulations for finite-diameter laser beams," *Lasers Surg. Med.*, **9**, 148-154 (1989).
6. R. Marchesini, C. Clemente, E. Pignoli, M. Brambilla, "Optical properties of *in vitro* epidermis and their possible relationship with optical properties of *in vivo* skin," *J. Photochem. Photobiol. B*, **16**, 127-140 (1992).
7. R. Graaff, A. C. M. Dassel, M. H. Koelink, F. F. M. de Mul, J. G. Aarnoudse, W. G. Zijlstra, "Optical properties of human dermis *in vitro* and *in vivo*," *Appl. Opt.*, **32**, 435-447 (1993).
8. J.M. Schmitt, G.X. Zhou, E.C. Walker, "Multilayer Model of Photon Diffusion in Skin," *J. Opt. Soc. Am. A*, **7**, 2141-2153 (1990).
9. I.D. Miller, A.R. Veith, "Optical modelling of light distributions in skin tissue following laser irradiation", *Lasers Surg. Med.*, **13**, 565-571 (1993)
10. W. Verkruijsse, J.W. Pickering, J.F. Beek, M. Keijzer, M.J.C. van Germert, "Modeling the effect of wavelength on the pulsed dye laser treatment of port wine stains", *App. Opt.*, **32**, pp.393-398 (1993)
11. X. H. Hu, "Efficient use of Q-switched lasers in the treatment of cutaneous lesions," in "Lasers in Surgery: Advanced Characterization, Therapeutics, and Systems V", ed. by R. R Anderson, *SPIE Proceedings*, **2395**, 586-591 (1995).
12. Z. Song, K. Dong, X.H. Hu, J.Q. Lu, "Monte Carlo Simulation of Converging Laser Beams Propagating in Biological Tissue", *App. Opt.*, **37**, pp.2944-2949 (1999)
13. K. Dong, Z. Song, J.Q. Lu, X.H. Hu, "Monte Carlo Simulation of Converging Laser Beams Propagating in Skin Tissue Phantoms", *Proceedings of SPIE*, **3590**, 4-10 (1999)
14. H.G. Burkitt, B. Young, J.W. Heath, *Wheater's Functional Histology*, 3<sup>rd</sup> ed., ch. 9 (Longman Group Limited, Edinburgh, 1993).
15. R.R. Anderson, J. A. Parrish, "The optics of human skin", *J. Invest. Dermatol.*, **77**, 13-19 (1981)
16. N. Garcia, E. Stoll, "Monte Carlo calculation for electromagnetic wave scattering from random rough surfaces", *Phys. Rev. Lett.*, **52**, 1798-1801 (1984).
17. A. A. Maradudin, T. Michel, A. R. McGurn, E. R. Mendez, "Enhanced backscattering of light from a random grating," *Ann. Phys.*, **203**, 255-307 (1990)
18. P. Tran, A. A. Maradudin, "Scattering of a scalar beam from a two-dimensional randomly rough hard wall: enhanced backscattering," *Phys. Rev. B*, **45**, 3936 (1992)
19. R.J. Sheuplein, A survey of some fundamental aspects of the absorption and reflection of light by tissue", *J. Soc. Cosmet. Chem.*, **15**, 111-122 (1964)
20. V.G. Peters, D.R. Wyman, M.S. Patterson, G.L. Frank, "Optical properties of normal and diseased human breast tissues in the visible and near infrared", *Phys. Med. Biol.*, **35**, 1317-1334 (1990)
21. T.L. Troy, D.L. Page, E.M. Sevic-Muraca, "Optical properties of normal and diseased breast tissues: prognosis for optical mammography", *J. Biomed. Opt.*, **1**, 342-355 (1996)

---

\* Correspondence: Email: [luji@mail.ecu.edu](mailto:luji@mail.ecu.edu); WWW: <http://bmlaser.physics.ecu.edu>; Tel: 252 328 1856; Fax: 252 328 6314

# Experimental Study of Optical Properties of Porcine Skin Dermis from 900 to 1500nm

Y. Du<sup>a</sup>, M. Cariveau<sup>b</sup>, G.W. Kalmus<sup>b</sup>, J. Q. Lu<sup>a</sup>, X.H. Hu<sup>a\*</sup>

<sup>a</sup>Department of Physics, <sup>b</sup>Department of Biology, East Carolina University, Greenville, NC 27858

## ABSTRACT

The weak absorption of near-infrared light by skin tissue has offered an important optical window for diagnostic possibilities with optical means including optical biopsy. The strong scattering of the near-infrared light by skin tissue, however, presents a great challenge to the modeling of light propagation through and the optical measurement of the tissue. We have measured transmittance and reflectance of fresh porcine skin and performed Monte Carlo simulations to inversely determine the absorption coefficient, scattering coefficient and asymmetric coefficient of tissue samples in the spectral range from 900 to 1500nm. The state of cellular integrity following optical measurements was verified using transmission electron microscopy (TEM). These results were correlated with the possible effects on the measurements of the tissue optical properties.

**Keywords:** tissue optics, light scattering, ultrastructure of skin tissue

## 1. INTRODUCTION

Unlike visible light, near-infrared (NIR) light can penetrate deeply into most biological tissue and therefore, optical imaging with NIR light for diagnostic purposes has stimulated studies on its functional imaging capability with the absence of ionizing radiation hazards. A fundamental problem in medical application of the NIR light is to understand the tissues' response to the radiation in terms of its optical properties. Extensive studies have been conducted in the visible and near-infrared regions on analysis of the light propagation and measurement of optical properties in biological tissue.<sup>1-6</sup> Nevertheless, the strong scattering of light in these spectral regions by most biological tissues has prevented the accurate determination of their optical parameters until recently.

The propagation of light in an optically thick turbid medium has been often understood in the framework of radiative transfer theory.<sup>7</sup> In this approach, the energy aspect of light propagation is described by an equation of radiation transfer and the response to the radiation by the medium, assuming macroscopic homogeneity, is characterized mainly by three parameters: the absorption coefficient  $\mu_a$ , the scattering coefficient  $\mu_s$  and an anisotropy factor  $g = \langle \cos\theta \rangle$ , where  $\theta$  is the scattering angle and  $\langle \rangle$  represents the ensemble averaging.<sup>4,7</sup> Experimentally, however, these parameters cannot be directly measured. To characterize the optical properties of biological tissues, inverse methods have to be used to determine the three parameters from the experimentally measured diffused reflectance, diffused transmittance and collimated transmittance.<sup>3,5,6</sup> Numerical methods have been used for the inverse calculation and among these the Monte Carlo method<sup>2, 8-11</sup> provides a versatile procedure to model accurately the light propagation in a turbid medium within the framework of radiative transfer theory. For statistical validity the Monte Carlo method requires intensive computing in tracking a large number of photons.

Optical characterization of tissues in terms of the three optical parameters defined above has not been available in the important part of the near-infrared region, from 900 to 1500nm, for any type of biological tissue. The lack of accurate data has motivated us to determine the optical parameters in this region. In this paper, we report our recent results obtained from porcine skin tissue on the measurements of reflectance, transmittance and inverse calculations of the optical parameters by the Monte Carlo method. The possible effect on optical measurements due to different tissue storage techniques was investigated by correlating the tissue ultrastructure with the determined optical properties for samples from 0-30 hours post-mortem. For this purpose, microscopic examination of cellular morphology using TEM has been conducted to study the correlation of optical measurements with the storage time and preservation methods of the porcine dermal tissue.

## 2. THE EXPERIMENTAL METHODS

A 30W tungsten lamp and a PC controlled monochromator (CM110, CVI Laser) with a 600 grooves/mm ruled grating ablazed at 120nm were used as the wavelength-tunable light source from 900 to 1500nm. The light output was modulated at 18Hz by a chopper and filtered by a long-pass filter (750nm) to remove the second order diffraction from the monochromator

grating. The output beam was collimated with a spherical lens of 100mm focal length before the tissue sample. To measure the diffused transmittance  $T_d$  and the diffused reflectance  $R_d$ , an integrating sphere (IS-080-SF, Labsphere, Inc.) of 8 inch diameter ( $R=101.6\text{mm}$ ) was employed to collect the diffuse light signal.<sup>12</sup> The light signal from the integrating sphere was detected by a GaAs photodiode and preamplified with a gain of  $10^{10}$  before it was sent to a lock-in amplifier (SR850, Stanford Research). We used a comparison method to determine  $T_d$  and  $R_d$  in which three light measurements were carried out. The first was obtained with the sample at the entrance port ( $P_T$ ), as shown in Fig. 1(a), the second with the sample at the exit port by rotating the sphere  $180^\circ$  ( $P_R$ ) and the third with the sample at the exit port and the sphere rotated  $20^\circ$  from the last position with the incident light striking on the wall ( $P_C$ ). A small baffle with the same diffuse reflective coating as the sphere wall was placed between the sample port and the detector to prevent the light detector from receiving direct light from the sample. In our measurement of  $P_C$ , though, the baffle did not block the first reflected light from the sphere wall reaching into the detector. Based on the analysis of light distribution inside the integrating sphere similar to those published earlier<sup>12,13</sup>, we find that  $T_d$  and  $R_d$  can be related to three light power signals as

$$R_d = \frac{AP_R}{A(1-f)P_C + A_sP_R} \quad \text{and} \quad T_d = R_d \frac{P_T}{P_R},$$

where  $A=4\pi R^2$  is the total surface area of the sphere,  $f$  is the area ratio of the three ports to the sphere and  $A_s = \pi(3.18)^2 \text{ mm}^2$  is the area of the sample exposed to the incident light beam. In experiments, each light measurement was conducted over the spectral region from 900 to 1500nm with a personal computer for scanning the grating and data acquisition from the lock-in amplifier. The integrating sphere setup has been calibrated against a SPECTRALON reflectance standard (SRS-80-020, Labsphere, Inc) from 900nm to 1500nm and the measured  $R_d$  agrees with the calibrated values within  $\pm 5\%$ .

To measure the collimated transmittance  $T_c$ , the collimated light was focused with a combination of a spherical lens of 400mm and a cylindrical lens of 75mm in focal length into a spot of about  $4\text{mm} \times 0.5\text{mm}$  in size at the focus. A 0.5mm slit was used to spatially filter the transmitted light from the sample. A separate GaAs photodiode was used behind the slit to detect the light signal with a preamplifier gain of  $10^7$ . The experimental error in the diffuse reflectance and transmittance measurements were estimated to be about  $\pm 5\%$ .<sup>12,13</sup> For the measurement of collimated transmittance, however, the error was increased to  $\pm 10\%$  because of the large fluctuation in the thickness measurement for the thin samples.

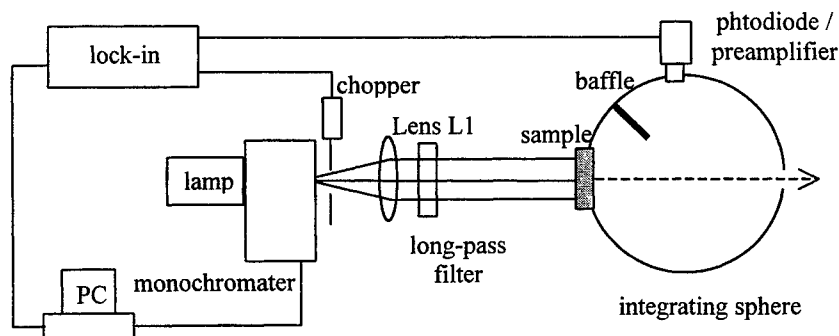


Fig. 1(a)  
The integrating sphere setup for measurements of the diffuse transmission  $T_d$ .

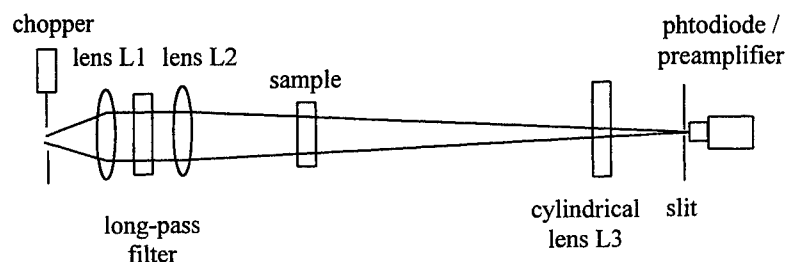


Fig. 1(b)  
The spatial filtering setup for measurements of the collimated transmission  $T_c$ .

Fresh porcine skin was obtained from the Department of Comparative Medicine, School of Medicine at East Carolina University. Immediately after the tissue was removed from animal, the samples were kept under two conditions: on top of crushed ice in a capped ice bucket or in Tyrode's solution refrigerated at  $4^\circ\text{C}$ . For the measurement of diffused reflectance  $R_d$

and transmittance  $T_d$ , the dermis was trimmed into  $20 \times 20 \text{ mm}^2$  squares. Using a specially designed microtome, this tissue was sectioned with thickness  $D$  ranging from 0.5 to 1mm at  $4^\circ\text{C}$  in a walk-in refrigerator room. The sample was sandwiched between two sapphire optical windows of 25mm diameter with saline solution between the tissue and the windows to reduce the effect of index mismatch at the rough surfaces of the tissue section. The rim of the gap between the two sapphire windows was sealed with Vaseline grease to prevent tissue dehydration during the measurement. After the measurements of  $T_d$  and  $R_d$ , tissue samples were fixed immediately for TEM. For measurements of collimated transmittance  $T_c$ , however, the above method could not provide uniformly thin sections of the dermis with thickness on the scales of  $100\mu\text{m}$ . Instead, we used an Ames Lab-tek cryostat to obtain sections of the dermis with thickness  $D$  ranging from 53 to  $236\mu\text{m}$  after the skin samples were stored on top of crushed ice for 5 hours post-mortem. Each section was carefully examined to ensure that no holes existed in the section and the thickness was satisfactorily uniform.

### 3. THE INVERSE CALCULATIONS

We first determined the attenuation coefficient  $\mu_t = \mu_a + \mu_s$  at each wavelength from the measurements of collimated transmittance  $T_c$  of 10 thin dermis samples. The dependence of  $T_c$  on the sample thickness  $D$  is plotted on a semi-log scale at each wavelength from 900nm to 1500nm. Assuming a Lambert-Beer's law for the collimated transmittance,  $T_c(D) = A \cdot \exp(-\mu_t D)$  with  $A$  describing the deflection of incident light at the surfaces of the tissue sample, the bulk attenuation coefficient  $\mu_t$  can be calculated from the slope of the curve  $\log(T_c)$  versus  $D$ .

The inverse calculation starts with fixed input optical parameters,  $\mu_t$  and  $n$ , and variable parameters,  $\mu_s$  ( $\mu_a = \mu_t - \mu_s$ ) and  $g$ , for the dermal tissue phantom. The diffuse transmission and reflectance  $T_d$  and  $R_d$  was calculated with a Monte Carlo simulation method as developed recently,<sup>10,11</sup> with the phantom geometry decided by experimental values. Briefly a tissue phantom slab with optically smooth surfaces, was used to simulate the tissue sample with the phantom geometry determined by the experimental condition. The tracked photons propagate inside the tissue phantom according to the optical parameters ( $\mu_s$ ,  $\mu_a$ ,  $g$ ) which ( $\mu_s$ ,  $g$ ) were used as the adjustable input parameters. Once transmitted into the tissue phantom, the photons were tracked individually until absorbed or escaped from the tracked region in the tissue phantom. The reflection and refraction probabilities of the tracked photons were determined randomly from a distribution function dictated by the Fresnel reflection formula. The refractive index of the tissue phantom was assumed to be a constant,  $n = 1.41$ , over the studied spectral region, between the value 1.37 adopted in ref.[9] and 1.5 in ref. [4]. When tracked photons emerged from the tissue phantom, they were categorized as specular reflection, collimated transmission, diffused reflection and diffuse transmission based on the propagation direction and location at a phantom surface. Upon the completion of the tracking process, the total numbers of the escaped photons in each category were tallied to compute the various reflectances and transmittances. The result of the calculated  $R_d$  and  $T_d$  were compared to the experimental values and an error function  $\delta$

$$\delta^2 = \left\{ \frac{(R_d)_{cal} - (R_d)_{mea}}{(R_d)_{mea}} \right\}^2 + \left\{ \frac{(T_d)_{cal} - (T_d)_{mea}}{(T_d)_{mea}} \right\}^2,$$

was calculated. The inverse calculation was repeated with a new set of  $\mu_s$  and  $g$  until  $\delta < 5\%$ . With proper choice of  $\mu_s$  and  $g$ , it usually took only a few iterations to achieve  $\delta < 1\%$ . For inverse calculations, we determined the dependence of the statistical fluctuation in the  $T_d$  and  $R_d$  calculations on the total number of tracked photons,  $N_0$ , and chose  $N_0 = 2.8 \times 10^5$  with negligible fluctuation in different runs of the Monte Carlo codes.

### 4. RESULTS

All optical measurements have been conducted at room temperature near  $25^\circ\text{C}$ . To determine the attenuation coefficient  $\mu_t$ , we used a conventional method of measuring the dependence of the collimated transmittance  $T_c$  on the sample thickness  $D$ . Fresh porcine skin dermis was frozen at  $-18^\circ\text{C}$  within 5 hours post-mortem. Ten sections were obtained using a cryostat microtome for the  $T_c$  measurements with the setup displayed in Fig. 1(b). The wavelength dependence of  $T_c$  was determined for each sample from 900 to 1500nm with 30nm per step. The results from two samples are shown in Fig. 2(a). At each wavelength, the  $T_c$  data from the ten samples were plotted against  $D$  on a semi-log scale and fitted to straight line, as shown in Fig. 2(b). Since  $\log(T_c) = \log A - 0.434\mu_t D$ , where the parameter  $A$  is always less than one and indicates the light deflection caused by the roughness and index mismatch at the sample surfaces. The attenuation coefficient  $\mu_t$  was determined at each wavelength from the slope of the fitting curves and the results are displayed in Fig. 2(c).



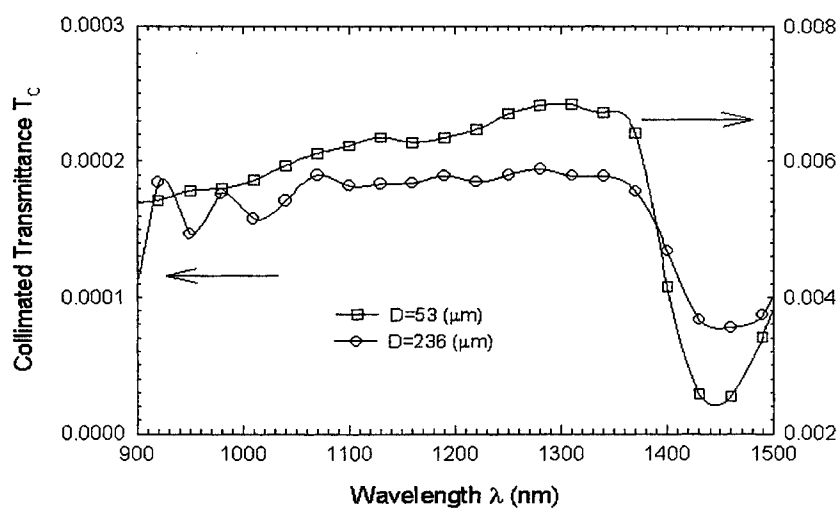


Fig. 2 (a)  
The collimated transmittance as a function wavelength measured from two samples.

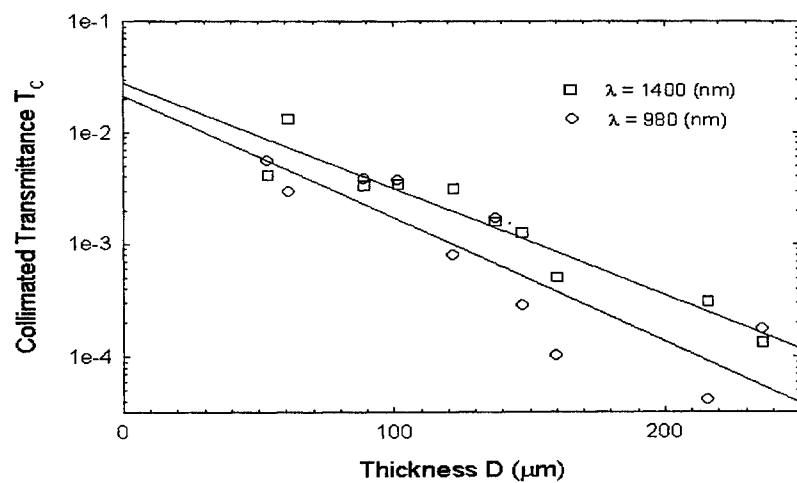


Fig. 2 (b)  
The collimated transmittance as a function of sample thickness measured from ten samples at two values of wavelength. The solid lines are the fitting straight lines used to calculate the attenuation coefficients from 900 to 1500nm.

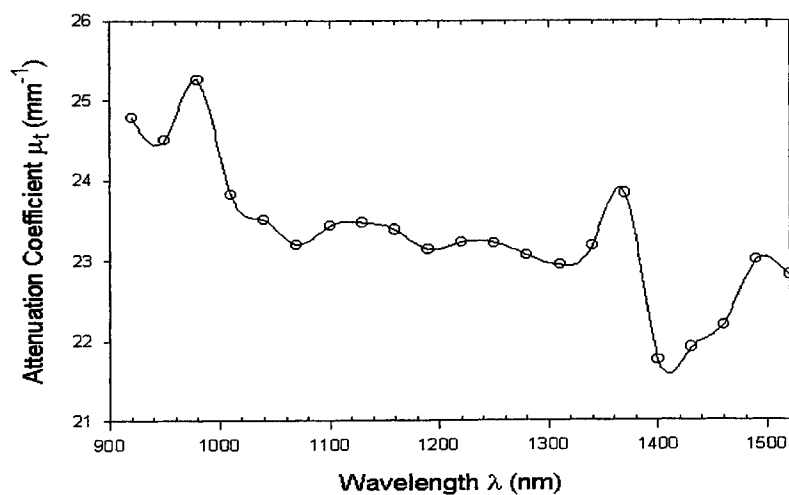


Fig. 2 (c)  
The attenuation coefficient determined from ten samples versus the wavelength.

The diffuse transmittance and reflectance were measured from samples stored under different conditions and at different post-mortem time  $T$  ranging from 0-30 hours. For each sample, inverse calculations with the Monte Carlo method discussed in the previous section have been performed to determine the value of  $\mu_s$  and  $g$  when the calculated values of  $T_d$  and  $R_d$  converge to the experimental values within 5% or less. Typical results on the calculated and measured values of  $T_d$  and  $R_d$  from a sample with  $T = 2$ (hours) and  $D = 930\mu\text{m}$  are plotted as a function of wavelength in Fig. 3(a) with the three optical parameter  $\mu_s$ ,  $\mu_a$  and  $g$  shown in Fig. 3(b).

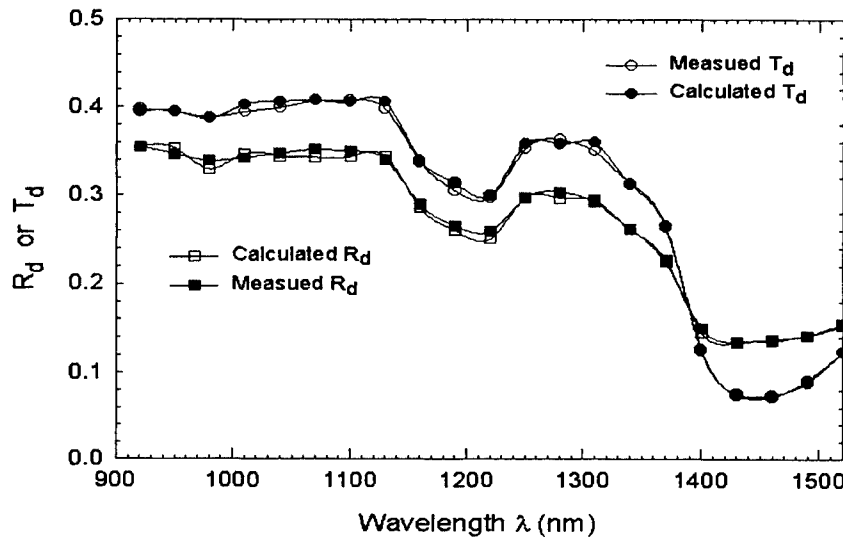


Fig. 3 (a)

The measured and calculated diffuse transmittance  $T_d$  and reflectance  $R_d$  as a function of wavelength from a porcine skin dermis sample stored on ice with postmortem time of 2 hours. The thickness of the sample  $D = 930\mu\text{m}$ .

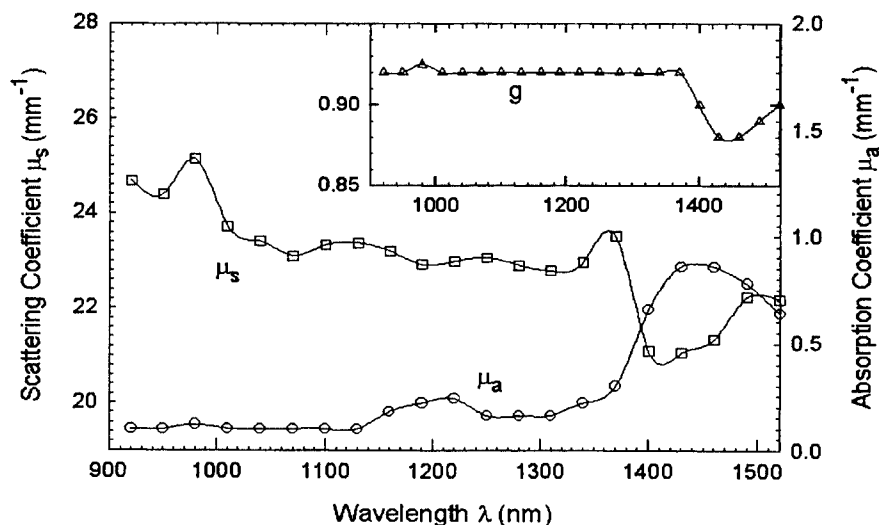


Fig. 3 (b)

The wavelength dependence of the scattering coefficient  $\mu_s$  and the absorption coefficient  $\mu_a$  of the same sample shown in Fig 3 (a). Insert: the anisotropy factor  $g$ .

The optical properties of dermal tissue may be dependent on postmortem time and storage conditions. The values of three optical parameters,  $\mu_s$ ,  $\mu_a$  and  $g$ , at three wavelengths of 980, 1370 and 1400nm from 19 samples were selected from our results to investigate this possible dependence. These results are shown in Fig. 4.

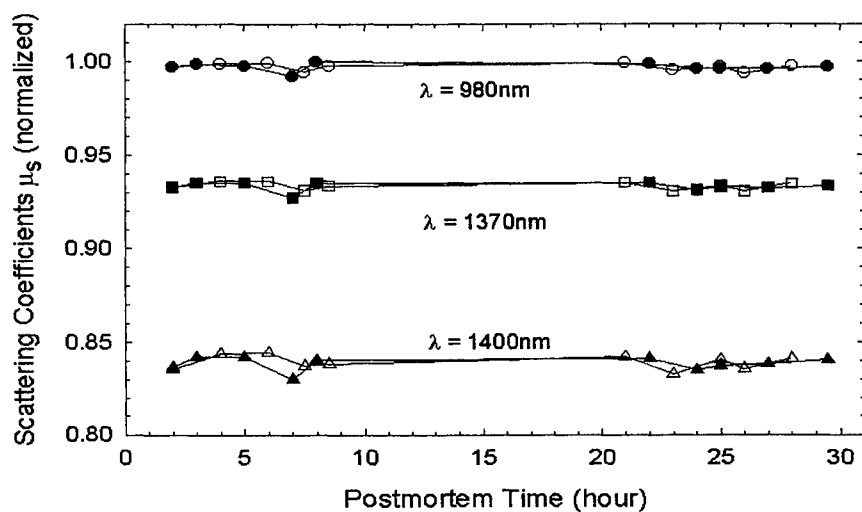


Fig. 4 (a)  
The scattering coefficient inversely determined from the transmittance and reflectance measurements of 19 skin dermal tissue samples with different postmortem time and storage conditions at three wavelengths. The solid symbols are from the samples stored in crushed ice and the empty symbols are from samples in Tyrode's solution. All data are normalized by the  $\mu_{s\_max} = 25.2 \text{ (mm}^{-1}\text{)}$ .

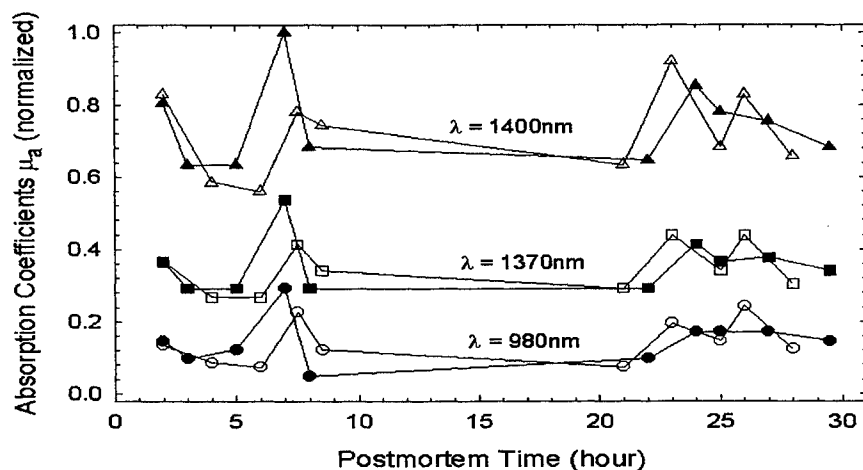


Fig. 4 (b)  
The absorption coefficient inversely determined from the transmittance and reflectance measurements of the same samples with different postmortem time and storage conditions at three wavelengths. The solid symbols are from the samples stored in crushed ice and the empty symbols are from samples in Tyrode's solution. All data are normalized by the  $\mu_{a\_max} = 0.82 \text{ (mm}^{-1}\text{)}$ .

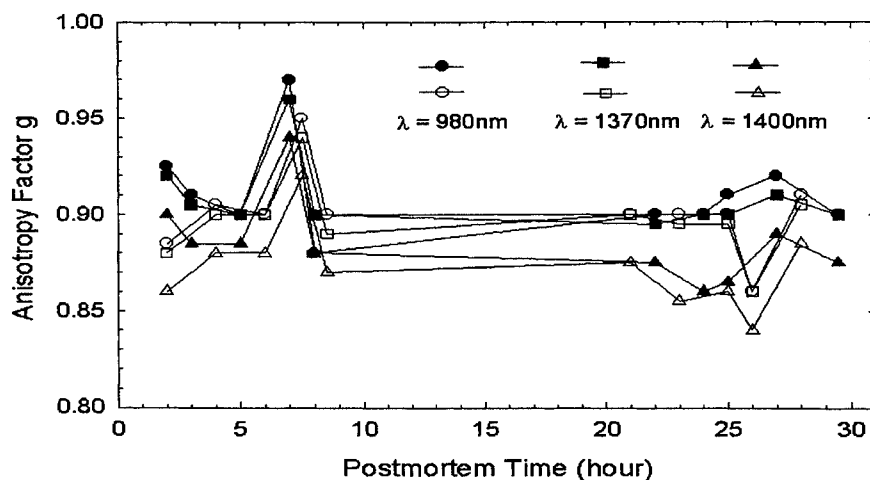


Fig. 4 (c)  
The anisotropic factor inversely determined from the transmittance and reflectance measurements of 19 skin dermal tissue samples with different postmortem time and storage conditions at three wavelengths. The solid symbols are from the samples stored in crushed ice and the empty symbols are from samples in Tyrode's solution.

The ultrastructure of the dermis has been examined through TEM to study the correlation between the cellular morphology and tissue optical properties. For this purpose all the tissue samples used in the optical measurements were fixed by standard TEM processing procedures. Briefly, samples were fixed in 10% gluteraldehyde buffered with NaCacodylate. After fixation,

samples were dehydrated in a series of alcohol solutions. The samples were then post-fixed in osmium tetroxide before infiltration with epoxy resin. Samples were embedded in epoxy at 64°C for 24 hours. The resulting blocks were trimmed prior to sectioning. A Sorvall ultramicrotome was used to produce sections approximately 1mm<sup>2</sup> and 60-70µm thick with a diamond knife. The samples were placed on copper coated grids and contrasted with lead stain and uranyl acetate. Grids were analyzed using a Philips 201 transmission electron microscope. From the TEM examination of all the tissue samples stored under different conditions, it has been determined that the ultrastructure of the tissue remains essentially intact up to 30 hours post-mortem. No observable changes in fibroblasts and collagen fibers were noted. Two TEM micrographs of a sample stored on ice and another stored in Tyrode's solution are displayed in Fig. 5.



Fig. 5 (a) TEM micrograph of a skin dermal sample stored in Tyrode's solution 24 hours post-mortem. Bar = 1µm.



Fig. 5 (b) TEM micrograph of a skin dermal sample stored on crushed ice 24 hours post-mortem.. Bar = 1µm.

## 5. DISCUSSION

From the results presented in this report, one can clearly see that the interaction between the near-infrared light and skin tissue is dominated by scattering due to the inherent microscopic inhomogeneity by cellular structures and tissue morphology. Since most optical measurements are carried out *in vitro*, it is very important to understand the effect of tissue conditions such as the integrity of the major skin cells and collagen fibers on the results of the measurements. The significance is of two fold: the clinical relevance of the *in vitro* data and the correlation between the microscopic structures of the tissue and the macroscopic optical properties. The word "macroscopic" refers to the experimental results obtained with the optically thick tissue samples.

Using a Monte Carlo simulation method within the framework of the radiative transfer theory, the scattering coefficient  $\mu_s$ , the absorption coefficient  $\mu_a$  and the anisotropy factor  $g$  have been inversely calculated from the experimentally measured collimated transmittance  $T_c$ , diffuse reflectance  $R_d$  and diffuse transmittance  $T_d$ . With this procedure, we were able to obtain the three optical parameters of porcine skin dermis by simulating the light propagation in tissue with the geometry and boundary conditions that are nearly identical to the experiments. From the favorable agreement between the calculated and measured  $T_d$  and  $R_d$ , shown in Fig. 3 (a), we concluded that the Monte Carlo simulation provides an excellent modeling tool for the inverse calculation. We note, however, two deficiencies in the current procedure. First, the effect of surface roughness

of the sectioned tissue samples is not considered. This leads to the overestimate of the scattering coefficient because the deflection of the incident light at the two surfaces of the sample are treated as a part of bulk scattering. Second, we assumed the average refractive index of the tissue to be a constant,  $n = 1.41$ , over the spectral region from 900 to 1500nm. The value of  $n$  has not been verified experimentally for skin dermis and, in any case, the assumption of  $n$  as a constant is not a good approximation in studying the light deflection due to the index mismatch at the tissue surfaces. Current investigations are underway to address these concerns.

From both Fig 3 (b) and Fig. 4, we observe a decreasing trend in the scattering coefficient  $\mu_s$  as the wavelength increase toward 1400nm while the anisotropy factor  $g = \langle \cos\theta \rangle$  remains as a constant around 0.92, indicating a feature of strong forward scattering. The nature of the scattering is consistent with the previous determination of the diffuse scattering coefficient (S) based on the Kebelka-Munk (KM) flux model.<sup>1</sup> In addition, the absorption coefficient  $\mu_a$  displays a peak between 1400 and 1500nm which can be associated with the absorption of water component in the skin dermis.<sup>14</sup> Significant differences do exist between previous results based on KM model<sup>1</sup> and that of water. First, the dominance of the light attenuation by scattering over absorption is evident from our result up to the end of the spectral region at 1500nm. Second, the increase in the absorption coefficient  $\mu_a$  from 1000nm to 450nm is more modest than that of water: a factor of 5 in the skin (see Fig. 3b) in contrast to a factor of nearly 100 in water.

Surprisingly, we noticed no observable changes in cellular morphology in samples stored on ice or in Tyrode's solution up to 30 hours post-mortem. The collagen fibers, which are the primary component of the dermis along with the fibroblasts appeared comparable to characteristics observed in the controls (data not shown). Thus, the different storage conditions and post mortem time, up to 30 hours, should have no impact on the optical properties measured. This is evident by the data presented in Fig. 4(a)-(c).

In summary, we have conducted optical measurements of skin dermis in the spectral region from 900nm to 1500nm and determined the scattering coefficient  $\mu_s$ , the absorption coefficient  $\mu_a$  and the anisotropic factor  $g$  within the framework of the radiative transfer theory. Based on these results, we investigated the effect of the tissue storage conditions and post-mortem time on the experimental data. We concluded that no significant changes occur in the microscopic structures of the dermal cells and collagen and the *in vitro* optical measurements can be consistently carried out on samples stored in crushed ice with postmortem time up to 30 hours.

## ACKNOWLEDGEMENT

Part of the numerical simulations was performed on the Origin 2000 computers through an allocation grant from the North Carolina Supercomputing Center. X.H. Hu would like to acknowledge the support through a research grant from the National Institute of Health (R15GM/OD55940-01).

## REFERENCES

1. R.R. Anderson, J.A. Parrish, "The optics of human skin," *J. Invest. Dermato.*, **77**, 13-19 (1981)
2. B. C. Wilson, G. Adams, "A Monte carlo model for the absorption and flux distributions of light in tissue," *Med. Phys.*, **10**, 824-830 (1983).
3. S. Ertefai, A.E. Profio, "Spectral transmittance and contrast in breast diaphanography," *Med. Phys.*, **12**, 393-400 (1985)
4. M.J.C. van Gemert, S.L. Jacques, H.J.C.M. Sterenborg, W.M. Star, "Skin optics," *IEEE Trans. Biomed. Eng.*, **36**, 1146-1154 (1989)
5. V.G. Peters, D.R. Wyman, M.S. Patterson, G.L. Frank, "Optical properties of normal and diseased human breast tissues in the visible and near infrared," *Phys. Med. Biol.*, **35**, 1317-1334 (1990)
6. T.L. Troy, D.L. Page, E.M. Sevick-Muraca, "Optical properties of normal and diseased breast tissues: prognosis for optical mammography," *J. Biomed. Opt.*, **1**, 342-355 (1996)
7. S. Chandrasekhar, *Radiative Transfer*, Oxford University Press, London, 1950
8. M. Keijzer, S. T. Jacques, S. A. Prahl, A. J. Welch, "Light distributions in artery tissue: Monte Carlo simulations for finite-diameter laser beams," *Lasers Surg. Med.*, **9**, 148-154 (1989).
9. R. Graaff, A. C. M. Dassel, M. H. Koelink, F. F. M. de Mul, J. G. Aarnoudse, W. G. Zijlstra, "Optical properties of human dermis *in vitro* and *in vivo*," *Appl. Opt.*, **32**, 435-447 (1993).
10. Z. Song, K. Dong, X.H. Hu, J.Q. Lu, "Monte Carlo simulation of converging laser beams propagating in biological tissues," *Appl. Opt.*, **37**, 2944-2949 (1999)

11. K. Dong, Z. Song, J.Q. Lu, X.H. Hu, "Monte Carlo Simulation of Converging Laser Beams Propagating in Skin Tissue Phantoms", *Proceedings of SPIE*, **3590**, 4-10 (1999)
12. J.A. Jacquez, H.F. Kuppenheim, "Theory of the Integrating Sphere", *J. Opt. Soc. Am.*, **45**, 450-470 (1955)
13. J.W. Pickering, C.J.M. Moes, H.J.C.M. Sterenborg, S.A. Prahl, M.J.C. van Gemert, "Two integrating sphere with an intervening scattering sample", *J. Opt. Soc. Am. A.*, **9**, 621-631 (1992)
14. G. Hale, M. Querry, "Optical constants of water in the 200nm to 200 micrometer wavelength region", *Appl. Opt.*, **12**, 555-563 (1973)

---

\* Correspondence: Email: [hux@mail.ecu.edu](mailto:hux@mail.ecu.edu); URL: <http://bmlaser.physics.ecu.edu>; tel: 252-328-6476; Fax: 252-328-6314

## **SESSION 8**

### **Women's Health and Light Scattering**

# Spatial variation of fluorescence in human breast tissues

A. Pradhan<sup>a</sup>, M. S. Nair, N. Ghosh<sup>1a</sup>, and A. Agarwal<sup>\*</sup>

Department of Physics, Indian Institute of Technology, Kanpur, IN 208016

<sup>\*</sup>G. S. V. M. Medical College, Kanpur, IN 208016

## ABSTRACT

Spatial variation of fluorescence intensity in human breast tissues was studied. A diffusion theory model describing fluorescence light energy distribution inside a thick and turbid medium like human tissue was developed. Experimental data were fitted with the theoretical model to obtain reduced scattering coefficient and absorption coefficient at different fluorescence wavelengths (530nm, 550nm and 585nm) with 488nm excitation of normal, malignant and benign breast tissues. Computed reduced scattering and absorption coefficients of malignant tissues were observed to be more as compared to the normal tissues and benign tumors.

**Keywords:** Fluorescence, Scattering coefficient, Absorption coefficient, Reduced scattering coefficient.

## INTRODUCTION

The study of photon migration in tissue is important in understanding the morphology of different tissue types. Knowledge of different optical transport parameters of tissue like scattering coefficient ( $\mu_s$ ), absorption coefficient ( $\mu_a$ ) and reduced scattering coefficient ( $\mu_s'$ ) is essential in diagnostic and therapeutic use<sup>1</sup>. Further, fluorescence energy distribution, specially its spatial variation in different tissue types is of considerable interest for extracting intrinsic fluorescence from bulk tissue fluorescence for diagnostic studies<sup>2</sup>. Heuristic approaches have been used to model propagation of photons through an optically thick and turbid medium such as human tissue<sup>3-6</sup>. All these methods provide knowledge about the different optical transport parameters of tissue. Elastic scattering has generally been used as a probe. It has been seen in several spectroscopic studies that fluorophores present in human tissue play a major role in the biochemical changes during progress of disease<sup>7</sup>. Hence, investigation of different optical transport parameters taking fluorescence as a probe may reveal additional information about the morphological changes in diseased environment as compared to elastic scattering experiments. This paper presents a three dimensional model for radial variation of fluorescence in flat tissue. The absorption coefficient ( $\mu_a$ ) and reduced scattering coefficient ( $\mu_s'$ ) at three different fluorescence wavelengths (530nm, 550nm and 585nm) of normal, benign and malignant (ductal carcinoma) breast tissues, excited by 488nm line of Ar-ion laser were computed, fitting the experimental data to the developed diffusion theory model.

## EXPERIMENTAL SET-UP

A schematic of the experimental set-up used for studying spatial variation of fluorescence in human breast tissues is shown in Fig 1. The set-up consists of Spectra Physics 5 Watt Ar-ion laser as an excitation source. The laser spot was focused to one end of an optical fiber of a linear array of fibers. The array was held in contact with the tissue by the help of a jig whose contact end was polished to a smooth finish. The fluorescence output from the other fibers of the array were detected with a double grating scanning spectrometer (SPEX 1877E) and a S1 photomultiplier tube. The optical fibers used for this purpose were 140  $\mu$ m in diameter and had a numerical aperture of 0.22. The fluorescence spectrum was recorded, one at a time, and the result was stored in a computer. Scanned fluorescence spectra from different output optical fibers situated at different radial positions of flat tissue surface gave the spatial variation of fluorescence in human breast tissue.



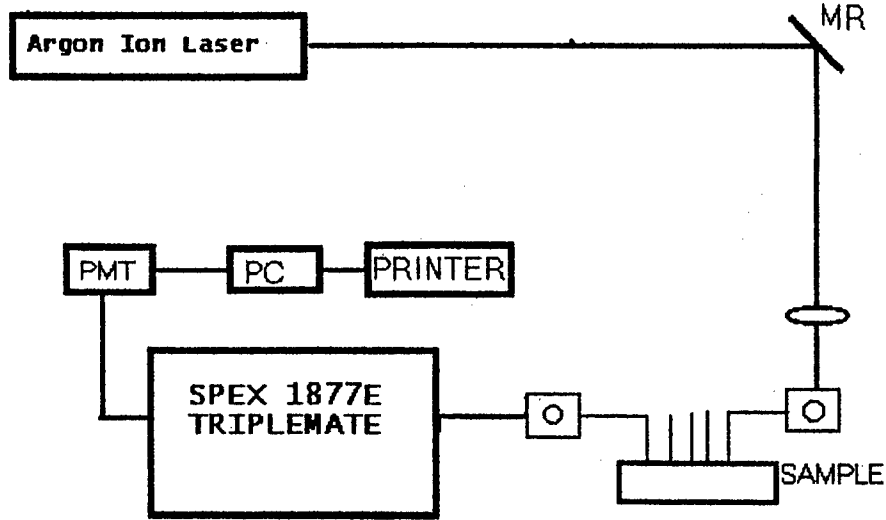


Fig 1. Schematic diagram of experimental set up

### Theoretical Model for Radial Variation of Fluorescence in Tissue:

To derive an analytical expression for radial dependence of fluorescence in flat tissue, the time independent transport equation of net change of diffuse fluorescence intensity was modified as<sup>8</sup>:

$$dI_d/ds = -\mu_t I_d(r,s) + (\mu_t/4\pi) \int p(s,s') I_d(r,s') d\omega' + \epsilon_n(r,s) \quad (1)$$

where  $I_d(r,s)$  is the diffuse fluorescence intensity at any point  $(r, s)$  of the medium and

$$\epsilon_n(r, s) = \phi \mu_a^f I^{exi}(r,s)$$

$\mu_t$  is the total extinction coefficient,  $\mu_s$  is the single scattering coefficient and  $\mu_a$ , the absorption coefficient of the medium.  $\mu_a^f$  is the absorption coefficient at excitation wavelength due to the fluorophores only and  $\phi$  is the fluorescence yield.  $I^{exi}(r, s)$  is the excitation energy distribution inside the tissue.

The first term in the right hand side of eqn. 1 is the total loss suffered by propagating fluorescence intensity due to absorption and scattering. The second term is the source function due to diffuse fluorescence intensity. The third term is distributed fluorescence source terms due to the presence of fluorophores inside tissue.

Diffusion equation for propagating fluorescence was then formulated using diffusion approximation to the transport equation (eqn. 1)<sup>9</sup>,

$$\nabla^2 U_d(r) - \mu_{eff}^2 U_d(r) = -3\phi \mu_a^f \mu_{tr} [U^{exi}_{tot}(r)] + 3/4\pi \nabla \cdot [U^{exi}_{tot}(r)] \quad (2)$$

where  $\mu_{eff} = (3\mu_{tr} \mu_a)^{1/2}$  is the effective attenuation coefficient and  $\mu_{tr} = \mu_s + \mu_a$  is the transport coefficient.

$U^{exi}_{tot}(r)$  is the average total intensity of the excitation light at any point inside the tissue. Instead of doing the rigorous solution of eqn.2, an equivalent point source located at  $(\rho_0, z_0)$  of the extended source  $Q^f(r)$  has been found and the expression for average diffuse excitation intensity  $U_d^{exi}(r)$  used in this case was that obtained by solving eqn. 2 in cylindrical co-ordinate  $(\rho, \phi, z)$ . Further, for a mismatched boundary, the boundary condition can be satisfied by setting the fluence equal to zero on an extrapolated boundary at a position  $z_b = 2AD$  where  $D = 1/3\mu_{tr}$  and  $A$  is a parameter dependent upon the refractive index of the medium and that of the surrounding medium<sup>10</sup>. Hence the position of the image source was found at a height of  $(z_0 + 2z_b)$  above the tissue surface. The fluorescence fluence at any radial position  $(\rho, 0)$  of tissue due to contribution from the equivalent isotropic point source inside tissue and the image source located outside tissue was finally worked out as:

$$R^f(r) = A_0 [z_0 (\mu_{eff} + 1/r_1) \exp(-\mu_{eff} r_1) / r_1^2 + (z_0 + 2z_b) (\mu_{eff} + 1/r_2) \exp(-\mu_{eff} r_2) / r_2^2] \quad (3)$$

where  $r_1^2 = z_0^2 + (\rho - \rho_0)^2$  and  $r_2^2 = (z_0 + 2z_b)^2 + (\rho - \rho_0)^2$

$A_0$ ,  $z_0$  and  $\rho_0$  are dependent upon the effective attenuation coefficient at excitation wavelength  $\mu_{eff}^{exi}$  and the relationships were worked out. Equation 3 describes the spatial variation of fluorescence involving  $\mu_a$  and  $\mu_{eff}$  at fluorescence emission

wavelength and  $\mu_{\text{eff}}^{\text{oxi}}$  at excitation wavelength. This model was fruitfully utilized to determine transport parameters of breast tissues at different fluorescence wavelengths excited by 488nm line of Ar-ion laser.

## RESULTS AND DISCUSSION

Fluorescence intensity at 530nm, 550nm and 590nm wavelengths collected from different radial positions were plotted with distance from excitation point to obtain the spatial variation curves at these wavelengths. Thus obtained spatial variation curves were fitted to the theoretical model describing fluorescence energy distribution (Eqn. 3). Livenberg - Marquardt algorithm was used for minimizing  $\chi^2$  in the curve fitting. Typical experimental profile of normal, malignant and benign tissues with their theoretical fits are shown in Figures 2, 3, and 4 respectively.

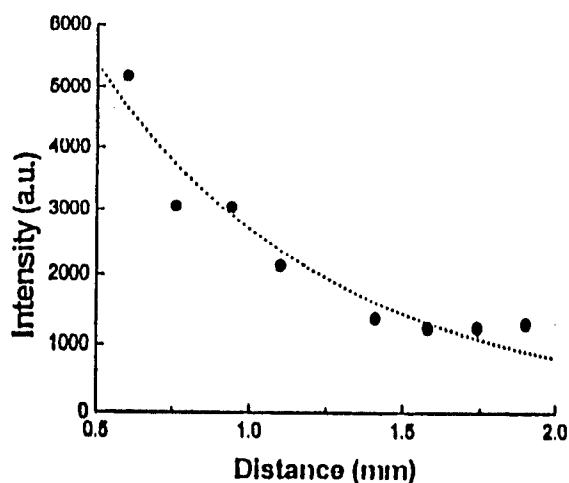


Fig 2. Spatial variation of fluorescence (550nm) in typical normal breast tissue with theoretical fit. Dotted curve represents theoretical fit to experimental points

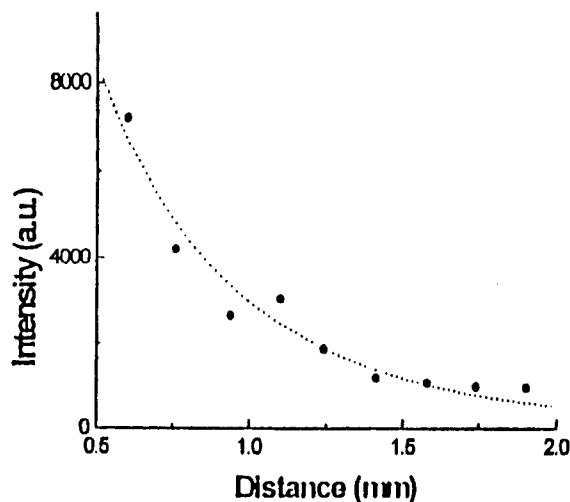


Fig 3. Spatial variation of fluorescence (550nm) in typical malignant breast tissue with theoretical fit. Dotted curve represents theoretical fit to experimental Points.

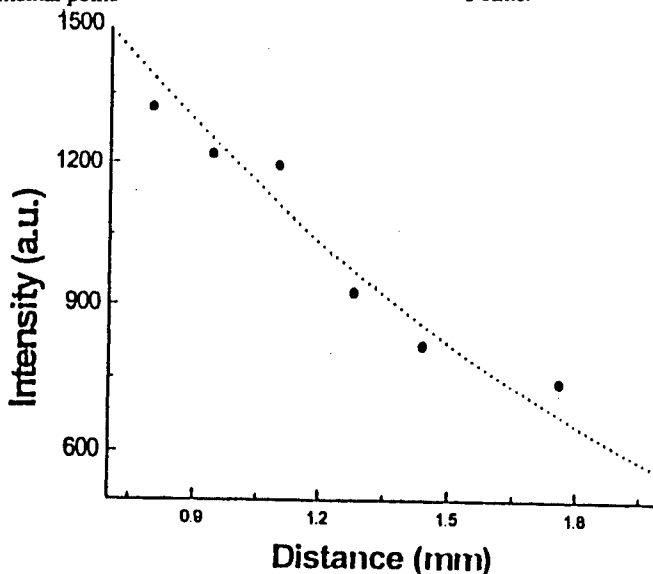


Fig 4. Spatial variation of fluorescence (550nm) in typical benign breast tissue with theoretical fit. Dotted curve represents theoretical fit to experimental points.

Experiments were carried out on 8 benign tumors, 4 malignant breast tissue samples and their normal counter parts. The mean absorption coefficients ( $\mu_a$ ) of normal, malignant and benign breast tissues at three different wavelengths with standard deviations are tabulated in Table 1. The corresponding computed mean reduced scattering coefficients ( $\mu_s'$ ) with standard deviations are listed in Table 2. Experiments were further carried on different tissue phantoms to check the accuracy of estimating  $\mu_s'$  and  $\mu_a$  using the model. Tissue phantoms were prepared with polystyrene microspheres as scatterers (0.61 $\mu$ m diameter) and riboflavin of known concentration as fluorophores. The experimentally obtained values of  $\mu_s'$  and  $\mu_a$  were in close agreement to the known  $\mu_s'$  and  $\mu_a$  values of tissue phantoms.

**Table 1**

Type of tissue	Value of absorption coefficients $\mu_a$ (/mm)		
	at		
	530nm	550nm	585nm
Malignant	0.16 $\pm$ 0.12	0.12 $\pm$ 0.05	0.09 $\pm$ 0.05
Benign	0.13 $\pm$ 0.05	0.11 $\pm$ 0.03	0.14 $\pm$ 0.05
Normal	0.07 $\pm$ 0.02	0.07 $\pm$ 0.02	0.05 $\pm$ 0.01

**Table 2**

Type of tissue	Value of reduced scattering coefficient( $\mu_s'$ )/mm at		
	530nm	550nm	585nm
Malignant	2.99 $\pm$ 0.05	3.62 $\pm$ 1.3	3.47 $\pm$ 1.2
Benign	2.33 $\pm$ 0.35	1.99 $\pm$ 0.15	1.98 $\pm$ 0.56
Normal	2.27 $\pm$ 0.05	2.17 $\pm$ 0.58	1.97 $\pm$ 0.52

The results show that the computed reduced scattering coefficients ( $\mu_s'$ ) of malignant breast tissues were significantly higher than normal tissues and benign tumors at the three wavelengths investigated whereas no significant differences in  $\mu_s'$  were observed between normal tissues and benign tumors. The computed absorption coefficients ( $\mu_a$ ) of malignant breast tissues were observed to be higher compared to normal tissues and benign tumors at both 530nm and 550nm wavelengths. No significant differences in  $\mu_a$  between malignant and normal breast tissues were observed at 585nm. Interestingly some of the benign tumors (with sharp fall in spectral profile around 590nm) show higher  $\mu_a$  as compared to both normal and malignant tissues.

Major fluorophores with 488 nm excitation are assigned to flavins which have an absorption band centered around 460 nm - 490 nm wavelength region. Flavins fluoresce in the visible wavelength region with peak centered at 530 nm<sup>11</sup>. The observed higher value of reduced scattering coefficients ( $\mu_s'$ ) of malignant tissues is possibly because of higher concentration of scatterers present in malignant tissues compared to the normal ones. Another cause may be the larger size of tissue scatterers in presence of malignancy<sup>12</sup>. A plausible cause for the observed higher absorption coefficients ( $\mu_a$ ) of malignant tissues as compared to the normal tissues and benign tumors at 530nm and 550nm wavelengths is the presence of higher concentration of chromophores and fluorophores in malignant tissues.

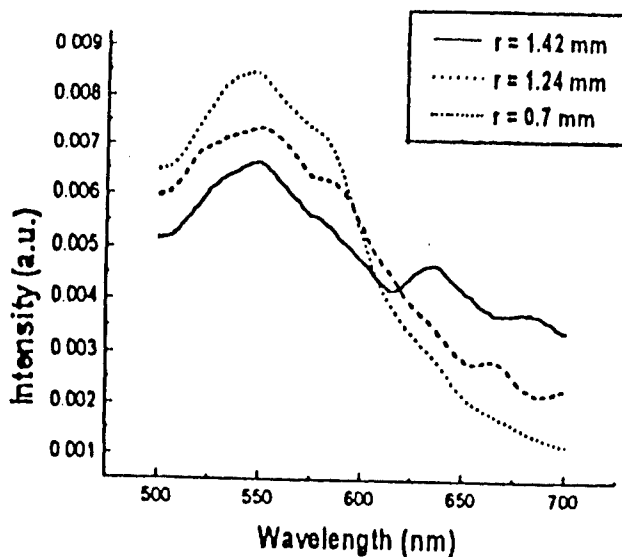


Fig 5. Normalized fluorescence spectra collected from different radial positions of typical normal breast tissue.

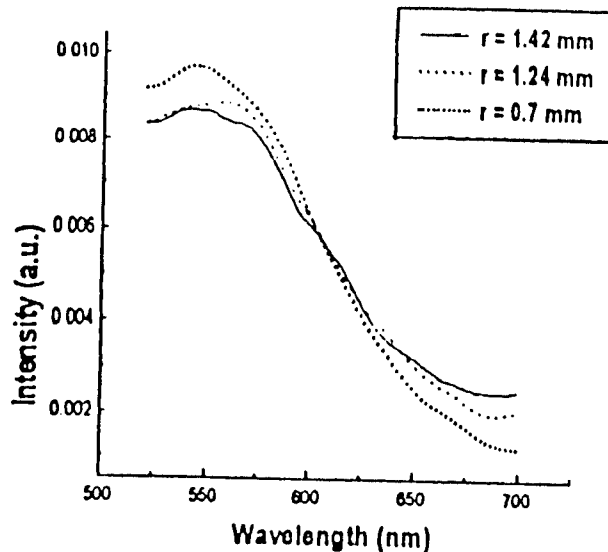


Fig 6. Normalized fluorescence spectra collected from different radial positions of typical malignant breast tissue.

Progressive broadening of fluorescence spectral shape was observed with distance from excitation point. Figure 5 shows the effect of progressive broadening in fluorescence spectral shape with distance from excitation point for a typical normal breast tissue. Similar normalized fluorescence spectra collected from different radial positions of a typical malignant breast tissue are shown in Figure 6. This effect was observed to be considerably more in normal tissue as compared to the malignant ones. The broadening of fluorescence spectra possibly originates from the wavelength dependent transport properties of tissue. Lower values of both absorption coefficients ( $\mu_a$ ) and reduced scattering coefficients ( $\mu_s'$ ) of tissue at higher wavelengths cause lesser loss of propagating fluorescence at higher wavelengths and consequently causes broadening of fluorescence spectral shape.

Further, a bump was observed in the spatial variation of fluorescence profile (about 1.1 mm away from the source) for almost all the tissue samples and in all the wavelengths investigated. This was attributed primarily due to the effect of fluorescence photo bleaching. It was observed that at the point of the bump in spatial variation curve, there was no significant broadening of fluorescence spectrum whereas at all the other points progressive broadening was observed. This suggests that at the point of bump total collected fluorescence is dominated by fluorescence contribution from localized fluorophores. Contribution of propagating fluorescence from the bleached area near the source is primarily due to the effect of fluorescence photo bleaching. The intensity ratio of the bump to the dip in the spatial variation profile was observed to be significantly more in almost all the malignant tissues investigated as compared to their normal counterparts. This implies that the effect of fluorescence photo bleaching is more prominent in malignant tissues as compared to the normal ones.

## CONCLUSION

Our study shows that both reduced scattering coefficients and absorption coefficients of malignant breast tissues are more compared to normal tissues and benign tumors. However, no significant differences in the absorption coefficients exist between normal and benign tumors. The differing values of the transport parameters can be related to the observed changes in the spectral profiles, which are more prominent in normal tissues as compared to the malignant ones. Effect of fluorescence photo bleaching on spatial dependence of fluorescence is observed to be more prominent in malignant tissues. This is being investigated.

## ACKNOWLEDGEMENT

Authors would like to acknowledge Dr.U.Das for valuable discussions. We also thank Dr. A. Rastogi for providing tissue samples.

## REFERENCES

1. A.J. Welsh, M.J.C Van Germert, W.M Star and B.C. Wilson, "Overview of tissue optics" in *Optical thermal response of laser irradiated tissue*, chap.2, A j Welsh and M.J.C van Germert (eds.), Plenum, New York, 1995.
2. Jun Wu, Michel S. Feld and Richard P. Rava, Analytical model for extracting intrinsic fluorescence in turbid media," *App. Opt.* **32**, pp. 3585-3595, 1993.
3. G.Yoon, S.A Prahl and A.J welsh, "Accuracies of diffusion approximation and its similarity relations for laser irradiated biological media," *Appl. Opt.* **28**, pp. 2250-2255, 1989.
4. Judith R. Mourant, Tamica Furelier, James Boyer, Tamara M. Jhonson and Irving J. Bigio, " Predictions and measurements of scattering and absorption over broad wavelength ranges in tissue phantoms," *Appl. Opt.* **36**, pp. 949-957, 1997.
5. R.A.J Groenhuis, H.A Ferwerda and J.J Ten Bosch, "Scattering and absorption of turbid materials determined from reflection measurements 1: Theory," *Appl. Opt.* **22**, pp. 2456-2462, 1983.
6. Anna M.K Nilson, Christian Sturesossen, David L. Liu and Stephan Anderson Engles, " Changes in spectral shape of tissue optical properties in conjunction with laser induced thermo therapy," *Appl. Opt.* **37**, pp. 1256-1267, 1998.
7. R.R.Alfano, A.Pradhan and G.C.Tang, "Fluorescence spectroscopy of tissue recovery of intrinsic fluorescence from measured fluorescence," *J.Opt. Soc. Am.B* **6**, pp. 1015-1023, 1989.
- 8-9. A. Ishimaru, *Wave propagation and scattering in Random Media*, Vol.1, Academic, Newyork, 1978.
10. T.J. Farrel, M.S. Patterson and B. C. Wilson, " A diffusion theory model of spatially resolved steady state diffuse reflectance for the non invasive determination of tissue optical properties in-vivo," *Med. Phys.* **19**, pp. 879-888, 1992.
11. R.R.Alfano, G.C.Tang, A.Pradhan, W. Lam, D.C. Choy and E. Opher, "Fluorescence spectra from cancerous and normal human breast and lung tissues," *IEEE J. Quant. Electron.* **23**, pp. 1806, 1987.
12. R.R.Alfano, S.G.Demos, A.J. Papadopoulos, H.Savage and Alexandra S.H., S. Schantz, "Polarization filter for biomedical tissue optical imaging," *Photochem. Photobio.* **66**, pp. 821-825, 1997.

---

<sup>a</sup> Correspondence: Email: asima@iitk.ac.in  
Fax: 011-91 0512 590914

<sup>1a</sup> Presently at CAT, Indore.

# Ultraviolet and blue 2-D fluorescence mapping of gynecological tissues

A. Katz<sup>a</sup>, Howard E. Savage<sup>b</sup>, Yuanlong Yang<sup>a</sup>, Fanan Zeng<sup>a</sup>, Jayson Rome<sup>a</sup>,  
Steven A. McCormick<sup>b</sup>, Rubina S. Cocker<sup>b</sup>, Yizhong Yu<sup>c</sup>, and R. R. Alfano<sup>a\*</sup>

<sup>a</sup>Institute for Ultrafast Spectroscopy and Lasers,  
The City College of New York, New York, NY 10031

<sup>b</sup>Dept. of Pathology, New York Eye and Ear Infirmary, New York, NY 10003

<sup>c</sup>Sarnoff Corporation, Princeton, NJ 08540

## ABSTRACT

Fluorescence images were acquired from gynecological tissues for multiple combinations of emission and excitation wavelengths in the ultraviolet and blue spectral regions. The wavelength combinations were selected to highlight different tissue molecules (collagen, elastin, tryptophan, NADH) whose fluorescence signatures have been shown to potential in the detection of malignancy. These images were analyzed to determine the size, shape and location of different tissue structures

**Keywords:** Optical biopsy, Native fluorescence, Cervical cancer detection

## 1. INTRODUCTION

The American Cancer Society estimates that there are 16,000 new cases and 5,000 deaths from cervical carcinoma per year.<sup>1</sup> In the United States, studies have shown that a significant fraction of women who have been diagnosed with cervical cancer, have had a normal Papanicolaou (Pap) test in the preceding 3-5 years<sup>2</sup>. The Pap test, the current standard for cervical cancer screening in the United States, is subject to errors on multiple levels, including sampling errors, reading errors by cytotechnicians and interpretation errors by pathologists. Sampling errors frequently result from an inadequate number of cells on the slide, failure to collect cells from the entire cervix, and menstrual blood or inflammation which can obscure abnormal cells. Estimates of Pap test sensitivity have ranged from 45 to 94%<sup>3</sup>. Retrospective studies have shown that 30% to 50% of women with cervical cancer had normal Pap smears in the previous 3-4 years.<sup>4</sup> One study reported that 62% of the false negative Pap smears could be attributed to sampling error by the clinician. The remaining errors were attributed to the cytotechnician (16%) and the pathologist (22%)<sup>5</sup>. In the presence of invasive cancer, the false negative rate of Pap smears may be significantly higher due to obscuring inflammation.<sup>6</sup> Improved screening techniques can significantly increase the potential for early detection, with the subsequent reduction in mortality.

Fluorescence spectroscopy has been shown to be a valuable *in vivo* tool for real-time, non invasive detection of cancer or precancer. Previous studies of gynecological tract tissue have shown that differences in the fluorescence signatures of tissues can be used to classify the tissue as either cancerous or normal. Das *et al*<sup>7</sup> investigated the fluorescence from *ex vivo* gynecological tissue and used a 340nm/440nm intra peak ratio with 300nm excitation to differentiate normal and tumor tissue of the cervix. Normal and benign tumor tissue had a lower ratio than the cancer tissue. Glassman *et al*<sup>8-10</sup> employed a combination of UV excitation and emission spectroscopy to distinguish normal from cancerous *ex vivo* gynecological tissue. In this work it was shown that, under 320 nm excitation, the ratio of emission intensities at the 383 nm and 460 nm peaks could distinguish malignant samples from normal and benign tumor. Ramanujam *et al*,<sup>11,12</sup> in an *in vivo* study demonstrated the ability to differentiate cervical interepithelial neoplastic from normal tissues. In that work, it was demonstrated that preneoplastic and neoplastic tissue could be distinguished from abnormal non-neoplastic tissue.

The goal of this work is to develop a fluorescence imaging system which can be used as a screening tool for cervical cancer. In this effort, fluorescence images were acquired from *ex vivo* normal and malignant gynecological tissue at multiple combinations of emission and excitation wavelengths in the ultraviolet and blue spectral regions. The wavelength combinations employed focused on the key tissue fluorophores (tryptophan, collagen, elastin, NADH) which have previously been used to successfully identify tumor in gynecological tissue. These images were analyzed to determine the shape and location of tissue

---

\*Correspondence: Email: [alfano@scisun.sci.ccnv.cuny.edu](mailto:alfano@scisun.sci.ccnv.cuny.edu), Telephone: 212-650-5531; Fax: 212-650-5530.

structures including tumors.

## 2. MATERIALS AND METHODS

The salient features of the system used to acquire the fluorescence images is as follows: The excitation source is a high power xenon lamp. A UV transmitting liquid light pipe delivers the excitation light to the sample. The light pipe is oriented nearly normal to the sample in order to optimize uniformity of illumination. Wavelength selection was made by narrow band interference filters. Intensity at the sample was approximately  $0.5 \text{ mW/cm}^2$ . The fluorescence was collected by a multi-element UV lens and imaged onto the photo cathode of a UV sensitive image intensifier. The image magnification was unity. Selection of the emission wavelength was also controlled by narrow band interference filters. The fluorescence signal was amplified by the image intensifier and relayed to a monochrome CCD video camera. The output of the CCD was transferred to a frame grabber mounted in a Personal Computer. Images were captured at  $640 \times 480$  pixels at a rate of 30 frames per second. The frame grabber uses an 8 bit analogue-to-digital converter to give a maximum of 256 grey levels per pixel. For each excitation and emission wavelength combination, 25 frames were acquired and stored for averaging and further processing. The spatial resolution of the system was limited by the image intensifier resolution to approximately  $100 \mu\text{m}$ .

Tissue samples were acquired from the National Disease Research Interchange. Tissues were stored at  $4^\circ\text{C}$ , and not chemically treated prior to image acquisition. After completion of the optical measurements, the samples were stored in formalin and transported to the pathology for histopathological analysis. Images were acquired at five combinations of excitation and emission wavelengths. These wavelengths were chosen based on prior studies which have shown that various intensity ratios calculated from these combinations have exhibited high accuracy in the ability to predict the presence of cancer. These combinations correspond to absorption or emission peaks from different tissue fluorophores. The emission peak from tryptophan is at  $340 \text{ nm}$ , from collagen at  $380 \text{ nm}$ , and both NADH and elastin emit at  $440 \text{ nm}$ . Collagen absorption peaks at  $340 \text{ nm}$ . The first filter combinations primarily measures emission from tryptophan, collagen, elastin and NADH.

## 3. EXPERIMENTAL RESULTS

Differences in emission intensity between normal and cancerous tissue images were observed. These differences were consistent with spectral differences observed in prior studies. Some of these differences can be seen in the fluorescence images from a malignant (S185) and a benign (S186) cervical tissue sample, as shown in Figs. 1 and 2, respectively. The  $340 \text{ nm}$  emission images, with  $\lambda_{\text{ex}} = 300 \text{ nm}$ , are shown in Figs 1(a) and 2(a) and the  $440 \text{ nm}$  emission images are shown in Figs. 1(b) and 2(b), respectively. The respective ratio maps,  $I_{340}/I_{440}$  for these two samples are shown in Figs. 1(c) and 2(c). The images have been inverted, i.e. darker regions represent either higher emission intensity ((a) and (b)), or higher ratio (c). Sample S185 is predominantly tumor with small regions of inflammation on the right side and bottom of the sample. Pathology has identified the S186 as consisting of a benign fiber muscular tumor located in the lower left half of the sample with areas of inflammation

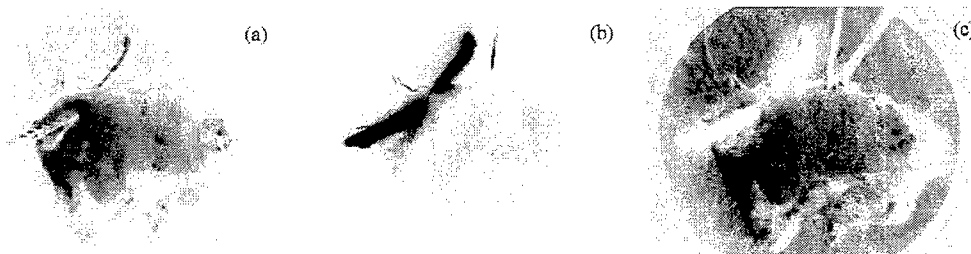


**Figure 1.** Fluorescence images from cancerous cervical tissue S185. (a)  $\lambda_{\text{ex}} = 300$ ;  $\lambda_{\text{em}} = 340 \text{ nm}$ . (b)  $\lambda_{\text{ex}} = 300$ ;  $\lambda_{\text{em}} = 440 \text{ nm}$ . (c) Ratio  $I_{340}/I_{440}$ .



**Figure 2.** Fluorescence images from benign tissue S186. (a)  $\lambda_{\text{ex}} = 300$ ;  $\lambda_{\text{em}} = 340 \text{ nm}$ . (b)  $\lambda_{\text{ex}} = 300$ ;  $\lambda_{\text{em}} = 440 \text{ nm}$ . (c) Ratio  $I_{340}/I_{440}$ .



**Figure 3.** Fluorescence images from cancerous cervical tissue S185. (a)  $\lambda_{ex} = 340$ ;  $\lambda_{em} = 380$  nm. (b)  $\lambda_{ex} = 300$ ;  $\lambda_{em} = 380$  nm. (c) Ratio  $I_{340}/I_{300}$ .

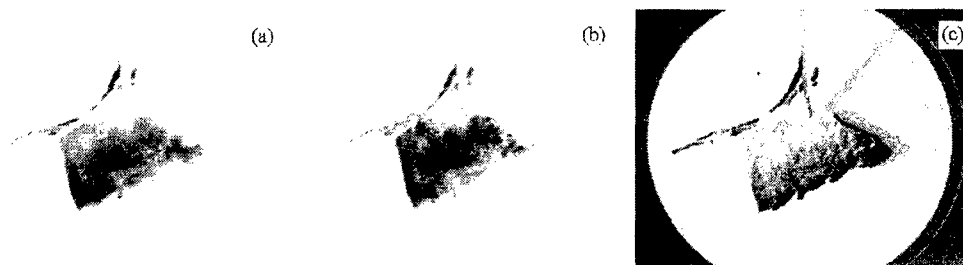


**Figure 4.** Fluorescence images from benign tissue S186. (a)  $\lambda_{ex} = 340$ ;  $\lambda_{em} = 380$  nm. (b)  $\lambda_{ex} = 300$ ;  $\lambda_{em} = 380$  nm. (c) Ratio  $I_{340}/I_{300}$ .

throughout the upper part of the tissue. The tissues were marked with a stitch on the upper left to assist pathology in orienting the samples relative to the fluorescence images.

It was observed that the  $I_{340}$  signal (tryptophan emission) from the cancer sample was higher than from the benign sample. The tumor regions of S185 also exhibited higher  $I_{340}$  signal than the non tumor regions. On the other hand, the  $I_{440}$  signal (NADH emission) from S185 was much weaker than from both the benign tumor and inflamed regions of S186. Consequently, the  $I_{340}/I_{440}$  ratio from the cancer sample is significantly larger than from the benign sample. This can be observed in the ratio maps of S185 and S186 (Figs 1(c) and 2(c), respectively). Significant is that the benign tumor and inflamed areas of S186 appear different from the cancer regions in S185, indicating that fluorescence measurements may be able to distinguish malignant tissue from either benign or inflamed tissues.

The  $\lambda_{em} = 380$  nm images from S185 and S186 for  $\lambda_{ex} = 340$  nm and  $\lambda_{ex} = 300$  nm are shown in Figs. 3(a)(b) and 4(a)(b), respectively. The images are inverted such that darker areas in the figures represents regions of higher emission intensity. The filter combination used to acquire the images in Figs. 3(a) and 4(a) primarily measure collagen emission. Almost no collagen signal is observed in the emission from the cancer sample while the collagen emission can be observed from both the benign tumor and inflamed regions of S186. Conversely, the  $I_{380}$  emission with  $\lambda_{ex} = 300$  nm is greater from the cancer sample than the benign sample. Examination of Fig. 3(b) reveals that the largest signal comes from the malignant regions of S185. Generating ratio maps for these samples further highlights the intensity differences. These  $I_{340}/I_{300}$  maps are shown in Figs. 3(c) and 4(c), in which the S185 ratio map is significantly than the benign sample.

In addition to being able to distinguish cancer from benign tissue by differences in emission intensity, features were observed in the fluorescence images which correlated with structures identified by histopathological analysis revealed additional structures in the tissues. The  $\lambda_{ex} = 340$ ,  $\lambda_{em} = 380$  nm fluorescence image from a normal uterine is shown in Fig. 5. Darker regions of the image represent higher intensity regions. Some of the structures identified by pathology and

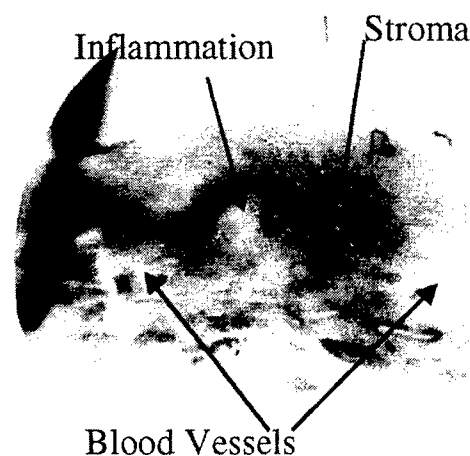


**Figure 5.** Fluorescence image of normal uterine sample,  $\lambda_{ex} = 340$ ,  $\lambda_{em} = 380$  nm.



visible in this image are: A region of stroma in the center of the tissue can be located by the higher collagen signal from the stroma area. Areas of inflammation to the left of the stroma exhibits weaker collagen emission. Multiple blood vessels are identified by lower intensity areas. Two of these vessels are identified in Fig. 5. Additional blood vessels were identified near the bottom of the sample. The increased blood absorption resulted in weaker fluorescence in this area.

### CONCLUSION

In conclusion, this work has demonstrated the UV fluorescence images corresponding to the emission wavelengths of collagen, NADH and tryptophan may be able to differentiate malignant tissue from normal, benign tumor or inflamed *ex vivo* tissues. It has also been demonstrated that different tissue structures such as blood vessels, can be identified by fluorescence images. The extension of this work to *in vivo* measurements may provide an effective method to identify cancerous or precancerous regions of the cervix and provide a valuable screening technique for early cancer detection.

### ACKNOWLEDGMENTS

This work was supported by grants from NASA and the Department of Energy.

### REFERENCES

1. S. L. Parker, T. Tong, S. Bolden, and P. A. Wingo, "Cancer statistics, 1996," *Ca-Cancer J. Clin.*, 65, 5-27 (1996).
2. H. Singleton and J. Orr, *Screening in Cancer of the Cervix*, Lippincott-Raven, Philadelphia, Pa., (1995)
3. H. M. Singleton, R. L. Patrick, W. W. Johnston, and R. A. Smith, "The current status of the Papanicolaou smear," *Ca Cancer J Clin*, 45, 305-320 (1995).
4. A. P. Korn, 1996., "Innovations in Pap Screening for Cervical Neoplasia," ([www.medscape.com/Medscape/WomensHealth/Journal/1996/v01.n10/w155.korn.html](http://www.medscape.com/Medscape/WomensHealth/Journal/1996/v01.n10/w155.korn.html))1996).
5. J. Gay, L. Donaldson, and J. Goellner, "False-negative results in cervical cytologic studies," *Acta Cytology*, 29, 1043-1046 (1985).
6. C. M. Stanbridge, B. A. Suleman, R. V. Persad, and e. al., "A cervical smear review in women developing cervical carcinoma with particular reference to negative cytology and the histologic age, false-type of the carcinoma," *Inter. J. Gyne. Ca.*, 2, 92-100 (1992).
7. B. B. Das, W. L. Glassman, R. R. Alfano, J. Cleary, R. Prudente, E. Celmer, and S. Lubicz, "UV-fluorescence spectroscopic technique in the diagnosis of breast, ovarian, uterus, and cervix cancer," *Laser-Tissue Interaction II*, 1427, S. L. Jacques, Ed., 368-373, SPIE Proceedings, Los Angeles, CA, 1991.
8. W. Glassman, C.-H. Liu, S. Lubicz, and R. R. Alfano, "Excitation spectroscopy of malignant and non-malignant gynecological tissues," *Lasers Life Sci.*, 6,, 99-106 (1994).
9. W. S. Glassman, C. H. Liu, G. C. Tang, S. Lubicz, and R. R. Alfano, "Ultraviolet excited fluorescence spectra from non-malignant and malignant tissues of the gynecological tract," *Lasers Life Sci.*, 5,, 49-58 (1992).
10. W. Sha Glassman, C. Liu, G. C. Tang, S. Lubicz, and R. R. Alfano, "Ultraviolet excited fluorescence spectra from non-malignant and malignant tissues of gynecological tract," *Lasers Life Sci.*, 4, 23-28 (1991).
11. N. Ramanujam, M. F. Mitchell, A. Mahadevan-Jansen, S. L. Thomsen, G. Staerckel, A. Malpica, T. Wright, N. Atkinson, and R. Richards-Kortum, "Cervical precancer detection using a multivariate statistical algorithm based on laser-induced fluorescence spectra at multiple excitation wavelengths," *Photochem. Photobiol.*, 64, 720-35 (1996).
12. N. Ramanujam, M. F. Mitchell, A. Mahadevan, S. Thomsen, A. Malpica, T. Wright, N. Atkinson, and R. Richards-Kortum, "Spectroscopic diagnosis of cervical intraepithelial neoplasia (CIN) in vivo using laser-induced fluorescence spectra at multiple excitation wavelengths," *Lasers Surg. Med.*, 19, 63-74 (1996).

# Visualization of Photon Propagation and Abnormality Detection

Jun Ge<sup>1</sup>, Zisheng Le and David Yun<sup>2</sup>

Laboratory of Intelligent and Parallel Systems, University of Hawaii  
492 Holmes Hall, 2540 Dole Street, Honolulu, HI 96822

## Abstract

An approach to computer assisted imaging diagnosis is introduced for tumor detection in tissues, using softer light sources and detection from both transmission and reflection. A 3D model, described by the diffusion equation, is developed to simulate the photon propagation inside human tissue to detect the tumor or other inclusions. The inclusion is modeled with a different absorption coefficient from that of the otherwise homogeneous media. The Alternating Direction Implicit (ADI) algorithm is used to solve the diffusion equation on each spatial grid at each time instance in an iterative manner. The data on a cut section of the model at a certain moment is visualized to be a picture according to the photon intensity value. Pictures of different moments can be linked to construct a dynamic movie for the presentation of the photon propagation procedure on a specific cut-plane. The movies show that in the homogeneous model the photon density has a symmetric concentric distribution on the plane opposite the source. When an off-center inclusion is introduced inside the model, a clear asymmetry appears. The shadow of the inclusion is determined by both the size and the location of the inclusion. If the inclusion is moved to the center, the symmetry is restored, though different from the original image. To reach a more precise result, the derivative of the intensity, with respect to the distance from the light source, is computed. From the dynamic derivative curves, the size of the inclusion can be estimated. Experiments verify the conclusion on inclusions of arbitrary dimensions which are larger than 5 mm. A scanning search strategy is proposed for unknown inclusions.

**Key words:** diffusion equation, simulation, visualization, Alternating direction implicit (ADI)

## 1. Introduction

Near-infrared (NIR) laser technology is being explored as a promising direction of cancer detection in its early stage. NIR laser has more benefits than the traditional X-ray or other computational tomography (CT) techniques because it is safe to the healthy tissue [1,2,5]. The photon travels inside the tissue more like a wave than a particle. In the physical application, the photons are assumed to be radiated by an extremely fast pulse laser, and the light propagates in a turbid scatter-dominated medium. The photon propagation through such media can be described by the Boltzmann transport equation. Due to the high scattering medium property of the human tissue, the light propagation can be described by the diffusion equation:

$$\frac{\partial}{\partial t} \varphi(r, t) = \text{div}(D \text{grad} \varphi(r, t)) - c \mu_a(r) \varphi(r, t) + s(r, t), \quad r \in \Omega, t \geq 0 \quad (1)$$

where  $\varphi(r, t)$  is the photon density at position  $r$  at time  $t$ ,  $\mu_a$  is the absorption coefficient, and  $s(r, t)$  is the source input.

The coefficient  $D$  is given by

$$D = \frac{c}{3(\mu_a(r) + \mu'_s(r))} \quad (2)$$

where  $\mu'_s(r)$  is the reduced scattering coefficient,  $c$  the speed of light. Given a model, the light propagation is simulated based on the impulse source input. The boundary condition is set to  $\varphi(x, t) = 0$ ,  $x \in \partial\Omega, t \geq 0$  in order to simulate the highly absorbing medium around the model. The human tissue has an absorption coefficient  $\mu_a$  to indicate the feature of media with respect to the given laser source. The tumor tissue has a different absorption coefficient other than the normal tissue while it keeps other parameters the same with normal tissue. Therefore, the human tissue with inclusion inside is simulated by a model with a specific distribution of absorption coefficient. The normal tissue is considered as the background media with a constant absorption coefficient, while the regions with particular absorption coefficient indicate the tumor tissues. The location and the size of the inclusion certainly play an important role in the propagation of photons. Because photons of NIR laser do not travel in straight line, the "shadow" resulted by the inclusion is quite different from what we get in X-ray image.

There are several image reconstruction algorithms such as Newton-Raphson iteration, Extended Kalman Filter, etc [9-11]. These algorithms deal with the output signals that are involved with the noise. However, these algorithms usually have problem in convergence and stability and are computational time cost. Visualization is an alternative approach to explore the

<sup>1</sup> Correspondence: Email: [gejun@spectra.eng.hawaii.edu](mailto:gejun@spectra.eng.hawaii.edu); Telephone: 808-956-7249

<sup>2</sup> Correspondence: Email: [dyun@spectra.eng.hawaii.edu](mailto:dyun@spectra.eng.hawaii.edu); <http://www-ee.eng.hawaii.edu/~uhlips/>; Tel: 808-956-7627; Fax: 941-1399

information of the inclusion. In this paper, by using Alternating Direction Implicit (ADI) algorithm in 3D<sup>[3,4,6]</sup>, models of different inclusion conditions are used to study the influence of the location and the size of inclusion. ADI has been proven to be a mature and effective algorithm for partial differential equations by computing the finite difference equation in all the directions separately. ADI is absolutely stable because of its implicit finite difference scheme. It is easy to be parallelized for large-scale equation, especially for the life-size model.

ADI computes the photon intensity in every spatial grid at every time step. These time-series volumetric data are mapped with respect to a color table. By cutting the rectangular model with a specified plane, a 2-D picture can be captured from any viewpoint. The time-series pictures are linked to build a dynamic "movie" of propagation procedure. Considering the possible location of detectors, only source-surface and detector-surface are used in this paper (Figure 1). In NIR laser propagation, the shadow of inclusion occurs not only on detector-surface, but also on source-surface. To enhance the effect of inclusion's influence, the photon density of the homogeneous model is subtracted from the corresponding values of model with inclusion inside.

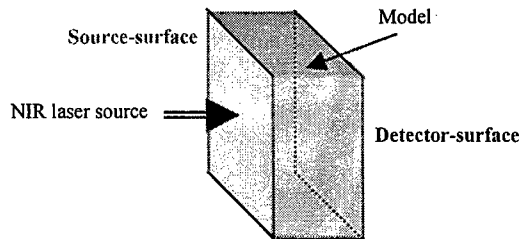


**Figure 1. Source-plane and Detector-plane**

Section 2 introduces the approach that visualizes the photon intensity distribution. A visualization tool is developed to demonstrate the procedure of photon propagation. Section 3 introduces the settings and conditions of the simulation experiments in this study. Section 4 presents the result of inclusion location influence. Based upon the peak position of subtraction pictures, it is easy to locate the center of inclusion approximately. In section 5, dynamic directional derivative curve is introduced into the analysis. The size of inclusion can be determined from the curves. Based on the detection results on the location/size of inclusion, a scanning search strategy is proposed for inclusion (tumor tissue) detection in section 6.

## 2. Visualization of Volumetric Data

There are many techniques available to visualize volumetric data, including section view, iso-surface and volume rendering. Among them, section view, which visualizes 3D data slice by slice, has advantage over others due to its simplicity, and is still in use mostly in the primary analysis stage where comprehensible 3D configuration is very difficult to establish. Based on section view technique, *VisualTool*, a visualization tool, is developed to visualize the volumetric data on controllable arbitrary cut plane. Curves, images and movies can be obtained to extract the detailed static and dynamic features of the volumetric data. Several aspects are considered in *VisualTool*.

The first problem encountered in visualization is color mapping: to establish a mapping relationship between the set of data and the set of colors<sup>[7,8]</sup>. In the research of photon propagation, the photon intensity varies greatly from  $10^{-5}$  to  $10^7$ . On the other hand, the colors available are limited due to the hardware and the sensibility of human eye. It is necessary to build a mapping relationship between data and color. When processing the data dynamically as well as statically, a successful mapping on dynamic volumetric data can reach good visualization effect, such as indicating the slight difference, showing the transition period of the procedure and so on. In order to get a satisfactory color mapping, several strategies are tested which include mapping fixed color to a specific data range, mapping data to color components and mapping data to a color index. After comparing the effect of these strategies, the method that maps a value  $v$  to a color index  $I$  is selected. The mapping function is defined as follows  $I = N \cdot \max(1/N, [\log_{10}(v+1)/\log_{10}(v_{Max}+1)])$ , where  $I$  is the  $i^{\text{th}}$  color in the sequence of total  $N$  colors that are pre-defined,  $v \in [v_{Min}, v_{Max}]$ , and  $0 < v_{Min} < v_{Max}$ . *VisualTool* provides several default color tables, including a rainbow color mapping in which all colors vary in the sequence of the rainbow color except the background color. Color mapping is an application-specific problem. A good mapping effect comes from a good pre-analysis on the data, including the range and the distribution. Also, color mapping is a particular data process problem. Searching for the best mapping is a challenging experiment task. This suggests that besides the default mapping it be better to provide ways by the user to define a specific problem-based color sequence to meet different requirements. *VisualTool* is able to accept a user-defined mapping table besides the default mapping.

The second problem is to select visualization style. In the application of photon propagation, several aspects, including photon propagation, section go-through, static view and dynamic curve view, etc., are required to demonstrate the dynamic volumetric data. In propagation style users are allowed to view the photon propagation procedure at a specific cut-plane. Go-through style provides users to walk through the model in geometry along a direction to check the photon distribution at a specific moment. Static view style allows users to view all the data on the same plane at a specific time. While dynamic curve view shows the time-series curves on the grids of interest. In fact, these styles are complementary in helping to appreciate and to understand the physical process from different viewpoints. A double-buffer technique is applied to improve the visualization quality. Figure 2 shows an example of data visualization on a cut-plane.

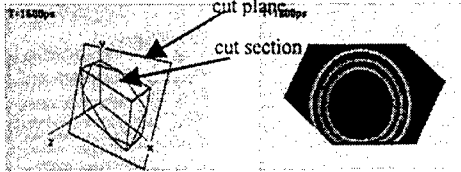


**Figure 2. Example of Cutting-plane Data Visualization**

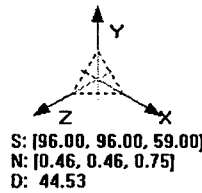


**Figure 3. Control Window**

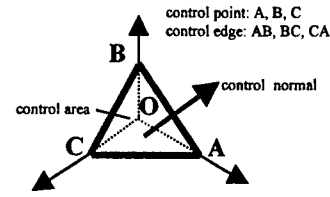


**Figure 4. Control Triangle**

The third aspect is the control of the viewer. The most important part in *VisualTool* is the control window design. In order to distinguish the window that contains the “graphics of visualized data” from the window that controls the viewpoint (cut-plane), the former is named application window and the latter control window, respectively. Once the cut-plane (the viewpoint) is adjusted by operating the control window, the corresponding application window starts to visualize the data on the new cut-plane. Figure 3 shows one status of the control window. Where,  $S:[96.00, 96.00, 59.00]$  means that the cut-plane intercepts three axis X, Y, Z at 96.00, 96.00 and 59.00 respectively;  $N$  is the normal direction of cut-plane, and  $D$  shows the distance from the original point to cut plane. Three operation methods are defined to control the cut-plane: moving control points, rotating control edges and dragging control normal. This kind of control design is novel and easy to understand. The control rules are in conformity with favorite operation habituation of users. User can always dominate the control of objects and have no limitation in physical space.

### 3. Experimental Settings and Conditions

The inclusion inside the model affects the distribution of photon intensity. Therefore, the possible inclusion inside the model can be located from the difference between the photon distributions comparing to the homogeneous case. However, the photons do not propagate in a straight line like X-ray. The traditional algorithms of image reconstruction are not applicable for NIR laser. A visual approach is presented to identify the inclusion by comparing the signal to the standard signal (of the homogeneous model). Experiments based on simulation results show the effectiveness of this method. A rectangular model ( $\Omega$  in Equation (1)) of  $180 \times 136 \times 70 \text{ mm}^3$  size with a cubic inclusion inside is used in the simulation. The length of the inclusion varies from 2 mm to 10 mm. The model size is large enough to satisfy the scatter-dominant condition of applying diffusion equation. The NIR laser source is placed at the center of one surface (Figure 1). The input signal from the source is considered to be an impulse signal. The output signals are the pulse-response signals on the grids at source-surface and detector-surface. To simplify the problem, the inclusion is moved in two dimensions only. The location of the inclusion changes at several different positions with respect to the location of the source (Figure 5).

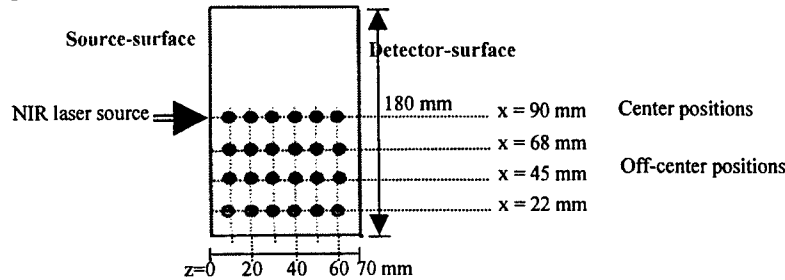


**Figure 5. Distribution of inclusion locations in 2D**

A total of 24 positions are selected for inclusion locations. They are in a 2D plane that is in the middle of Y-axis, which are symmetric with respect to model boundary. Therefore, the pulse response signals are the same on the symmetric grids with

respect to the middle line in Y-axis. Each time, there is one inclusion inside the model at one of the specified locations. When the inclusion is moved along the X-axis, the influence of the inclusion inside will be presented along X-axis as well.

ADI simulation algorithm is used to compute the photon intensity of each grid. The photon intensity values of the grids in source-surface and detector-surface are recorded for comparison. From the view point of practice, the information of both the source-surface and the detector-surface is important and available. A spatial grid size of 1mm is used in ADI simulation. Therefore, for each surface at one time step, there are  $180 \times 136$  grids (values) to construct the picture. Several optical parameters in Equation (1) and (2) are taken as follows, which are estimated under the clinic condition.

Background's absorption coefficient  $\mu_a = 0.0057 \text{ mm}^{-1}$ ;

Inclusion's absorption coefficient  $\mu_a = 0.06 \text{ mm}^{-1}$ ;

Reduced scattering coefficient  $\mu'_s(r) = 1.03 \text{ mm}^{-1}$ ;

Speed of NIR light  $C = 0.2254 \text{ mm/ps}$ .

#### 4. Visualization of Dynamic Subtraction Pictures for Location Influence

In ADI simulation, the photon intensity values in source-surface and detector-surface are collected at each time step as an array with dimension of  $180 \times 136$ . By using *VisualTool*, every number is converted to a color according to the predefined color table, thus the array to a picture. From the pictures, it can be found that the inclusion brings an extra "shadow" on both source-surface and detector-surface. Figure 6 shows the source-surface pictures and detector-surface pictures for two different inclusion sizes at the same location. Figure 7 shows the shadow resulted from an off-center inclusion of 5-mm size.

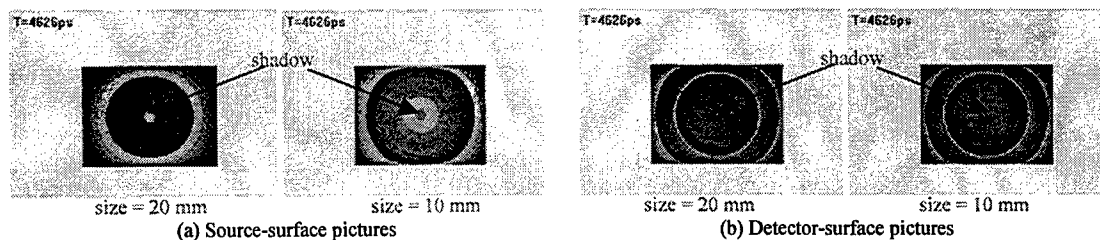


**Figure 6. Pictures of shadow with respect to different inclusion sizes**

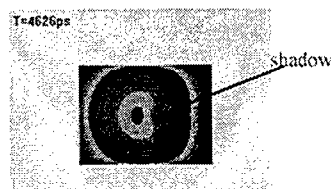


**Figure 7. Off-center shadow in source-surface**

However, the shadow becomes unclear enough the inclusion size is small. Furthermore, it is hard to distinguish the propagation distribution from the influence of the inclusion. Thus, a subtraction picture is introduced to ignore the normal distribution in the propagation and to enhance the inclusion influence even when the inclusion size is small. Each value in the  $180 \times 136$  array is the subtraction value of a heterogeneous model from a homogeneous model (model without inclusion inside) instead. In subtraction pictures, the difference between with and without the inclusion is compared. Figure 8 shows the subtraction pictures on detector-surface for inclusions with different sizes at the same location.

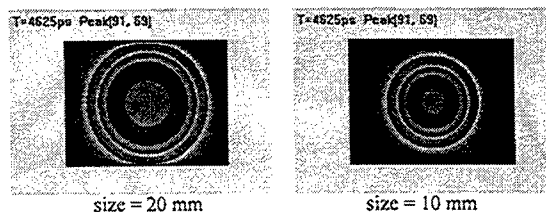


**Figure 8. Subtraction pictures of shadow with respect to different inclusion sizes on detector-surface**

In Figure 8, the brighter the color, the higher value the corresponding value is. It is obvious to discover the influence of the inclusion of larger size is more significant and apparent, which suggests subtraction picture is a better way to analyze the inclusion influence. The values in subtraction array show the difference of the response signals for a homogeneous model and a heterogeneous model. The difference of the response signals is so-called "inclusion shadow" resulted from the inclusion. The location where the difference reaches the maximum is considered as the center of the shadow.

For the inclusion in the center position, which is symmetric in geometry structure of the model, the shadow is of course in the center of the picture. It is important to explore the shadow when the inclusion is off-center. The shadows (with respect to the corresponding off-center locations in Figure 1) are compared to each other in order to discover the relationship between the shadow location and inclusion location. As in straight-line projection, such as X-ray, the shadow of the inclusion can be bounded by the straight line from the point light source and the edge of the inclusion. The center of the shadow should be almost on the straight line that connects the light source point and the inclusion center. However, for NIR laser propagation in the model, the dominant factor is scattering. The edge of the shadow is not clear because of the diffraction effect of wave. The subtraction pictures are used to explore the relationship. Figure 9 shows some pictures of detector-surface on different inclusion center location. The number on each picture is the center of the shadow. It is easy to discover that the center of the shadow is approximate to the position of the inclusion. Both the source-surface subtraction picture and the detector-surface subtraction picture have the similar conclusion.

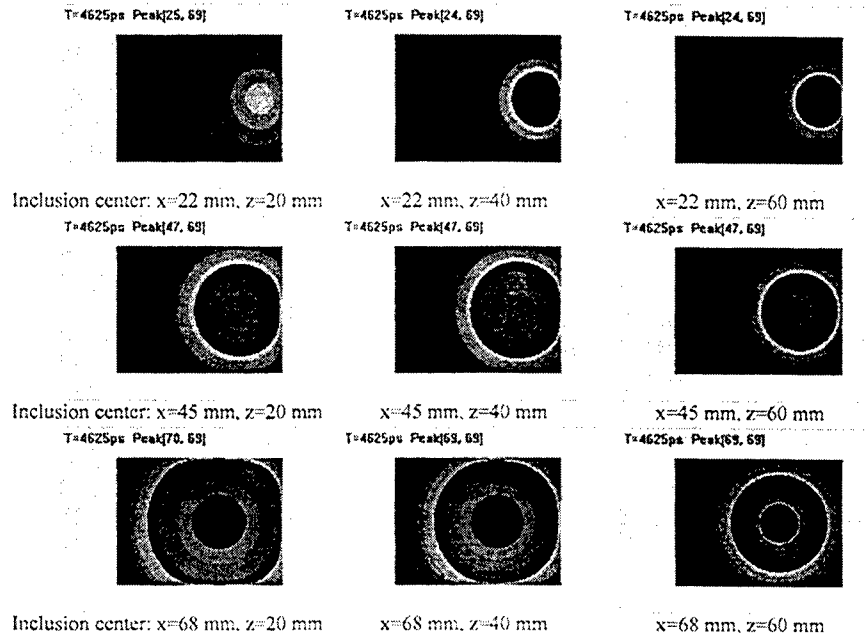


**Figure 9. Detector-surface subtraction pictures on detector-surface**

Table 1 and 2 show the positions of the corresponding shadow centers for different inclusion locations (as shown in Figure 1) on detector-surface and on source-surface. The shadow center is very close to center location in x- and y- coordinate. The distance to the surface does not have a lot of influence on the shadow. The closer the inclusion to the source in x-coordinate, the closer to the inclusion center the shadow center is.

Location of shadow center (x-coordinate)		X-coordinate for inclusion center		
z-coordinate of inclusion center	Z=10 mm	x=22 mm	x=45 mm	x=68mm
	Z=20 mm	24.5 mm	46.5 mm	69.5 mm
	Z=30 mm	24.5 mm	46.5 mm	69.5 mm
	Z=40 mm	24.5 mm	46.5 mm	69.5 mm
	Z=50 mm	23.5 mm	46.5 mm	68.5 mm
	Z=60 mm	23.5 mm	46.5 mm	68.5 mm

**Table 1. Shadow centers on the detector-surface (z=70 mm)**

Location of shadow center (x-coordinate)		X-coordinate for inclusion center		
		x=22 mm	x=45 mm	x=68mm
z-coordinate of inclusion center	Z=10 mm	23.5 mm	46.5 mm	68.5 mm
	Z=20 mm	23.5 mm	46.5 mm	68.5 mm
	Z=30 mm	23.5 mm	46.5 mm	68.5 mm
	Z=40 mm	23.5 mm	46.5 mm	68.5 mm
	Z=50 mm	24.5 mm	46.5 mm	68.5 mm
	Z=60 mm	25.5 mm	46.5 mm	68.5 mm

**Table 2. Shadow centers on the source-surface (z=0 mm)**

The visualization result of subtraction pictures shows that the shadow center is less relevant to the source location. The center of the shadow has the relationship with the center of inclusion as the diffraction projection shown in Figure 10 (c).

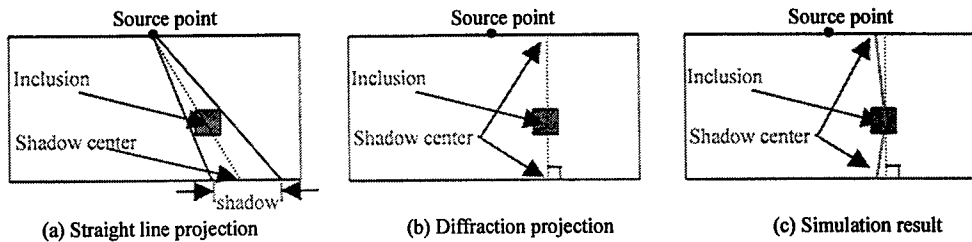
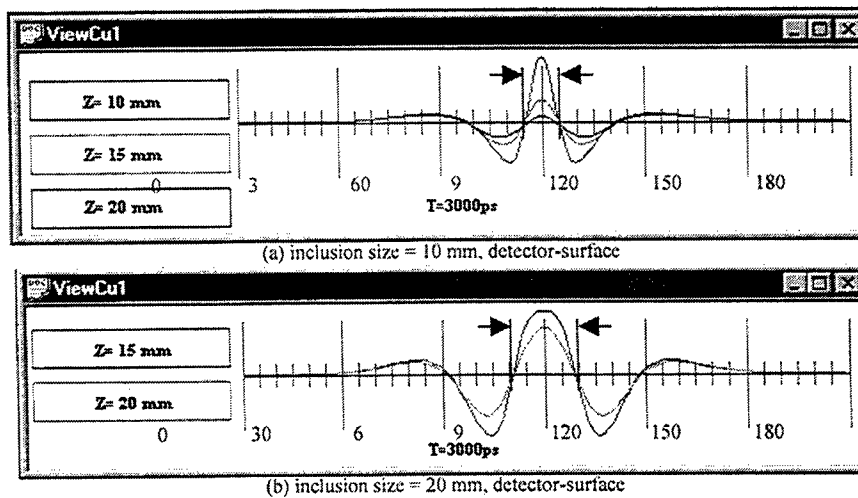


**Figure 10. Shadow of the inclusion**

The result shows that the location of the inclusion can be approximately identified by using the subtraction pictures on source-surface or detector-surface.

### 5. Further Exploration on Size Influence

To explore the inclusion further, derivatives along a line is used to determine the size of the inclusion. Since the shadow of the inclusion does not exactly match the center location when the inclusion is off-center, the influence of the inclusion's size is studied when assuming its location is found. In this case, the source is moved to the center of the shadow so that the shadow becomes symmetric at any direction. The directional derivative curve is computed on the pulse response at each time step. Only the line that passes through the shadow center is applied. The simulation result shows that the inclusion's size can be determined from the second order derivative curve. When the inclusion locates in the different distance to the source-surface and detector-surface, the derivative values are different. However, they intersect with the zero line at the same positions approximately. The distances between two intersection points are around the size of the inclusion. Figure 11 shows the results from the second order derivative curve on both source-surface and detector-surface and with different distances to the surface. Therefore, this result can be used to estimate the size of the inclusion.



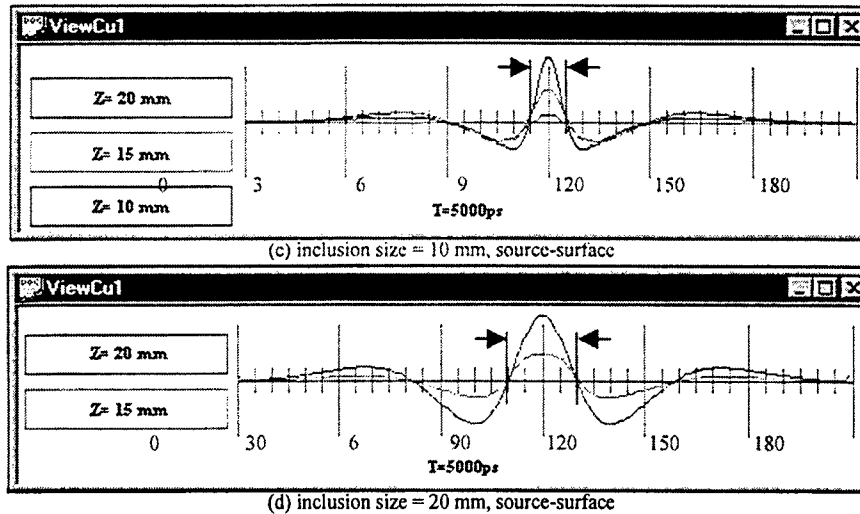


**Figure 11. The distance between two cross points to zero is around the size of inclusion**

## 6. Discussions

The experiments in Section 4 and 5 present some conclusions on determining both the location and size of the inclusion approximately through the visualization result. Based upon these results, a scanning strategy for inclusion detection is introduced as follows, with Location detection (Figure 12):

1. Given a rectangular model, use a point NIR laser source to provide impulse signal from one surface.
2. Record the pulse response on the source-surface and on the detector-surface, compute the subtraction pictures with respect to the pulse response of a homogeneous model.
3. Use *VisualTool* to locate the center of any shadow.
4. Move the laser source to the center of the shadow.
5. Repeat step 1-4 until the center of the shadow becomes the perpendicular projection of the source. Thus, the inclusion is identified in a 2-D range.
6. Repeat step 1-5 while the source is located on other model surfaces to locate the inclusion in other 2-D range.

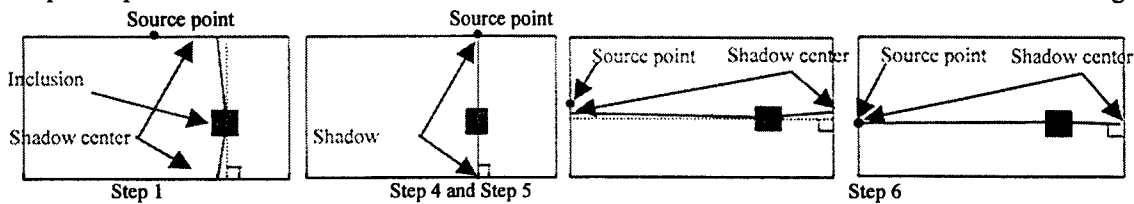


**Figure 12. Steps for location detection**

Size detection:

1. After finding the location of the inclusion, move the source to the correspondent position so that the shadow of the inclusion becomes symmetric in every direction.
2. Compute the second order derivative curve along the line that passes through the center of the shadow on the source-surface and detector-surface.
3. Measure the distance between two cross points with the zero value as the size of the inclusion.

The scanning approach makes use of visualization tool to detect the information (location and size) of the inclusion. It does not require extra iterative computation to solve any inverse equation. Therefore, it becomes a worthy approach in inclusion detection. The limitation of this approach is that the noise will bring false alert in detection. When the inclusion is deep inside the model, the shadow becomes not as strong as when the inclusion is near the source-surface or detector-surface.

## 7. Conclusions

Diffusion equation is used to analyze and visualize photon propagation for the detection of tumor or regular conditions inside human tissues. Visualization method is used in this paper to assist the detection of inclusions inside a tissue model. A *VisualTool* with color mapping is applied to visualize ADI simulation results. Simulation experiments show that an off-



center inclusion introduces the asymmetric phenomena in the response signal that is both visual and computable. The location of the shadow resulted from the inclusion is roughly independent of the source location. The location of the inclusion in 2D can be detected from the visualized shadow of the inclusion. Therefore, there is an interactive method by moving source position to find the inclusion location. From the second order directional derivative curve, the size of the inclusion can also be determined. A 2-step scanning strategy is proposed based on these conclusions to detect both the 3D location and the size. Response signals both on source-surface and on detector-surface can be used in visualization and detection. This work shows that combining computation and visualization for tumor detection constitutes a useful approach to computer assisted imaging diagnosis.

### References

1. C. Lindquist, R. Berg and S. Andersson-Engels, Numerical diffusion modeling of interfering photon density waves for optical mammography, SPIE Vol. 2326, 31-39, 1998
2. M. S. Patterson, B. Chance, B. C. Wilson, Time resolved reflection and transmittance for the non-invasive measurement of tissue optical properties, Applied Optics, Vol. 28, 2331-2336
3. W. H. Press, S. A. Teukolsky, W. T. Vetterling, B. P. Flannery, Numerical recipes in C: the art of scientific computing, 2nd edition, Cambridge University Press, 1994
4. D. W. Peaceman, H. H. Rachford, The numerical solution of parabolic and elliptic differential equations, J. Soc. Indust. Appl. Math., 3(1955), 28-41
5. R. Model, R. Hunlich, D. Richter, et al, Imaging in random media: simulating light transport by numerical integration of the diffusion equation, Proc. of Photon Transport in Highly Scattering Tissue, SPIE Vol. 2326, 11-22, Lille, France, 1994
6. J. Ge, D. Yun, Multigrid ADI algorithm for solving diffusion equation, Proc. of SPIE, Photonic Devices and Algorithms for Computing, SPIE Vol. 3805, p. 184-193, Denver, CO, USA, 1999
7. C. Healey, Choosing effective colours for data visualization, Proc. Visualization 1996, pp. 263-270, San Francisco, CA
8. C. Healey, Perceptual Colours and Textures for Scientific Visualization, SIGGRAPH 98 Course 32: Applications of Visual Perception in Computer Graphics, Orlando, Florida, 1998
9. M. Eppstein, D. Dougherty, et al, Biomedical optical tomography using dynamic parameterization and Bayesian conditioning on photon migration measurements, Applied Optics, Vol. 38, No. 10, p. 2138-2149, April, 1999
10. M. Klibanov, T. Lucas, R. Frank, New imaging algorithm in diffusion tomography, preprint
11. V. L. Syrmos, J. Yin, D. Yun, "The Photon Diffusion Equation: Forward and Inverse Problems," in IEEE Conference on Control Applications and IEEE Symposium on Computer-Aided System Design, Hawaii, Aug., 1999.

# The simulation comparisons of diffusion equation<sup>1</sup>

Jun Ge, Sixiang Nie, Vassillis Syrmos, David Yun<sup>2</sup>

Laboratory of Intelligent and Parallel Systems, University of Hawaii  
492 Holmes Hall, 2540 Dole Street, Honolulu, HI 96822

## Abstract

Near infrared laser (NIR) is being explored in clinic diagnosis of early-stage cancer. Diffusion equation is used as the mathematical model to describe photon propagation inside human tissues. In this paper, two numerical algorithms, ADI and FEM, are applied in solving the diffusion equation. All the algorithms reach a satisfactory precision on a human-tissue model of realistic size. Results from simulation and experimental are compared and show a good match. Further analysis on algorithm convergence for both spatial grid size and time step also shows the algorithmic stability. The multigrid version of both ADI and FEM are developed to save computational time and memory. The multigrid algorithms use fine grid size in the region of interest and coarse grid size elsewhere. Parallelization implementation is completed for all the algorithms in both share-memory mode and message passing mode. Numerical simulation experiments show that all simulators can serve as computed experiments, i.e. an alternative to physical experiments.

**Key words:** diffusion equation, simulation, multi-grid, model reduction, Finite element algorithm (FEM), Alternating direction implicit algorithm (ADI), parallelization

## 1. Introduction

The development of laser light sources the use of light in therapeutic and diagnostic medicine has increased rapidly. Especially in detecting the possible cancer tissue in women's breast, this technology is being researched widely nowadays because it has the advantage that light laser does not hurt healthy cells as X-ray does. Therefore, it is safer than X-ray in clinic use. For the laser impulse input of the wavelength located in a near infrared (NIR) region, the tissue constituents absorb less than for other wavelengths, allowing a thicker tissue sample to be examined. Human tissue is considered as a high-scattering media for the photons travelling inside.

The photon density wave propagation can be described by Maxwell's transport theory. However, it can be analytically solved only under some specific geometry. The transport equation in a general form has to be solved numerically. With the assumptions that the scattering dominates over the absorption and that detection is far away from the light source, the transport equation can be approximated to a parabolic diffusion equation as:

$$\frac{\partial}{\partial t} \varphi(r, t) = \text{div}(D \text{grad} \varphi(r, t)) - c \mu_a(r) \varphi(r, t) + s(r, t), \quad r \in \Omega, t \geq 0, \quad (1)$$

where  $\varphi(r, t)$  is the photon density on position  $r$  at time  $t$ ,  $\mu_a$  the absorption coefficient,  $s(r, t)$  the source input. Coefficient  $D$  is derived as

$$D = \frac{c}{3(\mu_a(r) + \mu'_s(r))},$$

where  $\mu'_s(r)$  is the reduced scattering coefficient which is much larger than  $\mu_a(r)$ ,  $c$  is the constant light speed in the media.

For the time-resolved systems, the output of the detector at time  $t$  is the number of photons that pass through the detector region during the last time interval. The output flux follows the Fick's law<sup>1</sup>:

$$J(x, t) = -D \frac{\partial \varphi(x, t)}{\partial n} \bigg|_{\partial \Omega} \quad (2)$$

where  $n$  is the normal direction on the boundary at position  $x$ .

<sup>1</sup> This research was supported in part by Hamamatsu Photonics K. K. of Japan

<sup>2</sup> Correspondence: Email: dyun@spectra.eng.hawaii.edu; http://www-ec.eng.hawaii.edu/~uhlips/; Telephone: 808-956-7627

A rectangular phantom, which is made of homogeneous epoxy media in absorption coefficient and scattering coefficient, is used to simulate the healthy breast tissue. Some absorber with abnormal absorption coefficient is placed inside to simulate the possible tumor tissue. To simplify the problem, only one absorber is placed in the center slab every time. Laser beam shots from one surface from several different points in turn. Detectors are placed on the opposite surface to collect the photons that reach the surface. Figure 1 shows the illustration of the system.

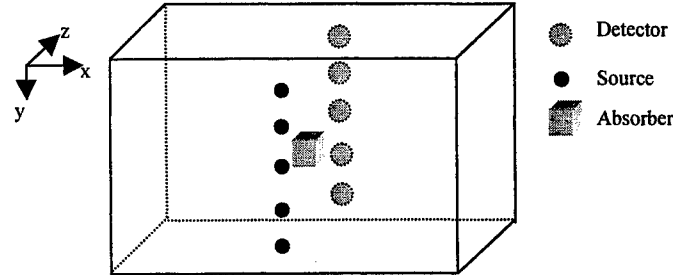


**Figure 1. Phantom with the location of laser sources, detectors and absorber**

In experimental equipment, the phantom is wrapped by black fabric as a strong absorber of photons. All the photons are supposed to be absorbed when reaching the boundary. Therefore, the boundary condition of equation (1) is considered to be zero during the whole procedure.

There is an amplifier process in the detector end of the time-resolved systems to enhance the signals received. Therefore, the number of photons (energy) collected is proportional to the real value. Time-percentage, an index denoted as  $T_{x\%}$ , is applied to explore important information in the phantom.  $T_{x\%}$  is defined as the solution in the integral

$$\int_0^{T_{x\%}} J(t) dt = x\% \cdot \int_0^{\infty} J(t) dt.$$

$T_{x\%}$  takes the advantage that the integral signal automatically eliminate the influence of noise in measurement which is assumed to be white noise.

In this paper, Alternating Direction Implicit (ADI) and Finite Element Method (FEM) are used to solve the diffusion equation in the given phantom geometry. Section 2 introduces the basic formulas of these two algorithms. The convergence on time step and spatial grid size is discussed. The simulation results of the two algorithms are compared and reach a good precision. Because of the huge amount of computational resource, multi-level spatial grid size algorithms are developed for both the algorithms in section 3. Simulation results are compared to that of the uniform-grid algorithm. Section 3 also introduces the parallelization implementation of both algorithms with their multi-grid versions to shorten the execution time. These are two approaches to speedup the computation and decrease the computational amount. Section 4 gives the conclusions of the numerical simulation of diffusion equation.

## 2. Algorithms for Diffusion Equation

Equation (1) is a partial differential equation for finite time length and for finite geometry size of three dimensions. Both ADI and FEM are stable and mature algorithms in solving PDEs. The difference between the two algorithms is that ADI is finite-difference scheme while FEM is finite-element scheme. Therefore, FEM does not use time-domain difference in the equation. In this paper, the spatial grid size is denoted as  $h$ , the time step as  $K$ .

### 2.1. Finite Element Method (FEM)

FEM is widely used in solving PDE problems. By using Galerkin approximation and choosing a series of basis functions  $\varphi_i(r)$ ,  $i=1, 2, \dots, N$  as

$$\varphi_i(r) = \begin{cases} 1, & r \in i\text{th cube} \\ 0, & \text{otherwise} \end{cases}$$

These special basis functions comprise an  $N$ -dimensional subspace to approximate the PDE in a state-space equation as

$$\begin{aligned} \dot{x}(t) &= Ax(t) + Bu(t) \\ y(t) &= Cx(t) \end{aligned} \quad (3)$$

where  $A \in R^{n \times n}$  is a block symmetric tridiagonal matrix,  $n$  is the number of total grids.

For model of life-size,  $n$  could be as large as  $10^6$  with respect to the grid size  $h$  applied in simulation. To reduce the size of problem, an orthogonal projection is built by using Kylov subspace theory to map state vector of  $n$ -dimension to a vector of hundreds of state variables. The solution of the small system is shown to be a good approximation of the original large system. Details of model reduction are discussed in reference paper [5]. FEM computes only the specified grids, which are considered as detectors. There is no discretization on time-domain in FEM algorithm.

## 2.2. Alternating Direction Implicit Method (ADI)

ADI algorithm is a generalized Crank-Nicholson method in solving partial differential equations. It solves the equation in three dimensions with three separate steps. Each step uses a third of a time step. A tridiagonal linear equation is derived in an one-dimensional "strip" with its neighbor grids. Based on step  $k$ , the equation for a dimension can be written as:

$$Ax^{(k+1)} = f(x^{(k)}), A \in \mathbb{R}^{n \times n}$$

where  $n$  is the size of the one dimensional strip. And

$$A = \begin{bmatrix} a & b & & & \\ b & a & b & & \\ & b & \ddots & \ddots & \\ & & \ddots & a & b \\ & & & b & a \end{bmatrix}, f(x^{(k)}) = -b \sum x_{neighbor}^{(k)} + dx^{(k)},$$

where

$$b = -\frac{K \cdot c}{3\mu_d h^2}, a = 1 - 2b + \frac{K \cdot c \cdot \mu_a}{6}, d = 1 + 4b - \frac{K \cdot c \cdot \mu_a}{6}.$$

The "strip" solutions for each grid on 3 directions are saved in each time step and used for next step. Different from the result of FEM, ADI gets solutions on all the grids but in discrete time steps. More details on ADI algorithm can be referred to [1] and [4].

## 2.3. Simulation experiments

The phantom in the experiment has a size of  $180 \times 136 \times 70 \text{ mm}^3$  (life-size) with related parameters as:

$$\mu_a = 0.0057 \text{ mm}^{-1}, \mu_s = 1.03 \text{ mm}^{-1}, c = 0.19467 \text{ mm} \cdot \text{ps}^{-1}, k = 1 \text{ ps}$$

If taking  $h=1 \text{ mm}$  as the grid size in computation, the memory requirement and the estimated execution time for a whole propagation process are listed in Table 1.

Table 1. Resource requirement for algorithms

	ADI	FEM
Memory	14.5 Mb	29.0 Mb
Execution time	44.5 hr	0.31 hr

The comparison between two experiments (for either simulation or measurement) is counted on  $T_{x\%}$  index only. The error is defined by a relative error as

$$\text{error}(y_1, y_2) = \max_{x\%} \left\{ \frac{|T_{x\%}(y_1) - T_{x\%}(y_2)|}{\text{average}(T_{x\%}(y_1), T_{x\%}(y_2))} \times 100\% \right\}$$

for two different cases  $y_1$  and  $y_2$ .

## 2.4. Comparison between FEM and ADI

Although FEM and ADI are dealing with the same diffusion equation, they use different theoretical methods to interpret the system, which makes the solutions different. However, the outputs should be close to each other. It is also a way to verify the validity of the implementations. Under several different grid sizes the simulation results are compared between the two algorithms. For the life-size phantom with the grid sizes of 4 mm, 2 mm and 1 mm, the relative errors are always less than 0.05% for  $T_{x\%}$  indices and 0.91% for curve comparisons in any randomly chosen grid. This also shows the validity of the implementation of both the algorithms.

## 2.5. Convergence on spatial grid size

When the grid size  $h$  changes, the simulation result will be different. To model the physical process correctly, a small  $h$  is required to describe the variation smoothly. From the view point of computation amount, a smaller  $h$  means more grids involved in computation, which makes the simulation resource (both time and memory) more critical for user. Several

simulation experiments are executed to test what is the proper grid size for an acceptable numerical precision. The relative errors for different grid sizes show the convergence of simulation on grid size.

**Table 2. Convergence of ADI and FEM (Tx% error)**

Grid size $h$	2 mm vs. 1 mm	1 mm vs. 0.5 mm	2 mm vs. 0.5 mm
ADI	0.90%	<b>0.53%</b>	1.39%
FEM	0.92%	<b>0.32%</b>	1.23%

It shows that both ADI and FEM reaches good convergence when grid size  $h = 0.5$  mm.

## 2.6. Convergence on time step (for ADI only)

ADI algorithm also reaches convergence for time step  $k$ . As an example, when  $h=1$  mm, the simulation outputs for different  $k$  are as in Figure 2. The relative errors show that when  $k$  gets smaller, the difference between two curves is smaller too. It is easy to be divergent when  $k$  increases. When  $h=1$  mm, the solution becomes divergent when  $k=3.5$  ps.

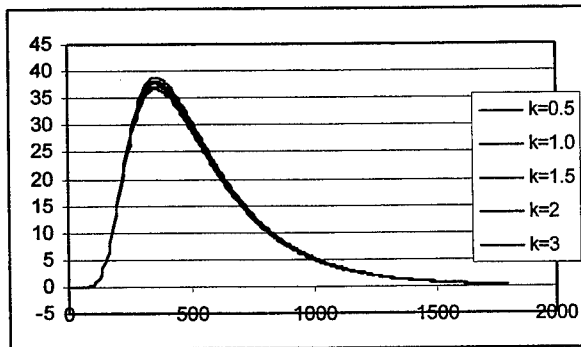


**Figure 2. Convergence of time step (ADI)**

**Table 3-a: Convergence for time steps (curve peak error)**

	K=0.5	K=1.0	K=1.5	K=2.0	K=3.0
K=0.5	-	<b>1.48%</b>	2.76%	3.87%	5.73%
K=1.0		-	1.26%	2.36%	4.18%
K=1.5			-	1.09%	2.89%
K=2.0				-	1.77%
K=3.0					-

**Table 3-b: Convergence for time steps (Tx% error)**

	K=0.5	K=1.0	K=1.5	K=2.0	K=3.0
K=0.5	-	<b>0.11%</b>	0.20%	0.28%	0.40%
K=1.0		-	0.09%	0.17%	0.30%
K=1.5			-	0.08%	0.20%
K=2.0				-	0.12%
K=3.0					-

FEM does not discretize on time domain.

## 3. Refinement of the algorithms

For the life-size phantom, ADI and FEM can not reach a very high resolution because of the huge computational amount when the grid size  $h$  becomes small. When  $h$  is cut to half, the required memory size will be increasing by 8 times in 3-D. The total computational amount will increase more because time step  $k$  should also be chosen to be a smaller value with respect to  $h$ . Usually, the computation amount increases by 16 times. To detect tumor tissue with size less than 1 mm, simulation has to run under 0.5 mm at least. As shown in Table 1, for  $h=1$  mm grid size, ADI needs 44 hours while FEM requires 29 Mb memory. When  $h=0.25$  mm, ADI would have use more than 2 months for one computation, while FEM would request 1.9G bytes memory, which are not acceptable for most computing request. Efforts are made on both decreasing the computational amount and having the code parallelized on the way to a high resolution.

### 3.1. Multigrid algorithms

To save the time cost and the memory cost in the algorithms. A multigrid method is proposed for the rectangular phantom in simulation. It focuses on the center part of the phantom to reach a high resolution as required. For the rest part, a coarse grid is applied. This method is combined with ADI algorithm and FEM algorithm, thus generalized to new algorithms--MADI and MFEM. The multigrid algorithms can reach the approximate precision of fine grid size in the region of interest (Figure 3). The coarse grid region provides approximate boundary information for the fine grid area so that the result in fine grid area can reach a very high precision<sup>[8]</sup>. In this method, important factors including sources, detectors and absorbers are all covered in the fine grid slab.

Multiple layers are used in multigrid algorithms so that there are transition grid sizes between the finest one and the coarsest one. 2-layer setting represents there are only fine grid size ( $h$ ) and coarse grid size ( $2h$ ), while 3-layer setting means there is an extra transition grid size ( $2h$ ) between the fine grid size ( $h$ ) and coarse one ( $4h$ ).

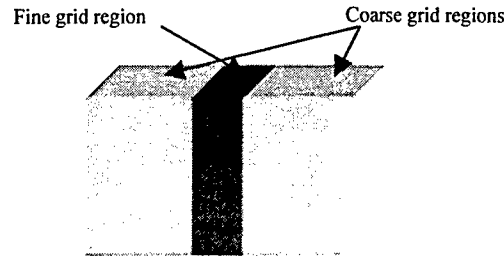


**Figure 3. Multigrid method on rectangular phantom**

The benefit of multigrid algorithm is significant. For example, to reach the same resolution of grid size, MADI has savings (both space and time) up to 80% for 2-level MADI, up to 95% for 3-level MADI. MADI is able to be generalized to higher number of levels so long as the relative conditions (block and boundary widths) remain true. At the same time, comparing the simulation output of MADI to that of ADI algorithm with uniform grid size, the Tx% error is as low as less than 0.61% for 2-block multigrid settings and less than 1.02% for 3-block multigrid settings.

The precision of multigrid algorithms is dominated by the thickness of the boundary grids and the width of center slab. The wider the fine-grid slab is, the thicker the affiliated boundary for fine grid block is, the more accuracy we can reach to the solution under the uniform fine-grid. This is proved both in theoretical method and simulation experiments.

The precision of ADI and MADI is also reached in realistic life-size phantoms. Figure 4 shows the curve comparison among MADI and ADI simulation results for resolution  $h=0.5$  mm. The Tx% relative errors are shown in Table 4.

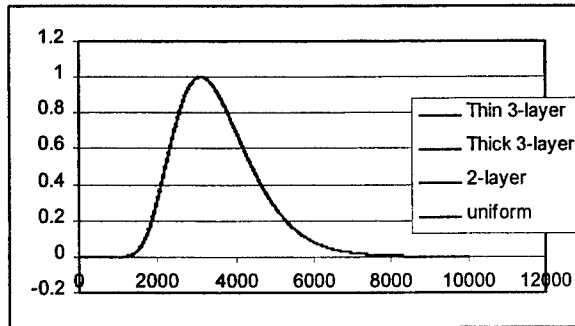


**Figure 4. Convergence of MADI algorithm on a small size phantom**

**Table 4. Tx% relative error for ADI and MADI**

	Uniform	2-layer	Thin 3-layer	Thick 3-layer
Uniform	-	0.61%	1.63%	1.02%
2 layers		-	1.00%	0.41%
Thin 3-layers			-	0.60%
Thick 3-layers				-

Here, "Thin 3-layer" MADI uses 3 layers where the layer for fine grid is 12 mm width. "Thick 3-layer" uses a 20 mm width fine grid layer instead for the region of interest (the center slab). The "thick 3-layer" result has a much higher precision than "thin 3-layer" comparing to result of uniform grid ADI.

In multigrid FEM algorithm, basis functions should be re-scheduled with respect to the specific multigrid layers. MFEM requires a wider fine grid slab (up to 40 mm) to guarantee the numerical precision comparing to FEM results. An comparison error of 0.41% is reached for MFEM.

### 3.2. Parallelization of algorithms

The other approach to speed up the simulation is to use parallel computing technique. Two common parallelization versions of simulator are implemented. One is Share Memory method (SMP), where multiple processors work on a same memory block simultaneously. The other is Message Passing Interface (MPI) method, where each processor has its own memory block and data are exchanged through messages among processors. Both the two methods are implemented and tested. For the algorithms discussed in this paper, SMP method is much better than MPI method because data in computation are strongly correlated, which means there are lots of communication in each step. Therefore, too much communication cost in MPI method makes the implementation unreasonable.

SMP parallel computing results are compared with the sequential version. The results show that both FEM and ADI simulator have good scalability for number of processors. Figure 5 and Table 5 show the parallel efficiency reaches 90.6% for MADI, 98.8% for FEM in 4-processor machine.

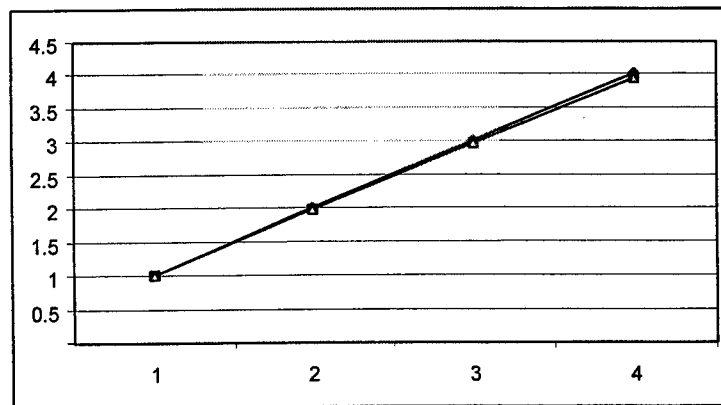


Figure 5: The speedup curve versus the processor number for FEM

Table 5-a: Parallelization-efficiency of parallelized MADI

SMP Efficiency	1 processor	2 processors	3 processors	4 processors
Standard execution time (s)	1281.399	640.699	427.133	320.350
Real execution time (s)	1281.399	646.241	452.726	353.440
Efficiency	100%	99.1%	94.3%	90.6%

Table 5-b: Parallelization-efficiency of parallelized FEM

SMP Efficiency	1 processor	2 processors	3 processors	4 processors
Standard execution time (hrs)	2:19:37	1:09:49	46:32	34:55
Real execution time (hrs)	2:19:37	1:09:66	46:56.86	35:21.00
Efficiency	100%	99.5%	99.0%	98.8%

### 3.3. Experimental validation

Simulation results are compared with experimental measurements. For 1 mm grid size simulation results, the Tx% error reaches as low as 1.27% for ADI algorithm and 1.58% for FEM algorithm. Considering the experimental error, it shows both the simulators reach a good approximation of the real system.

## 4. CONCLUSIONS

Although ADI and FEM algorithms are different ways for solving the PDE problem, the comparison of simulation results gives only small errors, which show the reliability and validity of both algorithms. The convergence on grid size is reached when the grid size comes down to 1 mm. Simulators are compared to each other and a very low comparison error (0.05% for Tx%, 0.91% for curve) is reached. Multigrid method is applied in both algorithms, which results a resource saving on computational time and memory up to 95%. Parallelization of the algorithms reach a scalability efficiency of 90.6% in Share Memory machines. When comparing with measurement data, the Tx% errors are as low as 1.27% (ADI) and 1.58% (FEM). This shows that both simulators can provide sufficiently good approximations to the experimental output of the photon propagation process. Consequently, the simulators can be used for advanced research in the form of "computed experiments", replacing real measurements wherever appropriate, and saving equipment cost and experimental time.

## REFERENCE

1. M. S. Patterson, B. Chance, B. C. Wilson, Time resolved reflectance and transmittance for the noninvasive measurement of tissue optical properties, *Applied Optics*, Vol. 28, No. 12, 2331-2336, 1989
2. B. Ohlsson, J. Gundersen, D. M. Nilson, Diaphanography: a method for evaluation of the female breast, *World J. Surg.*, 4, 701-705, 1980
3. R. Model, R. Hunlich, D. Richter, et al, Imaging in random media: simulating light transport by numerical integration of the diffusion equation, *SPIE Vol. 2326/11*
4. C. Lindquist, R. Berg and S. Andersson-Engels, Numerical diffusion modeling of interfering photon density waves for optical mammography, *SPIE Vol. 2326*, 31-39

5. Q. Su, V. L., Syrmos, D. Y. Y. Yun, A numerical algorithm for the diffusion equation using 3D FEM and the Arnoldi method, IEEE Trans. on medical imaging,
6. E. Okada, M. Schweiger, S. R. Arridge, Experimental validation of Monte Carlo and finite-element methods for the estimation of the optical path length in inhomogeneous tissue, et al, Applied Optics, Vol. 35, No. 19, 3362-3371, 1996
7. A. H. Hielscher, S. L. Jacques, L. Wang, et al, The influence of boundary conditions on the accuracy of diffusion theory in time-resolved reflectance spectroscopy of biological tissues, Physics in Medicine and Biology, 1995(40), 1957-1975
8. J. Ge, D. Yun, The multi-grid ADI algorithm in solving diffusion equation, accepted by SPIE 44th Annual Meeting, Vol. 3817, 184-193, Denver, CO, July, 1999.
9. Q. Su, V. L. Syrmos and D. Y. Y. Yun, A Numerical Algorithm for the Diffusion Equation Using 3D FEM and the Arnoldi Method, in American Control Conference, San Diego, CA, June, 1999.
10. V. L. Syrmos, J. Yin, D. Y. Y. Yun, The Photon Diffusion Equation: Forward and Inverse Problems, in IEEE Conference on Control Applications and IEEE Symposium on Computer-Aided System Design, Big Island, HI, August, 1999.
11. Y. Saad, Analysis of Some Krylov Subspace Approximations to Matrix Exponential Operator, SIAM J. Numer. Anal., Vol. 29, No. 1, 209-228, Feb. 1992.
12. R. Model, R. Hnlich, D. Richter, H. Rinneberg, H. Wabnitz and M. Walzel, Imaging in Random Media: Simulating Light Transport By Numerical Integration of the Diffusion Equation, SPIE, Vol. 2336, 11-22, Feb. 1995.



# Distributed-Source Approach to Image Reconstruction in Diffuse Optical Tomography

Ilya V. Yaroslavsky<sup>\*a</sup>, Anna N. Yaroslavsky<sup>a</sup>, Harold Battarbee<sup>a</sup>, Cynthia Sisson<sup>b</sup>, Juan Rodriguez<sup>a,c</sup>

<sup>a</sup>Louisiana State University Health Sciences Center, Shreveport, LA 71130-3932

<sup>b</sup>Louisiana State University – Shreveport, Department of Physics, Shreveport, LA 71115

<sup>c</sup>Centenary College, Department of Physics, Shreveport, LA 71134

## ABSTRACT

A novel approach to the quantitative image reconstruction in diffuse optical tomography is proposed. The special structure of the transport equation is used to formulate the iterative image reconstruction algorithm as a process updating the estimates of the optical properties from the solution of an intermediate tomographic problem. The ability of the technique to reconstruct simultaneously maps of both absorption and reduced scattering coefficients in 2D geometry is demonstrated using simulated frequency-domain data. The potential advantages of the new approach include its ability to fully retain the non-linear character of the inverse problem while at the same time avoiding either gradient or Jacobian calculations and eliminating the need in an additional regularization mechanism.

**Keywords:** Tissue imaging, inverse technique, regularization

## 1. INTRODUCTION

The practical utility of diffuse optical tomography rests with the ability of the technique to produce quantitative spatial images of the optical properties, such as absorption and (reduced) scattering coefficients. To date, several approaches to the reconstruction problem have been explored (See Ref.1 and literature cited therein). The most promising of them are centered on either linearized perturbation techniques<sup>e.g.2</sup> or gradient-based non-linear optimization schemes<sup>e.g.3</sup>. Significant progress has been achieved with both. However, the two approaches have a number of limitations. Specifically, as has been shown recently<sup>4</sup>, linearized algorithms are fundamentally limited in their ability to correctly describe the higher moments of the intensity, which makes a quantitative image reconstruction problematic. The gradient-based optimization methods, on the other hand, call for an update of either gradient or Jacobi matrix on each iteration, which may place a prohibitively high demand on computational resources, especially for 3D geometry. In addition, choice of a regularization technique best suited for the underlying physical model in the context of such a method still remains a challenging task.

In this paper, we propose a different approach to the image reconstruction problem. The technique makes use of the specific structure of the transport equation, which governs light propagation in a strongly scattering medium, and exploits this structure to formulate an iterative process of updating the estimates of the optical properties from the solution of an intermediate *linear* problem. At the same time, the *non-linear* nature of the initial inverse problem is fully preserved, and no linearizing assumptions are used.

## 2. DISTRIBUTED-SOURCE APPROACH AND INVERSE ALGORITHM

We start with the scalar transport equation. Without loss of generality, the problem is treated in the frequency domain. Let light transport occur in a convex domain  $G$  limited by boundary  $\partial G$ . Assuming instantaneous single scattering events and the absence of internal sources, the frequency-domain transport equation is (Ref.5)

---

\* Correspondence: Email: [iyaros@lsu-mc.edu](mailto:iyaros@lsu-mc.edu); Telephone: 318 675 7359; Fax: 318 675 6005

$$\mathbf{s} \cdot \nabla I(\mathbf{r}, \mathbf{s}, \omega) = -(\mu_t(\mathbf{r}) + i\frac{\omega}{c})I(\mathbf{r}, \mathbf{s}, \omega) + \frac{\mu_s(\mathbf{r})}{4\pi} \int_{4\pi} I(\mathbf{r}, \mathbf{s}', \omega) p(\mathbf{r}, \mathbf{s}, \mathbf{s}') d\Omega', \quad (1)$$

where  $I(\mathbf{r}, \mathbf{s}, \omega)$  is the frequency component of the specific intensity at position  $\mathbf{r}$ , direction  $\mathbf{s}$ , and angular frequency  $\omega$ ;  $\mu_t$  and  $\mu_s$  are the scattering and total attenuation coefficients, respectively;  $p(\mathbf{r}, \mathbf{s}, \mathbf{s}')$  is the scattering phase function; and  $c$  is the speed of light in the medium. Eq.(1) is supplied with the usual boundary conditions at  $\partial G$ .

For arbitrary point  $\mathbf{r}_G \in \partial G$  and direction  $\mathbf{s}$ , Eq.(1) can be transformed to integral form as

$$\begin{aligned} I(\mathbf{r}_G + u\mathbf{s}, \mathbf{s}, \omega) &= I(\mathbf{r}_G, \mathbf{s}, \omega) \exp\left(-\int_0^u \eta_t(\mathbf{r}_G + u'\mathbf{s}) du'\right) \\ &+ \frac{1}{4\pi} \int_0^u \mu_s(\mathbf{r}_G + u'\mathbf{s}) \left[ \int_{4\pi} I(\mathbf{r}_G + u\mathbf{s}, \mathbf{s}', \omega) p(\mathbf{r}_G + u\mathbf{s}, \mathbf{s}, \mathbf{s}') d\Omega' \right] \exp\left(-\int_{u'}^u \eta_t(\mathbf{r}_G + u''\mathbf{s}) du''\right) du', \end{aligned} \quad (2)$$

where  $\eta_t = \mu_t + i\omega/c$  and  $u$  is the distance counted from point  $\mathbf{r}_G$  in direction  $\mathbf{s}$ .

The complex signal  $J_D(\omega)$  collected by a detector  $D$  with small area  $\Delta S_D$  located at  $\mathbf{r}_D \in (G + \partial G)$  is determined by

$$J_D(\omega) = \Delta S_D \int_{(\mathbf{n}_D \cdot \mathbf{s}) > 0} I(\mathbf{r}_D, \mathbf{s}, \omega) (\mathbf{n}_D \cdot \mathbf{s}) h_D(\mathbf{s}, \omega) d\Omega, \quad (3)$$

where  $\mathbf{n}_D$  is the detector's internal normal and  $h_D(\mathbf{s}, \omega)$  is the detector's sensitivity function, which also accounts for signal losses at the detector-medium interface.

Substituting Eq.(2) into Eq.(3) and replacing the integration over the solid angle with integration over  $(G + \partial G)$ , one obtains

$$\begin{aligned} J_D(\omega) &= \int_{\partial G} I(\mathbf{r}, \mathbf{s}_D, \omega) \exp(-\sigma_D(\mathbf{r})) H_D(\mathbf{r}, \omega) \Delta\Omega_D (\mathbf{n}_G \cdot \mathbf{s}_D) dS \\ &+ \int_G \frac{\mu_s(\mathbf{r})}{4\pi} \left[ \int_{4\pi} I(\mathbf{r}, \mathbf{s}', \omega) p(\mathbf{r}, \mathbf{s}, \mathbf{s}') d\Omega' \right] \exp(-\sigma_D(\mathbf{r})) H_D(\mathbf{r}, \omega) \Delta\Omega_D dV, \end{aligned} \quad (4)$$

where

$$\begin{aligned} \mathbf{s}_D &= \mathbf{s}_D(\mathbf{r}) = (\mathbf{r}_D - \mathbf{r}) / |\mathbf{r}_D - \mathbf{r}|, \\ \Delta\Omega_D &= \Delta\Omega_D(\mathbf{r}) = \Delta S_D (\mathbf{s}_D \cdot \mathbf{n}_D) / |\mathbf{r}_D - \mathbf{r}|^2, \\ \sigma_D(\mathbf{r}) &= \int_0^{|\mathbf{r}_D - \mathbf{r}|} \eta_t(\mathbf{r} + u\mathbf{s}_D) du, \\ H_D(\mathbf{r}, \omega) &= \begin{cases} h_D(\mathbf{s}_D, \omega), & (\mathbf{s}_D \cdot \mathbf{n}_D) > 0 \\ 0, & \text{otherwise} \end{cases}, \end{aligned}$$

$\mathbf{n}_G(\mathbf{r})$  is the internal normal to  $\partial G$  at point  $\mathbf{r}$ . The signal at an extended detector with area  $S_D$  can be calculated by straightforward integration of Eq.(4) over  $S_D$ .

Thus, all detector readings can be calculated from the known distribution of the specific intensity with Eq.(4). We refer to this approach as "distributed-source approach". The validity of the concept has been previously verified in the framework of Monte Carlo simulations by comparing results with traditional Monte Carlo simulations<sup>6</sup>.

Simplifications of Eq.(4) are achieved by invoking two assumptions: 1) the direct contribution to the detected signal from the sources and boundaries (first term in RHS of Eq.4) is small and may be neglected; and 2) the diffusion approximation is valid. Then the similarity relations can be used and Eq.(4) is simplified to

$$J_D(\omega) = \int_G K_D(\mathbf{r}, \omega) Z_D(\mathbf{r}) dV, \quad (5)$$

where

$$K_D(\mathbf{r}, \omega) = \mu_{tr}(\mathbf{r}) U(\mathbf{r}, \omega) \exp(-i\omega t_D) H_D(\mathbf{r}, \omega) \frac{\Delta\Omega_D}{4\pi},$$

$$Z_D(\mathbf{r}) = \lambda(\mathbf{r}) \exp(-\tau'_D(\mathbf{r})), \quad (6)$$

$\lambda(\mathbf{r}) = \mu'_s(\mathbf{r}) / \mu_{tr}(\mathbf{r})$  is the reduced albedo;  $\mu_{tr}$  is the transport coefficient;  $\mu'_s$  is the reduced scattering coefficient;

$U(\mathbf{r}, \omega)$  is the total intensity in the frequency domain determined by the diffusion equation;  $\tau'_D(\mathbf{r})$  and  $t_D(\mathbf{r})$  are the reduced optical distance and time-of-flight from point  $\mathbf{r}$  to the detector  $D$ , respectively.

Under above stated assumptions, the inverse problem of diffuse optical tomography is formulated as follows: given set of measurements  $J_{nil}^*$  (index  $n=1..N$  enumerates sources, index  $i=1..I$  enumerates detectors, index  $l=1..L$  corresponds to frequency  $\omega_l$ ), estimate the spatial distributions of the absorption coefficient  $\mu_a(\mathbf{r})$  and the reduced scattering coefficient  $\mu'_s(\mathbf{r})$ . The refractive index is assumed known and uniform within the medium.

We approximate the spatially varying functions  $\mu_a(\mathbf{r})$  and  $\mu'_s(\mathbf{r})$  by dividing the volume of the medium into  $M$  voxels with constant optical properties. Eq.(5) can then be approximated as

$$J_{nil} = \sum_{m=1}^M \langle K_{nil} \rangle_m V_m Z_{im}, \quad (7)$$

where  $\langle \bullet \rangle_m$  stands for averaging over the volume of the voxel  $m$ ;  $V_m$  is the volume of the voxel  $m$ ;  $Z_{im}$  is an approximation of  $Z_m(\mathbf{r})$ , defined as

$$\ln Z_{im} = \ln \lambda_m - \sum_{q=1}^M W_{imq} (\mu_{tr})_q, \quad (8)$$

where  $W_{imq}$  is the contribution of the voxel  $q$  to geometrical path from voxel  $m$  to detector  $i$  (measured in units of length). If quantities  $\langle K_{nil} \rangle_m$  are known, Eqs.(7),(8) represent a *linear* tomographic problem that can be solved using an algebraic reconstruction technique. In order for Eqs.(7),(8) to have a unique solution, the following conditions should be met: 1)  $2NL \geq M$  (when both modulation and phase data are used), and 2)  $I \geq 2$ .

The iterative reconstruction algorithm based on the distributed-source approach consists of the following steps:

- 1) Set iteration counter  $k=0$ , obtain an initial guess of the optical properties and calculate initial  $Z_{im}^0$  using Eq.(6);
- 2) Increase iteration counter  $k=k+1$ , solve the forward model (diffusion equation in the frequency domain) for the distribution of the total intensity  $U_{ni}^k$  for all  $n, i$ ;
- 3) Calculate  $\langle K_{nil} \rangle_m^k$  for all  $n, i, l, m$ ;
- 4) Solve Eq.(7) for running estimates of  $Z_{im}^k$ ;
- 5) Solve Eq.(8) for update of the optical properties;

- 6) Calculate running estimates of  $J_{nil}^*$  using Eq.(7);
- 7) If measured and calculated signals are sufficiently close, exit; otherwise, go to step 2.

Eqs.(7),(8) still represent an ill-posed problem due to the fact that their respective matrices are typically poorly conditioned. Fortunately, no complete inversion of these matrices on each iteration is required. Rather, gradual rotation of these constantly changing matrices can be combined with the iteration process itself. There is a class of linear solvers, which are well suited for this task. We used Oschepkov-Dubovik scheme<sup>7</sup>. Numerical tests have shown that best convergence is achieved when just a single step of Oschepkov-Dubovik scheme is performed on each iteration. In order to balance contributions from different sources in Eq.(7) and from different areas in Eq.(8), the former was multiplied by  $\ln(\text{Mod}(J_{nil}^*))$ , and the latter by  $Z_{im}$ . This led to the following explicit formulas used in Steps 4 and 5 of the algorithm:

$$Z_{im}^k = Z_{im}^{k-1} \frac{\sum_{l=1, n=1}^{L, N} \left[ \text{Re}(J_{nil}^*) \text{Re}(\langle K_{nil} \rangle_m^k) + \text{Im}(J_{nil}^*) \text{Im}(\langle K_{nil} \rangle_m^k) \right] \ln(\text{Mod}(J_{nil}^*))^2}{\sum_{l=1, n=1}^{L, N} \left[ \text{Re}(J_{nil}^{k-1}) \text{Re}(\langle K_{nil} \rangle_m^k) + \text{Im}(J_{nil}^{k-1}) \text{Im}(\langle K_{nil} \rangle_m^k) \right] \ln(\text{Mod}(J_{nil}^*))^2}$$

$$(\mu_{ir})_m^k = (\mu_{ir})_m^{k-1} \frac{\sum_{i=1, q=1}^{I, M} E_{iq}^k W_{imq}}{\sum_{i=1, q=1}^{I, M} D_{iq}^k W_{imq}}, \quad \ln(\lambda_m^k) = \ln(\lambda_m^{k-1}) \frac{\sum_{i=1}^I E_{im}^k}{\sum_{i=1}^I D_{im}^k}, \quad (9)$$

$$E_{iq}^k = (Z_{iq}^k)^2 (-\ln Z_{iq}^k), \quad D_{im}^k = \left[ \sum_{q=1}^M \left[ W_{imq} (\mu_{ir})_q^{k-1} - \ln(\lambda_m^{k-1}) \right] (Z_{im}^k)^2 \right].$$

This technique realizes the idea of the "latent" matrix inversion, and, therefore, provides a built-in regularization mechanism.

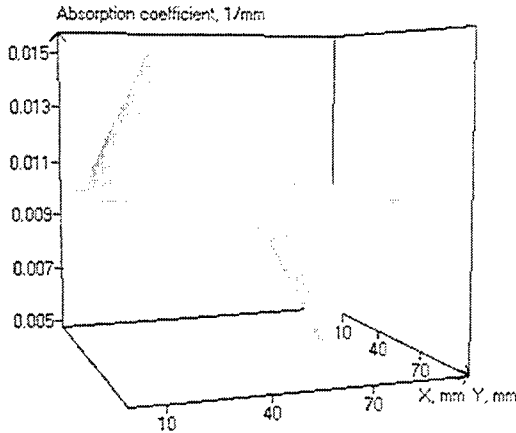


Fig.1. "True" spatial map of absorption coefficient for test medium used in numerical tests. Distribution of reduced scattering coefficient identical, with background value of 1.0 /mm, maximum of 1.5 /mm, and minimum of 0.5 /mm.

### 3. NUMERICAL TESTS

We have implemented the algorithm for 2D geometry. The MUDPACK package<sup>8</sup> was used to solve the frequency-domain diffusion equation. A series of numerical tests on simulated data have been conducted. One particular case is exemplified by Figs.1-3. The medium in this test represented a square area 100x100 mm, with 11x11 square voxels. The following background optical properties were used: absorption coefficient of 0.01 mm<sup>-1</sup> and the reduced scattering coefficient of 1.0 mm<sup>-1</sup>. Two pyramid-shaped inhomogeneities (See Fig.1) have been introduced. Matched boundary conditions were assumed. 20 sources and 16 detectors have been evenly distributed along the perimeter of the area. The detected signals at 20 frequencies ranging from DC to 950 MHz (at 50 MHz intervals) have been simulated using the forward solver and Eq.(7). A 2% noise has been added to the computed data to simulate experimental errors. Both "measured" intensities  $J_{nil}^*$  and calculated intensities  $J_{nil}$  have been normalized on

their maximal absolute value independently for each source  $n$ . Thus, only relative data have been used for reconstruction. The quality of the absorption coefficient reconstruction was characterized by the average absorption error  $\varepsilon_a$  defined as

$$\varepsilon_a = \frac{1}{M} \sqrt{\sum_{m=1}^M \frac{((\mu_a)_m - (\mu_a)_m^{true})^2}{((\mu_a)_m^{true})^2}}. \quad (10)$$

Average scattering error  $\varepsilon_s$  was defined analogously, with replacement  $\mu_a$  by  $\mu'_s$  in Eq.(10). Results of the reconstruction are shown in Figs.2,3. In both cases, the algorithm started with uniform distribution of the optical properties. Fig.2 demonstrates the case when the optical properties of the background are known and used as an initial approximation. Reconstructions in Fig.3 have been obtained using a poor initial approximation, imitating the situation when information on the background optical properties is unavailable. In both cases, positions and qualitative shapes of the inhomogeneities have been satisfactory reproduced. Quantitative assessment of the reconstruction errors is summarized in captions to Figs.2,3.

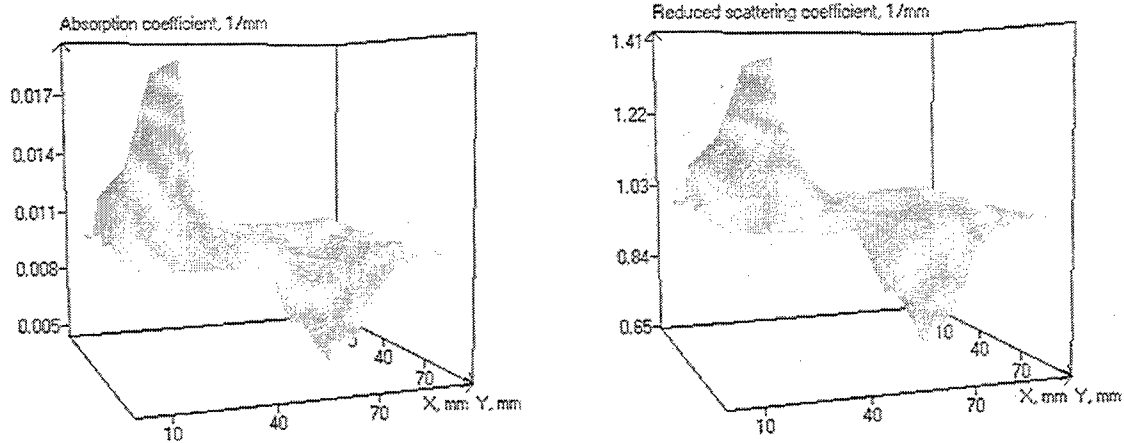


Fig.2. Reconstruction results when background optical properties were used for initial approximation. Initial  $\varepsilon_a = \varepsilon_s = 0.0123$ . Final  $\varepsilon_a = 0.0072$ ,  $\varepsilon_s = 0.0049$  (after 157 iterations).

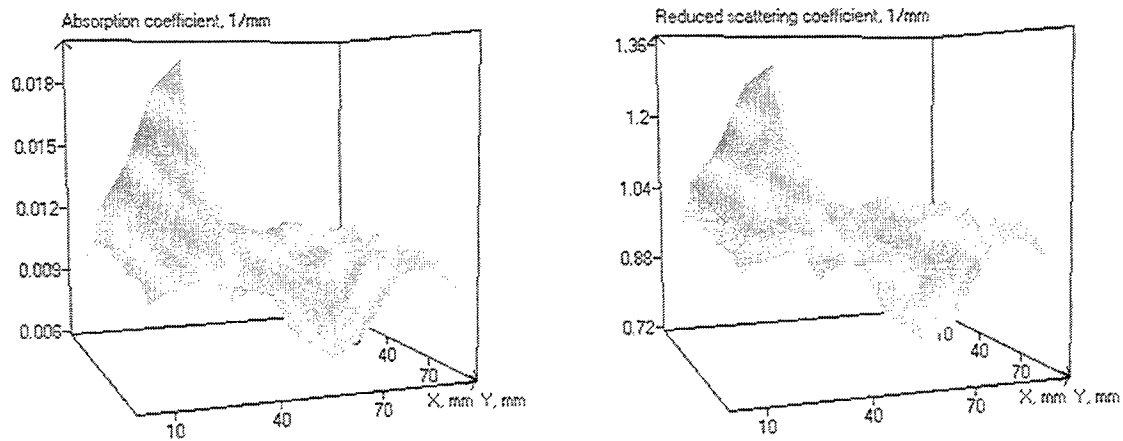


Fig.3. Reconstruction results when poor initial approximation was used ( $\mu_a = 0.007$  /mm,  $\mu'_s = 0.8$  /mm). Initial  $\varepsilon_a = 0.027$ ,  $\varepsilon_s = 0.0198$ . Final  $\varepsilon_a = 0.0096$ ,  $\varepsilon_s = 0.0066$  (after 100 iterations).

#### 4. DISCUSSION

The results of the numerical tests demonstrate the ability of the algorithm to reconstruct the spatial distribution of the optical properties for the range of parameters similar to those found in a typical experiment with a phantom of biological tissue. It should be noted that although the diffusion equation was used as a forward model in the present work, the distributed-source approach can also be applied in combination with a more accurate model of light transport, such as *e.g.* third-order approximation to the transfer equation<sup>9</sup>. A distinctive feature of the new approach is elimination of the necessity to estimate either gradient or Jacobi matrix of the system on each step of the iterative process. This factor may be especially important for full 3D reconstruction. At the same time, the non-linear character of the problem is completely retained. In addition, no external regularization parameters are required. Thus, reconstruction is achieved in a "natural" way.

#### 5. ACKNOWLEDGMENTS

This work was supported by the Biomedical Research Foundation of Northwest Louisiana. IVY and ANY are on leave from the Optics Department, Saratov State University (Russia).

#### REFERENCES

1. Arridge, S.R. and M. Schweiger. "Image reconstruction in optical tomography," *Phil.Trans.R.Soc.Lond.* 352(1997):717-726.
2. O'Leary, M.A., D.A. Boas, B. Chance, and H. Yonas. "Experimental Images of heterogenous turbid media by frequency-domain diffusing-photon tomography," *Opt.Lett.* 20(1995):426-428.
3. Hielscher, A.H., A.D. Klose, and K.M. Hanson. "Gradient-based iterative image reconstruction scheme for time-resolved optical tomography," *IEEE Trans.Medical Imaging* 18(1999):262-271.
4. Boas, D.A. "A fundamental limitation of linearized algorithms for diffuse optical tomography," *Optics Express* 1(1997):404-413.
5. Yaroslavsky, I.V., A.N. Yaroslavsky, V.V. Tuchin, and H.-J. Schwarzmaier. "Effect of the scattering delay on time-dependent photon migration in turbid media," *Appl.Opt.* 36(1997):6529-6538.
6. Yaroslavsky, I.V., A. Terenji, S. Willmann, A.N. Yaroslavsky, H. Busse, and H.-J. Schwarzmaier. "Small-volume tissue spectroscopy using photon-density waves: apparatus and technique," *Proc.SPIE* 3597(1999):465-473.
7. Oschepkov, S.L. and O.V. Dubovik. "Optimized iterative method for numerical solution of Fredholm integral equation of the first kind for positive definite values," *J.Atmospheric and Oceanic Physics* 30(1994):153-160.
8. Adams, J. "Multigrid Fortran software for the efficient solution of linear elliptic partial differential equations," *Appl.Math.Comp.* 34(1989):113-146.
9. Jiang, H. "Optical image reconstruction based on the third-order diffusion equation," *Optics Express* 4(1999):241-246.

# In Vivo Sized-Fiber Spectroscopy

T. P. Moffitt and S. A. Prahl

Oregon Medical Laser Center, 9205 SW Barnes Rd, Portland, OR 97225

## ABSTRACT

Sized-fiber array spectroscopy describes a device for measuring the absorption and reduced scattering properties of tissue. The device consists of two fibers with different diameters that measure the amount of light back-scattered into each fiber. Only one fiber emits and collects light at a time. Recent innovations allow for spatially limited measurement diffuse reflectance over a wavelength range of 500–800 nm. Reflection spectra of *in vitro* and *in vivo* porcine tissue are presented for a device with 200 and 600  $\mu\text{m}$  fibers to demonstrate its performance.

**Keywords:** Reflectance, Optical Biopsy

## 1. INTRODUCTION

In many fields of medicine, the knowledge of the optical properties of a tissue is important. The minimally invasive sized-fiber device described in this paper allows a simple and rapid means to determine optical properties. The device makes use of the fact that the amount of light backscattered into an optical fiber is affected by absorption and scattering properties of the tissue. In general, tissues with different scattering and absorption properties will scatter different numbers of photons back into the originating fiber. If only a single fiber is used, two samples with very different optical properties can backscatter the same number of photons. To distinguish between samples, a second measurement must be made using a different size fiber. Each size fiber has a different spatial resolution provided that the fibers are comparable to the optical path length in the tissue.

This paper begins with a description of the sized-fiber device and construction of the device. Next, *in vitro* porcine kidney reflection spectra are presented to show the measurement to measurement variation of repeated experiments. Finally, typical reflection spectra of several *in vivo* porcine tissues are presented.

The sized-fiber device was adapted to use white light measurements instead of a limited wavelength source from a laser,<sup>1</sup> literally giving the user a spectrum of information. This was made possible by a special bifurcated fiber,<sup>2–4</sup> which I shall refer to as a Y-fiber. A Y-fiber consists of a two smaller fibers coupled to a single larger fiber making a “Y” shaped junction with the three fibers as shown in figure 1. Each of the smaller fibers has a specific purpose: the function of one fiber is designated for light input from a lamp, the other fiber guides the output signal (backscattered photons) coming back from the large fiber to a spectrometer. This has the benefit of reducing background noise by separating the lamp light from the back-scattered light from the tissue. The sized-fiber device uses two Y-fibers with different core diameters, thus the descriptive name, sized-fiber spectroscopy. The two Y-fibers are joined together and inserted through a needle to measure a spatially limited diffuse reflection of tissue.

## 2. MATERIALS AND METHODS

The construction of a single Y-fiber begins with the preparation of the three fibers; two fibers, having a core diameter about half the diameter of the larger fiber core, and cut to 2 m in length. For these experiments, 100  $\mu\text{m}$  and 200  $\mu\text{m}$  fibers compose one Y-fiber, and the other Y-fiber by 300  $\mu\text{m}$  and 600  $\mu\text{m}$  fibers. The fibers are polished and 1 cm of the fiber jacket is removed. The use of glass-glass (core-cladding) fibers ensures that the cladding remains intact to the end of all fibers. The two smaller fibers are mounted side by side in an SMA connector. The large fiber is also mounted in an SMA connector. An SMA coupler connects the fibers together without the use of index matching oil or gel.

---

Direct correspondence to S.A.P, prahl@ece.ogi.edu; (503) 216-2197; <http://omlc.ogi.edu/>

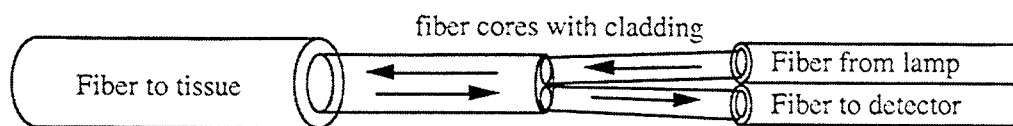


**Figure 1.** Three fibers are coupled together to form a Y-shaped junction. Light is guided from the lamp to the tissue; diffusely reflected light from the tissue is guided back to the detector, minimizing noise. The arrows indicate the direction of light travel which affect the measurements. With the noise minimized, very small reflectances ( $\sim 0.1\%$ ) are detectable.

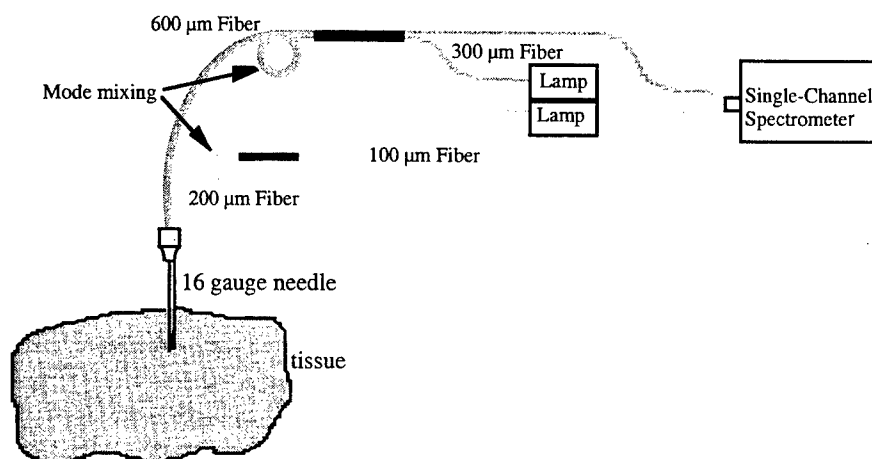


**Figure 2.** This is a schematic diagram for the sized-fiber measurements. Only a single spectrometer was available; the two Y-fibers share a single spectrometer. SMA fiber mounts are used to ease the switching of the fibers between measurements.

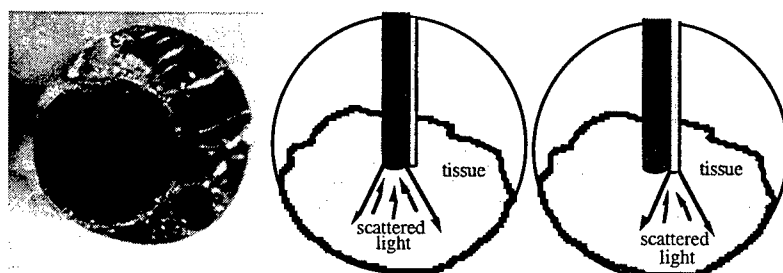


**Figure 3.** The far left picture shows the proximate location of the fiber faces fixed in epoxy which are inserted through a needle. The next two figures show how each fiber measures tissue independently.



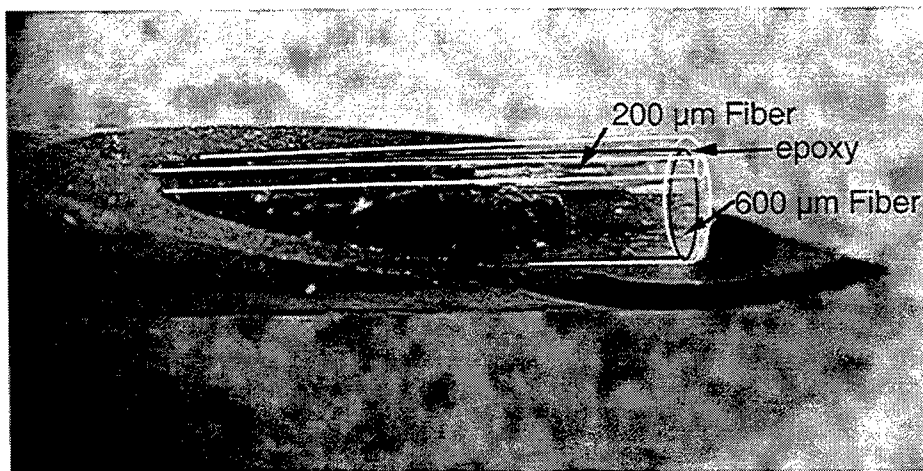


**Figure 4.** This is a picture of the needle probe with the fibers outlined for clarity. The fibers are fixed together in epoxy (also outlined) so that the faces are in the same plane. Tubing fixed to the fibers prevent the fibers from going any farther into the needle than shown. This gives consistent placement of the fibers in relation to the needle.

Before the sensing end of the Y-fibers are joined with a UV cured epoxy(191-M, Dymax corp, Torrington, CT), a series of procedures are taken to optimize the durability of the fibers. First, the two sensing fibers are threaded through a piece of tubing which extends 1.5 m in length. The purpose of the tubing is two-fold, to act as a depth stop for the fibers within the needle and to reduce any stresses on the fibers. The fibers are purposely epoxied to this tubing in the process of binding the fibers together. Next, an epoxy mold is made from two pieces of teflon tubing of differing diameters such that one tube just fits inside the other. The smaller diameter ( $\leq 800 \mu\text{m}$  inner diameter) piece of tubing, 4 cm in length is sliced lengthwise on one side of the tube and fit over the sensing fibers. The tubing should come in contact with the 1.5 m tubing so that epoxy will bind it to the fibers. Care is taken to align the fiber faces such that they lie in the same plane, before the other piece of tubing, 5 cm in length, is sleeved over the sliced tubing, completing the epoxy mold. The epoxy is inserted with a needle into the open end of the molding. The epoxy should overfill the 5 cm tube, run through the 4 cm tube and into the 1.5 m tubing which is positioned 3.2 cm from the end of the fibers. The 3.2 cm distance was chosen as the appropriate depth stop distance for a 1 inch 16 gauge needle (figure 4). The epoxy is then cured and the outer tubing is removed from the smaller tubing. The slicing of the inner tube greatly reduces the risk of breaking a fiber, saving much aggravation. Once the inner tube is peeled away any excess epoxy can be cut away from the face of the fiber faces. If necessary, the fibers can then be polished together in the epoxy.

Finally, the two fiber bundles of 300 and 100  $\mu\text{m}$  fibers are threaded through 1.5 m of teflon tubing for reinforcement and SMA connectors are fixed to the four loose fiber ends. The 300  $\mu\text{m}$  fiber bundle is coupled to the 600  $\mu\text{m}$  fiber and likewise the 100  $\mu\text{m}$  fibers to the 200  $\mu\text{m}$  fiber. Mode mixing loops are put into the 200 and 600  $\mu\text{m}$  fibers with the 1/2 m of exposed fiber between the reinforcement tubing and the SMA connectors. Mode mixing produces an exit half-angle of  $16.7^\circ$  in air for both the 200  $\mu\text{m}$  and 600  $\mu\text{m}$  fibers.

The experimental set up uses two tungsten-halogen lamps (LS-1, Ocean Optics, Inc.) to illuminate the sample and a spectrometer (S2000, Ocean Optics, Inc.) to measure the light backscattered into the fiber. The experimental apparatus is shown in figure 2. A 100 and 300  $\mu\text{m}$  fiber are each connected to a lamp. The remaining 100 and 300  $\mu\text{m}$  fiber connect to the spectrometer, one at a time, depending on which size fiber is making a measurement. A 100  $\mu\text{m}$  fiber connected to the spectrometer corresponds to a 200  $\mu\text{m}$  fiber reflectance; and so, only the lamp with the 100  $\mu\text{m}$  fiber is on. Likewise, a 300  $\mu\text{m}$  fiber connected to the spectrometer corresponds to the 600  $\mu\text{m}$  fiber reflectance in which case, the lamp with the 300  $\mu\text{m}$  fiber is used. A 1 inch 16 gauge needle is filled with distilled water, and then the epoxied fibers are inserted into the needle as far as allowed by the tubing depth stop. The needle and fibers are inserted into the tissue to be measured. The water aids the coupling of light between the tissue and the fiber. Measurements are recorded for both fiber sizes in air and water inside of a black box for subsequent normalization

of further measurements in terms of percent reflectance. The Fresnel reflectance for the glass/air and glass/water interfaces gives

$$R_{\text{air}} = \left( \frac{n_{\text{air}} - n_{\text{fiber core}}}{n_{\text{air}} + n_{\text{fiber core}}} \right)^2 = 3.5\%$$

and

$$R_{\text{water}} = \left( \frac{n_{\text{water}} - n_{\text{fiber core}}}{n_{\text{water}} + n_{\text{fiber core}}} \right)^2 = 0.22\%$$

respectively. The data is normalized using the 0.22% Fresnel reflectance signal in water,

$$R_{\text{tissue}} = 0.22\% \left( \frac{S_{\text{tissue}}}{S_{\text{water}}} \right)$$

where  $S_{\text{tissue}}$  and  $S_{\text{water}}$  are the raw signals of tissue and water respectively. The normalized reflectance is the same if  $S_{\text{water}}$  is replaced by  $S_{\text{air}}$  and 0.22% by 3.5% so that

$$R_{\text{tissue}} = 3.5\% \left( \frac{S_{\text{tissue}}}{S_{\text{air}}} \right)$$

The Fresnel reflection for the fibers in tissue is not subtracted away. Initially a Fresnel reflection of 0.22% for water was expected, since water is used to couple light from the fiber into the tissue. However, the raw signals for *in vivo* tissue are smaller than from water thus a negative reflectance would result if a 0.22% is subtracted from  $R_{\text{tissue}}$  to account for Fresnel reflections. The Fresnel reflection from tissue is less than that of water since the index of refraction is smaller for water than tissue ( $n_{\text{tissue}}$  is in the range of 1.37–1.45<sup>2</sup>). Data is recorded in 0.75 nm increments over the range of 400–1000 nm. Note, data is presented over the range of 500–800 nm since the noise dominates outside this range.

### 3. RESULTS

The sized-fiber device has been used to measure porcine tissues *in vitro* and *in vivo*. The device gives consistent measurements of tissues for both size of fibers. Figure 5 shows the typical variation for *in vitro* reflectance spectra for kidney. The signals from the two locations are expected to be different, since the kidney is not homogeneous. In figure 6, the reflectance from the 600  $\mu\text{m}$  Y-fiber is plotted against the reflectance of the 200  $\mu\text{m}$  Y-fiber for the 5 measurements in each location at a wavelength of 500 nm. Also, *in vivo* reflectances of the kidney are included on figure 6 which are notably smaller than the *in vitro* kidney. This was to be expected since more blood is present in live tissue. Moreover, the *in vitro* kidney was removed nearly a week prior to the time of measurement and may have dehydrated changing the index of refraction for the tissue. However, the sized-fiber technique demonstrates a high degree of sensitivity in measuring the small reflectance signals in *in vivo* tissue.

Furthermore, the sensitivity of the device during *in vivo* measurements demonstrate that the spectra noticeably changes as the needle and fibers pass from one tissue to the next. Figure 7 shows typical spectra of different tissues with both fiber sizes. The signal in real time remains quite constant, then will quickly change as the device passes from one tissue to the next. This indicates the the device returns information about the tissue that is immediately at the probe face, though the effect has not been fully quantified.

### 4. DISCUSSION

Although the spectra of tissue are fascinating, the sized-fiber method still lacks a simple algorithm to convert the reflectance measurements reported here into more useful information of the absorption and reduced scattering properties of the tissue.

Previous methods of sized-fiber spectroscopy did not achieve the high degree of sensitivity shown here.<sup>1</sup> Using Y-fibers has eliminated problems associated with optical alignment and have enhanced the ruggedness of the device. Requiring only a couple white light lamps, some optical fibers bundled together, and a detector or two, means the device is quite compact. The Y-fiber greatly reduces the cost of this technology by eliminating the need for many pricey optical components and equipment such as lasers, beam splitters, polarizers, optical choppers, and lock-in amplifiers used in previous methods of sized-fiber spectroscopy. Yet, replacing all the aforementioned equipment with a couple Y-fibers, greatly improves the signal to noise ratio making the *in vivo* measurements possible. The Y-fiber device is simple, rugged, compact, relatively inexpensive, and sensitive.

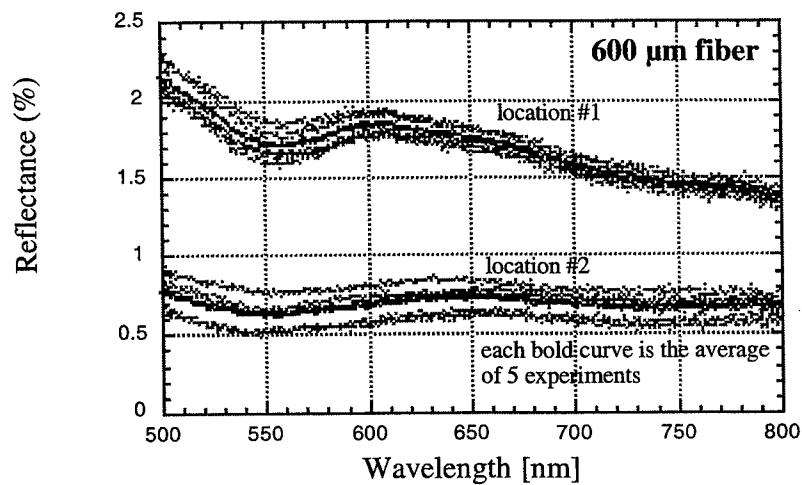
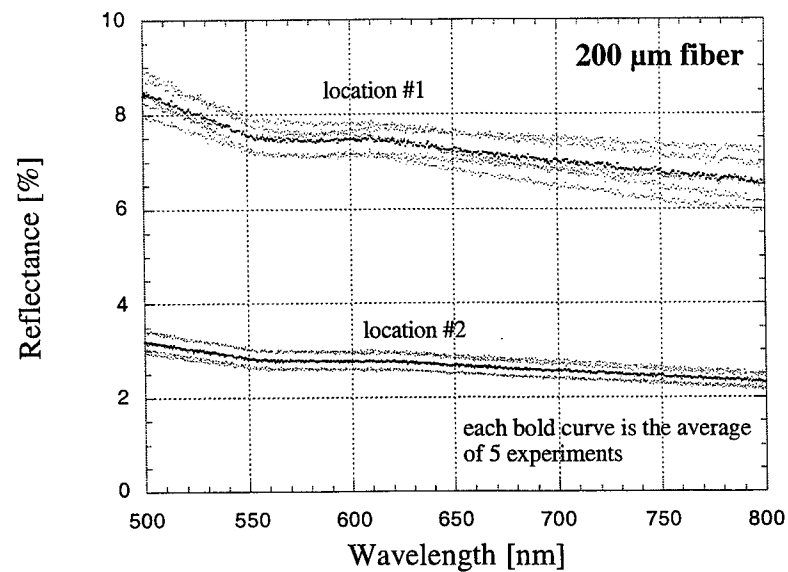


**Figure 5.** These typical *in vitro* spectra of kidney using a 200  $\mu\text{m}$  and 600  $\mu\text{m}$  fiber in a porcine kidney at two locations. Repeated experiments at each location show the measurement to measurement variation of signal. Since the kidney is not a homogeneous organ, it is not expected that the spectra be the same throughout the organ, and significant differences in reflectance were measured at the different locations.

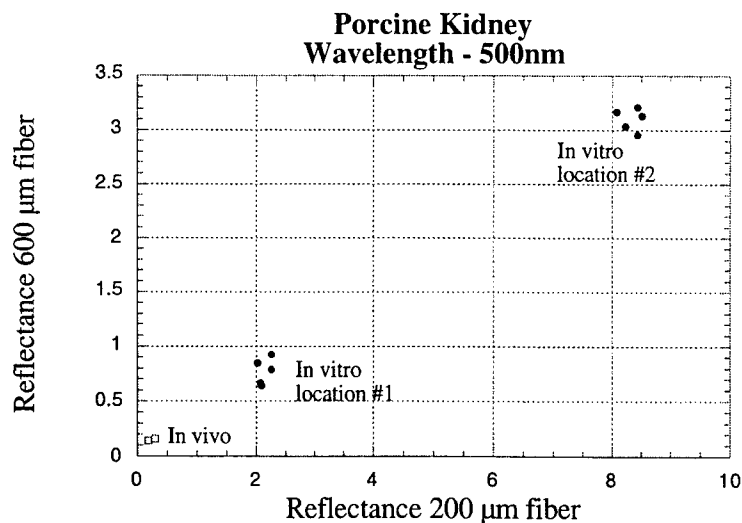


**Figure 6.** The measured reflectance of a 600  $\mu\text{m}$  fiber versus a 200  $\mu\text{m}$  fiber for *in vitro* measurements in two locations as well as for *in vivo* measurements of kidney. Expectedly, the *in vivo* reflectance is much smaller due to the presence of blood and other possible factors such as hydration levels.

## 5. ACKNOWLEDGMENTS

I would like to thank David Spain, Chris Sturges, and John Viator for their help and ideas on optical fibers. I would also like to thank Jeff Teach for his assistance with the *in vivo* experiments. And of course, I must give thanks to the Collins Medical Foundation for their financial support.

## REFERENCES

1. S. A. Prahl and S. L. Jacques, "Sized-fiber array spectroscopy," in *SPIE Proceedings of Laser-Tissue Interaction IX*, S. L. Jacques, ed., vol. 3254, pp. 348–352, 1998.
2. A. J. Welch and M. J. C. van Gemert, *Optical-Thermal Response of Laser Irradiated Tissue*, Plenum Press, 1995.
3. B. C. Wilson, M. S. Patterson, and S. T. Flock, "Indirect versus direct techniques for the measurement of the optical properties of tissues," *Photochem. Photobiol.* **46**, pp. 601–608, 1987.
4. B. C. Wilson, T. J. Farrell, and M. S. Patterson, "An optical fiber-based diffuse reflectance spectrometer for non-invasive investigation of photodynamic sensitizers *in vivo*," in *SPIE Proceedings of Future Directions and Applications in Photodynamic Therapy*, C. J. Gomer, ed., vol. IS 6, pp. 219–232, 1990.

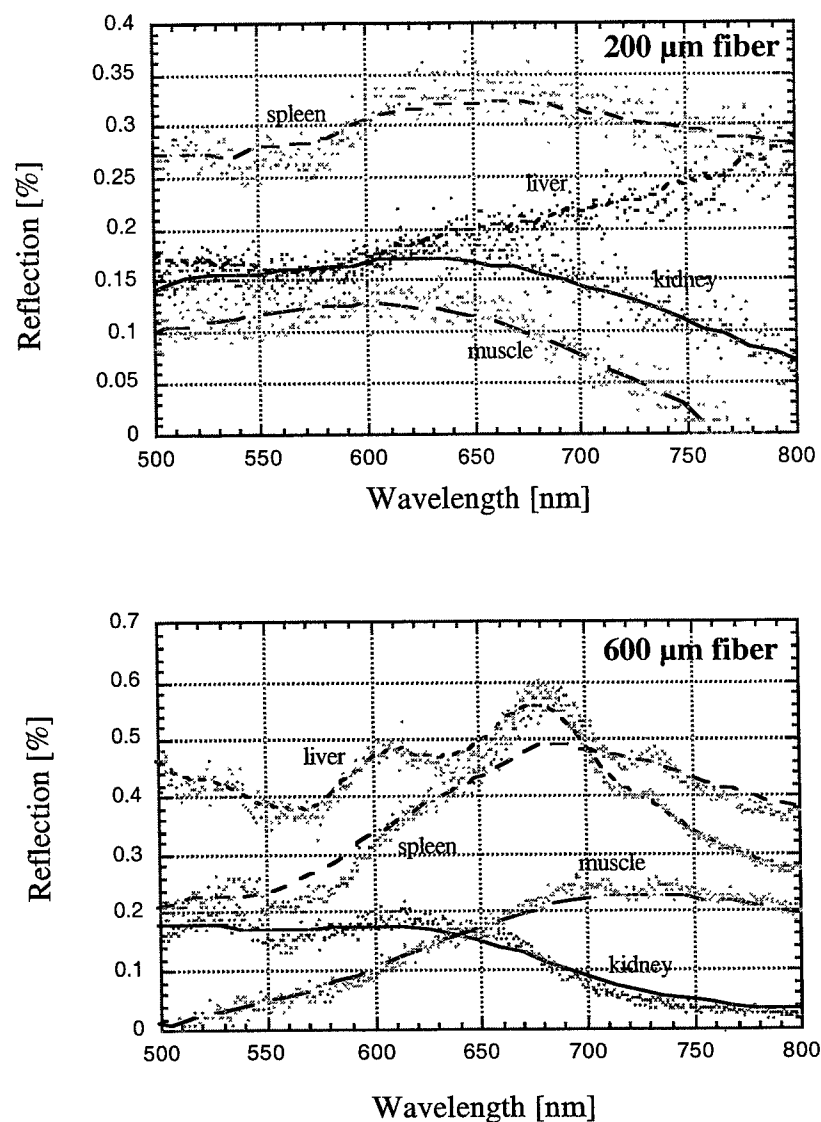


**Figure 7.** These are typical *in vivo* spectra using 200 and 600  $\mu\text{m}$  fibers in several porcine tissues; kidney, liver, spleen, and muscle. The signals are stable while the fibers in the needle are held in a particular site. Additionally, the signal changes abruptly when the needle passes from one tissue to another. The lines represent a smoothed average of the spectra.

# Validation of Self-Reported Skin Color via Analysis of Diffuse Reflectance Spectra of Skin

Robert A. Weersink<sup>a</sup>, Loraine A. Marrett<sup>b</sup>, Lothar D. Lilge<sup>a</sup>, Mark Purdue<sup>b</sup> and Stephen Walter<sup>c</sup>.

<sup>a</sup> Photonics Research Ontario, Biomedical Facility, 610 University Avenue, Toronto, Ontario, M5G 2M9

<sup>b</sup> Division of Preventive Oncology, Cancer Care Ontario, 620 University Avenue, Toronto, Ontario, M5G 2L7.

<sup>c</sup> Dept. of Clinical Epidemiology and Biostatistics, McMaster University, Hamilton, Ontario

## ABSTRACT

The validity of self-reported skin color was assessed by comparing the responses of a skin color survey with the external measure of diffuse reflectance spectrophotometry. Reflectance spectra of 108 subjects were measured at sites on the arm normally exposed to sunlight and sites normally unexposed to sunlight. The reflectance spectra were analyzed with a variety of discriminating algorithms, such as principal component analysis (PCA), and competitive neural networks. For subjects with light and dark skin, there was good correspondence between the survey results and groupings derived by the neural network analysis. For those people reporting medium skin color, the correspondence with the neural network groupings was poor. It was unclear if this was due to poor self-reporting or deficiencies in the spectral analysis.

**Keywords:** Reflectance Spectroscopy, Principal Component Analysis, Neural Networks

## 1. INTRODUCTION

Constitutive skin colour is an important predictor of skin cancer risk. Furthermore, self-perceived skin colour can be easily ascertained as part of a survey through use of one simple question (such as "What is the colour of your untanned skin (on the inner upper arm)?") with responses such as "light", "medium" and "dark". In the recently completed Canadian "National Survey of Sun Exposure and Protective Behaviour" 43% of adult (aged 15 and over) Ontarians reported that they had "light" skin; 47% reported "medium" skin colour; and 10% reported that they had "dark" skin<sup>1</sup>.

However, the validity of self-reported skin colour is not known. Many skin cancer investigators have actually used either reflectance measures, comparison with colour samples or interviewer assessment of skin colour, rather than self-report. But this is not possible in surveys to monitor population health and behaviour, for which data generally have to be collected by telephone or self-administered questionnaire (because of large sample size and substantial geographic dispersion).

The theory behind using reflectance to assess skin colour is that the lighter the skin the greater the amount of light will be reflected. The color of the skin is determined by 3 absorbers, hemoglobin, carotene and melanin, plus its scattering properties. In the context of skin cancer, it is believed that the amount of melanin in the epidermis is related to skin cancer risk. Therefore, we would like to measure reflectance as a function of wavelengths where this is the predominant quality of skin being assessed. Most investigators have used wavelengths in the vicinity of 650-680 nm, because there is little absorption by hemoglobin or carotene at this end of the spectrum, while there is still a small amount of absorption by melanin<sup>2</sup>.

Recently, however, investigators in Tasmania have reported finding that the strongest correlation between melanin density (measured in skin biopsies) and reflectance was when reflectance was assessed as the difference in reflectances at 420 nm and 400 nm<sup>3</sup>. The investigators argue that this is reasonable because melanin absorbs more light at these wavelengths, carotene makes only a very small contribution at these wavelengths, and absorption by hemoglobin is comparable at the two wavelengths. Thus, perhaps the hemoglobin effects are cancelled out leaving a better estimate of the contribution of melanin. This work has not been replicated and additionally, all subjects in this study were Caucasian.

The objective of this study was to assess the validity of self-reported "natural" skin color through comparison of responses to the skin color question used in the Canadian "National Survey of Sun Exposure and Protective Behaviours" with an objective measure obtained through diffuse reflectance spectrophotometry. Simple diffuse reflectance measurements made at several locations on the subjects' arms were analyzed with a variety of discriminating algorithms, such as principal component

analysis (PCA)<sup>4</sup>, and competitive neural networks<sup>5</sup>. The self-groupings obtained using these algorithms were then compared to the self-reported colors.

## 2. EXPERIMENT

One hundred and eight subjects were recruited for this study. Subjects completed a questionnaire requesting skin color, age, sex, and ethnic background. For comparison with other surveys, and to assess the relationship between reflectance and other important phenotypic characteristics, the subjects were also asked about ability to tan, tendency to burn and natural hair color.

### 2.1. Instrumentation

A schematic of the instrumentation is shown in Figure 1. Reflectance is measured by use of an integrating sphere probe, encased in a 2" cube of diffusing plastic. One face, which has a 1/4" porthole, is placed on the skin. When placed directly on the skin, the probe excluded all extraneous light except that originating from the light source. The probe was applied only with enough pressure to ensure that the port on the face of the probe is fully covered by the skin. White light from the QTH light source (Ocean Optics LS-1 Tungsten Halogen Light Source) is delivered to the top face of the probe via a 600  $\mu\text{m}$  optical fiber. At the probe, the light is collimated with a lens and directed to the skin surface filling the porthole on the bottom of the probe. A second optical fiber (400  $\mu\text{m}$  diameter) is connected to the integrating sphere perpendicular to the measurement face. This fiber collects the diffusely reflected light and directs it to a laptop controlled spectrophotometer (Ocean Optics S2000). The reflectance was measured from 400-1000 nm. A 99% reflectance standard (Lab Sphere) was used for the reference spectrum, while a dark spectrum was collected by placing the probe in a darkened environment such that no surface came in contact with the portal face.

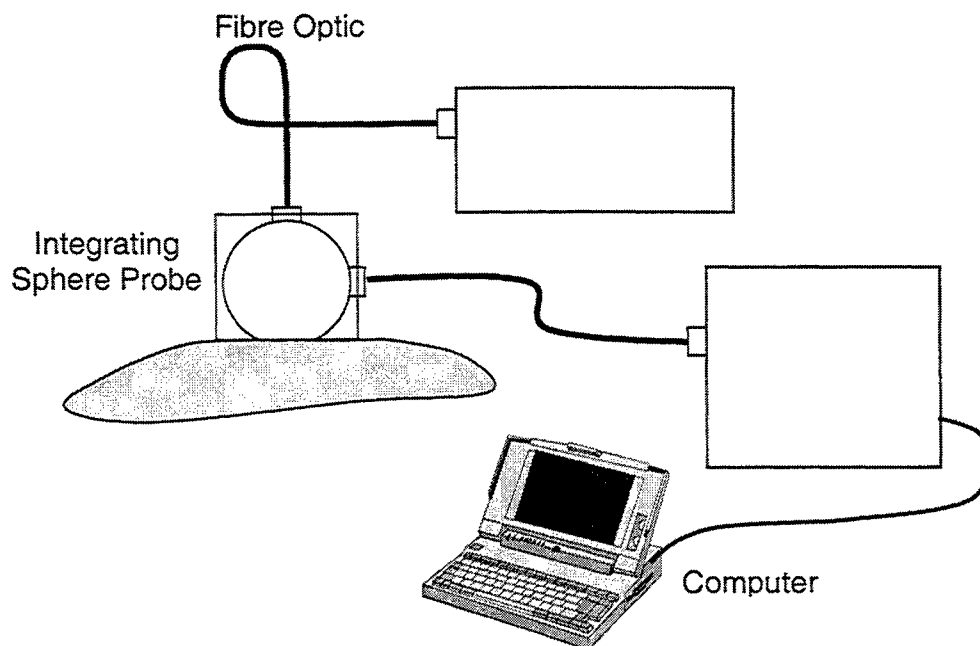


**Figure 1:** Schematic of reflectance measurement instrumentation.

### 2.2. Measurements

Reflectance spectra were measured at five locations on the subject's arm. Two locations were sun exposed sites (the top of the hand and the top of the forearm), and the other three locations were unexposed sites (on the inside of the arm between the elbow joint and the middle of the bicep muscle). Three spectra were collected at each location to ensure proper measurements were made. If all measured spectra were identical ( $R^2 > 0.99$  between spectra) then the spectra were averaged together.

Measurements were conducted at 10 sessions over a period of 5 weeks. Two individuals were measured at each session to monitor systematic measurement changes from session to session and to monitor measurement noise.

### 2.3. Spectral Analysis

The spectra were analyzed for clustering by two methods, principal component analysis (PCA) and self-organizing competitive neural networks. Analysis was performed with MATLAB version 5 using the MATLAB PLS and neural network toolboxes. PCA was performed on the data as measured, or preprocessed by mean centering or autoscaling to unit standard deviation across the spectrum. Little change was observed in the results regardless of the data preprocessing techniques. Neural network analysis was performed directly on the reflectance data. The competitive neural network works by computing the distance between an input vector (or spectrum) and the weighting vectors for each group. The weighting vector can be understood to be a representative spectrum of the group. The weight vector closest to the input vector is adjusted so that it is closer to the input vector. The process is repeated across the set of input vectors and repeated until the weights of the grouping vectors don't change. At this point, the input spectra are classified by measuring the distance between the input vector and the group vectors, with the input vector categorized by being placed in the closest group. The number of groups is an input parameter to the neural network. For this analysis, 3 groups were used to correspond to the number of groups used in the self-analysis survey.

## 3. RESULTS

The reflectance spectra of all 108 subjects at one of the unexposed sites is shown in Figure 2. Typical absorption bands are present in these spectra; hemoglobin peaks at 545 and 570 nm, and the water peak at 960 nm. Because of the small size of the collection port, the collected reflectance is only about half of the total diffuse reflectance. At longer wavelengths, the measured reflectance actually decreases, even though tissue absorption decreases and hence total diffuse reflectance should increase. This effect is due to the decreasing tissue scattering at longer wavelengths, and hence, longer wavelength light is more diffuse and escapes from the surface at larger distances from the point of entry. The port on the bottom of the probe is therefore collecting a smaller amount of the diffusely reflected light returning to the surface at longer wavelengths.

As described above, two individuals were measured at each of the 10 measurement sessions. For the 10 spectra collected at each measurement site per individual, there was a standard deviation of about 1% across the entire spectrum.

The exception to this was in the region of the hemoglobin peaks, where there was higher variation between measurement sessions. By comparing measurements made at different sites and at different sessions, it was concluded that the error between sessions was not due to any systematic differences in acquiring the data from one session to the next. Instead, the measured standard deviation represents the actual measurement error.

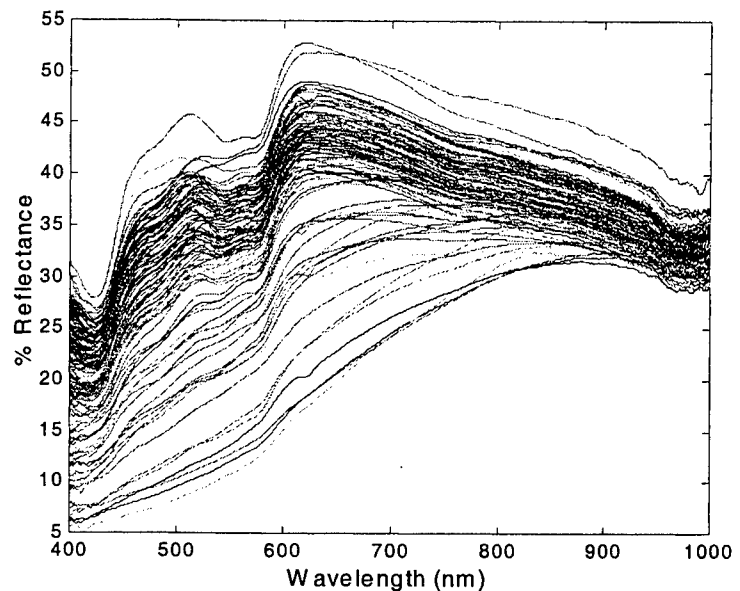


**Figure 2:** Reflectance spectra collected at one of the unexposed measurement sites.



### 3.1. PCA Analysis

The first four components of the principal component analysis explained 99% of the variation in the measured reflectance spectra, with over 80% of the variation covered in the first component alone. The first 3 principal components are shown in Figure 3. In typical clustering analysis using PCA, one plots the scores of the various components against each other. Such plots usually reveal some categorization of the data. For the spectra collected, such plots didn't categorize the data. Histograms of the scores of the first component indicated some grouping of the skin types. Therefore the score of the first component was compared to the self-reported skin color. Figure 4 shows the normalized scores of component 1 versus self-assessed skin color for measurements on an exposed and unexposed site. Normalized scores greater than 0.6 correspond well with self-assessments of dark skin. Separation between those reporting medium and light colored skin is more ambiguous.

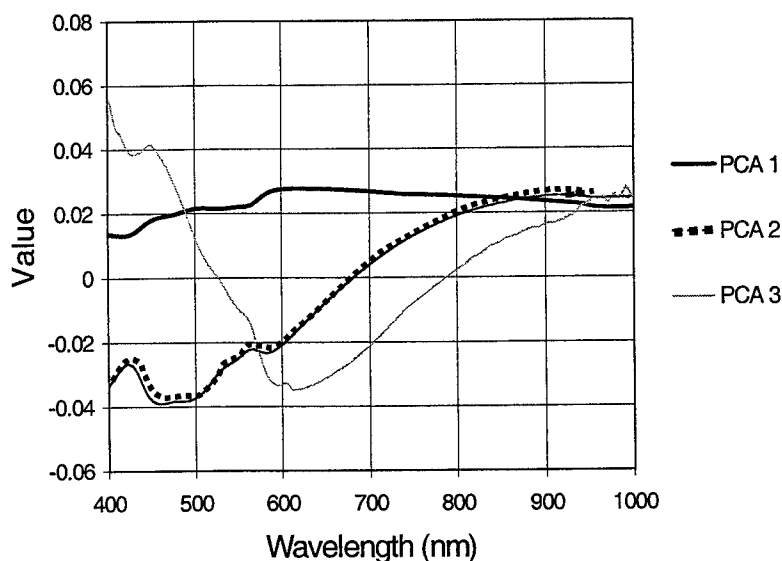


**Figure 3:** First three principal components as derived from PCA analysis of data in Figure 2.

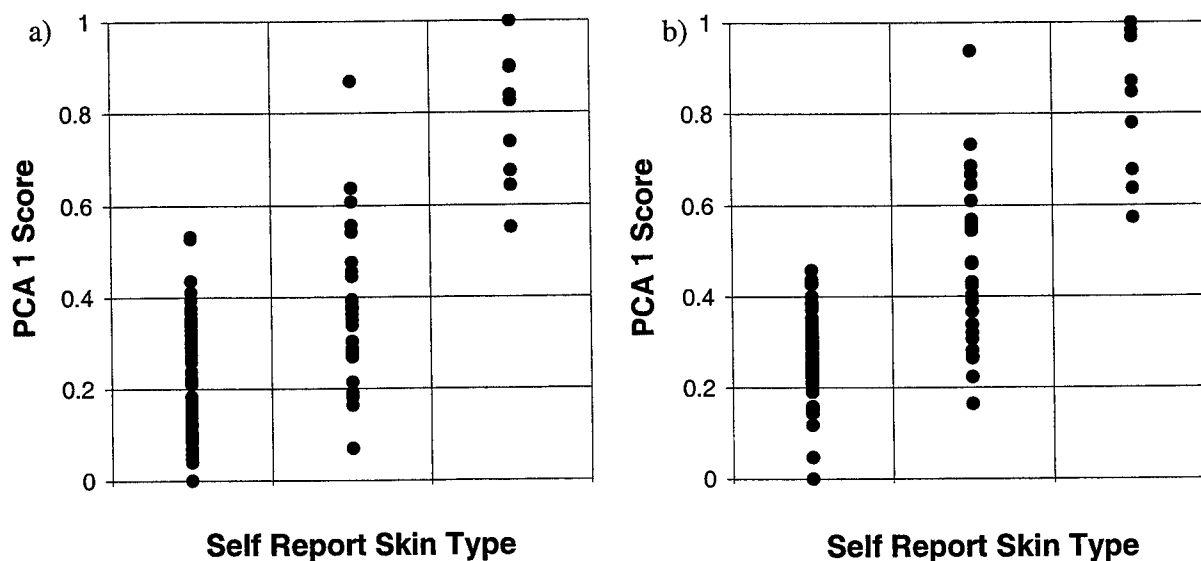


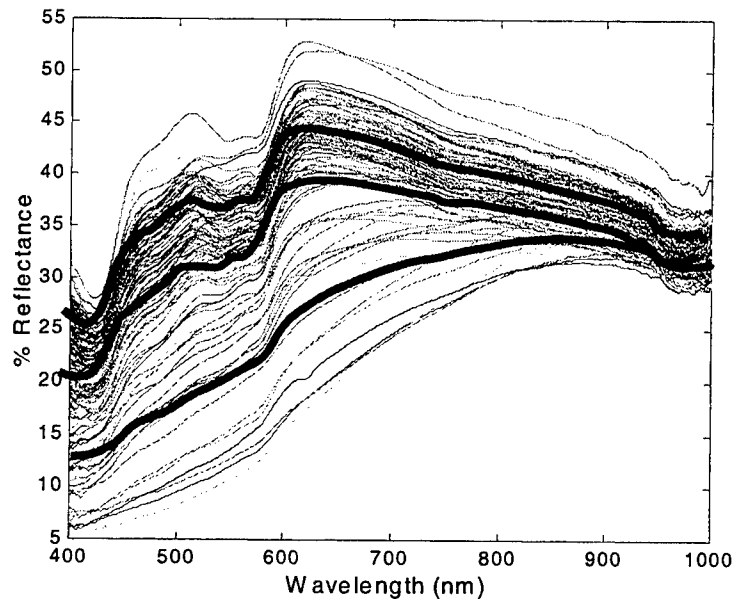
**Figure 4:** Normalized scores of first principal component versus self-assessed skin color for a) site exposed to sunlight and b) site not exposed to sunlight.

### 3.2. Neural Network Analysis

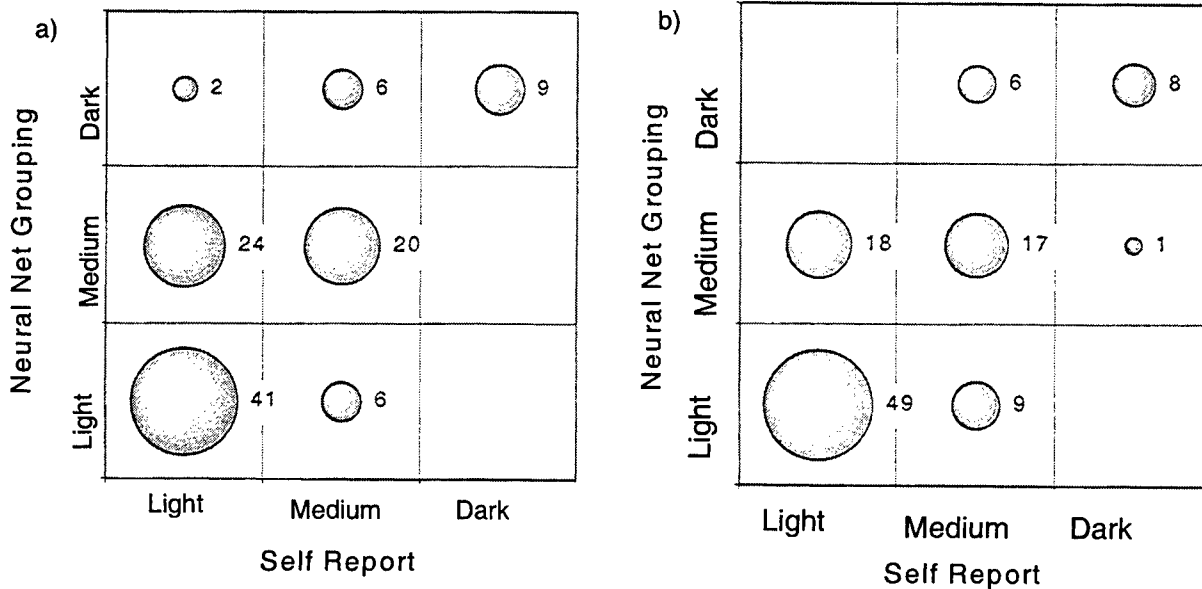
Figure 5 shows the reflectance spectra collected at one of the unexposed sites and the representative group spectra as determined by the neural network analysis. Three groups were used in the analysis to correspond to the number of groups used in the self-assessment question.

Figure 6 compares the neural net groupings for exposed and unexposed measurement sites with the self-assessments. Almost all of those assessing their skin color as dark are also grouped as having dark skin by the neural network. Likewise, the majority of those assessing themselves as having light colored skin are also assessed as having light colored skin by the neural network. However, there is little correspondence between those assessing themselves as medium skinned and the neural network grouping of medium skinned. For the unexposed site, only half of those reporting medium skin color are grouped in the medium skin color group by the neural network. The other half are evenly divided between light and dark groupings.

It does appear that most people are able to distinguish between actual skin color and color due to exposure to sunlight. The neural network groupings of skin color, when measured on the sun-exposed site, tend to group people as having darker skin than the subjects' own assessment of their skin color. Neural network groupings of the reflectance spectra measured on the unexposed site have a better correspondence to the self-assessed skin colors. The neural net groupings are also more evenly balanced around the line of perfect correspondence between the neural net groupings and the self-assessed skin color.



**Figure 5:** Reflectance spectra from Figure 2 and representative spectra of 3 groups as determined by neural network analysis. Representative spectra are thick black lines.



**Figure 6:** Neural network groupings versus self reported skin color for a) a site exposed to sunlight and b) a site not exposed to sunlight.

#### 4. DISCUSSION AND SUMMARY

The objective of the study was to assess the validity of self-reported skin color by comparing responses of a self-assessment of skin color with an external objective measure. In this case, the external objective measure was diffuse reflectance spectrophotometry. The measured spectra were analyzed for groupings into light, medium and dark skin by Principal Component Analysis and a competitive neural network algorithm.

It was found that PCA analysis of the reflectance data did not correspond well with the self-assessed skin colors, except for those reporting dark skin. The neural network analysis provided better correspondence with the self-assessed skin colors. However, it could not distinguish between medium skin color and either light or dark skin. It is unclear if this poor correspondence is due to poor reporting of skin color or inconclusive spectroscopic measurements and analysis. It may be more appropriate to use more than 3 groups in the neural network analysis to distinguish between those with very light skin, such as Northern Europeans, from those with moderately light skin, i.e. people with an ethnic origin from the middle of Europe. Also, the analysis may be somewhat biased by the large number of subjects who are by their own assessment light skinned. The population sampled corresponded well with the ethnic makeup of the local population, but the lack of dark skinned people may have placed a bias in the groupings by the neural network.

Future work in this study will include comparing the results of this study with previous studies. These studies generally examined reflectance at only one or two wavelengths. Also, we are examining ways of determining the melanin concentration directly from the reflectance spectra by fitting the main skin components to the spectra.

#### ACKNOWLEDGEMENTS

The authors would like to thank Sandrene Chong and Gini Hunter for the assistance during the study. The authors also would like to acknowledge the support of Cancer Care Ontario and Photonics Research Ontario.

---

<sup>1</sup> Ontario Sun Safety Working Group. Sun exposure and protective behaviours: Ontario report 1998. Toronto: Canadian Cancer Society (Ontario Division), 1998.

<sup>2</sup> A. Green, and N.G. Martin, "Measurement and perception of skin colour in a skin cancer survey," *British Journal of Dermatology* **123**, pp.77-84, 1990.

<sup>3</sup> T. Dwyer, H.K. Muller, H.K., L. Blizzard, R. Ashbolt and G. Phillips, "The use of spectrophotometry to estimate melanin density in Caucasians," *Cancer Epidemiology, Biomarkers and Prevention* **7**, pp. 203-6, 1998.

<sup>4</sup> E.R. Malinowski, *Factor Analysis*, John Wiley 1991.

<sup>5</sup> B.D. Ripley, *Pattern Recognition and Neural Networks*, Cambridge University Press, 1996.



## Poster Session

# Fluorescence study of normal, benign and malignant human breast tissues

A. Pradhan<sup>a</sup>, R. N. Panda, M. S. Nair, B. V. Laxmi, A. Agarwal\* and A. Rastogi\*

Department of Physics, Indian Institute of Technology, Kanpur, IN 208016

\* AA, G. S. V. M. Medical College, Kanpur, IN 208016.

## ABSTRACT

Fluorescence properties of flavins in normal, benign and malignant human breast tissues have been investigated between 500-700 nm using 488 nm excitation of an Ar-ion laser. The combination of fluorescence anisotropy and spectral profiles can distinguish normal, benign and malignant from one another. The fluorescence spectra may be characterized by two major bands with the width of the band at 580nm being the distinguishing parameter. The polarization study of human breast tissues shows higher anisotropy for the tumor tissues compared to their normal counterparts. The effects of multiple scattering on depolarization of fluorescence is confirmed by polarization measurements on thin tissue sections which show higher anisotropy values compared to the thick samples. An important observation is the increase in the difference of anisotropy values between some of the normal and malignant tumor samples while going from thick to thin tissues.

**Keywords:** Fluorescence, Depolarization, Anisotropy, Multiple Scattering, Malignant.

## INTRODUCTION

The use of optical spectroscopy for non-invasive probing of human tissue environment<sup>1</sup> is now an important area of research. Since the emission process contains a wealth of information that is related to fluorophores and its surroundings, fluorescence is unique among spectroscopic techniques<sup>2</sup>. Several groups have been investigating the use of fluorescence spectroscopy for possible cancer diagnosis and promising results have been achieved<sup>3-6</sup>. Fluorescence spectroscopic studies in human tissues may provide informations on progress of disease at the molecular level. Earlier work with excitation in the visible range however has not been quite rewarding<sup>7</sup>. The aim of this work is to use fluorescence depolarization to probe in more details in visible region, for any distinguishing features and more information on the environment of flavins, the major fluorophore in that region. These are coenzymes that play a role in oxidation-reduction processes of the tissues. Hence, they may play a major role in triggering tumor growth<sup>11</sup>. The size, shape or segmental flexibility of the fluorophores can also be probed by fluorescence depolarization measurements. In this paper we report diagnostic possibilities of flavoproteins using steady state fluorescence depolarization techniques and shape profile in the visible region for breast cancer.

## MATERIALS AND METHODS

Pathologically characterized thick (~4mm) tissues samples were obtained immediately after surgery. The experiments were done on the same day of operation, without any chemical treatment. Most of the tumor tissues studied were ductal carcinomas. The normal tissues were from the surrounding areas of the resected cancerous tissues.

The samples were excited with linearly polarized laser light of wavelength 488nm of an Ar-ion laser with a power of 2mw at the sample site. The light was focused on to a spot size of nearly 10 $\mu$ m on the front surface of the tissue. Luminescence from the front surface of the tissue was passed through an analyzer whose optical axis was set parallel or perpendicular to the optical axis of the polarizer. A depolarizer was placed before the spectrometer to ensure that the detection system does not give preference to any one of the selected direction of polarized luminescence. The fluorescence spectra were scanned using an SPEX-1877E triplemate blazed at 500nm and detected using a cooled S1 photomultiplier tube. Fluorescence anisotropy was estimated using the relation  $r(\lambda) = (I_{\parallel} - I_{\perp}) / (I_{\parallel} + 2I_{\perp})$ . For measurements samples were placed in optical cuvettes of 1 $\times$ 1 $\times$ 5cm<sup>3</sup>. Samples were in the form of thick and thin slices of thickness 4mm to 0.5mm respectively.

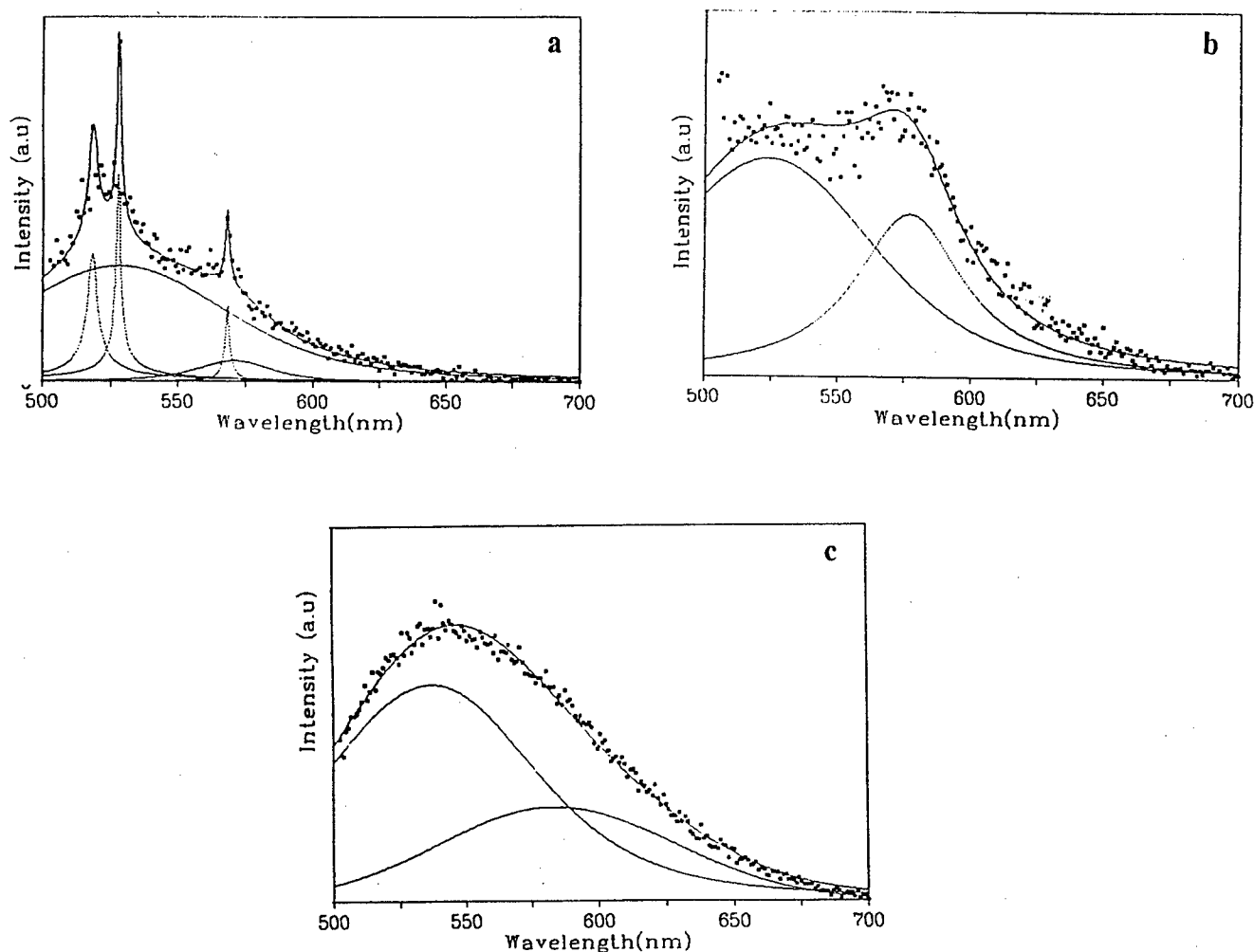


Fig.1 Fitted fluorescence spectral profiles for (a) Normal, (b) Benign, (c) Malignant Human Breast tissue.

## RESULTS AND DISCUSSION

Fig.1 shows the fitted fluorescence spectral profiles for normal, benign and malignant human breast tissues excited at 488nm. The emission spectra were characterized in general by a major wavelength band centered around 530nm. The fluorophores responsible for this band is believed to be mainly from flavins, eg: - FAD, FMN, and free riboflavins. This was supported by the emission spectra of the corresponding fluorophores in aqueous solution ( $10^{-5}$ M) peaked at 530nm<sup>7</sup>. In benign tumors the wavelength band at 580nm was remarkably prominent and the fluorescence profiles appeared to be broadened. To extract more information in this regard, the profiles were fitted to two voigt functions, one at 530nm and the other at 580nm. Assuming the 530 band to be from flavins, the peak position and FWHM of this band was fixed as according to the spectral profiles of aqueous solution of FAD measured by us.

Quantitatively, from the theoretical fits, a distinct difference was observed in the normal, benign and malignant tumors. The bandwidth of benign tumors was seen to be always less than 70nm. In comparison the same band is greater than 85nm in malignant tumors and normal tissue has a bandwidth of ~33nm. Based on the second band width a clear cut-off can be obtained for the three types of tissues. Fig.2 shows scatter plot of 20 samples analysed. These broader profiles indicate either presence of another fluorophore or different kinds of flavins<sup>8</sup> in tissue material and their possible interactions with various chemical species present in human breast tissues. Of particular interest is the distinguishing spectral feature of benign tumor, which is pathologically important. The spectral profiles of benign tumors also show an abrupt drop at around

590nm. This could be due to self-absorption effects. The spatial variation of fluorescence intensities have been studied to confirm whether the abrupt decrease is due to self absorption effects, or is an intrinsic property of tissue. The value of absorption coefficient at 590nm is seen to be higher in benign tumors. Hence, this shape may be due to self absorption effects<sup>12</sup>.

Three Raman peaks were observed at 1148.9, 1520.4, and 2891.8  $\text{cm}^{-1}$  in almost all normal cases, at different positions as reported<sup>13</sup>. The normal tissues were mostly yellow and fatty.

On the basis of polarized fluorescence spectra from normal, malignant and benign tissues, anisotropy was calculated. Experiments were done by varying thickness from 4mm to 0.5mm. Lower anisotropy values of the normal human breast tissues compared to benign or malignant tumor counter parts have been observed. Such kind of observations have been reported for skin tissues<sup>9</sup>. Fluorescence depolarization can occur due to Brownian rotational motion of the excited fluorophores in low and moderate viscosities<sup>7</sup>. Depolarization of any propagating light can also occur due to multiple scattering. Experiments were performed with thin tissue sections (0.5mm) to minimize multiple scattering effects. A larger increase in the anisotropy was observed in malignant tumors as compared to their normal counter parts in going from thick to thin, but in benign cases they were of the same order as normal. This is consistent with the fact that multiple scattering effects on excitation light and fluorescence is more in malignant tissues as compared to normal<sup>10</sup>. The above results also suggest that benign tumor, on the contrary, are not as affected by multiple scattering as malignant tumors. These results suggest that depolarization due to multiple scattering plays a dominant role in thick tissues and that it is higher in malignant tissues because of its higher cell density. This result is also consistent with higher values of reduced scattering coefficient of benign tumors, obtained from fluorescence light propagation model. The lower anisotropy in normal tissues compared to malignant tumors even in thin tissues where effect of multiple scattering has been reduced, suggest that other causes of fluorescence depolarization (eg: rotational motion of fluorophores or average size of rotationally mobile species) may be more dominant. Experiments with tissues of thickness in the single scattering region will be performed to confirm this.

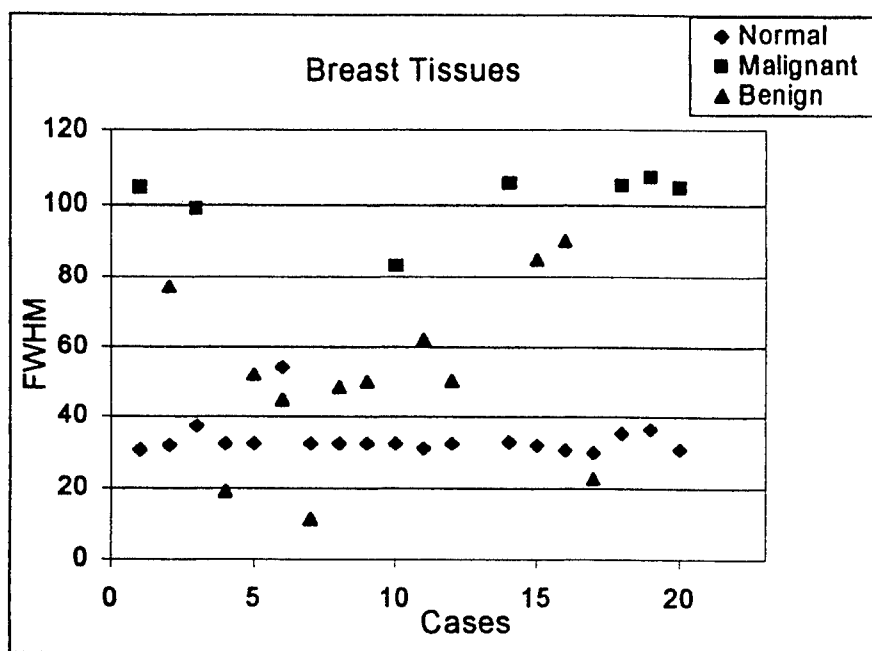


Fig. 2. A plot of D-parameter Vs no. cases for human breast tissues.

## CONCLUSIONS

To conclude, our in-vitro studies on human breast tissues show that characteristic information from shape of the fluorescence spectra and depolarization effects can provide a very good discrimination between cancerous, normal and benign breast tissues in the visible region. The results therefore suggest that a straightforward fluorescence spectral profile can itself provide excellent discrimination between malignant and benign, which is of pathological importance. The fluorescence depolarization results also throw light into effects of multiple scattering in the three different tissue types.



## ACKNOWLEDGEMENTS

The authors would like to acknowledge Dept. of Science and Technology (DST) for partial financial support. We also thank Nirmalya Ghosh for extensive discussions.

## REFERENCES

1. R.R. Alfano, G.C. Tang, A. Pradhan, M. Bleich, D.S.J. Choy, E. Opher, "Steady state and time resolved laser fluorescence from and tumor lung and breast tissues", *J. Tumor Marker Oncology*, 3, pp.165, 1988.
2. J.R. Lakowicz, *Principles of fluorescence Spectroscopy*, Plenum Press, New York, 1983.
3. C.C. Hoyt, R.R. Richards Kortum, B. Costells, B.A. Sucks, C. Kittrell, N.B. Ratliff, J.R. Kramer and M.S. Feld, *Laser surg. Med.*, 8, pp.1, 1988.
4. R.R. Richards Kortum, A. Mehta, G. Hayes, R. Cothren, T. Kolubayer, C. Kittrell, N.B. Ratliff, J.R. Kramer and M.S. Feld, *Amer. Heart J.*, 118, pp.381, 1989.
5. R. Alfano, B.B. Das, E. Celmer, R. Prudente, J. Cleary, "Light sheds light on cancer-distinguishing malignant tumors from benign tissues and tumors", *Bull. N. Y. Acad. Med.*, 67, pp. 143, 1991.
6. G.C. Tang, A. Pradhan, W.L. Sha, J. Chen, C.H. Liu, S.J. Wahl and R.R. Alfano, "Pulsed and cw laser fluorescence spectroscopy from cancer and chemically treated normal breast and lung tissues", *Appl. Opt.*, 28, pp.2337, 1990.
7. R.R. Alfano, A. Pradhan, G.C. Tang, "Optical spectroscopic diagnosis of cancer and normal breast tissues", *J. Opt. Soc. Am. B*, 6, pp. 1015, 1989.
8. R.R. Alfano, D.B. Tata, J.J. Cardero, P. Tomashefsky, F.W. Lango and M.A. Alfano, "Laser induced fluorescence spectroscopy from native cancerous and normal tissue", *IEEE J. Quantum Electron.*, 20, pp. 1507, 1984.
9. A. Pradhan, S.S. Jena, B.V. Laxmi, A. Agarwal, "Fluorescence Depolarization of normal and diseased skin tumor tissue", *SPIE* 98, 78, pp. 3250, 1998.
10. R.R. Alfano, S.G. Demos, A.J. Papadopoulos, H. Savage, Alexandra S. H., S. Schantz, "Polarization filter for biomedical tissue optical imaging", *Photochemistry & Photobiology*, 66(6), pp. 821, 1997.
11. S. Ghisla, V. Massey, J. Lhoste and S.G. Mayhew, "Fluorescence and optical characteristics of reduced flavins and flavoproteins", *Bio-chemistry*, 13, pp.589, 1974.
12. A. Pradhan, M.S. Nair, N. Ghosh, A. Agarwal, "Spatial variation of fluorescence in human breast tissues", to be printed in *SPIE* 2000.
13. R.R. Alfano, G.C. Tang, A. Pradhan, W. Lam, D.C. Choy and E. Opher, "Fluorescence spectra from cancerous and normal human breast and lung tissues", *IEEE J. Quant. Elect.* 23, pp 1806, 1987.

---

\* Correspondence: Email: asima@iitk.ac.in  
Fax: 011-91 0512/590914

# **Stoke's and anti - Stoke's characteristics of anaerobic and aerobic bacterias at excitation of fluorescence by low-intensive red light.**

## **Part I. Research of anaerobic bacterias**

Victor I. Masychev\*, Michail T. Alexandrov

ROSSLYN MEDICAL (UK) / Moscow Representative office

### **ABSTRACT**

Biopsy or photodynamic therapy of tumors are usually investigated by fluorescent diagnostics methods. Information on modified method of fluorescence diagnostics of inflammatory diseases is represented in this research (optical PNC-method). Anaerobic microorganisms (bacterias) are an often cause of these pathological processes. These microorganisms also accompany disbiotic processes in intestines.

Conducted reserches on studying the possibility of registration of monoculture of anaerobic microorganisms and their mixtures by the method of laser PNC-diagnostics. Stoke's and anti-Stoke's characteristics of 7 anaerobic and aerobic microorganisms (bacterias) types were researched.

A choice of the listed bacterias as objects of study connected with that these species of microorganisms, presenting a normal microbiocenosis and being obligatory anaerobes are the most often cause of purulent-inflammatory diseases of different localizations.

Moreover, at present very few facts are known about fluorescence of these bacterias under excitement by red light.

**Keywords:** in vivo autofluorescence, laser, spectroscopy, anaerobic and aerobic bacterias, PNC-diagnostics

### **1. INTRODUCTION**

Human organism consists big quantity of bacterias. Bacterial flora usually forms complicated and rather stable ecological system, which depends on peculiar features of human organism and can characterize ecosystem in norm and pathology.

Thus continuous search for relatively prime, inexpensive and informative methods allowing to estimate microecological shift of organism is well-taken and rather important. Such a method could be optical PNC-method[1-3]. The distinctive feature of the optical PNC-method in aspect of indication of informational signals, characterizing biotissue in normal and pathologi are application in analyzing of Stoke's and anty-Stoke's fluorescent radiation components, probing, reflected and backscattering radiation and other secondary optical radiations.

In elementary case at least three components of optical radiation are used – probing, backscattering and fluorescence radiation, which are detected simultaneously and analyzed by special algorithm.

In the first part of this article main attention is paid to research of anaerobic bacterias spectral characteristics. In the second part of the article the results of aerobic bacterias research will be published.

---

\*Correspondence: E-mail: VMasychev@rosslynmedical.com, Telephone: 7 095 258 2330; Fax: 7 095 258 2438

## 2. MATERIALS AND METHODS

The scheme of the experimental device is shown on fig. 1 The experimental device includes treatment-diagnostic "Oliver-101" system (produced by ROSSLYN MEDICAL, UK) intended for registration and studying of biological object spectrums (biotissues, microorganisms, physiological liquids etc.), and a tube (vial), having a volume about 10 cm<sup>3</sup> and held in special holder. The "Oliver-101" system has a fiber-optic device for delivery of probing radiation to an object of studying. The fiber-optic device simultaneously provides registration of backreflected, backscattering and fluorescent radiation from a bioobject. Optical signals from an investigated bioobject are guided to the entrance of the "Oliver-101" system and directed to the entrance of spectrum registering device. Monochromator with a dispersing element (linear dispersion 10nm/mm) enables to detect exciting radiation and fluorescence spectrums in the spectral region 520 – 850 nm. As photo receivers photodiode straightedge with a limiting sensitivity up to 10 photon/element on bacterial wavelength of 633 nm are used. Electrical signals from the photoreceiver are registered, displayed and processed by PC-computer. The distinguishing feature of the current research is that anti-Stokes components of optical PNC-signals of biological objects are being registering for the first time.

Developed software enables the "Oliver-101" system to operate in two diagnostic modes: a spectrum registering mode and a spectrum processing mode.

In a spectrum registering mode optical spectrums of bacterias was recorded in absolute values as dependencies of backscattering weakened signal intensity on a fixed wavelength of exciting radiation and of autofluorescence from wavelength (PNC-spectrums) [1]. In the spectrum processing mode the spectrums having been received during the registration are studied in details. In particular the processing mode enables to perform on spectrums some standard mathematical operations, to normalize spectrums and to compare them. Besides that, special programs allow on certain algorithms to select consider separate spectral ranges, to measure fluorescence power, to measure wavelength absolute value at maximums of spectral curves and to get numerical parameters, characterizing relative contribution of back scattering and fluorescent signals into radiation spectrums. In this work four types of microorganism's (bacterias) spectrums were researched:

- |                             |                     |
|-----------------------------|---------------------|
| 1. Bacteroides fragilis     | N 323               |
| 2. Clostridium perfringens  | tA N E <sub>5</sub> |
| 3. Fusobacterium necroforum | N 22                |
| 4. Campilobacter jejuni     | N 170               |

The choice of the listed bacterias was based on the fact that these species of microorganisms, presenting a normal microbiocenosis, in most cases are conditionally-pathogenic microbes (the exception is Campylobacter jejuni – causative agent in acute enteritis), cause purulent-inflammatory diseases of different localization and caries. Moreover at present very few facts about the bacterial fluorescent by red light excitement are known. Usually bacterias were kept in sealed tubes, opened just before each experiment.

### 3. STRATAGY OF THE STUDY UNDERTAKING

As far as fluorescent methods of analysis depend on many external factors, changing fluorescence of investigated substances, then in this research greater attention was paid to a fluorescence spectrum registration beginning with choosing of tube materials, solvent, conditions of undertaking the experiment and ending with factors, which prevent photodestruction (photobleaching) of investigated microorganisms in relation to laser probing radiation.

In particular, the applied tube was made of special optical glass, not having any observable fluorescence, what was confirmed by additionally conducted experiments. As solvent in experiments distilled water was used, which also showed no fluorescence in absence of analysing substance. To ensure impossibility of contamination by fluorescent, scattering and absorbing admixtures right in time of analysis other arrangements were made. It is particularly important when concentration of analyzing substance is close to the limits of sensitivity of given analytical method of fluorescence analysis. As far as fluorescence for many substances can extremely depend on temperatures, special measures on stabilization of temperatures indoors were taken. All measurements described below were performed at room temperature of  $20 \pm 1$  °C under normal atmospheric pressure. Besides, in experiments described below, pH parameter was constant and equal 7.

As it was noted above, many fluorescent substances, being intensively irradiated by natural or coherent light, absorb its and herewith decay. As a result of the instability intensity of fluorescence decreases right in time of measurements. It is obvious that destruction of microorganisms (bacterias) can bring about serious systematic mistakes. Because of it all analyzed bacterias every time were studied on photoresistance under one or another parameter of probing radiation. A degree of analyzed bacteria photodestruction depended on energy dose used. So while analyzing such unstable bacterias, energy doses, which do not bring about inconvertible bacteria photodestruction were used.

It is also necessary to emphasize that intensive probing light, focused in some point inside a tube, also can cause considerable local photodestruction. If the fluorescence emitted by this damaged solution area is measured, that under investigated spectrums can vary depending on optical focus position. They can be lowered under focused beam, and only after that, as in the tube diffusion occurs and in the point, where the light was focused initial conditions recovered, spectrum will go back to the initial values. So in this research optical systems of probing radiation delivery were used, which don't focus light inside the tube.

Studies were held at the following scheme.

On the first stage spectrums of each four bacterial types were researched. Each spectrum was registered in conditions of contact distal end of fiber with a surface of bacterial mixture in distilled water, placed in the tube (monosolutions). The power of probing laser radiation did not exceed 3 mW, time of spectrum registration varied within 0.02 and 5 sec. Herewith as it was mentioned above, laser energy radiation (not exceeding 0.015 J) did not bring about inconvertible photodynamic damaging of bacterias and their observable photobleaching.

On the second stage spectrums of bacterial mixtures (polysolutions) were studied. Their particularities and possibility of usage for each bacteria in under investigated mixtures were researched. In this case registered spectrums were shown by superposition of fluorescence of several bacterial species, located in solution in one common tube.

## 4. RESULTS AND DISCUSSION

### 4.1. Monobacterial mixtures

Dependences of absolute intensity of fluorescence on a wavelength at excitement of fluorescent by probing radiation of the He-Ne laser ( $\lambda=632.8$  nm) for four bacterias types are shown on Fig. 2-5. As it is seen from the figures bacterial mixtures in distill water, which was used as a dissolvent, show intensive fluorescence. Stoke's fluorescence can be located in red and nearest infrared spectral range (635-850 nm). Applying spectral registering device enables also to detect anty-Stoke's of fluorescence, i.e. light with less wavelength (more energy) than *exciting* light.

Emission in spectral region 590-630 nm is character for anty-Stoke's radiation.

Spectrums of fluorescence of all studied bacterias are characterized by one vastly denominated maximum in range 650 nm and by monotonous fading in the nearest infrared range. Different types of microorganisms in the experimental conditions are different in intensities of a fluorescent maximum and in integrated power of fluorescence. These factors can vary in 3-4 times for different types of bacterias. However, the differences are insufficient for reliable bacterial type identification with only these information factors. More specific and informative are amplitudes of backscattering probing radiation ( $\lambda=632.8$  nm). In combination with fluorescence, forming spectrums, their informational factors allow to characterize types of studied bacterias more uniquely, i.e. these factors might be used for indication and separation of observed monobacterias, since they in significant measure reflect specifics of the researched bioobjects.

Normalization of fluorescence spectrums allow to compare intensities and powers of under investigated bacterias fluorescence in particular when using the standards of comparison (fig. 6). The standard of comparison serves also as a factor of reproducibility of detected spectrums.

Reproducibility of researched spectrums were proved by detection of 15-30 spectrums, recording sequentially with time interval 5 sec. (fig. 7, 8). As it follows from the figures, measurement inaccuracy did not exceed  $\pm 2\%$  (fig. 7), inaccuracy in reproducibility of wavelength value in spectrum maximum did not exceed  $\pm 0.5$  nm (fig. 8), and inaccuracy in integrated power reproducibility – 1.5%. Fig. 7 illustrates data on reproducibility of optical spectrums. It is shown, that under long irradiation with chosen parameters effect of photodestruction did not revel itself at all.

The "Oliver – 101" system has a mode, providing countering and variation of excited light dose, in order to irradiate an object of studying only in a short period of measurement. At bacteria investigation it was shown that for quick spectral analysis it is preferable to use high - speed registration systems. The sensitivity of a system is better to raise by means of receiver sensitivity rather than increasing the intensity of exiting radiation. When studying unstable objects and having to

use very weak light sources, necessary sensitivity is completely defined by sensitivity of a receiver. At the analysis of such unstable substances as bacterias, it is recommended to use the beam of smaller intensity for excitement.

#### 4.2. Polybacterial mixtures

On the second stage spectrums of bacterial mixtures dissolved in distilled water were researched. Their peculiarities, possibility of identification of each bacteria from the mixture upon their distinctive spectrums and information features were studied. In this case detected spectrums were superposition of several bacteria's fluorescent spectrums located in one tube.

Fig. 10-12 show dependence of normalized signal intensity on wavelength while excitement of fluorescence by probing radiation 632.8 nm for three different bacterial mixtures. These mixtures are dissolved in distill water. Basic spectral characteristics proper to the investigated bacterias are the same for spectrums of their mixtures. Withal we should note a number of differences in the spectrums, distinctive for polybacterial mixtures. Intensity of fluorescence of mixtures is higher than intensity of fluorescence of each component. It is not observed stochiometrical relations between integral concentration of bacterias and integral power of fluorescence at study of spectrums of bacterial mixtures. Unlike monosolutions, spectral maximum of fluorescence for bacterial mixtures shifts to a long wave range. The shift depends on a quantity of bacterias under investigation, their species, concentrations and a number of other parameters. The biggest shift of the fluorescence maximum in the described above experiments was near 30 nm. This data shows integration between under investigated bacterias when they are in mixtures. A mechanism of such action is differ from straight proportional increasing of fluorescence power and depends on bacterial species and bacterial concentration. There is not heavy but observable competition between bacterias and products of their vital activity in mixtures, what is reflected on fluorescence spectrums. Under that, as it can be seen from spectral analysis (fig. 10-12), the most frequency shift in mixtures is specific for the mixtures containing bacteria No. 3 (*Fusobacterium necroforum*). Withal an accompaniment of bacterias No.1, No.2 and No.4 in the mixtures brings around not sufficient, but measured shifts of maximum fluorescence wavelength. However the most important experimental fact of the spectrum analysis is that the studied bacterial types did not actively participate in fluorescence quenching. We can regard this as an confirmation of light energy migration under the described interaction.

Revealed phenomena of potentiation fluorescent power and shift of fluorescent maximum, which are determined by each part of mixture and type of bacteria is of crucial importance for clinical usage, first of all in aspect of detection and evaluation the stage of pathological processes in which the studied microorganisms participate. Weak mutual influence and an absence of observable quenching of fluorescence allow to regard the integral factors of fluorescence power as an objective quantity and quality indicator of a pathologic hearth microbiocenosis. It allows to integrally evaluate presence and activity of microbes in under investigated biological object.

#### 5. CONCLUSIONS

1. The research of four bacterial types and their mixtures was performed by method of optical PNC-diagnostics while fluorescence excitation by red light. Main attention was paid to the research of fluorescence component of optical PNC-signals.
2. For the first time anty-Stoke's fluorescence of anaerobic bacterias was registered.

3. It is revealed that the characteristic wavelength of peak of fluorescence maximum for different investigated bacterias at probing radiation  $\lambda = 632.8$  nm does not depend on type of the object. It is a constant value  $650 \pm 0.5$  nm.
4. Different species of microorganism in conditions of experiments vary on intensities in the fluorescence maximum and on integral power of fluorescence.
5. It is revealed that fluorescence spectrums of under investigated microorganisms differ both in each fixed point of a spectral fluorescence curve and in fluorescence power in any spectral interval of fluorescence.
6. A relative input of each indicated parameter can vary, but the dominant parameters are the wavelength of fluorescence intensity peak and its integral power. Spectral changes of fluorescent as information parameters reflect specifics of under investigation objects (bacterias) incredibly weaker.
7. At bacterial mixture study it is revealed a phenomena of fluorescent power potentiation, which determined by the power of each component of the mixture. Herewith integral effect is not a linear superposition of each component of the mixture.
8. It is revealed that while studying fluorescence of bacterial mixtures it can be observed a shift of fluorescent peak in a long wave range up to  $30 \pm 1$  nm. The shift depends on set of under investigation bacterias, their types and concentrations and obtains in the described above cases  $30 \pm 1$  nm.
9. On the basics of the achieved results we can suppose that the most informative factors from the standpoint of clinical applications in detection and evaluation pathological processes, based on quality and quantity changes in microbiocenosis with participation of the specified bacterias are: a position of peak of fluorescence maximum, intensity in maximum, integral power and shift of fluorescence wavelength under of pathological processes.
10. Thereby, observed in clinical practice shift of maximum of fluorescent wavelength when recovery process in patients with inflammatory diseases can reflect quality and quantity changes in microflora and probably is not determined by changes in its Ph environment as it was supposed earlier.
11. Left shift of maximum of fluorescent integral factor characterises changes of quantity and quality microflora component of pathological hearth.
12. On the basics of the conducted researches we suppose that integral factors of fluorescent power are not specific, but objective factors of quantity and quality components of pathologic hearth microflora, allowing to evaluate integrally presence and activity of microbes in under investigation biological object (skin, disbacterios, purulent inflammatory wounds etc.)

## REFERENCES

1. V. Masyshev, M. Alexandrov, "Photon – undulatory nonlinear conversion optical emissions in biologic objects", Proceedings SPIE, vol. 3918 "Biomedical Spectroscopy: Vibrotional Spectroscopy and other Novel Techniques", Bellingham, WA, 2000.
2. V. Masyshev, M. Alexandrov, "Photon – undulatory nonlinear conversion optical emissions in biologic objects". IV International congress "Laser medical problems", pp. 233-234, Moscow, 1997.
3. V. Masyshev, M. Alexandrov, "Conception of Photon – undulatory nonlinear conversion optical emissions in biological tissues". Description of intellectual product, VNTIC, Moscow, 1999.

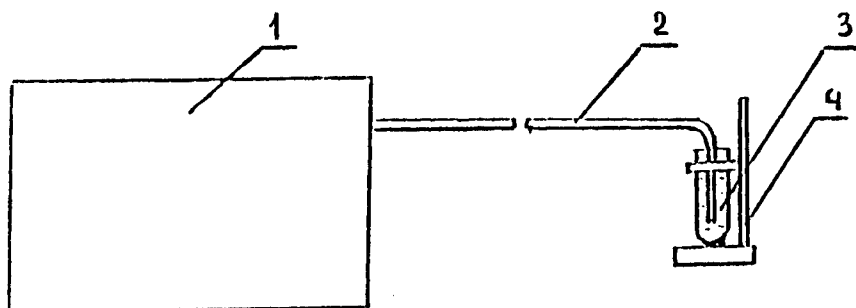


Fig. 1. Scheme of the experimental device: 1- the "Oliver -101" system; 2- fiber-optic device; 3-tube(vial); 4-holder

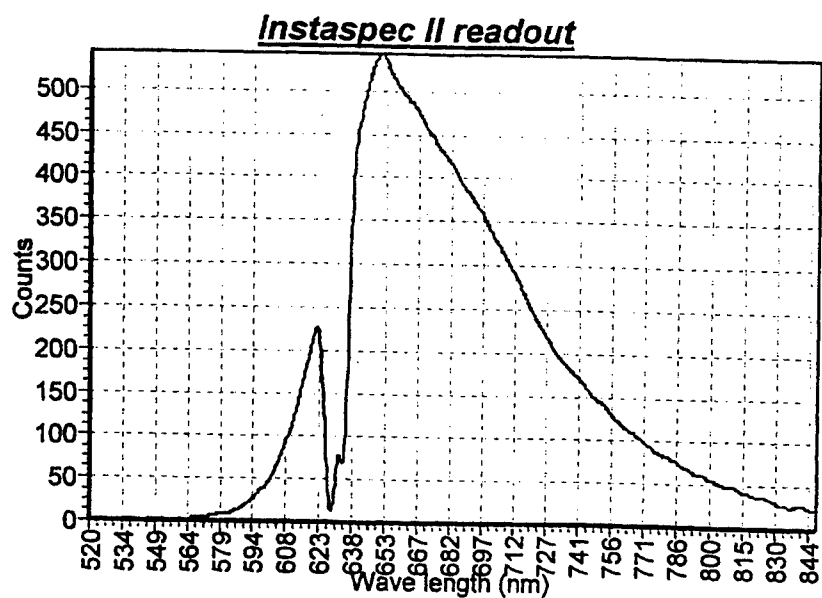


Fig. 2. Spectrum of monobacterial solution (suspension) *Bacteroides fragilis* in distill water



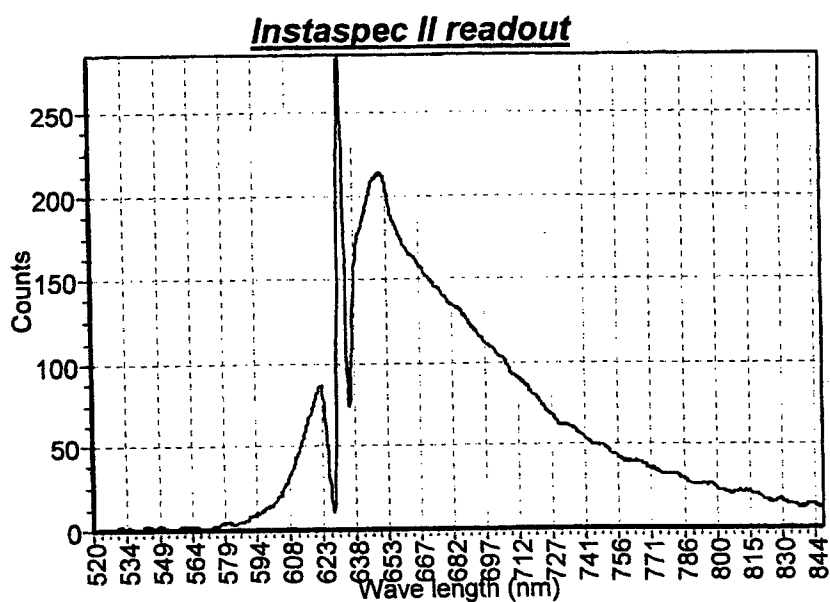


Fig. 3. Spectrum of monobacterial solution (suspension) *Clostridium perfringens* in distill water

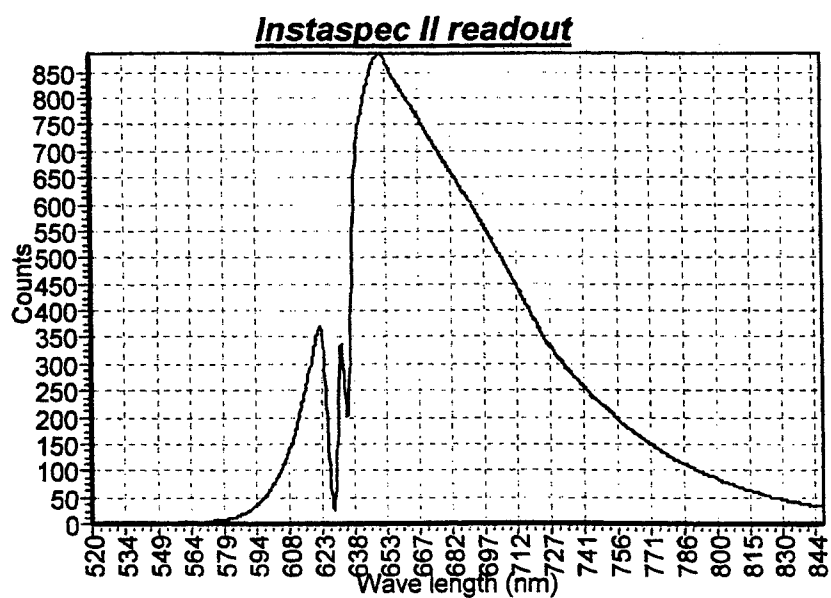


Fig. 4. Spectrum of monobacterial solution (suspension) *Fusobacterium necroforum* in distill water

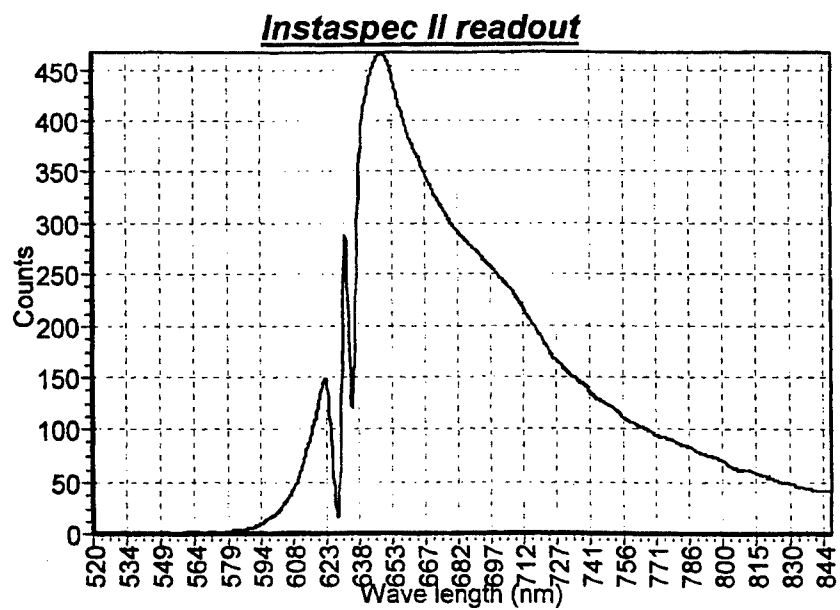


Fig. 5. Spectrum of monobacterial solution (suspension) *Campilobacter jejuni* in distill water

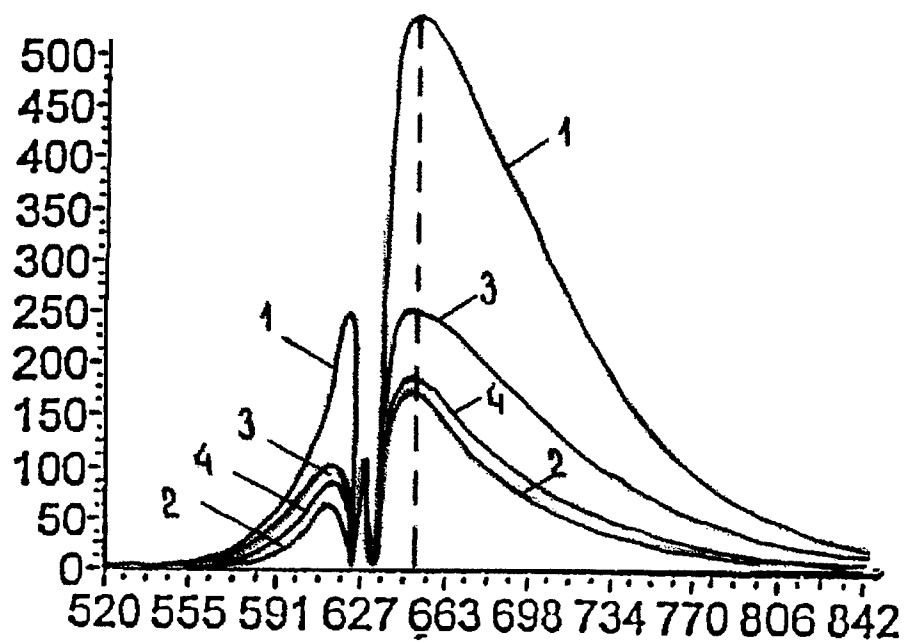


Fig. 6. Normalized spectrums of monosolutions (suspension) of 1-*Bacteroides fragilis*; 2-*Clostridium perfringens*; 3-*Fusobacterium necroforum*; 4-*Campilobacter jejuni*

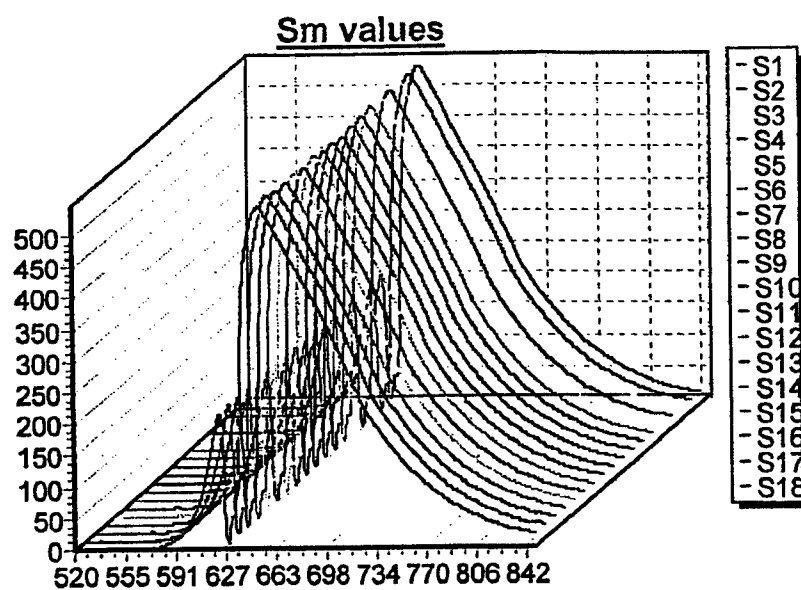


Fig. 7. Spectrums of monobacterial solution *Bacteroides fragilis* in distill water, recorded sequentially with time interval 5 sec

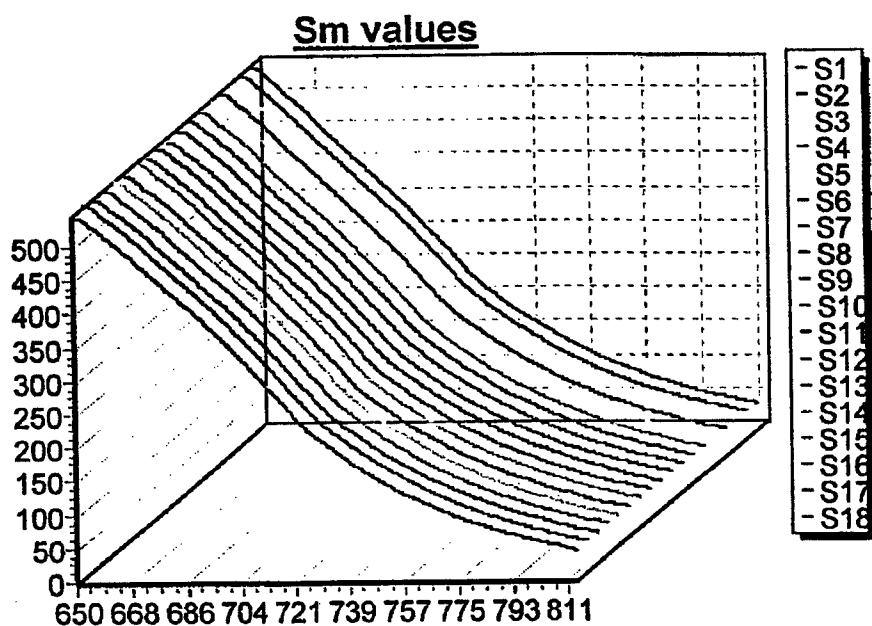


Fig. 8. Reproducibility of maximal amplitudes of fluorescence spectrums ( $\lambda_{\text{max}}=650$  nm)

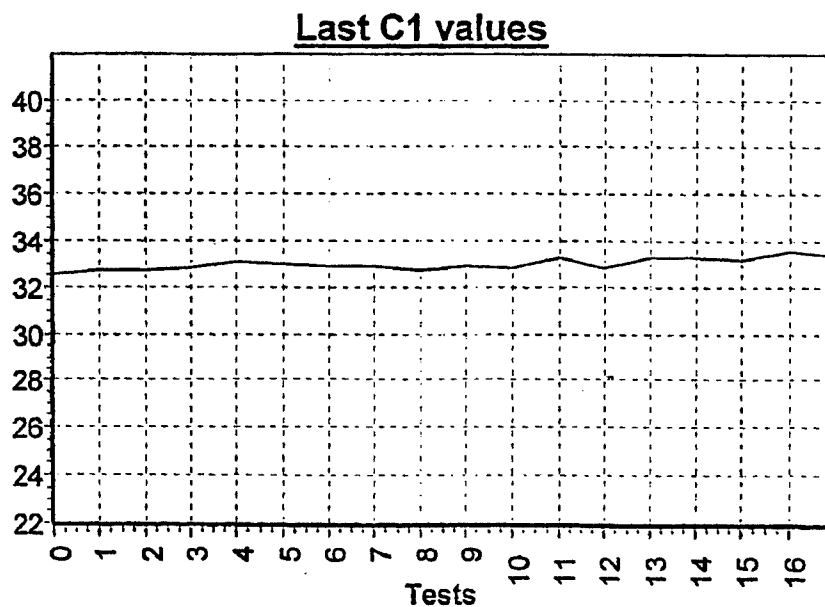


Fig. 9. Dependence of integral power of fluorescence (coefficient  $C_1$ ) on number of tests

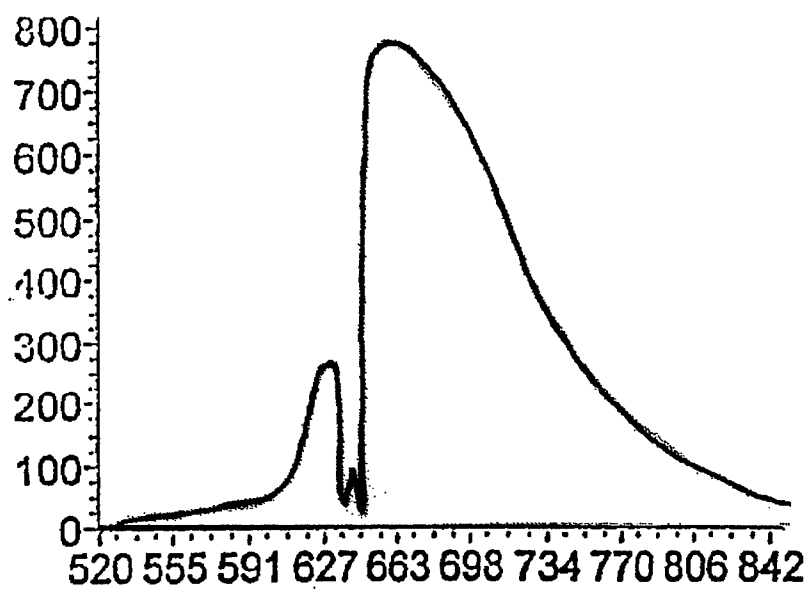


Fig. 10. Normalized spectrum of bacterial mixture (*Bacteroides fragilis* (No.1) and *Clostridium perfringens* (No. 2)) in distill water

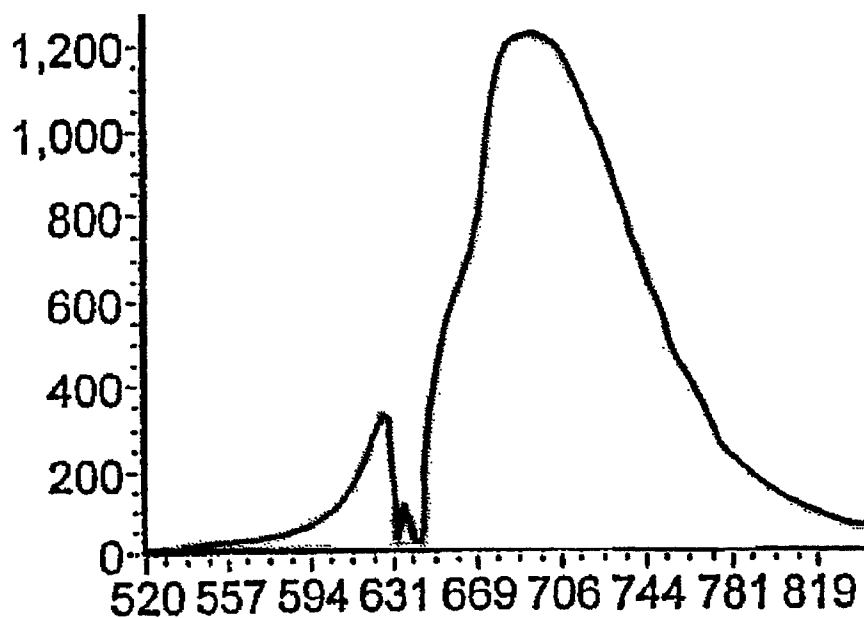


Fig. 11. Normalized spectrum of bacterial mixture (*Bacteroides fragilis* (No.1); *Clostridium perfringens* (No. 2) and *Fusobacterium necroforum* (No. 3)) in distill water

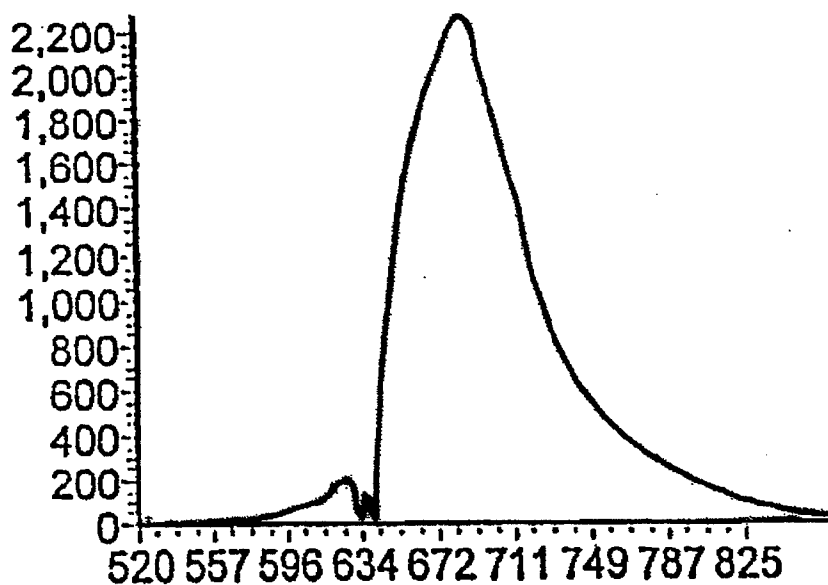


Fig. 12. Normalized spectrum of bacterial mixture (*Bacteroides fragilis* (No.1); *Clostridium perfringens* (No. 2); *Fusobacterium necroforum* (No. 3) and *Campilobacter jejuni* (No.4)) in distill water

# Effects of scattering particles concentration on light propagation through turbid media

Alexey N. Bashkatov, Elina A. Genina, Vyacheslav I. Kochubey, Valery V. Tuchin

Saratov State University, Astrakhanskaya 83, Saratov 410026, Russia

## ABSTRACT

Experimental study and computer simulation of light propagation in turbid media with different concentration of scattering particles are described. Gel phantoms with adding of Intralipid-20% as a model of living tissue have been investigated. Experimental results have shown existing of transmittance and reflectance saturation in dependence on volume fraction of the scatterers. The inverse adding-doubling method and Reyleigh-Gans approximation of the Mie theory were applied to describe the light propagation. The explanation of the experimental results is presented.

**Keywords:** phantoms, turbid media, scattering spectroscopy, inverse adding-doubling method, concentration effects

## 1. INTRODUCTION

One of the problem in clinical laser therapy is the prediction of light distribution in tissue. Wavelength range from 400 to 700 nm has a special significance because of its therapeutic applications. However, light propagation in tissue is complicated by the inhomogeneous and variable character of tissue. In addition, *in vitro* samples are expected to have different optical properties from *in vivo* samples. Nowadays, phantoms are widely used for study of light propagation in tissues.<sup>1-12</sup> Real tissues are usually densely packed systems of scatterers, therefore concentration effects should be accounted for.<sup>3,13-22</sup> In this paper we present the results of experimental study and computer simulation of effects of scattering particles concentration on light propagation through turbid media.

## 2. MATERIALS AND METHODS

In this study we used a commercially available computer-driven CARY-2415 spectrophotometer with integrating sphere to make total transmittance, and diffuse reflectance measurements in the 400-700 nm wavelength range for various turbid media (phantoms) which model living tissues. For each phantom diffuse reflectance  $R_d$  and total transmittance  $T_d$  were measured. The diffuse reflectance were calibrated on the basis of reflectance from standard reflectance plate (BaF<sub>2</sub>).

We used transparent gel, prepared from 10% aqueous solution of food gelatin, as a ground of the phantoms. Structure of gelatin gel was described in Ref. 23 and presented in Fig. 1. Gel was made turbid by adding of various quantity of Intralipid-20% suspension.<sup>1-3,6,8,9,12</sup> Concentrations of Intralipid-20% within samples were 0, 5, 10, 15, 20, 25, 30, 35, and 40% (vol/vol). The samples were prepared as tablets with diameter 25 mm and height 4 mm. The samples were placed on thin glass plates with thickness of 0.17 mm.

Since we used the food gelatin, which has its own strong absorption band in visible spectral range, we measured absorption coefficient of gelatin gel. The spectrum of measured absorption coefficient is presented in Fig. 2. Mie theory provides an exact computation of the scattering coefficient and the anisotropy factor of perfect spheres of arbitrary size.<sup>24,25</sup> To use Mie theory we considered the gelatin particles as spherical particles of the same volume. Scattering coefficient and anisotropy factor of the gelatin were calculated using Mie theory algorithm,<sup>24</sup> as a result there was shown that the scattering of gelatin can be neglected, so, only absorption of gelatin should be accounted for.

Optical properties of the Intralipid suspension can be found in Refs. 9, 12, the anisotropy factor is described by the formula.

---

Address all correspondence to Alexey N. Bashkatov. Tel: 8452 514693; E-mail: [bash@softhome.net](mailto:bash@softhome.net)

$$g = 1.1 - 5.8 \cdot 10^{-4} \cdot \lambda [nm] \quad (1)$$

Refractive indices of the samples were estimated using the law of Gladstone and Dale

$$n = n_g \eta_g + n_s \eta_s \quad (2)$$

where  $n_g$ ,  $n_s$ , and  $\eta_g$ ,  $\eta_s$  are the refractive indices and volume fractions of the ground substance (gelatin matrix and water) and substance which was used as a scatterers (Intralipid-20%), respectively. Refractive indices of the gelatin matrix and Intralipid-20% were found experimentally using Abbe refractometer as  $n = 1.3525$  and  $1.335$ , respectively.

The refractive indices for various wavelengths of water were calculated using dispersion formula from Ref. 26:

$$n_{H_2O} = 1.31848 + \frac{6.662}{\lambda [nm] - 129.2} \quad (3)$$

It is well known that the scatterers of Intralipid suspension are soybean oil particles, which wavelength dependent refractive index can be calculated using <sup>12</sup>

$$n_{soybean} = 1.451 + \frac{1.154 \cdot 10^4}{(\lambda [nm])^2} - \frac{1.132 \cdot 10^9}{(\lambda [nm])^4} \quad (4)$$

The refractive index of the gelatin particles was determined in Ref. 27 as  $n_{gp} = 1.533$ .

We used the inverse adding-doubling method that was developed by *Prahl et al.*<sup>28</sup> to calculate the absorption and scattering coefficients of turbid media (phantoms) from measured values of total transmittance and diffuse reflectance. To obtain optical properties of the investigated phantoms we used a computer program of *S.A. Prahl* (Oregon Medical Laser Center, USA; [www.omlc.ogi.edu](http://www.omlc.ogi.edu)).

To compare optical properties calculated using inverse adding-doubling method and Reyleigh-Gans approximation of the Mie theory, we determined the reduced scattering coefficient using the formula taken from Ref. 3.

$$\sigma'_s = \frac{9}{256 \cdot \pi} \left( \frac{m^2 - 1}{m^2 + 2} \right)^2 \cdot \left( \frac{\lambda}{n_{ex}} \right)^2 \cdot \int_0^\pi (\sin u - u \cos u)^2 \frac{(1 + \cos^2 \theta) \sin \theta (1 - \cos \theta)}{\sin^6 \left( \frac{\theta}{2} \right)} d\theta \quad (5)$$

where  $\sigma'_s = \sigma_s (1 - g)$ ,  $u = 2 \frac{2\pi a n_{ex}}{\lambda} \sin \left( \frac{\theta}{2} \right)$ ,  $\sigma_s$  is the scattering cross section,  $g$  is the average cosine of the

scattering angle,  $a$  is the radius of the scattering particle,  $\lambda$  is wavelength of the scattered light in vacuum,  $m = \frac{n_m}{n_{ex}}$  is the refractive index of the scatterers relative to the surrounding medium, and  $n_m$  and  $n_{ex}$  are refractive indices of the scattered particle and surrounding medium, respectively. Anisotropy factor  $g$  we calculated using Eq. 1.

In a multiple-scattering medium, the reduced scattering coefficient,  $\mu'_s$ , is related to  $\sigma'_s$  by<sup>14, 15, 20, 22</sup>

$$\mu'_s = N \sigma'_s \frac{(1 - \eta)^4}{(1 + 2 \cdot \eta)^2} \quad (6)$$

where  $\sigma_s'$  is given by Eq. 5,  $N$  is the total number of scattering particles per unit volume, i.e., the number density.  $N$  can be given as  $\eta/v_{par}$ , where  $\eta$  is the volume fraction of the particles relative to the total volume, and  $v_{par}$  is  $(4/3)\pi a^3$ . To account for the packing factor (Eq. 6) we should evaluate the volume fraction of the scatterers (soybean oil particles). For that the volume fraction of Intralipid (which was added to gelatin gel) was multiplied by 0.239. This coefficient accounts for real concentration of oil particles in Intralipid solution.<sup>12</sup>

### 3. RESULTS AND DISCUSSION

Figures 3-6 show the experimental results of optical properties of the investigated samples (phantoms) with various concentrations of the scatterers. Figure 3 presents the diffuse reflectance spectra of the gelatin phantoms with adding of various volume fractions of Intralipid-20% suspension. Figure 4 presents the total transmittance spectra of the gelatin phantoms with adding of various volume fractions of Intralipid-20% suspension. Figure 5 presents the Intralipid concentration dependence on the diffuse reflectance at three wavelengths. In this figure we see that diffuse reflectance has a slight saturation which depends on concentration (expressed in volume fraction) of the Intralipid suspension. Figure 6 shows concentration dependence of the optical density of the gelatin phantoms with adding of various volume fractions of Intralipid suspension. We define the optical density as  $D = -\log(T_d)$ . We see that the optical density saturates as concentration of Intralipid goes up. As was shown above the absorption properties of phantoms are defined by gelatin gel and scattering properties by Intralipid suspension. We assume that saturation of optical density and diffuse reflectance are connected with changes of scattering properties of phantoms. Using inverse adding-doubling method the scattering coefficients of phantoms were obtained. Anisotropy factor of the scatterers was calculated using Eq. 1. To obtain refractive indices of phantoms Eqs. 2-4 and data taken from Ref. 27 were used. Results of our calculations are presented in Figs. 7 and 8. Figure 7 shows that the scattering coefficients of the phantoms decrease with increasing of the wavelength. With increasing of Intralipid concentration the increasing of the scattering coefficients is observed. Figure 8 shows that determined scattering coefficient dependencies on concentration are saturated at high concentrations, which well correlate with saturation of measured optical density and diffuse reflectance which.

To compare data obtained using inverse adding-doubling method and Reyleigh-Gans approximation of the Mie theory, we used Eqs. 5, 6. Refractive index of the scatterers was calculated using Eq. 4. Refractive index of surrounding medium was estimated using Eqs. 2, 3 and data from Ref. 27. Anisotropy factor was calculated using Eq. 1. Different references present different values of scatterers radius of Intralipid suspension. For example, in Ref. 3 scatterers radius is about 250 nm, in Refs. 2, 12 it is 46.5 nm. Due to well fit to our experimental data we use value of scatterers radius equal to 34 nm.

The final result of our calculations is presented in Fig. 8. In general, a good fit of data obtained using inverse adding-doubling method and Reyleigh-Gans approximation (scatterers radius 34 nm) is received.

### 4. CONCLUSION

This paper discusses some aspects of tissue-like phantoms optical properties, especially phantoms with a high concentration of scatterers which corresponds to real tissues. Experimental study and computer simulation of light propagation in gelatin gel phantoms with adding of Intralipid-20% at high concentrations up to 40 % have been investigated. The saturation of transmittance and reflectance of phantoms in dependence on volume fraction of the scatterers was revealed. The inverse adding-doubling method and Reyleigh-Gans approximation of the Mie theory were applied to describe the light propagation.

It should be noted that transmission and reflectance spectra of the studied phantoms with a high concentration of scatterers are well correlate with corresponding spectra of real tissues, like the human eye sclera.<sup>26</sup>

### 5. ACKNOWLEDGMENTS

The research described in this publication was made possible in part by grant "Leading Scientific Schools" #96-15-96389 of the Russian Basic Research Foundation



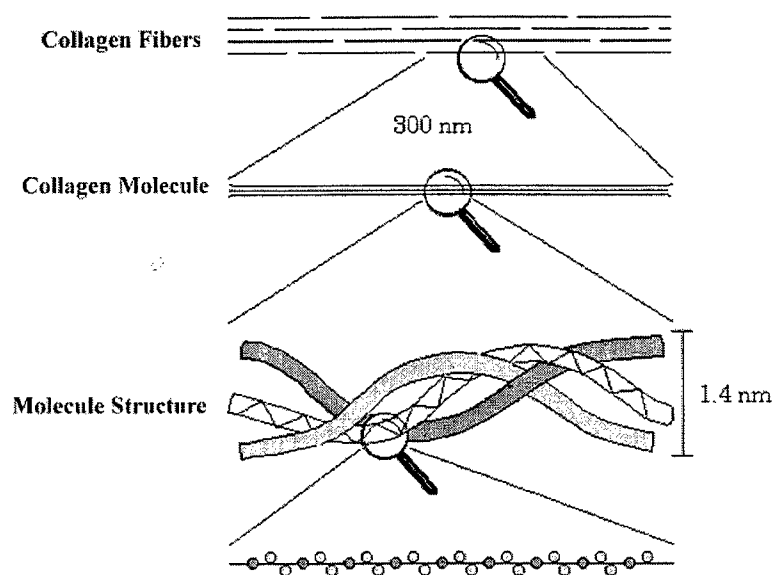


Figure 1. Structure of the gelatin particles

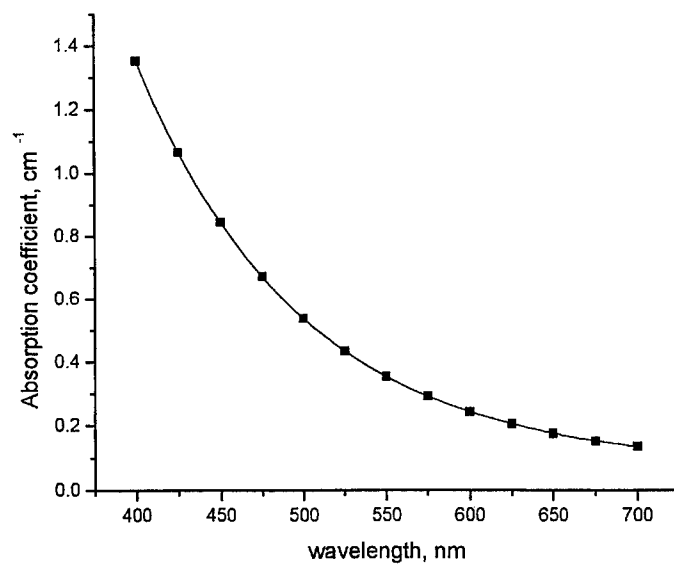


Figure 2. Absorption coefficient of the food gelatin gel.

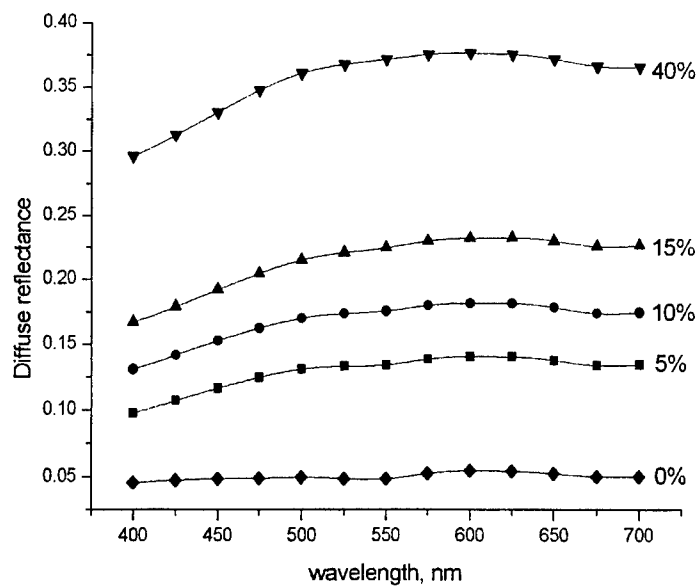


Figure 3. Diffuse reflectance spectra of the gelatin phantoms with adding of various volume fractions of 20%-Intralipid.

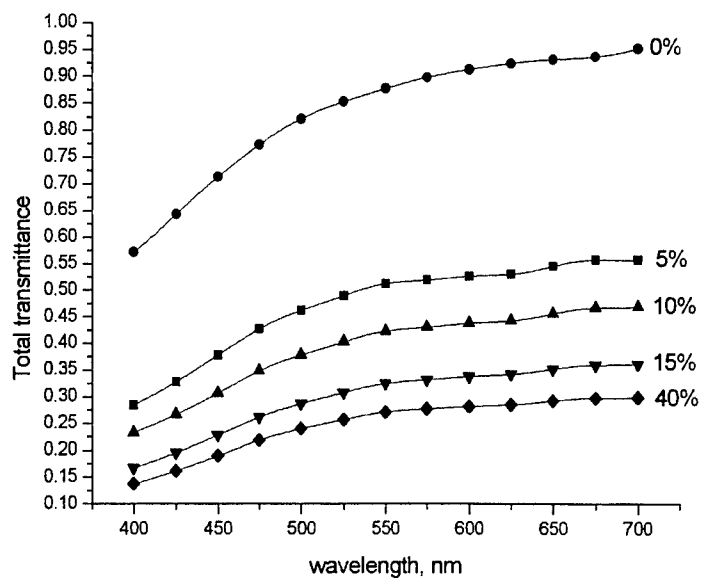


Figure 4. Total transmittance spectra of the gelatin phantoms with adding of various volume fractions of 20%-Intralipid.

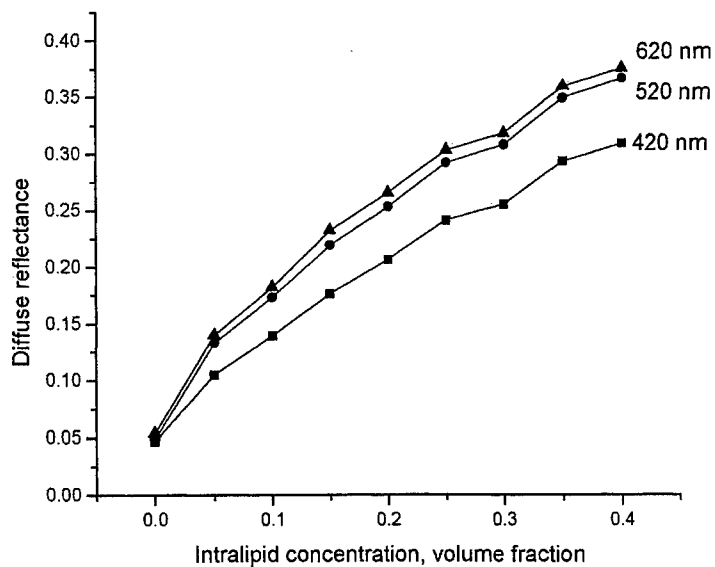


Figure 5. The diffuse reflectance of the gelatin phantoms with adding of various volume fractions of 20%-Intralipid.

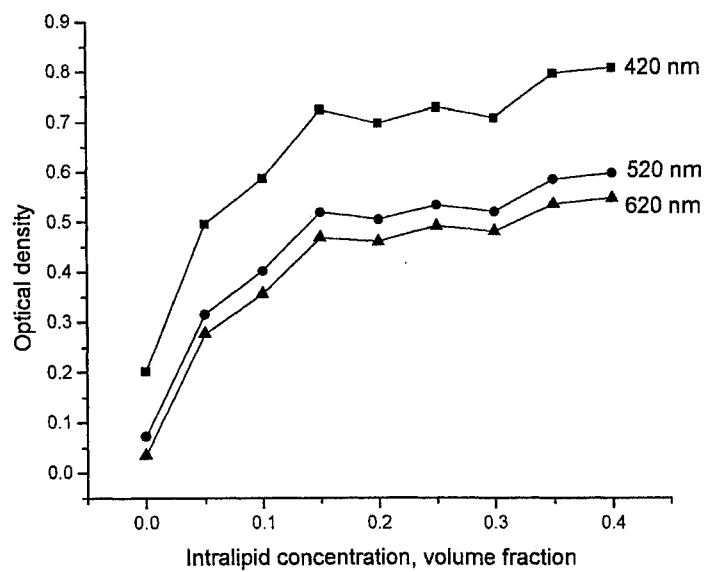
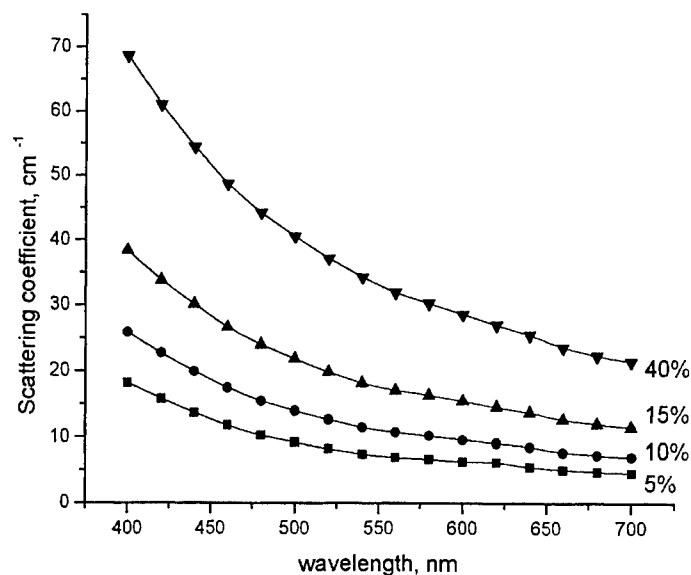
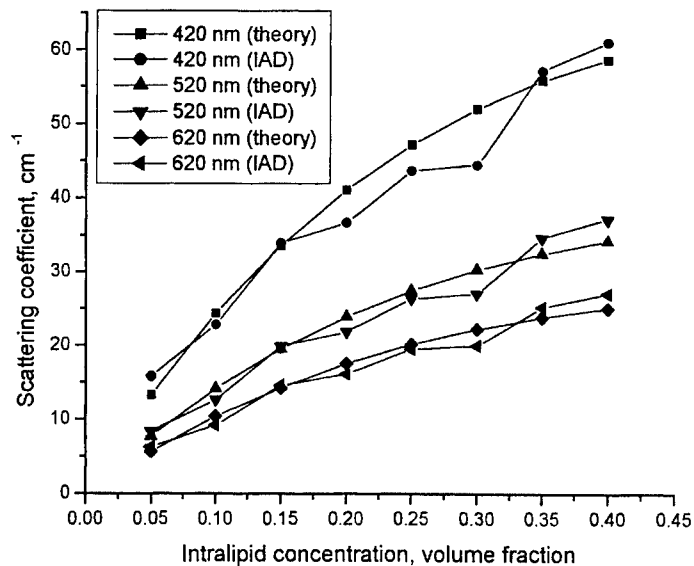


Figure 6. The optical density of the gelatin phantoms with adding of various volume fractions of 20%-Intralipid.



**Figure 7.** The scattering coefficient of the gelatin phantoms with adding of various volume fractions of 20%-Intralipid versus wavelength.



**Figure 8.** Dependencies of the scattering coefficient of the gelatin phantoms on Intralipid concentration calculated using inverse adding-doubling (IAD) method and Reyleigh-Gans approximation of the Mie theory (theory) at three wavelengths.

## REFERENCES

1. C.J.M. Moes, M.J.C. van Gemert, W.M. Star, J.P.A. Marijnissen, S.A. Prahl, "Measurements and calculations of the energy fluence rate in a scattering and absorbing phantom at 633 nm," *Appl. Opt.* **28**(12), pp. 2292-2296, 1989.
2. J.R. Mourant, T. Fuselier, J. Boyer, T.M. Johnson, I.J. Bigio, "Predictions and measurements of scattering and absorption over broad wavelength ranges in tissue phantoms," *Appl. Opt.* **36**(4), pp. 949-957, 1997.
3. H. Liu, B. Beauvoit, M. Kimura, B. Chance, "Dependence of tissue optical properties on solute-induced changes in refractive index and osmolarity," *J. Biomed. Opt.* **1**(2), pp. 200-211, 1996.
4. L.P. Danilova, S.P. Chernova, A.B. Pravdin, "Tissue-like phantoms: fluorescence under 405 nm excitation," *Proc. SPIE* **3726**, pp. 410-414, 1998.
5. K.E. Denisov, S.P. Chernova, A.B. Pravdin, "Fluorescence spectra of multilayered phantom of biotissue: Optimization of data collection," *Proc. SPIE* **3726**, pp. 163-166, 1998.
6. M. Kohl, M. Esseupreis, M. Cope, "The influence of glucose concentration upon the transport of light in tissue-simulating phantoms," *Phys. Med. Biol.* **40**, pp. 1267-1287, 1995.
7. J.M. Schmitt, G. Kumar, "Spectral distortions in near-infrared spectroscopy of turbid materials," *Applied Spectroscopy* **50**(8), pp. 1066-1073, 1996.
8. D.D. Royston, R.S. Poston, S.A. Prahl, "Optical properties of scattering and absorbing materials used in the development of optical phantoms at 1064 nm," *J. Biomed. Opt.* **1**(1), pp. 110-116, 1996.
9. S.T. Flock, S.L. Jacques, B.C. Wilson, W.M. Star, M.J.C. van Gemert, "Optical properties of Intralipid: a phantom medium for light propagation studies," *Laser in Surgery and Medicine*, **12**, pp. 510-519, 1992.
10. A.A. Oraevsky, S.L. Jacques, F.K. Tittel, "Measurement of tissue optical properties by time-resolved detection of laser-induced transient stress," *Appl. Opt.*, **39**(1), pp. 402-415, 1997.
11. A.A. Oraevsky, R.O. Esenaliev, S.L. Jacques, F.K. Tittel, "Laser opto-acoustic tomography for medical diagnostics: principles," *Proc. SPIE*, **2676**, pp. 22-31, 1996.
12. H.J. van Staveren, C.J.M. Moes, J. van Marle, S.A. Prahl, M.J.C. van Gemert, "Light scattering in Intralipid-10% in the wavelength range of 400-1100 nm," *Appl. Opt.* **30**(31), pp. 4507-4514, 1991.
13. A.N. Bashkatov, E.A. Genina, Yu.P. Sinichkin, N.A. Lakodina, V.I. Kochubey, V.V. Tuchin, "Estimation of glucose diffusion coefficient in scleral tissue," *Proc. SPIE* **4001**, 1999.
14. A.P. Ivanov, V.A. Lojko, and V.P. Dik, *Light Transportation in Densely Packed Dispersive Media*, Nauka i Technika, Minsk, 1988.
15. J.M. Schmitt, G. Kumar, "Optical scattering properties of soft tissue: a discrete particle model," *Appl. Opt.* **37**(13), pp. 2788-2797, 1998.
16. E.K. Chan, B. Sorg, D. Protsenko, M. O'Neil, M. Motamedi, A.J. Welch, "Effects of compression on soft tissue optical properties," *IEEE Journal of selected topics in quantum electronics* **2**(4), pp. 943-950, 1996.
17. A.Ya. Khairullina, "About mechanism of coherent and diffuse transmission monolayer of particles with different densities packing and optical properties," *Opt. and Spectr.* **53**(6), pp. 1043-1048, 1982.
18. A.N. Ponyavina, V.G. Vereshchagin, "Concentration effects during coherent scattering by big size particles with density packing," *J. Appl. Spectr.* **XL**(2), pp. 302-308, 1984.
19. A.N. Ponyavina, N.I. Silvanovich, A.A. Shevchenko, "About cooperating effects during radiation reflection from density packing scattering media," *J. Appl. Spectr.* **51**(4), pp. 670-675, 1989.
20. Ya.I. Granovsky, M. Ston, "Attenuation factor during light scattering by transparent particles," *J. Experimental and Theoretical Physics* **105**(5), pp. 1199-1207, 1994.
21. G.S. Dubova, A.Ya. Khairullina, "Diffuse transmission and reflection of thick low absorbing layer with close particles packing," *J. Appl. Spectr.* **37**(5), pp. 832-836, 1982.
22. A.P. Ivanov, S.A. Makarevich, A.Ya. Khairullina, "Radiation propagation in tissues and liquids with close particle packing," *J. Appl. Spectr.* **47**(4), pp. 662-668, 1987.
23. S. Lipgens, *Sol-Gel Transition in Water-in-Oil Microemulsions. Investigation on the Dynamics of Gelatin-Containing Systems*, Ph.D. Thesis, Cologne, 1997.
24. C.F. Bohren and D.R. Huffman, *Absorption and Scattering of Light by Small Particles*, Wiley, New York, 1983.
25. H.C. van de Hulst, *Light scattering by Small Particles*, Dover, New York, 1981.
26. V.V. Tuchin, I.L. Maksimova, D.A. Zimnyakov, I.L. Kon, A.H. Mavlutov, A.A. Mishin, "Light propagation in tissues with controlled optical properties," *J. Biomed. Opt.* **2**(4), pp. 401-417, 1997.
27. A. Seeboth, H. Hermel, "Gelatin films with embedded liquid crystals in the conoscopic ray," *Thin solid films*, **173**, pp. L119-L129, 1989.
28. S.A. Prahl, M.J.C. van Gemert, A.J. Welch, "Determining the optical properties of turbid media by using the adding-doubling method," *Appl. Opt.* **32**, pp. 559-568, 1993.



## Addendum

The following papers were announced for publication in this proceedings but have been withdrawn or are unavailable.

- [3917-01]      **Correlation of autofluorescence (AF) and ultrastructures of ex-vivo colorectal tissues and isolated living epithelial cells from primary cell cultures (PCC) of normal colon and hyperplastic and dysplastic: implications for early diagnosis, altered cell metabolism, and cytopathology**  
R. S. DaCosta, Univ. of Toronto (Canada) and Ontario Cancer Institute (Canada); H. Andersson, Univ. of Uppsala (Sweden); N. E. Marcon, St. Michaels Hospital (Canada); B. C. Wilson, Univ. of Toronto (Canada) and Ontario Cancer Institute (Canada)
- [3917-04]      **Time-resolved fluorescent lifetime imaging in tissue**  
D. W. Hattery, George Washington Univ. and National Institutes of Health; V. V. Chernomordik, National Institutes of Health; I. Gannot, Tel Aviv Univ. (Israel); M. H. Loew, George Washington Univ.; A. H. Gandjbakhche, National Institutes of Health
- [3917-13]      **Fluorescence photodetection of human lung cancer using prodrugs of 5-aminolevulinic acid: preliminary ex-vivo results**  
N. Lange, Swiss Federal Institute of Technology and Univ. Lausanne (Switzerland); H. van den Bergh, Swiss Federal Institute of Technology; P. Kucera, Univ. Lausanne (Switzerland)
- [3917-19]      **Detection of chemically induced precancerous skin tissues by UV-LIFS**  
J. J. Padilla, Ctr. Alexis Vautrin (France) and ITSON (France); E. Bossu, I. Fries, Univ. Henri Poincaré Nancy-I (France); V. Louis, E. Yvroud, Ctr. Alexis Vautrin (France); D. Notter, C. Vigneron, Univ. Henri Poincaré Nancy-I (France); F. H. Guillemin, Ctr. Alexis Vautrin (France)
- [3917-20]      **Improved oral cancer screening through the use of enhanced visual systems**  
D. L. Heintzelman, Indiana Univ. School of Medicine; U. Utzinger, Univ. of Texas/Austin; A. Gillenwater, M.D. Anderson Cancer Ctr./Univ. of Texas; R. R. Richards-Kortum, Univ. of Texas/Austin
- [3917-24]      **Monitoring neuron activity by OCT**  
J. Liu, A. Miyawaki, RIKEN—Institute of Physical and Chemical Research (Japan)
- [3917-32]      **Preclinical frequency domain optical tomography imager of breast abnormalities**  
M. V. Klibanov, J. Zeylikovich, A. A. Kharissov, S. V. Martakov, T. R. Lucas, Y.-T. Shih, J. L. Benson, Medical Optical Imaging, Inc.
- [3917-39]      **Problems of accuracy of the laser clinical fluorescence diagnostic and the ways to unify technique**  
D. A. Rogatkin, Moscow Regional Research and Clinical Institute (Russia); V. N. Svirin, State Enterprise (Russia); V. V. Tchernyi, Moscow Regional Research and Clinical Institute (Russia)

- [3917-41]      **Spectra distribution properties of ultraweak photon emission from biological system and biophoton coherence**  
Y. Zhu, South China Normal Univ.; Z. Zhu, Sony Semiconductor; Z. Guo, J. Ma, S. Li, South China Normal Univ.
- [3917-43]      **Qualitative classification of gastroenterological diseases in space of the Volterra kernel features on base of IR spectroscopy data**  
A. M. Akhmetshin, D. V. Shutin, Dnepropetrovsk State Univ. (Ukraine)
- [3917-45]      **Development of quantitative spectroscopy for cerebral hemoglobin measurement**  
B. W. Pogue, K. D. Paulsen, H. Kaufman, C. Abele, Dartmouth College
- [3917-46]      **Simplified apparatus for autofluorescence imaging in the bronchi**  
H. van den Bergh, M. Zellweger, D. Goujon, N. Lange, P. Grosjean, A. Radu, P. Monnier, G. A. Wagnières, Swiss Federal Institute of Technology



## Author Index

- Abele, Chris, Addendum  
 Achilefu, Samuel I., 80  
 Agarwal, Asha, 194, 240  
 Akhmetshin, Alexander M., Addendum  
 Alexandrov, Michail T., 244  
 Alfano, Robert R., 62, 75, 146, 150, 200  
 Ali, J. H., 75  
 Andersson, Helene, Addendum  
 Aruna, P., 16  
 Bartel, Sebastian, 43  
 Bashkatov, Alexey N., 256  
 Battarbee, Harold, 219  
 Benson, Jonathon L., Addendum  
 Bernstein, Paul S., 102  
 Bharghavi, S., 16  
 Bigio, Irving J., 67  
 Bogaards, Arjen, 2  
 Bolt, René A., 168  
 Bossu, Edwidge, Addendum  
 Briggs, Gavin M., 67  
 Bocker, C., 33  
 Brown, Stephen G., 67  
 Bugaj, Joseph E., 80  
 Canpolat, Murat, 33  
 Cariveau, Mickael J., 184  
 Celmer, Edward J., 150  
 Cheah, Horn Mun, 139  
 Chernomordik, Victor V., Addendum  
 Chia, Teck-Chee, 139  
 Choen, Francis Seow, 139  
 Cocker, Rubina S., 146, 200  
 Cohen, David, 93  
 DaCosta, Ralph S., Addendum  
 de Mul, Frits F. M., 168  
 Dekker, Erwin, 2  
 Demos, Stavros G., 62  
 Denisov, Nikolay A., 130  
 Dets, Sergiy M., 130  
 Diong, Cheong Hoong, 139  
 Dong, Ke, 176  
 Dorshow, Richard B., 80  
 Du, Yong, 184  
 Ermakov, Ignor V., 102  
 Espondo-Ramos, O., 33  
 Freyer, James P., 33  
 Fries, I., Addendum  
 Gandjbakhche, Amir H., Addendum  
 Ganesan, Singaravelu, 16  
 Gannot, Israel, Addendum  
 Ge, Jun, 204, 212  
 Gellermann, Werner, 102  
 Genina, Elina A., 256  
 Ghosh, N., 194  
 Gillenwater, Ann, Addendum  
 Goldfain, Ervin, 119  
 Goujon, Delphine, Addendum  
 Gowri, V. S., 16  
 Grosjean, P., Addendum  
 Grundfest, Warren S., 93, 109  
 Guillemin, François H., Addendum  
 Guo, Zhouyi, Addendum  
 Haruna, Masamitsu, 87  
 Hattery, David W., Addendum  
 Heintzelman, Douglas L., Addendum  
 Hielscher, Andreas H., 43  
 Hu, Xin-Hua, 176, 184  
 Hua, Jianwen, 56  
 Huang, Zhijian, 9, 56  
 Huang, Zhiwei, 139  
 Johnson, Tamara M., 33  
 Jongen, Armand J. L., 2  
 Kalmus, Gerhard W., 184  
 Kanger, Johannes S., 168  
 Kaplan, Peter D., 22  
 Katz, Alvin, 146, 200  
 Kaufman, Howard, Addendum  
 Khalil, Omar S., 168  
 Kharissov, Andrey A., Addendum  
 Klibanov, Michael V., Addendum  
 Kochubey, Vyacheslav I., 256  
 Koteeswaran, D., 16  
 Koutcher, Jason A., 150  
 Krishnan, S. M., 139  
 Kucera, Pavel, Addendum  
 Lakhani, Sunil, 67  
 Lange, Norbert, Addendum  
 Laxmi, B. V., 240  
 Le, Zisheng, 204  
 Lee, Sing, 139  
 Li, Shaoshan, Addendum  
 Lilge, Lothar D., 232  
 Lim, Tuan-Kay, 139  
 Liu, Jiyuan, Addendum  
 Loew, Murray H., Addendum  
 Lomberdo, J. M., 75  
 Louis, V., Addendum  
 Lu, Jun Q., 176, 184  
 Lucas, Thomas R., Addendum  
 Ma, Junfu, Addendum  
 Maarek, Jean-Michel I., 93, 109  
 Marcon, Norman E., Addendum  
 Marcu, Laura, 93, 109  
 Marret, Lorraine A., 232  
 Martakov, Sergey V., Addendum

Masyshev, Victor I., 244  
 Matanock, A., 33  
 McClane, Robert W., 102  
 McCormick, Steven A., 146, 200  
 Miyawaki, Atsushi, Addendum  
 Moffitt, Theodore P., 225  
 Monnier, Philippe, Addendum  
 Morimoto, Shigeto, 87  
 Maurant, Judith R., 33  
 Muthuvelu, K., 16  
 Nair, M. S., 194, 240  
 Nakamura, Mitsuo, 87  
 Nie, Sixiang, 212  
 Notter, Dominique, Addendum  
 Ohmi, Masato, 87  
 Padilla, J. J., Addendum  
 Panda, R. N., 240  
 Patrickyev, Igor, 156  
 Paulsen, Keith D., Addendum  
 Pickard, David C. O., 67  
 Pogue, Brian W., Addendum  
 Popp, Alois K., 22  
 Pradhan, Asima, 194, 240  
 Prah, Scott A., 225  
 Purdue, Mark, 232  
 Qu, Jianan Y., 9, 56  
 Radousky, Harry B., 62  
 Radu, A., Addendum  
 Rajagopalan, Raghavan, 80  
 Rastogi, A., 240  
 Richards-Kortum, Rebecca R., Addendum  
 Ripley, Paul M., 67  
 Rodriguez, Juan, 219  
 Rogatkin, Dmitrii A., Addendum  
 Rome, Jayson, 146, 200  
 Saunders, Christobel, 67  
 Savage, Howard E., 146, 200  
 Schantz, Stimson P., 146  
 Shakhurdin, Valintin I., 156  
 Shih, Yin-Tzer, Addendum  
 Shutin, Dmitriy V., Addendum  
 Sisson, Cynthia, 219  
 Staggs, Michael C., 62  
 Sterenborg, Henricus J. C. M., 2  
 Stetter, K., 33  
 Svirin, Vaytcheslav N., Addendum  
 Syrmos, Vassillis, 212  
 Techemyi, V. V., Addendum  
 Tuchin, Valery V., 256  
 Utzinger, Urs, Addendum  
 Valentine, Megan T., 22  
 van den Akker, J. Hanneke T. M., 2  
 van den Bergh, Hubert, Addendum  
 Vengadesan, Nam, 16  
 Vigneron, C., Addendum  
 Vitenson, J. H., 75  
 Wagnières, Georges A., Addendum  
 Walter, Stephen, 232  
 Wang, Wubao B., 75  
 Weersink, Robert A., 232  
 Wei, William I., 9  
 Weitz, David A., 22  
 Wilson, Brian C., Addendum  
 Wu, Xiaomao, 168  
 Yang, Yuanlong, 150, 200  
 Yaroslavsky, Anna N., 219  
 Yaroslavsky, Ilya V., 219  
 Yeh, Shu-Jen, 168  
 Yu, Yizhong, 200  
 Yuen, Po Wing, 9  
 Yun, David Y. Y., 204, 212  
 Yvroud, Edouard, Addendum  
 Zellweger, Matthieu, Addendum  
 Zeng, Fanan, 146, 200  
 Zeylikovich, Joseph, Addendum  
 Zheng, Wei, 139  
 Zhu, Yanbin, Addendum  
 Zhu, Zhaohui, Addendum